UNIVERSITÀ
DEGLI STUDI
DI PADOVA

KU LEUVEN

Università degli Studi di Padova
Department of Civil, Environmental and
Architectural Engineering

Katholieke Universiteit Leuven
Department of Materials Engineering

DEVELOPMENT OF INORGANIC POLYMERS FOR NEAR-ZERO ENERGY DWELLINGS

Guilherme António dos Santos Calado Marianito da Ascensão

Supervisor: Prof. Carlo Pellegrino

Co-Supervisor: Prof. Yiannis Pontikes

Dissertation presented in partial fulfilment of the requirements for the joint degree of:

Dottore di ricerca del Corso di dottorato in Scienze dell'ingegneria civile e ambientale by Universtà degli Studi di Padova

Doctor of Engineering Science (Ph.D.): Materials Engineering by KU Leuven

This dissertation was written with the financial contribution of the European Union's EU Framework Program for Research and Innovation Horizon 2020 under the Grant Agreement No 721185

November 2019

DEVELOPMENT OF INORGANIC POLYMERS FOR NEAR-ZERO ENERGY DWELLINGS

Guilherme António dos Santos Calado Marianito da Ascensão

Supervisor: Prof. Carlo Pellegrino
Co-Supervisor: Prof. Yiannis Pontikes

Members of the Examination Committee:

Prof. ____________________________

Prof. ____________________________

Prof. ____________________________

Dissertation presented in partial fulfilment of the requirements for the joint degree of:

Dottore di ricerca del Corso di dottorato in Scienze dell'ingegneria civile e ambientale by Universtà degli Studi di Padova

Doctor of Engineering Science (Ph.D.): Materials Engineering by KU Leuven

November 2019

2019, Universtà degli Studi di Padova - Department of Civil, Environmental and Architectural Engineering
GUILHERME ASCENSÃO, Via Antonio Vivaldi, 11, 24125 Bergamo (BG), Italy

Dedicated to:

My beloved parents and sweetheart

“*The most beautiful and deepest experience a man can have is the sense of the mysterious. (…) To sense that behind anything that can be experienced there is a something that our mind cannot grasp and whose beauty and sublimity reaches us only indirectly and as a feeble reflection (…). To me it suffices to wonder at these secrets and to attempt humbly to grasp with my mind a mere image of the lofty structure of all that there is.*”

From “My Credo” of Albert Einstein for the German League for Human Rights, 1932.

“(…) *what remains of our once rich land is like the body of a sick man, with the fat and soft earth having wasted away and only the bare skeleton being left.*”

Adapted from the English translations of Plato’s Atlantis dialogues of Benjamin Jowett, 1871.

Preface

Making a Ph.D. outside of the traditional academic settings was a challenging experience. Trying to keep a foot in academia and launch the other into the industry required from me intellectual, and sometimes even physical, acrobatic skills. Having experienced such diverse realities and being exposed to entirely different visions of the world that surround us has strengthened me professionally, scientifically, but more importantly, as a human being.

The following dissertation has benefited from many to which I wish to express my sincere gratitude. To my academic and industrial supervisors, I am grateful for their trust in my work and for the liberty conceded. Having the freedom to make my own mistakes and learn from them was a true privilege. To the many other professors, researchers, technicians, and colleagues from the University of Padua, KU Leuven, Heidelberg Cement Group and NEW MINE project I am thankful for the countless discussions that have greatly improved this dissertation; thank you to all for sharing your expertise and given me inspiration when most needed.

Finally, a word of immense gratitude to my parents and loved one for their endless support and self-sacrifice in so many moments. This journey was as much mine as theirs.

Abstract

Alkali activation has been emerging as a sustainable technology to produce innovative construction materials. Alkali-activated materials have been extensively investigated, but different levels of scientific understanding and industrial implementation can be found among several subgroups of such materials.

The most widely examined alkali-activated materials are commonly known as geopolymers. The scientific knowledge of their reaction mechanisms and structures is mature, and their market implementation fairly consolidated. Conversely, inorganic polymers (IP) is a different subgroup of alkali-activated materials since their chemistry does not exactly correspond to the definition of geopolymers. These systems are challenging but unlikely geopolymers can admit a wide range of precursors offering an opportunity to valorize low-value raw materials that include several wastes and industrial by-products. The diversity of precursors that can be used in IP production hinders the definition of production guideposts, and dedicated research is needed to define ad hoc mix designs according to the precursors' characteristics and envisioned applications.

This doctoral research was focused on the multiscale development of inorganic polymers and the conceptual design of sustainable and multifunctional materials for near-zero energy consume buildings. Vitrified residues produced during the thermochemical conversion of refused derived fuel were taken as a representative case study of a broad group of currently underutilized industrial by-products, namely calcium-iron-rich slags.

The aim of this work was to understand the fundamental processing parameters affecting the reaction mechanism involved in the formation of calcium-iron-rich IPs and their correlation with the chemical and physico-mechanical properties of the developed materials. The major technological constraints related to the use of such slags as IP precursors were examined, and the most suitable production conditions to obtain IP products with enhanced properties identified. A broad range of IP materials with engineered properties was developed and optimized. The efforts made in developing predictive models, in optimizing mixture proportions and in minimizing the shrinkage of IP binders and mortars are described. Optimized products characterized by a high dosage of residues in their composition, increased volumetric stability, excellent mechanical properties, and good residual characteristics after exposure to high temperatures were developed. The functionalization of IP mortars was addressed, and the effects of incorporating phase change materials in the mix design investigated. Lightweight IPs were developed using different processing routes, and their mechanical and thermal properties examined.

Different IP products were used to develop multi-layer sandwich panels that were both thermal insulating and reactive to temperature fluctuations. The problematics related to their upscaling were analyzed, and the production processes optimized. Semi-industrial sandwich panels were produced to demonstrate the feasibility of the solutions proposed.

The topic analyzed in this doctoral research and the insights provided are a significant contribution to the implementation of alkali-activation technology as a viable upcycling solution for industrial by-products, and particularly interesting to the construction sector in which current efforts to achieve lower environmental impacts are considerable. The use of calcium-iron-rich slags, like the ones produced in thermochemical conversion processes, in such production schemes is a plausible large-scale upcycling route that can absorb significant volumes of those residues and, by doing so, contribute to increasing the sustainability of industrial sectors in which such residues are produced.

Sommario

I leganti ad attivazione alcalina (nella formulazione originale inglese "*alkali-activated materials*") stanno sempre più affermandosi come soluzione tecnologica sostenibile ed innovativa nella produzione di materiali da costruzione. Molti lavori esistono al riguardo, ma il livello di comprensione scientifica e di implementazione industriale di questi materiali, varia a seconda dei diversi tipi di leganti ad attivazione alcalina a cui si fa riferimento.

I materiali ad attivazione alcalina più studiati sono i geopolimeri. I meccanismi e le reazioni coinvolte nella formazione di questi materiali sono ormai noti e consolidati da tempo nella comunità scientifica, così come la loro implementazione sul mercato. Un diverso sottogruppo dei materiali ad attivazione alcalina sono i polimeri inorganici ("*inorganic polymers*"). La loro chimica differisce dai geopolimeri in quanto non ottenuti dall'esclusiva attivazione alcalina di materiali allumino-silicatici. Gli polimeri inorganici derivano da sistemi chimicamente complessi ma sono allo stesso tempo versatili. Contrariamente ai geopolimeri infatti, i polimeri inorganici possono essere prodotti utilizzando una vasta gamma di precursori, offrendo quindi l'opportunità di valorizzare materie prime di basso costo che includono anche numerosi rifiuti e sottoprodotti industriali. Tuttavia, l'ampia varietà di questi materiali fa sì che studi ad hoc siano necessari per ogni potenziale precursore in funzione della sua composizione chimica e dell'applicazione finale prevista.

La presente tesi di dottorato è finalizzata allo sviluppo di materiali da costruzione funzionalizzati e sostenibili, utili alla realizzazione di edifici ad un consumo di energia quasi zero ("*near Zero Energy Building*, nZEB") e messi a punto attraverso lo studio di polimeri inorganici prodotti da rifiuti non altrimenti valorizzabili: le scorie vetrose ottenute dalla conversione termochimica di combustibili derivato da rifiuti (CDR). Caratterizzati da alti contenuti di Ca e Fe, questi residui possono essere considerati rappresentativi di un più ampio gruppo di rifiuti e sottoprodotti attualmente scarsamente utilizzabili e spesso destinati al conferimento in discarica.

Obiettivo principale del presente lavoro era quello di comprendere i meccanismi delle reazione coinvolte nella formazione di polimeri inorganici ottenuti dall'attivazione alcalina di queste scorie, e di determinarne le correlazioni con le proprietà chimiche e fisico-meccaniche del prodotto finale. Attraverso l'uso di modelli statistici predittivi, sono stati sviluppati, ottimizzati ed ingegnerizzati un'ampia gamma di polimeri inorganici. I risultati sperimentali riportati nel presente lavoro riguardano innanzitutto lo sviluppo e l'ottimizzazione di mix design, in grado di massimizzare il contenuto di scoria come precursore. Altro aspetto molto importante di studio ha riguardato la riduzione dei ritiri per una migliore stabilità volumetrica di leganti e malte prodotti a partire dagli polimeri inorganici ottimizzati. Eccellenti proprietà meccaniche e buone prestazioni residue dopo l'esposizione alle alte temperature, sono fra le principali proprietà analizzate che caratterizzano le formulazioni sviluppate.

Con lo scopo di ottenere un prodotto in grado di incrementare l'efficienza energetica degli edifici, un importante parte del lavoro ha riguardato la funzionalizzate del materiale sviluppato. L'ingegnerizzazione della microstruttura, per ottenere un materiale leggero e termicamente isolante, e l'aggiunta di materiali a cambiamento di fase ("*Phase Change Materials, PCMs*"), capaci di ridurre le fluttuazioni termiche, sono le due principali tematiche tecnologiche investigate. Tale studio ha portato alla realizzazione di panelli multistrato in grado di offrire entrambe le proprietà termiche desiderate. Attraverso l'ottimizzazione dei parametri di produzione, compatibili con i requisiti di scalaggio industriale, sono stati realizzati in laboratorio prototipi in scala naturale, che dimostrando la piena fattibilità tecnica delle soluzioni proposte.

Il tema proposto e gli approfondimenti forniti in questa tesi di dottorato sono di particolare interesse per il settore delle costruzioni, sempre più attento a soluzioni innovative capaci di ridurre l’impatto sull’ambiente. La valorizzazione di scorie ricche in calcio e ferro, così come proposta nel presente lavoro, rappresenta una plausibile via di riciclo su larga scala in grado di assorbire significativi volumi di scarti. Valorizzare questi rifiuti convertendoli in materiali da costruzione che, nella loro vita utile, consentono di ridurre l’impatto energetico degli edifici, ha quindi un elevato beneficio che è sia economico che ambientale.

Disclaimer

This oeuvre is the output of the scientific work of Ascensão. G compiled here in the form of a Ph.D. thesis. Despite the personal nature of a work of this kind, some investigations result from collaborative work with others that should be duly acknowledged.

This is the case of Chapter 3 of this thesis, which merges the results of several investigations that later resulted in international publications.

Ascensão. G conceptualized the research, performed the experiments, analyzed the collected data, and wrote the original manuscripts. The final publications, however, have greatly beneficiated form contributions of all co-authors, which are mentioned at the beginning of the respective section of Chapter 3.

The work detailed in section 3.5.3 and 3.5.4 was conducted collaboratively with the Sustainable Resources for Engineered Materials (SREMat) research group at the Department of Materials Engineering, KU Leuven. In particular, a close collaboration was held with Mr. Glenn Beersaerts and with Professor Yiannis Pontikes.

The research reported in 3.5.4 was headed by Ascensão. G and framed under the scope of this doctoral research. Hence, the results of such investigations are forcibly an integrant part of this doctoral thesis.

In the research activities described in 3.5.3 Ascensão, G. participated in the definition of the experimental activities and, in the realization of the experiments together with Beersaerts, G. The dissemination of the results gathered will be led by Beersaerts, G. but Ascensão, G. is actively contributing to the discussion and conclusions of this work. The discussion presented here of the work undertaken is an original work of Ascensão, G., that has been oriented to be cohesively integrated into this thesis and may not necessarily correspond to future publications.

This doctoral research was only possible thanks to funding and support from the European Union’s Horizon 2020 research and innovation programme under the Marie Skłodowska-Curie grant agreement No 721185. Nonetheless, the funders had no role in the design of the study, in the collection, analyses, and interpretation of data or the writing of this document. This doctoral thesis exclusively reflects the authors’ views, and the Agency cannot be held responsible for any use that may be made of the information it contains.

Contents

Chapter 1

Chapter 2

Chapter 3

Chapter 4

Chapter 5

Chapter 6

Chapter 7

Chapter 8

List of Figures

List of Tables

Abbreviations and Acronyms

2M	2-Methyl-2.4-Pentanediol
3DP	Powder-based three-dimensional printing
AAM	Alkali-activated materials
AFDZ model	Andreassen, Funk, Dinger and Zheng particle packing model
Al	Aluminum powder
AM	Additive manufacturing
ARSW	Aluminum scrap recycling waste
ATR	Attenuated total reflectance
BET	Brunauer–Emmett–Teller
BFS	Blast furnace slag
Bio-FA	Biomass fly-ah
BR	Bauxite residue
BSE	Backscattered electron images
CAGR	Compound Annual Growth Rate
CMC	Critical micelle concentration
CSA	Calcium Sulfoaluminate cement
CT	Computed tomography
DF	Direct foaming
DIW	Direct ink writing
DMS	Dimethylsiloxane
DoE	Design of experiment
EA	Air-entraining agents
EA	Expansive agent
EDAX	Energy dispersive x-ray
EDS	Energy-dispersive X-ray spectrometry
ELFM	Enhanced landfill mining
FA	Fly-ash
FTIR	Fourier-transform infrared spectroscopy
GGBFS	Ground granulated blast furnace slag
GHG	Greenhouse gases
HDPE	High-density polyethylene
HVAC	Heating, ventilation, and air conditioning
ICC	Isothermal conduction calorimetry
IP	Inorganic polymers
IS	In-situ foaming
ITZ	Interfacial transition zones
LDH	Layered Double Hydroxide
LHS	Latent heat storage systems
LW IPs	Lightweight inorganic polymers
LWA	Lightweight aggregates
MIP	Mercury intrusion porosimetry
MK	Metakaolin

MLWA	Micro lightweight aggregates (hollow glass microspheres)
MSW	Municipal solid waste
NAD	Nitrogen adsorption/desorption methods
NRC	Noise reduction coefficient
NZEB	Near zero-energy buildings
OM	Other methods
OPC	Ordinary Portland Cement
PC	Principal components
PCA	Principal components analysis
PCM	Phase change materials
PDF	Pair distribution function
PLA	Polylactic acid
PMMA	Polymethyl methacrylate
PPG	Polypropylene glycols
Pre-F	Pre-foaming methods
PS	Plasmastone
PSD	Particle size distribution
R&D	Research and development
RDF	Refuse-derived fuel
RM	Replica method
RM	Red mud
RSM	Response surface methodology
S/L ratio	Solid-to-liquid mass ratio
SCC	Self-compacting concrete
SCM	Supplementary cementitious materials
SDS	Sodium dodecyl sulfate
SEM	Scanning electron microscopy
SF	Silica fume
SFM	Sacrificial filler method
SHS	Sensible heat storage
SO	Sodium oleate
SPW	Steel-plat waste
SRA	Shrinkage reducing agents
SSA	Specific surface area
ST	Foam stabilizing agents
TCES	Thermochemical energy systems
TES	Thermal energy storage
WG	Waste glass
XPS	Extruded polystyrene
XRD	X-ray diffraction
XRF	X-Ray Fluorescence

Chapter 1

Introduction

1.1 Sustainable development and secondary raw-materials cycles: a global framework

After more than two centuries of rampant industrialization and mass production, the world's environment is reaching a tipping point. The increase of extreme weather events and regional crises due to resource shortages are raising public awareness for the environmental, social, political, and financial impacts of climate change. In this context, civil society is pressing governmental bodies to fully support the transition to greener social and economic models. Signed in 2016, the Paris agreement (EU-Commission, 2017) is the most relevant and emblematic transnational agreement in which most of the worlds' governments committed themselves to undertake efforts to keep the global temperature rise below 2 °C relative to pre-industrial levels, and to pursue the more ambitious target of keeping global warming under 1.5 °C by the end of the century.

Following the steps of this international commitment, more than 700 jurisdictions in 16 countries, that cover more than 130 million citizens, have declared the state of climate emergency. In countries like Canada and Portugal, parliaments have passed binding motions that pledge climate action as a national priority, while Britain was the first bipartisan parliament to unanimously support a motion in favor of a climate emergency declaration. In the US, a package of economic stimulus to facilitate decarbonization was proposed in Congress (US Congress, 2019). Although the Green New Deal has failed to pass, the vast public discussion of this motion made clear that the necessity for more sustainable economic growth models is now perceived globally.

The need for systemic changes in your societies is further highlighted when considering the projections for worldwide population growth and the expected increase of urbanization and living standards in developing and emerging countries. Guaranteeing better standards of wellbeing to a growing population while making a global effort to limit global warming will definitely require a redefinition of our current production methods and patterns of consumption.

In this scenario, transitioning from linear to circular economic models will be crucial to guarantee future materials' flows, while simultaneously contributing to reducing the greenhouse emissions associated with the extraction, processing, and transport of virgin raw materials. Besides, promoting domestic materials loops has become an urgent matter in many countries since China, by far the world's largest importer of secondary raw materials, has instituted the "Green Fence" policy that has banned the import of several post-consumer wastes and enforced more stringent contamination thresholds on the remaining ones. Despite the possible short- and long-term impacts of this measure on global recycling, it has an ethical silver lining of holding accountable western societies for their wastes and by-products, while exerts additional pressure to enforce more ambitious recycling and upcycling programs. Reintroducing wastes and by-products into the materials cycles raises considerable scientific and technical challenges that are further exacerbated when considering upcycling solutions. Thus, stimulating the transition to circular economies will be greatly dependent on creating and nurturing favorable landscapes for investments in innovation and R&D activities. This vision has been clearly embodied in the Commission proposal for European Research and Innovation budget for the period 2021-2027 that foresee a 23 billion euros increase relative to the former EU's Multiannual Financial Framework (EU-Commission, 2018).

In the context of the previous EU's Multiannual Financial Framework, the Horizon2020 (EU-Commission, 2013), the development of large-scale upcycling solutions had already attained crucial importance envisioning not only to promote more sustainable economic models but also to increase the EU' sovereignty in terms of recycling and secondary-raw materials supply.

1.2 Mining Europe's future

Within a framework of resource shortages and pressed by the urgent need for more circular economic models, EU's current and historical landfill sites are started to be considered as resource stocks, and their future mining has attracted substantial attention (Krook, 2012; Jones, 2013). The development of integrated processes able to rehabilitate degraded solids while recovering valuable materials in an environmentally responsible manner is being encouraged at EU level. The implementation of such regenerative enterprises able to upcycle the recovered materials and valorize all waste streams generated during the process has been embodied in the concept of Enhanced landfill mining (ELFM).

As the first step in this concept, mechanical shorting allows recovering waste fractions (e.g., metals, glass, and aggregates) that can be directly reintroduced into the materials cycles. However, these fractions only represent a reduced portion of the materials present in landfill sites, and the remaining fractions need to be valorized through thermal conversion (Danthurebandara, 2015a). In this field, thermochemical conversion processes are among a group of emerging technologies that aim to reclaim large volumes of low-value resources, such as industrial, municipal, and mined solid wastes from historical landfills and reintroduce them into the materials cycles in the form of added-value products. The primary outputs of these processes are energy and valuable metals, but an inorganic solid fraction is also generated. This inorganic fraction is molten and often solidified by water quenching, being afterward disposed or used in low-value applications (e.g., road paving). As thermochemical conversion processes continue to thrive and their worldwide implementation grows, the volumes generated of these vitrified residues are expected to increase. The development of added-value products using such secondary outputs can have a remarkably positive effect on the sustainability of thermochemical technologies, either directly, providing a supplementary value stream, or indirectly, by abolishing environmental impacts and costs associated with landfilling (Danthurebandara, 2015b).

Considering the expected volumes, the construction sector constitutes one of the few viable candidates to absorb significant portions of these industrial residues. From the perspective of manufacturers, integrate waste materials in production schemes represents an important opportunity to meet the environmental targets defined to the sector while simultaneously provide an opportunity to reduce production costs. Increasing the use of alternative feedstock materials by incorporating wastes and industrial by-products in the production process of cement and cement-based materials has long been identified as a vital strategy for the future of the construction sector. In fact, in the last decades, significant efforts have been made in this regard, of which a brief overlook will be given in the following section.

1.3 Sustainability of the construction sector

Accounting for around half of all materials used worldwide and representing between 5-8% of global CO_2 emissions due to human activities (Olivier, 2016), cementitious materials play a crucial role in the transition to circular development models. Despite the efforts already undertook by the cement industry to gradually transition towards more efficient and sustainable resource management models, more than 60% of CO_2 emissions in cement manufacturing comes from the chemical breakdown of limestone (Favier, 2018). Since this large portion of emissions is inherent to cement production, carbon neutrality is virtually impossible in cement production without using carbon capture and storage technologies. These technologies still require massive capital investments and elevated operating costs that smother their economic feasibility and prevent their worldwide widespread. For this reason, the short-term focus of the cement industry must and has been to minimize CO_2 emissions through improving the kiln efficiency and reducing electricity usage, using alternative fuels in manufacturing (e.g., municipal solid waste (MSW) and refuse-derived fuel (RDF)), using supplementary cementitious materials (SCM) to partially replace Ordinary Portland Cement (OPC) and in developing new hydraulic binders with lower calcination temperatures as sulfoaluminate cement (CSA), aether and celitement cements.

Complementary to the above actions that aim to reduce the environmental impact of cement and cement-based building elements, more recently, the development of binders which do not require the use of clinker but instead a chemical activator has regained attention. These materials can be found in the literature under the names of soil cements, soil silicate concretes, alkali-activated materials (AAMs), geopolymers, inorganic polymers (IPs), or low-temperature synthesized aluminosilicate glasses depending on a broader or more restrictive interpretation of those terms. Lastly, hybrid cements have also been proposed as an option to reduce clinker production and being an intermediate strategy that combines the use of low-concentration chemical activators with the residual use of cement. Despite the chemical differences between the mentioned alternative binders, they share the possibility of being partially or fully synthesized from a wide source of low-grade raw materials and industrial by-products, such as calcined clays, volcanic ashes, metallurgical and other glassy industrial residues such as the materials produced during thermochemical conversion processes.

The present work will be focused on the development of inorganic polymers from slags with a chemical composition similar to the glassy residues produced during the thermochemical conversion (i.e. gasification) of refused derived fuel produced from mined waste from historical landfill sites. The development of inorganic polymers envisioned not only to provide a large-scale upscaling route for those residues but to produce innovative materials with engineered properties able to meet the most stringent construction codes in terms of energy efficiency.

The insights provided here should not be understood as restricted to these types of residues but instead as a case study of a much broader spectrum of systems that comprise other CaO-FeO_x-Al_2O_3-SiO_2-rich inorganic polymers.

1.4 Notes on alkali activation terminology

The reaction of alkali solutions with solid silica and alumina-rich precursors was firstly reported more than a century ago when Kuehl (1908) tried to develop a material from a vitreous slag equally performant to Portland cement. From then on, a myriad of similar binding materials has been developed and framed under different definitions. As the most commonly spread definitions include alkali-activated materials, geopolymers, and inorganic polymers, some clarification of those terms is worthy in the introductory part of this work.

The most general interpretation of alkali-activated materials encompasses any binder formed by the reaction of an alkali metal source with a solid precursor. This broad definition covers the usage of (calcium)-aluminosilicate materials as solid precursors and alkali sources that include silicates, hydroxide, carbonates, aluminates, and sulfates (Provis, 2013). Phosphoric acid activation is also often associated with this terminology despite the different nature of the reactions involved. A more restrictive interpretation reserves the term alkali-activated materials for products produced from latent hydraulic precursors to which a low-concentrated alkali solution has been added to trigger their hydraulic features (Davidovits, 2015). Depending on the chosen definition, geopolymers can be either understood as a subset of alkali-activated materials where the binding phase is almost exclusively an aluminosilicate network or instead as a separate set of entirely different materials. Figure 1.4.1 illustrates the chemical classification of geopolymers when understood as a subset of alkali-activated materials with a higher alkali and aluminum and a lower calcium concentration.

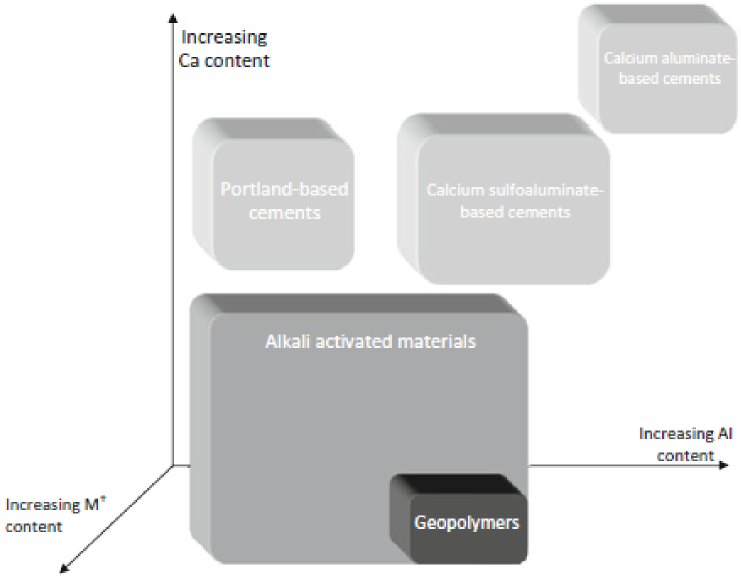

Figure 1.4.1 Schematic classification of alkali-activated materials, chemistry relative common binders (reproduced from Provis *et al.*, 2013).

Geopolymers were notoriously coined by Davidovits (2015) and, regardless of whether or not they are understood as a particular case of alkali-activated materials, their structure has been extensively described over the years. Geopolymers are defined as a fully polymerized cross-linked three-dimensional structure where alkali metals act as a charge balancing cations. Silica and aluminum are both present in tetrahedral coordination, and the hydrated gels formed are often described using a cement-analogous terminology as (M)-A-S-H, where M represents alkali cations, typically sodium (Na) or potassium (K). In order to avoid the formation of calcium silicate hydrates and promote the almost exclusive formation of (N/K)-A-S-H or (N/K)-A-(F)-S-H gels, limited calcium availability is required, hence calcinated clays (e.g. metakaolin) and low-calcium fly ashes have become the prevalent precursors used in geopolymers production.

As can be easily understood, such definition limits the concept of geopolymers and excludes systems of more complex chemistries as the ones that are the object of study here. A similar terminological gap was faced by the research community when describing the alkali activation of other calcium- and/or iron-rich abundant precursors (e.g., blast furnace slag and red mud). The term inorganic polymers (IPs) appeared as an attempt to suppress such terminological gap and embrace all materials formed by 3D connected networks of inorganic elements. The International Union of Pure and Applied Chemistry (IUPAC) has later standardized the definition of IPs as polymers or polymer networks with a skeletal structure that does not include carbon atoms (Alemán, 2007). However, it should be noticed that such definition is not restricted to completely amorphous structures and the presence of some crystalline phases is admitted. Therefore, the term "polymer" is not understood in his traditional sense but refers to the periodicity of the units created during polymerization.

Therefore, the term inorganic polymer can be used to describe any binding material resulting from the mixture of a reactive solid precursor and silicates or hydroxides solutions, without necessarily fulfilling the stoichiometric requirements of geopolymers.

According to the CaO-FeOx-Al_2O_3-SiO_2-rich nature of the precursors used in this work, the binding phases made thereof will clearly fall out of the definition of poly (sialate-(siloxo/disiloxo)) type structures, and therefore are better described as inorganic polymers.

1.5 Research outline

The technological potential of using alkaline activation technology to produce alternative binders has long been demonstrated. The substitution of calcinated clays and low-calcium fly ashes typically used in the production of geopolymers by low-grade and industrial by-products aims to further reduce the environmental footprint and production cost of alkali-activated products, and thus increase their competitiveness relative to OPC-based systems. However, as the sources of precursors are diversified and the complexity of their chemistry increased, further scientific and technical questions needed to be addressed in order to expand the available knowledge and gain market acceptance for these increasingly complex products. In addition, the large-scale implementation of inorganic polymers will also greatly depend on the development of innovative materials with superior performance relative to benchmark products. The latter can be a key differentiating factor with well-established competitors and thus facilitate their market penetration.

In this work, the vitrified residues produced during the thermochemical conversion of refuse-derived fuel (RDF) were taken as a representative case study of a broad group of currently underutilized industrial by-products, namely calcium-iron-rich slags. Conversely to geopolymers and calcium-rich IPs, the alkali activation of calcium-iron-rich residues has been investigated to a much less extent.

The aim of this work was to understand the fundamental processing parameters affecting the reaction mechanism involved in the formation of CaO-FeO_x-Al_2O_3-SiO_2-rich IPs and their correlation with the properties of the developed materials. The goal was to establish the first principles of the conceptual design of sustainable and innovative materials whose primary aim is to increase the energetic performance of residential dwellings. The major problematics related to upcycling solutions have been analyzed to identify the conditions suitable for IPs production, and the properties of the developed products were optimized according to the intended applications. In particular, IPs have been developed with engineered characteristics that enable the production of multi-layer panels that were both thermally insulating and reactive to temperature fluctuations.

The scientific and technological challenges faced during the development of those materials are described here, and the content of the chapters that compose this work can be briefly summarized as follows:

In Chapter 2, a general review of the state-of-the-art on alkaline activation technology is provided to introduce the reader to the main advantages, constraints, and specificities of different alkali-activated systems. Emphasis will be given to the production of IP binders from calcium and iron-rich silicate materials. More dedicated bibliographic reviews will be provided throughout this work when the assessment of a particular property or the engineering of IP with peculiar features makes it justifiable.

In the first section of Chapter 3, the results of parametric studies conducted to investigate the influence of several synthesis parameters on the IP binders' hardened properties are discussed. The most influential parameters were used to define the experimental domain of interest. Apart from kinetic, structural and physical analysis performed within this experimental domain, space distribution models of relevant IP properties were developed to create a robust tool to assist in ensuing developments.

As severe volumetric instability was identified as a criticality in the developed binders, Chapter 3 proceeds with the analysis of the impact of different shrinkage mitigation strategies. The shrinkage mitigation strategies analyzed included the development of mortars with optimized particle packing, the used shrinkage reducing agents (SRA), and the modification of curing regimes. As the single-use of each of these shrinkage mitigation strategies was insufficient to provide shrinkage values comparable to those of benchmark materials, the effects of combining multiple shrinkage mitigation strategies were also investigated.

In Chapter 4, the development of porous and lightweight inorganic polymers is addressed. A comprehensive bibliographic review was performed and analyzed according to principal component analysis (PCA) principles to identify the most promising processing routes. Based on such assessment, selected processing routes were employed to produce porous and lightweight $CaO\text{-}FeO_x\text{-}Al_2O_3\text{-}SiO_2$-rich IPs. The processing parameters affecting each processing route were identified and optimized in order to produce highly performant insulating materials.

Chapter 5 is dedicated to the functionalization of IP mortars and explores the possibility of incorporating phase change materials (PCMs) into the IPs mixture design. It was shown that phase change materials can be successfully used as passive thermal regulators in alkali-activated systems, even in severe climatic conditions. The fundamental proprieties of the developed thermally responsive mortars were investigated and found compatible with the requirements of common construction applications.

In Chapter 6, the high-temperature resistance of selected IP mortars was assessed. The effect of temperature and heating rate on post-heated properties and IPs' mineralogy is presented, and the potential of the developed products for high-temperature and fire-resistant applications is discussed.

In Chapter 7, the steps taken towards semi-industrial upscaling are presented and their results discussed. The description of the scale effects encountered, and measures undertaken to overcome their effects are provided.

Lastly, Chapter 8 contains the comprehensive conclusions of this work, and some recommendations for future research are given.

The topic analyzed here is of utmost interest to the construction sector and entities involved with thermochemical conversion processes. As these sectors try to reduce the environmental impacts associated with their industrial activities, the reintegration of wastes and by-products in production process is, and will continue to be, one of the main challenges to be overcome by industrial research. The work done serves the purposes of providing a comprehensive scientific background that meant to stimulate future industrial developments in this field.

References

Alemán, J. V., Chadwick, A. V., He, J., Hess, M., Horie, K., Jones, R. G., & Penczek, S. (2007). Definitions of terms relating to the structure and processing of sols, gels, networks, and inorganic-organic hybrid materials (IUPAC Recommendations 2007). Pure and Applied Chemistry, 79(10), 1801-1829. https://doi.org/10.1351/pac200779101801

Danthurebandara, M., Van Passel, S., Machiels, L., & Van Acker, K. (2015a). Valorization of thermal treatment residues in enhanced landfill mining: environmental and economic evaluation. Journal of Cleaner Production, 99, 275-285, https://doi.org/10.1016/j.jclepro.2015.03.021

Danthurebandara, M. (2015b). Environmental and Economic Performance of Enhanced Landfill Mining. Doctoral dissertation, KU Leuven. https://www.researchgate.net/profile/Maheshi_Danthurebandara/publication/304015502_Environmental_and_Economic_Performance_of_Enhanced_Landfill_Mining/links/57da38e908ae0c0081efc7b6.pdf

Davidovits, J. (2015). Geopolymer chemistry and applications. Geopolymer Institute. https://www.geopolymer.org/fichiers_pdf/geopolymer-book-chapter1.pdf

European-Commission (2013), Horizon 2020- Work programme https://ec.europa.eu/programmes/horizon2020/en/what-horizon-2020

European-Commission (2017), Paris Agreement. https://ec.europa.eu/clima/policies/international/negotiations/paris_en/

European-Commission (2018), Horizon Europe – the Framework Programme for Research and Innovation, laying down its rules for participation and dissemination. https://ec.europa.eu/commission/sites/beta-political/files/budget-may2018-horizon-europe-regulation_en.pdf

Favier, A., De Wolf, C., Scrivener, K., & Habert, G. (2018). A sustainable future for the European Cement and Concrete Industry: Technology assessment for full decarbonisation of the industry by 2050. ETH Zurich. https://doi.org/10.3929/ethz-b-000301843

Olivier, J. G. J., Janssens-Maenhout, G., Muntean, M., & Peters, J. A. H. W. (2016). Trends in global CO2 emissions: 2016 Report. Technical report, Joint Research Centre of the European Commission. https://www.pbl.nl/sites/default/files/cms/publicaties/pbl-2016-trends-in-global-co2-emisions-2016-report-2315.pdf

Jones, P. T., Geysen, D., Tielemans, Y., Van Passel, S., Pontikes, Y., Blanpain, B., & Hoekstra, N. (2013). Enhanced Landfill Mining in view of multiple resource recovery: a critical review. Journal of Cleaner Production, 55, 45-55. https://doi.org/10.1016/j.jclepro.2012.05.021

Krook, J., Svensson, N., & Eklund, M. (2012). Landfill mining: A critical review of two decades of research. Waste management, 32(3), 513-520, https://doi.org/10.1016/j.wasman.2011.10.015

Kuehl, H. (1908). U.S. Patent No. 900,939. Washington, DC: U.S. Patent and Trademark Office, https://patents.google.com/patent/US900939?oq=Kuhl%2c+H.+(1908).

Provis, J. L., & Van Deventer, J. S. (Eds.). (2013). Alkali activated materials: state-of-the-art report, RILEM TC 224-AAM (Vol. 13). Springer Science & Business Media, https://doi.org/10.1007/978-94-007-7672-2

US Congress, (2019) H.Res. 109: Recognizing the duty of the Federal Government to create a Green New Deal. https://www.congress.gov/116/bills/hres109/BILLS-116hres109ih.pdf

Chapter 2

Alkaline activation technology

Before presenting the materials developed here it is convenient to firstly present a review of the state-of-the-art on alkali-activated materials. As the early-age and hardened properties of those materials greatly depend on their chemical composition, reaction mechanisms, and structural assemblage, the most relevant groups of alkali-activated binders are summarized herein.

This review follows the broadest interpretation of alkali-activated materials, thus comprising any binding material formed by the reaction of a solid precursor with an alkali metal source. Hence, the alkali-activation of aluminosilicate materials that has been a topic of intense research was taken as baseline, being succeeded by the description of more relevant systems to this work, namely alkali-activated calcium-(alumino)-silicates and iron-silicates binders.

Despite the use of inexpensive non-corrosive activators such as alkaline carbonates and sulfates, been reported in the literature, the alkali activation solutions used in this work were limited to alkali silicates and hydroxides, as those are considered of relevance in industrial contexts (Provis, 2013). For coherence, the following section is exclusively focused on the chemistry and structures of such alkali-activated materials.

2.1 Chemistry and structure of alkali-activated materials

The formation of alkali-activated binders can be generally described as a five-stage process. In the first stage, the powdered precursors experience alkaline hydrolysis where their chemical structures are disrupted by the high alkalinity of activating solutions. The dissolution of amorphous phases occurs mostly in this stage, rapidly creating a supersaturated solution that is the primary driving force for polymerization (Van Deventer, 2007). A gelation phase follows where the initially formed gels gradually evolve towards more silica-rich structures (Provis, 2014). In the reorganization stage, the connectivity of the gel network is progressively increased until polycondensation reactions result in highly polymerized and disordered three-dimensional aluminosilicate networks. A significant part of the water in the system is consumed during the first stage of hydrolysis reactions, being later released as the reaction progresses.

The reaction mechanisms involved in the alkaline activation of aluminosilicate materials are schematically represented in Figure 2.1.1. The initial stages of this process are shared with alkali-activated materials other than aluminosilicate-derived binders.

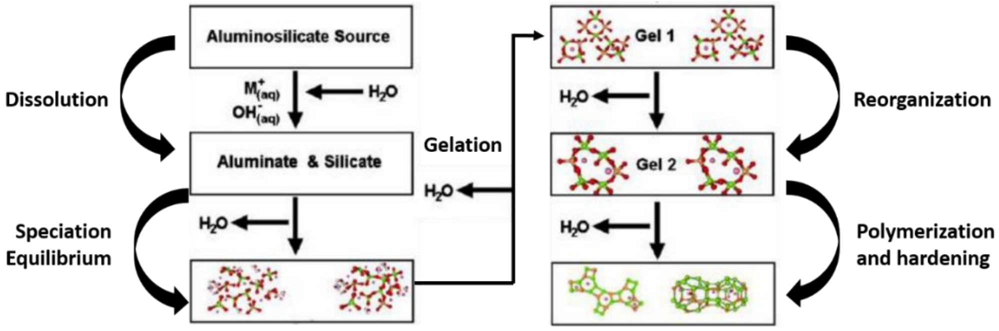

Figure 2.1.1 Schematically illustration of geopolymerization reactions (adapted from Duxson *et al.*, 2007)

The rearrangements undergone by dissolved species dictates the nanostructure and assemblage of binding phases. As calcium species strongly modify the nature of the reaction products formed, a useful methodology to first classify alkali-activated materials is based on the calcium content of their parent precursors. According to the availability of calcium species, alkali-activated materials can be divided into low or high-calcium systems. High-calcium systems are generally those having (Si+Al)/Ca molar ratios of approximately 1 (Provis, 2014). A schematic representation of the different reaction pathways and products formed is provided in Figure 2.1.2.

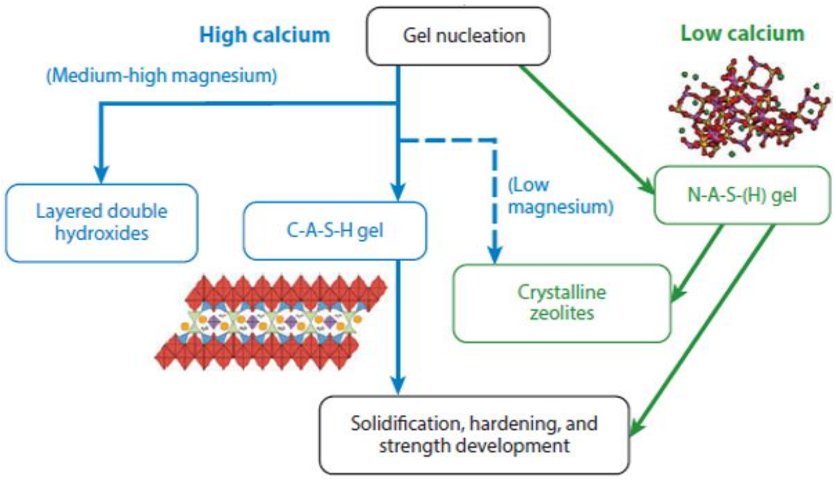

Figure 2.1.2 Reaction pathways and products of the alkaline activation of aluminosilicate precursors according to their calcium content (adapted from Provis *et al.*, 2014).

Low-calcium systems are synthesized from aluminosilicate precursors as metakaolin and class F fly ash, and the reaction products of their alkali-activation are primarily alkali aluminosilicate type gels (N/K–A–S–H). Hence, these alkali-activated systems are the only ones able to match the restricted definition of geopolymers as postulated by Davidovits (2017).

A broader group of calcium-(alumino) silicate materials can be used to synthesize high-calcium alkali-activated materials, with blast furnace slag being the most notable one. The significant increase of calcium availability in these systems modifies the nature of the binding phases formed to calcium aluminosilicate hydrates (C–A–S–H). The co-precipitation of these two types of gels is not mutually exclusive, and their coexistence has been reported in blended systems where high and low-calcium aluminosilicate materials had been used as precursors (Yip, 2005). As deep understanding of the fundamental differences between these systems is vital to properly design alkali-activated products suitable for different applications, a more detailed description of the reaction mechanisms and structure of the binding phases formed is provided.

2.1.1 Low calcium systems: Aluminosilicates

The molecular structure of aluminosilicate-derived binders can be described as a highly cross-linked 3D silicate network constituted by silico-aluminate linkages between SiO_4 and AlO_4 tetrahedrons with shared oxygen atoms (Provis, 2015). The insertion of tetrahedral aluminum into the silicate network results in a negative charge that is balanced by alkali cations provided in activating solutions. A structural model of the resulting structure is shown in Figure 2.1.3. Note that potassium cations are represented here as charge balance elements but similar structures will be formed when using sodium or cesium-based activators (Bell, 2008a,b).

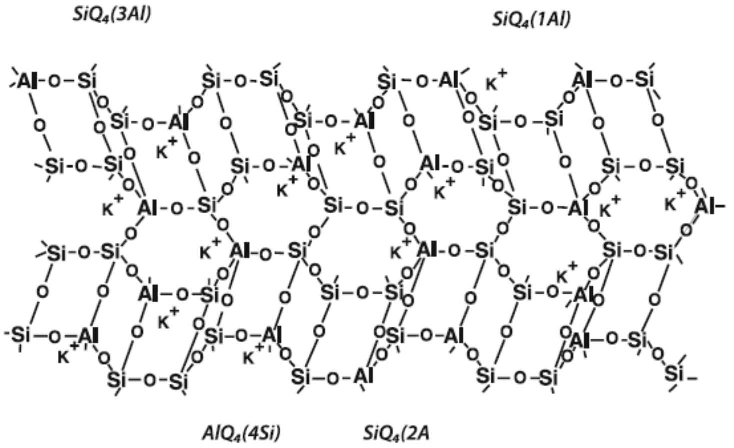

Figure 2.1.3 Representation of a 3D-structural model for a fully reacted potassium-activated aluminosilicate material (reproduced from Davidovits, 2017).

As previously mentioned, metakaolin and class F coal fly ash are the most significant aluminosilicates precursors used in alkali-activation technology (Provis, 2014). Although the described molecular structure is valid for their derived binders (Davidovits, 2017; Peys, 2018), additional details on their reaction mechanisms are pertinent.

The production of metakaolin involves the thermal treatment of kaolinitic clays. This process disrupts the clays' crystalline structure giving origin to a disordered and partially dehydroxylated material. The high reactivity of Al-O-Al bonds formed upon heating triggers alkaline hydrolysis reaction. The pH of the activating solution influences the dissolution rate, hence largely controlling the reaction kinetics. The instability of those bonds (i.e., dissolubility) explains the initial formation of aluminum-rich gels. The rupture of Al-bonds increments the accessibility of silicon sites, providing a gradual increase of silica units in the gel's structure. The dissolved species are later reorganized and polycondensate into three-dimensional polymeric structures. During mixture design, special attention should be given to guarantee the sufficient availability of silica species to avoid the precipitation of crystalline zeolitic structures (Provis, 2014).

The type of activation solution used, meaning the pH (that influences the dissolution rate) and the availability or absence of silica species, determines not only the reaction kinetics but also the microstructure of the gels formed (Hajimohammadi, 2010). Silicate solutions tend to produce more continuous and homogenous polymeric networks, thus ultimately providing less porous and more resistant alkali-activated materials.

Fly ashes instead are an industrial by-product from coal or biomass-based electric production, and their crystallographic and physical properties vary according to the feedstock materials and thermal conversion process used.

They typically present a nearly spherical morphology with a relatively high specific surface area, and sufficient reactivity to be used as precursors in alkali-activation reactions. The presence of some crystalline phases prevents fly ash complete dissolution (Kumar, 2007; Novais, 2016a), and unreacted particles act as growing sites for (N/K)-A-S-H gels. Despite the high heterogeneity of fly ashes, the reaction mechanisms and gels formed seem to be analogous to those of metakaolin-based systems (Provis, 2009; 2014).

Blended fly ash-metakaolin systems had also been successfully developed to overcome the poor reactivity of some fly ashes, in particular, biomass-ashes, and to tailor the reaction kinetics, the pastes' workability and the final properties of the developed materials (Van Jaarsveld, 2004; Novais, 2018).

Despite the technical possibility of using low-calcium alkali-activated materials to produce construction materials, the high cost of calcined clays has a severely detrimental impact on the economic viability of metakaolin-based products (Favier, 2018; You, 2019). On the other hand, fly ashes are already widely used as supplementary cementitious materials (SCM) in the cement industry, and potential areas of competition in the supply chain of these secondary raw-materials can be expected due to the growing number of EU directives that restrict coal-fired electric generation. The reduced availability of high-quality fly ashes will modify the market conditions, further impairing the competitiveness of fly-ash based alkali-activated materials.

Therefore, key applications for these materials can include high added-value niche markets were economic constraints are less relevant. Examples of those applications can include- among others- high-temperature applications, heavy metals adsorption from industrial wastewaters, or in conditioning and immobilization of radioactive wastes.

2.1.2 High calcium systems: Calcium-(alumino) silicates

Despite other metallurgic slags can be used as precursors in alkali-activation technology, the research in the field of high-calcium systems has been almost exclusively dedicated to blast furnace slag (BFS). Considering that BFS can no longer be considered a residue as it has already an established and growing market on blended cements, its use as a precursor in alkali-activated systems is only justifiable by the enhanced properties of the binders made thereof. The fast strength development and the reduced permeability of the microstructures formed - that is beneficial for many aspects related to durability - made BFS-based systems the most popular and commercially mature alkali-activated products.

A great amount of research has been done to describe in detail the reaction mechanisms and nanostructure of BFS-based systems. However, it is almost intuitive to recognize that the enhanced properties of BFS-based materials relative to their aluminosilicate counterparts must be somehow related to the role of calcium during alkali activation.

The alkali-activation of BFS is considered to follow a similar reaction pathway to pure aluminosilicates. As previously described in 2.1, alkali hydrolysis disrupts the precursors' structures, leaving calcium, alumina and silicate species available for reorganization, gelation, and later polycondensation. However, in calcium-rich systems, the pH of the alkaline medium assumes even more critical importance as the solubility of calcium species decreases at high pH. Hence, it is often reported that the use of silicate activating solutions greatly favors the increase of the reaction extension, and consequently strength development (Fernández-Jiménez, 1999; Provis, 2014). The reaction extension is further increased by the gradual formation of C-A-S-H type gels that reduce the availability of calcium species in the medium, further driving BFS dissolution.

The molecular structures formed in these materials present higher similarity to those observed in common OPC rather than to alkali-activated aluminosilicates. However, the alumina-substituted C–A–S–H gels formed in BFS systems are structurally distinct from the C–S–H, specifically having a lower Ca/Si molar ratio and a different ordering (Provis, 2014). The lower Ca/Si ratio and higher availability of aluminum in the gels formed reduce the degree of polymerization relative to aluminosilicate-systems and dreierketten chains of tobermorite-like gels are formed, Figure 2.1.4b (Provis, 2014). Chemically bonded water, calcium cations, and alkalis reside in the interlayer region. The latter also acts as a charge balance that compensates Si^{4+} replacement by Al^{3+} in the tetrahedral chains.

The presence of high amounts of aluminum and magnesium (>5 wt%, Gong, 2016) can also result in the formation of aluminum and magnesium-rich secondary reaction products, Figure 2.1.2. These secondary reaction products include Layered Double Hydroxide (LDH) phases such as hydrotalcite-like hydroxides, hydrous calcium aluminates or zeolites (Lothenbach, 2007; Bernal, 2013; Gong, 2016). The formation of these secondary phases can considerably beneficiate the long-term stability of the formed tobermorite-like structures, and therefore increase the service life of BFS-based alkali-activated products.

Another significant technological aspect of high-calcium systems is the possibility of using conventional admixtures (Provis, 2014). Conversely to geopolymers where admixtures traditionally used in the cement industry seem to have a reduced effect (e.g., superplasticizers), the higher similarity between the surface chemistry of C-S-H and C–A–S–H gels increases their effectiveness in BFS-based systems.

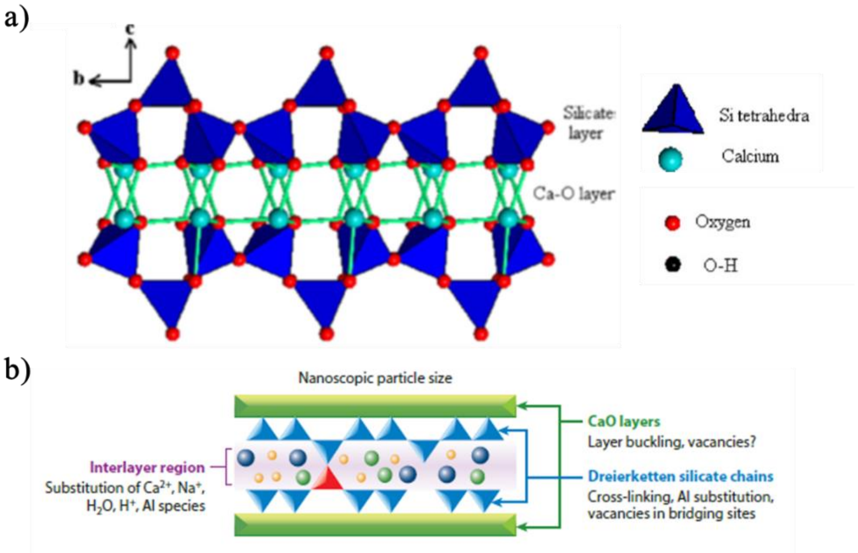

Figure 2.1.4 Projection of (a) tobermorite structure and (b) tobermorite-like C-A-S-H gel structure. In b), red triangles denote aluminum substitution in the silicon structure while the circle denotes interlayer species (adapted from Mostafa *et al.*, 2009 and Provis *et al.*, 2014).

2.1.3 Iron silicates

An extensive list of natural raw materials and industrial by-products has been used to synthesis Fe-rich inorganic polymers including volcanic ashes (Lemougna,2011a; 2013), natural Fe-rich clays (Lemougna, 2011b; Obonyo, 2014), bauxite residues (Ke, 2105; Hertel, 2016; Ascensão, 2017; Hertel, 2019), iron-nickel slags (Sakkas, 2014; Komnitsas, 2007; 2019) and copper slags (Onisei, 2015).

Deposits of volcanic ashes and debris are abundant and readily accessible in many regions of the world and have been used in the production of building materials since antiquity due to their pozzolanic activity. Despite the considerable variability in terms of their chemical composition, the major oxides present are usually SiO_2, Fe_2O_3, CaO, Al_2O_3, MgO, K_2O and Na_2O (Lemougna, 2016). As their reactivity towards alkali-activation largely depends on the parent magma, the potential of volcanic ashes to be used as a precursor is particularly case dependent, which has made difficult their systematic study. However, Lemougna *et al.* (2013) investigated the behavior of iron during the formation of inorganic polymers from volcanic ashes. They found that iron-bearing minerals, such as augite, can partially react and be integrated into the tetrahedral networks of inorganic polymers. Due to the homogenous distribution of the newly formed ferric phases, the properties of the produced IPs were not significantly impaired and compressive strength higher than 60 MPa (Lemougna, 2013) and good thermal stability were attained (Lemougna, 2011a).

In the case of natural Fe-rich clays, a thermal treatment similar to the one employed in metakaolin production is required to enhance reactivity. During this process, iron phases are transformed into hematite (Fe_2O_3), which has low solubility under alkali conditions and therefore does not significantly participate in the reaction. Hence, the reaction mechanisms and products formed are equivalent to geopolymers (see 2.2) with some impurities of crystalline hematite. Still, the use of Fe-rich calcinated clays can be advantageous in alkali-activation technology as the presence of iron increases the clays' structural disorder and therefore reduces the calcination temperature needed (Peys, 2018).

The large availability of Fe-rich metallurgical slags and the limitations imposed on their integration in cement manufacturing had brought attention to the potential use of these by-products as IP precursors. Ferronickel slags had been used to produce sodium-activated IPs with heat-resistant properties (Komnitsas, 2007; Sakkas, 2014; Komnitsas, 2019). The formation of sodalite, maghemite, thermonatrite and trona phases contributes to increasing post-heated mechanical properties and the durability of Fe-Ni-rich IPs. Copper slags have also been used to produce IP that show some similarities with BFS-based systems. The presence of silicate species in the activating solution was necessary to produce polymeric structures, and moderate levels of hydroxides were required to control the reaction kinetics (Onisei, 2015).

With a worldwide annual generation that surpasses 150 Mtonnes (Evans, 2016), bauxite residues (BR) constitute a severe environmental problem. As in some applications the admissible incorporation rates are restricted (e.g., common concrete), the valorization of bauxite residues in the production of alkali-activated products has been considered. A first approach includes using bauxite residues as partial replacement of more reactive and costly precursors, as metakaolin and blast furnace slag. Despite the environmental benefits of reintegrating BR in the materials cycle, the highly crystalline nature of bauxite residues hinders their significant participation in reaction and contribution to IPs' final properties (Ascensão, 2017). A considerably different approach was proposed by Ke *et al.* (2015) who calcined BR with sodium hydroxide pellets in order to produce the so-called “One-Part Geopolymers”. The thermal decomposition of the bauxite residues' original structure led to the formation of hydraulic compounds. The hydration of these phases results in the formation of zeolites and disordered binder gels, however with limited strength development (<10 MPa). A different calcination process was suggested by Hertel *et al.* (2016; 2019). By adding minor quantities of C and Si to bauxite residues, the carbothermic reduction of ferric iron into ferrous iron was achieved and the amount of molten phase increased. The inorganic polymers produced from modified-bauxite were able to develop compressive strength that exceeded 40 MPa.

Despite the attractive properties demonstrated, the molecular structure of Fe-rich IPs has been less investigated, and it is far less understood. Determining the fate of iron during alkali-activation of Fe-silicates precursors still requires comprehensive investigations but some recent works have given valuable insights. Early investigations had demonstrated that a small portion of Al^{3+} could be replaced by Fe^{3+} in octahedral sites (Gomes, 2010) being later shown that IPs produced from Fe-rich slags are structurally different from “Fe-enriched” aluminosilicate geopolymers in more than just Fe-Al substitution in tetrahedrally-coordinated sites (Simon, 2018). In-situ X-ray total scattering and subsequent pair distribution function (PDF) analysis were recently used to describe the formation mechanism of Fe-rich IPs, and it was found that the atomic rearrangements undergone by Fe-silicate species are heavily dependent on the alkali cation provided by the activating solution (Peys, 2019). It was reported that Fe^{2+} and Fe^{3+} oxidation states coexist in the binder phase under different forms. The Fe^{2+} is present as trioctahedral layers, while the participation of Fe^{3+} in the polymerized silicate network seems most likely. PDF analysis of matured specimens shows significant modifications in the structure attributed to long-term oxidization of the Fe^{2+} species present in the trioctahedral layers.

As the chemical composition of the vitrified residues produced during the thermochemical conversion of RDF contains significant calcium and iron contents (>20 wt%), their alkali-activation cannot be framed under the settings of calcium or iron-rich systems, as it may comprise elements of both. As the worldwide production of these types of residues grows and upcycling solutions are urgently needed, this work aimed to understand the principles of the alkali-activation of these complex $CaO\text{-}FeO_X$-rich systems and provided valuable insights on the development of IPs made thereof. This work was conducted envisioning the developed innovative materials with engineered properties that would be able to increase the energy efficacy of residential dwelling; nonetheless, the potential of the developed products should not be perceived as limited to those applications.

2.2 General considerations on mix design optimization

We are currently living during an era were significant transformations are happening to our society. The already visible effects of climate change and the scarcity or exhaustion of natural resources abundant not long ago require redefining the way we design, produce, consume, and dispose end-life products. Among others, fostering automation in manufacturing is expected to play a crucial role in reducing the environmental impacts of the industrial sector while offering the opportunity to manufacturers to increase the efficiency of their operations. National and EU incentives to develop the so-called "Industry 4.0" clearly reflects the necessity for a paradigm shift in current manufacturing practices (Morisson and Pattinson, 2019). The transition to self-cognitive, self-diagnosed and self-optimized production process is far away from becoming a transversal reality, and it will be necessarily a slow and incremental process. Emergent, high added-value industries and already heavily automated sectors (e.g., automobile sector) will naturally be more prone to incorporate new production methods into their value-chains, while in more conservative industrial segments such transition will be much slower.

In the construction sector, the design and execution of industrial experiments are still frequently performed by highly specialized experts in a field whose sole envision is to overcome a technology hurdle or to enhance a specific feature of a certain material. In the case of hydraulic and other binders, this is often done by tailoring the mix design and additives used and controlling any possible deleterious effects imposed by the latter. Although this approach has proven to be reliable, the reduced versatility of such production processes requires from manufacturers a tight quality control of the entire supply chain and constrains the selection of feedstock materials to widely available materials of well-known and stable composition. Abandoning these "one-off" established practices and developing resilient and adaptive mix designs able to accommodate higher degrees of variability on feedstock materials will allow incorporating so far unexplored resources, including some industrial by-products and waste products with expected environmental and economic benefits (Favier, 2018). This approach relinquishes the notion of rigorous control of inputs to ensure an output material that has proven to guarantee certain properties. Instead, a systematic description and holistic comprehension of the production process and feedstock materials are required to make it possible to intervene and adjust the mix design at any given time or/and to be able to predict the features of the finished product given a particular set of inputs materials.

Moreover, the current transition from prescriptive requirements to performance-based specifications also requires the adoption of versatility production methods, and this new approach towards manufacturing seems to be increasingly acknowledged by academia and by the construction sector itself. In fact, efforts have been made in the sector to mimic cutting-edge industries such as the pharmaceutical, where statistical and modeling tools are now current practice for decades. Among statistical tools, factorial experiments and response surface methodology (RSM) are becoming more common in industrial experimentation. Experiments with 2-levels factors are widely spread (Box, 2005) due to their relative simplicity and the small number of trials necessary to explore a large domain of an *n*-dimensional space of variables. Although the development and implementation of statistical models were not the primary scopes of this work, some statistical principles were employed during the design and execution of experiments, as well as to interpret their results. Some general considerations on factorial design, response surface methods, and principal components analysis will be provided in the next section along with a brief literature review of some works where such principles have been successfully implemented to produce and optimize alkali-activated materials.

2.2.1 Mix design optimization- a statistical approach

While everyone can easily acknowledge that in our daily life we are surrounded by multivariable phenomena, in laboratory experimentation, we tend to see the world as univariable. This may well reflect our natural tendency to control marginal variables to increase the accuracy of our experiments, hoping to lead ourselves towards replicable results and unquestionable scientific findings. Constraining all parameters during experimentation allows confidently identify the effects of a certain object of study, but this one-factor-at-a-time method of experimentation only provides information regarding the effects of a single factor in a selected and fixed set of conditions. To give a more general relevance to the estimated effects, different factors are often tested under several fixed sets of conditions. This time-consuming approach assumes that different factors would additively affect a particular response and neglect possible interactions of non-additive nature.

Factorial designs provide a multivariable experimental approach that assumes responses as being the result of non-additive effects, not excluding the opposite possibility, however. To perform a factorial design, a certain number of factors (variables) and a fixed number of levels that each factor can assume are selected. The dimensional space of research is defined by covering all possible combinations between factors and respective levels.

The two-level factorial designs are the simplest and most widely used, where each variable only assumes a minimum and maximum value. The number of experiments is dictated by 2^k where K stands for the number of variables studied. It should be noticed that it is not strictly necessary to only consider quantitative variables since qualitative factors are also admitted into factorial designs. The main advantage of these types of factorial design is allowing to explore a broad region of the factor space with a low number of experiments per factor. By interpreting the observations made is possible to characterize the research space and to determine promising directions for further examination. Moreover, the initial factorial design does not restrict at any given time the research space as it can be later augmented when a more thorough local examination is needed or expanded when results suggest further exploration outside of the initially defined boundaries. This process is frequently termed as *sequential assembly* (Box, 2005), and it was employed in the course of this work. Two-level factorial designs are also the base for *fractional* factorial designs. As the name suggests, in *fractional* designs only a chosen part (fraction) of the full factorial design is performed. This further reduces the number of experiments making these types of designs particularly valuable for factor-screening purposes and exploratory experimentation. As referred by Box *et al.* (2005), this allows separating the "*vital few*" from the "*trivial many*" as the active factor space is frequently of a lower dimension of the design space. Notice that a major influence might be manifested through the main effect of a factor or through interactions with others.

In *fractional* designs, not all the conceivable interactions are estimated. The effects of three or high-order interactions are assumed to be small enough to be inert, while the main effects keep being estimated without imposing a bias in the design. The higher-order terms are still considered in the research space, but their effects are confounded with those of lower order. Given a 2^4 factorial design as an example and considering A, B, C, D as the factors studied, the third-order abc effect can be confounded with the first-order effect of d. The main effect of d is no longer estimated indistinguishably from abc interaction, and the estimated effect reflects the sum $abc+d$. If one is prepared to assume third-order interactions as negligible, then the estimated confounded effect of abc and d can be assumed as the effect of d. A similar rationale is applied to all the estimated effects. Being aware of this alias structure is essential to distinguish random variation from experimental effects. The number of experiments in *fractional* factorial designs is given by the expression 2^{k-p} where k is the number of experiments of the original full factorial design, and p is given by the expression $\frac{1}{n} = (\frac{1}{2})^p$ where $\frac{1}{n}$ represents the fraction of the design intended.

Factorial designs were particularly useful during the screening stage of this work to investigate which factors exerted greater influence upon some fundamental properties of the developed alkali-activated materials without using a large number of experiments. The structure of the screening factorial designs and their results will be discussed later in this work.

Another powerful statistical tool that has found its place in many industrial applications is *principal component analysis*, often termed as PCA. PCA is a dimensional-reduction method frequently employed to analyze large sets of data where direct graphical representation is impossible. This statistical technique can be seen as a compromising solution where only significant information is retained while some accuracy loss is accepted for the sake of simplicity. In this way an initially large data set is reduced to highlight otherwise invisible patterns, similarities, and differences within the original set of data. The initial set of data is transformed by establishing a new set of variables (principal components, PCs) constructed as linear combinations of the initial ones while imposing orthogonality conditions to guarantee that the new variables remain uncorrelated. The newly construct principal components represent the directions within the initial *n*-dimensional space that explain the maximum amount of variance within the initial data set. Identifying these directions is to determine the space vectors that retain most of the information regarding the initial data set. Principal components will be constructed sequentially and always accounting for the direction that explains the largest variance remaining. Figure 2.2.1 shows a schematic representation of how PC directions are determined.

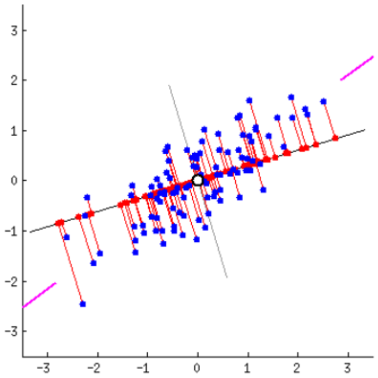

Figure 2.2.1 Schematic representation of how PCs directions are determined.

Once quantified the significance of each principal component to the total variance of the initial data set, the newly constructed set of PCs can be depleted from inert or almost inert PCs without the loss of relevant information. Since the number of PCs is equal to the number of the initial variables, keeping only a PC fraction will necessarily lead to a dimensional reduction. Once no vital information was lost during this process, any consideration concerning a particular PC would be as valid as any interpretation based on the original data set.

Analogously to factorial designs, PCA allows to separate the "*vital few*" from the "*trivial many*" but there are some fundamental conceptual differences to be considered. Briefly summarizing, factorial analysis estimates the influence of a certain set of variables in a certain set of responses while PCA builds a set of index variables based on initial responses to be later used for extracting relevant factors. An in-depth discussion concerning the similarities and differences between factorial designs and PCA will not be provided here; instead, some examples where statistical approaches were taken during the design and optimization of alkali-activated materials will be shown. The following section is mainly dedicated to factorial designs and surface response methodology since to this date, and to the best of our knowledge, only a few studied reported the use of PCA in cement-based materials and none on alkali-activated materials.

2.2.2 Optimization of AAMs using factorial experiments and response surface methodology

The wide range of feedstock materials that can be used as precursors is, without a doubt, one of AAMs most interesting features. This versatility tremendously increases alkali-activation technology attractiveness – both for environmental remediation and commercial purposes – but also poses significant challenges by increase the complexity of large-scale production operations.

As each (iron)-aluminosilicate-rich material exhibits its own dissolution and hardening mechanism when alkali-activated, the performance of end-materials largely depended on several factors such as the precursors mineralogical and chemical composition (Duxson, 2007), its particle fineness (Marjanović, 2014), the activator nature and its molar concentration (Duxson, 2007; Lizcano, 2012; Machiels, 2014) and, curing conditions (Novais, 2016b). Owing to this multitude of factors that contribute to AAMs properties, it is essential to develop robust mix designing tools to adapt and optimize AAMs formulations almost in real-time. Factorial designs and response surface methodology allow determining relationships between independent variables and responses making possible to optimize the mix design envisioning one or more target features (Box, 2005; Zahid, 2018). These techniques are frequently employed and widely accepted in several industrial fields, inclusive of cement and concrete manufacturing (Khayat, 2000) where can be included among the current best-practices. Examples of optimization processes performed by using response surface methodology can include the works of Cihan *et al.* (2013), Aldahdooh *et al.* (2013), and Mohammed *et al.* (2017), who optimize the strength development of ready-mix and fiber-reinforced concretes. Despite being successfully employed in OPC concrete mix design, response surface is only now starting to be introduced into the design process of alkali-activated products.

Sumabat *et al.* (2015) applied statistical design of experiments, multiple response optimization, and analytic hierarchy processes in the mix design of alkali-activated ternary blends. Red mud, rice hull ash, and diatomaceous earth were used as precursors, while a sodium silicate solution was used as an activator. Several technical (e.g., mechanical and thermal properties) and sustainability criteria (cost, embodied energy, and carbon footprint) were considered to modeling the expected responses and find the optimal mix proportions that maximized the overall desirability of the mix. An optimal mix formulation of 11.6 wt% red mud, 67.2 wt% rice hull ash and 21.2 wt% diatomaceous earth was proposed. Despite some fairly questionable assumptions (e.g., considering GHG emissions only within the production process boundaries or neglecting activator cost variability) and the fact that validation results were not presented, the predicted results included compressive strength of 13 MPa, thermal conductivity of 0.33 W/m°K, and a production cost of 0.15 US$/kg. Romagnoli *et al.* (2012; 2014) studied the fresh state properties of metakaolin (MK) and fly-ash (FA) AAMs using design of experiments approach. In both works, the effects of solid-to-liquid ratio, temperature and dispersant concentration (sodium polyacrylate) were investigated. Different reaction rates were observed between MK and FA systems, which were partially attributed to the different particle size distributions. The reduced superficial surface of FA particles was shown to slow dissolution. Yet, in both studies, solid-to-liquid ratio was found to be the dominant factor controlling the suspension viscosity, shear behavior, and yield stress. The dispersant concentration was less significant, while the effects of temperature were dependent on the precursor used.

Gao *et al.* (2016) investigated the effects of three factors (silica modulus, the concentration of the activating solution and solid-to-liquid ratio) on early strength development of alkali-activated slag. Based on the results gathered, compressive and flexural models were built, and a negative correlation between silica modulus and compressive strength was found. Increasing the concentration of the activating solution enhanced early strength development while the impact of solid-to-liquid ratio was less significant. The produced models were reasonably accurate for mortars with compressive strength > 5 MPa, where the difference between predicted and measured values did not exceed 15%. Hadi *et al.* (2017) employed Taguchi methods to maximize the strength development of GGBFS-based concrete. The effects of four parameters were investigated, the binder contents, activator-to-binder ratio, sodium silicate/hydroxide proportion, and sodium hydroxide concentration. The activator-to-binder ratio presented a negative correlation with compressive strength while the dosage of the binder was found to have an optimum value of 450 kg/m^3. Based on factorial analysis the relative contribution of each parameter was determined, identifying the activator-to-binder ratio as the most significant contribution to strength development (~ 70%). The optimized formulation presented insufficient setting times, and the partial replacement of GGBFS by fly ash, metakaolin, and silica fume was examined. Reducing the GGBFS dosage delayed polymerization reactions and prolonged setting time. However, decreasing calcium availability in systems resulted in the formation of less Ca-rich phases and led to poorer mechanical performances. Considering equal amounts of GGBFS replacement, it was concluded that FA provided the most suitable combination between setting time and compressive strength. Zahid *et al.* (2018) applied response surface optimization to modeling the effects of sodium hydroxide molarity, sodium silicate/hydroxide ratio and curing temperature on the properties of high calcium fly ash-based AAMs. They have developed statistical models to predict setting time, compressive strength, elastic modulus, first crack strength, flexural strength, flexural toughness, and ductility. After initial modeling and validation, a multi-objective optimization was performed. The optimal conditions proposed included the use of sodium hydroxide with molarity of 7.9, a sodium silicate/hydroxide ratio of 1.7 and a curing temperature of 70 °C. As can be seen in Figure 2.2.2, the optimal mix design accomplished desirability almost equal to 1 in several features and reached global desirability of 0.87. As shown in Table 2.2.1, the experimental validation of these results has shown a good agreement with the predicted values presenting an error margin inferior to 5%.

All the results mentioned here demonstrate that statistical methods can be successfully employed to investigate the most active factors and optimize the performance of AAMs. Moreover, the development of adaptive design solutions can further enhance the reliability of the production processes and decrease their susceptibility to feedstock materials variation. This was particularly relevant within the scope of this work since its primary aim was to develop added-value materials by upcycling a waste product produced during the advanced thermochemical conversion of landfilled materials. Given the intrinsic variability of the materials in landfills itself, considerable fluctuations in the composition of the vitreous residues generated can be expected. Therefore, this work followed a similar approach to the ones described herein, where factorial designs were employed to define experimental protocols, and surface response methodology was used to analyze the results gathered.

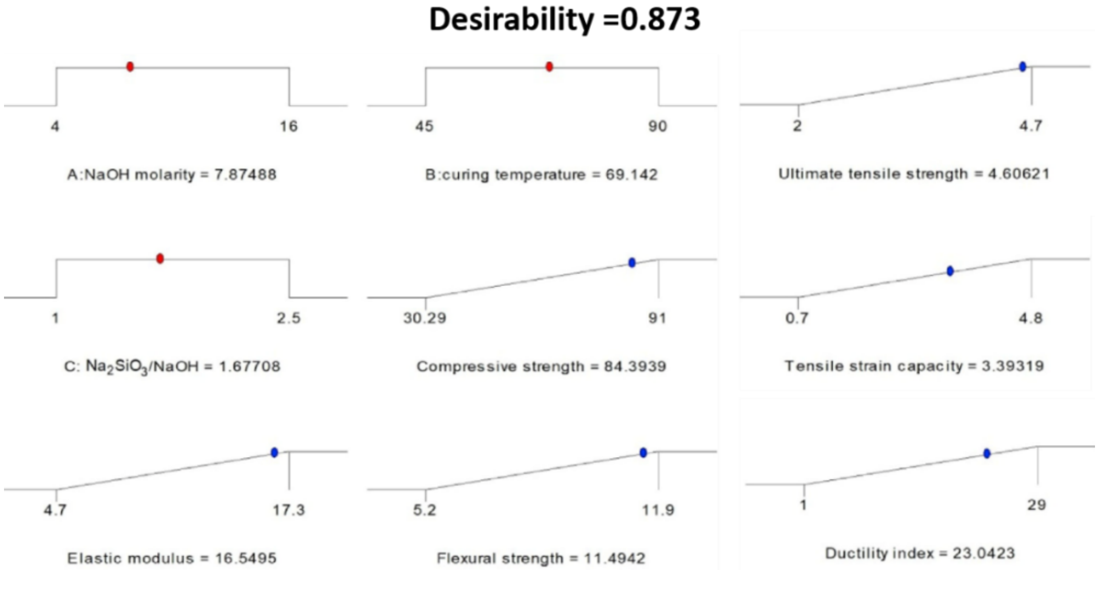

Figure 2.2.2 Desirability ramps for numerical optimization of different factors and responses (adapted from Zahid *et al.*, 2018).

Table 2.2.1 Predicted and experiment results for the optimal mix design (Zahid *et al.,* 2018).

Response	**Compressive strength (MPa)**	**Elastic modulus (GPa)**	**Flexural strength (MPa)**	**Flexural toughness (N.m)**	**Ductility index**	**Ultimate tensile strength (MPa)**	**Tensile strain capacity (%)**
Predicted	84.4	16.6	11.5	20.7	23.0	4.6	3.4
Experimental	81.2	15.9	10.9	21.2	22.2	4.4	3.2
Error (%)	3.7	4.7	4.8	2.6	3.8	3.9	4.4

References

Aldahdooh, M. A. A., Bunnori, N. M., & Johari, M. M. (2013). Evaluation of ultra-high-performance-fiber reinforced concrete binder content using the response surface method. Materials & Design (1980-2015), 52, 957-965. https://doi.org/10.1016/j.matdes.2013.06.034

Ascensão, G., Seabra, M. P., Aguiar, J. B., & Labrincha, J. A. (2017). Red mud-based geopolymers with tailored alkali diffusion properties and pH buffering ability. Journal of cleaner production, 148, 23-30. https://doi.org/10.1016/j.jclepro.2017.01.150

Bell, J. L., Sarin, P., Driemeyer, P. E., Haggerty, R. P., Chupas, P. J., & Kriven, W. M. (2008a). X-ray pair distribution function analysis of a metakaolin-based, KAlSi 2 O 6• 5.5 H 2 O inorganic polymer (geopolymer). Journal of Materials Chemistry, 18(48), 5974-5981. https://doi.org/10.1039/B808157C

Bell, J. L., Sarin, P., Provis, J. L., Haggerty, R. P., Driemeyer, P. E., Chupas, P. J.,& Kriven, W. M. (2008b). Atomic structure of a cesium aluminosilicate geopolymer: a pair distribution function study. Chemistry of Materials, 20(14), 4768-4776. https://doi.org/10.1021/cm703369s

Bernal, S. A., Provis, J. L., Walkley, B., San Nicolas, R., Gehman, J. D., Brice, D. G., & van Deventer, J. S. (2013). Gel nanostructure in alkali-activated binders based on slag and fly ash, and effects of accelerated carbonation. Cement and Concrete Research, 53, 127-144. https://doi.org/10.1016/j.cemconres.2013.06.007

Box, G. E., Hunter, J. S., & Hunter, W. G. (2005). Statistics for experimenters. In Wiley Series in Probability and Statistics. Wiley Hoboken, NJ, USA.https://doi.org/10.1198/tech.2006.s379

Cihan, M. T., Güner, A., & Yüzer, N. (2013). Response surfaces for compressive strength of concrete. Construction and Building Materials, 40, 763-774. https://doi.org/10.1016/j.conbuildmat.2012.11.048

Davidovits, J. (2017). Geopolymers: Ceramic-like inorganic polymers. J. Ceram. Sci. Technol, 8(3), 335-350. https://doi.org/10.4416/JCST2017-00038

Duxson, P., Fernández-Jiménez, A., Provis, J. L., Lukey, G. C., Palomo, A., & van Deventer, J. S. (2007). Geopolymer technology: the current state of the art. Journal of materials science, 42(9), 2917-2933.

Evans, K. (2016). The history, challenges, and new developments in the management and use of bauxite residue. Journal of Sustainable Metallurgy, 2(4), 316-331. https://doi.org/10.1007/s10853-006-0637-z

Favier, A., De Wolf, C., Scrivener, K., & Habert, G. (2018). A sustainable future for the European Cement and Concrete Industry: Technology assessment for full decarbonisation of the industry by 2050. ETH Zurich. https://doi.org/10.3929/ethz-b-000301843

Fernández-Jiménez, A., Palomo, J. G., & Puertas, F. (1999). Alkali-activated slag mortars: mechanical strength behaviour. Cement and Concrete Research, 29(8), 1313-1321. https://doi.org/10.1016/S0008-8846(99)00154-4

Gao, Y., Xu, J., Luo, X., Zhu, J., & Nie, L. (2016). Experiment research on mix design and early mechanical performance of alkali-activated slag using response surface methodology (RSM). Ceramics International, 42(10), 11666-11673. https://doi.org/10.1016/j.ceramint.2016.04.076

Gomes, K. C., Lima, G. S., Torres, S. M., de Barros, S. R., Vasconcelos, I. F., & Barbosa, N. P. (2010). Iron distribution in geopolymer with ferromagnetic rich precursor. In Materials Science Forum (Vol. 643, pp. 131-138). Trans Tech Publications. https://doi.org/10.4028/www.scientific.net/MSF.643.131

Gong, K., & White, C. E. (2016). Impact of chemical variability of ground granulated blast-furnace slag on the phase formation in alkali-activated slag pastes. Cement and Concrete Research, 89, 310-319. https://doi.org/10.1016/j.cemconres.2016.09.003

Hadi, M. N., Farhan, N. A., & Sheikh, M. N. (2017). Design of geopolymer concrete with GGBFS at ambient curing condition using Taguchi method. Construction and Building Materials, 140, 424-431. https://doi.org/10.1016/j.conbuildmat.2017.02.131

Hajimohammadi, A., Provis, J. L., & Van Deventer, J. S. (2010). Effect of alumina release rate on the mechanism of geopolymer gel formation. Chemistry of Materials, 22(18), 5199-5208. https://doi.org/10.1021/cm101151n

Hertel, T., Blanpain, B., & Pontikes, Y. (2016). A proposal for a 100% use of bauxite residue towards inorganic polymer mortar. Journal of Sustainable Metallurgy, 2(4), 394-404. https://doi.org/10.1007/s40831-016-0080-6

Hertel, T., Novais, R. M., Alarcón, R. M., Labrincha, J. A., & Pontikes, Y. (2019). Use of modified bauxite residue-based porous inorganic polymer monoliths as adsorbents of methylene blue. Journal of Cleaner Production, 227, 877-889. https://doi.org/10.1016/j.jclepro.2019.04.084Ke, X., Bernal, S. A., Ye, N., Provis, J. L., & Yang, J. (2015). One-Part Geopolymers Based on Thermally Treated Red Mud/NaOH Blends. Journal of the American Ceramic Society, 98(1), 5-11. https://doi.org/10.1111/jace.13231

Khayat, K. H., Ghezal, A., & Hadriche, M. S. (2000). Utility of statistical models in proportioning self-consolidating concrete. Materials and structures, 33(5), 338-344. https://doi.org/10.1007/BF02479705

Komnitsas, K., Bartzas, G., Karmali, V., Petrakis, E., Kurylak, W., Pietek, G., & Kanasiewicz, J. (2019). Assessment of Alkali Activation Potential of a Polish Ferronickel Slag. Sustainability, 11(7), 1863. https://doi.org/10.3390/su11071863

Komnitsas, K., Zaharaki, D., & Perdikatsis, V. (2007). Geopolymerisation of low calcium ferronickel slags. Journal of Materials Science, 42(9), 3073-3082. https://doi.org/10.1007/s10853-006-0529-2

Kumar, S., Kumar, R., Alex, T. C., Bandopadhyay, A., & Mehrotra, S. P. (2007). Influence of reactivity of fly ash on geopolymerisation. Advances in Applied Ceramics, 106(3), 120-127. https://doi.org/10.1179/174367607X159293

Lothenbach, B., & Gruskovnjak, A. (2007). Hydration of alkali-activated slag: thermodynamic modelling. Advances in cement research, 19(2), 81-92. https://www.researchgate.net/profile/Barbara_Lothenbach/publication/250071785_Hydration_of_alkali-activated_slag_Thermodynamic_modelling/links/00b49538dc20706168000000.pdf

Lemougna, P. N., MacKenzie, K. J., Jameson, G. N., Rahier, H., & Melo, U. C. (2013). The role of iron in the formation of inorganic polymers (geopolymers) from volcanic ash: a 57 Fe Mössbauer spectroscopy study. Journal of Materials Science, 48(15), 5280-5286. https://doi.org/10.1007/s10853-013-7319-4

Lemougna, P. N., MacKenzie, K. J., & Melo, U. C. (2011a). Synthesis and thermal properties of inorganic polymers (geopolymers) for structural and refractory applications from volcanic ash. Ceramics International, 37(8), 3011-3018. https://doi.org/10.1016/j.ceramint.2011.05.002

Lemougna, P. N., Melo, U. F. C., Kamseu, E., & Tchamba, A. B. (2011b). Laterite based stabilized products for sustainable building applications in tropical countries: review and prospects for the case of Cameroon. Sustainability, 3(1), 293-305. https://doi.org/10.3390/su3010293

Lemougna, P. N., Wang, K. T., Tang, Q., Melo, U. C., & Cui, X. M. (2016). Recent developments on inorganic polymers synthesis and applications. Ceramics International, 42(14), 15142-15159. https://doi.org/10.1016/j.ceramint.2016.07.027

Lizcano, M., Kim, H. S., Basu, S., & Radovic, M. (2012). Mechanical properties of sodium and potassium activated metakaolin-based geopolymers. Journal of Materials Science, 47(6), 2607-2616. https://doi.org/10.1007/s10853-011-6085-4

Machiels, L., Arnout, L., Jones, P. T., Blanpain, B., & Pontikes, Y. (2014). Inorganic polymer cement from Fe-silicate glasses: varying the activating solution to glass ratio. Waste and Biomass Valorization, 5(3), 411-428. https://doi.org/10.1007/s12649-014-9296-5

Marjanović, N., Komljenović, M., Baščarević, Z., & Nikolić, V. (2014). Improving reactivity of fly ash and properties of ensuing geopolymers through mechanical activation. Construction and Building Materials, 57, 151-162. https://doi.org/10.1016/j.conbuildmat.2014.01.095

Mohammed, B. S., Achara, B. E., Nuruddin, M. F., Yaw, M., & Zulkefli, M. Z. (2017). Properties of nano-silica-modified self-compacting engineered cementitious composites. Journal of cleaner production, 162, 1225-1238. https://doi.org/10.1016/j.jclepro.2017.06.137

Morisson, Arnault & Pattinson, Marc. (2019). INDUSTRY 4.0 Interreg Europe Policy Brief. https://www.interregeurope.eu/fileadmin/user_upload/plp_uploads/policy_briefs/INDUSTRY_4.0_Policy_Brief.pdf

Mostafa, N. Y., Shaltout, A. A., Omar, H., & Abo-El-Enein, S. A. (2009). Hydrothermal synthesis and characterization of aluminium and sulfate substituted 1.1 nm tobermorites. Journal of Alloys and Compounds, 467(1-2), 332-337. https://doi.org/10.1016/j.jallcom.2007.11.130

Novais, R. M., Ascensão, G., Seabra, M. P., & Labrincha, J. A. (2016b). Waste glass from end-of-life fluorescent lamps as raw material in geopolymers. Waste management, 52, 245-255. https://doi.org/10.1016/j.wasman.2016.04.003

Novais, R. M., Ascensão, G., Tobaldi, D. M., Seabra, M. P., & Labrincha, J. A. (2018). Biomass fly ash geopolymer monoliths for effective methylene blue removal from wastewaters. Journal of cleaner production, 171, 783-794. https://doi.org/10.1016/j.jclepro.2017.10.078

Novais, R. M., Buruberri, L. H., Ascensão, G., Seabra, M. P., & Labrincha, J. A. (2016a). Porous biomass fly ash-based geopolymers with tailored thermal conductivity. Journal of cleaner production, 119, 99-107. https://doi.org/10.1016/j.jclepro.2016.01.083

Obonyo, E., Kamseu, E., Lemougna, P., Tchamba, A., Melo, U., & Leonelli, C. (2014). A sustainable approach for the geopolymerization of natural iron-rich aluminosilicate materials. Sustainability, 6(9), 5535-5553. https://doi.org/10.3390/su6095535

Onisei, S., Lesage, K., Blanpain, B., & Pontikes, Y. (2015). Early age microstructural transformations of an inorganic polymer made of fayalite slag. Journal of the American Ceramic Society, 98(7), 2269-2277. https://doi.org/10.1111/jace.13548

Peys, A. (2018). Inorganic Polymers from CaO-FeO-SiO2 Slag: Processing, Reaction Mechanism and Molecular Structure. https://lirias.kuleuven.be/2243005?limo=0

Peys, A., White, C. E., Rahier, H., Blanpain, B., & Pontikes, Y. (2019). Alkali-activation of CaO-FeOx-SiO2 slag: Formation mechanism from in-situ X-ray total scattering. Cement and Concrete Research, 122, 179-188. https://doi.org/10.1016/j.cemconres.2019.04.019

Provis, J. L., & Bernal, S. A. (2014). Geopolymers and related alkali-activated materials. Annual Review of Materials Research, 44, 299-327. https://doi.org/10.1146/annurev-matsci-070813-113515

Provis, J. L., Palomo, A., & Shi, C. (2015). Advances in understanding alkali-activated materials. Cement and Concrete Research, 78, 110-125, https://doi.org/10.1016/j.cemconres.2015.04.013

Provis, J. L., & Van Deventer, J. S. J. (Eds.). (2009). Geopolymers: structures, processing, properties and industrial applications. Elsevier.

Provis, J. L., & Van Deventer, J. S. (Eds.). (2013). Alkali activated materials: state-of-the-art report, RILEM TC 224-AAM (Vol. 13). Springer Science & Business Media, https://doi.org/10.1007/978-94-007-7672-2

Romagnoli, M., Leonelli, C., Kamse, E., & Gualtieri, M. L. (2012). Rheology of geopolymer by DOE approach. Construction and Building Materials, 36, 251-258. https://doi.org/10.1016/j.conbuildmat.2012.04.122

Romagnoli, M., Sassatelli, P., Gualtieri, M. L., & Tari, G. (2014). Rheological characterization of fly ash-based suspensions. Construction and Building Materials, 65, 526-534. https://doi.org/10.1016/j.conbuildmat.2014.04.130

Sakkas, K., Panias, D., Nomikos, P. P., & Sofianos, A. I. (2014). Potassium based geopolymer for passive fire protection of concrete tunnels linings. Tunnelling and underground space technology, 43, 148-156. https://doi.org/10.1016/j.tust.2014.05.003

Simon, S., Gluth, G. J., Peys, A., Onisei, S., Banerjee, D., & Pontikes, Y. (2018). The fate of iron during the alkali-activation of synthetic (CaO-) FeOx-SiO2 slags: An Fe K-edge XANES study. Journal of the American Ceramic Society, 101(5), 2107-2118. https://doi.org/10.1111/jace.15354

Sumabat, A. K. R., Mañalac, A. J., Nguyen, N. T., Kalaw, M. E., Tan, R. R., & Promentilla, M. A. B. (2015). Optimizing geopolymer-based material for industrial application with analytic hierarchy process and multi-response surface analysis. Chemical Engineering Transactions, 45, 1147-1152.

Van Deventer, J. S. J., Provis, J. L., Duxson, P., & Lukey, G. C. (2007). Reaction mechanisms in the geopolymeric conversion of inorganic waste to useful products. Journal of Hazardous Materials, 139(3), 506-513. https://doi.org/10.1016/j.jhazmat.2006.02.044

Van Jaarsveld, J. G. S., Van Deventer, J. S. J., & Lukey, G. C. (2004). A comparative study of kaolinite versus metakaolinite in fly ash based geopolymers containing immobilized metals. Chemical Engineering Communications, 191(4), 531-549. https://doi.org/10.1080/00986440490277974

Yip, C. K., Lukey, G. C., & van Deventer, J. S. (2005). The coexistence of geopolymeric gel and calcium silicate hydrate at the early stage of alkaline activation. Cement and concrete research, 35(9), 1688-1697. https://doi.org/10.1016/j.cemconres.2004.10.042

You, S.; Ho, S. W.; Li, T.; Maneerung, T.; Wang, C. H. Techno-economic analysis of geopolymer production from the coal fly ash with high iron oxide and calcium oxide contents. J Hazard Materials 2019, 361, 237-244. https://doi.org/10.1016/j.jhazmat.2018.08.089

Zahid, M., Shafiq, N., Isa, M. H., & Gil, L. (2018). Statistical modeling and mix design optimization of fly ash based engineered geopolymer composite using response surface methodology. Journal of cleaner production, 194, 483-498. https://doi.org/10.1016/j.jclepro.2018.05.158

Chapter 3

Development and optimization of IP binders and mortars

3.1 Exploratory tests

The following section is based on a set of unpublished data in which the firstly produced inorganic polymers (IPs) are described. The influence of several synthesis and processing parameters on the IPs hardened properties were evaluated and used to restrict the number of variables considered in ensuing experiments and to define areas of interest for further examination.

Raw materials characterization

To mimic the chemistry of the vitreous material resulting from the gasification/vitrification of refuse-derived fuel from ELFM, a synthetic glass was produced and used as IPs' main precursor. The synthetic slag (also termed throughout this work as plasmastone or simply PS) was produced by melting a mixture of bottom ash, iron ore, and sand in a CO/CO_2 atmosphere at a volumetric ratio of 2. The molten slag was quenched using water jets and a water tank to ensure a predominantly glassy structure. A more detailed description of the slag production process is provided by Machiels *et al.* (2017).

X-ray fluorescence (Bruker AXS S8 Tiger spectrometer) was used to determine the chemical composition of the raw materials used. The oxide composition of the slag can be described as a quaternary CaO-FeO_x-Al_2O_3-SiO_2 system, and its chemical composition is provided in Table 3.1.1. The slag mineralogical composition was assessed by X-ray diffraction (XRD), conducted on a Bragg-Brentano configuration, Bruker D8 Advance diffractometer, equipped with LinxEye detector (Cu Kα radiation λ=1.54059 Å, divergence slit 0.5°, Soller slit set 2.5°+2.5°, 5-70° 2θ, t/step 0.04 s and step/size of 0.02 °) and phase identification by EVA software. As previously reported in slags produced using the same process (Machiels, 2014; Kriskova, 2015), plasmastone was confirmed to be nearly 100% XRD amorphous.

The vitrified slag was received in a granular form, being posteriorly dried, homogenized, and milled in 4 kg batches. The milling process comprised three different stages: i) a 30 min pre-grinding stage using a pre-grinder mill, ii) a 240 min grinding stage using a ball mill to further reduce the slag particle size, and iii) a final sieving using a 254 µm mesh to eliminate any remaining coarse granules. This grinding procedure was maintained throughout the work unless otherwise explicitly mentioned, as in section 3.5.5 where the influence of pre- and grinding process duration on the particle size distribution were investigated to optimize the particle size distribution of IP mortars. The particle size distribution of the as-received and powdered slags were determined by a laser particle analyzer (Malvern Mastersizer 3000) and are shown in Figure 3.1.1.

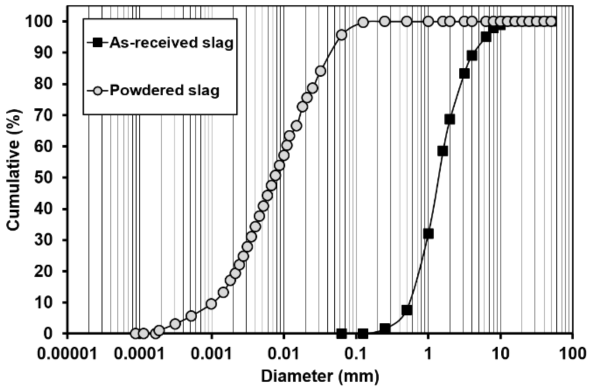

Figure 3.1.1 Slag particle size distribution before and after milling.

A multipycnometer (Quantachrome GmbH) was used to determine the slags' density, which was found to be 3.00±0.03 g/cm^3. The specific surface area (SSA) of the powdered precursor was determined by the Blaine method, being 450±20 m^2/kg. SSA was also determined using isotherm data according to the Brunauer–Emmett–Teller (BET) method (ISO 9277:2010), and a higher SSA value was observed, 1120 m^2/kg. The discrepancy between SSA values obtained using different testing procedures will be further addressed in section 3.5.4.

During the initial screening tests, an unknown batch of silica fume (SF_1) and metakaolin (MK, MetaStar® - Imerys Kaolin) were used as admixtures (wt% ≤7.0) to provide secondary sources of SiO_2 and Al_2O_3 and adjust binders' theoretical molar ratios assuming complete dissolution. Their oxide composition was determined by X-ray fluorescence and is presented in Table 3.1.1.

Table 3.1.1 Precursors' oxide composition in wt%.

Precursor	SiO_2	CaO	FeO_x	Al_2O_3	Others
Plasmastone	35	23	23	16	3
Silica fume	97	-	-	-	3
Metakaolin	52	-	-	44	4

Potassium and sodium hydroxide solutions (14M) were prepared by dissolving potassium (reagent grade, 85%, Carlo Erba, Italy) and sodium hydroxide beads (reagent grade, 97%, Carlo Erba, Italy) in demineralized water. All solutions used throughout this work were prepared in advance to allow them to cool down prior to the IP preparation. The potassium and sodium hydroxide solutions were diluted with varying amounts of demineralized water to adjust the concentration of activating solution and to achieve the binders' pre-defined S/L. The description of the experimental program and compositional parameters can be found in Table 3.1.2.

Binders' preparation and testing methods

Monolith samples of IPs pastes were synthesized following the procedure described by Ascensão *et al.* (2017) that involved: (a) the preparation of the alkaline medium by homogenizing the hydroxide solutions with demineralized water at 140 rpm for 300 s in a mortar mixer (Testing Bluhm & Beuerherdt Gmbh, Germany); (b) manually mixing the dried solid components in a plastic container; (c) mixing the solid and liquid components for 600 s at the same speed in the mortar mixer mentioned above. After mixing, the polymeric pastes were cast into 5x5x5cm^3 metallic molds and cured for 24 h at 20±1 °C and 95±1 % RH, being afterward demolded and cured at room conditions (20±1 °C; RH=65±5 %) until testing. The IP apparent density was determined by the relation between the weight and volume of each sample, while the compressive strength was determined using a Universal Testing Machine (Controls model) according to the EN196-1(2016).

Design of experiments

The experiments carried throughout this work, although different among them, were governed by some common denominators. The mix design should be able to provide materials that meet established technical requirements but also consider environmental and economic criteria. In that sense, the use of high contents of CaO-FeO_x-Al_2O_3-SiO_2 residues was established as a priority, and the use of alkaline activators and energy-intensive curing processes was restricted as much as possible. Plasmastone was defined as the main precursor being established that least 50 % of this residue had to be used in the solid part of the binders' formulations. Following this rationale, the single-use of hydroxide solutions was initially considered in these exploratory tests as silicate solutions represent between 50-80% of the production costs and environmental burdens of alkali-activated materials (Dimas, 2009; Abdulkareem, 2019). The beneficial impacts of using minor dosages of silicates in the activating solution will be discussed in section 3.3 where a comparative study between hydroxide and blended activating solutions was performed.

To firstly assess the impact of different synthesis parameters on AAM's properties, specimens corresponding to two half-*factorial* designs were produced. The compositional and synthesis factors considered, and their corresponding levels were selected based on available literature and are presented in Table 3.1.2. These screening experiments aimed to determine the most relevant processing parameters and reveal areas of interest for future research. Compressive strength and apparent density were considered adequate performance indicators to determine the parameters governing alkali-activation reactions and IPs' hardened state properties.

Table 3.1.2 Screening DoE- Experimental matrix of potassium and sodium activated pastes and evaluated responses.

DoE	**Run n° & code**	**Factors**				**Responses**	
		SiO_2/ (Al_2O_3+Fe_2O_3)	**m_2O/ SiO_2**	**S/L**	**Temp.**	**App. density (g/cm^3)**	**Compressive strength (MPa)**
KOH	PK7	2.50	0.17	2.25	20	2.25	44.1
	PK4	2.50	0.17	1.75	40	1.74	1.1
	PK2	1.95	0.23	1.75	40	1.97	19.7
	PK3	1.95	0.17	1.75	20	1.74	7.6
	PK6	1.95	0.17	2.25	40	2.12	28.7
	PK8	1.95	0.23	2.25	20	2.14	19.3
	PK5	2.50	0.23	1.75	20	2.01	47.2
	PK1	2.50	0.23	2.25	40	2.22	45.7
NaOH	PN1	2.50	0.23	2.25	40	2.11	18.1
	PN2	2.50	0.23	1.75	20	1.99	5.3
	PN5	1.95	0.33	1.75	20	2.06	0.6
	PN3	1.95	0.23	1.75	40	1.99	11.0
	PN6	1.95	0.23	2.25	20	2.20	0.5
	PN8	1.95	0.33	2.25	40	2.31	44.2
	PN7	2.50	0.33	1.75	40	2.04	5.1
	PN4	2.50	0.33	2.25	20	2.27	0.5

As RDF slags present relatively low contents of aluminum and significant amounts of iron on their bulk composition, $SiO_2/(Al_2O_3+FeO_x)$ molar ratio was considered during mix design instead of the frequently reported SiO_2/Al_2O_3 in iron-free aluminosilicate systems. This consideration is justified by the fact that iron compounds can, depending on its form, act either as network formers or as network modifiers, and have a remarkable influence on the reaction kinetics and the degree of crosslinking of the final polymeric structure. It should be emphasized here that Al substitution by Fe and/or Ca ions impose considerable changes in polymeric structures, and therefore, IPs are structurally different from conventional aluminosilicate geopolymers (see Chapter 2 for further details). Further considerations on the effects of iron and calcium "enrichment" of aluminosilicate structures will be provided later in this work.

The experimental matrix of the screening DoEs was defined and analyzed using commercially available software (i.e., R GUI and Minitab 18). As an example, the scripts employed to obtain the experimental matrixes of KOH-based IPs are provided below. A similar approach was followed throughout different chapters of this work, but the individual scripts will not be provided for the sake of conciseness.

```
#R-Script used to obtain the experimental matrix using potassium hydroxide in the activating solution.

SDoEK=FrF2(nruns = 8, ncenter = 0, nfactors = 4, replications = 1, repeat.only = FALSE, factor.names = list(X = c(1.95, 2.50), Y = c(0.17, 0.23), Z = c(1.75, 2.25), T = c(20, 40)), randomize = TRUE)
```

where X, Y, Z, and T represent $SiO_2/(Al_2O_3+Fe_2O_3)$ molar ratio, m_2O/SiO_2 molar ratio (representing m, Na or K cations), solid-to-liquid mass ratio, and curing temperature during the initial 24 h, respectively. Notice that the two 2-level half-factorial DoEs were produced independently and in a randomized order to avoid systematic experimental errors. No central points or replicates were produced at this stage. The two 2-level half-factorial DoE comprise eight experiments each, making a total sum of sixteen formulations. The type of alkali cation in the hydroxide solution was not considered as a factor, and each of the DoEs was designed individually. The levels of each factor were maintained equal except for m_2O/SiO_2 molar ratio. Lower values for this variable were selected for KOH-based systems since K^+ ions promote greater oligomer connectivity favoring the formation of more stable three-dimensional architectures, hence promoting higher strength development compared to their Na^+ counterparts (Poulesquen, 2011). In addition, potassium-based solutions also produce more viscous pastes, and therefore reducing m_2O/SiO_2 molar ratio increased the workability and setting time of the produced IPs.

The selection of different m_2O/SiO_2 ranges may hinder the direct comparison between NaOH and KOH systems, but a qualitative analysis was still possible. For computational simplicity all variables were computed in a binomial form (-1,+1), representing the lower and upper-level of each factor. Table 3.1.2 shows the experimental matrix including the sequence in which the specimens were produced while their bulk composition is presented in Table 3.1.3.

Table 3.1.3 Bulk composition of pastes produced during screening experimental designs.

DoE	Run n° & code	Solid precursors			Activating solution	
		PS	SF_1	MK	mOH	H_2O
KOH	PK7	60.0	6.6	2.6	14.9	15.9
	PK4	55.0	6.0	2.6	13.7	22.6
	PK2	62.5	0.0	1.2	15.9	20.5
	PK3	62.5	0.0	1.2	11.5	24.9
	PK6	68.1	0.0	1.2	12.5	18.3
	PK8	68.1	0.0	1.2	17.3	13.5
	PK5	55.0	6.0	2.6	19.0	17.3
	PK1	60.0	6.6	2.6	20.7	10.1
NaOH	PN1	60.0	6.6	2.6	19.4	11.6
	PN2	55.0	6.0	2.6	17.6	18.7
	PN5	62.5	0.0	1.2	21.7	14.7
	PN3	62.5	0.0	1.2	14.7	21.6
	PN6	68.1	0.0	1.2	16.0	14.8
	PN8	68.1	0.0	1.2	23.6	7.2
	PN7	55.0	6.0	2.6	25.8	10.5
	PN4	60.0	6.6	2.6	28.1	2.7

*** PS** = Plasmastone; **SF_1**= Sil**ica Fume; MK=** Metakaolin; **mOH=** potassium or sodium hydroxide.

Results and discussion

The responsiveness of IPs' apparent density and compressive strength to the modifications imposed on their composition and curing conditions were clearly observed. Apparent density ranged from 1.74 to 2.27 g/cm^3 while the variation of compressive strength at 7 d was even more significant, varying from 0.5 to 47.2 MPa. However, the selected parameters exerted different levels of influence on the measured properties. Figures 3.1.2 show examples of contour plots where the compressive strength of KOH systems was predicted as a function of $SiO_2/(Al_2O_3+Fe_2O_3)$ and solid-to-liquid. In Figure 3.1.2a, b variable T was fixed at level 0 (meaning 30 °C) while Y was fixed as -1 in Figure 3.1.2a ($m_2O/SiO_2=0.17$) and 1 in Figure 3.1.2b ($m_2O/SiO_2=0.23$). Conversely, in Figure 3.1.2c,d variable Y was fixed at level 0 ($m_2O/SiO_2=0.20$) while T was fixed as -1 in Figure 3.1.2c (20 °C) and 1 in Figure 3.1.2d (40 °C). A similar logic was applied in multiple configurations of constants and variables. It should be mentioned that in unreplicated *fractional* factorial designs the lack of degrees of freedom hinders the visualization of surface responses and to overcome such restriction a 5% standard deviation was assumed.

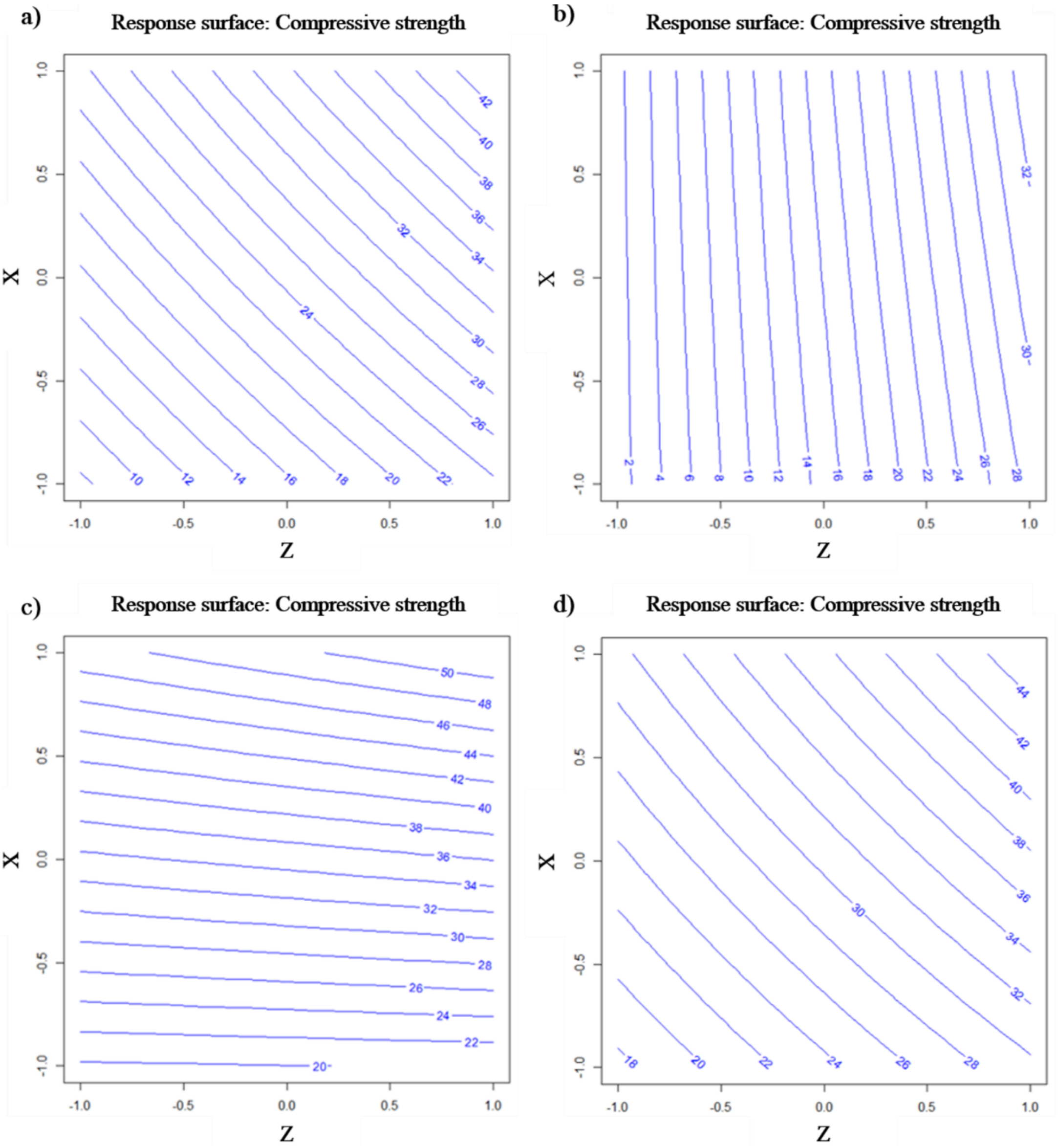

Figure 3.1.2 Examples of contour plots where the 7 d compressive strength of KOH-based IPs is predicted as a function of $SiO_2/(Al_2O_3+Fe_2O_3)$ molar ratio (X) and S/L ratio (Z).

In both *fractional* designs, rising $SiO_2/(Al_2O_3+Fe_2O_3)$ molar ratio led to an increase of strength development demonstrating that such compositional parameter significantly affects the formation of polymerized structures. IP structures are constituted of cross-linked SiO_4 tetrahedrons and increasing the availability of Si units promoted the formation of stronger Si-O-Si bonds, ultimately leading to the development of higher mechanical performances. Nonetheless, the $SiO_2/(Al_2O_3+Fe_2O_3)$ molar ratio in the composition of residues used here as precursor does not exceed 2.0 and, therefore, an increase in such synthesis parameter would forcibly require the use of considerable dosages of Si-rich admixtures or activating solutions. Despite the beneficial effects of raising $SiO_2/(Al_2O_3+Fe_2O_3)$ molar ratio, the ambition of this work was to maximize the volumes of FeO_x-CaO-rich slag reintroduced into the materials cycle while minimizing the use of activating solutions, additives, and admixtures. For those reasons, in ensuing experiments, $SiO_2/(Al_2O_3+Fe_2O_3)$ was fixed at 2.50 since IP binders with a compressive strength that surpasses 40 MPa after 7 d of curing could be produced without exceeding such threshold value (Table 3.1.2). Those compressive strength values are compliant with the requirements of a large group of applications in the construction sector. Moreover, further enhancements of strength development could be later achieved by proper mix design with $SiO_2/(Al_2O_3+Fe_2O_3)$ ratios lower than 2.50.

Curing temperature and m_2O/SiO_2 molar ratio as singular parameters had a small influence on strength development but their combined effect with $SiO_2/(Al_2O_3+Fe_2O_3)$ molar ratio and S/L ratio were significant in terms of strength development. In fact, the highest compressive strength (47.2 MPa) was achieved with the lowest curing temperature (20 °C) and decreasing K_2O/SiO_2 molar ratio had only resulted in a 7 % reduction of compressive strength (44.1 MPa). These two parameters have a direct impact on IPs production cost and environmental impact, and therefore low curing temperatures and K_2O/SiO_2 molar ratio should be promoted if possible. Later on this work, it will be shown that heat-curing at slightly elevated temperatures is beneficial to IPs' volumetric stability and strength development if water evaporation is avoided. In these tests, however, the specimens were not sealed during the first day of curing and, therefore the kinetic enhancement promoted by slightly elevated temperatures was counteracted by the rapid dehydration of the structure, resulted in some crack formation. These results agree with the findings of Iacobescu *et al.* (2017), who also had reported crack formation when heat-curing IP mortars produced from fayalitic slags. The type of activator had a determinant effect on efflorescence formation. The use of NaOH solutions had promoted the formation of severe efflorescence, while in KOH-based IPs no efflorescence was observed. Efflorescence formation can be partially attributed to the higher concentrations of NaOH activating solutions but also to the fact that Na^+ ions tend to be more weakly bonded to the aluminosilicate framework than their K^+ counterparts. In fact, even NaOH-based IPs synthesized with the lowest m_2O/SiO_2 molar ratio presented heavy efflorescence while in KOH-based IPs produced with equal m_2O/SiO_2 molar ratios no efflorescence was observed. The chemical composition of the white crystals formed was analyzed and confirmed to be sodium carbonates. The mechanism of sodium carbonates formation under natural carbonation has been previously described by Zhang *et al.* (2014). The formation of carbonate crystal confirmed that at least part of Na ions was not chemically bonded to the polymeric structure, demonstrating the excessive concentration of the activation solution. However, the formation of efflorescence did not have a direct detrimental effect on IPs' mechanical properties. The compressive strength of KOH-activated IPs ranged from 1.1 to 47.2 MPa after 7 d of curing, whereas in their NaOH counterparts ranged from 0.6 to 44.1 MPa. A similar trend was observed regarding apparent density. Thus, apparent density and strength development were not defined by the type of activator, but considering the higher dosages used and the heavy efflorescence formed in Na IPs, ensuing research and analysis were focused on potassium activated formulations.

On the other hand, increasing S/L ratio has a considerable beneficial impact on strength development. Higher S/L ratio led to superior mechanical performance that can be attributed to the combined effects of i) higher availability of dissolved species that increased the formation of binding phases, ii) the consequent reduction of porosity and increase of density and iii) the presence of higher amounts of undissolved particles which act as small-size aggregates and prevent crack propagation. This general trend was only modified when lowering SiO_2/ (Al_2O_3+Fe_2O_3) molar ratio which has obliterated the positive effect of increasing S/L ratio.

Nonetheless, these results allowed to foresee that increasing S/L ratio upper limits would result in enhanced mechanical performances, particularly if high SiO_2/ (Al_2O_3+Fe_2O_3) were maintained. To verify such predictions, PK7 formulation was selected to be reproduced with higher S/L ratios. The initial formulation (S/L=2.25) was tailored by progressively increasing S/L ratio by a factor of 0.25 up to S/L=3.0. The experimental error of the initial exploratory tests was also assessed by producing replicates of four KOH-based IPs. The IPs' apparent density and compressive strength, and corresponding standard deviations are shown in Table 3.1.4. As can be seen, reduced experimental variations were observed, attesting the robustness of the mix designs chosen.

Table 3.1.4 Reproducibility tests and sequential optimization trials.

	Code	Responses			
		App. density (g/cm^3)	STDEV	Compressive strength (MPa)	STDEV
Replicates	PK7	2.25	0.03	44.1	0.4
	PK7$_{rep}$	2.29		43.5	
	PK4	1.74	0.00	1.1	0.6
	PK4$_{rep}$	1.74		1.9	
	PK2	1.97	0.00	19.7	2.3
	PK2$_{rep}$	1.97		15.8	
	PK8	2.14	0.01	19.3	1.2
	PK8$_{rep}$	2.12		21.1	
Sequential Improvement	PK7	2.27	0.03	43.8	0.4
	PK7$_2$	2.23	-	44.8	-
	PK7$_3$	2.26	-	65.8	-
	PK7$_4$	2.35	-	74.6	-

The influence of increasing the S/L ratio on strength development was almost linear. The progressive increase of S/L rose compressive strength to a maximum value of 74.6 MPa in IPs produced with the highest S/L= 3.0 (PK7$_4$). It should be noticed that PK7 IPs were all cured at 20 °C and produced with a K_2O/SiO_2 molar ratio of 0.17. Such results validated the claims made based on the analysis of the results of exploratory tests and demonstrated that IPs can be synthesized with activating solutions of low concentration, cured at room temperature, and still exhibit elevated mechanical performances.

To further investigate the produced IPs, a new 2^3 full-factorial DoE was performed, and the results are discussed in the next section. The scope of the research was extended beyond the physical-mechanical properties and comprised fresh-state properties and microstructural analysis. In those experiments, SiO_2/ (Al_2O_3+Fe_2O_3) was fixed at 2.50, and S/L varied from 2.50 to 2.90. Despite significant effect seem unlikely, the impact of the KOH molarity was also assessed.

References

Abdulkareem, M., Havukainen, J., & Horttanainen, M. (2019). How environmentally sustainable are fibre reinforced alkali-activated concretes? Journal of Cleaner Production, 236, 117601. https://doi.org/10.1016/j.jclepro.2019.07.076

Ascensão, G., Seabra, M. P., Aguiar, J. B., & Labrincha, J. A. (2017). Red mud-based geopolymers with tailored alkali diffusion properties and pH buffering ability. Journal of Cleaner Production, 148, 23-30.https://doi.org/10.1016/j.jclepro.2017.01.150

Dimas, D., Giannopoulou, I., & Panias, D. (2009). Polymerization in sodium silicate solutions: a fundamental process in geopolymerization technology. Journal of Materials Science, 44(14), 3719-3730. https://doi.org/10.1007/s10853-009-3497-5

EN, B. (2016). 196-1: 2016. Methods of Testing Cement. Determination of Strength.

Iacobescu, R. I., Cappuyns, V., Geens, T., Kriskova, L., Onisei, S., Jones, P. T., & Pontikes, Y. (2017). The influence of curing conditions on the mechanical properties and leaching of inorganic polymers made of fayalitic slag. Frontiers of Chemical Science and Engineering, 11(3), 317-327. https://doi.org/10.1007/s11705-017-1622-6

ISO 9277:2010 Determination of the specific surface area of solids by gas adsorption–BET method. Geneva: International Organization for Standardization.

Kriskova, L., Machiels, L., & Pontikes, Y. (2015). Inorganic polymers from a plasma convertor slag: effect of activating solution on microstructure and properties. Journal of Sustainable Metallurgy, 1(3), 240-251. https://doi.org/10.1007/s40831-015-0022-8

Machiels, L., Arnout, L., Jones, P. T., Blanpain, B., & Pontikes, Y. (2014). Inorganic polymer cement from Fe-silicate glasses: varying the activating solution to glass ratio. Waste and Biomass Valorization, 5(3), 411-428. https://doi.org/10.1007/s12649-014-9296-5

Machiels, L., Arnout, L., Yan, P., Jones, P. T., Blanpain, B., & Pontikes, Y. (2017). Transforming enhanced landfill mining derived gasification/vitrification glass into low-carbon inorganic polymer binders and building products. Journal of Sustainable Metallurgy, 3(2), 405-415.https://doi.org/10.1007/s40831-016-0105-1

Poulesquen, A., Frizon, F., & Lambertin, D. (2011). Rheological behavior of alkali-activated metakaolin during geopolymerization. Journal of Non-Crystalline Solids, 357(21), 3565-3571. https://doi.org/10.1016/j.jnoncrysol.2011.07.013

Zhang, Z., Provis, J. L., Reid, A., & Wang, H. (2014). Fly ash-based geopolymers: the relationship between composition, pore structure and efflorescence. Cement and Concrete Research, 64, 30-41. https://doi.org/10.1016/j.cemconres.2014.06.004

3.2 Influence of microstructure on strength development

The following section is partially based on a conference paper entitled “Influence of microstructure on the mechanical strength of alkali-activated Fe-Si-Ca-rich materials” by Ascensão, G., Faleschini, F., Marchi, M., Segata & Pontikes, Y. published in the *Proceeding of the 4th International Symposium On Enhanced Landfill Mining,* page 285-290, February 2018, Mechelen, Belgium.

The mentioned paper covers investigations on hydroxide activated systems, and the experimental domain reported here was defined based on the considerations made in the previous section. The experimental domain was posteriorly expanded, being such expansion later justified in this work. A discussion on the use of silicate activating solutions is also included. In the following text, some adjustments were made relative to the original publication in order to incorporate additional insights and provide a more detailed discussion.

Introduction

The use of RDF residues as inorganic polymers precursors is incipient (EU Commission, 2016), and suggested applications are still limited to low-value applications (Machiels, 2017). However, Bosmans *et al.* (2013) highlighted that high-end secondary products could be developed from CaO-FeO_x-Al_2O_3-SiO_2-rich residues if in-depth research is conducted on novel waste-based products. Although sequential optimization path mainly focused on alkali-activated mortars’ hardened properties has been reported, systematic studies to assess the influence of compositional effects on fresh and hardened state properties of CaO-FeO_x-Al_2O_3-SiO_2-rich IPs binders are scarce.

Aiming to contribute to the design and conceptual development of value-added waste-based products, the scope of this work was to identify the effects of different processing parameters on the synthesis of IP binders. DoE methodology was used to evaluate the effect of three main compositional factors, their interaction, and the system responses.

Experimental

A two-level full factorial design with a central point was employed to assess the influence of three variables (S/L ratio, K_2O/SiO_2 molar oxide ratio and, KOH solution molarity) on the properties of the produced IPs. Their minimum and maximum values and the description of the experimental design are given in Table 3.2.1 and Table 3.2.2. The oxide composition of the slag used as main precursor can be found in Table 3.1.1. Silica fume and commercially available metakaolin (see Table 3.1.1) were used as admixtures at levels not exceeding 10 wt%.

Potassium hydroxide solutions were used to provide the alkaline medium (prepared using reagent grade hydroxide beads, 85%, Carlo Erba, Italy), and demineralized water was added to achieve the pre-defined S/L ratio. The use of M-silicates was not considered in this stage of development.

In PS3 and PS8 IPs, an additional 7.7 g/kg_{slurry} of demineralized water were provided to achieve the required flowability to cast the samples properly. The IP synthesis followed the procedure described in section 3.1. IP pastes were cast into $4x4x16cm^3$ molds and cured for 24 h at 20 °C and 95 % RH, being afterward demolded and kept at room conditions (20 °C and 65 % RH).

The pastes’ setting time was determined according to the EN 196-3:2016, and rheological measurements were performed using a ThermoHAAKE Rotovisco1 rheometer. Shear rates between 0 and 105 s^{-1} (up and down curves) were employed in a rheological profile with a total duration of 600 s. Down curves were fitted to the Herschel-Bulkley model and used to determine the pastes' viscosity, shear behavior, and yield stress.

The IPs' mineralogical composition was assessed by X-ray diffraction as described in section 3.1. Scanning electron microscopy (SEM - EVO® MA 15) equipped with energy dispersive X-ray spectrometry (EDS, AZtecEnergy) was used to evaluate the IPs microstructure. Archimedes method was employed to evaluate water absorption, while open porosity was estimated as described in the literature (Landi, 2013; Ascensão, 2017). Apparent density was determined by the relation between the weight and volume of each sample. The flexural and compressive strength were determined using a Universal Testing Machine (Controls model 50-C7022) according to the EN196-1:2016. The experimental error was assessed by testing a minimum of two samples produced independently for each formulation and curing age.

Table 3.2.1 Molar ratios of the 2^3 full-factorial design formulations.

Code	**Molar oxide ratios**				
	SiO_2/ (Al_2O_3+Fe_2O_3)	**K_2O/Al_2O_3**	**K_2O/ (Al_2O_3+Fe_2O_3)**	**K_2O/SiO_2**	**H_2O/K_2O**
PS1	2.50	0.91	0.51	0.200	10.98
PS2		0.77	0.43	0.170	13.94
PS3		0.91	0.51	0.200	8.81
PS4		0.77	0.43	0.170	11.35
PS5		0.84	0.47	0.185	11.09
PS6		0.91	0.51	0.200	10.98
PS7		0.77	0.43	0.170	13.94
PS8		0.91	0.51	0.200	8.81
PS9		0.77	0.43	0.170	11.35

Table 3.2.2 Two-level full-factorial design: studied variables and their respective levels. The central point formulation is highlighted in grey.

Code	**PS1**	**PS2**	**PS3**	**PS4**	**PS5**	**PS6**	**PS7**	**PS8**	**PS9**
S/L	2.50		2.90		2.70	2.50		2.90	
K_2O/SiO_2	0.200	0.170	0.200	0.170	0.185	0.200	0.170	0.200	0.170
KOH $_{mol/L}$	14				12	10			

Results and discussion

Setting time

Table 3.2.3 shows that the pastes' initial and final setting time were affected differently by the compositional parameters studied. The analysis of the standardized effects of each parameter demonstrated that the influence of such factors is time-dependent, and significant changes in setting times were promoted by S/L ratio and K_2O/SiO_2 molar ratio. The molarity of the initial activating solution had a much less significant impact (Figure 3.2.1). As S/L ratio decreased, the initial and final setting times were delayed, indicating a reduction in the precursor's reactivity and ensuing polymerization. As the solution content rose, the concentration of dissolved species and nucleation sites was reduced, which in turn, retarded the formation of IP networks (Arnout, 2017). For example, one can see that PS1 IPs were characterized by a final setting time of 275 min, while PS3 presented the lowest final setting time (175 min), representing a reduction of approximately 36%.

Table 3.2.3 IPs pastes setting times and rheological properties.

Code	Initial setting	Final setting	Yield stress (τ_0)	K	n	R
	Min.	Min.	Pa	(-)	(-)	(-)
PS1	209	275	149	1.6	1.3	0.996
PS2	290	360	120	2.8	1.1	0.994
PS3	93	175	302	0.4	1.7	0.996
PS4	165	233	295	1.4	1.4	0.998
PS5	184	245	201	1.3	1.3	0.997
PS6	155	225	119	1.2	1.2	0.994
PS7	297	355	99	1.1	1.1	0.994
PS8	115	189	269	1.6	1.6	0.997
PS9	133	198	253	1.3	1.3	0.996

Increase K_2O/SiO_2 molar ratio also promoted a reduction in setting times. The increase of the solution pH and a rise in the number of available ions in the activating medium had favored the precursors' dissolution (later discussed in detail) and enhanced the overall reaction kinetics.

By simply tailoring the three main factors investigated here, initial settings ranging from approximately 90 min up to 300 min were attained. Such a versatile nature of the developed IPs in terms of setting times allows foreseeing its use in different applications. Whereas in common building applications extended setting times are preferable, in some innovative applications (e.g., direct ink writing, DIW) shortened setting times are instead required.

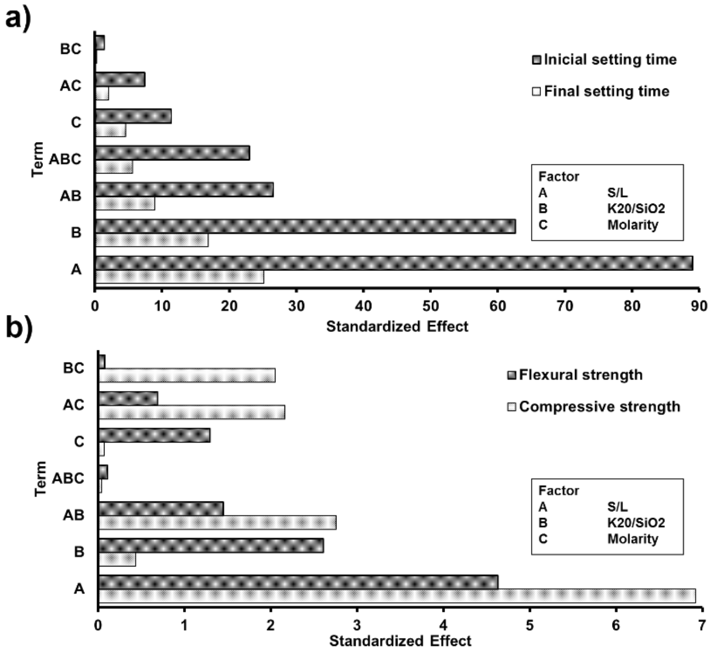

Figure 3.2.1 Standardized effects of the compositional parameters studied on a) setting time and b) flexural and compressive strength after 28 d of curing.

Rheological behavior

Rheological data were elaborated through commercial software and fitted using a three-parameter rheological model, the Herschel-Bulkley model (Equation 3.1):

$$\begin{cases} \tau = \tau_0 + K\dot{\gamma}^n & \tau > \tau_0 \\ \dot{\gamma} = 0 & \tau \leq \tau_0 \end{cases} \qquad (3.1)$$

where τ is the shear stress (Pa), $\dot{\gamma}$ is the shear rate (s^{-1}), and the H-B parameters are τ_0, K and n, being respectively the yield stress (Pa), the consistency factor (Pa s^n), and the flow index (R).

H-B parameters are reported in Table 3.2.3, and the high correlation coefficient (*R* above 0.99 for all IPs) indicates that the effects of each parameter could be assessed with a reasonable degree of confidence. The range of analysis was limited to the descendent part of the curve since correlation coefficients tend to be more stable in that branch of the curve. The analysis of H-B parameters has shown flow indexes (***n***) higher than 1. These results imply that power-equation is reproducing a shear-thickening behavior similar for instance, to self-compacting concretes (SCC).

The solid load in the suspension was enough to avoid the classical shear-thinning behavior displayed by many traditional suspensions, and yield stresses were considerably high, almost in all cases above 100 Pa. Such values of yield stresses are frequently observed in SCC and ordinary OPC-concrete but are much higher than those reported in alkali-activated pastes, < 35 Pa (Romagnoli, 2012). The shear-thickening behavior was particularly evident in IPs with higher S/L ratio. Figure 3.2.2 shows the overall flow curves of the analyzed mixtures, each one obtained with 150 experimental measurements. It is worth noting that, at a low shear rate, apparent viscosity values were considerably higher. In this range, the contribution of the Brownian forces was predominant. At higher shear rates, hydrodynamic effects were increased, and the particles forced to initiate motion, which resulted in a reduction of apparent viscosity.

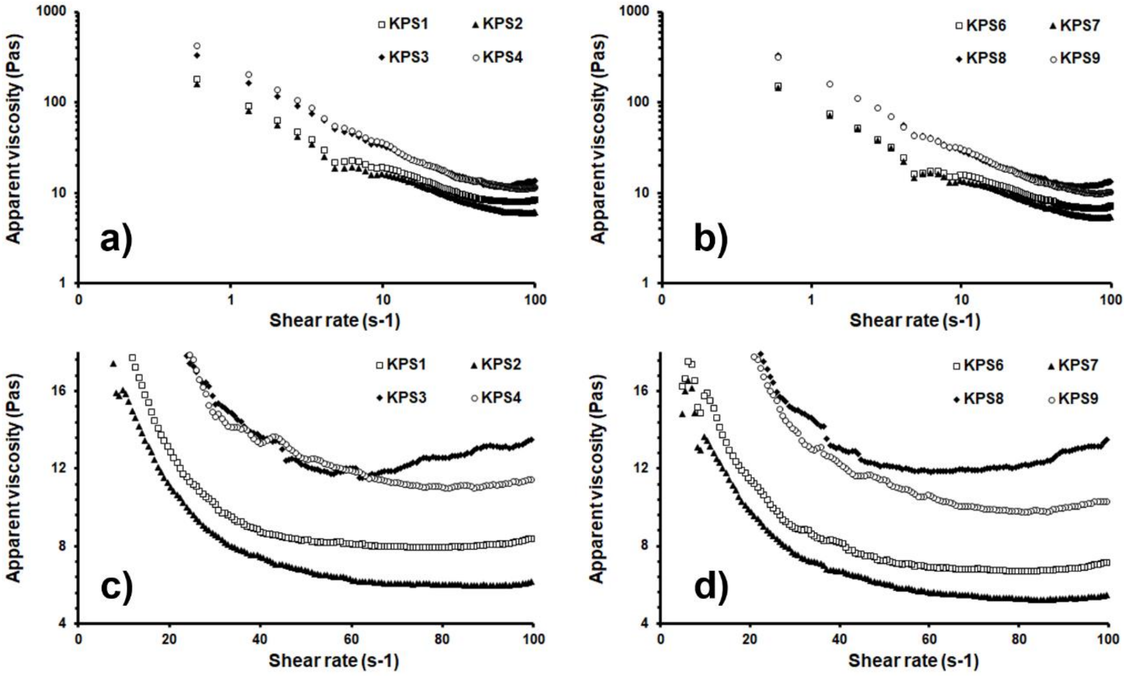

Figure 3.2.2 Flow curves of IP pastes activated with 14M (a and c) and 10M (b and d) potassium hydroxide solutions.

Properties of hardened pastes

Figure 3.2.3a and b show representative scanning electron microscopy (SEM) micrographs of IPs after 28 d of curing. Unreacted particles were detected, showing that precursors' complete dissolution did not occur. The high content of solid precursors limited dissolution, but all IPs exhibited a homogeneous matrix where undissolved particles act as small-sized aggregates. These results agree with previous findings (Machiels, 2014), which had reported samples with similar S/L ratios having a degree of precursor’s dissolution around 76%. The K_2O/SiO_2 molar ratio affected the precursors' degree of dissolution while changes in KOH molarity induced less pronounced microstructural changes. Although such quantification has not been performed, when comparing PS1 and PS2 (Figure 3.2.3), one can see that as the K_2O/SiO_2 molar ratio decreases, the content of unreacted particles rises. EDS analyses revealed a binder phase predominantly composed of Si, Al, Fe, Ca and K, while undissolved particles' spectra were in-line with the chemical composition of the parent slag (Figure 3.2.3b). Elemental mapping did not suggest crystalline precipitations, being in line with XRD data and SEM observations. The XRD patterns of the IPs binders had revealed their amorphous nature, with only one low-intensity crystalline diffraction peak identified as calcite ($CaCO_3$; PDF 01-088-1807), Figure 3.2.4.

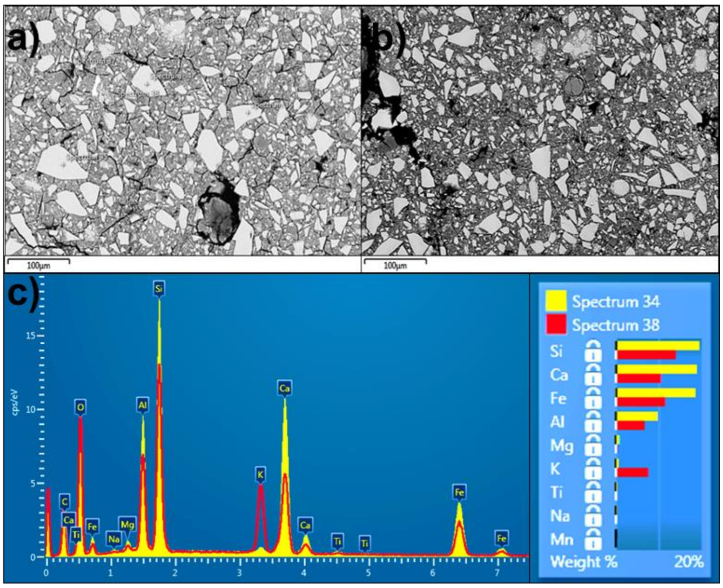

Figure 3.2.3 SEM micrographs of PS1 (a) and PS2 (b) and representative EDS spectra from PS1 where spectrum #34 shows unreacted particles and spectrum #38 the binder phase formed (c).

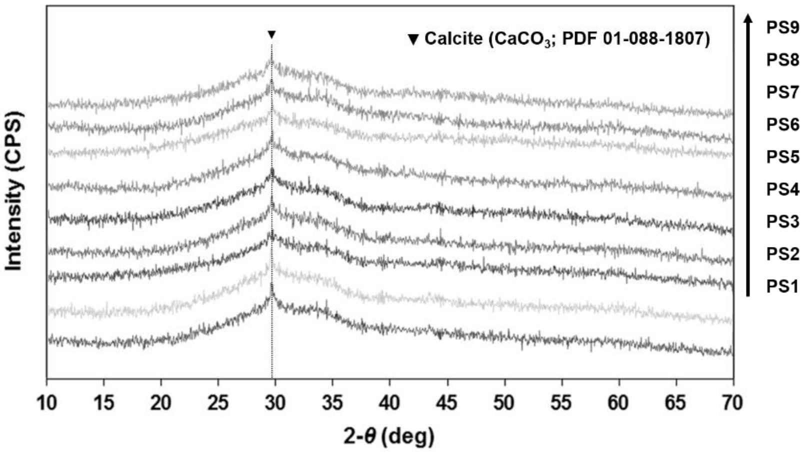

Figure 3.2.4 XRD patterns of IPs samples after 28 d of curing.

Spherical large size pores were observed in all IPs, which can be attributed to entrapped air during mixing; no correlation was found between the amount pores and their size and the studied compositional parameters. On the other hand, the length and size of micro-cracks seem to be governed by K_2O/SiO_2 molar ratio. Three simultaneous effects may contribute to such behavior: (i) crack development and propagation is limited by the presence of undissolved particles, which was incremented by lowering the K_2O/SiO_2 molar ratio (Machiels, 2014); (ii) a delay effect on elasticity development, as higher H_2O/K_2O ratios decrease the rate and total extent of binder formation, resulting in lower autogenous shrinkage (Beersaerts, 2017) and (iii) lower polymerization degree resulting in less intensive exothermic reactions that decrease the internal temperature during the polycondensation process, hence slower settings and hardening of the IP network (Machiels, 2017). Nonetheless, such pores and micro-cracks did not have a significant influence on open porosity and water absorption capacity, which suggests their closed nature and low connectivity (Table 3.2.4). S/L ratio determined the IPs density and open porosity, whereas increasing the K_2O/SiO_2 ratio contributed to further densification. Rising the K_2O/SiO_2 ratio maximized binder formation, leading to more homogenous binder matrixes. Regardless of the beneficial effect of limiting crack formation, PS3 and PS8 have shown the lowest water absorption and open porosity values. The impact of the initial solution molarity can also be seen, and IPs produced with 10 M KOH solutions were slightly less porous than their 14 M KOH counterparts. By combining high S/L and K_2O/SiO_2 ratios and using 10 M KOH solutions, IPs with the highest density were produced (2.30 ± 0.02 g/cm^3).

Table 3.2.4 IPs apparent density, open porosity, and water absorption after 7 and 28 d of curing.

Code	7th day			28th day		
	Apparent density	Open porosity	Water absorption	Apparent density	Open porosity	Water absorption
	g/cm^3	%	%	g/cm^3	%	%
PS1	2.23±0.01	0.6±0.1	0.3±0.0	2.21±0.00	2.3±0.1	1.0±0.0
PS2	2.14±0.00	1.4±0.1	0.7±0.0	2.13±0.01	3.0±0.2	1.4±0.1
PS3	2.28±0.02	0.3±0.1	0.2±0.0	2.29±0.04	1.0±0.0	0.4±0.0
PS4	2.20±0.04	0.6±0.2	0.3±0.1	2.27±0.01	1.5±0.0	0.7±0.0
PS5	2.25±0.01	0.5±0.1	0.2±0.0	2.21±0.01	1.3±0.2	0.6±0.1
PS6	2.21±0.01	0.6±0.1	0.2±0.0	2.20±0.01	1.6±0.4	0.7±0.2
PS7	2.15±0.00	1.1±0.1	0.5±0.0	2.13±0.01	2.1±0.1	1.0±0.0
PS8	2.28±0.02	0.4±0.1	0.2±0.0	2.30±0.02	0.7±0.2	0.3±0.1
PS9	2.22±0.02	0.8±0.1	0.4±0.0	2.25±0.01	1.2±0.1	0.5±0.0

IP's mechanical properties were measured after 7 and 28 d of curing, and the best mechanical performances were achieved by IPs produced with S/L=2.90, namely samples PS3, 4, 8, and 9 (Figure 3.2.5). Flexural strength diminished over time, while compressive strength exhibited the opposite trend. As previously reported by Arnout *et al.* (2017), polymerization reactions are not concluded after 7 d of curing, and the on-going reorganization of the structure can lead to increases of compressive strength over time. However, the increase of rigidity of highly cross-linked structures can also lead to poor flexural performances. A reduction of IP flexural strength over time was observed in all IPs varying from 15 to 46%. The distinct influence of each compositional parameter and their synergetic effects on strength development can be observed through its standardized effect shown in Figure 3.2.1, while the flexural and compressive surface responses are shown in Figure 3.2.6.

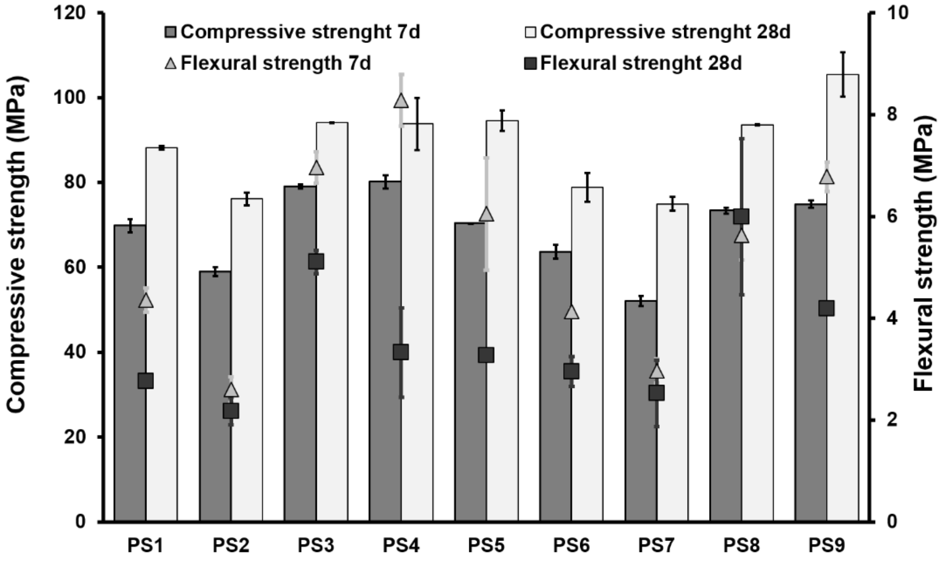

Figure 3.2.5 IPs flexural and compressive strength temporal evolution and corresponding standard deviations.

In general, decreasing the S/L ratio was detrimental to strength development and the dominant character of compositional factor affected both flexural and compressive strength. KOH molarity assumed a significant role regarding the development of flexural strength while its synergistic effects with S/L and K_2O/SiO_2 have a significant impact on compressive strength (Figure 3.2.6b). In high S/L ratio IPs, rise K_2O/SiO_2 molar ratio promoted better flexural strengths, whereas in IPs prepared with a lower S/L ratio no significant changes occurred. Compressive strength was particularly enhanced when K_2O/SiO_2 ratio was rose in IPs prepared with S/L = 2.50, but no evident beneficial effect could be seen at higher S/L ratios. In IP synthesis, compositional and processing parameters are often considered individually underestimating their combined effects. The results presented herein confirmed the relevancy of synergic effects on IP properties (as identifiable in Figure 3.2.1) and corroborated the necessity for more elaborate models that integrate not only singular compositional parameters but also their combined effects. These subjects are further addressed in the following sections.

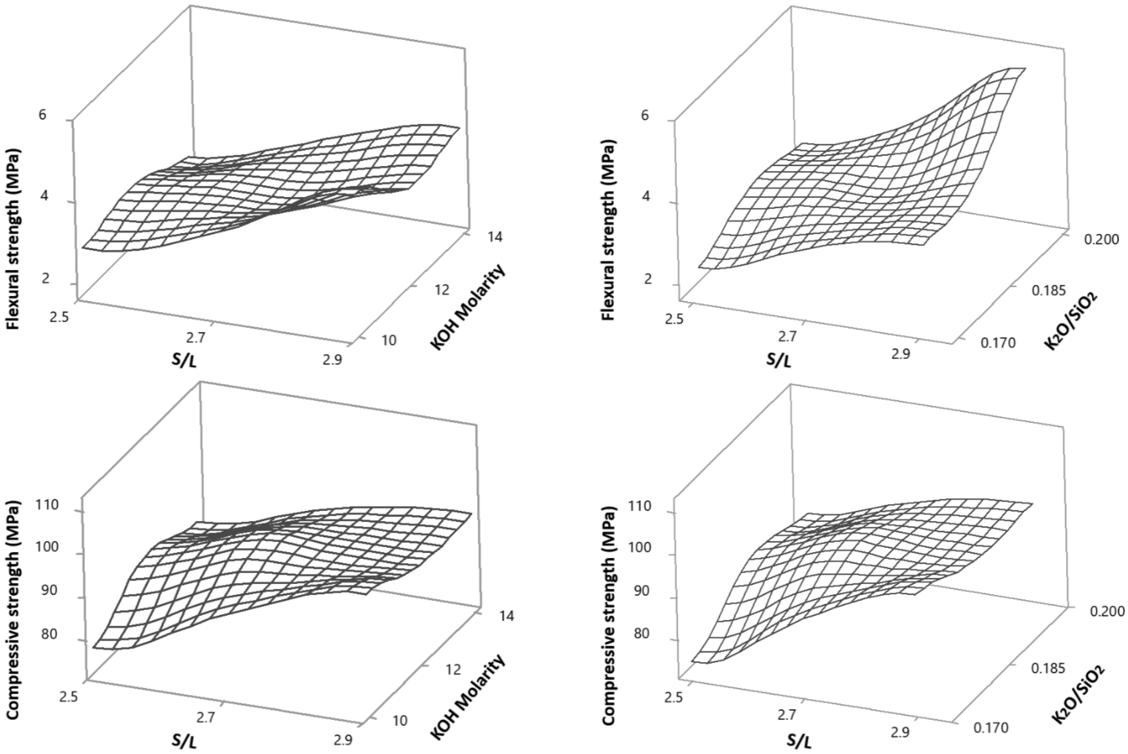

Figure 3.2.6 Influence of compositional parameters and their synergetic effects on IPs flexural and compressive strength after 28 d of curing.

Conclusions

In this work, IPs were synthesized with high contents of CaO-FeO_x-Al_2O_3-SiO_2-rich residues (86.7 wt%), no silicate solutions, and at low curing temperature (20°C). Results show that fresh and hardened properties can be controlled by proper mix design. S/L and K_2O/SiO_2 ratios were found to be the governing factors, whereas the influence of KOH molarity was less significant for the investigated properties. The produced IPs varied in final setting time (between 175 and 360 min) and rheological behavior (mainly shear-thickening), exhibited low open porosity (< 3.0%) and water absorption (< 1.4%), and had considerable flexural (up to 6 MPa) and compressive strength (up to 106 MPa) after 28 d of curing. The results herein constituted the basis for the development of predictive models used to tailor the mix design of CaO-FeO_x-Al_2O_3-SiO_2-rich IP binders and attain the envisioned properties while minimizing production costs and environmental burdens. This approach ultimately aims to make these materials more attractive to real-life applications and will be further discussed in the following section.

References

Arnout, L., Kriskova, L., Onisei, S., Machiels, L., Blanpain, B., & Pontikes, Y. (2017) Effect of the activating solution's chemistry and volume, on the processing and properties of Fe-Si-Ca-rich inorgnic Polymers. *In Proceedings of the 5th International Slag Valorisation Symposium* (pp. 341-344).

Ascensão, G., Seabra, M. P., Aguiar, J. B., & Labrincha, J. A. (2017). Red mud-based geopolymers with tailored alkali diffusion properties and pH buffering ability. Journal of Cleaner Production, 148, 23-30.https://doi.org/10.1016/j.jclepro.2017.01.150

Beersaerts, G., Arnout, L., Machiels, L., Elsen, J., & Pontikes, Y. (2017). Monitoring early-age crack formation in a Ca-Fe-Al-rich inorganic polymer. *In Proceedings of the 5th International Slag Valorisation Symposium* (pp. 345-348).

Bosmans, A., Vanderreydt, I., Geysen, D., & Helsen, L. (2013). The crucial role of Waste-to-Energy technologies in enhanced landfill mining: a technology review. Journal of Cleaner Production, 55, 10-23. https://doi.org/10.1016/j.jclepro.2012.05.032

EN, B. (2016). 196-1: 2016. Methods of Testing Cement. Determination of Strength.

EU Commission: Marie Skłodowska-Curie Actions, Innovative Training Networks, H2020-MSCA-ITN-2016- NEWMINE-Grant Agreement No 721185

Landi, E., Medri, V., Papa, E., Dedecek, J., Klein, P., Benito, P., & Vaccari, A. (2013). Alkali-bonded ceramics with hierarchical tailored porosity. Applied Clay Science, 73, 56-64. https://doi.org/10.1016/j.clay.2012.09.027

Machiels, L., Arnout, L., Jones, P. T., Blanpain, B., & Pontikes, Y. (2014). Inorganic polymer cement from Fe-silicate glasses: varying the activating solution to glass ratio. Waste and Biomass Valorization, 5(3), 411-428. https://doi.org/10.1007/s12649-014-9296-5

Machiels, L., Arnout, L., Yan, P., Jones, P. T., Blanpain, B., & Pontikes, Y. (2017). Transforming enhanced landfill mining derived gasification/vitrification glass into low-carbon inorganic polymer binders and building products. Journal of Sustainable Metallurgy, 3(2), 405-415.https://doi.org/10.1007/s40831-016-0105-1

Romagnoli, M., Leonelli, C., Kamse, E., & Gualtieri, M. L. (2012). Rheology of geopolymer by DOE approach. Construction and Building Materials, 36, 251-258. https://doi.org/10.1016/j.conbuildmat.2012.04.122

3.3 Modeling IPs binders' properties

In the following section, the most influential compositional parameters, i.e. S/L and K_2O/SiO_2 molar ratio, were used to define an experimental domain envisioning the development of predictive models. Apart from their impact on IP properties, the dosage of the activation solution (meaning S/L ratio) and its concentration (meaning K_2O/SiO_2 molar ratio) are also vital in determining the economic viability and sustainability of the proposed solutions, which is also considered during the following discussion. The experimental domain was populated with several formulations, and interpolation methods were used to compute surface responses of the properties assessed. The effects of introducing silicates in the activating solution were determined by confronting the surface responses constructed based on hydroxide and silicate-activated IPs. The content of this section has not been published and is firstly discussed here.

3.3.1 Introduction

The variability of industrial residues can potentially compromise the industrial implementation of alkaline activation technology. Thus, robust and resilient mix designs able to accommodate the variability of secondary raw materials should be developed to allow engineering the IPs properties by controlling major synthesis parameters.

Therefore, the development of predictive tools assumes critical importance and aiming to contribute to the latter, the effect of two main compositional factors (K_2O/SiO_2 molar ratio and S/L ratio), their interaction, and the IP responses were evaluated here.

As fundamental properties for many construction applications, open porosity, water absorption, apparent density, flexural, and compressive strength were selected as key performance indicators. The system boundaries were found experimentally, and predictive models were constructed based on natural neighborhood interpolation for two different maturation ages, 7 and 28 d. This work constitutes the conceptual foundation of a reliable and straightforward method for, given the prescribed synthesis restrictions, controlling and predicting the properties of CaO-FeO_x-Al_2O_3-SiO_2-rich IPs. Similar studies can be later conducted to build analog models for other fundamental properties such as porosity distribution and connectivity. This approach is expected to generate a valuable compendium of user-friendly models that can be used as screening tools to select IP binders based on one or more specific features required for envisioned applications.

3.3.2 Parameters definition and spatial distribution of experiments

Based on the results of the previous sections, the starting point formulation was defined to present an S/L ratio of 2.5 and K_2O/SiO_2 molar ratio of 0.20. The experimental domain initially considered encompassed a research area defined by S/L varying from 1.3 to 3.2, and K_2O/SiO_2 molar ratios ranging from 0.14 to 0.26, Figure 3.3.1a.

Laboratory experimentation has shown that combining the upper and lower limits of the variables investigated did not allow the production of viable binders. Although equally impossible, the explanations behind such impossibility at these conditions were rather different. While IP binders produced with S/L ratio of 1.3 and the lowest concentrated activating solution (0.14) were not consolidated after 24 h of curing, flash setting occurred at the opposite extreme of the experimental domain. The former would later consolidate after a few days of curing, but such prolonged settings are not compatible with the requirements of the construction sector. Besides, such IPs presented a fragile structure that could hardly be handled. For those reasons, the formulations mentioned above were excluded, and the experimental domain was redefined.

The initial research area was divided into two sub-regions of interest, further termed as blocks 1 and 2, Figure 3.3.1a. Binders located in block 2 (high S/L region) were expected to present higher mechanical performances and lower production costs. Therefore, exploring this region was of particular interest for applications where certain levels of structural performance are required. Conversely, IPs located in block 1 (low S/L region) were expected to present reduced densities given their lower solid load. Despite a decline in strength development be anticipated, such area was worthy of being explored in order to identify low-density binders later used in the development of porous and lightweight materials (see Chapter 4). The results gathered from both regions were complemented by two extra data points presenting an S/L ratio of 2.85 and 1.90, and K_2O/SiO_2 molar ratio of 0.23 and 0.17, respectively. The data set was constructed, and a schematic representation of the newly defined system boundaries is shown in Figure 3.3.1b.

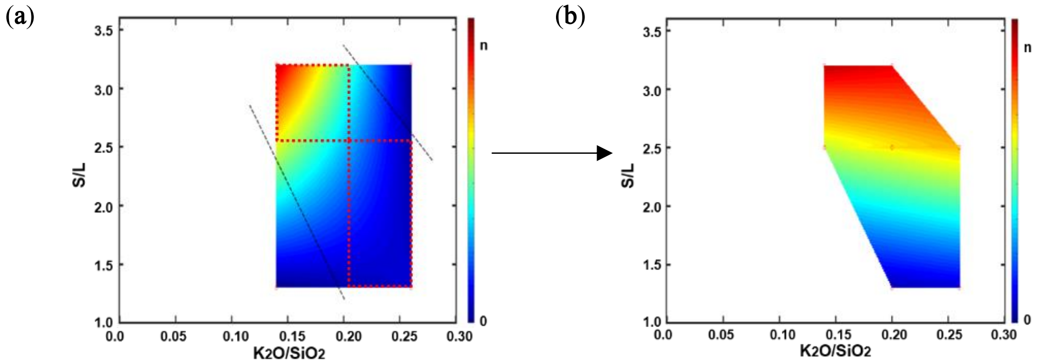

Figure 3.3.1 Initially considered experimental domain (a) and research area defined by the integration of the two regions of interest later considered.

3.3.3 Materials and methods

The slag described in the previous sections was maintained as the IPs' main precursor. In order to simplify the binders' formulations, the number of solid constituents was reduced to two. The observations made in section 3.1 had shown that IPs binders with SiO_2/ (Al_2O_3+Fe_2O_3) molar ration as low as 1.95 could be successfully produced, and therefore the use of metakaolin was avoided from here on. Densified silica fume (SF, Microsilica Grade 940, ELKEM®, Norway) was used as a secondary source of SiO_2. The SF was composed of (in wt%) 95.0 SiO_2, and minor elements such as CaO, Fe_2O_3, and Al_2O_3 were considered negligible (<0.5 wt%). SF specific surface area was measured by BET method and found to be approximately 22200 m^2/kg. Potassium hydroxide and silicate solutions were used to provide the alkaline medium, and demineralized water was added to achieve the pre-defined S/L ratio. The limits of the compositional factors investigated in blocks 1 and 2 and the bulk composition of KOH- and K_2SiO_3-activated binders are shown in Table 3.3.1 and 3.3.2, respectively.

Table 3.3.1 Compositional factors investigated and bulk composition of KOH-activated binders.

Block	Code	Factors		Solid precursors		Activating solution		
		K_2O/SiO_2	S/L	PS	SF	KOH	K_2SiO_3	H_2O
1	K4	0.20	1.30	52.4	4.1	13.9	0.0	29.6
	K7	0.26	1.30	52.4	4.1	18.2	0.0	25.4
	K8	0.20	2.50	66.3	5.2	17.5	0.0	11.0
	K9	0.26	2.50	66.3	5.2	23.0	0.0	5.6
2	K8	0.20	2.50	66.3	5.2	17.5	0.0	11.0
	K11	0.14	2.50	66.3	5.2	11.7	0.0	16.9
	K12	0.20	3.20	70.7	5.6	18.2	0.0	5.3
	K13	0.14	3.20	70.7	5.6	12.5	0.0	11.3
Extra points	K16	0.23	2.85	68.6	5.4	20.5	0.0	5.1
	K17	0.17	1.90	60.8	4.8	13.3	0.0	21.2

Table 3.3.2 Compositional factors investigated and bulk composition of K_2SiO_3-activated binders.

Block	Code	Factors		Solid precursors		Activating solution		
		K_2O/SiO_2	S/L	PS	SF	KOH	K_2SiO_3	H_2O
1	K3	0.20	2.50	67.4	4.1	16.9	4.8	6.9
	K4	0.20	1.30	52.4	4.1	13.9	0	29.6
	K6	0.26	2.50	67.4	4.1	22.4	4.8	1.4
	K7	0.26	1.30	52.4	4.1	18.2	0	25.4
2	K1	0.20	3.20	72.1	4.1	17.6	6.2	0
	K2	0.14	3.20	72.1	4.1	11.5	6.2	6.1
	K3	0.20	2.50	67.4	4.1	16.9	4.8	6.9
	K10	0.14	2.50	67.4	4.1	10.9	4.8	12.8
Extra points	K14	0.23	2.85	69.9	4.1	20.0	5.5	0.5
	K15	0.17	1.90	61.4	4.1	12.8	2.8	18.9
3	K20	0.14	3.30	72.7	4.1	11.5	6.5	5.3
	K21	0.06	3.30	72.7	4.1	3.3	6.5	13.5
	K22	0.06	3.10	71.5	4.1	3.3	6.1	15.0
	K23	0.14	3.10	71.5	4.1	11.4	6.1	6.9
	K24	0.10	3.20	72.1	4.1	7.4	6.2	10.2
Extra points	K18	0.08	3.20	72.1	4.1	5.3	6.2	12.3
	K25	0.10	3.30	72.7	4.1	7.4	6.5	9.4
	K26	0.10	3.10	71.5	4.1	7.3	6.1	11.0
	K27	0.20	2.85	69.9	4.1	12.2	5.5	3.3
	K28	0.14	2.85	69.9	4.1	11.2	5.5	9.3
	K29	0.10	2.85	69.9	4.1	7.3	5.5	13.2
	K30	0.08	2.85	69.9	4.1	5.3	5.5	15.2

The preparation of all binders followed the procedure already described in section 3.1, and all $4x4x16cm^3$ IP samples were cured for 24 h at 20 °C and 95 % RH, being afterward demolded and kept at room conditions (20 °C and 65 % RH). Water absorption, open porosity, apparent density, flexural and compressive strength were determined as described in section 3.2. To minimize the experimental error a minimum of three samples per formulation and curing time were produced independently.

3.3.4 Results and discussion

The properties and temporal evolution of IP samples of blocks 1, 2 and the two extra experimental points are shown in Table 3.3.3 and 3.3.4. A third block of K_2SiO_3-activated binders and seven additional experimental points can also be seen in Table 3.3.4. These IPs were not considered in this first stage of analysis, corresponding to posterior optimization steps later discussed.

Although the visualization is difficult due to the plethora of data in Table 3.3.3 and 3.3.4, some general trends can be observed. The IP produced presented a predominantly closed-porosity structure with water absorption and open porosity values not exceeding 15 and 26% in silicate and hydroxide activated binders, respectively. Such values were increased as curing progressed, but significant increases were only observed in IPs produced with the lowest S/L (1.30). The increase of porosity observed on those IPs can be explained by the excess of activation solution provided that led to the formation of visible cracks during drying processes. The negative water absorption values observed in some IPs can be attributed to the fragile nature of the binders formed, which have resulted in some superficial degradation during water immersion. The existence of leaching on those samples may also have contributed to such results (Chapman, 2011), although most likely to a less significant extent. The introduction of silicates in the activating solutions promoted the formation of denser structures and a visible reduction on the number of cracks formed.

Nevertheless, S/L ratio was the dominant factor dictating water absorption and open porosity levels. Flexural strength was only marginally affected by the type of activating solution used, while significantly higher apparent densities and compressive strengths were achieved when silicate solutions were used. In both types of systems, apparent density was slightly reduced at later ages. The evaporation of unbounded water from the pore structures and its effects on the binders' performance are deeply discussed in section 3.5.4.

The effects of the compositional parameters studied become much more evident when analyzing the spatial distribution and the surface responses predicted by the developed interpolation models. Figure 3.3.2 shows the surface responses after 28 d of curing, where it can be seen that no significant modifications occurred in terms of water absorption and flexural strength when silicates were introduced in the activating solutions. Conversely, the increase of apparent density and compressive strength was particularly evident when elevated S/L ratios were used.

Apart from the higher densities, the reduced crack formation, and the enhanced mechanical performance of IPs produced with a high S/L ratio, it was also interesting to notice the minor decay of compressive strength provoked when K_2O/SiO_2 molar ratio was reduced. This observation is particularly relevant when considering K_2SiO_3-activated systems with S/L ratio above 2.75. Compressive strength above 75 MPa was attained by all K_2SiO_3-activated binders located in block 2, which suggested that the concentration of the activating solution could be significantly reduced without imposing significant deleterious impacts on mechanical properties. It was also observed that reducing K_2O/SiO_2 molar ratio extended the binders' setting time and workability, being also recommended to increase the economic viability of building materials made thereof (Dimas, 2009, Abdulkareem, 2019).

For the above-mentioned reasons, the experimental domain of K_2SiO_3-activated systems was further expanded to lower K_2O/SiO_2 regions while limiting the minimum S/L to 2.85. A 2^2 DoE with a central point in K28 formulation was performed (termed as block 3 in Table 3.3.2). Six additional formations (K25-30) were synthesized to further populate the research area in order to increase the accuracy of the predictions made. The results gathered were then integrated into the pre-developed predictive models. The results K18 formulation were initially excluded from the data set to verify the accuracy of the predictions made.

With the exception of flexural strength, well-defined surface responses were obtained by the expanded models. Such patterns confirm that S/L and K_2O/SiO_2 molar ratios can describe the experimental domain, although more elaborate models may be necessary to predict flexural strength. However, the water absorption capacity (<5%), apparent density (approximately 2.15 g/cm^3), and compressive strength (approximately 90 MPa) of K18 were reasonably predicted, Figure 3.3.3.

Table 3.3.3 Compositional factors analyzed and the responses of KOH-activated binders.

Block	**Code**	**Factors**		**Responses**									
		K_2O/ SiO_2	**S/L**	**H_2O abs. 7d (%)**	**H_2O abs. 28d (%)**	**Open por. 7d (%)**	**Open por. 28d (%)**	**ρ 7d (g/cm^3)**	**ρ 28d (g/cm^3)**	**Flex. strength 7d (MPa)**	**Flex. strength 28d (MPa)**	**Comp. strength 7d (MPa)**	**Comp. strength 28d (MPa)**
1	K4	0.20	1.30	6.1±0.1	14.5±0.7	10.7±0.1	26.6±1.0	1.62±0.01	1.39±0.02	2.4±0.2	1.8±0.7	13.9±0.6	7.0±0.3
	K7	0.26	1.30	3.3±0.6	11.7±1.5	5.9±1.0	21.3±2.7	1.71±0.03	1.55±0.01	2.0±0.1	1.7±0.7	20.3±0.2	12.3±2.6
	K8	0.20	2.50	0.0±0.1	0.2±0.4	0.0±0.1	0.5±0.1	2.20±0.01	2.18±0.01	1.8±0.0	1.0±0.3	79.4±1.7	103.8±0.7
	K9	0.26	2.50	-0.3±0.1	0.1±0.0	-	0.1±0.0	2.34±0.02	2.31±0.01	3.2±0.3	1.5±0.1	76.0±0.3	89.4±5.4
2	K8	0.20	2.50	0.0±0.1	0.2±0.4	0.0±0.1	0.5±0.1	2.20±0.01	2.18±0.01	1.8±0.0	1.0±0.3	79.4±1.7	103.8±0.7
	K11	0.14	2.50	0.8±0.2	1.0±0.4	1.7±0.3	2.0±0.5	2.08±0.01	2.05±0.02	0.9±0.1	1.2±0.3	59.1±0.7	61.4±1.0
	K12	0.20	3.20	-0.3±0.1	-0.2±0.0	-	-	2.39±0.00	2.41±0.02	4.8±0.0	7.3±0.1	94.9±3.2	123.9±2.2
	K13	0.14	3.20	0.1±0.0	0.0±0.0	0.3±0.0	0.1±0.0	2.27±0.00	2.28±0.01	1.2±0.1	1.7±0.1	89.2±2.2	120.1±4.7
Extra points	K16	0.23	2.85	-0.3±0.0	-0.2±0.0	-	-	2.36±0.01	2.33±0.01	5.2±0.3	5.0±0.5	87.5±1.9	109.1±4.2
	K17	0.17	1.90	3.1±0.3	4.9±0.3	6.2±0.7	9.6±0.7	1.88±0.03	1.83±0.02	0.6±0.0	1.4±0.0	23.5±1.1	27.9±0.1

Table 3.3.4 Compositional factors analyzed and the responses of K_2SiO_3-activated binders.

Block	Code	Factors		Responses									
		K_2O/ SiO_2	S/L	H_2O abs. 7d (%)	H_2O abs. 28d (%)	Open por. 7d (%)	Open por. 28d (%)	ρ 7d (g/cm^3)	ρ 28d (g/cm^3)	Flex. strength 7d (MPa)	Flex. strength 28d (MPa)	Comp. strength 7d (MPa)	Comp. strength 28d (MPa)
1	K3	0.20	2.50	0.3±0.0	0.3±0.0	0.8±0.1	0.6±0.0	2.26±0.00	2.28±0.01	2.3±0.1	2.3±0.1	93.6±5.3	115.8±0.2
	K4	0.20	1.30	6.1±0.1	14.5±0.7	10.7±0.1	26.6±1.0	1.62±0.01	1.39±0.02	2.4±0.2	1.8±0.7	13.9±0.6	7.0±0.3
	K6	0.26	2.50	0.3±0.0	0.0±0.0	0.6±0.0	0.0±0.0	2.24±0.07	2.41±0.00	2.9±0.1	2.2±0.2	91.9±1.1	119.2±2.1
	K7	0.26	1.30	3.3±0.6	11.7±1.5	5.9±1.0	21.3±2.7	1.71±0.03	1.55±0.01	2.0±0.1	1.7±0.7	20.3±0.2	12.3±2.6
2	K1	0.20	3.20	-0.1±0.0	0.2±0.1	-	0.4±0.1	2.48±0.01	2.48±0.01	3.9±0.1	6.9±0.5	114.4±10.9	155.0±7.1
	K2	0.14	3.20	0.3±0.0	0.5±0.0	0.6±0.1	0.8±0.0	2.37±0.01	2.37±0.02	3.0±0.2	3.4±0.3	128.6±2.7	162.8±1.9
	K3	0.20	2.50	0.3±0.0	0.3±0.0	0.8±0.1	0.6±0.0	2.26±0.00	2.28±0.01	2.3±0.1	2.3±0.1	93.6±5.3	115.8±0.2
	K10	0.14	2.50	0.7±0.0	0.8±0.2	1.6±0.1	2.1±0.0	2.20±0.01	2.20±0.02	1.4±0.1	1.3±0.0	78.7±0.9	97.6±4.9
Extra points	K14	0.23	2.85	-0.2±0.1	-0.2±0.0	-	-	2.43±0.00	2.41±0.01	4.8±0.8	4.0±1.6	110.3±0.0	131.7±7.8
	K15	0.17	1.90	2.1±0.0	2.2±0.2	4.2±0.0	4.5±0.4	1.92±0.00	1.91±0.01	0.8±0.0	0.7±0.2	45.5±8.1	55.2±2.4
3	K20	0.14	3.30	0.2±0.1	0.1±0.0	0.4±0.2	0.3±0.1	2.41±0.03	2.41±0.03	4.9±0.8	5.2±1.1	96.9±9.8	174.7±9.2
	K21	0.06	3.30	8.6±0.2	8.0±0.4	17.8±0.9	18.0±1.1	2.02±0.00	2.00±0.03	N.A	N.A	13.8±0.6	24.9±4.8
	K22	0.06	3.10	6.0±0.7	5.2±0.0	13.5±1.6	11.9±0.9	2.06±0.05	2.02±0.01	N.A	N.A	7.8±1.0	20.4±9.9
	K23	0.14	3.10	0.2±0.0	0.2±0.0	0.5±0.0	0.5±0.0	2.34±0.02	2.37±0.00	3.5±0.0	3.6±0.1	101.2±7.5	127.5±17.3
	K24	0.10	3.20	0.4±0.1	0.5±0.0	1.1±0.0	1.2±0.0	2.23±0.00	2.22±0.01	6.3±0.7	6.3±0.4	86.6±2.6	114.7±4.3
Extra points	K18	0.08	3.20	1.2±0.0	1.4±0.2	2.7±0.0	3.3±0.4	2.14±0.10	2.22±0.03	6.5±0.1	7.1±0.7	88.2±5.0	100.5±8.5
	K25	0.10	3.30	-	0.7±0.0	-	1.6±0.0	-	2.32±0.03	-	4.6±0.0	-	132.5±3.4
	K26	0.10	3.10	-	1.0±0.0	-	2.3±.0	-	2.26±0.02	-	5.8±0.6	-	118.8±3.9
	K27	0.20	2.85	-	0.1±0.0	-	0.1±0.0	-	2.37±0.01	-	6.1±1.5	-	122.9±16.2
	K28	0.14	2.85	-	0.3±0.0	-	0.7±0.1	-	2.33±0.00	-	1.6±0.1	-	115.9±6.9
	K29	0.10	2.85	-	1.7±0.2	-	3.9±0.4	-	2.18±0.00	-	5.9±0.4	-	92.2±0.5
	K30	0.08	2.85	-	1.6±0.5	-	3.0±0.4	-	2.13±0.02	-	6.4±0.9	-	102.6±6.8

N.A- under the limit of detection.

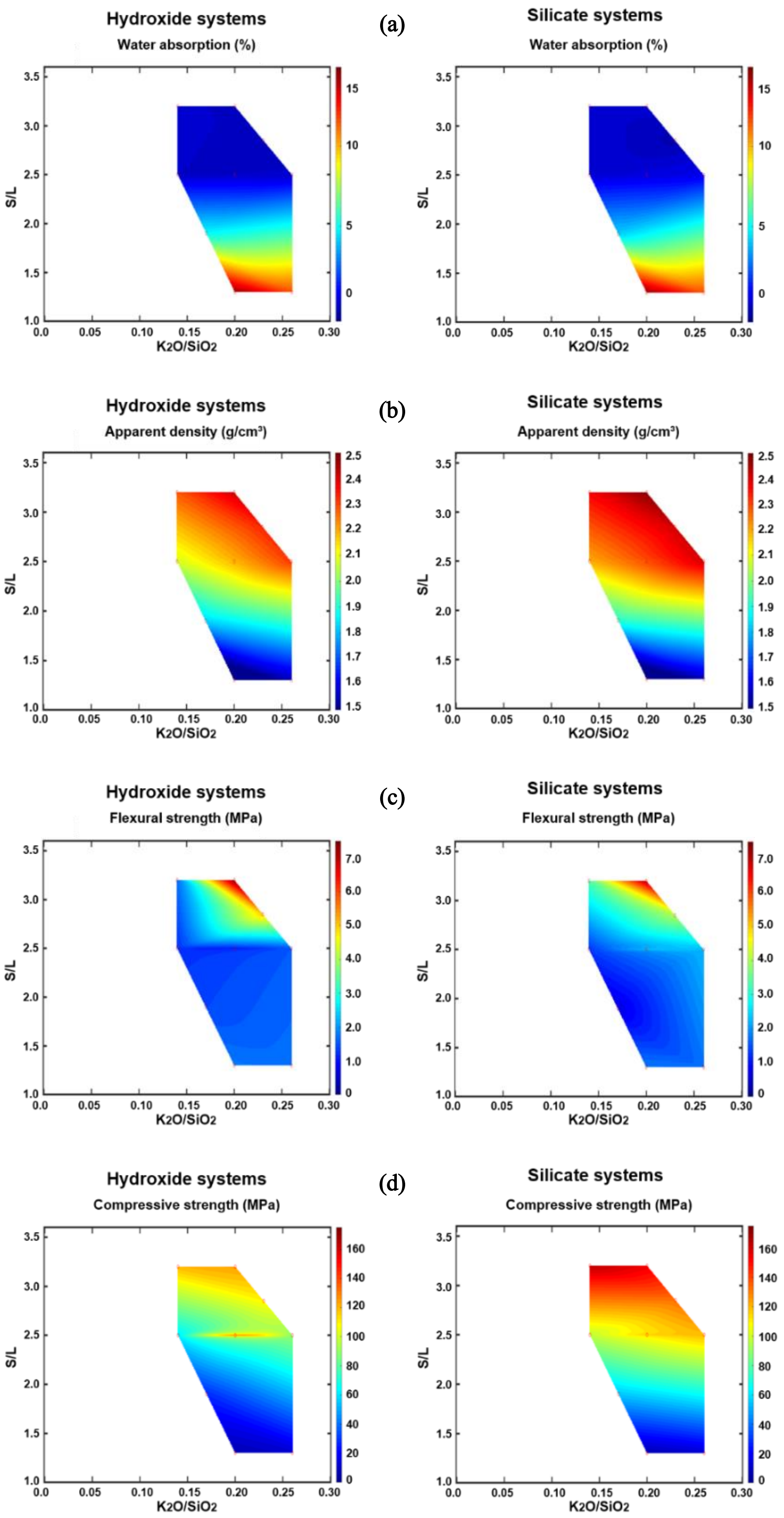

Figure 3.3.2 IPs' surface responses after 28 d of curing in terms of a) water absorption, b) apparent density, c) flexural strength and d) compressive strength.

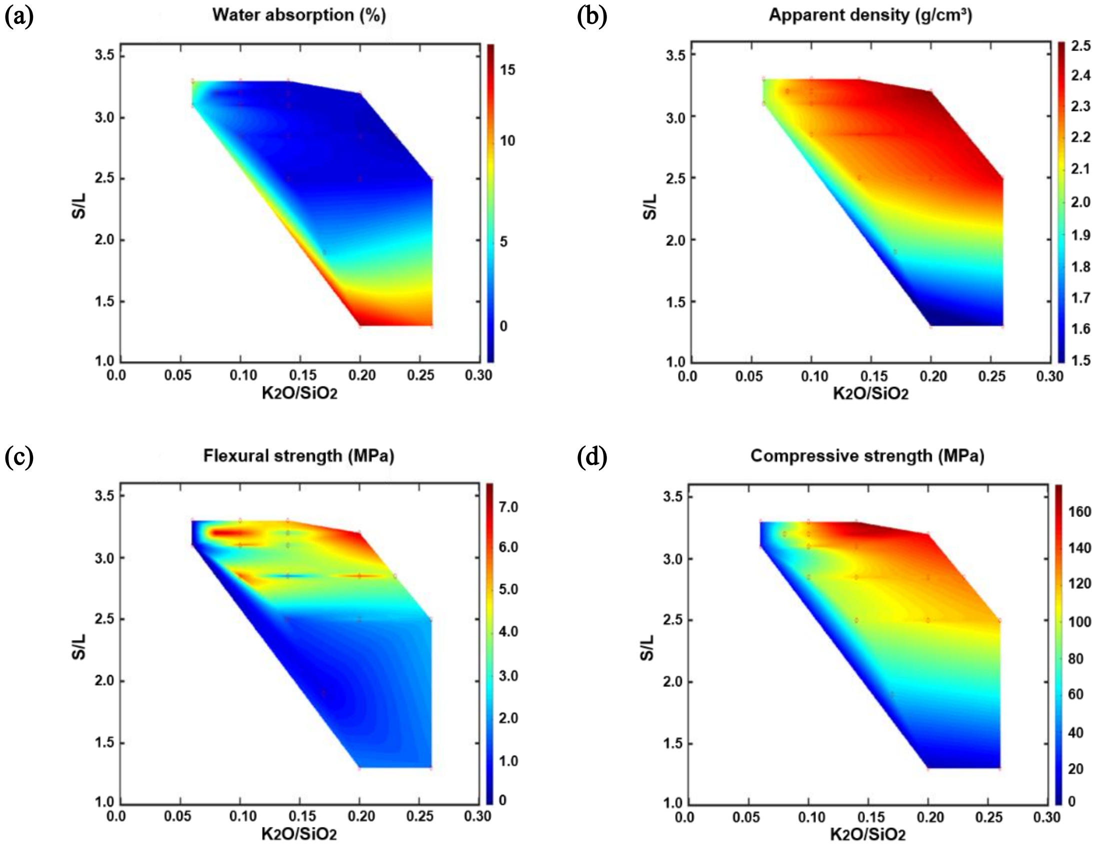

Figure 3.3.3 Expanded surface responses of K_2SiO_3-activated IPs after 28 d of curing in terms of a) water absorption, b) apparent density, c) flexural strength and d) compressive strength.

3.3.5 Preliminary economic assessment

Independently of the target application, the large-scale application of CaO-FeO_x-Al_2O_3-SiO_2 IPs will be affected by its economic viability. Therefore, identifying the possibility of decreasing the cost of raw materials through proper mix design while maintaining IPs' properties constitutes a relevant insight into the development of novel waste-based products. Therefore, the constructed models were further extended beyond IPs technical properties and used to preliminary assess the production cost of K_2SiO_3-activated binders within the experimental domain. This preliminary analysis is based on laboratory experimentation and should not be understood as an estimation of IPs' real production costs. Nonetheless, such analysis is still useful and provides a breakdown cost analysis for the binders developed here. The raw materials' prices and boundaries considered in this analysis are schematically represented in Figure 3.3.4.

As no estimation of the market price of the slag used here as the main precursors was found, three different scenarios were considered. As a baseline scenario, the cost of the slag was assumed equal to the price of fly-ash produced within a 150 km distance between the supplier and production site, 0.06 €/kg (Cristelo, 2015). A more challenging scenario was taken into consideration by doubling the expected price of the slag. As the best-case scenario, the price of the slag was assumed zero but the conservative nature of such assumption should be acknowledged here. As taxes on landfilling grow exponentially, particularly in EU countries, additional revenue streams may be available for binders' manufacturers.

Silica fume was purchased at the price of 0.85€ /kg, while the cost of KOH and K_2SiO_3 solutions was calculated based on the market price of anhydrous potassium silicate powder and potassium hydroxide pellets (Smolik, 2008; Cristelo, 2015). Costs related to processing were not included in this analysis but can be assumed equal in all formulations.

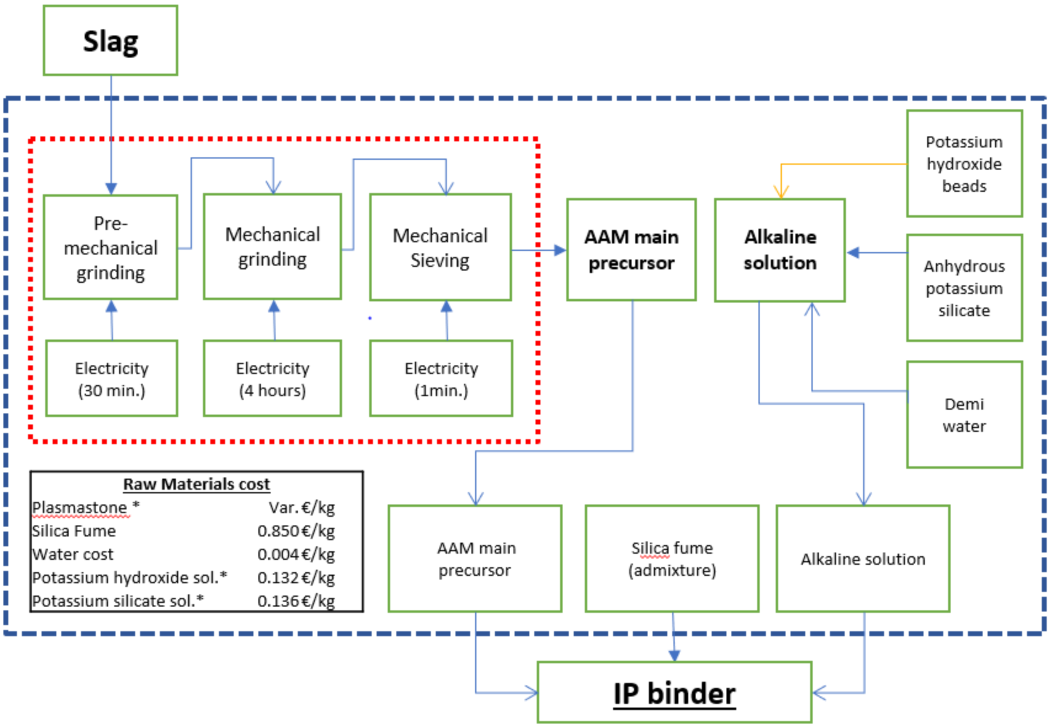

Raw Materials cost	
Plasmastone *	Var.€/kg
Silica Fume	0.850€/kg
Water cost	0.004€/kg
Potassium hydroxide sol.*	0.132€/kg
Potassium silicate sol.*	0.136€/kg

Figure 3.3.4 Raw materials costs and boundaries of preliminary economic assessment. The boundaries of the production process analyzed are delimited in blue while inputs not considered are marked in red.

In Figure 3.3.5, the spatial distribution of IPs costs can be seen according to the three different scenarios assumed. Given the fixed prices assumed for admixtures and activating solutions and the considerable dosage of slag used in all formulations (> 90 wt% of solids), the cost of the binder was mainly dictated by the prince of the slag. However, it can be seen that even when considering the worst-case scenario, the estimated financial costs did not surpass 350 €/m^3. Taking into account that aggregates typically represent more than three-quarters of the mass in mortars and concrete production, significant cost reduction can be anticipated from introducing aggregates in the mix design. Reducing the binder dosage per m^3 was one of the reasons why IP mortars were later developed in this work. Moreover, if the best-case scenario is considered, the cost of the raw materials needed to produce a cubic meter of IP binder decreases to values lower than 150 € independently of the synthesis conditions used.

Nevertheless, synthesis conditions have also severely affected IP raw materials cost. Decrease K_2O/SiO_2 molar ratio generally reduced the binder cost while the impact of S/L ratio was dependent on the slag cost.

It can also be seen that binders located in blocks 1 and 3 (see Table 3.3.2) presented the lowest production costs independently of the scenario assumed, further justifying the selection of those binders to produce lightweight and high-resistance IPs, respectively. The red dot inserted in Figure 3.3.5 identifies K18 formulation whose raw materials cost varied between 105 and 280 €/m^3 depending on the scenario assumed. This cost range shows that K18 binders can be competitive in the market of alkali-activated binders as similar raw materials costs have been reported for fly-ash, copper slag, and red mud-based IPs (80-100 €/m^3) (Cristelo, 2015; EIT Raw materials, 2018). In these studies, the cost of the main precursor was considered null or not exceeding 0.06 €/kg, being, therefore, equivalent to the most optimistic scenarios considered here.

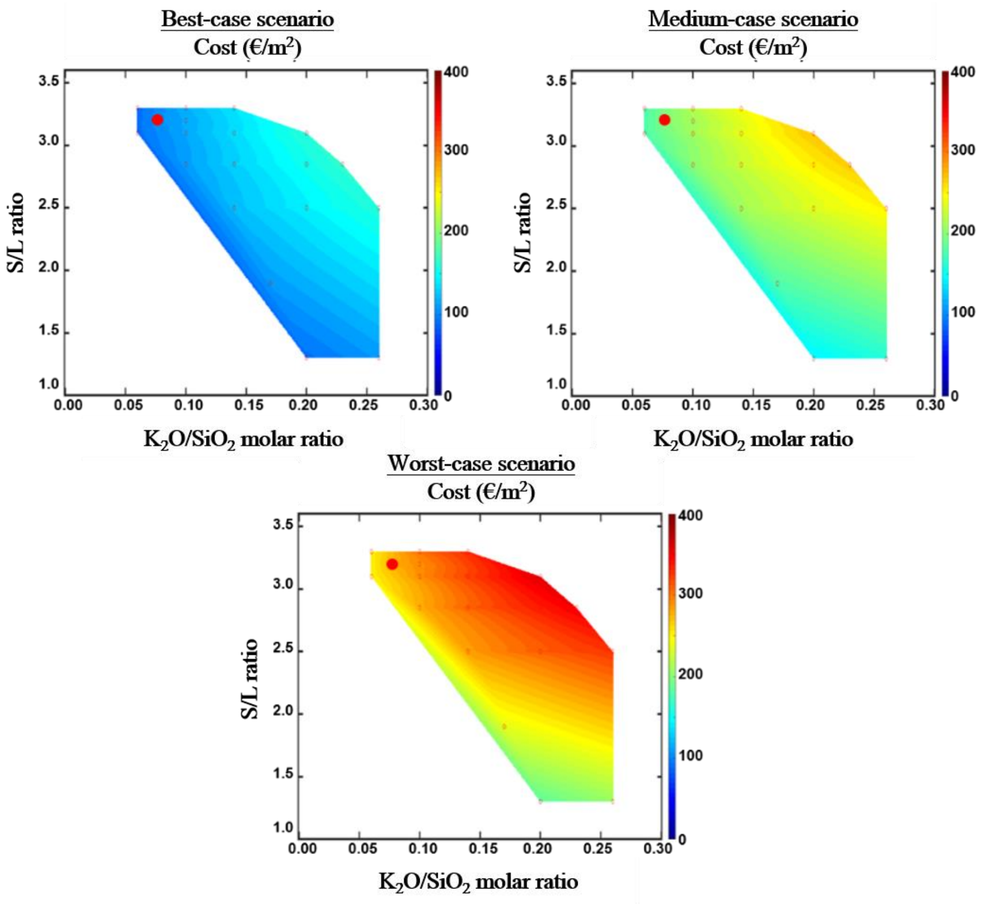

Figure 3.3.5 Prediction of raw materials costs based on different economic scenarios.

3.3.6 Conclusions

Considering the simple interpretation of the prediction methods proposed and their interactive nature -meaning that accuracy can be progressively increased with further experimental realizations- the developed models can be a helpful tool to assist developers and manufacturers in the selection of synthesis parameters to produce binders with adequate properties and cost for different applications. In fact, two different lines of research were defined based on the developed surface responses.

The first line of research was dedicated to further investigate the alkali-activation reaction and products formed in the area defined here as block 1. The interest in such an area is justifiable by the increased porosity and reduced apparent density of IPs located in this region, which was particularly relevant when considering the development of insulation materials.

The second line of research was dedicated to the development of high-strength IPs, where K18 formulation was selected as the starting binder. Despite the absence of visible cracks, the volumetric stability of K18 samples was monitored and revealed the existence of extensive shrinkage. A comprehensive investigation was performed to describe the shrinkage mechanisms involved and to develop different shrinkage mitigation strategies.

Future efforts to develop the models presented here may allow to analyze a growing number of compositional parameters and extend the type of variables considered to encompass additional economic and environmental factors, and in this way, predict the effects of modifying synthesis parameters in a holistic manner.

References

Abdulkareem, M., Havukainen, J., & Horttanainen, M. (2019). Enviromental assessment of alkali-activated mortars using different activators. In Proceedings of the 17th International Waste Management and Landfill Symposium.

Cristelo, N., Miranda, T., Oliveira, D. V., Rosa, I., Soares, E., Coelho, P., & Fernandes, L. (2015). Assessing the production of jet mix columns using alkali activated waste based on mechanical and financial performance and CO2 (eq) emissions. Journal of Cleaner Production, 102, 447-460. https://doi.org/10.1016/j.jclepro.2015.04.102

Chapman, C., Taylor, R., & Deegan, D. (2011). Thermal plasma processing in the production of value added products from municipal solid waste (MSW) derived sources. In Proceedings 2nd International Slag Valorisation Symposium. Leuven (pp. 147-161). https://www.researchgate.net/profile/David_Deegan/publication/229043335_Thermal_Plasma_processing_in_the_production_of_value_added_products_from_municipal_solid_waste_MSW_derived_sources/links/5433f2150cf294006f72e3a9.pdf

Dimas, D., Giannopoulou, I., & Panias, D. (2009). Polymerization in sodium silicate solutions: a fundamental process in geopolymerization technology. Journal of Materials Science, 44(14), 3719-3730. https://doi.org/10.1007/s10853-009-3497-5

EIT Raw Materials projects: Innovation in Motion: Red mud and Copper slag valorization in Engineered Products, Feasibility Study, 2018

Smolik I. (2008) Geopolymers - market analysis Heidelberg Cement Technology Center GMBH

3.4 Reaction kinetics and structural analysis of low-density binders

The following section describes the outcomes of research activities conducted to further examine the IPs defined in the previous section as block 1. The scope of these activities was to gain a deeper knowledge of how the reaction kinetics and products formed varied within this experimental domain to later facilitate the selection and adjustment of binders used to produce IP insulating materials.

This section is based on a paper entitled "Reaction kinetics and structural analysis of alkali activated Fe-Si-Ca-rich materials" by Ascensão, G., Marchi, M., Segata, Faleschini, F., & Pontikes, Y., published in the Journal of Cleaner Production, 119065, 2019.

Introduction

This work describes the outcomes of a study conducted to investigate the influence of S/L ratio, K_2O/SiO_2 molar ratio, and type of activation solution on reaction kinetic and structural development of CaO-FeO_x-Al_2O_3-SiO_2–rich IPs. IPs were synthesized with alkali hydroxide and alkali hydroxide/silicate type activators to investigate the kinetic and structural impact of soluble silicates on the activating solution. Combining multiple characterization techniques - isothermal conduction calorimetry (ICC), X-ray diffraction (XRD) and infrared spectroscopy (FTIR) - to analyze reaction kinetics and the products formed upon alkali activation has previously provided valuables insights on metakaolin (Zhang, 2012; Zhang, 2013), GGBFS (Gebregziabiher, 2015) and fly-ash (Zhang, 2014) based systems. However, dissolution and hardening mechanisms vary according to the parent precursor used, depending on its mineralogical and chemical composition (Duxson, 2007), particle fineness (Marjanović, 2014), and precursors to activating solution ratio (Ascensão, 2018) for a given temperature and pressure.

The considerable Ca and Fe content of RDF slags significantly modifies the reaction kinetics, which challenges accurate prediction of the reaction products. Van Deventer *et al.* (2007) reported that Ca^{2+} and $Fe^{2+/3+}$ cationic species rapidly dissolve and precipitate, providing a large number of extra potential nucleation sites. The accelerating effect of higher Ca amounts can result in the removal of the OH^- ions from the solution, which has a net effect of lowering the pH. A decrease in the solution pH will affect the further dissolution/precipitation rate and reduce the solution supersaturation levels. These competing effects hamper the definition of a general reaction kinetic model, but Salman *et al.* (2015) observed very early exothermic peaks and concluded that these may be related to enhanced reaction kinetics due to the hydrolysis of Si-O-Ca and Ca-O-Ca linkages. Daux *et al.* (1997) showed that, under slightly alkaline conditions, the precipitation of dissolved Fe was much faster than Si and Al, which can also lead to a considerable pH decay and result in slower reaction progressions. However, the use of Ca-rich admixtures in Fe-rich IPs was shown to further accelerate the reaction kinetics on one hand, but to reduce the reaction extension on the other (Beersaerts, 2019). Most important, however, are the modifications imposed on the reaction products formed. When considerable amounts of Ca species are available, the formation of C-S-A-(F)-H type products is favored (see Chapters 1 and 2). These reaction products are significantly different from (N/K)-A-(F)-S-H products formed in IPs, which has a great repercussion on the structural characteristics and properties of the final material.

In addition to the availability of Ca and Fe species and their impact on dissolution stage, the reaction kinetics, phase development, and IP final properties are also insignificantly influenced by the precursor to activating solution ratio (Ascensão, 2018); the activator nature (Zhang, 2012); and its molar concentration (Machiels, 2014).

Therefore, understanding the basic principles and dominant compositional factors affecting the alkali activation of CaO-FeO_x-Al_2O_3-SiO_2–rich residues is fundamental to incentivize the valorization of those residues. Aiming to contribute to the latter, the influence of three main compositional parameters on the synthesis of IP binders was investigated. The effects of S/L ratio, alkali concentration, and soluble silicates in the activation solution on the reaction kinetics and IPs structural assemblage were examined and correlated to the physico-mechanical properties of the developed materials.

Experimental

The detailed description of the precursors and activating solutions used in these experiments can be found in Table 3.3.4. Isothermal conduction calorimetry (ICC) measurements were conducted at 20 °C in a 3116-1 TAM 83 Air (TA Instruments, USA) using an internal mixing procedure. In ICC measurements, the solid raw materials (2.0g) and the activating solution were stored in the admix ampoule for a minimum period of 12h prior to the experiments to guarantee stable conductions. Once the activating solution was injected using the equipment' syringes, the pastes were mixed for 1 minute using an internal mini-blender (TA Instruments, 2019). One replicate of each mixture was tested, and the average values are reported. A similar procedure was used to prepare three control pastes using demineralized water as a solution. Control pastes replicate the same conditions of their polymeric counterparts, both in terms of S/L ratios and precursor proportions. The data collected from the control trials were used to account for the heat released due to wetting processes.

IP pastes were synthesized and cured following the procedure described in section 3.1, and their setting time determined according to the EN 196-3:2016. The IPs mineralogical composition was assessed by X-ray diffraction (XRD). XRD samples were collected from mechanical testing, then milled, sieved and dried in low vacuum at 40 °C for 3h hours before testing. Replicates of K7 samples with dimensions of 4x4x1 cm^3 were produced and cured in sealed and non-sealed conditions, and their mineralogical evolution monitored over time. Thinner samples were produced to reduce the influence of thickness and guarantee a homogeneous (if any) CO_2 exposure and carbonation. Prior to XRD acquisition, the samples were crushed in an agate mortar, sieved ($\leq$90µm), and dried in a low vacuum chamber (MMM VVCell model) overnight. The chemical bonding of IP structures was analyzed using the attenuated total reflectance (ATR)-FTIR method. Absorbance spectra were collected from 4000 to 380 cm^{-1} at a resolution of 2 cm^{-1} and 32 scans per single measurement. Three IR spectra were collected per sample, and the average result is reported herein.

Two experimental programs were defined to assess the impact of different synthesis parameters on the reaction kinetics and their correlation with IP properties. The first experimental program, EP1- that corresponds to block 1 of KOH-activated IP- was defined to evaluate the influence of S/L ratio and K_2O/SiO_2 molar ratio on the reaction kinetics. The second batch of IP samples was prepared to evaluate the impact of introducing soluble silicates into the activating solution (experimental plan 2, EP2).

Results and discussion

ICC testing

Figure 3.4.1a, b show the heat evolution rate and cumulative heat evolution of polymeric pastes where no soluble silicates were introduced into the activating solution (EP1), whereas Figure 3.14c, d show the effect of potassium silicates on pastes' kinetic evolution (EP2). The first exothermic peak (termed peak I) appeared immediately after mixing followed, in some cases, by a second smaller and broader peak (termed peak II). Peak I required less than 5 minutes to reach the maximum heat release rate in all pastes. The initial exothermic peak is often attributed to instant sorption of the activating solution at the precursors' surface and ensuing dissolution processes. The slag' dissolution was promoted by the highly alkaline environments and, depending on synthesis parameters (e.g., precursors SSA), can occur instantly after the wetting of the precursors. The heat evolution rate was monitored for 168 h, and no peaks were recorded after the initial 72 h. The considerable alkali concentration and the high specific surface area of the precursors promote the fast nucleation of aluminosilicate gels and the rapid setting of IP pastes, which hinders reorganization or crystallization at later stages (Zhang, 2012). These results are in agreement with previous works where it was demonstrated that high Si/Al ratios increase structural stability and reduce the formation of zeolite-like crystalline structures (Duxson, 2007).

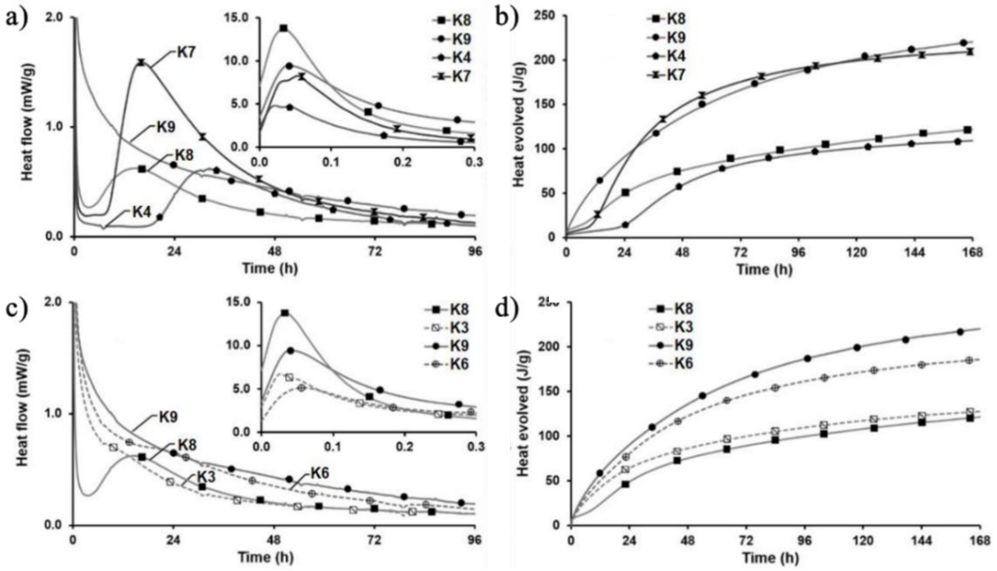

Figure 3.4.1 Isothermal calorimetry curves of IP pastes a) and c) heat evolution rate of EP1 and EP2 systems, respectively; and b) and d) cumulative heat evolved in EP1 and EP2 systems, respectively. The inserted graph in a) and c) shows a close-up of the initial heat peak (peak I). In c) and d), open symbols and dashed lines are used for identifying EP2 systems.

Table 3.4.1 shows the maximum heat released from IP pastes and respective control systems. The heat evolution rate of the control groups was monitored for a period of 24h. As expected, no peaks were recorded after the initial 5 minutes. The exothermic peak in the control systems can be attributed solely to wetting processes, while the difference in the magnitude of peak I between the pastes and their control groups can be seen as the result of dissolution processes. Thus, kinetic data demonstrates that both physicochemical processes (wetting and dissolution) coexist in the initial reaction stage and contribute to the magnitude of peak I. The different magnitudes of peak I in the control groups reflect the differences in S/L ratios and solids' mixture portions.

In EP1, the heat release in the control systems increases as S/L ratio rises, which suggests that, under the conditions tested here, the solid content is the rate-controlling factor on heat release, due to wetting processes. On the other hand, the released heat attributed to dissolution did not present a consistent trend: K8>K9; K4<K7; K8>K4; and K9≈K7. In low K_2O/SiO_2 ratio pastes, heat release due to dissolution processes rose as the solid content increased, but in pastes with $K_2O/SiO_2=0.26$, such increase was less significant.

Concerning S/L ratio, two distinct trends can be seen. At low S/L, the magnitude of peak I increases as alkali concentration rise. As alkali concentration in the activating solutions rises, the potential to hydrolyze T-O (T=Al, Si) bonds in the precursor's increases. Salman *et al.* (2015) suggest that the reaction kinetics may also be enhanced due to the hydrolysis of Si-O-Ca and Ca-O-Ca linkages. However, when considering pastes with S/L=2.50, the increase of alkaline solution reduced peak I magnitude (K8>K9), which indicates lower immediate dissolution. The kinetic data of K9 pastes seem to suggest that combining high S/L and K_2O/SiO_2 ratios reduces the solution activity at early stages of reaction. However, the characteristic deceleration after the initial peak was less pronounced. This demonstrates the continuous nature of the reaction and denotes the contribution to peak I of oligomerization and polymerization processes, which occur in parallel with the dissolution of silicates and aluminates units (Figure 3.4.1a, b). The absence of peak II in K9 heat flow curves, which is commonly attributed to gelation and polymerization stages, supports the idea of such a reaction mechanism. Therefore, the combined effect of increasing the content of highly reactive precursors and the alkalinity of the activating solution is to accelerate the dissolution and nucleation stages, which promotes the immediate achievement of the critical concentration necessary to start the IP network formation. As a result, K9 peak I and II appear to overlap in the isothermal calorimetric curves, broadening the exothermic peak but reducing its maximum magnitude. The anticipation of peak II corroborates the latter either as the S/L ratio increases from K4 to K8, or as K_2O/SiO_2 rises from K4 to K7, with similar trends being expected for K9.

Table 3.4.1 Maximum heat release of IP pastes and respective control systems. The difference between the initial peak magnitude of the IPs and its control groups is represented by Δ magnitude.

Experimental	Code	Peak I maximum	Control maximum	Δ magnitude
		mW/g	mW/g	mW/g
EP1	K8	13.74	3.98	9.77
	K9	9.38	3.98	5.40
	K4	4.65	0.82	3.83
	K7	7.11	0.82	6.29
EP2	K8	13.74	3.98	9.77
	K3	6.10	2.70	3.40
	K9	9.38	3.98	5.40
	K6	5.09	2.70	2.39

It should be noted that peak I in K4 and K7 pastes were not sharp. One possible explanation for such a phenomenon is the formation of transient products at very early stages of reaction when different physicochemical processes coexist. Such phenomena seem to be prompted by less concentrated systems but did not present a significant impact on the reaction extent after 7 d (Figure 3.4.1b). The cumulative heat curve shows that the amount of heat released in the early stage (initial 24h) is increased by rising solid content. However, higher K_2O/SiO_2 ratios anticipate the initial heat release.

At later stages, the reaction progression is mainly governed by the K_2O/SiO_2 ratio, which suggests a similar degree of precursor dissolution at a given K_2O/SiO_2 molar ratio. However, when comparing K8-K4 and K9-K7, very distinct mechanical performances were observed (see Table 3.3.3). The formation of silica-rich gels is known to have a significant role in strength development (He, 2016) and the higher content of highly reactive SF in K8 and K9 most likely contributed to increased formation of polymeric and hydration products, thus promoting IPs' stability. Furthermore, lowering S/L ratio resulted in severe cracks formation, possibly due to the existence of severe drying shrinkage, which turn, diminished the stability of the polymeric structures formed. The above hindered the direct correlation between the isothermal profiles of K4 and K7 samples and their mechanical performance.

The effects of soluble potassium silicates on reaction kinetics are shown in Figure 3.4.1c, d. The introduction of potassium silicates in the activating solution exerted a considerable influence on heat flows. In K3 and K6 pastes, the second exothermic peak was suppressed, and the heat release associated with the precursors' immediate dissolution was considerably diminished (Table 3.4.1). Nonetheless, the already available Si species in the activating solution accelerated the gelation and polymerization stages, which resulted in a single small, broad exothermic peak. K_2O/SiO_2 molar ratio remains the governing parameter determining the reaction extent, but distinct trends between K3 and K6 and their silicate-free counterparts were found. The presence of silicates in the activating solution was expected to increase the formation of reaction products, generating higher cumulative heat release (Salman, 2015). In fact, K3 presented higher cumulative heat release values than K8. In these pastes, the slight reduction of hydroxides in the activating solution - implying a lower degree of precursors dissolution - was compensated by the higher formation of reaction products, increasing the overall cumulative heat release after 7 d (Figure 3.4.1d). IPs apparent density and mechanical strength results (see Table 3.3.4) had shown further densification being promoted by silicate solutions, which corroborates isothermal data. Despite similar densification and increase of mechanical strength observed when comparing K6 and K9 samples, the cumulative heat released was shown to be reduced in K6. The combined effect of a high K_2O/SiO_2 molar ratio along with the introduction of potassium silicates in the activating solution was found to considerably increase the viscosity of K6, which might have affected the pastes' homogeneity during ICC experiments. Thus, kinetic data is not in line with the rest of K6 characterization.

Finally, it should be mentioned that reactions (both in EP1 and EP2) did not cease within the testing period as the cumulative heat curves still presented positive slopes. Ongoing reactions after 7 d can still cause minor structural rearrangements and have an impact on IP strength development.

Setting time

The pastes setting times are shown in Table 3.4.2. In KOH-activated systems, both S/L ratio and K_2O/SiO_2 molar ratio influenced the formation of consolidated IPs, however to considerably different extents. Setting rate was governed by S/L ratio whose increase significantly shortened the pastes' open times. However, one can see that increasing S/L ratio when using highly concentrated activating solutions lead to a five-fold reduction of final setting whereas in lowest concentrated systems such reduction was less significant.

Table 3.4.2 IPs' initial and final setting time.

Experimental	Code	Initial setting	Final setting
		Min.	Min.
EP1	K8	191	253
	K9	60	105
	K4	653	712
	K7	523	591
EP2	K8	191	253
	K3	55	100
	K9	60	105
	K6	49	92

The increase in K_2O/SiO_2 molar ratio further enhanced the network formation rate leading to shorter setting times. By combining high S/L ratio and K_2O/SiO_2 molar ratios final setting times of approximately 105 min were obtained in KOH-activated IPs. These results are in good agreement with ICC measurements, which had shown the highest heat release during the initial days of reaction on those IPs. Moreover, the effects on the pastes' setting times described in section 3.1 were confirmed despite the different compositions of the IPs analyzed here.

The introduction of silicate species in the activating solutions further shortens setting times. The reduction was particularly notable in systems with a low K_2O/SiO_2 molar ratio where the initial and final setting times were reduced to approximately one third. In those systems, the increased concentration of Si units in the dissolution medium has hastened gelation and network formation. This accelerating effect occurs despite the lower pH of silicate solutions which reduces the amount of dissolved species from the parent precursors. The smaller exothermic peaks observed at early ages in K3 confirm lower dissolution levels, which however, were greatly compensated by the Si units provided in the activating solution.

Nonetheless, in systems with K_2O/SiO_2=0.26, such accelerating effects were almost negligible. In the case of K9, the high pH of the activating solution used already allowed to reach the critical concentration of dissolved species in short time, hence rendering the effects of silicates on setting less relevant. However, reaction pathways may have been altered with preferential polymerization occurring with the readily available Si units of the activating solution, possibly partially hindering the precursors' dissolution. Still, all the K_2SiO_3-activated pastes presented acceptable initial setting times (>45 min) not being activating solutions limited to hydroxides.

XRD analysis

Figure 3.4.2a shows the XRD patterns of the precursors used in these experiments. PS and SF patterns exhibited a pronounced hump between 20-40º and 15-30º 2θ, respectively, confirming their predominantly amorphous nature. The XRD pattern of SF presents only one crystalline peak which has been identified as moissanite (SiC), present as an impurity.

By comparing the precursors and IP patterns, it is evident that IPs binders retain a mainly amorphous structure (Figure 3.4.2a-c). However, no significant shifts in the hump center towards higher 2θ values were observed, as previously reported in metakaolin-based systems (Zhang, 2012). Sharp peaks appeared in the IPs' patterns revealing the formation of new crystalline phases whose presence and intensity vary according to the synthesis conditions. Figure 3.4.2b and c show the XRD patterns of IPs from EP1 and EP2 after 28 d of curing. Calcite (CaCO3; PDF 01-088-1807) was identified in all patterns while vaterite (CaCO3; PDF 01-074-1867), a metastable phase of calcium carbonate, be detected only when low S/L ratio and no potassium silicates were used. Alkali-activated materials are prone to carbonation, which is generally attributed to the i) high pH of the pore solution which facilitates the capture and hydration of atmospheric CO_2, which then reacts with calcium species to form calcium carbonate species; and ii) the carbonation of reaction products at atmospheric conditions (Salman, 2015). In EP1, as S/L ratio diminished, the number of pores and cracks rose, facilitating the access of atmospheric CO_2 to the pore solution and inner reaction products. Consequently, lowering the S/L ratio enhanced the formation of carbonated species and the matrix carbonation.

A crystallinity increase can be seen in Figure 3.4.2b. Such an increase of crystallinity promoted by lowering S/L ratios agrees with previous findings (Provis, 2005) and is consistent with ATR-FTIR observations presented in the following section. Furthermore, Figure 3.4.2e shows the mineralogical variation of K4 and K7 according to the probe collection location (surface and bulk samples). External surfaces, being more exposed to atmospheric CO_2, presented high-intensity crystalline peaks, whereas, in the overall sample, only low-intensity crystalline peaks were detected. Such results suggest that atmospheric CO_2 exposure prompted calcite formation, and additional experiments (XRD in samples matured in sealed conditions) were conducted to correlate such carbonated products to atmospheric carbonation and to monitor the IPs' mineralogical evolution over time.

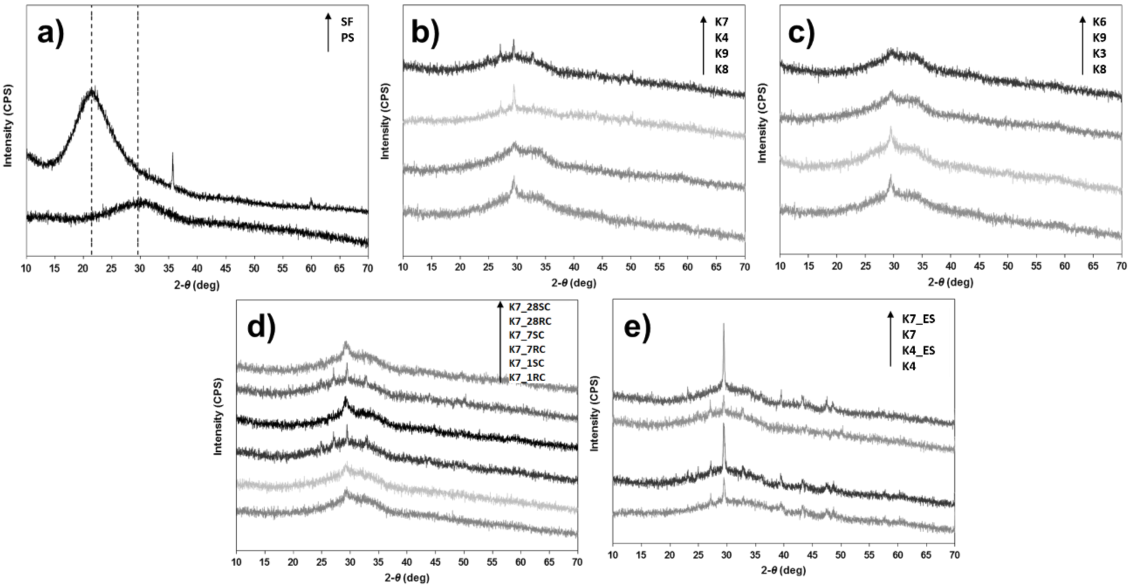

Figure 3.4.2 XRD patterns of raw materials and IP samples: a) slag and silica fume; b) and c) IPs after 28 d of curing at room conditions, EP1 and EP2 respectively; d) K7 temporal evolution upon different curing conditions and e) mineralogical variation of K7 pastes according to collection site (surface or bulk samples).

In Figure 3.4.2d, IPs cured in room conditions are denoted as K7_RC, and the preceding number indicates the maturation age, e.g. K7_28RC corresponds to K7 sample, cured for 28 d in room conditions. At early stages, in both sealed and non-sealed samples, only a small intensity crystalline peak was identified as calcite (CaCO3; PDF 01-088-1807). The similarity between the XRD patterns suggests that, even during mixing, Ca^{2+} released from precursor during dissolution reacts with atmospheric CO_2. Moreover, the slight increase of the crystalline peak intensity over time in sealed samples can be explained by the presence of entrapped air, which continued to react with available calcium species (Figure 3.4.2d). After 7 d, in non-sealed K7 samples vaterite was identified and calcite peak intensity had risen. The same trend was observed at later stages, with vaterite being the only identified phase in non-sealed samples (Figure 3.4.2d). These results seem to confirm CO_2 exposure as the predominant factor contributing to IPs' carbonation. However, dedicated research is still needed to fully describe the carbonation mechanisms involved, as no conclusive evidence is available yet.

In Figure 3.4.2c, the XRD patterns of EP2 samples are shown. One can see that introducing soluble silicates in the activating solution has a minor impact on the formation of crystalline phases. Similar carbonated products with peaks of comparable intensity were identified in all EP2 samples, indicating similar carbonation extension. No vaterite was detected in K3 and K6 samples. In both EP1 and EP2, the influence of the K_2O/SiO_2 molar ratio was found to be minor, but a small decrease in the crystalline peaks' intensity can be seen when K_2O/SiO_2 rises. Increasing the K_2O/SiO_2 molar ratio contributed to the further densification of IP samples (Table 3.3.4), which might have partially limited the access of atmospheric CO_2 to samples' inner regions, and by doing so, limit the formation of carbonated species. Carbonation mechanisms seem to be mainly due to atmospheric CO_2 exposure and related to the density of the IPs structures formed. The results show a considerable impact of S/L ratio, where increasing the K_2O/SiO_2 molar ratio and introducing soluble silicate in the activating solution further reduced the formation of carbonated products. Therefore, an effective way to minimize the formation of carbonated products may consist of maximizing IP densification through compositional and synthesis design.

Matrix and pore solution carbonation may also have a beneficial impact and enhance the IPs' performance in some applications, however. Monoclinic-domatic crystals are known to have high hardness and molar volume, and by filling the porous structure they can contribute to increasing the IPs' mechanical resistance as so as extend its service life. With the exception of K4 and K7 samples, the compressive strength increased during the testing period due to structure consolidation (Table 3.3.3 and 3.12). It is worth noting, however, that the apparent density rose only in K8 and K3. In the latter, the formation of carbonated products may have been able to compensate for water lost upon curing and contribute to the IPs' densification.

ATR-FTIR analysis

The attenuated total reflectance-Fourier transform infrared spectroscopy (ATR-FTIR) method has been extensively used to characterize the chemical bonding of inorganic polymeric structures (Kriskova, 2015). Synthesis parameters affect gel development and hence determine the IP's mechanical performance. ATR-FTIR measurements were performed on samples with at least 90 d of curing; under this condition, gels were assumed to be in a near stable state.

Figure 3.4.3 shows the IR spectra of the starting slag and the chemical bonded structures of IPs made thereof. The IR spectra of PS showed three main peaks that correspond to a) the T-O (T=Al, Si) bonds stretching and bending vibrations at 471 cm^{-1}; b) Si–O bonds bending vibration at 699 cm^{-1}; and c) the asymmetric and symmetric vibration of Si–O–T bonds at 907 cm^{-1} (Komnitsas, 2007; Criado, 2007; Saikia, 2008).

The presence of Fe oxide phases is often denoted in IR spectra by a band at around 600-700 cm^{-1} (Hertel, 2016); in this case, it overlapped with the band corresponding to Si–O bonds' bending vibration. All IP samples presented the same peaks of the main precursor, albeit with a different shape, intensity, and position. The peak at 471 cm^{-1} shifted to lower wavenumbers and was positioned at around 434 cm^{-1}. No systematic correlation was observed between the compositional parameters studied here and the amplitude of the shift. The peak at 907 cm^{-1} was also relocated to higher wavenumbers, which can be attributed to the dissolution of the precursor and the formation of a new, more Si-rich material, possibly with a greater amount of Si-units in higher coordination (Peys, 2017).

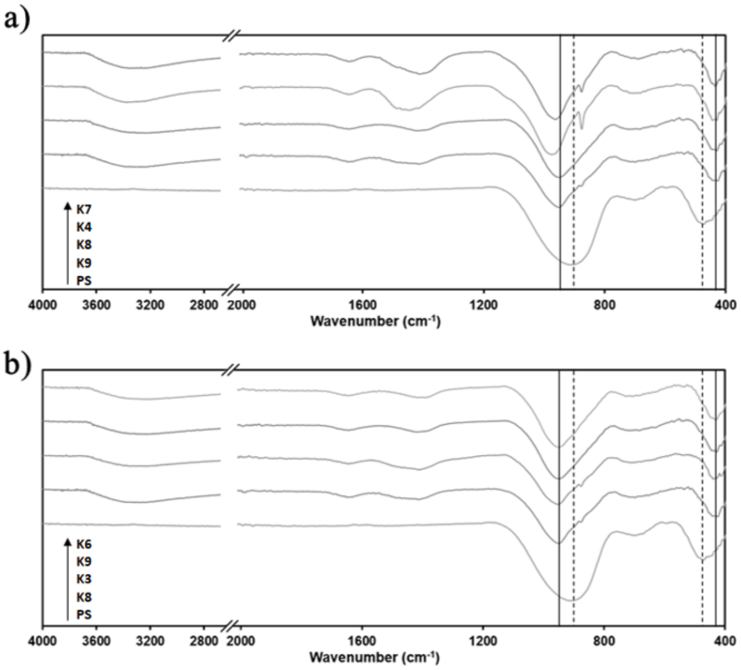

Figure 3.4.3 FTIR spectrum of IP samples: a) effect of S/L and K_2O/SiO_2 molar ratio, EP1, and b) impact of soluble potassium silicate addition, EP2.

When comparing the spectra of EP1 samples, it can be seen that lower S/L ratios promote higher peak displacements relative to PS, indicating differences during the polymerization reaction and in the final binder structure. The shift of the Si-O-T band towards higher wavenumber values indicates the formation of more Si-rich reaction products at later stages of the reaction when the S/L ratio rises. These results are in agreement with previous findings reported by Hajimohammadi *et al.* (2017). However, the introduction of soluble silicates in the activating solution did not induce considerable changes to the position, shape, or intensity of this peak, which suggests the formation of similar reaction products (Figure 3.4.3b). Nonetheless, the displacement of these two peaks relative to the precursors' spectra, observed both on EP1 and EP2, confirms the reorganization of the chemical structure, which agrees with XRD measurements discussed previously. Moreover, three new peaks were formed. The broad peak between 2500 and 3700 cm^{-1} and the smaller peak at around 1645 cm^{-1} represent H_2O molecules on the IP structure, corresponding to H-O-H bonds' deformation and the O-H groups' stretching vibrations, respectively. The different processing parameters tested have a small impact on the peak at around 1645 cm^{-1}. However, increasing the solid content and introducing soluble silicates in the activator narrowed the broader peak at 2500-3700 cm^{-1} and decreased its intensity, indicating a decrease in the amount H2O molecules present. A small peak between 1400 and 1450 cm^{-1} appears in all IPs' spectra, and a fourth peak located between 870 and 880 cm^{-1} appeared in samples K8, K3, K4, and K7. Those peaks represent the O-C-O stretching vibrations from carbonate groups. The formation of such carbonate groups is often attributed to the reaction of free Ca cations with atmospheric CO_2 (Salman, 2015) and are in agreement with XRD data presented previously. ATR-FTIR data corroborated that the formation of carbonated species is greatly enhanced when lowering the S/L ratio.

Strength development

The temporal evolution of the IPs' flexural and compressive strength and corresponding standard deviations can be seen in Table 3.3.3 and Table 3.3.4. Despite considerable differences in heat evolution between K8 and K9 pastes, after 7 d of curing they both presented similar compressive and flexural strength results. More intense exothermic reactions indicated higher degrees of polymerization, binder formation, and further densification, but as previously suggested lowering the K_2O/SiO_2 molar oxide ratio may have a beneficial effect on IPs' mechanical performance. Four simultaneous effects may contribute to such behavior: (i) the lower dissolution of the precursors and subsequent gel formation result in lower shrinkage values; (ii) crack development and propagation is now limited by the presence of undissolved particles which was increased by lowering the K_2O/SiO_2 molar ratio (Machiels, 2014); (iii) a delayed effect on stiffness development (E-modulus), as higher H_2O/K_2O ratios decrease the rate of IP binder formation, resulting in lower autogenous shrinkage (Beersaerts, 2017); and (iv) less intensive exothermic reactions decrease the internal temperature during the polycondensation process, hence preventing crack formation (Machiels, 2017). In fact, K8 presented the highest compressive strength increase and lower flexural strength loss over time of all samples in block 1. Thus, these results show that an increase of the reaction extent and binder formation do not intrinsically increase the IPs' mechanical performance, and a certain degree of undissolved particles should be promoted in the mix design. Further, K4 and K7 presented very low compressive and flexural strengths even after 28 d of curing. Despite the similar cumulative heat release of formulations K8-K4 and K9-K7 after 7 d, suggesting a similar reaction extent, lowering the S/L ratio results in severe crack formation and compromised the stability of the hardened bodies.

On the other hand, the introduction of soluble silicates had a positive impact on IPs' mechanical performance. As can be seen in Table 3.3.4, apparent density increases following the introduction of soluble silicate despite there being no notable impact on reaction kinetics or mineralogical composition. The consolidation of the polymeric structure overtime was also positively affected, resulting in higher compressive and flexural strengths at later ages. Similar results were observed in other sections of this work where IPs were produced with higher S/L and lower K_2O/SiO_2 molar ratios. It is worth mentioning, however, the minor reduction of flexural strength over time in samples K8 and K9. Such results suggest that soluble silicates promote denser but less prone to shrinkage structures and, by doing so, contribute to the IPs' increased strength development. The effects of drying shrinkage in strength development will be later discussed in detail, but a good correlation was found. Further, K6 and K3 presented comparable mechanical properties, confirming that a certain degree of undissolved particles is favorable to strength development and can compensate for less extensive reactions.

Conclusions

In this experimental work, kinetic and structural analysis of CaO-FeO_x-Al_2O_3-SiO_2-rich inorganic polymeric binders was performed, and their fresh and hardened properties were correlated to the reaction progression. Results showed that IPs present adaptable properties that can be controlled by proper mix design. The S/L ratio was found to govern IPs' early-age reaction kinetics, whereas the K_2O/SiO_2 molar ratio controlled their cumulative heat release. Notwithstanding this, lowering K_2O/SiO_2 had a beneficial effect on IPs' mechanical performance when no silicate species were present in the activating solution. The effect of introducing soluble silicates into the activating solution was less significant on reaction kinetics but did lead to IPs with more densified structures and enhanced mechanical performance. Despite the differences between the formulations of block 1 and those in the remaining research area, these results can also explain the extremely enhanced mechanical performance of binders produced with silicate solution, high S/L and low K_2O/SiO_2 molar ratios in block 2 and 3.

Thus, it was shown that by properly combining the effect of the studied parameters, alkali concentration can be reduced without negatively affecting strength development. These results have also shown how it is possible to accommodate slags' variability and tailored the IP properties solely by controlling the production process. The insights provided here were later used in the development of insulating IPs in order to achieve the defined criteria of acceptability in terms of apparent density while maintaining acceptable mechanical performances.

References

Ascensão, G. Faleschini, F., Marchi, F., Segata, M., & Pontikes, Y. (2018) Influence of microstructure on mechanical strength of alkali-activated Fe-Si-Ca-rich materials. *In Proceedings of the 5th International Symposium on Enhanced Landfill Mining* (pp. 285-289).

Beersaerts, G., Arnout, L., Machiels, L., Elsen, J., & Pontikes, Y. (2017). Monitoring early-age crack formation in a Ca-Fe-Al-rich inorganic polymer. *In Proceedings of the 5th International Slag Valorisation Symposium* (pp. 345-348).

Beersaerts, G., Ascensão, G. & Y Pontikes, Y. (2019). Modifying the pore size to minimise shrinkage by curing and using reactive and non-reactive additives in an Fe-rich inorganic polymer mortar. Cement and Concrete Research (in press)

Criado M, Fernández-Jiménez A, Palomo A (2007) Alkali activation of fly ash: effect of the SiO_2/Na_2O ratio: part I: FTIR study. Microporous Mesoporous Mater 106:180–191. https://doi.org/10.1016/j.micromeso.2007.02.055

Daux, V., Guy, C., Advocat, T., Crovisier, J. L., & Stille, P. (1997). Kinetic aspects of basaltic glass dissolution at 90 C: role of aqueous silicon and aluminium. Chemical Geology, 142(1-2), 109-126. https://doi.org/10.1016/S0009-2541(97)00079-X

Duxson, P., Fernández-Jiménez, A., Provis, J. L., Lukey, G. C., Palomo, A., & Van Deventer, J. S. (2007). Geopolymer technology: the current state of the art. Journal of Materials Science, 42(9), 2917-2933. https://doi.org/10.1007/s10853-006-0637-z

Gebregziabiher, B. S., Thomas, R., & Peethamparan, S. (2015). Very early-age reaction kinetics and microstructural development in alkali-activated slag. Cement and Concrete Composites, 55, 91-102, https://doi.org/10.1016/j.cemconcomp.2014.09.001

Hajimohammadi, A., Ngo, T., Mendis, P., Kashani, A., & van Deventer, J. S. (2017). Alkali activated slag foams: the effect of the alkali reaction on foam characteristics. Journal of Cleaner Production, 147, 330-339, https://doi.org/10.1016/j.jclepro.2017.01.134

He, P., Wang, M., Fu, S., Jia, D., Yan, S., Yuan, J. & Zhou, Y. (2016). Effects of Si/Al ratio on the structure and properties of metakaolin based geopolymer. Ceramics International, 42(13), 14416-14422, https://doi.org/10.1016/j.ceramint.2016.06.033

Hertel, T., Blanpain, B., & Pontikes, Y. (2016). A proposal for a 100% use of bauxite residue towards inorganic polymer mortar. Journal of Sustainable Metallurgy, 2(4), 394-404, https://doi.org/10.1007/s40831-016-0080-6

Komnitsas K, Zaharaki D (2007) Geopolymerisation: a review and prospects for the minerals industry. Miner Eng 20:1261–1277. https://doi.org/10.1016/j.mineng.2007.07.011

Kriskova, L., Machiels, L., & Pontikes, Y. (2015). Inorganic polymers from a plasma convertor slag: effect of activating solution on microstructure and properties. Journal of Sustainable Metallurgy, 1(3), 240-251. https://doi.org/10.1007/s40831-015-0022-8

Machiels, L., Arnout, L., Jones, P. T., Blanpain, B., & Pontikes, Y. (2014). Inorganic polymer cement from Fe-silicate glasses: varying the activating solution to glass ratio. Waste and Biomass Valorization, 5(3), 411-428. https://doi.org/10.1007/s12649-014-9296-5

Machiels, L., Arnout, L., Yan, P., Jones, P. T., Blanpain, B., & Pontikes, Y. (2017). Transforming enhanced landfill mining derived gasification/vitrification glass into low-carbon inorganic polymer binders and building products. Journal of Sustainable Metallurgy, 3(2), 405-415.https://doi.org/10.1007/s40831-016-0105-1

Marjanović, N., Komljenović, M., Baščarević, Z., & Nikolić, V. (2014). Improving reactivity of fly ash and properties of ensuing geopolymers through mechanical activation. Construction and Building Materials, 57, 151-162, https://doi.org/10.1016/j.conbuildmat.2014.01.095

Peys, A., Arnout, L., Hertel, T., Iacobescu, R. I., Onisei, S., Kriskova, L., & Pontikes, Y. (2017). The use of ATR-FTIR spectroscopy in the analysis of iron-silicate inorganic polymers. *In Proceedings of the 5th International Slag Valorisation Symposium*: (pp. 385-388).

Provis, J. L., Lukey, G. C., & van Deventer, J. S. (2005). Do geopolymers actually contain nanocrystalline zeolites? A reexamination of existing results. Chemistry of Materials, 17(12), 3075-3085, https://doi.org/10.1021/cm050230i

Saikia B, Parthasarathy G, Sarmah NC (2008) Fourier transform infrared spectroscopic estimation of crystallinity in SiO_2 based rocks. Bull Mater Sci 31:775–779.

Salman, M., Cizer, Ö., Pontikes, Y., Snellings, R., Vandewalle, L., Blanpain, B., & Van Balen, K. (2015). Cementitious binders from activated stainless steel refining slag and the effect of alkali solutions. Journal of Hazardous Materials, 286, 211-219, https://doi.org/10.1016/j.jhazmat.2014.12.046

TA Instruments: TAM Air Isothermal Calorimetry (2019). http://www.tainstruments.com/wp-content/uploads/TAM-AIR-brochure.pdf

Van Deventer, J. S. J., Provis, J. L., Duxson, P., & Lukey, G. C. (2007). Reaction mechanisms in the geopolymeric conversion of inorganic waste to useful products. Journal of Hazardous Materials, 139(3), 506-513. https://doi.org/10.1016/j.jhazmat.2006.02.044

Zhang, Z., Provis, J. L., Wang, H., Bullen, F., & Reid, A. (2013). Quantitative kinetic and structural analysis of geopolymers. Part 2. Thermodynamics of sodium silicate activation of metakaolin. Thermochimica Acta, 565, 163-171, https://doi.org/10.1016/j.tca.2013.01.040

Zhang, Z., Wang, H., Provis, J. L., Bullen, F., Reid, A., & Zhu, Y. (2012). Quantitative kinetic and structural analysis of geopolymers. Part 1. The activation of metakaolin with sodium hydroxide. Thermochimica Acta, 539, 23-33, https://doi.org/10.1016/j.tca.2012.03.021

Zhang, Z., Wang, H., Zhu, Y., Reid, A., Provis, J. L., & Bullen, F. (2014). Using fly ash to partially substitute metakaolin in geopolymer synthesis. Applied Clay Science, 88, 194-201, https://doi.org/10.1016/j.clay.2013.12.025

3.5 Development of shrinkage mitigation strategies for high-performance binders and mortars

The acceptance and large-scale implementation of AAMs will greatly depend on their performance in which volumetric stability is a key factor. In fact, high susceptibility to shrinkage of IPs is frequently reported (Cartwright, 2014; Lee, 2014), which presents a major compromising factor to the widespread adoption of the alkaline activation technology. The high shrinkage of IPs is related to reaction mechanisms and the reaction products form. During the alkali hydrolysis that initially disrupts the precursor's glassy structure, a significant amount of water is consumed. As dissolution continues and the concertation of dissolved species in the medium increases, oligomers start to be formed, which later further crosslinks to create polymers. The recombination and reorganization of these polymers result in a significant volume contraction (chemical shrinkage) and release of the water consumed during dissolution (Duxson, 2007). This water remains in the pore structure of the binder without being chemically bonded (Pacheco-Torgal, 2012). The existence of significant amounts of free-water later results in severe shrinkage which leads to severe crack formation. Different mechanisms contribute to the IPs' volumetric instability. Autogenous shrinkage begins once the material initiates to consolidate and is driven by self-desiccation (Neto, 2008). Self-desiccation is generated in the pores as the pore solution continues to react with the pore surface to form additional binding phases. The saturation of the pores is reduced, and capillary pore tensions are generated (Jensen, 2001). Additional shrinkage results from evaporation processes when the materials are exposed to an open environment (drying shrinkage).

Methods to mitigate shrinkage have been extensively developed for OPC-based systems, however much fewer successful investigations have been reported in field alkali-activated systems, particularly when (FeO_x)-CaO-rich slags are used as precursors. As the binder selected to be the base of high-performance materials was found to present considerable shrinkage values (>20 mm/m), a comprehensive investigation was performed to evaluate the effectiveness of different shrinkage mitigation strategies.

3.5.1 The effects of calcium oxide-rich admixtures on IPs' fresh and hardened properties

The initial part of the following section is based on a conference article entitled "The effects of CaO-rich admixtures on controlling drying shrinkage of alkali-activated materials" by Ascensão, G., Faleschini, F., Marchi, M., Segata & Pontikes, Y. published in the *Proceedings of the 6th International Slag Valorization Symposium*, April 2019, Mechelen, Belgium. In this conference paper, the effects of calcium oxide-rich admixture on fundamental fresh and hardened properties of IPs binders was analyzed.

The second part of this section is based on a manuscript entitled "Increasing the dimensional stability of CaO-FeO_x-Al_2O_3-SiO_2 alkali-activated materials: on the swelling potential of calcium oxide-rich admixtures" by Ascensão, G., Marchi, M., Segata, Faleschini, F. & Pontikes, Y. in Detritus journal (in press). In this second work, the impacts of CaO-rich admixtures were further characterized and complementary insights on the phenomena affecting IPs volumetric stability were given.

Taken as a single chapter, these two publications provide a holistic overview of the effects, potential, and limitations of this shrinkage mitigation strategy. In both publications, the same binder was used as a reference corresponding to the formulation K18 described in Table 3.3.4. In the following text, adjustments were made relative to the original publications for the sake of cohesion and brevity.

Introduction

Alkali activation can be a viable valorization route for a broad group of low-grade and waste materials but the high susceptibility of AAMs to shrinkage can potentially limit their attractiveness for real-life applications.

In isothermal conditions, autogenous and dry shrinkage occur simultaneously, though the mechanisms involved are rather different. Autogenous shrinkage can be defined as physico-chemical phenomenon that results from chemo-mechanical and hygro-mechanical interactions (Mounanga, 2011). The former is due to the difference between the absolute density of the reaction products and the starting materials (also known as chemical shrinkage), while the latter results from tensile stresses generated during the emptying of the pores as the hydration reaction progress (also known as self-desiccation). In IP synthesis, a high solid content is often used to achieve good mechanical performances and enhanced durability. Imposing such synthesis conditions, however, leads to the refinement of the pore structures, which inevitably enlarges capillary stress in partially filled pores, and so contributes to high autogenous shrinkage (Lee, 2014). Moreover, the high viscosity of silicate solutions, like the ones used here, considerably increases the viscosity of the activating solution, contributing to a further rise in surface tension in partially filled pores (Sakulich, 2013). Additional shrinkage results from evaporation processes that take place when the materials are exposed to an open environment (referred to as drying shrinkage).

In the cement industry, the swelling potential of calcium oxide-based admixtures has been successfully used to counteract shrinkage effects (Ono, 1971; Chanvillard, 2007; Corinaldesi, 2015; Yang, 2019). Hydroxide formation from quicklime hydration has been broadly reported (Chen, 2012) but cement and IPs' chemistry are entirely distinct, and the use of calcium compounds to compensate for shrinkage may affect the polymerization process and products formed (see Chapter 1 and 2).

Van Deventer et al. (2007) investigated the effect of Ca^{2+} during the alkali activation of fly-ash and suggested that such cationic species rapidly dissolve and precipitate, providing a large number of extra potential nucleation sites. Kellermeier et al. (2010) investigated the progress of calcium carbonates in inorganic silica-rich environments and proposed that growing amorphous calcium carbonate particles can promote the spontaneous polymerization of silica. These accelerating effects will compete with the removal of the OH− ions from the solution, which has the net effect of lowering its pH. A decrease in solution pH will, in turn, affect further dissolution and precipitation processes, thus reducing supersaturation, which is the primary driving force for polymerization (Van Deventer, 2007). In addition, the stability of calcium-containing precipitates also depends upon the medium composition and pH (Van Deventer, 2007), which render it difficult to define a general kinetic reaction model and to predict the effects of calcium-rich admixtures in specific mix designs. Nonetheless, Salman et al. (2015) observed very early exothermic peaks during the alkali activation of Ca-rich slags, from which the authors concluded that they must be related to the enhancement of reaction kinetics due to the hydrolysis of Si-O-Ca and Ca-O-Ca linkages. As previously mentioned, additional Ca sources may also change the nature of the reaction products formed, hence altering the phenomena affecting their volumetric stability.

Further, the scarce existing literature on the use of calcium oxide-based admixtures to control IPs shrinkage is focused on precursors with low-iron content (Yuan, 2014; Velandia, 2016) and appreciable levels of the latter will infer with the polymerization reaction and increase the complexity of the reactions' mechanisms involved. Daux et al. (1997) studied the dissolution of basaltic glasses and observed that Fe species are dissolved and precipitated faster than Si and Al. Van Deventer et al. (2007) reported that reactive Fe species will most likely behave similarly to Ca2+, precipitating as hydroxide or oxy-hydroxide and decreasing the pH of the solution. Gomes et al. (2010) used 57Fe Mössbauer spectroscopy to determine the fate of iron during alkali activation and found that a small portion of Al^{3+} could be replaced by Fe^{3+} in octahedral sites. Nonetheless, Simon et al. (2018) demonstrated that IPs produced from Fe-rich slags are structurally different from "Fe-enriched" aluminosilicate geopolymers, in more than just Fe-Al substitution in tetrahedrally-coordinated sites. In recent work, Peys et al. (2019) used in situ X-ray total scattering and subsequent pair distribution function (PDF) analysis to describe the formation mechanism of Fe-rich alkali-activated materials. They found that the atomic rearrangements undergone by Fe-silicate species are heavily dependent on the alkali cation provided by the activating solution. In the case of sodium, the atomic correlations of the parent precursors are maintained in the intermediate products, while potassium solutions induce an increase in the coordination number of Fe species. Moreover, it was reported that Fe^{2+} and Fe^{3+} oxidation states coexist in the binder phase under different forms. The Fe^{2+} state was observed to be present as trioctahedral layers, while the participation of Fe^{3+} in the polymerized silicate network seemed most likely. Additionally, PDF analysis of matured specimens has shown significant modifications, suggesting the long-term oxidization of the Fe^{2+} species present in the trioctahedral layers.

From the above, it seems evident that many questions remain unanswered to enable a full understanding of the structural role of iron during alkali activation and, to a larger extent, to describe the effects of calcium "enrichment" in Fe-rich systems. Hence, the effects of CaO-rich admixtures on reactions kinetics of Fe-Ca-rich systems and the products formed could not be unraveled from the available literature, neither as their impact on IP properties.

Hence, the feasibility of using CaO-based admixtures to mitigate shrinkage phenomena on Fe-rich systems was assessed, while simultaneously investigating their impact on fundamental properties of fresh pastes and hardened IP specimens. Aiming to gain deep knowledge on the effects of CaO-rich admixtures, the impacts of such admixtures on setting time, autogenous and drying shrinkage, porosity, microstructure, mineralogy, and strength development were evaluated. The results confirmed that CaO-rich admixtures can be used to increase the long-term volumetric stability of $CaO\text{-}FeO_x\text{-}Al_2O_3\text{-}SiO_2$-rich IPs. A holistic overview of their effect is provided, and an optimal dosage prescribed.

.

Experimental

The K18 formulation was selected as the reference binder in this investigation. The description of the starting materials and mixture portions of the reference binder can be found in sections 3.1 and 3.2, respectively. A commercially available CaO-rich material (Expandex C-NEW, Sika, Italy) was used as an expansive agent (EA). EA was determined to be mainly composed of CaO 73.0, SiO_2 3.6 and MgO 1.5 and minor contents of Fe_2O_3, Al_2O_3, K_2O, TiO_2, Na_2O, Mn_2O_3, SO_3, SrO, P_2O_5 (all less than 1.0 wt%), with 20.6 wt% loss on ignition (LOI). Trace amounts of calcite ($CaCO_3$; PDF 00-005-0586), lime (CaO; PDF 00-037-1497) and portlandite ($Ca(OH)_2$; PDF 00-004-0733) were detected in XRD patterns; possibly due to partial hydration and subsequent carbonation, Figure 3.5.1.

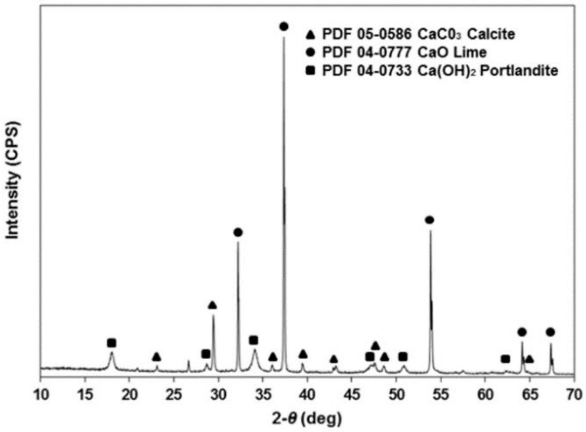

Figure 3.5.1 X-ray diffraction patterns of the expansive agent (EA).

Three EA dosages (1, 2 and 3 wt% of solid precursors) were added to the reference paste (here referred to as EA0), and the corresponding IPs were termed as EA1, EA2, and EA3, respectively. The detailed description of the reference binders can be seen in Table 3.3.4. It should be noted that the analyzed pastes differ only by the amount of EA, whereas the other mix components were kept constant. All IPs were synthesized following the procedure described in section 3.1 modified by employing 2 extra minutes for mixing the EA.

The IPs setting time was determined as prescribed by EN196-3:2016. In order to investigate the dynamics of autogenous shrinkage, a laser measurement system was used, as shown in Figure 3.5.2. The set-up consisted of two laser units horizontally aligned and directed to lightweight reflectors placed on top of the pastes. A polypropylene foil was used to isolate the pastes from direct contact with the metallic mold and to minimize water evaporation. The distance between the lasers and the reflectors was recorded continuously for 10 d and the sum of the relative displacements was converted into linear deformation.

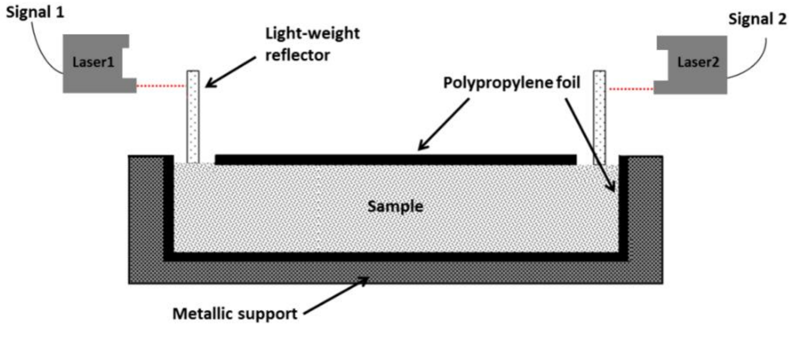

Figure 3.5.2 Schematic representation of autogenous shrinkage measurement apparatus.

To further evaluate the long-term impact of Ca-rich compounds on drying shrinkage, two types of samples were produced. For preliminary measurements, six samples (2x2x16 cm^3) were produced according to EN12617-4:2002. On selected formulations, two samples (4x4x16 cm^3) were produced with a metallic spindle (type I), according to EN 12617-4:2002. The IPs were kept for 24 h at 20±1 °C and 95±1 % RH, being afterward demolded and cured at room conditions (20±1 °C; RH=65±5 %). The length variation of samples was monitored using a dial gauge with a sensitivity of 0.001 mm for up to 56 d after casting. Weight variation (with a precision of 0.01 g) was recorded during the same period. The samples' volume and apparent density were determined according to EN12390-1 and EN12390-7:2007 and used to estimate water absorption and open porosity. For each formulation, the flexural and compressive strength of two samples was determined according to EN196-1:2016. The mineralogical composition of hardened samples was assessed by X-ray diffraction (XRD) as described in section 3.1. Unharmed samples were collected from mechanical testing, then ground, sieved and low vacuum dried (40 °C) for 3 h prior to testing. The mineralogical evolution of the samples was monitored on the 1st, 3rd, 7th, and 28th d of curing. Scanning electron microscopy (SEM - EVO® MA 15) equipped with energy dispersive X-ray spectrometry (EDS, AZtecEnergy) was used to evaluate the differences in morphology and microstructure of the produced IPs after 28 d of curing. All backscattered electron images (BSE) were acquired using a 20 kV acceleration voltage and a work distance of 10.0 mm.

The IPs' pore size distribution was investigated by mercury intrusion porosimetry (MIP). Fractured samples from mechanical tests at 28 d of curing were collected and dried in a vacuum chamber for 5 hours (45 °C) prior to testing. A mercury surface tension of 0.48 N/m and a contact angle of 141.0° were set for the MIP measurements.

Results and discussion

Setting time

EA addition aimed to counteract shrinkage by combining its swelling potential with the reduction of free water in the system. However, it was possible that calcium compounds affect the nature of the reaction products, resulting in the formation of calcium silicate hydrate phases or calcium hydroxide precipitates depending on the medium conditions (Van Deventer, 2007). Under highly alkaline conditions, Ca-forms can rapidly dissolve and precipitate as $Ca(OH)_2$, providing extra nucleation sites accelerating the formation of polymeric networks (Temuujin, 2009). On the other hand, (i) the formation of calcium silicate hydrates removes silicate species from the activating medium and (ii) the formation of Ca-precipitates decreases the pH of activating solution due to the removal of OH- ions, hindering further the dissolution of more stable Si elements. These competing effects influence the reaction kinetics and products formed, which ultimately determine the IP properties. Seeking to minimize the disturbance of reaction mechanisms, EA was introduced only after the precursors' initial wetting/dissolution phase. Rising EA content was shown to accelerate setting time, suggesting that increasing calcium availability enhances the reaction kinetics, Figure 3.5.3. The final setting varied between 90 and 79 min, for EA0 and EA3, respectively, representing a reduction of 12 %. The impact was even more significant to the initial setting where a maximum reduction of 26 % was observed. These results were in line with the findings of Guo *et al.* (2015) who observed that even a small addition of calcium compounds rises setting and early yield stress. EA2 and EA3 present the most shortened but comparable initial setting times. When higher EA levels were attempted, flash settings occurred, thus limiting EA dosage.

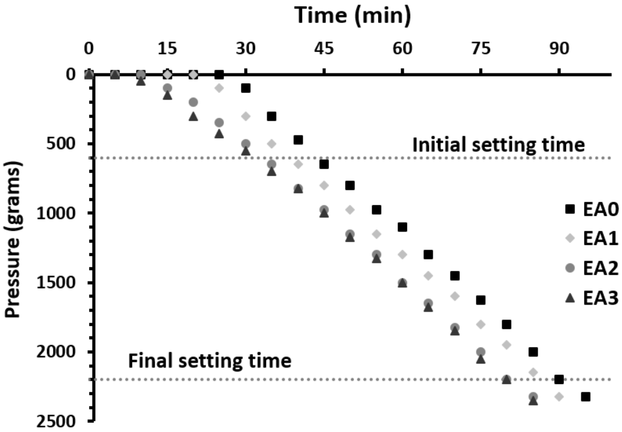

Figure 3.5.3 Setting time of IP pastes as a function of EA content.

Autogenous shrinkage

Figure 3.5.4 shows length variation due to autogenous shrinkage of the analyzed IPs as a function of EA content and time. It can be seen that the reference paste (K18) presented high linear deformation after the testing period. In the initial stage of the reaction, considered to be the timeframe from mixing until the initial setting time (≈42 minutes, Figure 3.5.3) capillary stresses can be negligible, and autogenous shrinkage is mainly attributed to chemical contraction. Thus, it is interesting to notice that shortly after that period, the autogenous shrinkage progression rate drastically reduces in the reference paste, which may indicate the point at which chemical shrinkage ceases and self-desiccation begins to dominate.

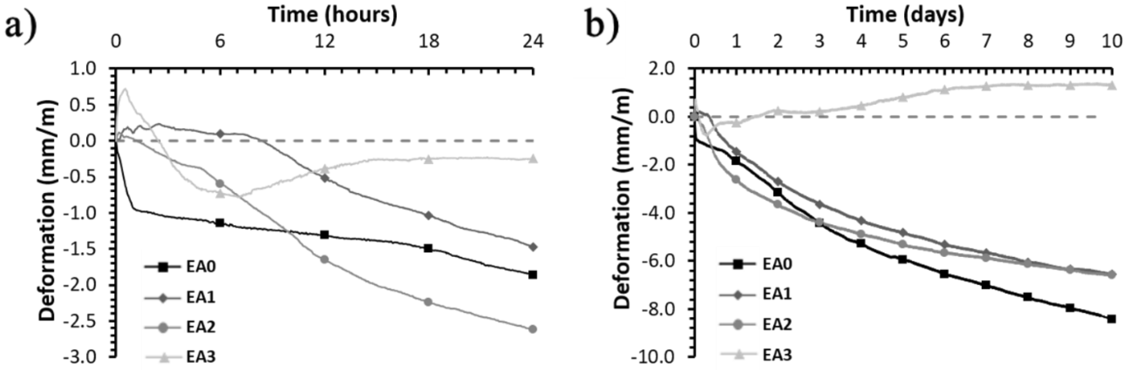

Figure 3.5.4 Autogenous shrinkage as a function of shrinkage reducing agent content: a) initial 24 h and b) evolution until 10 d of curing.

The addition of calcium-rich admixtures was expected to urge the formation of calcium hydrates species and/or increase the rate of formation of polymeric gel (Van Deventer, 2007; Guo, 2015) or promote the spontaneous Si-polymerization (Kellermeier, 2010), which could potentially affect both chemical and self-dissection processes. Figure 3.5.4b shows that the addition of CaO reduced autogenous shrinkage during the test period. In fact, samples with 1.0 and 2.0 wt% EA underwent approximately 20.0% less length variation than the reference paste, while with higher EA dosages a slight expansion occurred. As calcium oxide was introduced, its finer fraction immediately hydrated and induced an initial expansion, as can be seen in Figure 3.5.4a. Depending on the EA content, such expansion was able to partially mitigate or overcome early age autogenous shrinkage. The distinct behavior of EA1 and EA2 at a very early age is still not clear. Yet, as the reaction progresses, self-desiccation becomes the dominant shrinkage process and the addition of 1.0 and 2.0 wt% EA could only minimize its effects.

When 3.0 wt% EA was used, the initial chemical expansion was followed by a period in which self-desiccation imposed a considerable volumetric contraction. The continuous EA hydration was later able to mitigate such a contraction, with only a slight expansion visible after 10 d.

These results indicate that CaO-rich admixtures can, in fact, be used to control IPs' autogenous shrinkage, but more detailed analysis should be conducted to assess the possible influence of factors such as i) CaO homogeneous dispersion, b) early age relaxation effects and c) expansion restriction due to a rigid set-up.

Drying shrinkage

Drying shrinkage occurs due to the loss of internal water to the external environment through evaporation processes and has been identified as a relevant shrinkage mechanism in AAMs (Cartwright, 2014; Lee, 2014). It should be mentioned that the results discussed in this section comprise the contributions of all forms of shrinkage and should be understood as the total shrinkage.

Figure 3.5.5a, b shows the linear deformation and mass variation of 2x2x16 cm^3 samples up to 56 d. In all samples drying shrinkage was a continuous process, with the highest value recorded in the reference paste after 56 d of curing (21.4 mm/m). As CaO content rose, drying shrinkage was progressively reduced to a minimum of 7.9 mm/m when 3.0 wt% EA was used (-63%). In all IPs, between 76% and 85% of the total drying shrinkage was observed within the initial 7 d of curing and a high degree of dimensional stability was reached after 28 d. Mass loss varied between 3% and 4% and occurred mainly in the initial 7 d of curing. Total shrinkage has shown a direct correlation with mass loss. The reference binder (K18) presented the highest shrinkage and mass loss while increasing EA dosage progressively reduced the magnitude of those values. Nonetheless, all IPs presented low open porosity (< 4 %) and water absorption capacity (< 2 %), and slight increasing density as EA rises, from 2.22 up to 2.32 g/cm^3.

As previously mentioned, the addition of calcium compounds can contribute to the formation of calcium hydrate species and /or increase the rate of formation of polymeric Si-rich materials. If the former occurs, expanded reaction products are formed and the free water available in the polymeric structures reduces. If the latter, calcium compounds contribute to an increase in the formation of polymeric gel and more stable structures are obtained, thus enhancing the IPs' volumetric stability. The microstructural changes imposed by EA addition along with their effect on pore size distribution will be discussed in the following sections.

Given that surface area may considerably interfere with evaporation processes and consequently affect drying shrinkage, probes of selected IPs with different superficial area per unit of volume ratios (h) were produced and monitored over 56 d. The results show that by reducing *h*, linear deformation decreases, but the magnitude of such reduction mainly depends on EA presence (see Figure 3.5.5c, d). In the reference binder, the final linear deformation was decreased by 16 % while its mass variation increased by 12 %. On EA2, reducing *h* resulted in a comparable mass loss after 56 d, but shrinkage was diminished by 9 %. In both cases, a more progressive mass loss was promoted, which contributes to a decrease in capillary stress at early ages and an increase in the volumetric stability of polymeric structures.

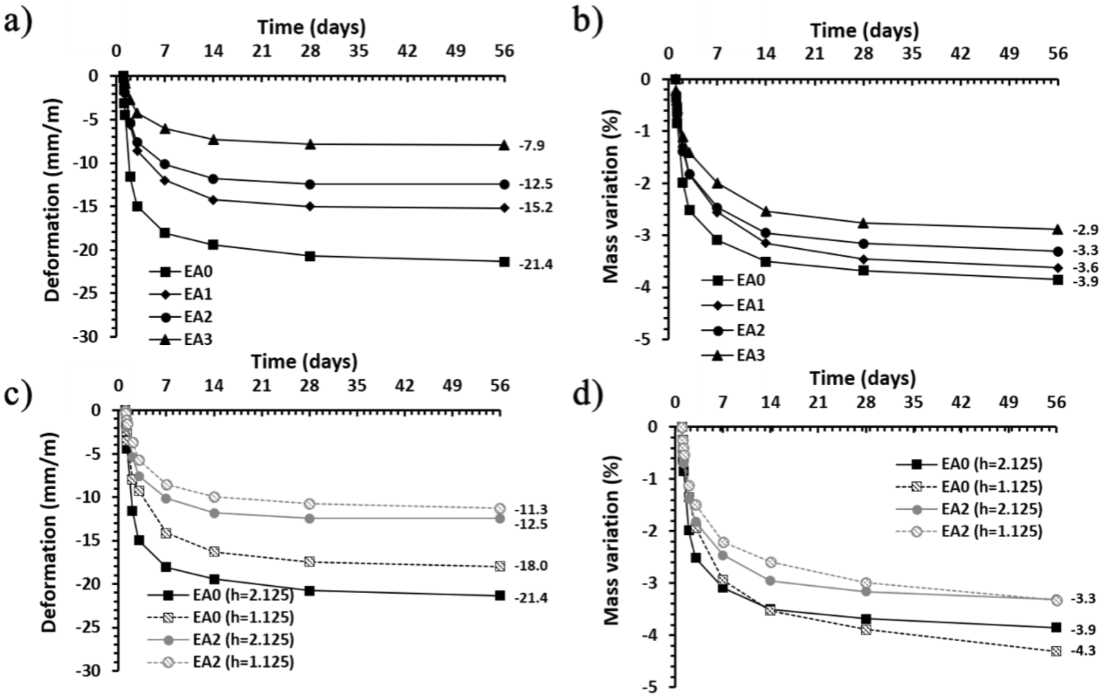

Figure 3.5.5 Linear deformation (a, c) and specific mass variation (b, d) as a function of time, EA content, and surface-to-volume ratio (*h*).

XRD analysis

Figure 3.5.6 shows the IP XRD patterns, in which it is evident that binders retain a mainly amorphous structure. No significant shift of the broad hump center towards higher 2θ values was observed. A sharp peak was visible in all patterns, revealing calcite ($CaCO_3$; PDF 00-005-0586) as the prevalent crystalline phase formed.

At later ages, and with increasing EA content, vaterite ($CaCO_3$; PDF 01-074-1867), a metastable phase of calcium carbonate, was identified (Figure 3.5.6b-d), but the pronounced broad hump and the low magnitude of vaterite's secondary peaks make it hard to postulate its presence with certainty. The almost exclusive formation of calcite agrees with to work of Lakshtanov *et al.* (2009), who has shown that polymeric silica serves as nucleation sites for calcite. Moreover, the formation of calcium carbonate species in IPs has been associated with the high pH of the pore solutions that facilitates the reaction of calcium species with atmospheric CO_2 (Salman, 2105). Along with the presence of calcium species and highly alkaline pore solutions, IPs microstructure also has a determinant effect on the formation of calcium carbonates as it controls the access of atmospheric CO_2 to the pore solution and inner reaction products.

Thus, although the addition of EA increases the availability of calcium species, an increase in calcium carbonates was not observed, as XRD patterns show (Figure 3.5.6). In fact, the increased availability of calcium compounds led to the formation of denser structures when EA content does not exceed 2.0 wt% (detailed in the "Microstructure" and "Porosity" sections), which restricts atmospheric CO_2 diffusion and so limits the advance of carbonation. However, this does not apply to the EA3, where an increase in calcium oxide availability is followed by a slight increase of porosity (Figure 3.5.8a), even though carbonation levels remain roughly the same. One explanation may lay in the fact that EA3 samples present a considerably different pore size distribution comprising considerably larger pores, as shown by MIP measurements (Figure 3.5.8b). Despite increased levels of porosity, the reduction of the pores' specific surface area decreased contact area with atmospheric CO_2, hence reduced the formation of carbonated species.

Nonetheless, the formation of calcite, which was verified in all samples, can contribute to IPs' densification by filling the porous structures and thus enhancing samples' volumetric stability and mechanical properties as it will be shown later.

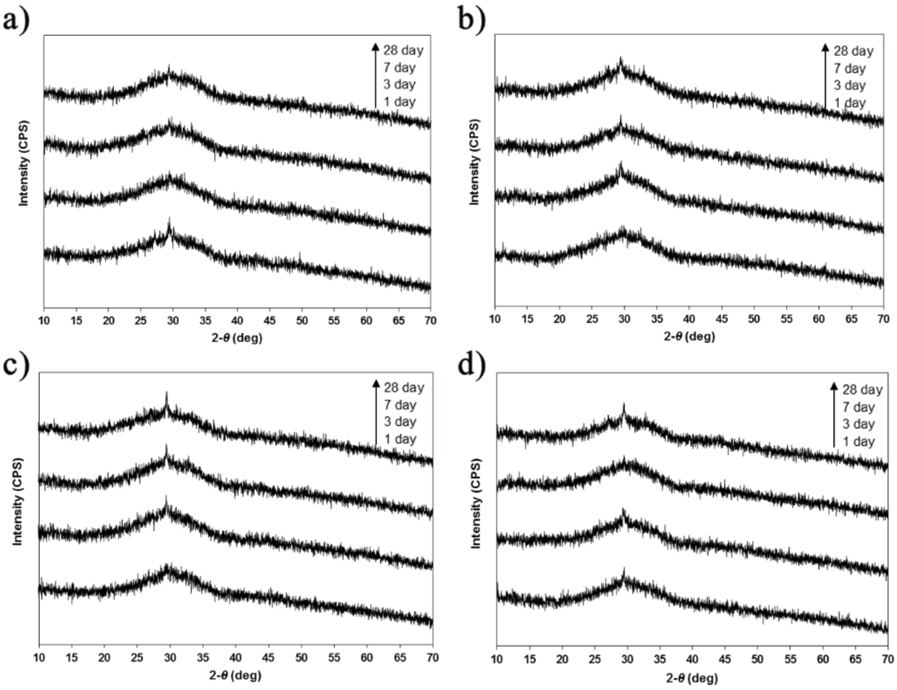

Figure 3.5.6 IPs XRD patterns and their temporal evolution as a function of EA: a) reference binder (K18); b) 1.0 wt% EA; c) 2.0 wt% EA and d) 3.0 wt% EA.

Microstructure

Figure 3.5.7 shows representative backscattered electron imaging micrographs of IPs produced with distinct amounts of EA. A binder phase was formed in all samples, but the existence of unreacted particles confirms that complete dissolution was not achieved (Figure 3.5.7a). The high solid-to-liquid ratio used (3.20) may have limited precursors' dissolution, but all IPs show a homogeneous matrix in which undissolved particles acted as small-sized aggregates (Figure 3.5.7a-f). These results are in agreement with previous findings (Machiels, 2014), which reported samples with similar S/L ratios as having a degree of precursor's dissolution of 76 wt%. Although the quantification of unreacted particles has not been performed, a slight decrease in the number of unreacted particles seems to be promoted as EA content rises.

Depending on the solutions' saturation level with respect to amorphous silica, calcium carbonates can urge the polymerization of silica in their vicinity (Kellermeier, 2010), thus accelerating IPs' polymerization. On the other hand, the formation of Ca-precipitates decreases the activating solution pH due to the removal of OH^- ions, limiting the precursors' dissolution and reduces the medium's supersaturation level. As previously demonstrated, increasing EA content led to shorter setting times, which, combined with the reduction of unreacted particles, suggests that the former is favored when small amounts of calcium oxide are added to an already Ca-rich system.

EDS analysis was performed on selected unreacted particles revealing a homogeneous composition constituted by the chemical elements of the main solid precursor (not shown here for the sake of brevity). Some metallic artifacts were detected (as individuated in Figure 3.5.7b), which were mainly composed of FeO_x>90.0 wt%.

The binder phase of the reference sample has shown to be composed of approximately SiO_2: CaO: Fe_2O_3: Al_2O_3: K_2O = 2:1:1:0.5:0.2, except for some circular areas where an increased content of Si elements was observed (i.e., circular areas identified in Figure 3.5.7b).

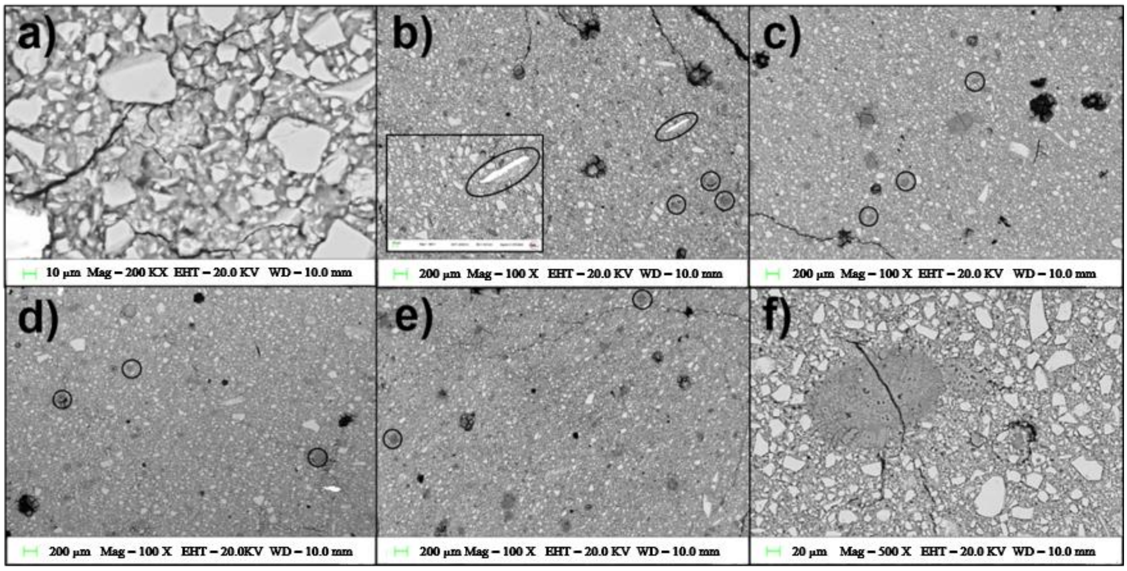

Figure 3.5.7 Backscattered electron imaging micrographs of IPs' microstructure and close-ups of selected areas after curing for 28 d: a) reference binder phase and unreacted particles; b) K18 microstructure; c) 1.0 wt% EA; d) 2.0 wt% EA; e) 3.0 wt% EA and f) Ca-rich binder phase. The insert circles in b-e show Si-rich binder phases.

The higher Si content in these areas may suggest that silica fume particle dissolution occurs at these locations and, due to mobility restrictions imposed by the high viscosity and short open time of the pastes, local heterogeneities were formed in the gel phase (Figure 3.5.7 b-e). These small circular areas were detected in all samples, however, with a growing Ca content as EA rose. Furthermore, EA-containing samples exhibited areas where a Ca-rich gel phase predominated. Figure 3.5.7 shows one of those areas in which the binder phase is mainly constituted by a Ca-rich gel (approx. SiO_2: CaO: Fe_2O_3: Al_2O_3: K_2O = 1:2:0.1:0.2:0.03). In all samples, cracks pierced the binder phase as the undissolved particles limited their propagation. Crack formation and development was particularly severe in Ca-rich binder phases, of which Figure 3.5.7f is a representative example. Yet, Ca-rich areas represent a small portion of the binder phase; the cracks formed on those areas are being compensated by the formation of denser and less fractured structures on a macroscopic level. As can be seen in Figure 3.5.7b-e, as EA content increases up to 2.0 wt%, fewer and finer cracks were formed, while with higher EA dosages more cracks were induced. These results are corroborated by MIP data (detailed in the "Porosity" section), which revealed higher and broader porosity in EA3 IPs. Further, some spherical pores were observed, especially in the reference and EA1, which can be attributed to air trapped during mixing. Those pores nearly vanished in EA2 and EA3 IPs, further contributing to the production of dense and mechanically strong polymeric structures as shown in Figure 3.5.9.

Porosity

Pores could be grouped into four main categories according to size: i) micropores, <1.25 nm; ii) mesopores ranging from 1.25-25 nm; iii) macropores ranging from 25-5000 nm; and iv) air voids and pre-existing microcracks >50000 nm (Collins, 2000). Micropores are inherent to reaction products whereas capillary pores (comprising both meso- and macropores) can be seen as the residual unfilled spaces between them. Drying shrinkage will greatly depend upon capillary pore size distribution, as it determines the extension and stresses generated by water loss during curing.

Figure 3.5.8 presents the cumulative and relative pore size distribution of IPs samples as a function of EA content. Micropores were outside of the range of measurement and therefore their relative volume is considered negligible. In all IPs, most of the pores had a pore radius <25 nm and a higher volume of mesopores is concentrated around 5 nm. The amount of mesopores (vol%)

increased as CaO dosage rose, from 59 vol% in EA0 sample to 68 vol% in EA2 and decreased to 57 vol% in EA3. EA3 hastened viscosity and setting may have compromised their proper confinement and particle packing, increasing the number of voids and cracks in these samples. In fact, Figure 3.5.8b shows that EA3 were the only IPs containing a proportion of pores with dimensions higher than 10000 nm. These results are in good agreement with the increased amount of visible cracks present on those IPs relative to EA2 (Figure 3.5.7b-e) and with the reduction of strength development demonstrated in Figure 3.5.9.

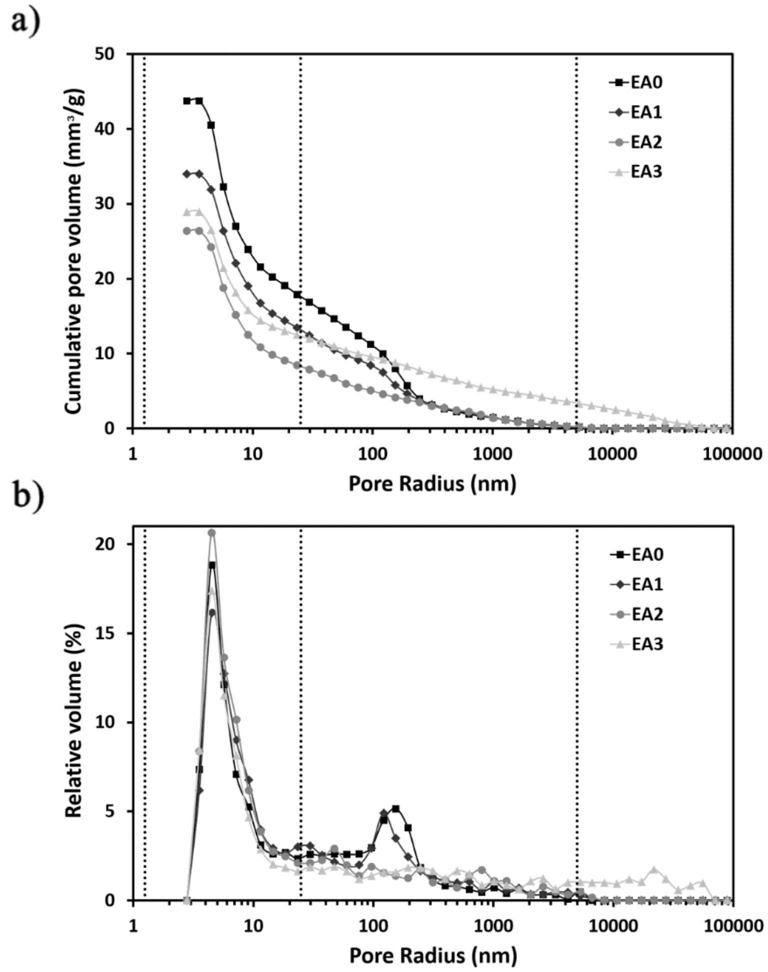

Figure 3.5.8 Cumulative pore volume (a) and relative pore size distribution (b) of samples after 28 d of curing.

Strength development

Figure 3.5.9 shows the IPs flexural and compressive strength after 28 d of curing. EA2 achieved the highest compressive strength while EA0 presented the best flexural performance. Increasing Ca content caused the refinement of the structure resulting in denser and more compact matrixes (Figure 3.5.9). These results are supported by existing literature (Van Deventer, 2007; Guo, 2015) and in line with the increase of apparent density observed as EA dosage rose, from 2.22 up to 2.32 g/cm^3.

With the exception of EA3, the compressive strength increased as the EA content rose, while the flexural strength exhibited the opposite trend. As suggested by Temuujin *et al.* (2009), the fine microstructure produced by CaO addition may cause heterogeneous nucleation and crystallization. Also, EA3 shortened setting did not give time for proper casting and de-airing, contributing to the decrease of mechanical performance observed. In general, the results indicated that EA had a positive impact on compressive strength development while the increase of rigidity of structures led to the decrease of its flexural strength. This trend was similar to what was observed when calcium was added in metakaolin (Granizo, 2002; Guo, 2015) and fly-ash (Temuujin, 2009; Guo, 2015) - based systems but in contrast with findings reported for blast furnace slag systems (Yuan, 2014). The latter is probably linked to the already high content of Ca available in the system. The distinct strength development of different systems stretches the necessity to fully comprehend the role of cationic elements and elucidate the relation of its content and form with the reaction products formed.

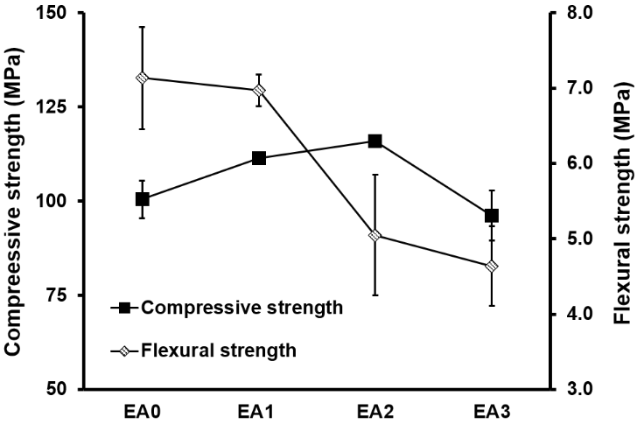

Figure 3.5.9 IPs mechanical properties after 28 d of curing. The lines are drawn as a guide to the eye.

Conclusions

The use of a CaO-rich admixture to increase the dimensional stability of $CaO\text{-}FeO_x\text{-}Al_2O_3\text{-}SiO_2$-rich IPs and its effect on setting time, autogenous and drying shrinkage, porosity, mineralogy, microstructure and, strength development were investigated. Drying shrinkage was confirmed as the governing mechanism affecting IPs volumetric stability, however negligible after the initial 28 d of curing. The contribution of autogenous shrinkage to IP total shrinkage was found to less significant.

The reference pastes presented the highest drying shrinkage while increasing the dosage of shrinkage reducing agent (EA) was found to reduce drying shrinkage up to 63%. The reduction of drying shrinkage was proportional to EA content; however, elevated dosages of such admixture were found to considerably hasten the pastes' setting times and have a detrimental impact on IPs microstructure. On the other hand, small dosages of CaO-rich admixtures did not induce significant changes in the IPs' mineralogical evolution and promoted the formation of denser microstructures. The produced IPs presented low open porosity (< 4.0%) and water absorption (< 2.0%).

Considering the effects EA on setting time and strength development, an optimal admixture dosage of 2.0 wt% was therefore recommended. At this dosage, autogenous and linear drying shrinkage was considerably reduced, while a reasonable fluidity and setting time were maintained to guarantee that the samples were cast properly. Furthermore, it was shown that EA2 samples presented enhanced compressive strength (116 MPa) relative to its parent binder (K18, 100 MPa) and maintained a flexural strength above 5 MPa.

In summary, the results presented here confirmed that CaO-rich admixtures can be used to increase IP's long-term volumetric stability. A holistic overview of the effects of such admixture was provided and an optimal dosage prescribed.

3.5.2 Improving the volumetric stability IP binders with polypropylene glycols

This section is partially based on a conference article entitled “The effects of polypropylene glycols on the properties of Fe-rich alkali-activated materials” by Ascensão, G., Faleschini, F., Vleugles, J., Rahier, H., Marchi, M., Segata & Pontikes, Y. published in the *Proceedings of the 17th International Waste Management and Landfill Symposium,* September 2019, Sardinia, Italy.

However, in the following text, the characterization of the inorganic polymers produced was extended and the spectrum of analysis enlarged to provide a more comprehensive understanding of the effects of polypropylene glycols in alkali-activated systems.

Introduction

Despite the technical advantages of AAMs, such as rapid strength development and good fire and chemical attack resistance (Pacheco-Torgal, 2008; Shi, 2011; Kalina, 2018), their high susceptibility to shrinkage can hinder their wider use and several admixtures/additives have been tested attempting to reduce such phenomena. Among them, organic compounds, such as polypropylene glycols (PPG), have been used to synthesize organic-inorganic polymers showing promising results both in metakaolin and blast furnace slag-based systems (Palacios, 2007; Catauro, 2015). PPG are non-ionic surfactants having both a hydrophilic and hydrophobic chains and such amphiphilic character reduces the surface tension at the pore solution/air interface. In addition, the introduction of PPGs is known to broaden the pore size distribution in IPs structures, further reducing internal capillary stresses.

Following the theoretical model proposed by Szleifer *et al.* (1990), the decrease in surface tension will be proportional to the polymeric chain length of PPG. In fact, Kalina *et al.* (2018) reported that PPG solutions with a higher molar weight (longer hydrophobic chain) present lower surface tension and smaller concentrations allow to reach the critical micelle concentration (CMC). Those results suggest that PPGs with higher molar weights might be more suitable candidates to be used as shrinkage reducing agents in IPs. Yet, it was shown later that raising the volume of the micelles can cause an irregular PPGs dispersion, resulting in heterogeneous shrinkage and higher total length variation of blast furnace slag prismatic samples after 28 d of curing.

Palacios *et al.* (2007) studied the effects of PPGs on alkali activation reaction kinetics and reported that PPG delays and intensifies the precipitation of reaction products. The nature of the reaction products was also affected by the presence of PPGs, prompting the formation of more Si-rich products. Although no mineralogical changes have been reported, the impact on IPs’ mechanical performance was evident. The addition of > 2.0 wt% PPG considerably raised flexural strength, while no substantial changes in compressive strength were induced. On the other hand, Kalina *et al.* (2018) reported that the impact of PPGs on mechanical properties was dependent on the molar weight. Low molar weight PPGs had a detrimental effect on compressive strength while longer hydrophobic chains could promote a slight increment.

In summary, PPGs seem to enhance IPs volumetric stability but their effectiveness and effect on IPs’ properties are widely dependent on the synthesis conditions, and their impact on Fe-rich systems remains largely unknown. Therefore, the following section is dedicated to the assessment of the efficiency of different polypropylene glycols (PPG) as shrinkage-reducing agents in Fe-rich IPs. The effects of the PPG molecular weight and dosage on the drying shrinkage, porosity, and mechanical properties of the resulting IPs were investigated and are discussed herein.

Experimental

The K18 formulation was taken as the reference binder also here (S/L =3.20; K_2O/SiO_2=0.08). The detailed description of the binder can be found in section 3.3. Commercially available polypropylene glycols with two distinct molecular weights (400 and 1000 Mn, Alfa Aesar, Italy) were introduced in the activating solution during its preparation in amounts up to 5.0 wt% of the solid precursors' weight. With the exception of the reference formulation (RPa), all IPs were coded after PPG molar weight and content. For instance, 1000PPG3 stands for samples were PPG content of 3.0 wt% with molar weight of 1000 Mn was added in the activating solution.

The pastes' setting time was determined as prescribed in EN196-3:2016. For each formulation, six samples (2x2x16 cm^3) were produced with a metallic spindle (type II) in each extremity according to EN 12617-4:2002. PPG-containing IPs were cured at room temperature under the conditions described in 3.3. Low curing temperature allowed the direct comparison with a previously discussed shrinkage mitigation strategy and avoided any possible thermal degradation of the organic compounds (PPGs). The IPs length variation was monitored using a dial gauge up to 28 d after casting, and the weight variation was recorded during the same period. Mass and length variation refer to the initial IPs' individual measurement taken upon demolding (24 h after mixing). Similar to the investigations performed to assess the use of CaO-admixtures as SRA, a second batch of samples of selected formulations was produced to assess the impact of surface area in drying shrinkage processes.

For each formulation, two samples (4x4x16 cm^3) were prepared and cured under the same conditions. The IPs volume and apparent density were determined according to EN12390-1 and EN12390-7:2007, respectively. Flexural and compressive strength were determined according to EN196-1:2016. The pore size distribution was investigated by mercury intrusion porosimetry (MIP) with a mercury surface tension of 0.48 N/m and a contact angle of 141.0 °. Fractured samples from mechanical tests were collected and dried for 5 h at 45 °C in a low vacuum chamber prior to MIP measurements. Scanning electron microscopy (SEM - EVO® MA 15) was used to evaluate the effects PPG on IPs morphology and microstructure after 28 d of curing.

Results and discussion

Setting time

Table 3.5.1 shows the effects of PPG dosage and molecular weight on IPs setting time. Independent of PPG molecular weight, setting time was extended as the added dosage rose. These results agree with the findings of Palacios *et al.* (2007) who had reported a delay in the precipitation of reaction products when introducing PPG into alkali-activated systems. Depending on the molecular weight of the PPG used, the final setting of IPs containing 5 wt% PPG varied between 103±1 and 111±8 min, which represents an increase of 13 and 21 min relatively to the parent binder. The impact of PPGs was even less significant to the initial setting where a maximum increase of 16 min was observed in 1000PPG5. Nonetheless, increasing PPG molecular weight seems to have an impact on the polymerization reaction, promoting a slight increase in setting times. As will be later discussed, this also led to different morphologies and lower strength development of IPs produced with PPG with longer hydrophobic chains.

However, in all IPs produced here, modifications on setting time provoked by PPGs were marginal, particularly if dosages do not exceed 3 wt%. Conversely to CaO-rich admixtures, the rapid setting was not a limiting factor when considering using PPG as shrinkage reducing agents.

Table 3.5.1 Initial and final setting time of PPG-containing IPs.

PPG molar weight	Code	Initial setting	Final setting
		Min.	Min.
-	RPa	42±2	90±6
400	400PPG1	47±4	88±4
	400PPG3	49±1	93±6
	400PPG5	54±1	103±1
1000	1000PPG1	50±2	92±1
	1000PPG3	55±4	100±6
	1000PPG5	58±5	111±8

Drying shrinkage

The high drying shrinkage of IPs has been extensively reported in the literature (Palacios, 2007; Catauro, 2015; Kalina, 2018), and it was shown to assume a dominant character on mass and volume changes over time of the reference binder considered here (K18). The considerable drying shrinkage observed in when using CaO-rich admixtures were used as SRA pointed out the necessity to develop additional shrinkage-control strategies. The shrinkage and mass variation as a function of time for PPG molar weights of 400 and 1000, are given in Figure 3.5.10.

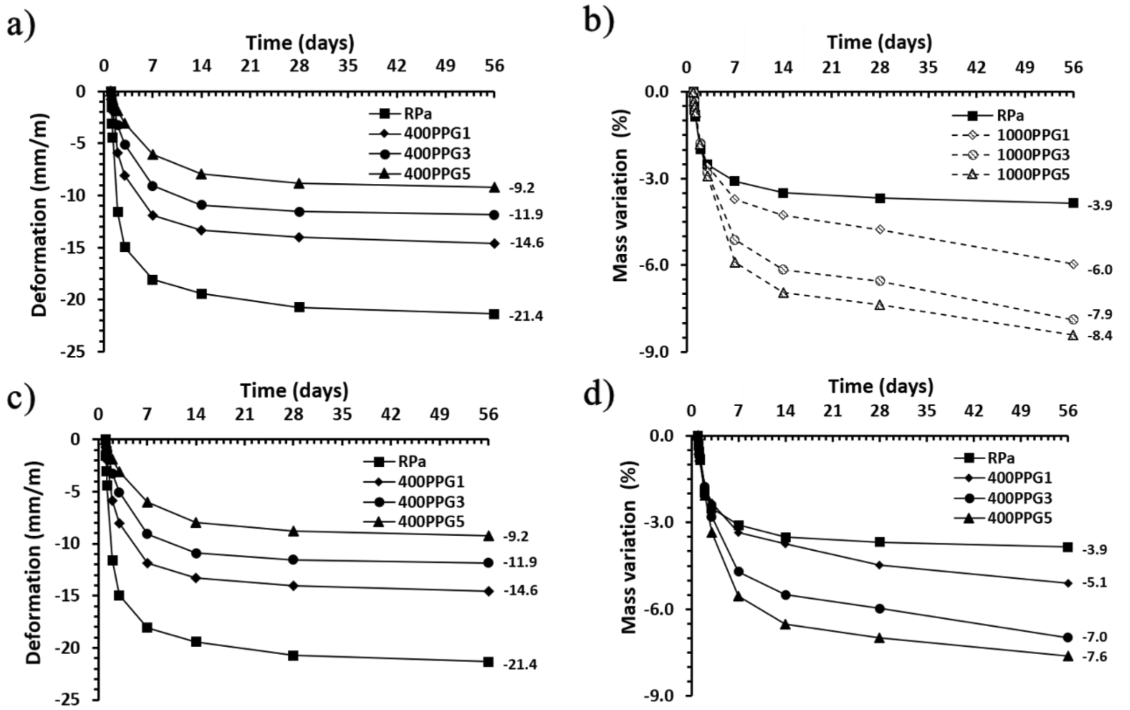

Figure 3.5.10 Linear deformation (a, c) and mass variation (b, d) as a function of time for different PPG molar weights and loadings.

In all IPs, mass loss was a continuous process through the testing period, although more pronounced during the initial 7 d of curing; accounting for 75-85% of the total mass loss. It can be seen that the organic phase content governs mass loss, while the influence of molar weight was less significant. To a given dosage, PPG with higher molar weight systematically presented higher mass loss values. These results are in agreement with the findings of Kalina *et al.* (2018) who reported that PPG solutions with a higher molar weight have lower surface tensions, thus being expected to facilitate water evaporation from the polymeric structures.

Independently of the organic phase used (PPG 400 or PPG 1000), mass loss after 7 d increased with increasing PPG addition, meaning that a more sudden water egress occurs. These results are in contrast with linear shrinkage measurements where the opposite trend was observed. In fact, Collins *et al.* (2000) suggested that the mechanism of drying shrinkage on IPs cannot be entirely attributed to water egress and ascribed critical importance to the pore size distribution in determining its progression and magnitude, which will be later discussed.

To evaluate the influence of the samples' surface area on drying shrinkage, the volumetric stability of 3PPG400 and 3PPG1000 samples with lower surface-to-volume ratio (*h*) was determined. Similar to IPs where CaO-rich admixtures were used as SRA, reducing *h* resulted in comparable specific mass variations but decreased the IPs linear deformation after 56 d of curing, Figure 3.5.11a, b. The shrinkage reduction in PPG-containing IPs was comparable to the reference binder, ranging from 12 to 14%.

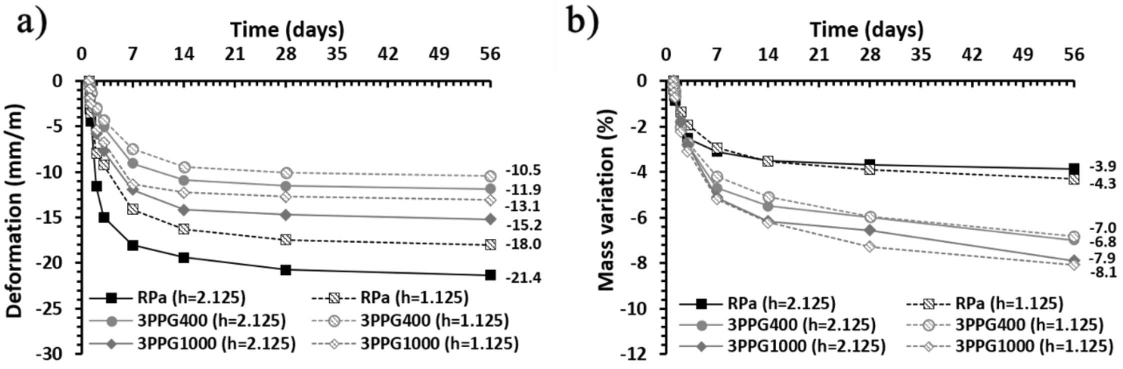

Figure 3.5.11 Linear deformation (a) and specific mass variation (b) as a function of time and surface-to-volume ratio (*h*).

Morphological analysis

Figure 3.5.12 shows representative backscattered electron imaging micrographs of K18, 3PPG400 and 3PPG1000 binders. As can be seen, the parent binder presented a dense microstructure, in which few porous could be seen, Figure 3.5.12a. Independently of the length of their polymeric chain, the introduction of 3.0 wt% PPG significantly increased the amount of pores formed in the IPs microstructures. The formation of structures containing higher levels of porosity and, pores of broader dimensions decreases internal stresses generated during water evaporation and, hence explains the increase volumetric stability of PPG-containing IPs observed in Figure 3.5.11. No significant differences could be observed between the morphology of 3PPG400 and 3PPG1000 IPs which was in good agreement with their similar shrinkage values after 28 d of curing (≈14 mm/m). However, Table 3.5.2 shows that IPs apparent density further decreases when using PPG of higher molecular weight, which suggests increased levels of porosities on those IPs. The pores structures formed were later characterized by MIP techniques that confirmed a systematic effect of PPG molar weight in the determination of the volume and size of pores formed. Still, the porosity and density of IP binders were mainly determined by PPG dosage as can be seen in Table 3.5.2. SEM micrographs of higher magnification did not show significant modifications on the morphology of the binding phases formed and EDS analyses confirmed their similar composition, predominantly Si, Al, Fe, Ca and K. Independently of their molecular weight, PPG does not seem to affect the nature of the phases formed, and therefore modifications on shrinkage and strength development can be related to the increase and enlargement of the porous formed as shown by MIP data.

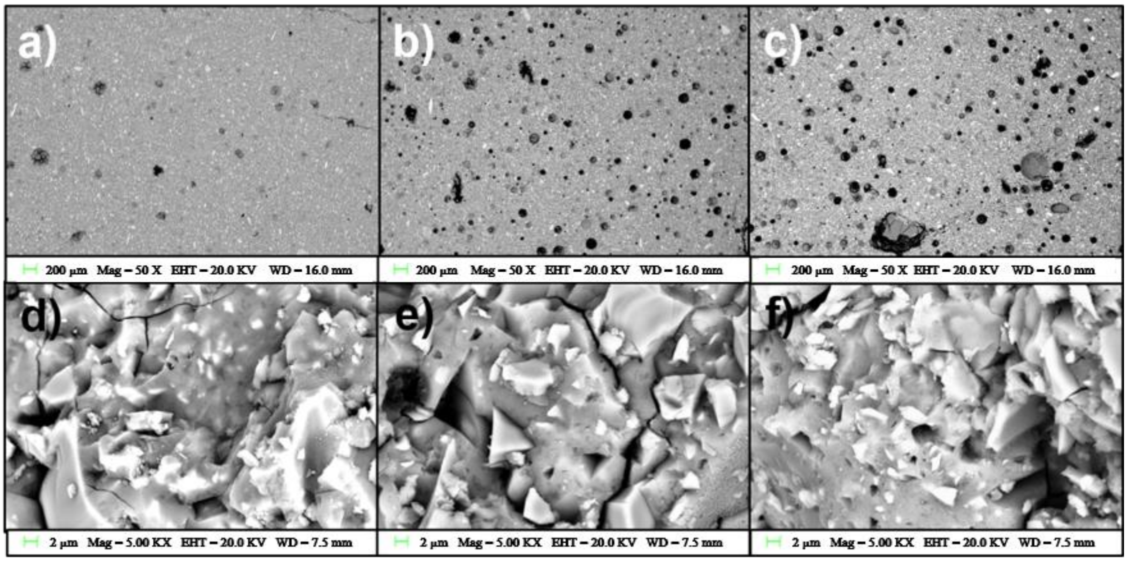

Figure 3.5.12 SEM backscattered electron imaging micrographs of RPa (a, d), 400PPG3 (b, e) and 1000PPG3 pastes (c, f) after 28 d of curing.

Table 3.5.2 IPs apparent density after 28 d of curing.

PPG molar weight	Code	Apparent density (g/cm^3)
-	RPa	2.22±0.04
400	400PPG1	2.12±0.01
	400PPG3	2.13±0.03
	400PPG5	2.08±0.01
1000	1000PPG1	2.10±0.06
	1000PPG3	2.09±0.02
	1000PPG5	2.05±0.01

Pore size distribution

Figure 3.5.13 shows the pore size distribution of purely inorganic and PPG-containing IPs. In general, MIP data show that PPG-containing IPs have higher porosity values and a broader pore size distribution relative to purely inorganic matrices. As PPG content increased, a more porous structure was formed. A systematic effect of the PPG molar weight was also observed since a higher cumulative pore volume was promoted by PPG 1000, Figure 3.5.13c.

Furthermore, as PPG content raised, the relative proportion of mesopores decreased, while the amount of macropores increased. The amphiphilic character of the PPGs, which intrinsically reduces the surface tension at the pore solution/air interface, was further complemented by a reduction of the capillary forces due to a pore size enlargement. Moreover, the surfactant molar weight also affected the pore size distribution. At low dosages (1.0 wt%), PPG of smaller polymeric chains contributed to form structures with fewer mesopores and a higher absolute amount and percentage of macropores. As the dosage of PPG increased, the differences between the porous structures formed became less significant, being even observed an increase of the macropores average size in samples produced with PPG1000. Such an increase of pore size in IPs produced with oligomers of a longer chain explains their higher specific mass variations over time.

Conversely, the IPs volumetric stability was clearly favored by the addition of shorter oligomers. Figure 3.5.10b, d shows that all PPG-containing IPs presented lower deformation relative to purely inorganic material (RPa), but IPs produced with PPG with lower molar weight presented the smallest shrinkage over time. Similarly, to the mass variation, linear deformation increased continuously within the timeframe of the present study, but mainly in the initial 7 d of monitoring (77-90% of the total length reduction).

Considering drying shrinkage, a progressive micromechanical process, a more homogeneous pore size distribution decreases the local capillary tensile forces, hence reducing the resulting total shrinkage (Wittmann, 1976; Collins, 2000). The higher miscibility of shorter oligomers results in a more regular dispersion, thence avoiding local heterogeneities and reducing the total length variation. Drying shrinkage seems to be mainly controlled by the organic phase content rather than its molar weight. It is interesting to notice that at lower concentrations (1.0 wt%), distinct PPGs have a similar effect on IPs shrinkage, whereas, at more elevated dosages, significant differences arose. This can indicate that at low concentration, PPG molar weight did not compromise its homogeneous dispersion, whereas if higher dosages were used such may not be guaranteed. Another possible explanation for such discrepancies can lay under the fact that oligomers of longer chains may require smaller dosages to reach their critical micelle concentration. Above the critical concentration, the surface tension remains relatively constant and providing extra PPG has limited impact on porous structures. However, the interaction of PPG with the particles being unknown, it is not clear how much the critical micelle concentration increases due to the removal of adsorbed molecules.

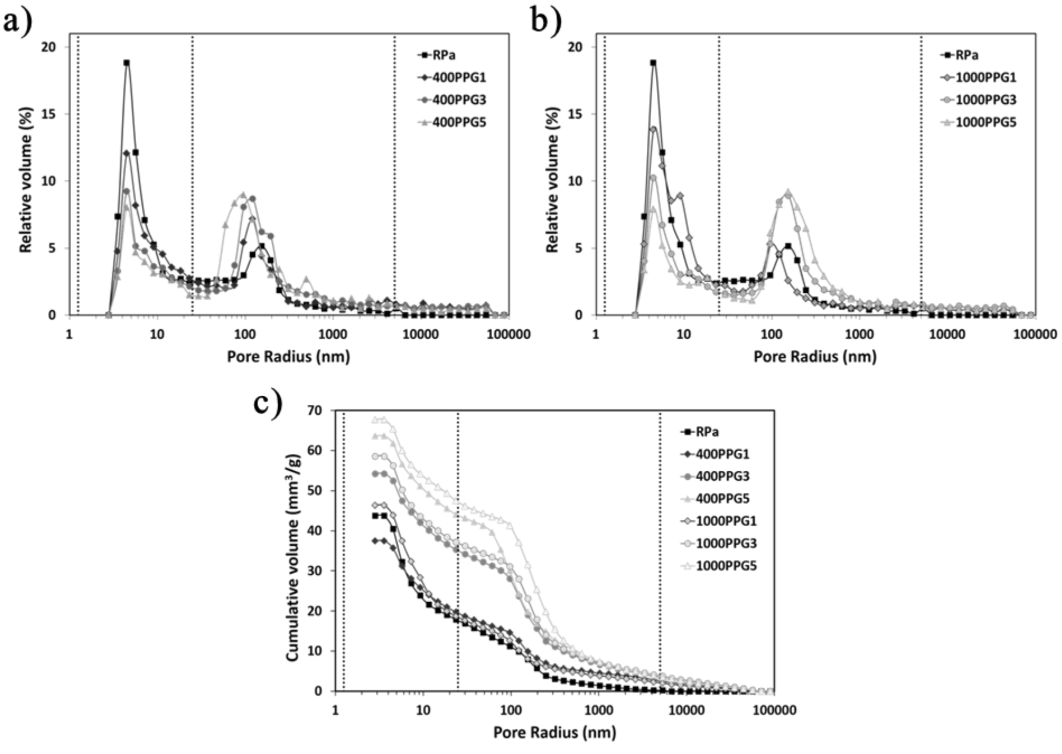

Figure 3.5.13 Relative pore size distribution (a, b) and cumulative pore volume (c) of IP after 28 d of curing.

Strength development

The compressive and flexural strength were measured after 28 d of curing and the influence of PPG content and molar weight on IPs mechanical properties assessed. The reference binder (K18) reached the highest flexural and compressive strength, and PPG addition had a consistent detrimental impact on strength development (Figure 3.5.14). The reduced mechanical performance was mainly governed by PPG content, whereas the influence of molar weight was less significant. An abrupt decay on the IP pastes' mechanical properties when PPG dosages above 3.0 wt% were used can be seen. The differences between 400PPG and 1000PPG samples reinforce the dependence of micelle formation and PPG dispersion. In both batches, the compressive and flexural strength reduced as PPG content rose, being in line with findings reported in metakaolin and BFS based systems (Palacios, 2007; Catauro, 2015,) and consistent with the increased porosity observed in Figure 3.5.14b. However, the distinct strength development of different systems requires a full comprehension of the role of polymeric glycols during the polymerization of Fe-rich systems and the nature of the interactions occurring between organic and inorganic components. Nonetheless, all the produced IPs presented a reasonable flexural (> 2.0 MPa) and compressive (> 50.0 MPa) strength after 28 d of curing, making them suitable for the majority of common construction applications.

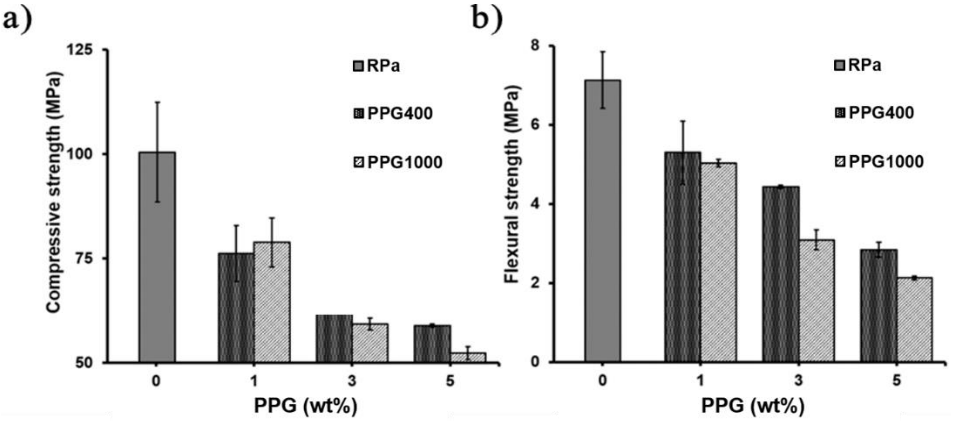

Figure 3.5.14 Influence of PPG content and molar weight on compressive (a) and flexural strength (b) after 28 d of curing.

Conclusions

Aiming to contribute in overcoming one of the major technical drawbacks for the wide of Fe-rich alkali activated materials, namely their high shrinkage, this work assessed the feasibility of using polypropylene glycols (PPG) as shrinkage reducing agents and investigated the effect of molar weight and dosage of the organic phase on the volumetric stability, porosity and strength development of IPs.

The experimental results have shown that PPG-containing systems have reduced shrinkage relative to pure inorganic matrices. The drying shrinkage was found to decrease as the organic phase content rises and its molar weight decreases. The beneficial impact on drying shrinkage was attributed to the combined effect of reduced surface tension of the pore solution and changes imposed on the porous structure. Both tested PPGs, with different molecular weight, increased the porosity (up to 55%) and average pore size (from 13 nm up 160nm), promoting the formation of mesopores at the expense of micropores; where capillary stresses are considerably lower. IPs reduce shrinkage values were favored by the addition of organic oligomers with shorter polymeric chains but was mainly controlled by PPG content rather than its molar weight. At a fixed dosage, lowering PPG molar weight ensures a more regular distribution which positively affected drying shrinkage. The maximum reduction of drying shrinkage achieved was 58%. The beneficial effect that polypropylene glycols exert on IPs volumetric stability was accompanied by a deleterious impact on strength development. Increasing amounts of PPG resulted in lower flexural and compressive strengths, being reduced from 7.1 to 2.0 and from 100.5 to 52.4 MPa, respectively.

Despite the significant decay in strength development provoked PPG, shrinkage values comparable to those reached when using the high dosages of CaO-rich admixtures as SRA were attained. As the impact of PPG on setting time was marginal, the use of organic SRAs was considered preferable relative to reactive admixtures, such as CaO.

In the same line of research, a parallel investigation was maintained in collaboration KU Leuven where the effects on porosity and shrinkage of an organic (2-Methyl-2.4-Pentanediol) and reactive admixture (GGBFS) were explored, and the results of such investigation will be discussed in the following section.

3.5.3 Minimize IPs shrinkage with 2-Methyl-2.4-Pentanediol and GGBFS

The following section is based on an article in preparation entitled “Modifying the pore size to minimize shrinkage by curing and using reactive and non-reactive additives in a Fe-rich inorganic polymer mortar” by Beersaerts, G., Ascensão, G. & Pontikes, Y.

This article results from a collaboration performed with Mr. Glenn Beersaerts, on the development of effective shrinkage mitigation strategies. The effects of curing conditions on IPs volumetric stability were firstly investigated (see section 3.5.4), but the use of organic and reactive SRA justifies the inclusion of these results here.

Relatively to the work that will be presented in section 3.5.4, the field of research was broadened by combining different curing conditions with the use of organic SRA (2-Methyl-2.4-Pentanediol) and the partial replacement of the parent Fe-rich precursor by ground granulated blast furnace slag, GGBFS.

In this investigation, a Fe-rich slag other than most widely used throughout this work was used as a precursor and therefore the produced binders and mortars were forcibly different from the ones previously reported. Nonetheless, the insights gathered allowed to describe the effects of 2-Methyl-2.4-Pentanediol and GGBFS on IPs’ volumetric stability and identify a promising shrinkage mitigation strategy that was later replicated in mortars produced form a CaO-FeO_x-Al_2O_3-SiO_2-rich slag.

In the following section, the main results of this investigation were summarized by Ascensão, G. but the ensuing text may not necessarily correspond to the final publication.

Introduction

Inorganic polymers (IPs) can be synthesized from Fe-rich residues, and the resulting material can present mechanical properties comparable to OPC-based systems. However, IPs are notably prone to shrinkage partially due to the nature of the reactions involved in their synthesis as previously described. Apart from plastic deformation in the fresh state due to polymerization reactions, chemical shrinkage also comprises autogenous deformation. Autogenous shrinkage began once the material starts to be stiffer and is driven by self-desiccation (Neto, 2008). Self-desiccation is generated in the pores as the pore solution continues to react with the pore surface to form additional binding phases. The saturation of the pores reduces, and capillary pore tensions are generated (Jensen, 2001). Additional shrinkage results from the evaporation process when the materials are exposed to an open environment (drying shrinkage). The size of the pores determines the stresses generated by capillary pore tensions according to the Young-Laplace equation, which means that as the pore radii decrease higher pore pressure will be developed (Wittmann, 1976; Collins, 2000).

Methods to mitigate shrinkage have been extensively developed for OPC-based systems, however much fewer successful investigations have been reported in the field of alkali-activated systems, particularly when (FeO_x)-CaO-rich slags are used as precursors. The influence of different curing temperatures has been assessed (Mastali, 2018), being demonstrated the beneficial impacts of curing at slightly elevated temperatures on IPs volumetric stability and strength development. The use of shrinkage reducing agents (SRA) such as polypropylene glycols has also been investigated here. The addition of such SRA intends to facilitate water evaporation and by doing so reduce the stresses that form in the IP structure, but their effectiveness is often challenged by the high alkalinity of the activation medium (Palacios, 2004). Apart from SRA, the binders' chemical composition and structure can be also modified by partially replacing the parent precursors by hydraulic admixtures such as OPC and CSA (blended cements), or anhydrite and periclase (Yuan, 2014; Li, 2019). It has been previously shown in section 3.5.1, that CaO-rich additives can be used to reduce the shrinkage of Fe-rich IPs with the added benefit of enhancing strength development. Yet, was also observed a considerable decrease in setting time as the additive dosage rose, imposing significant limitations on such shrinkage mitigation strategy. Extremely reduced setting times or even flash setting were observed when using minor dosages of OPC and CSA as shrinkage reducing agents, and therefore such experiments will not be presented here. However, introducing reactive admixtures in calcium-deficient systems may not be problematic and therefore was attempted here as the slag used as precursor presented a low Ca content (4 wt%).

Depending on the nature of the additives and admixtures used, different modifications on the binder chemistry, morphology and pore structure can be imposed on Fe-(Ca)-rich IPs and the development of suitable and competitive solutions needs further investigation. Hence, the effects on shrinkage behavior of 2-methyl-2.4-pentanediol (2M) and the partial replacement of a Fe-slag by GGBFS attempted. The autogenous and drying shrinkage of Fe-rich mortars and the forces driving such phenomena were investigated here. The impact of these two shrinkage mitigation strategies was analysed individually and in combination. In addition, different curing regimes were used to assess the significance of curing conditions in the volumetric stability of developed IPs. The partial replacement of Fe-rich residues by GGBFS and the addition of 2M were combined with different curing regimes in an attempt to achieve minimal shrinkage. The aim of this research was to identify an optimal mix design able to provide Fe-rich IPs mortars with shrinkage values compliant with current constructions codes and comparable to benchmark materials.

Precursor's characterization and mortars preparation

A Fe-rich slag from the Cu-metallurgical industry was used as the main precursor in this work. The slag's bulk chemical composition was determined by X-Ray Fluorescence (XRF, spectrometer PW 2400, Philips) and its crystalline composition analyzed by X-Ray Diffraction (D2 Phaser XRD, Bruker). The particle size distribution milled slag was determined by laser diffraction (LS 13 320, Beckman Coulter) while the slags' density and specific surface area were measured according to the ASTM-B417-64 and EN 196-6 standard, respectively. IP pastes were prepared by mixing for 1 m the powdered slag (KO) with a potassium alkali-silicate solution (SiO_2/K_2O =1.7; 65 wt% H_2O). The mixtures' overall S/L ratio was 0.38. Three 2M dosages (1, 2 and 3 wt% over slag mass) were introduced in the activation solution prior being to introduced to the powdered materials. In the case of slags' partial replacement, GGBFS was firstly mixed with the remaining Fe-rich slag in the dry state. Mortars were produced by adding sand (Sibelco, M31 type) in precursors/sand mass ratio of 1.5. An additional minute of mixing at low speed was provided to homogenize the binder with aggregates, followed by 30 seconds of high-speed mixing. IPs mortars were cast in metallic 4x4x16 cm^3 molds and kept for 24 h at 20±1°C and 95±5 %RH. Afterward, IPs were demolded and cured according to the conditions described in Table 3.1.3. Heat cured samples were kept 3 d at 60±1 °C and 95±5 % RH being afterward kept at room conditions. The detailed description of the mortar's mixture design is provided in Table 3.5.3.

Methods

To investigate the influence of 2M and GGBFS in the reaction kinetic of IP pastes, calorimetry experiments were conducted on an isothermal calorimeter at 20 °C (TAM Air, TA Instruments).

The plastic and autogenous shrinkage were determined by monitoring the length of corrugated tubes filled with IP mortars, according to ASTM C 1698. To determine drying shrinkage 4x4x16cm^3 prismatic samples were produced with a metallic spindle (type II) in each extremity according to EN 12617-4:2002. The samples were kept for 24 h at 20± 1 °C and 95±5 % RH. Afterward, the samples were demolded, and their initial length measured and a dial gauge used to monitored length variations until 28 d after mixing. Flexural and compressive strength were determined after 28 d with an Instron 5985 according to the EN 196-1 standard.

The pore size distribution of IP mortars was investigated by mercury intrusion porosimetry (MIP). IP mortars were dried for 24 h at 50 °C prior to performing the experiments to ensure a residual amount of water in the pore structure. A pre-step of low-pressure Hg intrusion was set (up 30 psi), being afterward raised until 30 000 psi.

Microstructural characterization was performed using a Philips XL30 FEG Scanning Electron Microscope (SEM) using cross-section samples coated with a 5nm Pt layer. High-resolution backscattered electron (BSE) images were collected using a 20kV beam, a spot size 5 and a working distance 10.0 mm. Elemental point analysis was performed with an energy dispersive x-ray (EDAX) detector.

Table 3.5.3 Experimental design.

Code	Mixture portion (wt%)					Curing conditions
	KO	Solution	Sand	2M	GGBFS	
02MA	100	38	150	0	0	Ambient
12MA	100	38	150	1	0	Ambient
22MA	100	38	150	2	0	Ambient
32MA	100	38	150	3	0	Ambient
32MH	100	38	150	3	0	Heat
02M15GA	85	38	150	0	15	Ambient
02M15GH	85	38	150	0	15	Heat
32M15GA	85	38	150	3	15	Ambient
32M15GH	85	38	150	3	15	Heat

Results and discussion

Precursor characterization

In Table 3.5.4 the bulk chemical compositions of KO slag and GGBFS are given. KO slag was mainly composed of Fe_2O_3, SiO_2, and Al_2O_3, with a residual amount of CaO also being present. GGBFS bulk composition was dominated by CaO, SiO_2 and Al_2O_3 and a considerable amount of MgO. According to XRD experiments, KO slag was predominately amorphous (92.7 wt%) with a minor portion of spinel (6.5 wt%) and metallic iron (0.7 wt%). Conversely, the commercial GGBFS selected was fully amorphous (Ecocem, 2018). The PSD distribution, density and specific surface area of KO and GGBFS can be seen in Table 3.5.5.

Table 3.5.4 Chemical composition of the Cu-slag and GGBFS used as precursors (% by mass).

	Fe_2O_3	SiO_2	CaO	Al_2O_3	ZnO	MgO	Cr_2O_3	P_2O_5	Na_2O	SO_3	Other
KO slag	41	32	4	11	2	1	2	2	2	n.d.	3
GGBFS	1	33	42	12	n.d.	8	n.d.	n.d.	1	2	1

*n.d. – not detected

Table 3.5.5 Particle size distribution distribution, density and specific surface area of KO and GGBFS.

	Density g/cm^3	SSA cm^2/g	D10 µm	D50 µm	D90 µm
KO slag	3.41	7700	1.2	4.8	17.2
GGBFS	2.90	4500	2.9	12.5	31.4

ICC measurements

The heat released during the initial 24 h of the reaction of 02MA, 32MA, and 02M15GA pastes was determined to assess the impact of 2M and GGBFS in the system reactivity. As can be seen in Figure 3.5.15, the addition of a 3 wt% dosage of 2-Methyl-2.4-pentanodiol did not provoke any relevant effect on the reaction progression. In 02MA and 32MA pastes, similar dissolution peaks were observed followed by equal induction periods and polymerization peaks. These results were different from the findings of Bilek *et al.* (2016), who had reported a significant delay in reactivity provoked by 2M introduction in alkali-activated systems. These results suggest that 2M may affect the reactivity differently depending on the binders' chemical composition. However, more detailed research should be conducted to further investigate eventual correlations.

On the other hand, the substitution of 15 wt% of KO slag by GGGFS significantly modified the heat flow during the initial 24 h of reaction. After the initial dissolution period, the second exothermic was considerably augmented and anticipated reaching its maximum after 1.5 h. Despite the larger dimension and reduced surface area of GGBFS particles, the rapid precipitation of abundant Ca and Mg phases change the precipitation of binding phases and lead to higher early heat flows. However, it can be seen that the early exponential increase ceases after 4 hours, evolving afterward in a more incremental manner. Conversely, GGBFS-free samples had shown lower heat-releasing rates during the first 5 h of reactions, having later rapidly evolved towards a steady increase state. The cumulative heat released by GGBFS-containing samples was surpassed after 8 h of reaction suggesting higher levels of reactivity of the reference mixtures at later ages.

Having in consideration the thermodynamic differences involved in the formation of distinct binding phases, one factor that could have contributed to the reaction kinetics of GGBFS-containing binders was excessive initial precipitation of Ca and Mg species. These precipitates can deposit on the surface of the less reactive slags' particles and act as a passivating layer that impedes the contact with the alkaline medium, and therefore preventing their dissolution.

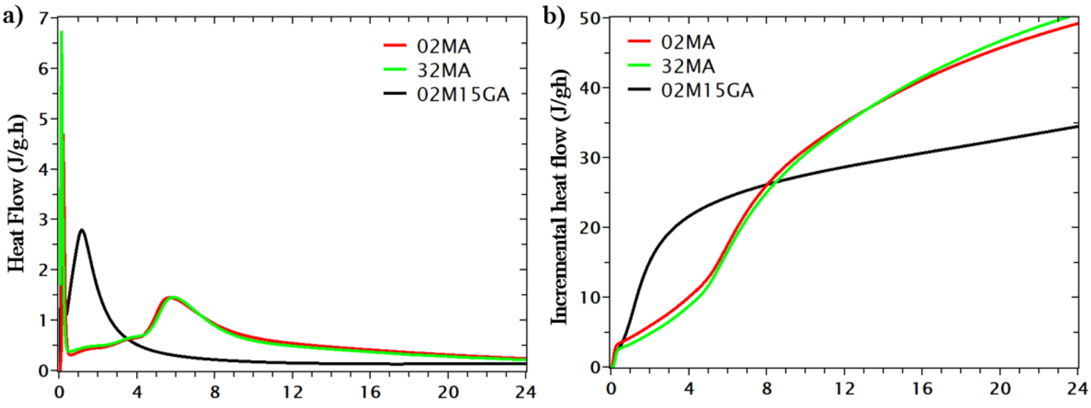

Figure 3.5.15 Effect of 2-Methyl-2.4-pentanodiol addition and slag partial replacement by GGBFS on (a) heat flow and (b) cumulative heat release during the initial 24 h of reaction.

Chemical shrinkage

Corrugated tubes determine the chemical shrinkage of certain binding material. The measurements comprise both plastic and autogenous deformation components and the transition between plastic and hardened state can be identified by changes in the rate of shrinkage. As can be seen in Figure 3.5.16a, the reference sample (02M) exhibit shrinkage during the initial 12 h of reaction. However, 4 h after mixing the shrinkage rate decreases, signing the end of plastic deformation and evidencing the beginning of polymerization. These results coincided with the heat flow peak observed in Figure 3.5.16a further supporting the formation of polymeric networks around this period. Despite the lower rates, shrinkage continued until 12h where reaches the maximum value of 1.1 mm/m. After this period an expansive behavior occurred at the hardened state that fully counteracted the initial plastic and autogenous shrinkage. The total value of expansion was around 6.4 mm/m and the post-expansion contraction evolved towards a plateau value of 4.6 mm/m, Figure 3.5.16b.

The partial replacement of Fe-rich slag by GGBFS drastically modified shrinkage patterns of IP mortars, Figure 3.5.16a. In GGBFS-containing samples, no expansive reactions occurred and a continuous shrinkage was observed. A change on the shrinkage slope was observed after 1 h that reinforces the calorimetric results (Figure 3.5.16a) and confirms that polymerization starts and plastic shrinkage ceases 1 h after the binders' preparation. Despite the faster polymerization, plastic shrinkage values were maintained similar to those 02M samples at around -0.4 mm/m. A progressive increase of autogenous shrinkage was observed until the 7 d of curing, reaching the maximum value of 2.3 mm/m.

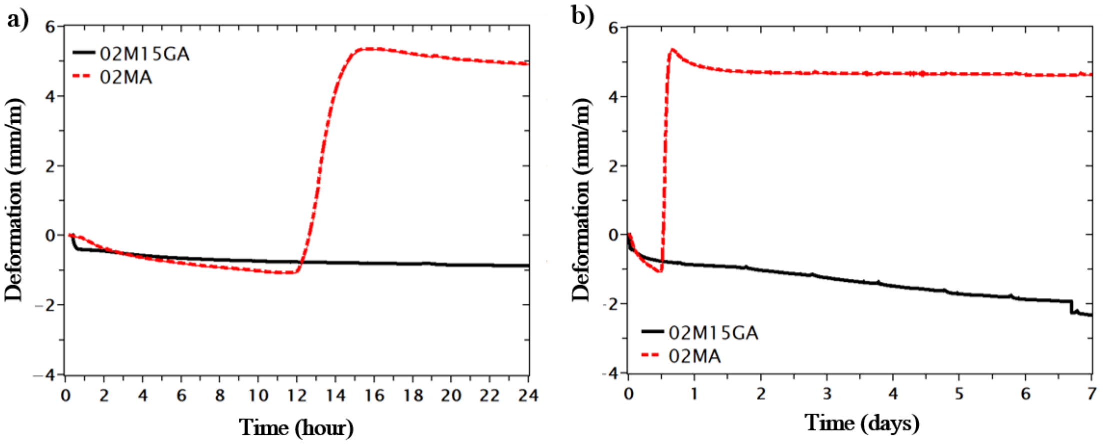

Figure 3.5.16 Effect slags' partial replacement by GGBFS on samples chemical shrinkage.

Drying shrinkage and weight loss

Despite high autogenous shrinkage values that can be found in the literature, drying shrinkage has been extensively reported as the governing mechanism affecting the volumetric stability of alkali-activated materials. To evaluate the effectiveness of 2M as a drying shrinkage reducing agent, IP mortars with four different 2M dosages (0, 1, 2 and 3 wt%) were produced and monitored for 28d. Figure 3.5.17a,b show that independently of the concentration used, drying shrinkage and weight loss occurred mostly during the initial 7 d of curing, evolving later towards plateau values. Consequently, weight loss can be related to IPs volumetric changes, confirming the predominantly drying nature of the shrinkage mechanism involved. Despite the different binders and SRA, similar weight loss and drying shrinkage patterns have been observed in section 3.5.1 and 3.5.2 further corroborating drying shrinkage as the most relevant phenomena and the initial 7 d of curing as the most critical period in terms of drying shrinkage. After 28 d, the reference samples presented the highest shrinkage, 5.0 mm/m, and the addition 1 wt% of 2M have only a marginal beneficial effect being the shrinkage observed 4.7 mm/m. Yet, doubling 2M dosage led to a significant decrease of drying shrinkage to 1.8 mm/m, representing a reduction of over 60 %. When further increase 2M dosage to 3 wt% the minimum shrinkage value of 1.4 mm/m was reached. However, the shrinkage observed in 32MA samples shows reduced effectiveness of increasing 2M dosage above 2 wt%.

After 28 d, weight loss was proportional to 2M dosage ranging from 3.6 to 5.4 wt%, Figure 3.5.17b. These results confirm that 2M favors evaporation, and by doing so, reduces the internal stress generated resulting in lower shrinkage values. Heat-curing the samples decreased shrinkage by 38 % (Figure 3.5.17a), confirming the observations made in section 3.5.4. A reduction in a weight loss of 19% was also observed in 32MH relative to 32MA.

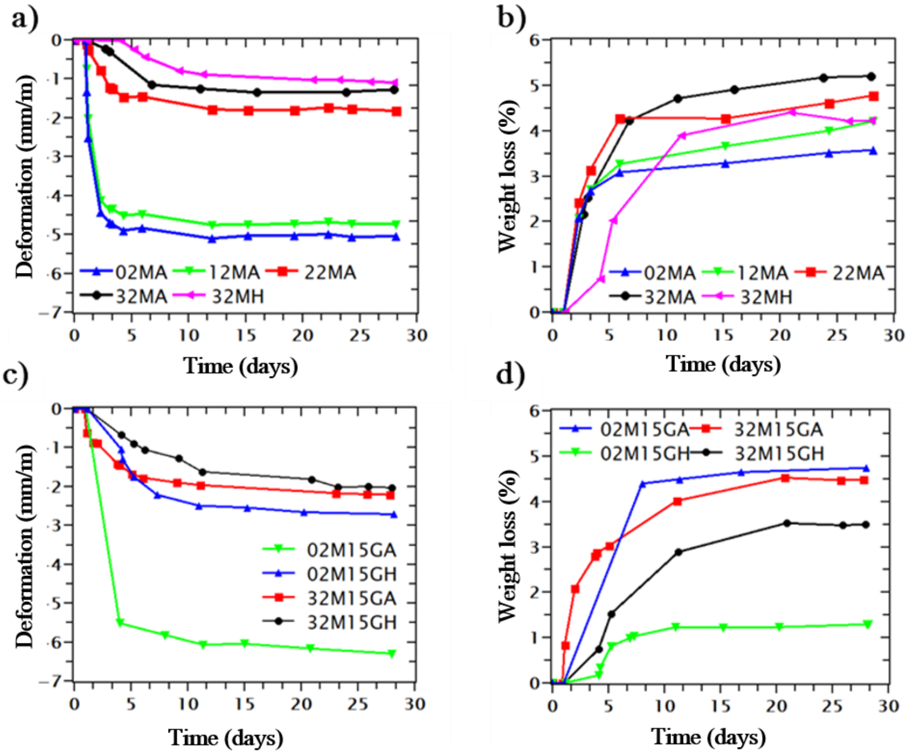

Figure 3.5.17 Effect of 2-Methyl-2.4-pentanodiol dosage (a, b) and slags' partial replacement by GGBFS (c, d) on shrinkage and weight loss during the initial 28 d curing.

The substitution of Fe-rich slag by GGGFS was detrimental to the mortars' volumetric stability as significantly higher of drying shrinkages were observed. GGBFS-containing mortars cured at room conditions (02M15GA) presented the highest shrinkage values recorded (6.3 mm/m) and heat-curing those samples was only able to partially compensate the adverse effect of GGBFS, Figure 3.5.17c.

The combined effects of 2M and GGBFS were evaluated by adding 3 wt% of 2M to GGBFS-containing samples. In ambient-cured mortars (02M15GA) the addition of 2M significantly decreased drying shrinkage to 2.2 mm/m, representing a reduction of more than 65%. In the case of GGBFS-containing mortars, the effect of heat-curing was cancelled, and no further reductions of drying shrinkage were promoted. In these systems, weight loss also occurred mostly in the initial 7 d of curing and followed a similar pattern to drying shrinkage. The addition of 2M does not significantly alter weight loss of blended mortars cured at room conditions (≈-4.5%), while heat-curing GGBFS-containing mortars provoked a significant reduction (-1.5%). The introduction of 2M in the heat-cured blended mortars (32M15GH) increased weight loss to 3.5%, once again suggesting some competition between the effects of 2M and heating curing in GGBFS-containing systems.

Autogenous and drying shrinkage were combined in Figure 3.5.18 to provide a compressive overview of GGBFS on the mortars' shrinkage behavior from mixing until 28 d of curing. It can be clearly seen that despite the higher drying shrinkage of GGBFS-containing mortars, it was the absence of early age expansion that ultimately dictated the overall shrinkage pattern. Similar expansive behavior has been observed in section 3.5.4 when a comparable slag was used as a precursor. It is also interesting to notice that mortars made form a Fe-Ca-rich precursor described in section 3.5.4 exhibit a shrinkage pattern equal to the GGFBS-containing mortars reported here. To a certain extent, the GGBFS addition modified the system chemistry and approximated the initial Fe-rich precursor to the Fe-Ca-rich slag used in section 3.5.4. In both cases no expansion behavior occurred and a continuous increase of shrinkage was observed. Possible explanations to the lack of expansive reaction can lay under the lower amount metallic particles on Ca-rich systems- in the case of GGBFS-containing mortars due to a dilution effect- and due to the formation of different reaction products of a more C-A-S-H type.

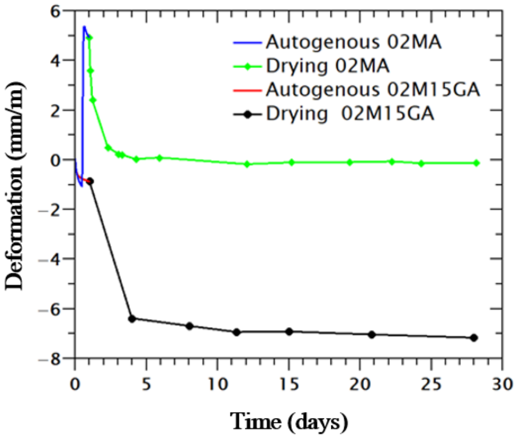

Figure 3.5.18 Effect of GGBFS partial replacement on mortars’ total shrinkage during 28 d of curing.

The correlation between water evaporation and drying shrinkage is better to identify in Figure 3.5.19. The responsiveness of shrinkage to weight loss is as strong the slopes of the curves, meaning that samples can endure evaporation processes with or without considerable effects on shrinkage. Figure 3.5.19a shows the influence of 2M dosage and the responses are clearly clustered in two groups. Weight loss was increased when 2M dosages exceeded 1 wt% but a considerable decrease of the curves’ slope showing that in 22MA and 32MA mortars lower internal stress was generated, thus resulting in lower shrinkage values. These results are in an agreement with the total porosity and average pore size increase shown in Figure 3.5.22. Figure 3.5.19a also shows very similar slopes between 22MA and 32MA mortars indicating that increase 2M above 2 wt% has limited efficiency.

In Figure 3.5.19b, three groups of samples are clearly identified that correspond to 2M and GGBFS-containing mortars, and to samples were 2M was added to the activating solution of GGBFS-containing mortars. The 2M-free mortars presented the strongest responsiveness. The slag partial replacement by GGBFS significantly increased the total weight loss and shrinkage. The high shrinkage of GGBFS-containing systems has been attributed to the significant visco-elastic or plastic behavior of Ca-rich IPs (Ye, 2017) and the high weight loss suggests the existence of a considerable amount of residual water in the pore structure of GGBFS-containing mortars. Heat-curing reduced weight loss and shrinkage proportionally and therefore significant modifications on the responsiveness were not observed. These results can be explained by the enhanced strength development promoted by heat-curing that increases the binders' resistance to the internal stresses generated during evaporation. On the other and, the decrease in weight loss can be attributed to the increase of hydration reactions and to the higher amount of water entangled in pore structures constituted by pore of smaller dimensions.

The second group of curves includes 32MA and 32MH mortars. In this cluster of curves, a weak dependence between weight loss and shrinkage behavior was shown. The amphiphilic character of 2M and the enlargement of the pore size distribution allowed to increase the amount of water evaporated while reducing the stresses generated. In this regard, the effects 2M are comparable to those of PPGs described in section 3.5.2.

The third group of curves shows the combined effects of 2M and GGBFS. The introduction of GGBGS in 2M-containing mortars increased drying shrinkage and reduced the amount of evaporated water. As will be shown later, the GGBFS introduction has reduced the pore size even in 2M-containing mortars that explain the increase of shrinkage observed. The contradictory effect of 2M and GGBFS on pore size distribution resulted in mortars with an intermediate performance. Therefore, the use of GGBFS is not advisable if minimum shrinkage values are intended.

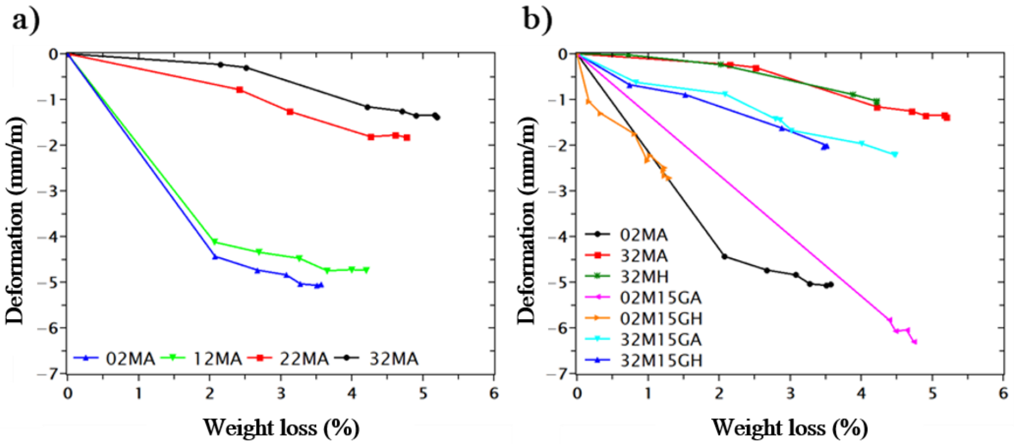

Figure 3.5.19 Mortars shrinkage as a function of weight loss and (a) 2-Methyl-2.4-pentanodiol dosage and (b) slags' replacement by GGBFS.

Microstructural analysis

Figure 3.5.20 shows the SEM micrographs of 02MA and 32MA mortars. The largest grains correspond to sand aggregates while small-sized light-grey grains show partially unreacted particles of the parent precursor. The addition of 2M cleary resulted in the formation of less dense microstructures with spherical pores being abundantly observable on 32MA samples. These large pores can act as drains at early ages and concentrate a considerable amount of water that can later evaporate without generating substantial capillary stresses.

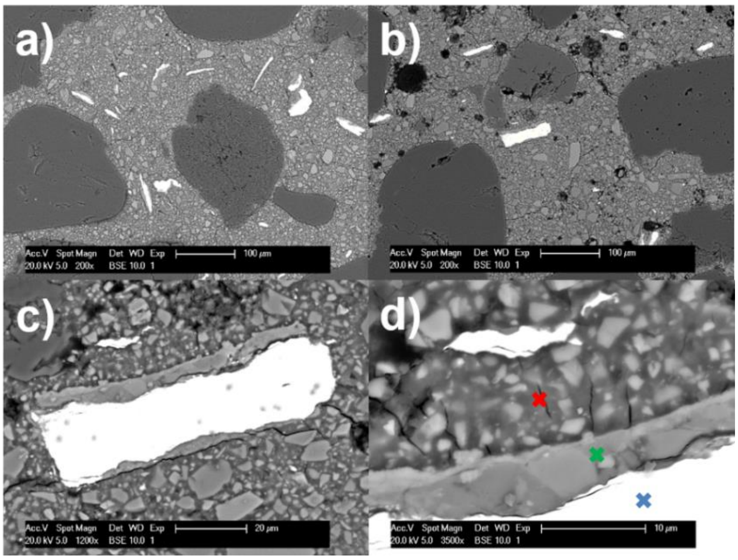

Figure 3.5.20 Backscattered electron imaging micrographs of a) 02MA and b) 32MA mortars. In c) and d) high-resolution micrographs of a metallic Fe particle are given. Colorful crosses in d) identify three different phases: the metallic Fe particle itself (in blue), Fe-rich binder (in red) and spinel (in green).

The withe elongated particles were identified as metallic Fe particles. High-resolution SEM micrographs of a metallic Fe particle are shown in Figure 3.5.20c, d. In these micrographs three distinct phases can be seen, the metallic Fe particle itself, the Fe-rich binder and a third phase that reassembles an interfacial transition zone. However, elemental identification provided in Figure 3.5.21b shows that Fe particles are surrounded by spinel, most likely formed during the slags' quenching process. It can also be seen that spinel and the metallic Fe remained partially unreacted while the amorphous fraction of the parent precursors was preferentially dissolved. Despite particularly large Fe particles have remained almost unreacted, smaller particles like the shown in Figure 3.5.20d are more prone react with the alkali medium and can possibly explain the expansion behavior observed 02MA mortars. Yet, the expansion observed only took place after the hardening of the mortar - but in a period were high visco-elasticity was sufficiently high- implying that oxidation reaction does not occur instantaneously. The delay observed in oxidation reactions can be possibly related to the size of metallic Fe particles present in parent precursors. Smaller Fe particles with increased surface area would have accelerated the expansion, being the opposite also true. As previously mentioned, the introduction of GGBFS prevents expansion due to the rapid formation that surrounds metallic grains and acts as a passivation layer at later stages.

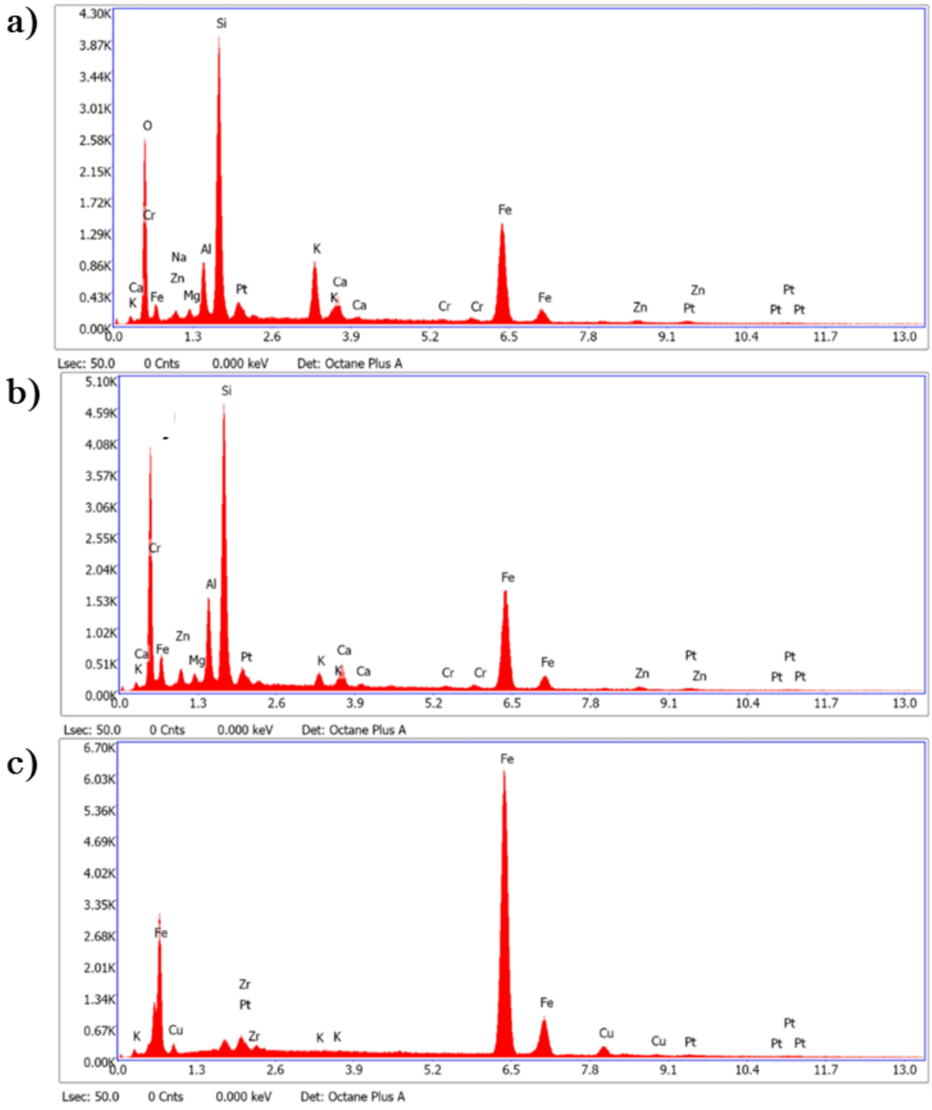

Figure 3.5.21 XRD patterns of different phases detected in the vicinity of metallic iron particles being a) Fe-rich IPs binder, b) spinel and c) spectrum of the metallic iron particle itself.

Pore structure analysis

Table 3.5.6 shows the mortars' bulk density and apparent porosity determined by the Archimedes method, and the total porosity and mercury volume intrusion measured by MIP. It can be observed that different porosity percentages were obtained which can be explained by the different methodologies of the techniques used. Yet, a similar trend was maintained showing the consistency of the data collected and validating the following discussion on the effects of 2M and GGBFS.

The mortars' total porosity ranged from 8 to 23 % according to MIP measurements while the bulk density varied from 2.4 to 2.6 g/cm^3. Total porosity was not significantly altered by heat-curing while only a slight reduction was promoted by the introduction of GGBFS. The effects of 2M addition on total porosity were evident with two-fold increases of total porosity being observed when 3 wt% of 2M was added in the activation solution. The increase provoked by 2M was even higher in GGBFS-containing mortar, being the total porosity value almost tripled. These changes in the mortars' total porosity agree with the changes in responsiveness observed in Figure 3.5.19.

Table 3.5.6 Bulk density, total porosity, and intruded volume.

Code	Bulk density g/cm^3	Total app. porosity $\%_{mass}$	Total porosity (MIP) $\%_{vol.}$	Intruded V. / total V. (MIP)
02MA	2.58	6.25	10.44	7.28
32MA	2.42	10.5	20.48	12.44
32MH	2.33	16.13	18.25	12.43
02M15GA	2.51	6.13	7.46	5.01
02M15GH	2.60	5.75	8.73	5.46
32M15GA	2.44	7.94	21.32	11.41
32M15GH	2.48	9.13	23.71	13.89

The incremental and cumulative mercury intrusion volume is shown in Figure 3.5.22. In all mortars, the majority of pores were observed in the region between 0.1 and 2 µm. However, some patterns could also be identified in the outlying areas 0.005 and above 50 µm. Blended systems containing 2M had the highest porosity in this region followed by 02M15GA and 02M15GH mortars. Despite the higher total porosity of imposed by 2M addition, it can be also observed that 2M single-use resulted in a porous structure mostly defined in the range of 0.1 and 2 µm. In the mesopores region, meaning pores with diameters bellow 0.025 µm, pore formation can be related to the rearrangement of gel pore structure and binding phase formation, particularly of C-S-H phases (Mindess, 2003). The introduction GGBFS into the binders' composition resulted in a considerable increase of CaO concentration in the systems, and therefore, the higher formation of calcium silicate hydrates phases in these systems was expected. In Figure 3.5.22b the pores' cumulative volume is shown. It can be seen, that in GGBFS-containing mortars up to 20% of the pore volume can be attributed to these pores. Yet, it should be mentioned this region is located near to limit of detection of MIP instruments and therefore should be regarded carefully.

The capillary pores defined in the region between 0.01 – 10 µm result form to the presence of interstitial water in the IP structure (Mindess, 2003) and can be related to the formation of capillary stresses and consequently drying shrinkage. The modifications imposed on the binders' chemical composition by GGBFS and/or 2M addition had a clear reflection in the pore structures formed. The coarsest pore size distributions were obtained in mortars where 2M was single-used independently of the curing conditions imposed. The overlapping of 02MA and 02MH pore size distribution is supported by the similar porosity values observed in Table 3.5.6. On the other hand, the partial replacement of Fe-rich slag by GGBFS resulted in porous structures mainly constituted by pores of smaller dimensions. In these systems, heat curing further promoted the formation of closer structures, which increased the mortars' density contributing to raising compressive strength, Figure 3.5.24. By combining GGBFS and 2M intermediate pore size distributions were produced and a minimal increase of total porosity was observed relative to 32MA and 32MH mortars.

From the MIP data, the average pore size diameter can be also calculated, being plotted against the mortars drying shrinkage in Figure 3.5.23. Three different groups of mortars can be identified. The first group comprises the reference mortar (02MA), and 2M-free blended mortars with an average pore size of around 0.2 µm. The introduction of 2M doubles the average pore size in 32MA and 32MH mortars, while a third intermediate group is constituted by mortars where both 2M and GGBFS were used. Apart from the increase of the total porosity, the significant increase of the average pore size provoked 2M further contributed to the reduction of the internal capillary stress generated. The decrease of shrinkage in 2M-containing mortars results from these combined effects.

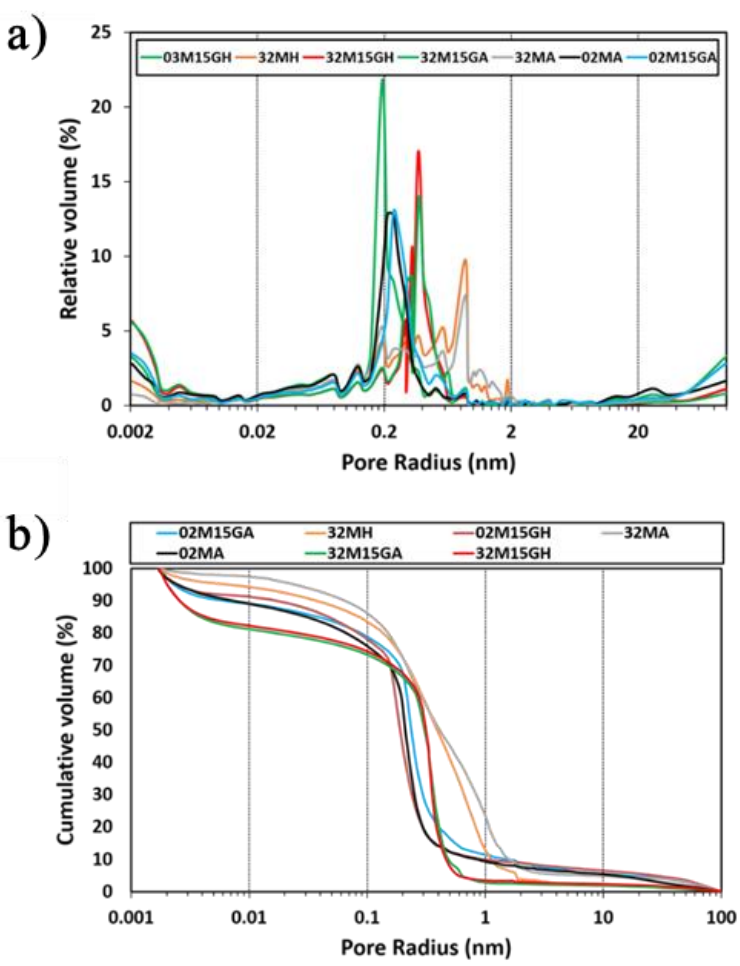

Figure 3.5.22 Relative pore size distribution (a) and cumulative pore volume (b) of the mortars after 28 d.

The responsiveness of shrinkage to modifications in pore size distribution is further supported by the elevated drying shrinkage of blended systems and the intermediate values of GGBFS-2M containing mortars. The only exception to this correlation was 02M15GH mortars. In these mortars, weight loss values were significantly lower which implies a reduced amount of water available to be evaporated, hence less significant capillary stresses being generated. In addition, heat-cured mortars presented the highest strength development (Figure 3.5.24) which rose the stiffness of the binders and their ability to withstand capillary stresses. These findings do not agree with the high drying shrinkage values of GGBFS alkali-activated materials reported in the literature (Collins, 2000). However, the porous structures reported were mostly composed of mesopores (82%) while in the Fe-rich IPs described here macro-pores are predominant. Moreover, increases of mesoporosity when heat-curing alkali-activated materials were also reported and related to the enhancement of reactivity and increased formation of binding phases (Sindhunata, 2006). This is also the case for GGBFS-containing mortars, but not for 2M mortars where no modifications on the reaction kinetics occurred and the promotion of large pores by 2M addition dominated heat-curing effects and consequently defined the pore size distribution.

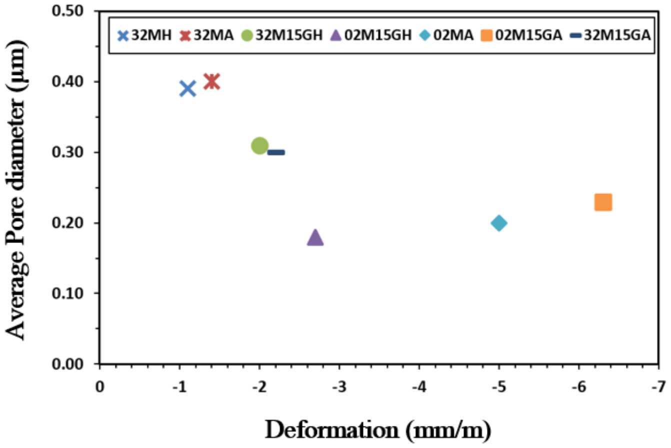

Figure 3.5.23 Responsiveness of mortars' volumetric stability to average pore size.

Mechanical properties

The compressive and flexural strength of the IP mortars after 28 d of curing is shown in Figure 3.5.24. The reference mortar 02MA present a compressed strength of 49±1 MPa which was not considerably affected by 2M addition independently of dosage used. Increase 2M dosage only led to slightly decrease compressive strength being the minimum value being reached by the 32MA mortars, 46±6 MPa. The higher standard deviation can be explained by the more porous nature of these samples. Heat-curing has significantly increased the compressive strength of mortars containing 3 wt% 2M, reaching the value of 67 MPa and which represents a 45% increase relative to 32MA mortars. The highest strength development of heat-cured had already been demonstrated in this work. High 2M dosages also have beneficiated flexural strength being raised up to 7 MPa and representing a maximum increase of 53% when compared to 02MA mortars. The increase of 2M dosage and the inverse decrease of shrinkage favored flexural strength development as they are directly related (Kuenzel, 2012). Heat-curing further decreased shrinkage and consequently increase the flexural strength of mortars containing 3 wt% of 2M up to 9MPa. The slag partial replacement by GGBFS considerably decreases the compressive strength of mortars cured at ambient conditions, from 49±1 MPa to 34±1 MPa. Notwithstanding, heat-curing was able to redeem such deleterious effect of GGBFS addition, being a compressive strength of 99±3 MPa obtained in 02M15GH mortars.

At ambient conditions, the combined effect of 2M and GGBFS was notoriously positive as the compressive strength of 32M15GA mortars was increased to 65±4 MPa. Such mechanical results considerably outstand the compressive strength of 02M15GA and 02MA mortars and are comparable those of 32MH samples. The increase of compressive strength in GGBFS-containing mortars provoked by 2M can be related to the decrease of shrinkage. Heat-curing further rose compressive strength to 87±3 MPa which was only surpassed by 02M15GH mortars. Upon heating, 2M addition did not rose strength development due to the increased total porosity that most likely overwhelmed the beneficial effect of reducing shrinkage.

The flexural strength of GGBFS-containing mortars was significantly enhanced by heat-curing. Mortars 02M15GH have shown an almost four-fold increase in flexural strength relatively to 02M15A mortars, 2.3 and 8.5 MPa, respectively. Heat-curing enhances the reaction kinetics which along with extra source Ca provided by GGBFS developed a binder that can resist more easily capillary pore pressure, resulting in a decrease of shrinkage and increased flexural strength. An even higher increase was observed when 2M was added to heat-cured GGBFS-containing, being reached the maximum value of 9.7 MPa. Similar to GGBFS-free mortars, reductions in shrinkage had favored higher flexural strength development.

Heat-curing, in particular, allowed the formation of stronger binders in both GGBFS and 2M-containing mortars that can endure higher capillary stresses, and in turn, reduce shrinkage and increased strength development. The correlation between shrinkage and strength development is particularly evident in the case of flexural strength, Figure 3.5.24b

In a general overlook of the strength development, it can be said that heat-cured GGBFS-containing mortars, with or without the addition of 2M, presented the highest flexural and compressive strengths. In these mortars, shrinkage did not surpass 3 mm/m, representing a reduction of over 50% relative to the reference mortar, 02M. Yet, in applications where the allowed shrinkage thresholds are even more restrictive, the 2M single-addition has higher potential as a shrinkage mitigation strategy if one is willing to accept some reduction in mechanical performance. Also, in the case of 2M-containing mortars, heat-curing can partially compensate the loss in compressive strength.

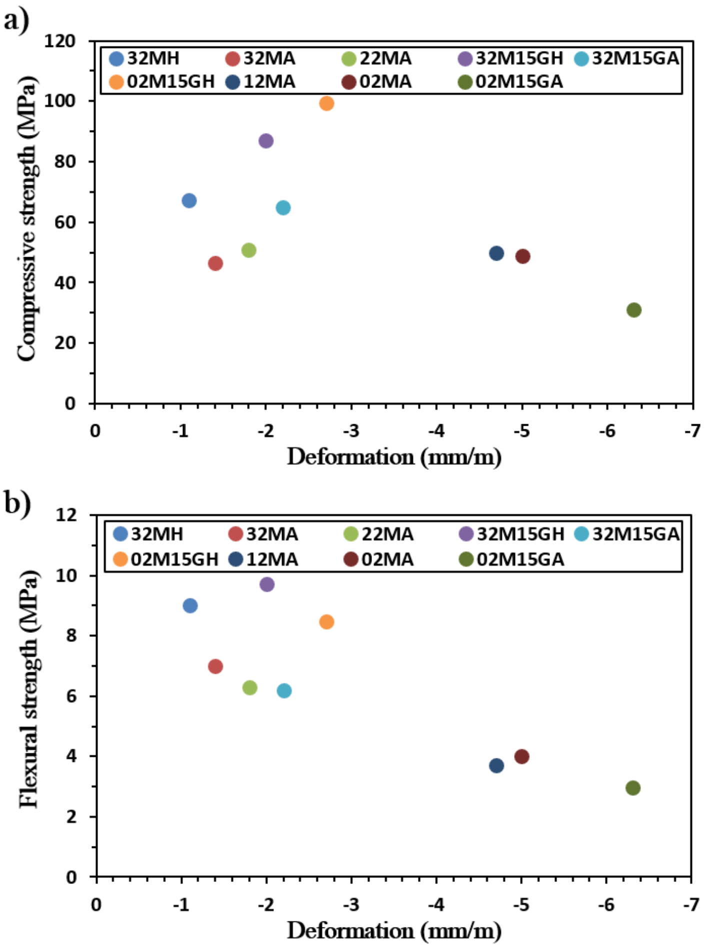

Figure 3.5.24 Mortars' compressive and flexural strength after 28 d of curing.

Conclusions

Different shrinkage mitigation strategies were investigated in an attempt to increase the volumetric stability of Fe-rich IP mortars. It was found that the chemical composition of the parent precursors should be carefully considered when designing AAMs. Metallic iron content was shown to be particularly important to determine the volumetric stability of IP mortars. Autogenous shrinkage was generally low, and the oxidation of metallic Fe could fully counteract drying shrinkage in GGBFS-free mortars.

In the reference mortars (02MA) drying was a dominant shrinkage mechanism with values above 5 mm/m. The observed weight loss was explained by a lack of hydration reactions that result in a considerable amount of residual water in the structure. The total porosity did not surpass 10 % and was mainly characterized by capillary pores.

The introduction 2M in the activating solution increased total porosity and modified the pore size distribution. Enlarged pores significantly reduced drying shrinkage values as 2M content rose but increasing dosages above 2 wt% had limited efficiency. Heat-curing 2M-containing mortars further reduced drying shrinkage and can be used as a complementary shrinkage mitigation strategy to obtain lower shrinkage, limit 2M addition or increase the mortars' mechanical performance.

At ambient conditions, the partial substitution of Fe-rich slag by GGBFS resulted in increased shrinkage values and poor mechanical properties. Heat-curing was able to reduce shrinkage and significantly increase strength development.

In summary, both shrinkage mitigation strategies tested here had beneficiate the volumetric stability of Fe-rich mortars. Heat-curing has the added benefit of not intervene in the mortars' chemical composition and therefore not requiring specialized personal. It could be also concluded that 2M and GGFS are both valid admixtures for Fe-rich IPs and their use should be mostly determined by the precursors' chemistry and envisioned properties. While 2M it is advisable to systems where a considerable reduction of drying shrinkage is needed, the partial replacement of Fe-rich slag by GGBFS may be a suitable compromise solution to partial reduce drying shrinkage while enhancing mortars' mechanical performance if heat curing is provided. The combined use of 2M and GGBFS was detrimental, lower shrinkage values were attained with 2M single-use while higher strengths were observed in 2M-free mortars.

Moreover, it was previously shown in section 3.5.1 that CaO-rich admixtures considerably reduced the IPs' workability and setting time, and therefore the potential of introducing GGBFS in the mix design as a shrinkage mitigation strategy in CaO-FeO_x-rich systems -as IPs produced from RDF slags- may be limited.

In the following section, the results of a follow-up investigation performed to gain deeper knowledge into the influence of curing regimes on IPs volumetric stability are discussed. The performance of calcium "deficient" mortars similar to the ones described here was compared with mortars produced from RDF slags in order to assess how curing regimes affect differently the properties of Fe and Fe-Ca-rich systems.

Later in section 3.6, the insights gathered in this work on the beneficial effects of 2M will be transposed to CaO-FeO_x-Al_2O_3-SiO_2-rich mortars produced from binders developed in 3.3, which combined with the findings of the following sections allowed to achieve alkali-activated products with minimal shrinkage values.

3.5.4 The impact of different curing regimes on IP mortars volumetric stability

The following section is based on an article entitled "Shrinkage and mitigation strategies to improve the dimensional stability of $CaO-FeO_x-Al_2O_3-SiO_2$ inorganic polymers" by Ascensão, G., Beersaerts, G., Marchi, M., Segata, Faleschini, F. & Pontikes, Y. published in Materials, 12 (22), 3679, 2019.

This article reports the results of an investigation conducted by Ascensão, G. during his staying in KU Leuven. Despite the formulations described here do not exactly match the ones reported in 3.3, the findings of this investigation on the shrinkage mechanisms affecting Ca-Fe-rich IPs and related mitigation strategies were relevant to this work and therefore are reported. Two (CaO)-$FeO_x-Al_2O_3-SiO_2$ slags were used as case studies to deeply investigate IPs shrinkage mechanisms and assess the different influence curing regimes in the volumetric stability of Fe and Fe-Ca-rich systems. The best-practices were later transposed to mortars formulations produced that are reported in 3.3.

In the following text, adjustments were made relative to the original publication in order to better frame the work and to avoid unnecessary repetitions.

Introduction

Despite the expected economic and environmental benefits of alkali-activated binders, IPs are still slowly deploying as a commercial complement to traditional cementitious materials. Their high susceptibility to shrinkage is identified as one of the major technical factors that limits the IPs large-scale implementation (Cartwright, 2014; Lee, 2014). In fact, high shrinkage values were also observed in the $CaO-FeO_x-Al_2O_3-SiO_2$-rich binders developed in 3.3. The shrinkage mitigation strategies previously attempted were able to significantly reduce IPs shrinkage but further reduction was still needed in order to be compliant with construction codes and standards where low shrinkage values are recommended.

The IPs shrinkage can be mainly attributed to two different processes: autogenous and dry shrinkage. In open conditions, these processes occur simultaneously but the mechanisms involved are rather different. Autogenous shrinkage can be defined as a physico-chemical phenomenon resulting from chemo-mechanical and hygro-mechanical interactions (Mounanga, 2011). The former results from the difference between the absolute density of the reaction products and the starting materials (also known as chemical shrinkage), while the latter is driven by the progressive emptying of the initially saturated pore structure as the reaction progresses (also known as self-desiccation). Self-desiccation may generate considerable tensile stresses at the menisci, resulting in severe inwards contraction of the pore structure. These hygro-mechanical processes are rather analogous to drying shrinkage phenomena occurring when water leaves the system - through evaporation- generating tensile stresses, which causes further volumetric contraction. The aforementioned shrinkage mechanisms can be easily linked to the shrinkage behavior of traditional cements. Unfortunately though, the most commonly used superplasticizers and shrinkage reducing agents are not effective as the chemistries of cement and IP binders are entirely different (Beersaerts, 2019).

Existing literature shows that IPs shrinkage mechanisms and their magnitude are heavily compositional dependent. Lee *et al.* (2014) showed that shrinkage characteristics are primarily dependent on the precursors and the activating solution provided, and from the reaction products made thereof. Yet, the existing literature on the shrinkage behavior of $CaO-FeO_x$-rich IP systems is surprisingly scarce (Mastali, 2018). Considering that shrinkage mechanisms can be inferred by reaction mechanisms and the formation of different binders' structures (Peys, 2019), shrinkage mechanisms (and magnitudes) different than the previously demonstrated in 3.3.3 could affect the volumetric stability of $CaO-FeO_x-Al_2O_3-SiO_2$-rich IPs produced from RDF slags.

In order to assess how curing regimes affect the properties of FeO_x and CaO-FeO_x-rich IPs, two different slags were used as case studies and, the robustness of the developed shrinkage mitigation strategies evaluated.

IP pastes and mortars were cured at (i) room conditions, (ii) in slightly elevated temperatures (60°C-2d) and (iii) in a water-saturated environment. IP pastes were used to examine the reaction kinetics and products formed while mortars were made to characterize the 28 d pore structures, autogenous shrinkage, drying shrinkage and strength development. Understanding the effect of precursor's composition and curing conditions on IPs shrinkage was fundamental to later, in combination with the use of SRA, develop optimized IP mortars with minimal shrinkage values.

Experimental

Materials

Two vitreous slags were used as precursors for IP binders. The slags, further termed as PS and KO, were engineered to present chemical compositions representative of common non-ferrous metallurgy slags (KO slag) and, vitrified residues originating from thermal treatment of municipal wastes (PS slag). The latter corresponds to the slag used as the main precursor throughout this work. The detailed production process of each slag can be found in Onisei *et al.,* 2015 and Machiels *et al.,* 2017, respectively. The main components of both slags are SiO_2, Al_2O_3, CaO, and FeO_x; the main differences among them was FeO_x/CaO and FeO_x/SiO molar ratios. Both slags were received as granules and they were dried and milled before use. Commercial standardized sand (M31, Sibelco, Belgium; 99.5 wt% SiO_2) was used as aggregate and its particle size distribution is given in Figure 3.5.25. An activating solution, with a SiO_2/K_2O molar ratio of 1.60 and 70.0 wt% H_2O was prepared by dissolving potassium hydroxide beads (reagent grade, 85.0%, Honeywell, Belgium) in a commercial potassium silicate solution supplied by Silmaco, Belgium (SiO_2/K_2O molar ratio of 3.20 and approximately 60.0 wt% H_2O) and demineralized water. The solution was prepared at least 24 h in advance to allow it to cool down prior to IPs preparation.

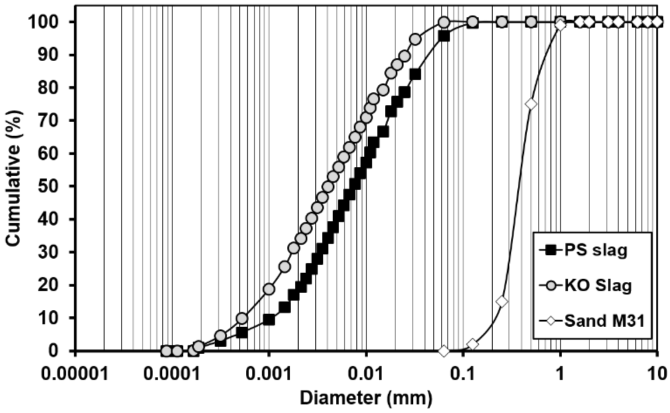

Figure 3.5.25 Precursors and aggregates particle size distribution.

Methods

X-ray fluorescence (Bruker AXS S8 Tiger spectrometer) was used to determine the bulk chemical composition of each powdered slag. The Fe oxidation state of each slag was quantified as described by Close *et al.* (1958). The crystallinity of slags and IP pastes were assessed by X-ray diffraction (XRD), carried out on the diffractometer already described in 3.1 and phase identification was performed using EVA software (database ICDD-PDF-2). The particle size distribution of was determined by a laser particle analyzer (Malvern Mastersizer 3000) and the powdered slags surface area was determined via nitrogen adsorption/desorption methods (NAD) (ISO 9277, 2010) and Blaine method, according to the EN 196-6 (EN 196-6, 2018). NAD experiments record the adsorbed/desorbed nitrogen quantity as a function of the pressure imposed, allowing a deeper characterization of the structure of the powdered slags. Different evaluation methods- such as standard isotherms (t-plots), Langmuir, BET and BJH (Zeng, 2015) have been proposed to evaluate NAD SSA values; the T-plot method was used herein.

The generated heat flow in IP pastes was determined by isothermal conduction calorimetry (ICC) at 20 °C following an external mixing procedure. The slags (10 g) and the activating solutions were stored for 24h at 20 ±0.5 °C prior to the experiment, being afterward, mixed for 1 min using an external mini-blender. Each mixture was replicated once to guarantee data repeatability, and the average values are reported here.

The synthesis procedure of IP mortars involved: i) introducing the slag to the activating solution and mixing (in a Hobart N-50 mixer) at low speed (139 rpm) for 60 s; (ii) adding quartz sand aggregates to the blend and mix for another 60 s at the same speed; and (iii) mixing 30 s at high shear (285 rpm). After mixing, the mortars were cast into 4x4x16 cm^3 stainless steel molds, sealed with plastic film and cured for 24 h at room temperature (20±0.5 °C and 65±5.0 % relative humidity). After curing, the samples were demolded and kept under different curing conditions as described in the ensuing section.

The chemical structure of the IP pastes and the slags were analyzed using attenuated total reflectance (ATR)-FTIR (ALPHA 2 FTIR spectrometer, Bruker) method. For this purpose, 2x2x2 cm^3 paste samples were produced following the procedure described previously but without the addition of aggregates to the blend. Prior to each test, the IP samples were grinded with mortar and pestle. The spectra were analyzed in the reflectance transmission mode with a resolution of 2 cm^{-1}.

The IP mortars' density was determined by the relation between the weight and volume of each sample; their flexural and compressive strength was determined using a Universal Testing Machine (Instron 5985e) according to the EN196-1:2016 (EN 196-1, 2016). At least three samples for each formulation, curing conditions and curing age were tested.

The autogenous shrinkage of IP mortars was investigated according to ASTM standard C1698 (ASTM C1698-09: 2014). Two replicates of each mortar formulation were produced and used to fill corrugated polyethylene tubes. To evaluate the total shrinkage, IP mortars (4x4x16 cm^3) were prepared with a metallic spindle (type I), according to the EN 12617-4 (BS EN 12617–4, 2002). A minimum of two samples per each formulation and curing conditions were produced. The pore size distribution of each sample was investigated by mercury intrusion porosimetry (PASCAL 140, Thermo Scientific) as already previously described throughout 3.5.

Experimental conditions

All mortar mixtures were designed for a constant solution/slag mass ratio of 0.38 and a slag-to-aggregate mass ratio of 1.50 (Table 3.5.7). Three curing conditions were imposed on the different slag-based IP mortars to assess the impact of slags' characteristics and curing environment on the shrinkage mechanisms. The selected curing conditions comprised: i) ambient curing, ii) slightly elevated temperatures (60 °C for 2 d), and iii) a 100 % relative humidity (RH) environment at room temperature. The described conditions exclude the initial 24 h period where all samples were kept in the molds following the conditions described in 2.1. After demoulding, the ambient cured IPs were exposed to room temperature (20±0.5 °C) and 65±5.0 % humidity. This experimental condition allowed to determine the total shrinkage during curing and replicate the most likely environment in common construction applications. The second batch of specimens was thermally treated for 48h at 60 °C after demoulding. The samples were sealed with a plastic film during thermal treatment to prevent severe drying. Such condition guarantees that water egress is avoided and given that plastic shrinkage already took place during the initial 24h of curing (before samples' demoulding), it can be assumed that autogenous is the predominant shrinkage mechanism during the thermal treatment. It should be noticed that slightly elevated temperatures are known to increase precursors' degree of reaction and to accelerate the reaction kinetics resulting in the formation of different reaction products and porous structures (Van Jaarsveld, 2002; Zhang, 2012; Zhang, 2013; Novais, 2016). Therefore, the results gathered will describe these combined effects preventing direct comparison with autogenous shrinkage processes occurring at room temperature. Notwithstanding, such curing conditions were imposed to assess if an increase of reaction kinetics and a faster consolidation of the polymeric network was able to sufficiently enhance strength development to withstand the tensile stresses generated onwards and increase IPs volumetric stability over time. The IP autogenous shrinkage at room temperature was determined by using corrugated tubes. Under this type of conditions (room temperature and absence airflow), no volumetric phenomena are expected to occur other than chemical shrinkage (during plastic stage) and self-desiccation as the reaction progresses. Direct comparison with shrinkage values registered in room-cured samples was expected to allow the determination of the predominant character of drying or autogenous shrinkage.

The third batch of specimens was cured in a water-saturated environment. Similarly to corrugated tubes measurements, it is assumed that no drying shrinkage takes place. Since plastic shrinkage already occurred during the first day of curing, these trials intended to confirm the magnitude of autogenous shrinkage while determining possible late-stage effects promoted by such environmental conditions, such as the possible oxidation of Fe.

Table 3.5.7 Mortars mixture composition and slag-to-liquid and solid-to-liquid mass.

Formulation	Mixture portion (wt%)				Slag/liquid	Solid/liquid
	PS	KO	Solution (aq.)	Agg.	(g/g)	(g/g)
PSm	34.72	-	13.20	52.08	2.63	6.57
KOm	-	34.72	13.20	52.08		

Results and discussion

Precursors' characterization

The KO chemical composition is presented in Table 3.5.8. The composition of PS is included for direct comparison and it can be seen that the slag presented comparable amounts of SiO_2 but very distinct contents of FeO_x and CaO. PS slag presented a FeO_x/CaO bulk ratio of around 1.0 while such ratio in the KO slag was approximately 13.0. The Al_2O_3 content in the PS slag was slightly higher than in the KO slag but the overall $SiO_2/(Al_2O_3+FeO_x+CaO)$ molar ratio was lower, i.e. 0.82 and 1.24 for PS and KO slag, respectively. In low-Al_2O_3 systems, it is particularly important having the latter ratio in consideration since calcium and iron compounds have a remarkable influence on the reaction kinetics and products formed (Van Deventer, 2007; Peys, 2019). Lastly, the iron phases were found to be predominantly in the bivalent oxidation state in both slags, being 92 % and 94%, in the PS and KO slags, respectively.

Table 3.5.8 Representative oxide composition of the precursors used.

	Fe_2O_3	SiO_2	CaO	Al_2O_3	MgO	P_2O_5	Na_2O	Other
KO_{slag}	41	32	4	11	1	2	2	3
PS_{slag}	23	35	23	16	1	0	0	2

Along with slags' bulk oxide composition, particle size distribution (PSD) and specific surface area (SSA) are key parameters influencing precursors' dissolution rate and degree. To a given precursor, alkali activation solution and precursor/solution ratio, PSD and SSA control the activating solution sorption process, ensuing dissolution and gel formation. Hence, such physical parameters considerably influence the reaction kinetics and products formed; thus, ultimately determining binders' properties (e.g. shrinkage).

Figure 3.5.25 shows the slags' particle size distribution. KO slag has a higher content of smaller particles but both precursors were characterized by similar distributions with all particles being smaller than 0.1mm. SSA values determined by the Blaine method were found to be 5500 ± 400 and 4500 ± 200 cm^2/g for KO and PS slag, respectively. In NAD experiments, the absorption volume showed a linear dependence on the absorbed thickness, in which the SSA of each slag is given by the slope of the T-plot. The SSA of KO slag was higher than for the PS slag, i.e., 1.0049 and 0.5470 m^2/g, respectively. By comparing these results with SSA values obtained through the Blaine method, it can be seen that SSA values are systematically higher according to the latter (Table 3.5.9). The explanation for such discrepancy can lie on the fact that NAD methods were originally developed to determine SSA of predominantly flat-surfaced materials under the assumption of pores with cylindrical geometry and due to the porosity of slags' particles itself. Nonetheless, both methods indicate that KO has a larger internal accessible area, further confirming laser scattering and Blaine measurements. Lastly, KO has a higher slag density than PS, i.e. 3.41 versus 2.97 g/cm^3 of the latter (Table 3.5.9). Such a difference is mostly related to the much higher iron content of the KO slag.

Table 3.5.9 Precursors' density and specific surface area measured by the Blaine and NAD methods.

Code	Density (g/cm^3)	Blaine (cm^2/g)	T-Plot (m^2/g)
PS_{slag}	3.00	4500±200	0.55
KO_{slag}	3.41	5500±400	1.01

ICC testing

Figure 3.5.26 shows the heat evolution rate and cumulative heat evolved of the alkali-activated KO and PS pastes. The reaction kinetics in AAMs are often characterized by two, and sometimes three, exothermic peaks depending on the used precursor and synthesis conditions (Zhang, 2012). The first exothermic peak (peak I) appears immediately after mixing the powdered precursor with the activation solution. This peak is attributed to wetting and instant sorption of the activating solution on the precursors' surface and ensuing dissolution reactions. Wetting, sorption and dissolution processes can be enhanced by rising precursors' SSA, and therefore increased magnitudes could be expected as SSA rises. Figure 3.5.26a shows the heat evolution rate during the initial 30 min of reaction. As can be seen, due to the instantaneous nature of peak I, employing ICC with pastes' external preparation did not allow to determine the maximum heat release. However, the initial isothermal data seem to suggest that PS pastes present superior sorption and initial dissolution. These results indicate that precursors' dissolution and isothermal data cannot be solely attributed to precursors' SSA, but also reflect the difference in slags' density and reactivity. In fact, both precursors are complex glasses where network formers and modifiers influence the degree of structural disorder and therefore their reactivity towards an alkali solution. Moreover, is still not consensual whether Fe species present in glassy phases act as network formers or network modifiers, further increasing the complexity and uncertainty concerning the dissolution mechanisms involving Fe-rich precursors. The glasses' complex chemistry did not allow to clearly identify the individual effects of each element, but the very early stage of reaction seems to be mainly governed by precursor's chemistry instead of their physical characteristics (SSA). After peak I, both pastes presented the characteristic deceleration period followed by a second exothermic peak (peak II). Peak II is commonly attributed to the oligomerization and polymerization stage. The magnitude of peak II, and the time corresponding to its maximum, varied notably according to the precursor used. KO pastes presented a much broader, smaller and delayed peak II compared to PS (Figure 3.5.26b). In a first attempt, some parallelisms can be drawn from the simplified and widely described case of alkali-activated metakaolin (MK), even though the chemistries of the precursors used in this work were more complex. In this system, the reaction starts with the hydrolysis of T-O (T=Al, Si) bonds followed by the polymerization of initially Al-rich phases, which will be progressively converted into more Si-rich phases as the reaction continues (Mastali, 2018). Despite the most likely structural differences existing between

MK, KO and PS systems, the slightly higher availability of Al species in PS pastes compared to KO ones was enough to expect a shorter time required to reach the supersaturation level and to initiate polymerization. In addition, both precursors used in this work presented significant Ca and/or Fe contents which further complicated the description of the kinetics. Detailed information on the competing effects provoked by Ca^{2+} and Fe$^{2+/3+}$ cationic species can be found in 3.2. KO pastes presented a second exothermic peak which is much broader and smaller compared to PS pastes, which indicates that in systems with similar chemistries, the effect of OH^{-} ions removal may prevail (Figure 3.5.26b,d). Daux *et al.* (1997) showed that, under slightly alkaline conditions, the precipitation of dissolved Fe is much faster than Si and Al, which could lead to a considerable pH decay in KO pastes, resulting in slower initial reaction progression. In fact, a higher cumulative heat release in PS pastes can be seen at early age, Figure 3.5.26. Yet, it was later observed that after the initial 24 h, the heat release of KO pastes was still considerably high, while in PS pastes it was less significant. This may indicate higher precursors' dissolution degree, which is consistent with the increased mechanical performance exhibited by KO mortars cured at room temperature, Figure 3.5.33. As both precursors were composed of approximately the same SiO$_2$ bulk content, extending the reaction may promote the formation of more silica-rich gels which are known to have a significant contribution to strength development (He, 2016). It should be mentioned that the reaction of both KO and PS pastes were not completed after 550 h since the cumulative heat curves still present positive slopes. The ongoing reactions can still cause microstructural rearrangements and have an impact on IP strength development. Lastly, a small third exothermic peak was identified only in PS pastes, appearing approximately after 72 h, Figure 3.5.26c. This third peak suggests a residual reorganization or crystallization at later stages in PS pastes (Zhang, 2012) but further work is needed to shed light on the precise mechanisms involved here.

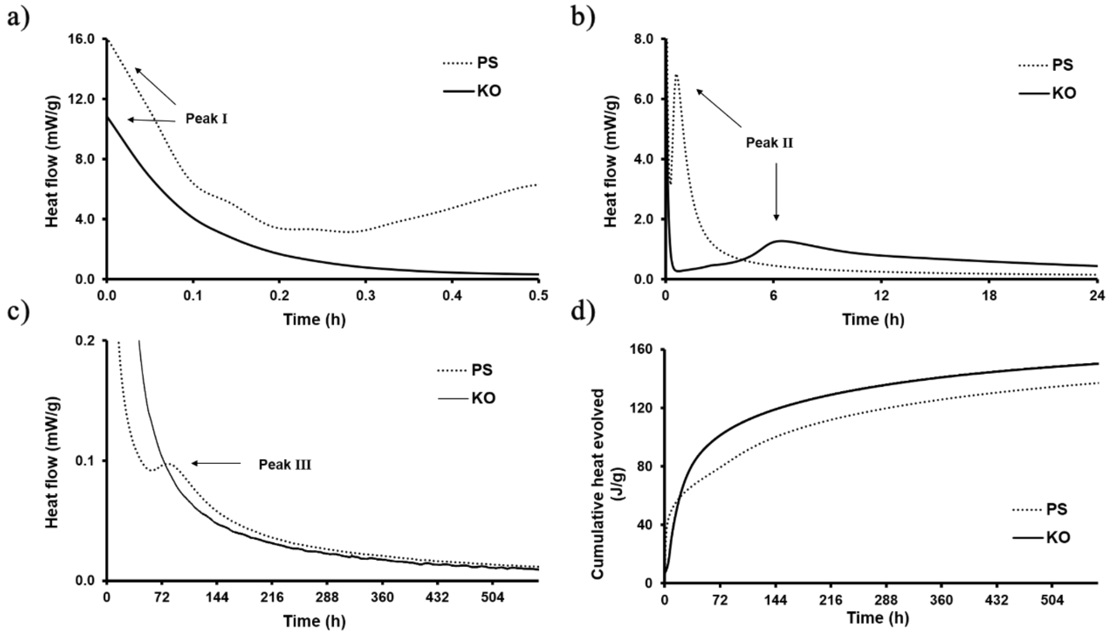

Figure 3.5.26 Isothermal calorimetry curves of alkali activated pastes. Heat evolution rate during the initial: (a) 30 min and (b) 24h period while (c) shows a close-up of a secondary heat peak detected on PS pastes (peak III). The cumulative heat release is shown in (d).

XRD analysis

Figure 3.5.27 shows the XRD patterns of the precursors used in these experiments and of the IPs pastes made therefrom. PS slag pattern exhibited a pronounced hump between 20-40° 2θ confirming the predominantly amorphous nature of the slags and IPs. In KO slag such hump was less visible, probably due to the considerable content of iron that increases the patterns' background baseline. Still, the absence of significant crystalline phases in both slags reveals their glassy nature, thus suggesting high solubility towards an alkali medium. These observations support ICC data, where a significant exothermic reaction took place immediately when the alkaline solution was introduced into the precursors.

When comparing precursors' and pastes' patterns, it is evident that the produced binders mainly retained the structure of their parent precursor, see Figure 3.5.27. No significant crystalline phases were formed after 28 d, regardless of the curing conditions used. The absence of carbonated products suggests low susceptibility of both binders to atmospheric carbonation, which however should be experimentally proved. The XRD patterns of pastes cured in a saturated environment are not provided here but no mineralogical differences are expected.

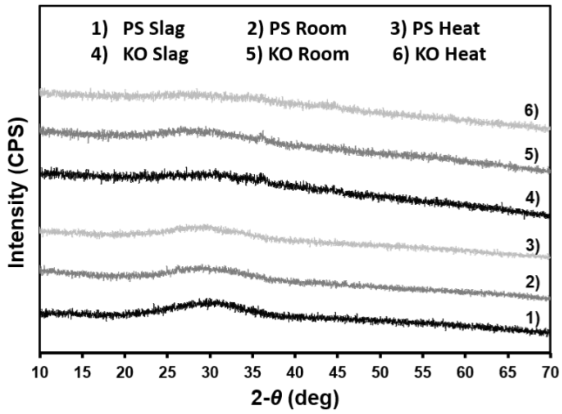

Figure 3.5.27 XRD patterns of precursors (1-4) and alkali activated pastes made therefrom cured at room (2-5) and slightly elevated temperatures (60°C-2d; 3-6). All the XRD patterns were collected after 28 d of curing.

ATR-FTIR analysis

Figure 3.5.28 shows the IR spectra of PS and KO pastes cured under different curing conditions. Despite the different curing conditions, all the produced IPs presented similar peaks, albeit with different shape, intensity, and position (Table 3.5.10). The three main peaks correspond to: I) the T-O (T=Al, Si) bonds stretching and out-of-plane bending vibrations, also known as rocking band, at 440 cm^{-1}; II) Si–O bonds in-plane bending vibration at 700 cm^{-1} and III) the asymmetric and symmetric vibration of Si–O–T bonds, also known as stretching band, at 970 cm^{-1} (Komnitsas, 2007; Criado, 2007; Saikia, 2008).

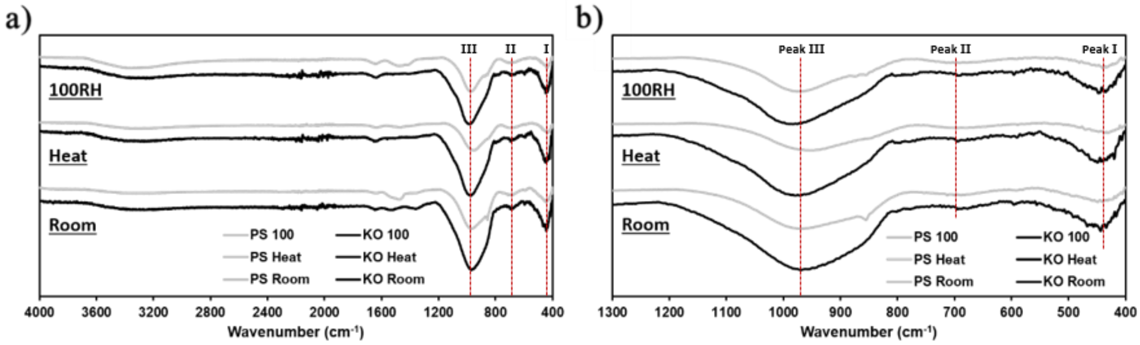

Figure 3.5.28 FTIR spectra of IP pastes cured under different conditions. (a) Full spectra collected; (b) close-up of low wavenumber region.

Some minor shifts in the location of the rocking band peaks are visible but no systematic correlation was revealed between its location and the precursors' chemistry or curing conditions studied here. In the case of Fe-rich silicates, the band corresponding to in-plane bending appears overlapped with a characteristic band of iron oxide phases located around 600-700 cm^{-1} (Hertel, 2016). This overlapping makes difficult to attribute this peak to Si–O in-plane bending or to the vibration of Fe-O or [FeO_4] units. Nonetheless, the location of this peak remained roughly unchanged (≈ 700 cm^{-1}) in all samples. On the other hand, the location of the stretching band peak (≈ 900 cm^{-1}) was clearly influenced by the curing conditions imposed. Comparing KO pastes, it is interesting to see that the minimum value of the stretching band for the room-cured samples was located at the lowest wavenumbers. The relocation of this peak to higher wavenumbers suggests that heat treatment and curing in a steam-saturated environment promoted the formation of more polymerized reaction products as a completely polymerized 3-dimensional glass will have the Si-O-Si stretching band around 1100 cm^{-1} (Dalby, 2006). These results can be explained by the increase in reaction degree of KO, leading to the formation of more Si-crosslinks, and/or to Fe oxidation processes. Despite the oxidation mechanism of Fe is not been fully understood yet, the work of Peys *et al.* (2019) demonstrated that oxidation reactions are not driven by atmospheric air since it still happens in inert environments. In their work, the connectivity of the silicate network does not seem affected by oxidation reactions neither suffer modifications due to late age oxidation. Yet, curing conditions may have affected the incorporation of Fe^{3+} species into the silicate networks and hence change the amount of available non-bridging oxygens in the system, contributing to an increase of the degree of polymerization of the formed structures. The formation of more polymerized structures is in agreement with mechanical strength results discussed later in this work where samples cured at room conditions presented the lowest flexural and compressive strength. A similar effect was only observed in PS pastes cured in a saturated environment. In all IPs, four other bands were formed. The broad peak between 2500-3700 cm^{-1} and the smaller peak around 1630 cm^{-1}, corresponding to the H-O-H bonds deformation and O-H groups stretching vibrations, respectively. The use of different precursors and curing conditions had a minor impact on these peaks, being only visible a slight decrease of intensity in the peak located at 2500-3700 cm^{-1} on heat-cured samples. This can indicate a small reduction of the amount of H_2O molecules present in these samples. A small peak between 1400-1450 cm^{-1} is present in all IPs' spectra but less pronounced in heat-cured samples. A fourth peak, located around 855 cm^{-1}, appeared in samples cured at room conditions and in a water-saturated environment. The latter two peaks can be attributed to the O-C-O stretching vibrations from carbonate groups. The formation of such carbonate groups is often attributed to the reaction of alkali cations with atmospheric CO_2 (Salman, 2015; Kriskova, 2015).

Table 3.5.10 Location of main IR peaks in PS and KO pastes.

Code	Curing cond.	Peak band I (cm^{-1})	Peak band II (cm^{-1})	Peak band III (cm^{-1})
PS	Room	448.5	712.0	970.4
	Heat	430.9	693.4	947.6
	Saturated	439.2	698.6	975.5
KO	Room	443.3	694.5	969.3
	Heat	449.5	694.5	970.4
	Saturated	447.5	693.4	982.8

Shrinkage behavior of IPs mortars

Autogenous shrinkage

Figure 3.5.29 shows the autogenous shrinkage of KO and PS mortars. PS mortars presented high autogenous shrinkage after 7 d (≈-2.9 mm/m) being several times higher than those reported in OPC systems and slightly above those reported in BFS-fly ash alkali activated mortars (Lee, 2014). Possible explanations for this high autogenous shrinkage can be the large chemical shrinkage, the high saturation degree of the porous structure, the poor stiffness and the fine pore structures of alkali activated materials (Cartwright, 2014). After the very initial stage of the reaction, KO mortars have a very distinct autogenous shrinkage behavior. Approximately 8 h after mix, KO mortars started to exhibit a considerable expansion behavior which overcomes the initial plastic shrinkage. It's interesting to notice that the inflection point on KO shrinkage coincided with the heat flow peak (peak II) detected in ICC measurements. Secondary exothermic peaks are associated with polymerization reactions, which may suggest that the observed expansion is related to IPs skeleton formation and ongoing reactions during that period. Autogenous expansion has not been broadly reported in AAMs but the oxidation of metallic Fe in KO slag may partially explain the observed expansion. Crystallization stresses generated due to the supersaturation of the pore solution may have also contributed to such expansion. Sant *et al.* (2011) attributed expansive behaviour in AAMs to crystallization stresses generated due to the supersaturation of the pore solution with portlandite phases. A similar supersaturation with portlandite phases seems unlikely in KO mortars, but the considerably high FeO$_x$ content of the phases formed may have interfered with crystallization processes. Other possible explanations may include formation of ettringite due to the presence of SO$_3$. Bumanis *et al.* (2017), recently explored the used iron sulfite rich (FeSO$_3$) precursors to generate sulfur dioxide and create porous materials. The described foaming reactions typically occur in a short timeframe after mixing implying that the contact between the metallic species and the alkaline medium would have been prevented during the initial hours of reaction. Moreover, the formations of gaseous phases typically have severe repercussions on IPs microstructure increasing total porosity and reducing IP density and mechanical resistance. None of the latter was observed in KO mortars being in the iron oxidation and in the crystallization process that the explanation may reside.

The expansion was followed by a post setting period where self-desiccation imposed some volumetric contraction, Figure 3.5.29. Considerable differences in binder's chemical shrinkage and mortars degree of saturation, stiffness and pore size distribution may also have further contributed to accentuating the differences between the autogenous shrinkage of KO and PS mortars and a more thorough analysis of mortars porous structure will be provided later in this work.

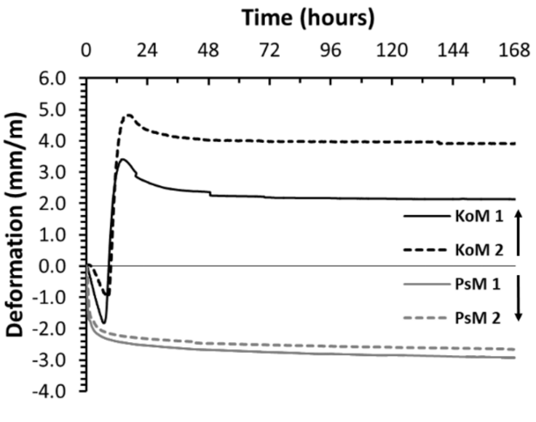

Figure 3.5.29 Autogenous shrinkage of alkali-activated mortars.

Drying shrinkage and weight loss

Similar to cementitious materials, drying shrinkage in AAMs is related to water loss in the pores, which results in significant capillary stresses. Curing conditions affect the stresses generated at the pore solution, which in turn, determine the shrinkage behavior of alkali-activated materials. Curing at slightly elevated temperatures has shown to be an effective strategy to increase the volumetric stability of AAMs (Bakharev, 1999; Thomas, 2017). Thomas *et al.* (2017) reported shrinkage reductions up to 75% in alkali-activated fly ash and granulated blast-furnace concretes. However, the chemistries of the systems investigated in this work are completely different, and the effectiveness of such a shrinkage mitigation strategy in Fe-rich systems was unknown. As drying shrinkage is a hygrothermal process, the dimensional stability of IPs was also evaluated in when cured in steam-saturated environment where no significant water transferences occur. The results of specific mass variation and total drying shrinkage of alkali-activated mortars cured in different conditions are shown in Figure 3.5.30.

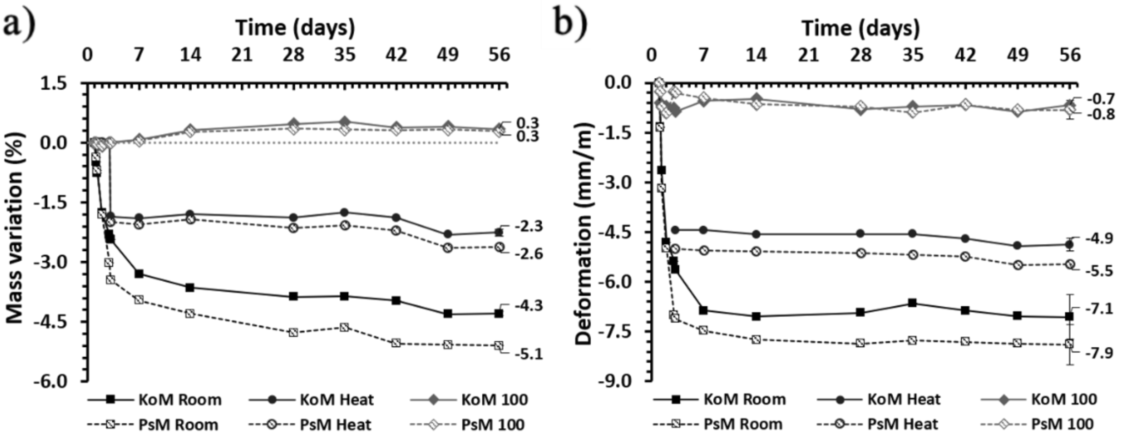

Figure 3.5.30 Mass variation (a) and drying shrinkage (b) of alkali-activated mortars cured under different conditions.

Independently of the precursor used (KO or PS), the total drying shrinkage at room conditions mainly occurred in the initial 7 d of curing, evolving afterward towards a plateau value. These results were consistent with the expectations based on existing literature (Bakharev, 1999; Cartwright, 2014; Lee, 2014) and the authors' previous findings. The drying shrinkage of PS mortars was larger compared to KO mortars, -7.9 and -7.1 mm/m, respectively. Isothermal data show more intense reactions in KO pastes at room temperature, which may indicate the formation of more binding phases. Despite no significant differences have been observed in FTIR and XRD results, the formation of more reaction products seems to be supported by the higher strength development of KO mortars at room conditions (Figure 3.5.33). These results are in agreement with the findings of Thomas *et al.* (2017) who reported that stiffer alkali-activated concretes presented improved dimensional stability. The total porosity of PS mortars was found to be slightly higher compared to KO mortars (54.6 and 52.1 mm^3/g) but the smaller average pore size in PS mortars may further contribute to increasing the capillary tensile forces generated, hence increasing shrinkage deformation at room conditions. The accompanying mass variation has shown to be a more gradual process that continued along the 56 d of curing. The mass loss followed a similar trend to drying shrinkage, being greater in PS mortars and occurring primarily in the initial 7 d of curing. From the above observations, it can be concluded that the highest volumetric stability of KO mortars cured at room conditions can be attributed to several complementary phenomena, including the amount of reaction products formed and the characteristics of their microstructures. When accounting for shrinkage/expansion occurred during the initial 24 h after mixing, that comprises the binder's plastic phase, the difference between the two mortars is further exacerbated. Considering the most extreme cases in the initial 24 h as reference values, the overall shrinkage of PS mortars was found to be approximately -9.8 mm/m after 7 d of curing at room conditions, see Figure 3.5.31a. On the other hand, the plastic expansion observed in KO mortars could partially mitigate the subsequent drying shrinkage, leading to an overall shrinkage of -2.5 mm/m for the same period, Figure 3.5.31b. It should be noticed that total drying shrinkage values comprise the contribution of autogenous processes occurring during the hardened state. It is interesting to mention the similarities between the shrinkage values of samples cured in saturated environments, where the exclusive existence of autogenous shrinkage can be assumed, and the long-term autogenous shrinkage measured using corrugated tubes which confirms the less significant role of autogenous shrinkage on binders' hardened state.

Thermal treatment was found to decrease the magnitude of drying shrinkage and accelerate the drying rate in both mortars. The water loss mainly occurred during the 48 h of thermal treatment and its total value was considerably lower than in room-cured samples. KO and PS mortars present similar mass loss, 2.3 and 2.6 % by mass, respectively. However, and similar to room-cured samples, a slightly higher mass loss was observed in PS mortars, which suggests a consistent correlation between the precursor's chemical composition and samples' weight loss. The formation of finer porous structures at slightly elevated temperatures was confirmed by MIP experiments (see Figure 3.5.32) and the reduction of the mean pore size is often associated with the increase of shrinkage, due to the increases of the capillary tensile stress (Thomas, 2017). Nonetheless, thermal curing promoted faster consolidation of polymeric structures and enhance strength development, Figure 3.5.33. The development of a stiffer solid network enables heat-treated mortars to accommodate higher tensile stresses generated during drying, reducing the total drying shrinkage by 30%. Similar to room-cured samples, heat-treated KO mortars presented superior volumetric stability if compared to PS mortars, as their total drying shrinkage was lower by 0.6 mm/m after 56 d of curing, Figure 3.5.30. These results show that, independently of the curing regime and modifications imposed on the pore structures, KO mortars presented enhanced volumetric stability relative to their PS counterparts. Moreover, when combining the autogenous and total drying shrinkage, one can see that heat-cured KO mortars present minimal shrinkage (0.1mm/m), while the thermal treatment was only able to reduce PS mortars shrinkage to 7.4mm/m.

Mortars cured under a steam-saturated environment exhibited higher dimensional stability along the testing period, which denotes the vital role of water evaporation on AAM shrinkage processes. In these IPs, shrinkage resulted exclusively from autogenous processes and roughly coincided with the results presented in Figure 3.5.29. Autogenous expansion of moist-cured mortars in the hardened state seems to be slightly affected by the precursor's different reactivity. However, the reduced magnitude of these results makes it difficult to postulate such a conclusion. Moist-cured samples presented a slight increase of mass during the initial 14 d of curing which can be attributed to the partial filling of open pores.

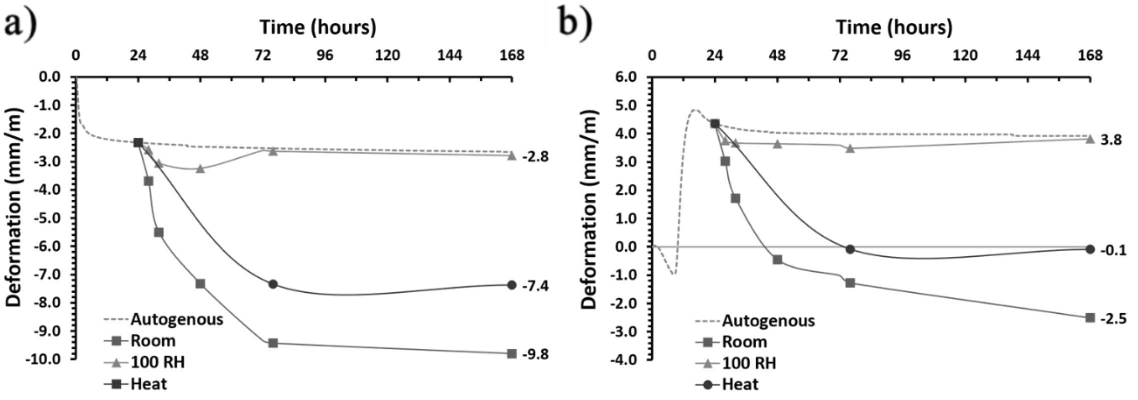

Figure 3.5.31 Combined representation of autogenous and total shrinkage of alkali-activated mortars cured under different conditions: (a) PS mortars and (b) KO mortars.

Mercury intrusion porosimetry

The porosity of IPs is known to largely influence their shrinkage processes and therefore the pore size distribution of PS and KO mortars were evaluated, and results are discussed here in detail. Pores can be characterized according to their size and grouped in four main categories: i) micropores, <1.25 nm, ii) mesopores ranging from 1.25-25 nm, iii) macropores ranging from 25-5000 nm and iv) air voids and pre-existing microcracks >5000 nm (Collins; 2000). Micropores are inherent to reaction products whereas capillary pores (comprising both meso- and macropores) can be seen as the residual unfilled spaces between reaction products and in-between aggregates and binding phases. Drying shrinkage greatly depends on capillary pore size distribution since it affects the amount of stresses generated by water egress during curing. Capillary stresses result from the difference between the atmospheric pressure at the meniscus and the internal pressure of the pore solution. The internal capillary pressures increase as the meniscus radii become smaller, augmenting the forces exerted on adjacent pore walls and promoting higher shrinkage strains. The tortuosity and connectivity of pore structures are also important parameters affecting water movements in porous structures and the tensile stresses generated.

Figure 3.5.32 shows the pore size distribution of room and heat-treated mortars. In general, MIP data show that mortars cured at room conditions have higher porosity values and a broader pore size distribution. The average cumulative pore volume of samples cured at room conditions was 54.6 and 52.1 mm^3/g in PS and KO mortars, respectively. A systematic effect of heat curing was observed but more evident in KO mortars. Heat treatment reduced the pore volume of PS and KO mortars to 43.7 and 37.6 mm^3/g, respectively; representing a 20 and 28 % reduction. Thermal treatment also influenced the pore size distribution by decreasing the relative proportion of macropores, while promoting an increase in the amount of mesopores. A reduction of macropores' average size was visible in both mortars. Slightly elevated temperatures modify the reaction kinetics and increase the amount of reaction products formed (Van Jaarsveld, 2002; Zhang, 2012; Zhang, 2013 Novais, 2016), hence promoting the formation of finer and less porous structures. The higher amount of reaction products contributes to partially filling the capillary pores, thus reducing the total pore volume and the average pore size. Filling capillary structures also contribute to form higher amounts of closed pores, which are able to encase water in their structure and thus reduce evaporation. The formation of denser structures is in agreement with the results in Table 3.5.11, where heat-treated samples presented the highest density values. The formation of less porous microstructures also contributed to enhancing the strength development of heat-cured IPs (Figure 3.5.33), as will be discussed in the following section.

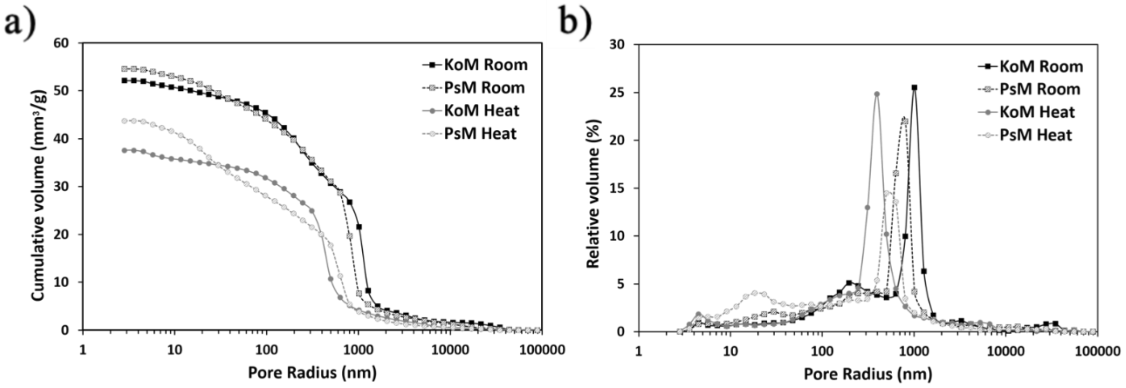

Figure 3.5.32 Cumulative pore volume (a) and relative pore size distribution (b) of room and heat-treated mortars.

Table 3.5.11 IPs bulk density and corresponding standard deviations.

Code	Curing cond.	Bulk density			
		1st day	4th day	28th day	56th day
		g/cm^3	g/cm^3	g/cm^3	g/cm^3
PS	Room	2.37±0.02	2.29±0.01	2.26±0.01	2.25±0.01
	Heat	2.39±0.01	2.34±0.01	2.34±0.02	2.33±0.02
	Saturated	2.38±0.01	2.38±0.01	2.38±0.02	2.38±0.02
KO	Room	2.39±0.02	2.33±0.02	2.29±0.02	2.29±0.02
	Heat	2.39±0.01	2.35±0.00	2.34±0.02	2.34±0.01
	Saturated	2.34±0.01	2.34±0.01	2.36±0.01	2.33±0.03

Mechanical Properties

Figure 3.5.33 shows the flexural and compressive strength temporal evolution of IP mortars (mechanical properties were evaluated at 28 and 56 d), that were subjected to different curing conditions. KO mortars cured at room conditions presented slightly higher compressive strength results when compared to PS mortars. In both room-cured mortars, compressive strength values tend to decrease with curing time, while flexural strength increases in PS mortars. A similar increase in flexural strength of metakaolin-based geopolymers cured at ambient temperature was reported by Kuenzel *et al.* (2012). A critical molar water ratio was suggested in which a uniform physical contraction in the gel microstructure can cause an increase in flexural strength, while further drying induced more shrinkage and resulted in a decrease of flexural performance. The definition of the critical molar water ratio is most likely related to the gel structures, which in this work is directly correlated to the slags' reactivity. The increase of flexural strength observed in PS mortars may suggest that a critical molar water ratio is being approached during curing, and possibly achieved around the 56th d of curing. In KO mortars such water molar ratio must have been achieved during the initial 28th d of curing, followed by the loss of flexural strength. Further investigation should be performed to determine how the slags' reactivity defines the required time to achieve such critical molar water ratio, but the results herein suggest that higher FeO_x/CaO molar ratios in the precursors' composition accelerated such phenomena. Calorimetric data shown demonstrated that long term reactions still occur and may contribute to the formation of reaction products. Yet, the continuous mass loss and drying shrinkage eventually overwhelmed this positive effect and the mechanical performance of room-cured mortars is decreased.

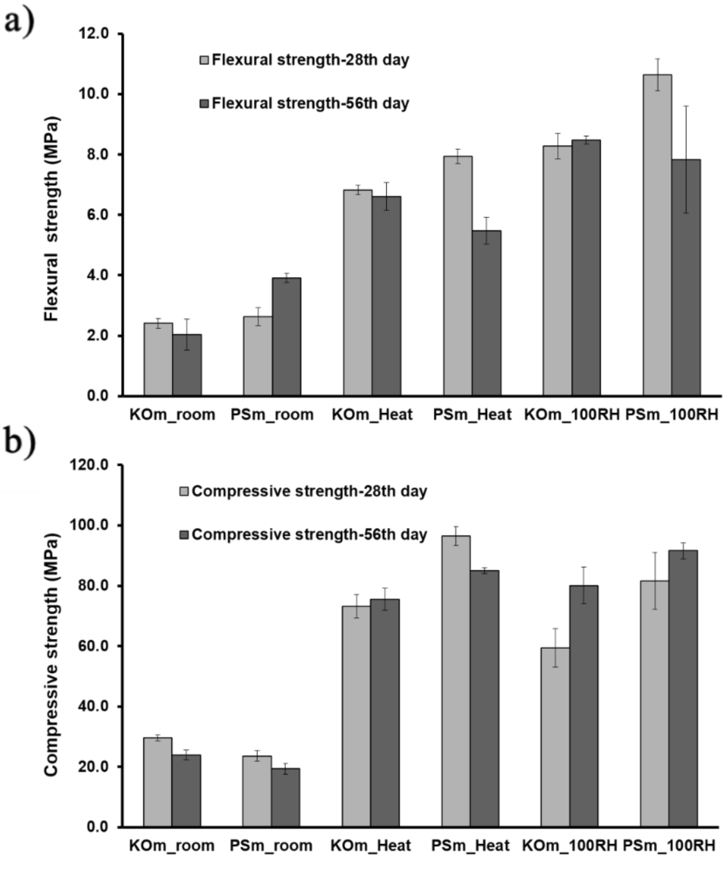

Figure 3.5.33 Flexural (a) and compressive strength of mortars (b) at different ages (28 and 56 d). Average results and corresponding standard deviations are provided.

Moist and heat curing notoriously increased strength development but a significant reduction of samples mechanical performance at later ages was also visible. Thermal treatment accelerated the formation of rigid networks, reduced the magnitude of drying shrinkage and decreased samples' total porosity. All these factors contributed to an increase in mortars' mechanical performance. In room cured samples, a small decay of compressive strength was observed at later ages that can be related to the continuous increase of drying shrinkage that may have been sufficient to provoke the formation on addition cracks or to enlarge already existing ones from the 28 to the 56 d of curing. In heat-cured mortars a similar decrease in compressive strength was not expected since most reactions/binder rearrangements took place during thermal treatment. The stable mechanical properties of KO mortars agree with such premises. However, PS binder chemistry seems to be susceptible to degradation over time, suggesting that precursors similar to KO may beneficiate the formation of more stable reaction products at slightly elevated temperatures. Similar decays of strength are not abundantly reported in the literature. Bakharev *et al.* (1999) have reported a decay in the compressive strength of heat-cured mortars but unfortunately no explanations for such decrease were provided by authors. The long-term evolution of PS binders and mortars and, the motifs to such decreases in compressive strength at later ages still need to be further investigated and no conclusive evidence is available yet.

In steam-saturated environments, the continuous water supply that acts as a reaction catalyst and/or as a transport medium in alkali activation along with a near absence of drying shrinkage in these conditions resulted in samples with high flexural and compressive strength, Figure 3.5.33. After 28 d of curing, moisture-cured IPs showed a flexural strength of 8.3 MPa and 10.7 MPa, and compressive strength of 59.3 MPa and 81.6 MPa, for KO and PS mortars, respectively. With the exception of PS mortars where a decrease in flexural strength was observed at later ages, mortars' mechanical features increased with curing time. According to the above results, it can be concluded that the deterioration of the mechanical performance observed in room-cured samples can be primarily attributed to drying shrinkage processes. A similar deleterious influence can be assumed for the initial 28 d of curing.

Conclusions

In the present work, the different effects of curing regimes on the shrinkage of CaO- and CaO-FeO_x-rich IP mortars were investigated. The precursors' reactivity and curing conditions were found to severely affected IPs shrinkage mechanisms and magnitude. The volumetric changes occurring during binders' plastic stage were defined by the precursors' nature. In the case studies analyzed here, considerable autogenous shrinkage or expansion has been observed, depending on the precursor used. However, regardless of precursors' bulk composition, drying shrinkage at room conditions was identified as the governing mechanism affecting IPs volumetric stability, whereas autogenous shrinkage was less significant. The characteristics of the precursors affected the reaction kinetics and porous structured formed, thus modifying mortars' pore size distribution and greatly influencing the drying shrinkage behavior.

Thermal treatment promoted a decrease in porosity and the redistribution of pores to lower dimensions, but it was found to be an effective shrinkage-control strategy as it reduced the total shrinkage by 30% either in CaO- or CaO-FeO_x-rich IP mortars.

As expected, in moisture-cured IPs, drying shrinkage was found to be negligible and corresponded to the results of corrugated tube autogenous shrinkage in the hardened stage. As thermal treatment, also moist curing promoted higher volumetric stability and considerably improved IPs mechanical features.

Despite being more favorable to low-calcium systems, heat and moist curing were found to be viable shrinkage mitigation strategies also for IPs produced for CaO-FeO_x-rich residues. Such curing conditions were later replicated in mortars produced from binders developed in 3.3 and, combined with the use of 2-Methyl-2.4-Pentanediol to produce IP mortars with minimal shrinkage.

Although these curing regimes may not be of practical interest in ready-mix concrete applications, they may facilitate the large-scale application of CaO-FeO_x-Al_2O_3-SiO_2 IPs in the market segments where such conditions can be more easily employed, as it is the case of the precast multilayer panels developed in Chapter 7.

3.5.5 Replacement of natural aggregates and particle packaging optimization

In the previous sections, it could be seen that considerably lower shrinkage was observed in IP mortars compare to IP pastes. These results were, however, observed in works that resulted for collaborations with KU Leuven in which the precursors and mix designs examined did not exactly correspond to the binders described in section 3.3. It was, therefore, necessary to evaluate the effectiveness of this shrinkage mitigation strategy in the CaO-FeO_x-Al_2O_3-SiO_2 IPs developed here.

Based on the considerations made in section 3.3, K18 formulation was selected as the starting binder to produce IP mortars and evaluate the magnitude of eventual improvements in the volumetric stability of the developed products.

Introduction

Aggregates are a key part of cement-based products representing between 60 to 75% of their volume and about 70 to 85% of their mass. The combination of aggregates with hydraulic binders reduces production costs and enhances the properties of the final composite material, being volumetric stability one of the aspects that are most greatly benefited.

The preeminently inert nature and dimensional stability of commonly used aggregates (i.e. natural gravel, sand and, crushed rock) along with the reduction of the binder portion in the mix design significantly reduce the susceptibility of mortars and concretes to shrinkage compared to cement pastes.

Despite the chemical differences between hydraulic binders and the IP binders investigated here, similar effects on volumetric stability could be expected in alkali-activated products. In fact, considerably lower values of shrinkage were observed in sections 3.5.3 and 3.5.4 when IP mortars were examined relative to the IP pastes described in 3.5.1 and 3.5.2.

In order to demonstrate the effectiveness of this shrinkage mitigation strategy and to assess the magnitude of the shrinkage reduction achieved in materials produced from RDF slags, normalized sand was first introduced into the mix design. Apart from drying shrinkage (the dominant shrinkage mechanism), the effects of binder-to-aggregates ratio (B/A) on fresh and hardened state properties of mortars were evaluated.

In this section, no SRA or heat-curing regimes were employed to properly quantify the impacts of introducing aggregates in the mix design without intermingling their effects with other shrinkage mitigation strategies.

Following the principle of maximal usage of residues, the possibility of replacing natural aggregates by granulated slag was also investigated. Such an approach intended to safeguard natural resources and increase the amount of RDF slags reintroduced in the materials cycle, while simultaneously maximizing the cost-benefit of the developed products.

Similar to cement-based products where particle size distribution can be manipulated in order to enhance mechanical and durability properties, the gradation of slag aggregates was tailored to improve particle packaging.

Several particle packing models have been proposed in the literature (e.g., Fuller, Bolomey, Andreassen, AFDZ) but all of them are based on the same concept of minimizing the voids between large particles and filling them with smaller-size aggregates or fillers, which thereby increases packing density and reduces the amount of binder per unit of volume. Figure 3.5.34 illustrates the concept of improving particle packing by properly combining aggregates of different dimensions.

Among those models, Fuller distribution is one of the most well-described and widely used methods. Fuller and Thompson (1907) proposed continuous aggregates gradations to attain maximal packing density and minimal porosity, which in turn, optimized strength development. In this classical gradation theory, each aggregate is assumed spherical and the optimal volume percentage of each aggregate fraction is described by the following equation:

$$U(i) = 100\left(\frac{i}{D_{max}}\right)^h$$

where, *i* is the average diameter of the aggregate in each size fraction (mm), *U(i)* is the cumulative volume of aggregate under *i* mm (%), D_{max} is the maximum diameter of aggregates (mm) and *h* the is Fuller exponential.

The volume percentage of different fractions of slag aggregates was calculated according to Fuller distribution and the fresh and hardened state properties of IP mortars examined. The correlation between the properties of IP mortars and binder-to-aggregate ratio (B/A) and, the type of aggregates used (normalized sand or slag aggregates) was investigated.

Apart from environmental and economic considerations, drying shrinkage, setting time, and strength development were taken as key performance indicators used to select the most appropriate mix designs, later used produced optimized IP mortars with minimal shrinkage values in section 3.5.6.

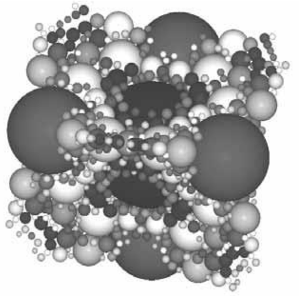

Figure 3.5.34 Illustrative representation of optimal particle packing (reproduced from Geisenhanslüke & Schmidt *et al.*, 2004).

Experimental

Materials and methods

To evaluate the impact of different types of aggregates and B/A ratios, K18 formulation was selected as the starting binder. The production procedure, mixture portions, and properties of the K18 binder can be found in 3.3. The mortar production followed the same mixture procedure previously described in 3.3, only being added an additional min to incorporate the aggregates in the mixture.

In the first batch of samples, normalized CEN-Standard sand (NormenSand, Germany) was used according to EN 196-1. The sand specific grain size distribution ranged between 0.08 and 2.00 mm, and have a moisture content that did not exceed 0.2 wt% which was considered negligible during mix design. The mass ratio between the parent binder and sand varied from 0.64 to 1.00 and the characteristics of the mix portions are provided in Table 3.5.12.

The second batch of IP mortars was produced using pre-processed RDF aggregates as sand substitutes. For this purpose, as-received granular RDF slag was submitted to distinct pre-processing procedures to achieve different particle size distributions. The slag granules were milled in 4 kg batches using a pre-grinder for a period that was progressively increased from 1 to 30 min. Further reduction of PSD was achieved by adding a second grinding stage in a ball mill for 1 h. The PSD of the different aggregate fractions was determined by a laser particle analyzer (Malvern Mastersizer 3000) and is shown in Figure 3.5.35. The PSD of the finely milled slag used as a precursor is also given for comparison, corresponding to the slag grinded from a total period of 4 h and 30 min.

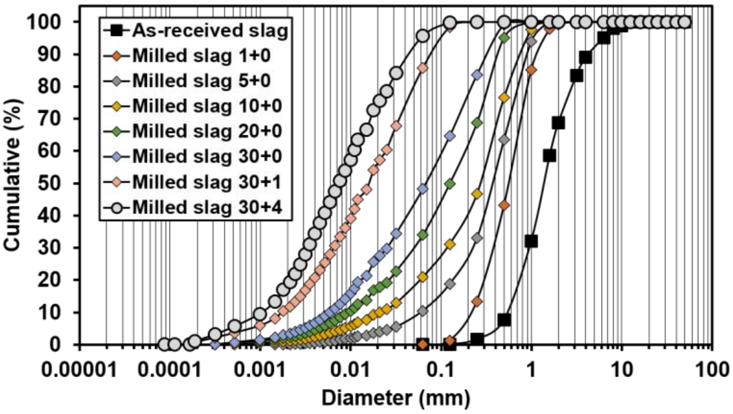

Figure 3.5.35 Particle size distribution of as-received granular slag and after different pre-processing procedures. Milled slag 30+4 refers to finely milled slag used as the binder main precursor while the remaining fractions are refer to according to the different milling times.

As can be seen, the diameter of the slag granules was progressively reduced as the milling time rose. In the slag milled for 1 h and 30 min, a substantial increase of the volume of very fine particles (<0.01 mm) was observed, resembling the PSD of the slag used as the precursor. Given the amorphous nature of RDF slags and the substantial increase SSA, this fraction would be considerably dissolved and participate in the mixture mostly as a precursor. At this point, it should be acknowledged that slag granules do not behave as inert aggregates analogs to normalized sand as their outer layers will still endure alkaline hydrolysis, partially react and contribute to polymerization reactions. However, finely milled materials are typically necessary to enhance the precursors' reactivity to significant levels and, therefore, if the gradation of slag aggregates is restricted to relatively large particles limited disturbance of the binder reaction kinetics and product formed were expected. Binder-aggregates bonds and the formation of interfacial transition zones will be discussed when examining the mortars' mechanical properties.

In order to increase packing density and produce highly dense structures, Fuller exponentials ranging from 0.33 to 0.50 are recommended (Gong, 2015). A Fuller distribution with an exponential (*h*) equal to 0.50 was considered in this work. The selection of such value results in a stepper curve that, in practice, intended to limit the amount of fine and highly reactive aggregates used. To define optimal mixture portions, the PSD of each aggregate fraction was classified into 24 classes, ranging 0.0018 to 2.0 mm, and simulation analyses were performed to determine mix combinations of different fractions that deliver granulometric distributions with minimal sum of squares of residuals (method of least squares) relative to the Fuller's theoretical curve. In Figure 3.5.36, two examples of the outputs of theses simulations are given.

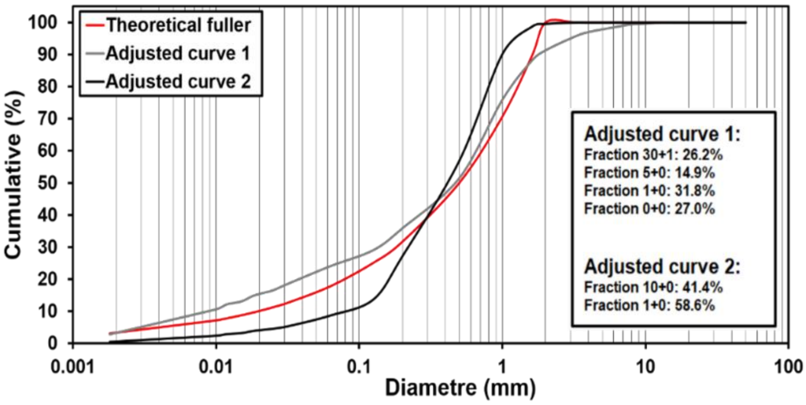

Figure 3.5.36 Fullers' theoretical particle size distribution and two examples of adjusted curves using pre-processed slag aggregates.

The adjusted curve n°1 corresponds to the PSD produced by combining the different slag fractions that delivered minimal residuals values. It can be seen, that curve n°1 follows a similar trend to Fuller's gradation curve, which, however, slightly exceeded the optimal volume of particles with diameters below 0.1 mm and over 1.5 mm.

Limit the portion of fine particles was considered necessary to restrict the interference in binders' kinetics and the PSD was, therefore, modified. Slightly higher residuals were admitted but the volume of particles with diameters below 0.1 mm was limited to 10 vol%. From the technical point of view, reducing the number of fractions used was also preferable to increase simply of milling and mixing processes. Precedence should and was given to course fractions where shorted milling processes are required. It can be seen that curve n°1 required the use of 4 different fractions while in the case of curve n°2 only two roughly milled fractions were necessary.

For this reason, the aggregates used here to produce IP mortars followed the distribution of curve n° 2. The density of both slag fractions was determined to be approximately 3.0 g/cm^3 - which defines them as high-density aggregates- considered equal and, their mass ratio set to be 1.41:1 in the mortars mix design. The characteristics of the mortar portions can be seen in Table 3.5.12, where the mortars produced are coded according to their parent binder, B/A mass ratio and type of aggregates used.

The mortars produced were characterized in terms of setting time, drying shrinkage, water absorption and open porosity, apparent density, and flexural and compressive strength after 28 d curing. All characterization tests were conducted as previously described for IP binders and the detailed description of the procedures can be found in section 3.3.

Table 3.5.12 Mortars mix portions (wt%).

Code	Binder	Agg.	Solid precursors		Solution	Aggregates			B/A	RDF slag total
			PS	SF		Sand	1+0	10+0	wt/wt	wt%
Ref. binder	K18	-	72.1	4.1	23.8	-	-	-	-	72.1
M18|0.64		Sand	28.1	1.6	9.3	61.0	-	-	0.64	28.1
M18|0.76			31.1	1.8	10.3	56.8	-	-	0.76	31.1
M18|0.88			33.7	1.9	11.1	53.2	-	-	0.88	33.7
M18|1.00			36.0	2.0	11.9	50.0	-	-	1.00	36.0
MP18|0.76		Slag	31.1	1.8	10.3	-	33.3	23.6	0.76	88.0
MP18|0.88			33.8	1.9	11.1	-	31.2	22.0	0.88	86.9

Results and discussion

Setting time

Table 3.5.13 shows that the initial and final setting time of the IP mortars produced. Independently of the conditions used, the setting time of IP mortars does not coincide with the setting time of K18 binder. As the phenomena of stiffening, setting and hardening are physical manifestations of progressive polymerization reactions, reducing the binder portion in mix design was not expected to significantly affect setting times. However, this did not turn out to be true in the systems produced here.

In sand mortars, setting times were progressively reduced as the sand dosage rose. The shortest initial and final setting time were observed in M18|0.64 mortars, 32 and 40 min respectively, representing a 24 and 56% reduction relative to K18 binder. As normalized sand is mainly composed of quartz, the dissolution of Si species seems an unreasonable explanation for this unexpected behavior. Possible explanations may include the absorption of water released during polymerization reactions on the sand particles surface, which in turn increase the medium concentration and accelerate ongoing rearrangements of the polymeric structure. Fine sand particles may also act as nucleation sites with a similar accelerating effect. Despite further examination still be required to determine the exact mechanism(s) contributing to such phenomena, a consistent acceleration pattern was observed. Nonetheless, all sand mortars presented initial setting time higher than 30 min, being therefore compliant with EN specifications for different types of cement. If longer setting times are required, the binder composition can be modified according to section 3.3 or the sand dosage can be simply reduced. The use of retardant admixtures is also an alternative solution to extend setting times which, however, will not be discussed here.

Setting times were differently affected when slag aggregates were introduced in the mix. Higher reductions were observed in both initial and final setting times. The lowest setting times were observed in MP18|0.76 mortars, 27 and 35 min, respectively, representing a 36 and 61% reduction relative to the initial and final setting of the parent binder, Table 3.5.13. Mortars with B/A ratio of 0.64 were produced but their hastened setting time prevented their proper cast, and therefore those mortars were discarded of further analysis.

Conversely to sand, the amorphous nature of slag aggregates makes foreseeable some degree of dissolution of the outer layers of slag particles, which increases the concentration of the medium and hasten supersaturation, and in turn accelerate the formation of consolidated polymeric structures. Similar to sand, undissolved slag particles may also act as nucleation sites further accelerating setting. It can be seen that increasing the dosage of aggregates reduced the initial setting to levels not admissible by EN specifications. Hence, when using such reactive aggregates, B/A ratios must be limited to 0.88 in the systems developed here.

Table 3.5.13 Setting time of IP mortars produced with different aggregates and binder-to-aggregates ratios.

Code	Binder	Agg.	Initial setting	Final setting	Δ Initial setting	Δ Final setting
			Min.	Min.	%	%
Ref. binder	K18	-	42	90	-	-
M18|0.64		Sand	32	40	-24	-56
M18|0.76			34	42	-19	-53
M18|0.88			37	47	-12	-48
M18|1.00			39	49	-7	-46
MP18|0.76		Slag	27	35	-36	-61
MP18|0.88			31	40	-26	-56

Drying shrinkage and weight loss

The drying shrinkage and specific mass variation of IP mortars produced with different aggregates and B/A mass ratios are shown in Figure 3.5.37. Independently of the conditions used, a significant reduction of drying shrinkage was observed relative to the parent binder, which demonstrates the general beneficial impact of aggregates and confirms the results gathered in 3.5.3 and 3.5.4.

In sand-based mortars, the reduction of drying shrinkage was proportional to sand content, ranging from 3.6 to 6.6 mm/m, which represents a reduction of 69 to 83% relative to the K18 binder. The introduction of sand aggregates did not change, however, drying shrinkage progression. Like it was observed in K18 pastes, drying shrinkage mainly occurred in the initial 7 d of curing, evolving afterward towards a plateau value. These results are in line with the observations made in previous sections.

In Figure 3.5.37b, the mass variation occurring during the initial 56 d of curing is shown. It can be seen that no significant modifications were observed relative to the K18 binder. Such mass loss result from the combined effects of lowering the binder portion in the system, and thereby the amount of free water available, and the higher density of IP mortars (see Table 3.5.12). The progressive increase of mass loss values as the B/A ratio rose has shown good agreement with drying shrinkage, as inert aggregates do not take part in evaporation processes.

It was also interesting to notice the lower shrinkage values of the mortars examined here when compared to the mortars described in section 3.5.4 cured at room conditions (-7.9 mm/m). These results can be mainly explained by the higher S/L of the binder used and the increased dosage of aggregates. Other factors that can have contributed to such notorious reduction include the higher concentration of Si species in the binder that favors the formation of more stable polymeric architectures and, the distinct gradation of the sand aggregates used.

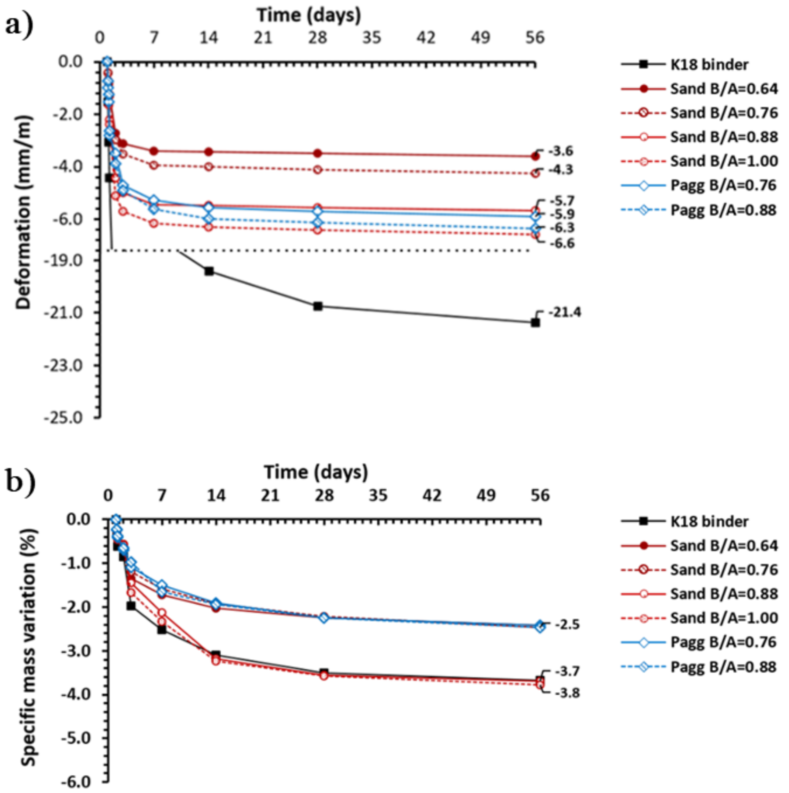

Figure 3.5.37 Drying shrinkage (a) and specific mass variation (b) of IP mortars produced with different aggregates and binder-to-aggregates mass ratios.

The drying shrinkage of mortars produced with slag aggregates was slightly increased relative to their sand counterparts. Similar to the reduction of setting times, these results can be attributed to the partial dissolution and participation in the reaction of these aggregates. The initial volume reduction due to partial dissolution and, the formation of additional binding phases that endure significant shrinkage (as can be seen in the case of K18 binder), increased the total drying shrinkage of mortars where slag granules were used as aggregates. However, shrinkage results comparable to those of sand-based mortars were attained, which demonstrates the general effectiveness of this shrinkage mitigation strategy.

Moreover, in these mortars, the total content of slag excessed 85 wt% of the mixture, whereas in sand-based mortars such values do not exceed 40 wt%, Table 3.5.12. Increasing the volumes of RDF slags reintroduced into the materials cycle by valorising such residues both as IP precursors and aggregates meets the most fundamental aspiration of this work, which is to foment and maximize industrial symbiosis between the energy and construction sectors to raise the sustainability of such production processes. Economic and environment gains are also driven by reducing to less than half the activating solution required per volume of produced material in mortars relative to the parent binders.

Physical-mechanical characterization

Strength development was considered the third key performance indicator to assess the efficiency of introducing different dosages and types of aggregates into the mix design of the alkali-activated materials developed here.

Table 3.5.14 showed the water absorption, open porosity, apparent density and, flexural and compressive strength of IP mortars produced with different aggregates and B/A ratios. As can be seen, open porosity and water absorption were only marginally affected by the different types and dosages of aggregates used, not exceeding 3 and 7%, respectively. Yet, water absorption and open porosity were slightly increased as B/A ratio rose, which can be related to an increase of the volume of micropores inherent to the higher amount of binding phases formed. Nonetheless, the small magnitude of open porosity also confirms the proper gradation of the aggregates used. In fact, apparent density was considerably increased when introducing aggregates into the mix, particularly in the case of slag aggregates with a density of approximately 3.0 g/cm^3. Such an increase of apparent density was not transposed into the mortars' strength development, however. The parent binder presented the highest flexural and compressive strength after 28 d of curing at room temperature, 7 MPa and 100 MPa, respectively. Independently of the type and dosage of aggregates used lower but comparable flexural strengths were attained. In sand-based mortars flexural strength ranged from 4.8 MPa to 5.3 MPa while in slag-based mortars such value varied from 5.1 MPa to 5.4 MPa, representing a reduction of 24 to 32% relative to K18. Reduced compressive strengths were also observed in IP mortars but in this case, the influence of the type of aggregate and B/A ratio was more visible. In sand-based mortars compressive strength varied from 52.2 MPa to 60.0 MPa, representing a maximum reduction of 43%. The maximum compressive strength was achieved by M18|0.76 mortars, which along with the highest apparent density observed suggests slight improvements in particle packing. Replacing natural sand by slag aggregates enhanced the mortars' compressive strength up to 37%, reaching a maximum value of 77.1 MPa. As previously described when examining the mortars' setting time, the amorphous nature of slag aggregates favors their partial dissolution in alkaline mediums, which in turn, contributes to increasing the amount of binding phases formed. The higher compressive strength of slag-based mortars also seems to discard the formation of fragile of interfacial transition zones and corroborate the good bonding between the polymeric networks formed and undissolved slag particles.

Table 3.5.14 Water absorption, open porosity, apparent density and, flexural and compressive strength of IP mortars produced with different aggregates and binder-to-aggregates ratio after 28 d of curing.

Code	Binder	Agg.	H_2O abs.	Open por.	ρ	Flex. strength	Comp. strength
			%	%	g/cm^3	MPa	MPa
Ref. binder	K18	-	1.4±0.2	3.3±0.4	2.22±0.03	7.1±0.7	100.5±8.5
M18|0.64		Sand	2.0±0.1	4.9±0.4	2.40±0.00	4.8±0.1	52.2±3.4
M18|0.76			2.2±0.1	5.3±0.4	2.42±0.03	5.3±0.1	60.0±1.8
M18|0.88			2.3±0.1	5.6±0.4	2.38±0.04	4.9±0.4	54.0±2.6
M18|1.00			2.5±0.1	6.2±0.4	2.41±0.04	5.1±0.6	56.2±2.7
MP18|0.76		Slag	1.8±0.2	4.7±0.4	2.63±0.01	5.4±0.2	73.6±0.4
MP18|0.88			2.0±0.1	5.3±0.0	2.61±0.00	5.1±0.1	77.1±2.7

In summary, introducing aggregates into the IP mix design has a significant deleterious effect on strength development but all mortars presented compressive strength above 50 MPa after 28 d of curing, and therefore compatible with the requirements of most of the common construction application applications. The replacement of natural sand by slag aggregates led to higher compressive strength values with the added benefit of reducing the content raw materials used. Both sand and slag aggregates also imposed important modifications on the specimens' failure mechanisms and the brittle nature of IP pastes was avoided.

Conclusions

The effectiveness of introducing aggregates into the IPs design mix as a shrinkage mitigation strategy was investigated and the effects of such modifications in key performance indicators examined.

Drying shrinkage in IPs mortars was considerably lower than the values observed in K18 binder. Although generally beneficial, drying shrinkage was found to be greatly dependent on the dosage and type of aggregates used. When normalized sand was used, drying shrinkage was progressively reduced as sand dosage rose, with the minimum value of 3.6 mm/m attained at B/A ratios of 0.64. The mortars' apparent densities were considerably increased relative to the starting binder while open porosity and water absorption were only marginally increased. Setting time and strength development were significantly reduced when aggregates were introduced into the mix, but kept compliant with the specifications and requirements of common construction applications.

The replacement of sand by RDF slag aggregates further reduced the mortars setting time, which limits B/A ratios to values superior to 0.88. Such restrictions prevented slag-based mortars to reach shrinkage values comparable to those of sand-based mortars, but such aggregates were still able to deliver IPs mortars with drying shrinkage values of less than one-third of their parent binders (≈ 6 mm/m).

Due to the higher density and reactive nature of slag aggregates, denser mortars with enhanced mechanical propertied were produced when using such aggregates.

The efficiency of such shrinkage mitigation strategy was slightly impaired when replacing normalized sand but the total content of slag on those mortars excessed 85 wt% of the total mixture, whereas in sand-based mortars such value does not surpass 40 wt%. Increasing the volumes of RDF slags reintroduced into the materials cycle by valorizing such residues both as IP precursors and aggregates meets the most fundamental aspiration of this work, which was to foment and maximize industrial symbiosis between the energy and construction sectors to raise the sustainability of their production processes. Further economic and environmental gains are also driven by reducing to less than half the activating solution required per volume of produced material in mortars relative to the parent binders.

Considering the above-mentioned environmental and economic factors and, the key performance indicators analysed, MP18|0.88 formulation was selected as the reference mortar in the following optimization stage, where the insights gathered throughout the previous sections will be combined to produced IP mortars with an elevated dosage of RDF residues, minimal shrinkage values and mechanical with properties comparable to benchmark materials in the construction sector.

References

ASTM C1698-09: 2014-Standard Test Method for Autogenous Strain of Cement Paste and Mortar, ASTM International, West Conshohocken, PA.

Bakharev, T., Sanjayan, J. G., & Cheng, Y. B. (1999). Effect of elevated temperature curing on properties of alkali-activated slag concrete. Cement and Concrete Research, 29(10), 1619-1625. https://doi.org/10.1016/S0008-8846(99)00143-X

Beersaerts, G., Ascensão, G. & Y Pontikes, Y. (2019). Modifying the pore size to minimise shrinkage by curing and using reactive and non-reactive additives in an Fe-rich inorganic polymer mortar. Cement and Concrete Research (in press)

Bílek, V., Kalina, L., Novotný, R., Tkacz, J., & Pařízek, L. (2016). Some issues of shrinkage-reducing admixtures application in alkali-activated slag systems. Materials, 9(6), 462. https://doi.org/10.3390/ma9060462

British Standards Institution, BS EN 12617–4:2002 Products and systems for the protection and repair of concrete structures. Test methods, Determination of Shrinkage and Expansion, Milton Keynes, UK, 2002, p. 14.

BS EN 12617-4:2002 Products and systems for the protection and repair of concrete structures. Test methods. Determination of shrinkage and expansion

Bumanis, G., Vitola, L., Bajare, D., Dembovska, L., & Pundiene, I. (2017). Impact of reactive SiO2/Al2O3 ratio in precursor on durability of porous alkali activated materials. Ceramics International, 43(7), 5471-5477. https://doi.org/10.1016/j.ceramint.2017.01.060

Cartwright, C., Rajabipour, F., & Radlińska, A. (2014). Shrinkage characteristics of alkali-activated slag cements. Journal of Materials in Civil Engineering, 27 (7), B4014007. https://doi.org/10.1061/(ASCE)MT.1943-5533.0001058

Catauro, M., Papale, F., Lamanna, G., & Bollino, F. (2015). Geopolymer/PEG hybrid materials synthesis and investigation of the polymer influence on microstructure and mechanical behavior. Materials Research, 18(4), 698-705. http://dx.doi.org/10.1590/1516-1439.342814

Chanvillard, G., Boivin, S., Thierry, J., Guimbal, F., Garcia, D. (2007). U.S. Patent No. 20090305019A1. Washington, DC: U.S. Patent and Trademark Office.Chen, W., & Brouwers, H.

Chen, W., & Brouwers, H. J. H. (2012). Hydration of mineral shrinkage-compensating admixture for concrete: An experimental and numerical study. Construction and Building Materials, 26(1), 670-676. https://doi.org/10.1016/j.conbuildmat.2011.06.070

Close, P., Shepherd, H. M., & Drummond, C. H. (1958). Determination of several valences of iron, arsenic and antimony, and selenium in glass. Journal of the American Ceramic Society, 41(11), 455-460. https://doi.org/10.1111/j.1151-2916.1958.tb12894.x

Collins, F., & Sanjayan, J. G. (2000). Effect of pore size distribution on drying shrinking of alkali-activated slag concrete. Cement Concrete Research, 30(9), 1401-1406. https://doi.org/10.1016/S0008-8846(00)00327-6

Corinaldesi, V., Donnini, J., & Nardinocchi, A. (2015). The influence of calcium oxide addition on properties of fiber reinforced cement-based composites. Journal of Building Engineering, 4, 14-20. https://doi.org/10.1016/j.jobe.2015.07.009

Criado M, Fernández-Jiménez A, Palomo A (2007) Alkali activation of fly ash: effect of the SiO_2/Na_2O ratio: part I: FTIR study. Microporous Mesoporous Mater 106:180–191. https://doi.org/10.1016/j.micromeso.2007.02.055

Dalby, K. N., & King, P. L. (2006). A new approach to determine and quantify structural units in silicate glasses using micro-reflectance Fourier-Transform infrared spectroscopy. American Mineralogist, 91(11-12), 1783-1793. https://doi.org/10.2138/am.2006.207

Daux, V., Guy, C., Advocat, T., Crovisier, J. L., & Stille, P. (1997). Kinetic aspects of basaltic glass dissolution at 90 C: role of aqueous silicon and aluminium. Chemical Geology, 142(1-2), 109-126. https://doi.org/10.1016/S0009-2541(97)00079-X

Duxson, P., Fernández-Jiménez, A., Provis, J. L., Lukey, G. C., Palomo, A., & Van Deventer, J. S. (2007). Geopolymer technology: the current state of the art. Journal of Materials Science, 42(9), 2917-2933. https://doi.org/10.1007/s10853-006-0637-z

EN, B. (2016). 196-1: 2016. Methods of Testing Cement. Determination of Strength.

EN, B. (2018). 196-6: 2018- Methods of testing cement - Part 6: Determination of fineness.

Fuller, W. B., & Thompson, S. E. (1907). The laws of proportioning concrete. American Society of Civil Engineers, Vol.33, 1907, pp.223-298.

Geisenhanslüke, C., & Schmidt, M. (2004, September). Methods for modelling and calculation of high density packing for cement and fillers in UHPC. In Proceedings of the International Symposium on Ultra-High Performance Concrete, Kassel, Germany (pp. 303-312).

Gomes, K. C., Lima, G. S., Torres, S. M., de Barros, S. R., Vasconcelos, I. F., & Barbosa, N. P. (2010). Iron distribution in geopolymer with ferromagnetic rich precursor. In Materials Science Forum, 643, 131-138. https://doi.org/10.4028/www.scientific.net/MSF.643.131

Gong, C., Zhang, J., Wang, S., & Lu, L. (2015). Effect of aggregate gradation with fuller distribution on properties of sulphoaluminate cement concrete. Journal of Wuhan University of Technology-Mater. Sci. Ed., 30(5), 1029-1035. https://doi.org/10.1007/s11595-015-1268-5

Granizo, M. L., Alonso, S., Blanco-Varela, M. T., & Palomo, A. (2002). Alkaline activation of metakaolin: effect of calcium hydroxide in the products of reaction. Journal of the American Ceramic Society, 85(1), 225-231. https://doi.org/10.1111/j.1151-2916.2002.tb00070.x

Guo, X., & Shi, H. (2015). Metakaolin-, fly ash-and calcium hydroxide-based geopolymers: effects of calcium on performance. Advances in Cement Research, 27(10), 559-566. https://doi.org/10.1680/jadcr.14.00081

He, P., Wang, M., Fu, S., Jia, D., Yan, S., Yuan, J. & Zhou, Y. (2016). Effects of Si/Al ratio on the structure and properties of metakaolin based geopolymer. Ceramics International, 42(13), 14416-14422, https://doi.org/10.1016/j.ceramint.2016.06.033

Hertel, T., Blanpain, B., & Pontikes, Y. (2016). A proposal for a 100% use of bauxite residue towards inorganic polymer mortar. Journal of Sustainable Metallurgy, 2(4), 394-404, https://doi.org/10.1007/s40831-016-0080-6

ISO, I. (2010). 9277: 2010 Determination of the specific surface area of solids by gas adsorption–BET method. Geneva: International Organization for Standardization.

Jensen, O. M., & Hansen, P. F. (2001). Autogenous deformation and RH-change in perspective. Cement and Concrete Research, 31(12), 1859-1865. https://doi.org/10.1016/S0008-8846(01)00501-4

Kalina, L., Bílek, V., Bartoníčková, E., & Krouská, J. (2018). Polypropylene Glycols as Effective Shrinkage-Reducing Admixtures in Alkali-Activated Materials. ACI Materials Journals, 115(2). http://doi.org/10.14359/51701099

Kellermeier, M., Melero-Garcia, E., Glaab, F., Klein, R., Drechsler, M., Rachel, R., & Kunz, W. (2010). Stabilization of amorphous calcium carbonate in inorganic silica-rich environments. Journal of the American Chemical Society, 132(50), 17859-17866. https://doi.org/10.1021/ja106959p

Komnitsas K, Zaharaki D (2007) Geopolymerisation: a review and prospects for the minerals industry. Miner Eng 20:1261–1277. https://doi.org/10.1016/j.mineng.2007.07.011

Kriskova, L., Machiels, L., & Pontikes, Y. (2015). Inorganic polymers from a plasma convertor slag: effect of activating solution on microstructure and properties. Journal of Sustainable Metallurgy, 1(3), 240-251. https://doi.org/10.1007/s40831-015-0022-8

Kuenzel, C., Vandeperre, L. J., Donatello, S., Boccaccini, A. R., & Cheeseman, C. (2012). Ambient temperature drying shrinkage and cracking in metakaolin-based geopolymers. Journal of the American Ceramic Society, 95(10), 3270-3277. https://doi.org/10.1111/j.1551-2916.2012.05380.x

Lakshtanov, L. Z., & Stipp, S. L. S. (2009). Silica influence on calcium carbonate precipitation. Geochimica et Cosmo chimica Acta Supplement, 73, A716. 2009GeCAS..73Q.716L

Lee, N. K., Jang, J. G., & Lee, H. K. (2014). Shrinkage characteristics of alkali-activated fly ash/slag paste and mortar at early ages. Cement and Concrete Composites, 53, 239-248. https://doi.org/10.1016/j.cemconcomp.2014.07.007

Li, Z., Zhang, W., Wang, R., Chen, F., Jia, X., & Cong, P. (2019). Effects of Reactive MgO on the Reaction Process of Geopolymer. Materials, 12(3), 526. https://doi.org/10.3390/ma12030526

Machiels, L., Arnout, L., Jones, P. T., Blanpain, B., & Pontikes, Y. (2014). Inorganic polymer cement from Fe-silicate glasses: varying the activating solution to glass ratio. Waste and Biomass Valorization, 5(3), 411-428. https://doi.org/10.1007/s12649-014-9296-5

Machiels, L., Arnout, L., Yan, P., Jones, P. T., Blanpain, B., & Pontikes, Y. (2017). Transforming enhanced landfill mining derived gasification/vitrification glass into low-carbon inorganic polymer binders and building products. Journal of Sustainable Metallurgy, 3(2), 405-415.https://doi.org/10.1007/s40831-016-0105-1

Mastali, M., Kinnunen, P., Dalvand, A., Firouz, R. M., & Illikainen, M. (2018). Drying shrinkage in alkali-activated binders–a critical review. Construction and Building Materials, 190, 533-550. https://doi.org/10.1016/j.conbuildmat.2018.09.125

Mindess, S., Young, J. F., & Darwin, D. (2003). Concrete. Prentice Hall, Upper Saddle River, New Jersey, 2.

Mounanga, P., Bouasker, M., Pertue, A., Perronnet, A., & Khelidj, A. (2011). Early-age autogenous cracking of cementitious matrices: physico-chemical analysis and micro/macro investigations. Materials and Structures, 44(4), 749-772. https://doi.org/10.1617/s11527-010-9663-z

Neto, A. A. M., Cincotto, M. A., & Repette, W. (2008). Drying and autogenous shrinkage of pastes and mortars with activated slag cement. Cement and Concrete Research, 38(4), 565-574. https://doi.org/10.1016/j.cemconres.2007.11.002

Novais, R. M., Ascensão, G., Seabra, M. P., & Labrincha, J. A. (2016). Waste glass from end-of-life fluorescent lamps as raw material in geopolymers. Waste management, 52, 245-255. https://doi.org/10.1016/j.wasman.2016.04.003

Onisei, S., Lesage, K., Blanpain, B., & Pontikes, Y. (2015). Early age microstructural transformations of an inorganic polymer made of fayalite slag. Journal of the American Ceramic Society, 98(7), 2269-2277. http://hdl.handle.net/1854/LU-7006236

Ono, Y., Taketsume, Y., Ogura, H., Takizawa, T. (1997). U.S. Patent No. 3801339A. Washington, DC: U.S. Patent and Trademark Office.

Pacheco-Torgal, F., Castro-Gomes, J., & Jalali, S. (2008). Alkali-activated binders: A review: Part 1. Historical background, terminology, reaction mechanisms and hydration products. Construction and Building Materials, 22(7), 1305-1314. https://doi.org/10.1016/j.conbuildmat.2007.10.015

Pacheco-Torgal, F., Labrincha, J., Leonelli, C., Palomo, A., & Chindaprasit, P. (Eds.). (2014). Handbook of alkali-activated cements, mortars and concretes. Elsevier.

Palacios, M., & Puertas, F. (2004). Stability of superplasticizer and shrinkage-reducing admixtures Stability of superplasticizer and shrinkage-reducing admixtures in high basic media. Materiales de Construcción, 54(276), 65-86. https://doi.org/10.3989/mc.2004.v54.i276.256

Palacios, M., & Puertas, F. (2007). Effect of shrinkage-reducing admixtures on the properties of alkali-activated slag mortars and pastes. Cement concrete Research, 37(5), 691-702. https://doi.org/10.1016/j.cemconres.2006.11.021

Peys, A., White, C. E., Rahier, H., Blanpain, B., & Pontikes, Y. (2019). Alkali-activation of CaO-FeOx-SiO2 slag: Formation mechanism from in-situ X-ray total scattering. Cement and Concrete Research, 122, 179-188. https://doi.org/10.1016/j.cemconres.2019.04.019

Saikia B, Parthasarathy G, Sarmah NC (2008) Fourier transform infrared spectroscopic estimation of crystallinity in SiO_2 based rocks. Bull Mater Sci 31:775–779.

Sakulich, A. R., & Bentz, D. P. (2013). Mitigation of autogenous shrinkage in alkali activated slag mortars by internal curing. Materials and Structures, 46(8), 1355-1367. https://doi.org/10.1617/s11527-012-9978-z

Salman, M., Cizer, Ö., Pontikes, Y., Snellings, R., Vandewalle, L., Blanpain, B., & Van Balen, K. (2015). Cementitious binders from activated stainless steel refining slag and the effect of alkali solutions. Journal of Hazardous Materials, 286, 211-219, https://doi.org/10.1016/j.jhazmat.2014.12.046

Sant, G., Lothenbach, B., Juilland, P., Le Saout, G., Weiss, J., & Scrivener, K. (2011). The origin of early age expansions induced in cementitious materials containing shrinkage reducing admixtures. Cement and Concrete Research, 41(3), 218-229. https://doi.org/10.1016/j.cemconres.2010.12.004

Shi, C., Jiménez, A. F., & Palomo, A. (2011). New cements for the 21st century: The pursuit of an alternative to Portland cement. Cement Concrete Research, 41(7), 750-763. https://doi.org/10.1016/j.cemconres.2011.03.016

Simon, S., Gluth, G. J., Peys, A., Onisei, S., Banerjee, D., & Pontikes, Y. (2018). The fate of iron during the alkali-activation of synthetic (CaO-) FeOx-SiO2 slags: An Fe K-edge XANES study. Journal of the American Ceramic Society, 101(5), 2107-2118. https://doi.org/10.1111/jace.15354|

Sindhunata,, Van Deventer, J. S. J., Lukey, G. C., & Xu, H. (2006). Effect of curing temperature and silicate concentration on fly-ash-based geopolymerization. Industrial & Engineering Chemistry Research, 45(10), 3559-3568. https://doi.org/10.1021/ie051251p

Szleifer, I., Ben-Shaul, A., & Gelbart, W. M. (1990). Chain packing statistics and thermodynamics of amphiphile monolayers. Journal of Physical Chemistry-US, 94(12), 5081-5089. https://doi.org/10.1021/j100375a060

Temuujin, J. V., Van Riessen, A., & Williams, R. (2009). Influence of calcium compounds on the mechanical properties of fly ash geopolymer pastes. Journal of Hazardous Materials, 167(1-3), 82-88. https://doi.org/10.1016/j.jhazmat.2008.12.121

Thomas, R. J., Lezama, D., & Peethamparan, S. (2017). On drying shrinkage in alkali-activated concrete: Improving dimensional stability by aging or heat-curing. Cement and Concrete Research, 91, 13-23. https://doi.org/10.1016/j.cemconres.2016.10.003

Van Deventer, J. S. (2007). Geopolymer technology: the current state of the art. Journal of Materials Science, 42(9), 2917-2933, https://doi.org/10.1007/s10853-006-0637-z

Van Jaarsveld, J. G. S., Van Deventer, J. S. J., & Lukey, G. C. (2002). The effect of composition and temperature on the properties of fly ash-and kaolinite-based geopolymers. Chemical Engineering Journal, 89(1-3), 63-73. https://doi.org/10.1016/S1385-8947(02)00025-6

Velandia, D. F., Lynsdale, C. J., Provis, J. L., Ramirez, F., & Gomez, A. C. (2016). Evaluation of activated high volume fly ash systems using Na2SO4, lime and quicklime in mortars with high loss on ignition fly ashes. Construction and Building Materials, 128, 248-255. https://doi.org/10.1016/j.conbuildmat.2016.10.076

Wittmann, F. H. (1976). On the action of capillary pressure in fresh concrete. Cement and Concrete Research, 6(1), 49-56. https://doi.org/10.1016/0008-8846(76)90050-8

Yang, L., Shi, C., & Wu, Z. (2019). Mitigation techniques for autogenous shrinkage of ultra-high-performance concrete–A review. Composites Part B: Engineering, 107456. https://doi.org/10.1016/j.compositesb.2019.107456

Ye, H., Cartwright, C., Rajabipour, F., & Radlińska, A. (2017a). Understanding the drying shrinkage performance of alkali-activated slag mortars. Cement and Concrete Composites, 76, 13-24. https://doi.org/10.1016/j.cemconcomp.2016.11.010

Yuan, X. H., Chen, W., Lu, Z. A., & Chen, H. (2014). Shrinkage compensation of alkali-activated slag concrete and microstructural analysis. Construction and Building Materials, 66, 422-428. https://doi.org/10.1016/j.conbuildmat.2014.05.085

Zeng, Q., Li, K., Fen-Chong, T., & Dangla, P. (2015). Pore structure of cement pastes through NAD and MIP analysis. Advances in Cement Research, 28(1), 23-32. https://doi.org/10.1680/adcr.14.00109

Zhang, Z., Provis, J. L., Wang, H., Bullen, F., & Reid, A. (2013). Quantitative kinetic and structural analysis of geopolymers. Part 2. Thermodynamics of sodium silicate activation of metakaolin. Thermochimica Acta, 565, 163-171, https://doi.org/10.1016/j.tca.2013.01.040

Zhang, Z., Wang, H., Provis, J. L., Bullen, F., Reid, A., & Zhu, Y. (2012). Quantitative kinetic and structural analysis of geopolymers. Part 1. The activation of metakaolin with sodium hydroxide. Thermochimica Acta, 539, 23-33, https://doi.org/10.1016/j.tca.2012.03.021

3.6 Development and characterization of optimized mortars

Introduction

The work presented in this section merges the insights gathered throughout Chapter 3 on the mix design of IP binders and mortars produced from RDF slags. The production of alkali-activated mortars with optimized properties is addressed and the efficiency of combining different shrinkage mitigations strategies examined.

In the previous sections, IP mortars with optimized particle packing and total content of RDF residues that exceeded 85 wt% were produced presenting high strength development, acceptable setting times and, reduced shrinkage relative to their parent binder. Despite the considerable reduction observed, additional shrinkage mitigation strategies were still required to further increase the volumetric stability of the products developed here to levels comparable to those of benchmark materials.

In section 3.5.4, the impacts of heat curing on the volumetric stability of IP mortars were investigated. Heat curing was found to be a simple and effective shrinkage-control strategy as it reduced the total shrinkage of $CaO\text{-}FeO_x\text{-}Al_2O_3\text{-}SiO_2$-rich mortars by 30%. In addition, denser microstructures were produced, contributing to increasing the mortars' mechanical performance. The reduced levels of porosity observed are also expected to positively contribute to the durability of the developed products.

As there is no intervention on the chemical composition of the binders, the industrial implementation of such a mitigation strategy will not require further modifications on the mix design, which in turn, simplifies the production processes and avoids the need for specialized workers and ad-hoc solutions. The environmental impacts associated with such curing regimes can be mitigated by using renewable energy sources while capital investments can be minimized by relying on pre-existing infrastructures used on related production processes, as pre-cast and autoclaved concrete elements.

Considering these factors, precedence was given to such a shrinkage mitigation strategy. Nonetheless, shrinkage reducing admixtures were still necessary to produce IP mortars with adequate volumetric stability. In Chapter 3 different shrinkage reducing admixtures were investigated and their effectiveness and impacts on the properties of $CaO\text{-}FeO_x\text{-}Al_2O_3\text{-}SiO_2$-rich systems examined.

The use of calcium-rich shrinkage reducing agents (CaO and GGBFS) was able to increase the volumetric stability of AAMs but found to considerably reduce their workability and setting time. The potential of such admixtures was therefore limited in the IPs mortars developed here. Similar limitations were not observed, however, when organic compounds (polypropylene glycols, PPGs and 2-methyl-2.4-pentanediol, 2M) were used as shrinkage reducing agents. Among those, the 2M was found more effective and less detrimental to the strength development of AAMs.

Aiming to achieve IPs mortars with minimal shrinkage and high mechanical performance, MP18|0.88 mortars developed in 3.5.5 were further optimized by combining heat-curing regimes with the addition of 2M into the mix design.

The single and combined effects of those shrinkage mitigation strategies were assessed in terms of apparent density, drying shrinkage and, flexural and compressive strength after 28 d of curing.

Unlikely section 3.5.5, where the modifications imposed on mortars' setting times by different types and dosages of aggregates were examined and considered a key performance indicator, no significant changes are foreseeable here and the values presented in Table 3.5.13 can be taken as reference.

Such a claim is grounded on the heat curing regime considered (previously described in section 3.5.4), being slightly elevated temperatures only employed 24 h after the reaction start, and therefore long after the mortars' initial and final set. Likewise, it was observed in section 3.5.3 that the introduction of 2M into the mortars mix did not alter the binders' reaction kinetics or shortened of the setting time of the mortars made thereof.

A second batch of IP mortars was produced using K30 as the starting binder (see mix portions in section 3.3). The same shrinkage mitigation strategies were employed and the effects of modifying the parent binder were assessed. The realization of such experiments intended to produce IP mortars with enhanced flowability and extended open times, while determining possible deleterious effects on volumetric stability and strength development.

The optimized mortars would later be used in Chapter 5 as a reference when the functionalization of alkali-activated materials was addressed.

Results and discussion

Table 3.6.1 shows the apparent density, flexural and compressive strength of the parent IP binders and mortars made thereof. As previously discussed in 3.5.5, MP18| 0.88 mortars are considerably denser than their parent binder (K18) presenting, however, an inferior mechanical performance. Based on the findings made in 3.5.4, heat curing was expected to produce denser microstructures and enhance strength development. In fact, higher densities and compressive strengths were observed in heat-cured IP mortars (MP18|0.88H), not corresponding to the magnitude of the increases observed in section 3.5.4, however.

The explanation for such reduced densification and increase of compressive strength being promoted by heat curing regimes resides on the synthesis conditions initially imposed. The high S/L ratio of the parent binder (K18) along with the reactive nature of aggregates used, accelerated the consolidation of the networks formed, limiting the mobility in the pore solution and consequently minimizes the effects of elevated temperatures on the reaction kinetics.

The introduction of 3 wt% 2M reduced the apparent density and compressive strength of heat-cured mortars by 5 and 32%, respectively. Such results agree with the findings made in section 3.5.3, where the addition of 2M modified the pore size distribution and increased the total porosity of CaO-FeO$_x$-rich IP mortars. Despite the reduction observed, apparent density and compressive strength above 2.50 g/cm^3 and 50 MPa were maintained, which suffices the requirements of common construction applications. No modifications on the mortars' workability were noticed, further corroborating the limited interference of 2M on the reaction progression previously shown in 3.5.3.

Table 3.6.1 The effect of the binder composition, 2M dosage and, curing conditions on mortars' apparent density and, flexural and compressive strength after 28 d of curing.

Code	B/A	SRA	Curing cond.	ρ	Flex. strength	Comp. strength
	(wt/wt)	(wt%)		(g/cm^3)	(MPa)	(MPa)
K18 binder	-	0.0	Room	2.22±0.03	7.1±0.7	100.5±8.5
MP18|0.88	0.88	0.0	Room	2.61±0.00	5.1±0.1	77.1±2.7
MP18|0.88H		0.0	Heat	2.65±0.03	-	80.3±3.4
MP18|32M0.88H		3.0	Heat	2.52±0.04	-	55.0±2.2
K30 binder	-	0.0	Room	2.13±0.02	6.4±0.9	102.6±6.8
MP30|0.88	0.88	0.0	Room	2.41±0.06	-	30.1±0.5
MP30|0.88H		0.0	Heat	2.58±0.03	-	74.2±4.2
MP30|32M0.88H		3.0	Heat	2.54±0.05	7.1±0.3	66.4±3.7
MP30|22M0.88H		2.0	Heat	2.49±0.05	8.0±0.3	67.3±5.1

Modifying the starting binder to K30 formulation, had a severe impact on the strength development of room cured mortars. In Table 3.6.1, can be seen that the compressive strength of MP30|0.88R mortars barely reached 30 MPa after 28 d of curing, while exceeded 75MPa in the case of their MP18|0.88R counterparts. The lower apparent density of MP30|0.88R mortars can be attributed to the density of the parent binder, while the reduction in strength development is most likely related to the combined effects of decreasing the supersaturation levels of the solution and, the increase of amount free water in the structures, which in turn, augments shrinkage (see Figure 3.6.1) and crack formation.

However, the lower saturation levels and slower consolidation of K30 binders and mortars made thereof, was beneficial when considering heat-cured mortars. Contrary to MP18|0.88 mortars where heat-curing only increased compressive strength by 4%, a 2.5-fold increase was observed. Higher mobility in the pore solution favored a greater enhancement of the reaction kinetics, beneficiating the effectiveness of heat-curing regimes. The deleterious effect of 2M to the strength development of heat-cured mortars was also minimized in MP30|0.88H mortars. Considering an equal 2M dosage of 3 wt%, compressive strength was reduced by approximately 10%, while such a decrease in MP18|0.88H mortars surpassed 30%. Conversely to MP18|0.88H where a considerable decrease of density was provoked by the addition of 2M into the design, only a minor decrease of apparent density was observed. These results show the greater impact of 2M on denser microstructures, further supported by must higher reduction of compressive strength in MP18|0.88H. Reducing 2M dosage to 2 wt% had a positive but limited impact on strength development, Table 3.6.1. Still, all heat-cured 2M-containing mortars presented flexural strength >7 MPa and compressive strength above >65 MPa.

Independently of the curing conditions and SRA dosage used, both MP18 and MP30 mortars presented satisfactory workability, density, and strength development. Thus, the acceptance of the developed products will be greatly dependent on their volumetric stability.

Figure 3.6.1 shows the weight loss and drying shrinkage of IP mortars produced with different binders, 2M dosages and, cured under different curing regimes. Similar to other IP products previously examined, mass loss and drying shrinkage occurred progressively but it is only significant in the first days of curing.

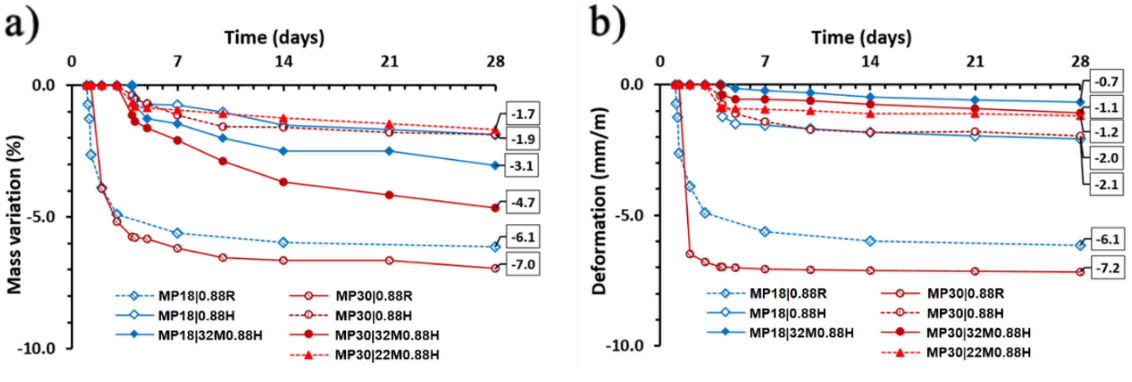

Figure 3.6.1 Mass variation (a) and drying shrinkage (b) of IP mortars produced with different binders, 2M dosages and, cured under different curing regimes.

As expected, room cured MP30|0.88 mortars presented higher weight loss and shrinkage values than their MP18 counterparts. After 28 d, the shrinkage in MP30|0.88 mortars reached 7.2 mm/m, while increasing the parent binder S/L ratio reduced shrinkage to 6.1 mm/m. Interestingly those values had an almost exact correspondence in terms of weight loss, demonstrating once again the relevance of drying processes in the volumetric stability of AAMs.

Nonetheless, heat curing vanished the differences between MP18 and MP30 mortars and comparable weight loss and shrinkage values were attained, approximately 1.9% and 2 mm/m, respectively. The higher similarity between M18 and M30 heat-cured mortars and their room cured counterparts was in line with the apparent density and compressive strength results shown in Table 3.6.1.

Yet, the introduction of 3 wt% 2M affected differently those mortars. The higher mass loss in MP30|32M0.88H agrees with the reduced density and lower mechanical resistance observed. All this evidence points out to increased levels of porosity relative to MP18|32M0.88H mortars, which did not have a positive reflection on shrinkage, however. Despite more open structures being formed, the increased amount of free-water in the systems possibly rose the total tensile stresses generated, resulting in slightly less stable IP structures. Notwithstanding, both MP18|32M0.88H and MP30|32M0.88H mortars presented low shrinkage, 0.7 and 1.1 mm/m, values comparable to those of self-leveling concrete (≈ 1m/mm). Furthermore, when decreasing 2M dosage to 2 wt% drying shrinkage was marginally higher, reaching 1.2 mm/m after 28 d of curing.

Considering the minor impact in the mortars' volumetric stability, it would be advisable to further reduced 2M dosage, however in 3.5.3 the existence of critical 2M concentration near 2 wt% has been demonstrated.

Regardless of the starting binder used, it was shown that heat-curing and 2M can be used as a complementary shrinkage mitigation strategies provenly able to deliver highly dense IP mortars with considerable mechanical performance and enhanced volumetric stability.

The main difference found between heat-cured 2M-containing MP18 and MP30 mortars was their workability. As extended open times are preferable in industrial contexts, MP30|22M0.88H was selected to produce the outer layers of sandwich-type panels later described in Chapter 7.

Fine concrete elements, with high surface-to-volume ratios, are prone to differential drying shrinkage often manifested through the extensive crack formation and bending. To preliminarily evaluate the occurrence of these phenomena when considering upscaling stages, 15x15x1.5cm^3 samples of MP30|22M0.88H mortars were produced, Figure 3.6.2.

After demolding, the samples were kept at room conditions and no cracks were visible in the samples' surfaces, and after more than 1 year since casting no signs of bending are visible either.

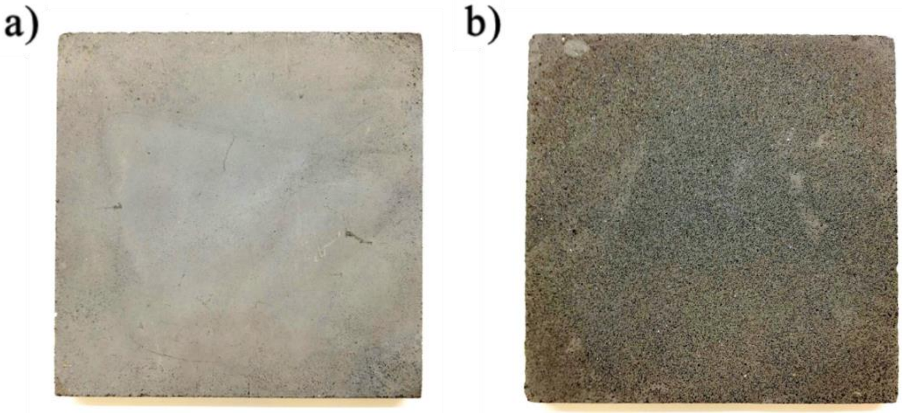

Figure 3.6.2 Surface of MP30|22M0.88H mortar (a) as demolded and (b) after polishing.

When colored aggregates are used in concrete, they are often exposed at the surface of elements. The aggregates are exposed for their visual appearance in order to esthetically valorize final product. As the development of economically viable products was an integral part of this work, the possibility of replicating such products using the developed mortars was also attempted.

Several methods can be employed to expose concrete aggregates, such as the removal of the mortar's surface by sand or water blasting, bush hammering or acid washing. Another common but less intrusive and labor-intensive method involves treating the surface of casting molds with products that compromise the formation of fully reacted reaction products. Vegetable oils are known to interfere with the alkali activation reaction playing a role similar to the retardants used to avoid the formation of hydrated products in OPC-based elements.

The internal surfaces of the molds used to cast 15x15x1.5cm^3 samples were abundantly brushed with vegetal oil and the mortars' surfaces polished using 120 grit paper sand after 28 d of curing. Figure 3.6.2 shown the visual appearance of MP30|22M0.88H mortars before and after polishing. As can be seen, a homogenous surface where shining RDF aggregates could be clearly identified was obtained after polishing. Therefore, this common industrial practice can be used to increase the market value of IP products produced form RDF slags, further showing the potential and versatility of the products developed here.

Conclusions

The results of combining the usage of a specific organic SRA (2-methyl 2.4 pentanediol) and curing conditions (3 d at 50 °C after 1 d of standard curing in sealed conditions at 20 °C) were explored, being shown able to reduce drying shrinkage of MP18|0.88 from 6.1 to 0.7 mm/m after 28 d of curing. The addition of 2M was found to have a profound impact on strength development but all the produced mortars presented compressive strength above 55 MPa after 28 d of curing. The mortar formulation was later modified sequentially in order to increase its workability and to reduce SRA dosage. Modifying the mortars' initial binder resulted in an increase of shrinkage values while reducing SRA dosage from 3 wt% to 2 wt% slightly rose the shrinkage values. Conversely, the higher mechanical performance in heat-cured 2M-containing mortars was attained when K30 formulation was used as starting binder and by reducing 2M dosage to 2 wt%.

Regardless of the starting binder used, combining multiple shrinkage mitigation strategies could be used to deliver highly dense IP mortars with considerable mechanical strength and enhanced volumetric stability. The volumetric stability of fine elements of IP was preliminary assessed being found no signs of crack formation or bending.

The modification of the visual appearance of the sample's surface was also proven possible by using a simple method to expose the mortars' aggregates.

Chapter 4

Development of insulation materials from alkali-activated binders

The following chapter starts by presenting the current framework for insulation building materials with particular emphasis on recent developments on alkali-activated insulation materials. The market prospects for the insulation segments are also discussed. A detailed description of the different processing routes used to produce insulating AAMs is presented to introduce the reader to the historical analysis later performed. Based on the findings of such analysis, the most promising processing routes were identified, and several porous and lightweight IPs were produced. The overall performance of the developed materials was examined and framed under the requirements of EU construction codes.

The data set, the discussions, and conclusions made throughout Chapter 4 have not been published and are firstly presented here.

4.1 Introduction

The public requirement for less energy-intensive buildings has been vastly supported by regulatory authorities that gradually enforced legislation that promotes near-zero energy buildings (NZEB). In this scope, O'Grady *et al.* (2017) highlighted the need for proper thermal insulation by reporting that about 75% of EU buildings are energy inefficient and attributing critical importance to the thermal performance to the buildings' envelopes. Increase the thermal insulation of buildings can be achieved by incorporating into building elements phase change or low conductive materials (insulating foams) or by using lightweight cement-like materials with tailored thermal insulation properties. To this date, employing polymer foams (e.g., polystyrene and polyethylene) and mineral wools (glass and rock wools) remain the most widely spread construction technique to increase buildings' thermal performance. Table 4.1.1 shows the typical thermophysical properties of conventional insulating materials (Vaou, 2010). Despite their excellent properties, the production, use, and post-life of polymer foams and mineral wools present significant challenges. The use of polymer foams poses substantial public health and environmental risks. The formaldehyde and furfuryl alcohols present in their chemical composition are suspected to be toxic and even carcinogenic for humans (Mazzon, 2015), and the carbon dioxide or hydrochlorofluorocarbons used in their production have considerable effects on ozone depletion and global warming (Papadopoulos, 2005). Also, polymer foams present poor fire resistance and release toxic fumes when exposed to high temperatures. On the other hand, mineral wools are non-combustible and can endure temperatures up to circa 750 °C. Their corrosive-resistant nature, the large variety of products available with different densities, and their easy installation make mineral wools attractive for various fields of application. However, mineral wools can cause severe skin irritation problems, and their insulation performance is considerably affected by humidity levels. The production of mineral wools also requires energy-intensive processes, and similarly to polymer foams, after-life recycling solutions are still scarce.

Table 4.1.1 Typical thermophysical properties of conventional insulating materials (Vaou *et al.,*2010).

Material	Apparent density (kg/m^3)	Compressive strength (MPa)	Thermal conductivity (W/m°K)	Maximum appl. temperature (°C)	Fire Class
Extruded polystyrene	20-80	100-700	0.025-0.035	75	B1-B2
Expanded polystyrene	18-50	70-450	0.029-0.041	80	B1-B2
Glass wool	13-100	16	0.03-0.045	500	A1-A2
Rock wool	30-180	0.01-69	0.033-0.045	750	A1-A2

In this context, the development of highly performant lightweight cement-like materials has been proposed as a viable alternative method for buildings' energy conservation. The use of lightweight cementitious materials has grown in the last decades in applications such as partition walls and prefabricated elements. However, the production of ordinary Portland cement also releases significant quantities of carbon dioxide (around 0.80 to 0.85 tons of CO_2/ton cement) (Velandia, 2016), and OPC- based insulating elements also present some technical shortcomings such as poor fire resistance (Panias, 2015). In that sense, replacing OPC binders by alkali-activated materials (geopolymers and inorganic polymers) has attracted attention also for thermal insulation purposes. Their less energy-intensive production process and lower associated greenhouse gas emissions can be seen by manufacturers as an adequate response to the current market demand for eco-friendlier and energy-efficient insulating materials.

Furthermore, the possibility of using industrial wastes in the production of lightweight inorganic polymers can represent an important valorization route for internally produced wastes and/or facilitate synergetic interactions with proxy industries. Replacing the use of prime raw materials (e.g., cement, gravel, sand) by internally or locally available low-value industrial wastes (e.g., by-pass dust, fly ash from MSW incineration) can significantly reduce manufacturing costs with the added benefit of allowing tighter control of supply chains. At this point, it is fair to acknowledge that other innovative insulating technologies are being developed in parallel. Aerogels and vacuum insulating panels (Baetens, 2010; 2011) are known to present attractive thermal insulation features, but their mainstream production and application in the construction sector still face considerable technical and economic constraints.

Conversely, several studies have demonstrated that lightweight IPs can present several of the properties required for industrial production of insulation materials. Excellent chemical and thermal stability (Cartwright, 2014; Van Deventer, 2007), good nailing ability (Duan, 2016), low permeability (Van Deventer, 2007) and thermal conductivity (Vaou, 2010), and reasonable mechanical proprieties have been reported in the literature.

Despite these promising results, the performance of lightweight IPs largely dependents on a multitude of compositional and processing factors. The need for extensive comprehension of each supply stream and production process justifies the continuous growth of research in this field, Figure 4.1.1a.

As can be seen in Figure 4.1.1b, several methods have been investigated to produce lightweight IPs. According to Bai *et al.* (2018), processing methods can be divided into five main categories: direct foaming (DF), replica method (RM), sacrificial filler method (SFM), additive manufacturing (AM) and other methods (OM). In the following section, these methods will be discussed with particular emphasis on direct foaming method. Direct foaming is commonly used to produce lightweight IPs and is considered one of the most mature processing routes for large scale production.

This work was focused on the development of thermal insulating materials, but porous and lightweight IPs have shown promising features in other fields of application. Future applications for the developed CaO-FeO_x-Al_2O_3-SiO_2O porous and lightweight IPs may include wastewater decontamination (Novais, 2018a; Hertel, 2019), pH regulation (Novais, 2019; Ascensão, 2017), membrane and membrane supports (Okada, 2011; Ge, 2015), catalysts, catalyst supports and scaffolds (Papa, 2015), high-temperature processes and acoustic insulation (Zhang, 2015).

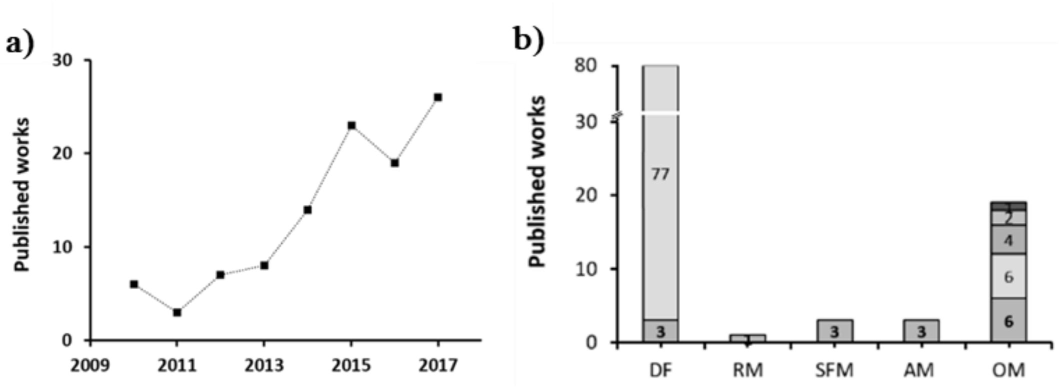

Figure 4.1.1 Works published on porous inorganic polymers: a) with porosity superior of 50 vol% or bulk density inferior to 0.7 g/cm^3, b) divided according to the processing method employed. In b) DF stands for direct foaming and comprise 3 papers on phosphate-based IPs; RM stands for replica method; SFM for sacrificial filler method; AM for additive manufacturing; and OM stands for others methods comprising 1 paper on templating and surface interaction, 2 papers on phosphate-based IPs, 4 papers using porous spheres or granules, 6 papers on reactive emulsion templating and 6 papers where no blowing agent was used. Data collected from Bai *et al.*, 2018.

4.2 Processing routes in lightweight AAMs

Direct foaming

Direct foaming is the most common method to produce lightweight materials. Like in many cement-based lightweight materials, porous IPs structures can be produced by incorporating gaseous phases during the pastes' plastic state. Numerous direct foaming routes are described in the literature, but they can be generally divided into two major groups depending on whether the gaseous phases are generated in-situ (using blowing agents) or are entrapped from the surrounding atmosphere (using air-entraining agents).

Mechanical frothing can be realized either by introducing air-entraining agents into the mix or by using pre-foaming methods. In pre-foaming methods, foam generators or tanks are used to produce the foam separately, being later gently homogenized with the polymeric pastes (Zhang, 2015; Hajimohammadi, 2018). Despite the differences between these two approaches, they both aim to incorporate large volumes of air into the structure of fresh IP pastes.

Conversely, the in-situ generation of gaseous phases is achieved by adding chemical or physical blowing agents. Physical blowing agents promote the formation of porous structures due to phase transitions (e.g., liquid sublimation), but the complex production methods involved rend this technique of no practical interest for conventional construction materials and therefore was not considered for this work. On the other hand, chemical blowing agents promote chemical reactions in which one of the reaction products is a gaseous phase (typically O_2 and H_2, but also others such as ammonia and sulfur dioxide (Bumanis, 2017)). Chemical blowing agents frequently reported in the literature include hydrogen peroxide (Novais, 2016a-c; Hajimohammadi, 2017a), aluminum (Ascensão, 2017; Novais, 2018b) and silicon powders (Medri, 2013), silica fume (Papa, 2016), silicon carbide (Prud'homme, 2015), sodium hypochlorite (Böke, 2015), aluminum nitrate and iron sulphite (Bumanis, 2017) and sodium perborate (Abdollahnejad, 2015).

The chemical reactions undergone by different blowing agents in alkaline mediums were vastly investigated and were summarized by Bai *et al.* (2018):

$$2H_2O_2 \rightarrow 2H_2O + O_2\,(g) \tag{4.2.1}$$

$$2Al + 2mOH + 2H_2O \rightarrow 2mAlO_2 + 3H_2(g) \tag{4.2.2}$$

$$Si + 2mOH + H_2O \rightarrow m_2SiO_3 + 2H_2(g) \tag{4.2.3}$$

$$2NaOCl \rightarrow 2NaCl + O_2\,(g) \tag{4.2.4}$$

$$AlN + mOH + 2H_2O \rightarrow mAlO_2 + NH_3\,(g) \tag{4.2.5}$$

$$4NaBO_3 + H_2O \rightarrow 2NaOH + Na_2B_4O_7 + 2O_2\,(g) \tag{4.2.6}$$

Where m stands for potassium or sodium according to the activation solution used.

From the above-mentioned blowing agents, hydrogen peroxide and aluminum powder are the most extensively investigated in the literature, and his simple application method has shown the ability to provide porous IPs with good insulation properties.

Novais *et al.* (2016a-c) investigated the use of hydrogen peroxide to produce waste glass and biomass fly ash-based alkali-activated materials. In their works, no stabilizing agents were used, and clear correlations were found between the hydrogen peroxide content and the volume, area, number, and shape of the pores formed, Figure 4.2.1. Increase the amount of blowing agent rose the relative amount of large pores and resulted in lower apparent densities, compressive strength, and thermal conductivities. In general, no significant mineralogical changes occurred when hydrogen peroxide was introduced but some modifications on the reaction kinetics and pastes' rheology were observed (Novais, 2016c). As the content of hydrogen peroxide increased, yield stress was reduced, and setting times extended. Exothermic peaks associated with polymerization reactions have shown lower intensity and occurred slightly sooner. Nonetheless, by adequately selecting the blowing agent dosage, activating solution, solid-to-liquid ratio, and curing conditions, self-bearing materials were produced with total porosities as high as 81 % and density and thermal conductivity as low as 440 kg/m^3 and 0.08 W/m°K, respectively, Figure 4.2.1. A summarized description of the results gathered in these works is provided in Table 4.2.1.

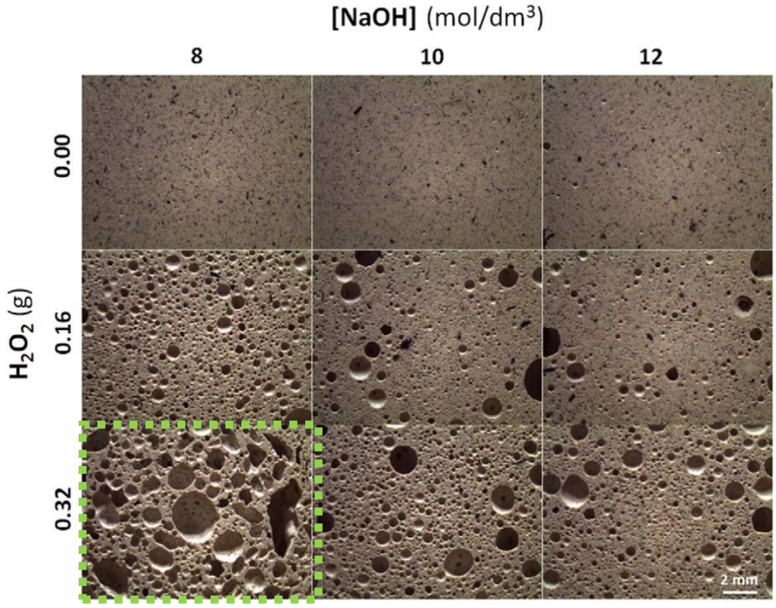

Figure 4.2.1 Optical images of biomass fly-ash based porous inorganic polymers produced with different hydrogen peroxide dosages and sodium hydroxide solutions of different molarity. Dashed lines identify the samples with better insulation performance (adapted from Novais *et al.,* 2016c)

The use of aluminum powder as a blowing agent has also become increasingly popular in the development of porous AAMs. Romagnoli *et al.* (2015) investigated the effect of rheological properties on the chemical foaming of MK-based alkali-activated materials. The pastes viscosity was shown to control gas generation and pores' coalescence and evolution, leading higher viscosities to enhanced levels of porosity. The rheological properties of alkali activated pastes can be engineered by controlling several processing parameters such as - among others- solid-to-liquid ratio or K_2O/SiO_2 molar ratio, or by modifying curing regimes (Henon, 2012; Novais, 2016b), foaming agents and dosages, or adding surfactants and thickening agents (Hajimohammadi, 2018). Henon *et al.* (2012) investigated the effects of curing parameters (e.g., temperature, thermal cycle) to modify the viscosity of pastes and control the foaming process and morphology of the porous formed. They have concluded that increasing temperature led to faster foaming processes and raised the total volume of pores. In addition, two-step temperature cycles had shown to be able to control the pore size distribution and form more homogeneous pore structures. Novais *et al.* (2016b) also evaluated the effects of the initial curing temperature on the properties of waste-containing foams. The results of their work shown that polymerization reactions are accelerated and intensified when the temperature rises while the incorporation of aluminum powder further contributed to reducing the setting time of foamed pastes. The characteristics of the porous structures were mainly controlled by the aluminum powder dosage and solid-to-liquid ratio. Solid-to-liquid ratio, meaning the viscosity of the pastes, was considered the prevailing factor affecting the connectivity between pores. By properly controlling the combined effects of curing temperature, solid-to-liquid ratio, and aluminum powder dosage, lightweight (430 kg/m^3) IPs with low thermal conductivity (0.78 W/m°K) were produced.

Nonetheless, the development of porous AAMs has been primarily focused on systems where metakaolin and fly ash are used as major precursors (see Table 4.2.1). More recently, Ascensão *et al.* (2017), Hertel *et al.* (2019), Denissen *et al.* (2019) and others started to explore the possibility of using of Fe-rich precursors to produce foamed IPs. Ascensão *et al.* (2017) and Hertel *et al.* (2019) used bauxite residues to produce porous IPs for pH regulation and water decontamination purposes. Despite the different scope of application, valuable insights on the foaming process and porous structures formed can be taken from these works. In both studies, increasing the aluminum powder dosage and lowering the solid load in the mix design decreased the bulk density and mechanical performance of the foamed materials. Self-bearing capacity ($\approx$1 MPa in compressive strength) and porosity levels that exceeded 80% were reported. However, it is interesting to notice that in these works very distinct solid loads were used, and surfactants were not strictly necessary to produce highly porous materials. The differences in the chemical composition of the precursors and processing parameters used should not be neglected when analyzing these results but these works had shown that Fe-rich IPs with proper porous structures can be produced using different methods to control the pastes' rheological features.

Denissen *et al.* (2019) investigated the factors influencing the synthesis of fayalite-based foamed IPs. They have confirmed the observations of Henon *et al.* (2012) that suggested that the effects of slightly elevated temperatures in in-situ foaming processes are not altered by the presence of iron species. Furthermore, it was reported that chemical foaming is a time-dependent process in which the moment of the addition of the foaming agent can have a significant impact on the homogeneity of the pore structures formed. Postponing the addition of aluminum powder up to 30 minutes after mixing was recommend, but such may be only required if proper rheological conditions are not reached before.

As can be concluded from the results described, the production of porous IPs using in-situ foaming methods depends on a delicate balance between the rheological proprieties of the pastes, polycondensation reactions, and the formation of gaseous phases. The reaction of metallic elements must be prompted before the structure gains considerable rigidity, but the pastes should have enough viscosity to guarantee the enclosure of the gaseous phases formed. The characteristic of the porous structure (pore volume, pore size distribution, and connectivity) will be determined by such kinetic balances, which in turn, will dictate the insulation properties of the produced IPs.

Moreover, blowing agents will also have an impact on polymerization reactions and chemical assemblage of the products formed. Hajimohammadi *et al.* (2017b) investigated the effects of aluminum powder on the phase evolution of fly-ash AAMs and found that increasing the availability of Al species induces significant differences during the gel network development. The ready availability of Al species at very early ages changes the driving force for polymerization as the preferential dissolution of Al species from fly-ash particles would no longer occur. The reduction of Al dissolution from fly-ash results in more Si-rich gels at early ages and the characteristic induction period became inexistent. However, the precipitation of aluminum hydroxide gels on the surfaces of fly-ash particles conceals their dissolution which delays strength development. It was later observed that the gelation of aluminum hydroxide particles and their polymerization released sodium hydroxide back to the pore solution. The gelation of such reaction products and the higher availability of cationic species can explain the slight enhancement of the mechanical performance of Al-containing samples over time. In addition, it was confirmed the higher amount of water consumed in Al-containing samples (being in line with equation 4.2.2), which might have further contributed to strength development at later ages. It should be mentioned that in this work Al-containing samples were introduced in a vacuum chamber after mixing to remove the gaseous phases formed and provide a reliable comparison between the mechanical features without accounting porosity effects. As the gaseous products formed were removed and the mechanical strength of binder itself remained on a similar or even slightly superior level, one can conclude that the differences imposed by metallic aluminum on reaction kinetics and products formed do not dictate a reduction in the mechanical strength of the binder.

Lastly, Papa *et al.* (2016) used the oxidation of metal silicon impurities present in the silica fume (0.7 wt% of free Si^0) to produce alkali-activated foams. The reactivity of silicon impurities towards different alkaline mediums was investigated, and significant differences in total pore volume, accessible porosity, and pore size distribution were reported. When silica fume was single-used as a precursor, potassium-based solutions were found to promote higher levels of porosity (85 vol%) and more homogeneous porous structures that contained larger amounts of macropores. Reducing the thickness of the interpore walls improved the insulating properties, having those samples the lowest thermal conductivity values of 0.12 W/m°K. It is particularly relevant to highlight the work of Papa *et al.* (2016) here since throughout this work silica fume was used as an admixture to provide a secondary source of Si species. Carefully selection was undertaken to ensure that highly pure silica fume was employed to not intermingle the effects of the foaming methods applied with hydrogen production due to silica fume decomposition. During the development of non-porous binders, no significant porosities were observed further confirming the reduced quantity of free Si^0 present in the chemical composition of the silica fume used.

It should be noticed that mechanical frosting and chemical foaming routes are not mutually exclusive and can be coupled. In fact, in-situ generated gas bubbles tend to coalescence and suffer from drainage and Ostwald ripening processes. The combination of these effects produces poorly distributed pore sizes, and surfactants are frequently employed as stabilizing agents to control the pore accessibility and to achieve more regular pores size distributions (Bai, 2018; Denissen, 2019). The amphiphilic character of surfactants allows them to be absorbed in the gaseous-liquid surface and diminish the bubbles’ tendency to coalesce while minimizing Ostwald ripening effects.

Table 4.2.1 List of porous alkali activated materials produced by direct foaming method.

Precursors	**Blowing agent**	**Blowing agent dosage**	**Stabilizing agents**	**Stabilizing agents' dosage**	**Density (g/cm^3)**	**Compressive strength (MPa)**	**Thermal conductivity (W/m°K)**	**Ref.**
WG/MK	H_2O_2	0.03-0.60	-	-	0.82-1.26	2.9-11.2	-	Novais, 2016b
Bio-FA/MK	H_2O_2	0.03-1.20	-	-	0.56-1.20	1.2-9.0	0.11-0.43	Novais, 2016a
Bio-FA/MK	H_2O_2	0.16-0.32	-	-	0.44-0.72	0.3-2.5	0.08-0.14	Novais, 2016c
Bio-FA/MK	Al	0.02-0.08	SDS	0.05	0.43-0.85	0.6-4.0	0.08-0.17	Novais, 2018b
RM/MK	Al	0.03-0.10	-	-	0.47-0.86	0.7-5.8	-	Ascensão, 2017
WG/SPW/ARSW/MK	$Al+AIN+FeSO_3$	Not specify	-	-	0.38-0.47	1.1-2.0	0.14-0.15	Dembovska, 2017
FA	Al	0.05	Polypropylene fib.	0.025	0.89-0.92	5.5-10.9	0.21-0.39	Rickard, 2014
FA	H_2O_2	0.5-1.5	SDS	0.1-4.0	0.58-1.34	2.6-12.2	-	Korat, 2017
MK	H_2O_2	0.05-0.13	Protein	0.03-0.05	0.47-0.80	2.1-11.2	-	Bai, 2018
MK	SiC	0.65-5.21	-	-	0.27-0.40	-	0.08-0.12	Pru'homme, 2015
FA	Al	0.01-0.03	Fatty acid, amide and sodium salt of sulphonic acid sol.	1.00	0.73-0.74	≈ 2.0		Masi, 2014
FA	H_2O_2	0.10-0.30		1.00	0.72-0.94	1.7-4.6		Masi, 2014
MK	H_2O_2	2.0	Not specify	0.05	0.45-0.65	-	0.15-0.19	Hajimohammadi, 2017b
MK	Si	0.03-0.24	DMS or Epojet®	10	0.25-0.86	0.7-11.0	0.10-0.11	Roviello, 2017
FA	Al	0.07-0.20	Not specify	-	0.73-0.74	3.3-3.7	-	Ducman, 2016
FA	H_2O_2	0.5-2.0	Not specify	-	0.66-1.00	3.7-9.3	-	Ducman, 2016
FA/MK	H_2O_2	1.0-2.0	Not specify	0.03-0.05	0.23-0.45	0.1-1.2	0.07-0.11	Samson, 2018
Modified RM	Al	0.10-0.30	Sodium oleate	0.03	0.38-0.75	1.1-2.8	-	Hertel, 2019
Fayalite-Slag	Al	0.2	SB-2 Sika	≈0.02	0.57-0.83	0.7-2.0	-	Denissen, 2019

* WG = waste glass; MK = metakaolin; Bio-FA = biomass fly-ah; RM = red mud; SPW = Steel-plat wast; ARSW = Aluminum scrap rcycling waste; FA = Fly ash; H_2O_2 = hydrogen peroxide; Al = aluminum powder; SF = silica fume; SDS = sodium dodecyl sulfate; DMS = dimethylsiloxane.

Replica method

Polymeric templates are often used in the sintering of ceramic foams. Ceramic pastes are impregnated into templates that act as confinement structures during the pastes' plastic state. Sintering at high temperatures degrades the templates and leaves behind a finished product with a well-defined structure. The low cost and versatility of this method had made it popular in the ceramic industry, as it allows to control the porous structure by merely using templates with adequate levels of porosity and desirable pore size distribution.

A similar rationale was followed by Kovářík *et al.* (2017), who used a mixture of calcined kaolin, clay, precipitated silica and chamotte to produce IP binders. Polyurethane templates were impregnated with the IP binder and sintered at different temperatures ranging between1100-1300 °C, and the produced porous materials presented good dimensional stability upon sintering (dimension shrinkage < 8%), a maximum open porosity of 88 vol% and compressive strength up to 0.9 MPa. The schematic representation of this replica template process is provided by Kovářík *et al.* (2017) and reproduced here in Figure 4.2.2.

By definition, alkali activated materials are produced without sintering, and the materials produced are better classified as glass-ceramics. However, the use of alkali activation principles was employed to produce the green material which justifies its inclusion in this section.

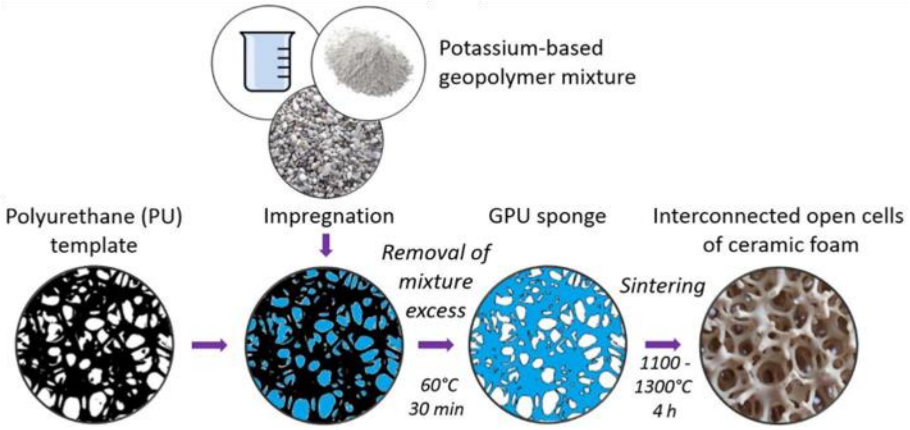

Figure 4.2.2 Schematic representation of the replica method used to produce porous inorganic polymers (reproduced from Kovářík *et al.*, 2017).

Sacrificial filler method

The sacrificial filler method can be seen as an inverted version of the replica method. In this processing route, sacrificial templates are surrounded by ceramic or inorganic pastes and let consolidate at near room temperatures. The sacrificial templates are later removed by a thermal or chemical process, and a negative replica of the template structure is obtained. Franchin *et al.* (2015) used a metakaolin and fly-ash to produce porous lattice structures. Polylactic acid (PLA) filaments were used to 3D printing sacrificial templates later removed in a three-step process. The biphasic product was firstly immersed in an alkaline solution to promote the partial degradation of PLA templates. PLA was then extracted using hot water and the remaining porous structures were thermally treated for 24 h at 330 °C. The final lattices presented total porosity up to 77 vol% while in the struts itself total porosity was circa 47 vol%. These results have shown that sacrificial methods can be successfully employed to produce lightweight IPs, but this rather complex production method may compromise its applicability in real-size construction elements. A simpler alternative sacrificial method was proposed by Papa *et al.* (2015). In their work, porous hierarchical AAMs were produced by ice-templating. Metakaolin and potassium silicate solutions were used to produce the starting pastes to which after a consolation period a surplus of water was added. When subjected to sublimation under reduced pressure, ice crystals were formed in the aqueous solution acting as sacrificial templates. In this case, the removal of the sacrificial template was simply done by thawing and drying. The products formed presented a lamellar porous structure corresponding to the freezing direction and total porosities up to 83 vol%. Furthermore, this technique allows for easy control of the porosity levels solely by modifying the content of added water.

Additive manufacturing

Applying additive manufacturing principles (AM) to produce inorganic polymers is expected to expand the technical frontiers of alkaline activation technology while further reducing its production cost and environmental impacts. Similarly to cementitious materials, raising the level of automation incorporated in IPs production will allow to build structures of complex geometry without traditional casting methods and with precise control of the structures formed. Among AM technologies, powder-based three-dimensional printing (3DP) and direct ink writing (DIW) have been employed to produce alkali-activated materials. Xia *et al.* (2016; 2018) investigated the effect of several parameters on powder bed printability of slag-based AAMs. Parameters such as bed particle size distribution, surface quality, density, droplet penetration, and binder saturation level were monitored and correlated to the printing accuracy and strength development of printed bodies. The printed AAMs presented limited compressive strength, although enough to endure de-powdering and post-processing treatments. Simple post-processing methods, consisting of immersing green samples in silicate, metasilicate, or fly ash solutions, were able to increase the mechanical performance more than 1000%, being the highest compressive strength reported 30 MPa. The superior compressive strength of post-processed samples was attributed to continuous polymerization in the presence of alkaline solutions that promoted an increase of the binding phases formed, hence reinforcing the bonds between powder particles. Pre- and post-processed bodies presented some anisotropic features showing higher dimensional accuracy and mechanical strength along with the axis correspondent to the jetting direction. However, all the printed AAMs were highly porous structures with porosity levels up to circa 60 vol%.

Instead of 3DP, AAMs can also be printed using direct ink writing techniques (DIW). The main constraints to implementing DIW in the manufacturing of alkali-activated products concern the proper control of rheological properties. The rheology should be tailored to provide good pumpability and sufficiently long printing times while simultaneously guarantee minimal shrinkage and deformation of unsupported struts. In this sense, Beersaerts *et al.* (2019a) engineered the rheological properties of Fe-rich AAMs towards direct ink writing. Fine sand, silica fume, and attapulgite were added to a reference Fe-rich paste, and a printable IP was obtained. The pastes' rheological properties were found to be determined by the degree of crosslink of silicate networks (Beersaerts, 2019b). Flow behavior was severely affected by colloidal concertation which could be controlled by modifying the solid load, the SiO_2/Na_2O molar ratio, and H_2O content. The yields stress increased as SiO_2/Na_2O rose due to the promotion of stronger physically bonded colloids but the rheological behavior of all Fe-rich pastes could be fitted with a Herschel-Bulkley model. Franchin *et al.* (2017) used DIW to produce metakaolin and fly ash-based porous lattices. The produced bodies present a high level of porosity varying from 50 to 71 vol%. The microstructural analysis did not reveal any significant cracks or defects in the struts and reasonable compressive strength values were obtained, ranging from 2 to 12MPa.

It should be highlighted that the printed AAMs cannot be classified as porous or lightweight materials since they typically presented low porosity levels and densities above 1000 kg/m^3. However, additive manufacturing techniques offer the possibility of design complex structures that can be potentially used to produce building elements with geometries that confer them reduced weight and desirable thermal properties (e.g., lattices, honeycombs).

Additionally, further manipulation of the mix design can enhance the thermal insulating features of printed IPs. This concept is illustrated in the work of Zhong *et al.* (2017), who used graphene oxide to 3D print porous and conductive polymeric structures. Within the scope of thermal insulating materials, the addition of hollow glass spheres, cenospheres, porous AAMs, or other small size porous materials can further reduce the density and thermal conductivity of printed AAMs.

Other methods

Even when no pore-forming agents are used, AAMs typically present some micro and mesopores. These pores are generated during network formation, and their size, volume and amount are intrinsically correlated to compositional factors. Following this rationale, Ge *et al.* (2015) tried to augment the intrinsic porosity of AAMs by properly engineering the mixture design. They found that when providing $SiO_2/Al_2O3 = 2.96$, $Na_2O/Al_2O_3 = 0.8$ and $H_2O/Na_2O = 19$ molar ratios, samples with total porosity higher than 60 vol% can be produced without using pore-forming agents. The produced samples presented pores ranging from 10 and 1000 nm and compressive strength higher than 18 MPa.

Another strategy that has been proposed to produce porous AAMs includes the in-situ formation of surfactants by saponification routes (Medpelli, 2014; Cilla, 2014). Vegetable oils underwent saponification in highly alkali environments generating carboxylate surfactants, glycerides, and water-soluble molecules of glycerol. Once the polymeric structure is consolidated, glycerol molecules can be extracted using warm water leaving behind a highly porous structure, Figure 4.2.3. The work of Cilla *et al.* (2014) compared the physical properties of foamed AAMs produced by different processing routes (in-situ hydrogen formation, saponification, and combining the latter). By combining in situ saponification and hydrogen formation, samples with total porosity higher than 80 vol% and compressive strength of 0.5 MPa were produced. A more detailed analysis of the pore structure revealed well-connected open pores (open porosity ~70 vol%) with small average cell size and high specific surface area. The features of these porous structures can be particularly attractive in applications where high permeability and specific surface area are required (e.g. water decontamination).

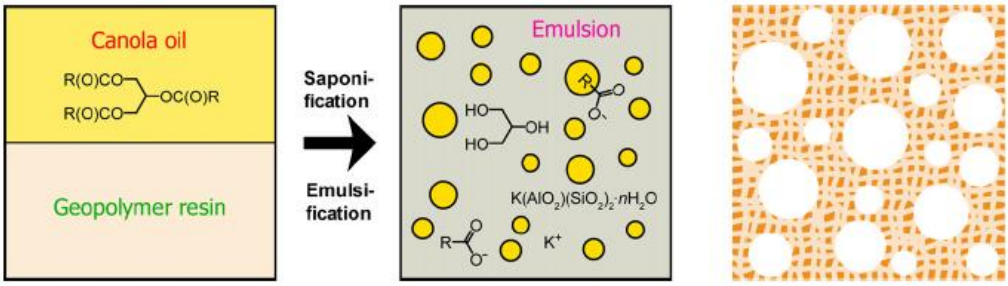

Figure 4.2.3 Schematic representation of emulsion templating method used to produce inorganic polymers (reproduced from Medpelli *et al.,* 2014).

Another approach frequently taken to develop insulation elements based on AAMs is to combine a dense polymeric matrix with lightweight aggregates. These lightweight materials can be either previously produced porous AAMs or other abundant lightweight materials such as perlite (Vaou, 2010), vermiculite (Medri, 2015), expanded glass aggregates (Palmero, 2015; Huiskes, 2016), extruded or expanded polystyrene (Colangelo, 2018; Kakali, 2018), cork granules (Roper, 2017; Novais, 2019), rubber scraps (Wang, 2019). A similar principle can be employed even at a smaller scale using hollow glass microspheres or cenospheres (Nematollhi, 2017; Lu, 2019; Hajimohammadi, 2019).

4.3 Market analysis and prospects

The use of thermal insulating components in building aims to reduce indoor thermals fluctuations without the extensive use of heat and cooling systems. Proper levels of thermal comfort are passively guaranteed, and the higher initial investments are compensated by a significant reduction of operative costs. Additionally, the need to reduce greenhouse emissions in the industrial, residential, and non-residential sectors led to the enforcement of mandatory energy efficiency requirements into recent retrofitting and construction codes, further driving the growth on the insulating market. Hence, the global market for thermal insulating materials is estimated to continue to grow with a projected compound annual growth rate (CAGR) of 3.65% between 2017 and 2022, nearly reaching 29.62 billion US dollars by 2022 (Markets and markets, 2017). The non-residential segment is projected to be the fasted growing market segment until 2020. In Europe and North America, the growth of the non-residential sector is expected to be driven by real estate investments and manufacturing activities, while in Asia-Pacific health and social care buildings assume a more relevant role. Nevertheless, the residential segment accounts for the largest market share, and some regional growth is expected in North America, Western Europe, and Asia-Pacific regions (Transparency Market Research, 2017).

By type of product used, clear regional distinctions can be made. Polymer foams such as polystyrene, polyurethane, and phenolic foams are widely used in the Asia-Pacific region, while the European and US markets are dominated by mineral wool products (Markets and markets, 2017). Polystyrene foams and glass wools dominate the global building insulation market, either in terms of value and volume, due to their thermal properties, versatility, low cost, and wide range of available commercial products. The thermal insulation market of polymer foams and mineral wools is mature and well-consolidated. The most relevant players operating in this segment include BASF SE, Saint-Gobain S.A., Knauf Insulation, Inc., Rockwool International, Johns Manville Corporation, Owens Corning, Paroc Group Oy, GAF Materials Corporation, Kingspan Group, and Beijing New Building Material, Ltd.

As previously mentioned, both polymer foams and mineral wools present some technical shortcomings and pose significant public health and environmental risks. Major industrial players had recognized this criticality and are adopting growing strategies base on the acquisition and development of innovative insulating building materials to expand their product portfolio.

From the perspective of cement and concrete manufactures, the technical shortcomings of polymer foams and mineral wools can represent a competitive advantage, and the lightweight concrete segment has been identified as a priority. Similarly to polymer foams and mineral wools, the lightweight concrete market continuous to growth globally driven by stringent construction codes and the increasing demand for energy-efficient materials. The interest of the construction sector in stimulating demand can be seen by the growing number of patents and technical publications on lightweight and ultra-lightweight concrete, which illustrates the increasing dispute of this market segment.

Lightweight concrete is typically characterized by good energetic efficiency parameters such as density lower than 2000 kg/m^3 and thermal conductivities ranging from 0.2 to 1.0 W/m°K (ACI committee, 2003). Traditional lightweight elements increase the buildings' thermal performances but present non-structural features. Despite the efforts made to satisfy both thermal and structural requirements, commercial solutions that combine good insulation and structural characteristics are still scarce to this date.

In the insulation segment, the production of lightweight concrete can envision different purposes and can be classified into two main categories: lightweight aggregates and aerated concretes. In the scope of this work, the production of lightweight aggregates was not foreseen and therefore, the analysis of this market segment is not provided. Aerated concretes can be divided according to their production method as foamed or autoclaved aerated concrete. The global market of foamed concrete is estimated to grow with a projected CAGR of 5.9%, reaching 430 Million US dollars by 2022 (Markets and markets, 2017). The foamed concrete market is projected to grow faster in the building segment and consolidate its position in the infrastructure sector. The global market for autoclaved aerated concrete is estimated to continue to grow with an expected CAGR of 7.3% and surpassing the 10 billion US dollars by 2024 (Transparency Market Research).

By type of product, autoclaved aerated concrete blocks dominated the global market in 2015, accounting for around half of the market size in terms of revenue. During the forecasted period, this market segment is estimated to continue to grow with a CAGR of 7.8%. This growth can be primary justified by the enforcement of environment protection amendments and rules that are severely detrimental to the main competitors in this segment (e.g., traditional red bricks).

Region-wise, Europe presented the highest share of the aerated concrete market in 2015, representing 34% in terms of revenue. Europe's' hegemony in this market segment is attributed to wide acceptance of lightweight concretes in the region and to the highly competitive environment with the presence of a large number of manufacturers (Transparency Market Research). The European market will continue to dominate the global market in terms of revenue, but considerable regional growth is expected in the Asia Pacific region (8.2% CAGR). In developing economies such as China and India the establishment of significant markets is not expected due to the highly cost-sensitive nature of consumers in these regions.

Globally the most relevant players operating in the production of lightweight concrete include Xella Group, H+H International, SOLBET, ACICO, AERCON AAC, UltraTech Cement Ltd., Biltech Building Elements Limited, AKG Gazbeton, Eastland Building Materials Co., Ltd. Brickwell and UAL Industries Ltd.

In this very competitive environment introducing new insulation materials can represent a significant competitive advantage and disrupt the market in favor of more innovative players. In such a context, lightweight IPs can be seen as promising candidates as they can be produced with tailored porous microstructures to guarantee low thermal conductivity values, and their chemical structure can provide enhanced high-temperature resistance (even compared to OPC concrete). The admission of lightweight IPs in this market segment might not be exclusively dictated by technical requirements since the possibility up-stream significant volumes of low-grade materials may result in reduced production costs and confers to lightweight IPs an eco-friendly character that meets the current market demands. The development of insulating materials that can be produced from low-grade or waste materials and withstand high-temperature exposure can close the existing markets loopholes and represent a significant commercial advantage in this market segment. Despite the latter, the building industry is known to be a conservative and the competition with well-established insulation products might be hampered by the absence of standardized certification protocols and customers' long-term experience with alkali-activated products.

References

Abdollahnejad, Z., Pacheco-Torgal, F., Félix, T., Tahri, W., & Aguiar, J. B. (2015). Mix design, properties and cost analysis of fly ash-based geopolymer foam. *Construction and Building Materials*, *80*, 18-30 https://doi.org/10.1016/j.conbuildmat.2015.01.063

ACI Committee 213. Guide for structural lightweight-aggregate, concrete; 2003.

Ascensão, G., Seabra, M. P., Aguiar, J. B., & Labrincha, J. A. (2017). Red mud-based geopolymers with tailored alkali diffusion properties and pH buffering ability. *Journal of cleaner production*, *148*, 23-30. https://doi.org/10.1016/j.jclepro.2017.01.150

Baetens, R., Jelle, B. P., & Gustavsen, A. (2011). Aerogel insulation for building applications: a state-of-the-art review. *Energy and Buildings*, *43*(4), 761-769. https://doi.org/10.1016/j.enbuild.2010.12.012

Baetens, R., Jelle, B. P., Thue, J. V., Tenpierik, M. J., Grynning, S., Uvsløkk, S., & Gustavsen, A. (2010). Vacuum insulation panels for building applications: A review and beyond. *Energy and Buildings*, *42*(2), 147-172. https://doi.org/10.1016/j.enbuild.2009.09.005

Bai, C., & Colombo, P. (2018). Processing, properties and applications of highly porous geopolymers: a review. *Ceramics International*, *44*(14), 16103-16118. https://doi.org/10.1016/j.ceramint.2018.05.219

Beersaerts, G., Pontikes, Y. (2019a). Developing A 3D printable inorganic polymer derived from a Fe-rich slag. *In Slag Valorisation Symposium: Science, Innovation & Entrepreneurship in Pursuit of a Sustainable World.* https://www.researchgate.net/profile/Glenn_Beersaerts/publication/332719156_DEVELOPING_A_3D_PRINTABLE_INORGANIC_POLYMER_DERIVED_FROM_AN_Fe-RICH_SLAG/links/5cc5ce164585156cd7b98a2c/DEVELOPING-A-3D-PRINTABLE-INORGANIC-POLYMER-DERIVED-FROM-AN-Fe-RICH-SLAG.pdf

Beersaerts, G., Vananroye, A., Sakellariou, D., Kriskova, L., Clasen, C., Pontikes, Y. (2019b). Rheology of an inorganic polymer paste derived from an Fe-rich slag. Journal cement and concrete research (article in press)

Böke, N., Birch, G. D., Nyale, S. M., & Petrik, L. F. (2015). New synthesis method for the production of coal fly ash-based foamed geopolymers. *Construction and building materials*, *75*, 189-199 https://doi.org/10.1016/j.conbuildmat.2014.07.041

Bumanis, G., Vitola, L., Bajare, D., Dembovska, L., & Pundiene, I. (2017). Impact of reactive SiO2/Al2O3 ratio in precursor on durability of porous alkali activated materials. *Ceramics International*, *43*(7), 5471-5477. https://doi.org/10.1016/j.ceramint.2017.01.060

Cartwright, C., Rajabipour, F., & Radlińska, A. (2014). Shrinkage characteristics of alkali-activated slag cements. Journal of materials in civil engineering, 27(7), B4014007. https://doi.org/10.1061/(ASCE)MT.1943-5533.0001058

Cilla, M. S., Morelli, M. R., & Colombo, P. (2014). Open cell geopolymer foams by a novel saponification/peroxide/gelcasting combined route. *Journal of the European Ceramic Society*, *34*(12), 3133-3137.https://doi.org/10.1016/j.jeurceramsoc.2014.04.001

Colangelo, F., Roviello, G., Ricciotti, L., Ferrándiz-Mas, V., Messina, F., Ferone, C., & Cheeseman, C. R. (2018). Mechanical and thermal properties of lightweight geopolymer composites. Cement and Concrete Composites, 86, 266-272. https://doi.org/10.1016/j.cemconcomp.2017.11.016

Dembovska, L., Bajare, D., Ducman, V., Korat, L., & Bumanis, G. (2017). The use of different by-products in the production of lightweight alkali activated building materials. Construction and Building Materials, 135, 315-322. https://doi.org/10.1016/j.conbuildmat.2017.01.005

Denissen, J., Kriskova, L., & Pontikes, Y. (2019). Kinetics of pore formation and resulting properties of lightweight inorganic polymers. Journal of the American Ceramic Society. https://doi.org/10.1111/jace.16301

Duan, P., Yan, C., Zhou, W., & Luo, W. (2016). Fresh properties, mechanical strength and microstructure of fly ash geopolymer paste reinforced with sawdust. *Construction and Building Materials*, *111*, 600-610. https://doi.org/10.1016/j.conbuildmat.2016.02.091

Ducman, V., & Korat, L. (2016). Characterization of geopolymer fly-ash based foams obtained with the addition of Al powder or H2O2 as foaming agents. *Materials characterization*, *113*, 207-213. https://doi.org/10.1016/j.matchar.2016.01.019

Franchin, G., & Colombo, P. (2015). Porous geopolymer components through inverse replica of 3D printed sacrificial templates. *Journal of Ceramic Science and Technology*, *6*(2), 105-111. https://doi.org/10.4416/JCST2014-00057

Franchin, G., Scanferla, P., Zeffiro, L., Elsayed, H., Baliello, A., Giacomello, G., & Colombo, P. (2017). Direct ink writing of geopolymeric inks. *Journal of the European Ceramic Society*, *37*(6), 2481-2489. https://doi.org/10.1016/j.jeurceramsoc.2017.01.030

Ge, Y., Yuan, Y., Wang, K., He, Y., & Cui, X. (2015). Preparation of geopolymer-based inorganic membrane for removing Ni2+ from wastewater. Journal of hazardous materials, 299, 711-718. https://doi.org/10.1016/j.jhazmat.2015.08.006

Global Autoclaved Aerated Concrete (AAC) Market: Rising Focus on Use of Environment-friendly Construction Materials to Drive Growth. http://www.mynewsdesk.com/in/pressreleases/global-autoclaved-aerated-concrete-aac-market-rising-focus-on-use-of-environment-friendly-construction-materials-to-drive-growth-says-tmr-164183

Hajimohammadi, A., Ngo, T., & Mendis, P. (2017b). How does aluminium foaming agent impact the geopolymer formation mechanism?. Cement and Concrete Composites, 80, 277-286. https://doi.org/10.1016/j.cemconcomp.2017.03.022

Hajimohammadi, A., Ngo, T., & Mendis, P. (2018). Enhancing the strength of pre-made foams for foam concrete applications. Cement and Concrete Composites, 87, 164-171. https://doi.org/10.1016/j.cemconcomp.2017.12.014

Hajimohammadi, A., Ngo, T., Mendis, P., Nguyen, T., Kashani, A., & van Deventer, J. S. (2017a). Pore characteristics in one-part mix geopolymers foamed by H2O2: the impact of mix design. *Materials & Design*, *130*, 381-391. https://doi.org/10.1016/j.matdes.2017.05.084

Hajimohammadi, A., Ngo, T., Provis, J. L., Kim, T., & Vongsvivut, J. (2019). High strength/density ratio in a syntactic foam made from one-part mix geopolymer and cenospheres. *Composites Part B: Engineering*, *173*, 106908. https://doi.org/10.1016/j.compositesb.2019.106908

Henon, J., Alzina, A., Absi, J., Smith, D. S., & Rossignol, S. (2012). Porosity control of cold consolidated geomaterial foam: temperature effect. *Ceramics International*, *38*(1), 77-84. https://doi.org/10.1016/j.ceramint.2011.06.040

Hertel, T., Novais, R. M., Alarcón, R. M., Labrincha, J. A., & Pontikes, Y. (2019). Use of modified bauxite residue-based porous inorganic polymer monoliths as adsorbents of methylene blue. *Journal of Cleaner Production*, *227*, 877-889. https://doi.org/10.1016/j.jclepro.2019.04.084

Huiskes, D. M. A., Keulen, A., Yu, Q. L., & Brouwers, H. J. H. (2016). Design and performance evaluation of ultra-lightweight geopolymer concrete. Materials & Design, 89, 516-526. https://doi.org/10.1016/j.matdes.2015.09.167

Kakali, G., Kioupis, D., Skaropoulou, A., & Tsivilis, S. (2018). Lightweight geopolymer composites as structural elements with improved insulation capacity. In *MATEC Web of Conferences* (Vol. 149, p. 01042). EDP Sciences. https://doi.org/10.1051/matecconf/201814901042

Korat, L., & Ducman, V. (2017). The influence of the stabilizing agent SDS on porosity development in alkali-activated fly-ash based foams. *Cement and Concrete Composites*, *80*, 168-174.https://doi.org/10.1016/j.cemconcomp.2017.03.010

Kovářík, T., Křenek, T., Rieger, D., Pola, M., Říha, J., Svoboda, M., & Kadlec, J. (2017). Synthesis of open-cell ceramic foam derived from geopolymer precursor via replica technique. *Materials Letters*, *209*, 497-500. https://doi.org/10.1016/j.matlet.2017.08.081

Lu, B., Qian, Y., Li, M., Weng, Y., Leong, K. F., Tan, M. J., & Qian, S. (2019). Designing spray-based 3D printable cementitious materials with fly ash cenosphere and air entraining agent. Construction and Building Materials, 211, 1073-1084. https://doi.org/10.1016/j.conbuildmat.2019.03.186

Markets and markets. [cited 2019, 18/05]; Available from: ⟨http://marketsandmarkets.com/⟩]

Masi, G., Rickard, W. D., Vickers, L., Bignozzi, M. C., & Van Riessen, A. (2014). A comparison between different foaming methods for the synthesis of light weight geopolymers. *Ceramics International*, *40*(9), 13891-13902.https://doi.org/10.1016/j.ceramint.2014.05.108

Mazzon, E., Habas-Ulloa, A., & Habas, J. P. (2015). Lightweight rigid foams from highly reactive epoxy resins derived from vegetable oil for automotive applications. European Polymer Journal, 68, 546-557. https://doi.org/10.1016/j.eurpolymj.2015.03.064

Medpelli, D., Seo, J. M., & Seo, D. K. (2014). Geopolymer with hierarchically meso-/macroporous structures from reactive emulsion templating. Journal of the American Ceramic Society, 97(1), 70-73. https://doi.org/10.1111/jace.12724

Medri, V., Papa, E., Dedecek, J., Jirglova, H., Benito, P., Vaccari, A., & Landi, E. (2013). Effect of metallic Si addition on polymerization degree of in situ foamed alkali-aluminosilicates. *Ceramics International*, *39*(7), 7657-7668. https://doi.org/10.1016/j.ceramint.2013.02.104

Medri, V., Papa, E., Mazzocchi, M., Laghi, L., Morganti, M., Francisconi, J., & Landi, E. (2015). Production and characterization of lightweight vermiculite/geopolymer-based panels. Materials & Design, 85, 266-274. https://doi.org/10.1016/j.matdes.2015.06.145

Nematollahi, B., Ranade, R., Sanjayan, J., & Ramakrishnan, S. (2017). Thermal and mechanical properties of sustainable lightweight strain hardening geopolymer composites. Archives of Civil and Mechanical Engineering, 17(1), 55-64. https://doi.org/10.1016/j.acme.2016.08.002

Novais, R. M., Ascensão, G., Buruberri, L. H., Senff, L., & Labrincha, J. A. (2016c). Influence of blowing agent on the fresh-and hardened-state properties of lightweight geopolymers. *Materials & Design*, *108*, 551-559. https://doi.org/10.1016/j.matdes.2016.07.039

Novais, R. M., Ascensão, G., Ferreira, N., Seabra, M. P., & Labrincha, J. A. (2018b). Influence of water and aluminium powder content on the properties of waste-containing geopolymer foams. *Ceramics International*, *44*(6), 6242-6249. https://doi.org/10.1016/j.ceramint.2018.01.009

Novais, R. M., Ascensão, G., Seabra, M. P., & Labrincha, J. A. (2016b). Waste glass from end-of-life fluorescent lamps as raw material in geopolymers. *Waste management*, *52*, 245-255. https://doi.org/10.1016/j.wasman.2016.04.003

Novais, R. M., Ascensão, G., Tobaldi, D. M., Seabra, M. P., & Labrincha, J. A. (2018a). Biomass fly ash geopolymer monoliths for effective methylene blue removal from wastewaters. *Journal of cleaner production*, *171*, 783-794. https://doi.org/10.1016/j.jclepro.2017.10.078

Novais, R. M., Buruberri, L. H., Ascensão, G., Seabra, M. P., & Labrincha, J. A. (2016a). Porous biomass fly ash-based geopolymers with tailored thermal conductivity. *Journal of cleaner production*, *119*, 99-107. https://doi.org/10.1016/j.jclepro.2016.01.083

Novais, R. M., Carvalheiras, J., Seabra, M. P., Pullar, R. C., & Labrincha, J. A. (2019). Red mud-based inorganic polymer spheres bulk-type adsorbents and pH regulators. *Materials Today*. https://doi.org/10.1016/j.mattod.2019.01.014

O'Grady, M., Lechowska, A. A., & Harte, A. M. (2017). Quantification of heat losses through building envelope thermal bridges influenced by wind velocity using the outdoor infrared thermography technique. *Applied energy*, *208*, 1038-1052. https://doi.org/10.1016/j.apenergy.2017.09.047

Okada, K., Isobe, T., Katsumata, K. I., Kameshima, Y., Nakajima, A., & MacKenzie, K. J. (2011). Porous ceramics mimicking nature—preparation and properties of microstructures with unidirectionally oriented pores. *Science and Technology of Advanced Materials*, *12*(6), 064701. https://doi:10.1088/1468-6996/12/6/064701

Palmero, P., Formia, A., Antonaci, P., Brini, S., & Tulliani, J. M. (2015). Geopolymer technology for application-oriented dense and lightened materials. Elaboration and characterization. Ceramics International, 41(10), 12967-12979. https://doi.org/10.1016/j.ceramint.2015.06.140

Panias, D., Balomenos, E., & Sakkas, K. (2015). The fire resistance of alkali-activated cement-based concrete binders. In F. Pacheco-Torgal, J.A. Labrincha, C. Leonelli, A. Palomo, P. Chindaprasirt, Handbook of Alkali-activated Cements, Mortars and Concretes (pp. 423-461). Woodhead Publishing. https://doi.org/10.1533/9781782422884.3.423

Papa, E., Medri, V., Benito, P., Vaccari, A., Bugani, S., Jaroszewicz, J. & Landi, E. (2015). Synthesis of porous hierarchical geopolymer monoliths by ice-templating. Microporous and Mesoporous Materials, 215, 206-214. https://doi.org/10.1016/j.micromeso.2015.05.043

Papa, E., Medri, V., Kpogbemabou, D., Morinière, V., Laumonier, J., Vaccari, A., & Rossignol, S. (2016). Porosity and insulating properties of silica-fume based foams. Energy and Buildings, 131, 223-232. https://doi.org/10.1016/j.enbuild.2016.09.031

Papadopoulos, A. M. (2005). State of the art in thermal insulation materials and aims for future developments. Energy and buildings, 37(1), 77-86. https://doi.org/10.1016/j.enbuild.2004.05.006

Prud'homme, E., Joussein, E., & Rossignol, S. (2015). Use of silicon carbide sludge to form porous alkali-activated materials for insulating application. *The European Physical Journal Special Topics*, *224*(9), 1725-1735 https://doi.org/10.1140/epjst/e2015-02494-7

Rickard, W. D., & Van Riessen, A. (2014). Performance of solid and cellular structured fly ash geopolymers exposed to a simulated fire. Cement and Concrete Composites, 48, 75-82.https://doi.org/10.1016/j.cemconcomp.2013.09.002

Romagnoli, M., Leonelli, C., Kamseu, E., & Gualtieri, M. (2015). Effect of viscosity on the geopolymer porosity. Geopolymers: The route to eliminate waste and emissions in ceramic and cement manufacturing, 71-74. ISBN 978-1-326-37732-8

Roper, D. S., Kutyla, G. P., & Kriven, W. M. (2017, January). Properties of cork particle reinforced sodium geopolymer composites. In Developments in Strategic Ceramic Materials II: A Collection of Papers Presented at the 40th International Conference on Advanced Ceramics and Composites, January 24-29, 2016, Daytona Beach, Florida (Vol. 36, No. 7, p. 79). John Wiley & Sons. https://doi.org/10.1002/9781119321811.ch8

Roviello, G., Menna, C., Tarallo, O., Ricciotti, L., Messina, F., Ferone, C., ... & Cioffi, R. (2017). Lightweight geopolymer-based hybrid materials. *Composites Part B: Engineering*, *128*, 225-237.https://doi.org/10.1016/j.compositesb.2017.07.020

Samson, G., & Cyr, M. (2018). Porous structure optimisation of flash-calcined metakaolin/fly ash geopolymer foam concrete. *European Journal of Environmental and Civil Engineering*, *22*(12), 1482-1498. https://doi.org/10.1080/19648189.2017.1304285

Van Deventer, J. S. J., Provis, J. L., Duxson, P., & Lukey, G. C. (2007). Reaction mechanisms in the geopolymeric conversion of inorganic waste to useful products. *Journal of Hazardous Materials*, *139*(3), 506-513. https://doi.org/10.1016/j.jhazmat.2006.02.044

Vaou, V., & Panias, D. (2010). Thermal insulating foamy geopolymers from perlite. *Minerals Engineering*, *23*(14), 1146-1151. https://doi.org/10.1016/j.mineng.2010.07.015

Velandia, D. F., Lynsdale, C. J., Provis, J. L., Ramirez, F., & Gomez, A. C. (2016). Evaluation of activated high volume fly ash systems using Na2SO4, lime and quicklime in mortars with high loss on ignition fly ashes. Construction and Building Materials, 128, 248-255. https://doi.org/10.1016/j.conbuildmat.2016.10.076

Wang, R., Gao, P., Tian, M., & Dai, Y. (2019). Experimental study on mechanical and waterproof performance of lightweight foamed concrete mixed with crumb rubber. Construction and Building Materials, 209, 655-664. https://doi.org/10.1016/j.conbuildmat.2019.03.157

Xia, M., Nematollahi, B., & Sanjayan, J. (2018). Influence of binder saturation level on compressive strength and dimensional accuracy of powder-based 3D printed geopolymer. In Materials Science Forum (Vol. 939, pp. 177-183). Trans Tech Publications https://doi.org/10.4028/www.scientific.net/MSF.939.177

Xia, M., & Sanjayan, J. (2016). Method of formulating geopolymer for 3D printing for construction applications. *Materials & Design*, *110*, 382-390 https://doi.org/10.1016/j.matdes.2016.07.136

Zhang, Z., Provis, J. L., Reid, A., & Wang, H. (2015). Mechanical, thermal insulation, thermal resistance and acoustic absorption properties of geopolymer foam concrete. *Cement and Concrete Composites*, *62*, 97-105. https://doi.org/10.1016/j.cemconcomp.2015.03.013

Zhong, J., Zhou, G. X., He, P. G., Yang, Z. H., & Jia, D. C. (2017). 3D printing strong and conductive geo-polymer nanocomposite structures modified by graphene oxide. Carbon, 117, 421-426. https://doi.org/10.1016/j.carbon.2017.02.102

4.4 Historical analysis of lightweight alkali-activated materials

To define the most adequate processing route to produce lightweight materials from a certain alkali-activated system, extended bibliographic reviews are usually performed to identify optimal performances in terms of a specific feature or good compromise solutions typically between thermal conductivity and mechanical properties. Direct performance-based confront is often used without resorting to any metric system. Using this kind of approach leaves room for subjective interpretation, especially when multiple features are considered. Therefore, in this work, a different approach was attempted by using PCA techniques to identify the main parameters affecting the production of lightweight alkali-activated materials and to determine the most promising processing routes. In this analysis, the distinction between geopolymers and inorganic polymers was not considered being both framed as alkali-activated materials.

A data-based was construct based on 70 scientific articles covering the period from 2010 to 2019 and comprising different processing routes that include: in-situ foaming (IS), the use air-entraining agents (EA), combining the latter (IS+EA), pre-foaming (Pre-F), combining pre- and in-situ foaming (Pre-F+IS), use lightweight materials as aggregates (LWA) and combining the use of lightweight aggregates with in-situ foaming (LWA+IS) or air-entraining agents (LWA+EA). Replica, sacrificial, and saponification routes were not considered in this database due to its high complexity that renders them of less practical interest for large-scale applications. Ice-templating was also excluded due to the still infant stage of this method that is evident by the scarce literature available. Although additive manufacturing could be used to produce lightweight construction elements, these methods were not in the scope of this work and therefore were not considered either.

The dataset was constructed based on four fundamental properties, i.e., apparent density, thermal conductivity, flexural, and compressive strength. Despite the known influence of precursors chemical composition and synthesis conditions (e.g., S/L, SiO_2/Al_2O_3, curing temperature) on AAMs' properties, such were not considered as the scope of this analysis was to independently identify general trends regarding distinct processing routes. In general, two entries were included in the dataset for each work corresponding to the lowest and highest apparent density reported, excluding dense reference samples. When apparent density was not reported, the minimum and maximum thermal conductivity or compressive strength were defined as the selection criteria. In some cases, were different processing routes were used in the same work, two entries for each processing route were considered. This decision was based on the realization that is a recurrent practice to first single-use in-situ foaming agents (IS) and air-entraining agents (EA) to study their individual effects and later combine the two (IS+EA) to achieve better insulation properties. The summarized description of the dataset is provided in Table 4.4.1.

Table 4.4.1 Dataset main characteristics.

	Min.	**1st Q.**	**Median**	**Mean**	**3st Q.**	**Max.**	**Missing data points (NA's)**
App. density (kg/m^3)	0.226	0.449	0.670	0.745	0.895	2.370	17
Flex. Strength (MPa)	0.100	0.330	0.900	2.024	2.500	12.000	127
Comp. strength (MPa)	0.060	1.100	2.100	4.589	4.000	50.000	29
Thermal cond. (W/m°K)	0.030	0.098	0.150	0.189	0.210	0.670	80

The dataset was centered and scaled, and a PCA analysis was performed considering all principal components. The percentage of explained variance rose as the number of components increased, but approximately 80 % of the variance in the dataset could be explained with two principal components (Figure 4.4.1a). Figure 4.4.1b shows the percentage of the variance of each variable explained by two principal components. As can be seen, more than 75 % of the variance of each variable can be explained solely by the first two principal components. In other words, during the conversion of the initial variables (a four-dimensional vector-space) into two PCs only 20 % of the total information was lost, never representing more than 30 % of the information of a single variable. Therefore, variables and runs could be transformed into PC1-PC2 bi-dimensional spaces (loading and score plots, respectively) without losing a significant portion of information and without significantly compromising the conclusions made thereof.

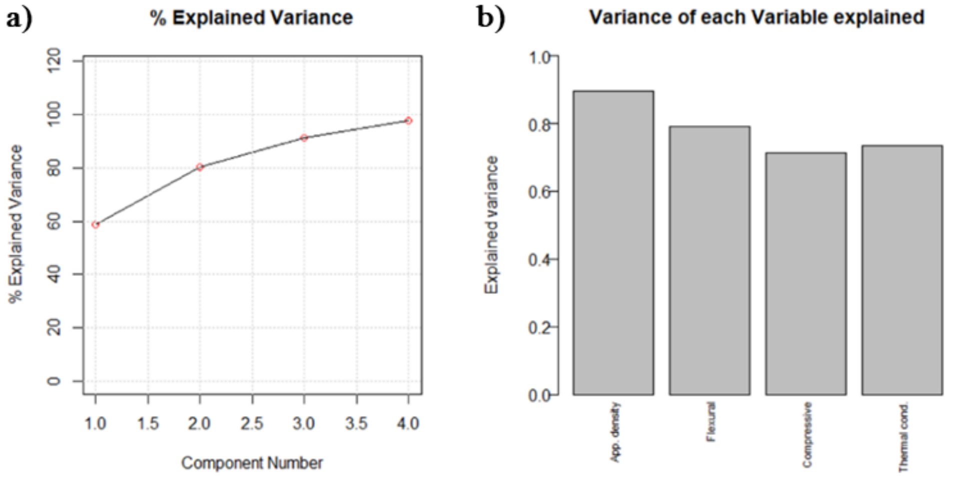

Figure 4.4.1 Cumulative explained variance according to the number of principal components (a) and variance in each variable explained by two principal components (b).

Figure 4.4.2a presents the loading plot, while Figure 4.4.2b shows the score plot according to the processing route used to produce lightweight AAMs. The loading plot shows a general correlation between strength development and thermal conductivity. All these variables are in the same quadrant indicating some degree of correlation. This means that an increase of compressive strength will most likely correspond to an increase in strength and thermal conductivity. However, one can see that flexural strength is predominately defined by PC2 while compressive strength and thermal conductivity were shown to be affected, in different magnitudes, by both PC1 and PC2. The loading vector of compressive strength was mainly defined by PC1, while PC2 assume more significant importance on thermal conductivity. Thus, as PC1 and PC2 explain different percentages of the variability in the dataset, a reduction in one of these responses will not be translated into an equal reduction of the second.

The loading vector of apparent density was shown to be also located in the positive section of the PC1 (the principal component that explains 58.8% of the variability) but in the positive section of PC2. This means that a direct correlation between apparent density and the other variables studied cannot be postulated. However, this loading plot seems to suggest that low thermal conductivity and high compressive strength can be achieved by increasing apparent density. This somehow contra intuitive result may be explained by differences in binders’ chemistries that can modify the thickness and density of interpore walls, and therefore the insulating and mechanical properties of the materials.

More interesting to observe was the influence of the different production methods in the characteristics of lightweight AAMs. The pre-foaming method was shown to provide AAMs with high compressive strength but poor insulating properties. Coupling pre-made foams with the in-situ formation of gaseous phases or lightweight aggregates was shown to reduce thermal conductivity and apparent density but resulted in poor mechanical properties. The results of single-use of lightweight aggregates have shown to be dispersed along the PC1 direction. The small coordinate in PC2 means that lightweight aggregates mainly affect compressive strength and only to a minor extent thermal conductivity, apparent density, and flexural strength. These observations do not imply that lightweight AAMs with low thermal conductivity cannot be produced using lightweight aggregates. Instead, the data in Figure 4.4.2b shows that producing AAMs with low thermal conductivity using lightweight aggregates is possible if one is willing to sacrifice mechanical performance. In fact, Novais *et al.* (2019) produced AAMs using cork granules as aggregates and reported thermal conductivity values as low as 0.07W/m°K, but in samples with compressive strength values of 0.2 MPa.

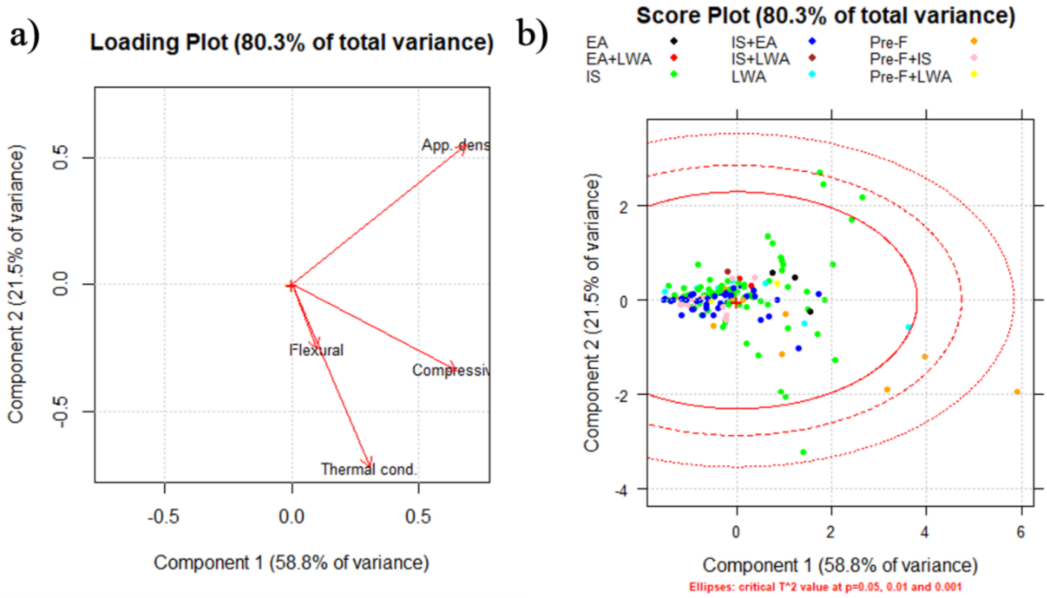

Figure 4.4.2 Loading plot (a) and score plot (b) according to the processing route used to produce lightweight AAMs.

The results from samples produced by single using air-entraining agents and combine those with lightweight aggregates are all located near the score plot origin. This means that such production methods are not adequate to produce highly performant insulating materials, but rather good comprise solutions with moderate mechanical properties and relatively high thermal conductivity. On the other hand, in-situ foaming results have shown considerable dispersion in PC2 in the positive section of PC1, but a relatively clustered and homogeneous distribution in the negative section of PC1. The vectors of apparent density and thermal conductivity are both defined in the positive section of PC1 but with significant components in PC2 that have opposite directions. As a consequence, the thermal conductivity of in-situ foamed samples can be reduced to a certain extent without necessarily reducing apparent density. On the other hand, this also implies that increasing apparent density is not necessarily translated into an increase in mechanical performance. Despite the relation between apparent density and mechanical properties been vastly described in the literature, such might not be sustained when considering the production of lightweight AAMs as an all but only valid when considering a specific mixture or processing route. In the negative section of PC1, the contribution of PC2 becomes less significant denoting a more direct correlation between the considered variables. The PC1 components of apparent density and compressive strength vectors are almost equivalent, meaning that, beyond a certain threshold, reduce AAMs apparent density also requires to diminish their compressive strength, and to a minor extent also flexural and thermal conductivity. Still, it interesting to notice that in negative section of PC1, where highly performant insulating materials are expected to be located, the PC1 vector components of compressive strength and thermal conductivity assume very different magnitudes. This realization implies that in order to reduce thermal conductivity one has to sacrifice a higher portion of compressive strength. The result from lightweight AAMs produced using in-situ foaming and air-entraining agents are mainly located in the same region of PC1, without a significant contribution of PC2. Therefore, the general trends and conclusions drawn from single using in-situ foaming agents remain valid. Nonetheless, an evident displacement of the results can be seen in the direction of the compressive strength vector. This general pattern suggests that using air-entraining agents may have a positive effect on the production of insulation materials by increasing their mechanical performance without significantly increase thermal conductivity. These observations are in line with the stabilizing effect of air-entraining agents and the formation of more regular pores size distributions reported in the literature (Bai, 2018; Denissen, 2019).

4.5 Development of porous and lightweight inorganic polymers

The following sections describe the different stages of the development of IP-based insulation materials. As a guideline to this work, acceptability criteria were defined, and the discussion will be focused on the efforts made to be compliant with those target features. The acceptability criteria considered three fundamental properties of insulating materials, apparent density, thermal conductivity, and compressive strength (Table 4.5.1).

Table 4.5.1 Target properties of IPs insulating materials.

Stage	Apparent density (g/cm^3)	Thermal conductivity (W/m°K)	Compressive strength (MPa)
1	0.50-0.80	0.10-0.15	> 4.0
2	<0.50	<0.10	Self-bearing capacity

These acceptability criteria were firstly used to further analyze the PCA results in Figure 4.4.2b. The two intervals of apparent density and thermal conductivity defined in the acceptability criteria were represented by two levels (medium (M) and low (L)) and a third level was added to indicate superior values, represented by H (higher). The results of compressive strength at 28 d were only divided into two levels (high (H) and low (L)) having 4.0 MPa as a threshold value. Data points missing in the dataset are represented in score plots as black dots. A combined analysis of the score plots in Figure 4.4.2b and Figure 4.5.1 reveals that the most promising processing routes to be compliant with the target features defined in the first stage of development are located around the origin. In this region, moderated apparent density and thermal conductivity values were observed, while compressive strength values higher than 4 MPa can still be reached. The processing routes displayed in this area were predominantly in-situ foaming (IS) and combining in-situ foaming and air-entraining agents (IS+EA). The usage of pre-made foams (Pre-F) also provided some results in this area, but the large dispersion in the data of this processing method makes anticipate the need for careful mix design to render this processing route effective.

For the second stage of development more stringent targets were established in terms of apparent density thermal conductivity. Meet such demanding features required to translocate the areas of interest in score plots in the opposite direction of the respective component vectors. As a result, only a small group of formulations was able to be compliant with all acceptability criteria, being those mainly produced using in-situ foaming agents with or without the addition of air-entraining agents. The inclusion of lightweight aggregates into the mix design also demonstrated the ability to provide some results in this restricted area but, as in the case of pre-made foams, the dispersion of the results of this processing route should be acknowledged. This PCA analysis did not intend to prescribe a specific processing route to achieve lightweight IPs with a certain set of characteristics but to evidence processes that were most likely to succeed in providing IPs compliant with the defined acceptability criteria based on historical analysis. Based on these results some processing routes were excluded a priori and efforts were concentrated in the fewer remaining processing routes, namely pre-made foams, in-situ foaming with or without the use of air-entraining agents and the used of lightweight aggregates.

The terms porous and lightweight inorganic polymers will be used here to distinguish insulating materials produced via different methods. Porous inorganic polymers (hereafter porous IPs) were produced using in-situ foaming methods with or without using air-entraining and stabilizing agents, while the term lightweight inorganic polymers (hereafter 'LW IPs') will be used to described materials resulting from the incorporation of lightweight aggregates into inorganic polymeric matrixes.

The different stages of the development of thermal insulation IPs from the initial screening tests until the selection of a mixture design later used to produce medium-scale prototypes of a multi-layer panel will be described. Apart from the selection of the most adequate processing routes and the compliance with the technical criteria previously defined, a special focus will be given to the effective use of admixtures, additives, and activating solutions.

Screening tests were first performed to confirm the information provided by the historical PCA and to evaluate the applicability of the general trends observed to CaO-FeO$_x$-Al$_2$O$_3$-SiO$_2$ rich IPs. When justifiable, after the initial screening trials, a more thorough investigation was performed to evaluate the impacts of several processing parameters and investigate their effects on IPs' fundamental properties (e.g., mechanical properties, apparent density, and thermal conductivity).

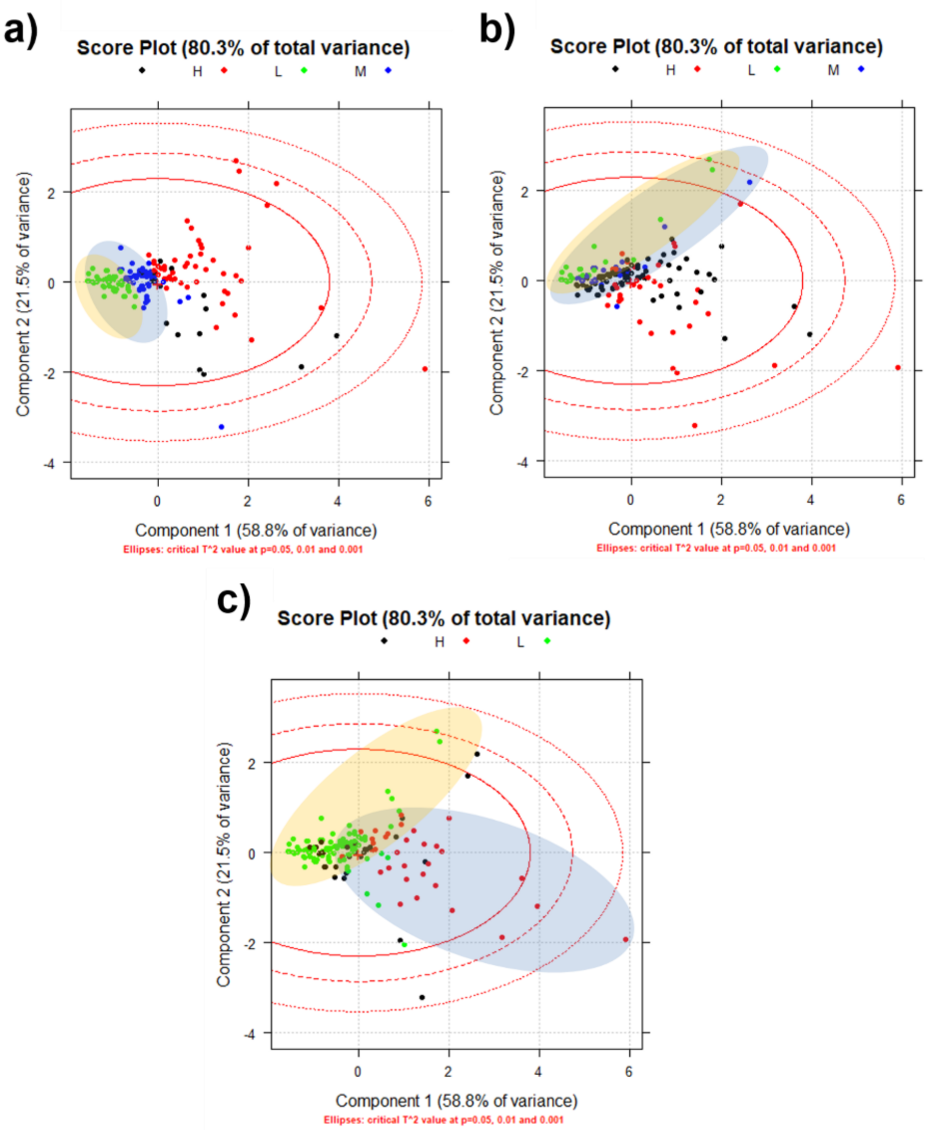

Figure 4.5.1 Score plot according to acceptability criteria: a) apparent density, b) thermal conductivity, and c) compressive strength at 28 d of curing. The acceptability criteria are plotted according to Table 4.5.1, represented here by H, L, M for high, low and medium levels, respectively. Data points missing in the dataset are represented here by black dots. The inserted circles cluster the results according to the target features in each development stage; blue areas represent samples compliant with the features defined in the first stage of development, while yellow areas represent the more stringent features defined in the second stage.

4.5.1 Porous inorganic polymers

Binder preparation

A CaO-FeO$_x$-Al$_2$O$_3$-SiO$_2$ rich slag was used as the main solid precursor used to produce porous and lightweight IPs, while silica fume was used as an admixture. As an alkaline activator, a 14 M potassium hydroxide solution was used. The binder composition was prepared based on a previously developed binder and corresponded to the formulation K7 in Table 3.3.3. The selection of this binder to produce porous and lightweight materials was based on its lower apparent density and slightly higher mechanical performance relative to K4 (see Table 3.3.3). When justifiable some modifications were made on the binder composition which will be described and discussed.

4.5.1.1 Pre-foaming methods

The scope of these exploratory experiments was to determine the conditions able to produce stable porous IPs using pre-foaming methods to assess the stability of the produced bodies. In preliminary tests, different stabilized foams and addition dosages by vol./vol.% were added to 100 g of the selected binder. The foams were produced by high-speed mixing a commercial air-entraining agent (a fatty alcohol ethoxylate), a methyl hydroxyethyl cellulose foam stabilizer (mass ratio ranging from 1:1 to 3:1) and water. Foams with different water dosages (up to ≈ 95% H_2O mass) were manually introduced to the binder on volumes ranging from 200 to 500%. The foams were able to sustain themselves before being introduced to the binder, but some burst of their structure occurred during the homogenization process. However, the foamed structures did not entirely collapse upon mixing and allowed the setting of the fresh pastes. Based on experimental observations, a slightly elevated temperature (40 °C) was set during the initial stage of curing to increase the reaction kinetics and promote faster setting. The porous IPs were kept up to 72 h in such environment but in general, could be demolded after 48 h. The specimens' densities were proportional to the volume of foam incorporated and ranged from 0.69 to 0.81 g/cm^3 after 7 d of curing. Figure 4.5.2 shown a sample produced with 500 vol./vol.% of pre-made foam to illustrate the porous structures formed.

Figure 4.5.2 Illustrative image of porous IPs produced using pre-foaming methods.

All samples could be demolded and manually handled but exhibit dusty surfaces and a fragile structure. Such undesired phenomena were considerably aggravated as higher foam volumes were introduced to the binder. Apart from strength losses associated with the increased amount of pores and voids in the structure, the addition of considerable volumes of a water-based foam may have unbalanced the reaction kinetics, and in turn, jeopardize strength development. The strength development of the porous IPs produced with pre-made foams could be optimized by adjusting the parent binder mix design. However, increase the solid load and/or the activating solution concertation was expected to promote further collapse of the foamed structure, and increase the samples' apparent density, moving away even further from the acceptability criteria defined. These preliminary observations seem to confirm the results gathered from the historical PCA, where the large dispersion of the data from pre-foaming methods made anticipate a considerable sensitivity of this processing method. Such variability and the success of this processing route seem to be intrinsically associated with the precursor's chemical and physical properties (e.g. density, particle size distribution), and therefore was disregarded from further testing.

4.5.1.2 In-situ foaming methods

A set of experiments was performed to explore the foaming potential of different in-situ pore-forming and air-entraining agents. As one of the most commonly and successfully used additives employed in the production of insulation materials, aluminum powder was selected as one of the pore-forming agents to be tested, and the effects of their single and combined use with air-entraining agents were investigated. Like pre-foaming methods, the combined use of fatty alcohol ethoxylate and methyl hydroxyethyl cellulose was considered. In these experiments, such agents were directly added in their powder form to the binders. In in-situ foaming trials, these admixtures were added in a mass ratio of 3:1.

All samples were produced following the procedure described in 3.3 being after employed 2 extra minutes to mix the pore-forming agents. In cases where the aluminum powder was used as the main pore-forming agent, air-entraining agents were pre-added to the activating solution. Such decision was ground on the available literature (Liu, 2016; Hertel, 2019) in which fly ash and Fe-rich porous IPs with densities lower than 0.40 g/cm^3 were produced in a similar manner. To evaluate the impact of each of these foaming strategies on the characteristics of the produced IPs, factorial design of experiments were performed and the results will be described in the following sections. The discussion will be focused on the characteristics of the porous microstructures formed and how they were translated into the insulating character of the produced IPs. Several properties were analyzed and will be discussed when justifiable but special emphasis will be given to apparent density, compressive strength, and thermal conductivity. The combined use of different in-situ foaming strategies are also discussed.

4.5.1.2.1 Metallic aluminum powder

Screening tests

To preliminary assess the foaming potential of metallic elements, a fixed dosage (0.20 wt%) of aluminum powder (particle size range 7–15 μm, Alfa Easer, purity 99.5%) was introduced to the binder selected in previous experiments (K7, Table 3.3.3). The dosage of Al powder was established based on available literature (Novais, 2018b; Hertel, 2019) and previously laboratory experimentation (Ascensão, 2017). These samples were named after their starting binder being added an A2 mark referring to Al addition. All samples were cured during 24 h at slightly elevated temperature (50 °C), being afterward demolded and stored at room conditions until testing.

As can be seen in Table 4.5.2, the physical and mechanical properties of K7 binders were only marginally impacted by the addition of Al powder. The low S/L ratio of this binder did not produce a mixture sufficiently viscous to guarantee that a significant portion of the gaseous phases formed during Al decomposition remained entrapped within the IP structure. Thus, the addition of Al powder to K7 binder had a nearly null impact in terms of apparent density (-1.3%), compressive strength (-7.3%) and thermal conductivity (-0.7%). However, the slight reduction observed and the different decreases of apparent density and thermal conductivity between K7 and K7_A2 during drying reveals the formation of distinct microstructures. Upon drying, K7 apparent density and thermal conductivity were reduced by 0.6 and 39.8 %, while in K7_A2 higher reductions were observed 4.5 and 42.3%, respectively. The higher reduction of apparent density and thermal conductivity denotes that- despite not being enough to produce highly porous materials- a portion of the hydrogen formed remained entrapped in the IP structure during plastic state, which may have later facilitated water evaporation.

Table 4.5.2 The effects of adding 0.20 wt%* aluminum powder on K7 binder.

	K7	K7_A2
Compressive strength 28 d (MPa)	12.3±2.6	11.4±2.1
Apparent density 28 d (g/cm^3)	1.56±0.1	1.54±0.1
Dry apparent density 28 d (g/cm^3)	1.55±0.1	1.47±0.1
Thermal conductivity 28 d (w/m°K)	0.457	0.454
Dry thermal conductivity λ 28 d (w/m°K)	0.275	0.262
Specific heat capacity 28 d (J/m^3·°K)	$1.6 \cdot 10^6$	$1.6 \cdot 10^6$
Dry specific heat capacity 28 d (J/m^3·°K)	$1.2 \cdot 10^6$	$1.1 \cdot 10^6$
Thermal diffusivity 28 d (m2/s)	$2.9 \cdot 10^{-7}$	$2.9 \cdot 10^{-7}$
Dry thermal diffusivity 28 d (m^2/s)	$2.3 \cdot 10^{-7}$	$2.3 \cdot 10^{-7}$

* % based on precursors mass (slag + silica fume).

As these preliminary results suggested that binders with higher viscosities were necessary to entrap the gaseous phases formed, K7 binder was modified by increasing the S/L ratio of the mix and substitute the potassium hydroxide solution used by a combination of potassium hydroxide and silicates solutions. The Blaine of the slag used in the following experiments was also reduced to 2700 cm^2/g, instead of the 4500 cm^2/g used when first developing the binders' formulations in section 3.3. The influence of PSD on the foaming process and strength development of porous IPs will be also discussed here.

Screening trials revealed that by imposing such modifications on the parent binder, the same aluminum powder dosage (0.20 wt%) was able to effectively produce foamed AAMs. As the porous structures produced comprised a considerable amount of large-size and apparently non-connected pores, a surface-active agent (sodium oleate ($CH_3(CH_2)_7CH{=}CH(CH_2)_7COONa$, purity 82%, Sigma-Aldrich) was used in an attempt to homogenize and increase the connectivity of the pore structure. A full factorial design of experiments was performed and the impacts of Al powder and sodium oleate dosage on IPs strength development and insulating properties evaluated.

Design of experiments

The binder selected to perform the initially DoE corresponded to K30 formulation and the detailed description of their mixture portions can be seen in Table 3.3.3. A full factorial 2^2 DoE was conducted being the variables considered the sodium oleate (SO) and aluminum powder (Al) dosage. All samples were named after the dosage of such additives, being their upper and lower limit shown in Table 4.5.3. A minimum of two 4x4x4 cm^3 replicates was produced employing the same production and curing procedures adopted during the screening trials.

Table 4.5.3 shows the average apparent density and compressive strength of the produced porous IPs after 2 d of curing. As can be seen, the apparent density and compressive strength of SA42 are not included in Table 4.5.3 as the samples produced with such elevated dosages of SO and Al powder were too fragile to be demolded. The impossibility of collecting data in this point of the design forced the redefinition of the experimental conditions and, therefore the examination of the remaining samples was anticipated.

Table 4.5.3 Experimental factors and evaluated responses of porous IPs produced by combining aluminum powder and sodium oleate.

Code	Factors		Responses	
	Sodium oleate (wt%)	Aluminum powder (wt%)	Apparent density (g/cm^3)	Compressive strength (MPa)
SA00	0.000	0.000	2.08±0.06	76.1±6.2
SA02	0.000	0.200	0.74±0.00	0.8±0.4
SA40	0.040	0.000	1.90±0.01	51.2±2.9
SA42	0.040	0.200	-	-

The analysis of the experimental domain using surface response methodology was invalidated but interesting observations based on the reaming results can still be made. The reduced apparent density and compressive of SA02 relative to their parent binder (SA00) show that the modifications imposed on K7 binder effectively increased the ability to entrap gaseous phases within the IPs structures. The porous IPs formed (SA02) were compliant with the first criteria of acceptability in terms of apparent density but fail in reaching reasonable mechanical resistance. Despite late-age reactions might have resulted in some strength development, compressive strength values near to 4 MPa after 28 d of curing seem unlike.

The effects of single-use SO can also be seen in Table 4.5.3. The impacts of the tested dosage of such additive could be mainly seen on strength development (-33%) but a slight reduction of apparent density was also visible (-8.7%). Nonetheless, the produced materials cannot be classified as lightweight materials due to their high apparent density values, and therefore good thermal insulation properties were not expected.

To further investigate the combined effects of SO and Al powder addition, a new factorial DoE was conducted. In this new DoE, the maximum dosage Al powder was maintained at 0.20 wt% while SO was limited to 0.030 wt%, Table 4.5.4. In addition, as the previous results show that porous IPs could be successfully produced from binders with 2.85 S/L, it was interesting at this stage to explore the surrounding experimental domain to investigate the possibility of further optimize thermal insulating properties. Therefore, S/L was included as the third variable and the original 2^2 DoE transformed in a 2^3 full factorial DoE. The upper and lower limit of each variable can be seen in Table 4.5.4, being a central point formulation also included. As before, all samples were named after the dosage of the additives used and, in this case, also S/L, where 270, 285 and 300 stands for the parent binder S/L ratio (Table 4.5.5). The foamed IPs were produced and cured as in the previous DoE but in this case, only tested after 28 d of curing.

Table 4.5.4 Experimental matrix of the 2^3 full factorial DoE and the respective value of each variable per formulation.

Code	DoE parameters Sodium oleate (wt%)	 Aluminum powder (wt%)	 S/L
SOAL00|270	0.000	0.000	2.70
SOAL02|270	0.000	0.200	2.70
SOAL30|270	0.030	0.000	2.70
SOAL32|270	0.030	0.200	2.70
SOAL151|285	0.015	0.100	2.85
SOAL00|300	0.000	0.000	3.00
SOAL02|300	0.000	0.200	3.00
SOAL30|300	0.030	0.000	3.00
SOAL32|300	0.030	0.200	3.00

* % based on precursors mass (slag + silica fume).

Table 4.5.5 Mixture portions of the binder's formulations with different S/L (by mass %).

	Mixture portion (wt%)					
Code	Slag	Silica fume	KOH (14M)	K_2SiO_3	H_2O	S/L
SOAL00|270	68.9	4.1	5.3	5.3	16.5	2.70
SOAL00|285	69.9	4.1	5.3	5.6	15.1	2.85
SOAL00|300	70.9	4.1	5.3	5.9	13.8	3.00

Volumetric expansion

The strength development and thermal properties of foamed materials are intimately correlated to their foaming process. Factors as pore size distribution and connectivity play a vital role in determining such features, but volumetric expansion itself provides a simple indication of how the mechanical and thermal properties IPs may be affected. Moreover, knowing the level of expansion allows to approximately determine the amount of IP required to fulfill a certain volume, and therefore avoid unnecessary use of material and its excessive confinement during the foaming process. Table 4.5.6 shows the volumetric expansion (vol%) experienced by IPs during the first 24 h of curing at 50 °C.

Table 4.5.6 Volumetric expansion experienced in the 24 h of curing, and apparent density and compressive strength after 28 d of curing of porous IPs produced using Al powder and sodium oleate as pore-forming and surface-active agents.

Code	Expansion (vol. %)	Apparent density 28 d (g/cm^3)	Compressive strength 28 d (g/cm^3)
SOAL00|270	0.00±0.0	2.08±0.00	23.0±5.3
SOAL02|270	95.9±1.9	0.75±0.02	1.1±0.0
SOAL30|270	2.6±0.1	1.96±0.03	25.2±2.8
SOAL32|270	86.8±4.3	0.53±0.02	0.8±0.0
SOAL151|285	99.0±1.0	0.82±0.04	0.9±0.1
SOAL00|300	0.00±0.0	2.17±0.01	40.6±2.6
SOAL02|300	83.0±6.5	0.84±0.06	1.6±0.1
SOAL30|300	2.5±0.1	1.96±0.02	30.9±2.7
SOAL32|300	97.1±4.9	0.52±0.00	1.0±0.0

As it would be expected, only Al-containing samples experienced significant expansions (>80 vol%) as in the remaining ones no gas-releasing agent was used. More interesting to observe was the distinct effect of SO at different S/L ratios. The interactions between those two variables and their combined effects on IPs foaming are better observed in Figure 4.5.3. For simplicity, the variables were converted to its binomial form where -1 and 1 stand for each variable lower and upper limit, respectively. As can be seen, in formulations were no SO was used, increase S/L reduced the volumetric expansion. The elevated S/L ratio in those formulations has reduced their ability to be foamed most likely due to an excessive increase of the binders' specific weight that augmented the gas bubbles' tendency to collapse. These results agree with the increase of apparent density and compressive strength observed between SOAL02|270 and SOAL02|300 samples. It should be mention that an increase of apparent density and compressive strength was also observed between SOAL00|270 and SOAL00|300, confirming the different microstructures formed between samples with different S/L ratios, Table 4.5.6.

Conversely, when 0.030 wt% SO was added to the mixture, increasing S/L ratio did not result in reduced expansions. In fact, the expansion of SOAL32|300 was higher relative of SOAL32|270, Table 4.5.6. The increased expansion revealed the positive impact of SO on the stability of the gas bubbles formed. Surface-active agents reduce drainage and Ostwald ripening processes, which in turn, avoided the gas bubbles collapse. This positive effect of SO it even further visible when comparing samples with an equally high S/L ratio. However, the opposite trend was observed in samples produced with 2.70 S/L which once more demonstrates the interaction between those variables. Therefore, when using Al powder as a gas releasing agent, SO is necessary for high S/L condition to obtain expansion levels similar to those observed at low S/L without its addition. However, the maximum expansion was reached in the central point formulation (99 vol%), showing the existence of an optimal combination between the Al and SO dosages and S/L ratio around this region of the experimental domain. This finding is particularly relevant if the scope of application requires to maximize expansion or to optimize the production process of porous IPs for thermal insulating purposes. In this region of the experimental domain the dosage of Al powder and SO were reduced by half and an intermediate quantity of activating solution is required, Table 4.5.5.

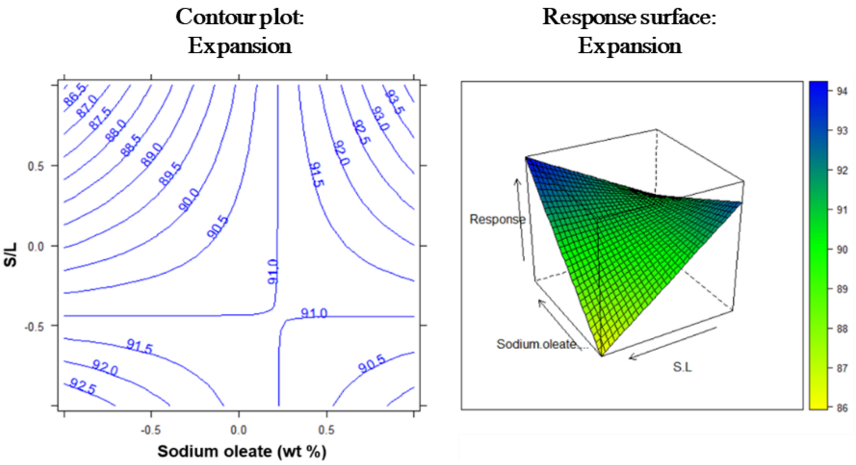

Figure 4.5.3 Contour plot and expansion surface response as a function of sodium oleate dosage and S/L ratio when a fixed dosage of aluminum powder is provided (0.20 wt%).

Apparent density

Similarly to expansion, the most noticeable reductions of apparent density were provoked by Al powder. The apparent density of Al-containing samples varied from 0.75 to 0.84 g/cm^3 when no SO was used. Despite the single-addition of SO did not have significantly reduced the samples' apparent density relative to the parent binders (<10 %), their combined use with Al-powder resulted in the lowest apparent densities observed, less than 0.54 g/cm^3. As can be seen in Figure 4.5.4, as SO dosage rose, apparent density was reduced independently of S/L ratio. However, the minimum SO dosage required to achieve a certain apparent density slightly increases as S/L ratios raise. The crucial role of the dosage of gas releasing agents is also depicted when one considers the apparent density of the central point formulation. As can be seen in Table 4.5.6, the apparent density of IPs produced with of 0.10 wt% of Al-powder and 0.015 wt% SO (SOAL151|285, 0.82 g/cm^3) was higher than what could be expected if similar S/L and SO dosage was employed along with 0.20 wt% of Al-powder, Figure 4.5.4. Nonetheless, the central point formulation provides an alternative solution to produce porous IPs nearly compliant with the first criteria of acceptability, while halving the dosage of additives required.

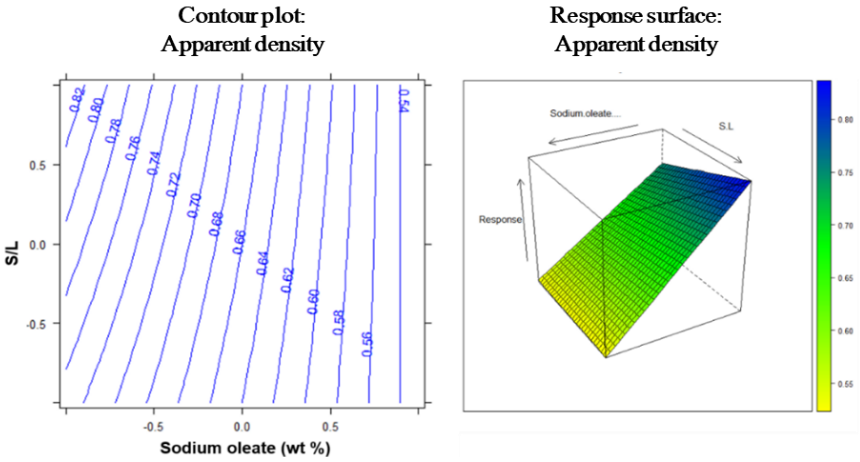

Figure 4.5.4 Contour plot and apparent density surface response as a function of sodium oleate dosage and S/L ratio when a fixed dosage of aluminum powder is provided (0.20 wt%).

Strength development

Table 4.5.6 shows the IPs compressive strength after 28 d of curing. Strength development shows similar patterns to apparent density which suggests a strong correlation between those responses. Increasing S/L ratio of additive-free binders from 2.7 to 3.0 resulted in a nearly two-fold increase of compressive strength, 23.0 and 40.6 MPa, respectively. A smaller increase in strength was also promoted by raising S/L ratio of single-doped Al-powder and SO IPs. Figure 4.5.5 shows the surface responses of single-doped IPs were increasing S/L rose compressive strength by approximately 50 % on IPs were only SO was used, while in Al-containing IPs such increase was less significant. The almost vertical lines displayed in Figure 4.5.5b demonstrate that the effects of Al-powder are almost independent of S/L, while the effects of SO are much more dominated by the later.

In Table 4.5.6 it can also be seen the deleterious impact of SO in the strength development of Al-containing IPs. Adding 0.03 wt% SO to SOAL02 samples reduced their compressive strength by 27 and 38 %, depending on the S/L used. The minimum compressive strength was reached by SOAL32|270 samples (0.8 MPa) and the compressive strength of the central point formulation did not surpass 1 MPa (Table 4.5.6). Despite the enhanced foaming process and maximum expansion observed in the central region of the experimental domain, it is also true that formulations in this area are not able to provide porous IPs with extremely reduced apparent density considerable mechanical performance. Conversely, it also means that Al and SO dosage can be reduced by half without significantly affect the properties of the produced IPs. None of the IPs produced with Al-powder presented compressive strength that surpassed 4 MPa - rendering them inadequate for applications where significant bearing-load capacity is required – but all the porous IPs presented self-bearing capacity. According to the second set of properties defined in the acceptability criteria, self-bearing capacity is acceptable if low apparent density and thermal conductivity are provided. In fact, the samples produced by combining high dosages of Al-powder and SO (SOAL32|270 and SOAL32|300) presented the lowest apparent densities, almost reaching the second threshold value in terms of apparent density (0.50 g/cm^3).

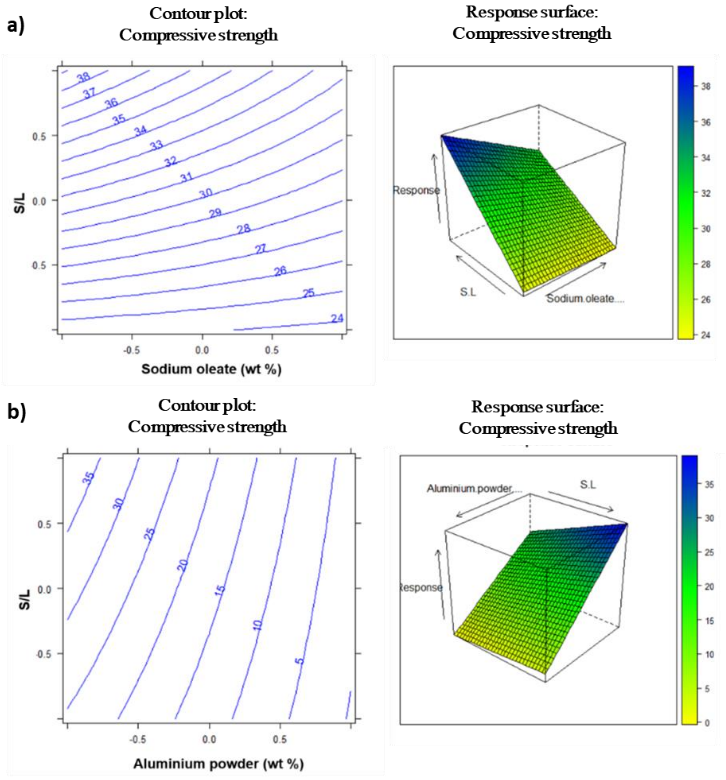

Figure 4.5.5 Contour plot and compressive strength surface response of single-doped IPs as a function of (a) sodium oleate dosage and S/L ratio and (b) aluminum powder dosage and S/L ratio.

Influence of precursor’s fineness

The precursor's particle size distribution (PSD) is known to affect the reaction kinetics and phase formed upon alkali activation. In general, increasing the precursor’s surface area promotes faster and higher dissolution levels and raises the binding phases formed, thus favoring the formation of more resistant structures. As modifying the reaction kinetics also significantly affects the rheological properties of alkali-activated pastes, evaluate the influence of particle size distribution in in-situ foaming processes was also worthy. In the DoE’s discussed above the Blaine of the slag used as the main precursor was 2700 cm^2/g. Modifications on the precursor’s PSD were imposed only by adjusting the milling procedures whereas the starting granular vitreous material was maintained. As so, no chemical modifications on the precursor's composition were made, only on its physical characteristics. The effects of precursors PSD on the foaming process and characteristics of the porous IPs produced by in-situ foaming strategies were examined in the central point formulation of the full factorial DoE described in Table 4.5.4. The mixture portions were maintained, being the only difference the Blaine of the main precursor (1800, 2700 and 4500 cm^2/g). To identify such differences from here on those samples will be referred to as 18SOAL, 27SOAL, and 45SOAL.

Figure 4.5.6 shows the expansion experienced by IPs produced with distinct precursors during the initial 24 h of curing. Reducing the precursors of Blaine from 2700 to 1800 cm^2/g incremented the binders’ ability to expand by approximately 15 %. The deleterious effect on expansion provoked by an increase in the precursor’s surface area was even more visible in 45SOAL samples. In those samples, the expansion did not surpass 30 vol. %, corresponding to a decrease of over 70% relative to 27SOAL. As can be seen in Figure 4.5.7, the morphology of the porous structure was also significantly affected by the precursor’s PSD. In IPs produced from precursors with the lowest Blaine (1800 cm^2/g, on the left), a homogenous porous structure mainly constituted by small spherical and connected pores was formed. Increasing the precursors Blaine seems to have reduced pore size and elongated their predominantly spherical morphology. Further increase the precursors Blaine led to the formation of more closed structures characterized by the existence of some large voids.

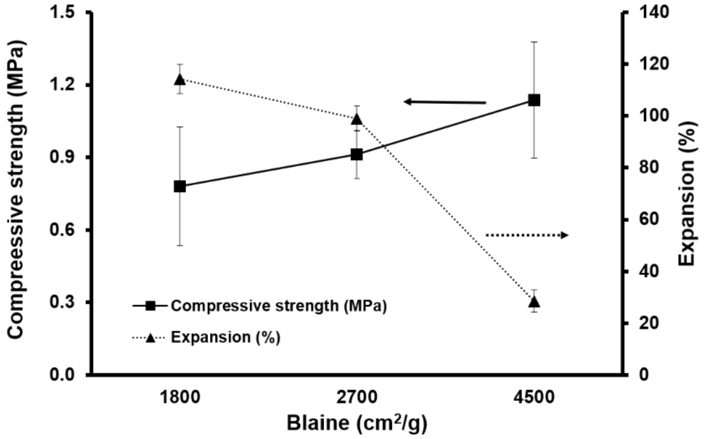

Figure 4.5.6 Compressive strength of porous IPs after 28 d of curing and their expansion during the initial 24 h as a function of the main precursor Blaine value. The lines are drawn as a guide to the eye.

The increasingly closed structures formed as the precursors Blaine rose is in line with the reduction in expansion and agrees with the significant decay observed in 45SOAL samples. Possible explanations for such macroscopic modifications may include the increase of early-age viscosity promoted by hastened and more extensive dissolution process, which can lead to the partial collapse of the gas bubbles formed. Other factors such as uneven dispersion of pore-forming agents and/or the mineralogical differences between binding phases formed may also have affected the binders’ ability to be foamed. The large-size pores observed in 45SOAL seem to corroborate the uneven dispersion of Al-powder (Figure 4.5.6), and reduced gains in mechanical strength can be attributed to physical factors such as modifications on the pore size distribution, on the total volume of pores, pore wall thickness, and pore connectivity. However, the reduced values and considerable standard deviations of compressive strength values makes difficult to postulate any definite conclusion without further investigations.

Figure 4.5.7 Image of porous IPs produced using precursors with different particle size distribution (Blaine value growing from left to right).

As in the case of strength development, the morphological differences also had a minor effect on apparent density and thermal characteristics, Table 4.5.7. Drying processes were not affected by differences in the porous structures formed as in all samples apparent density was reduced between 21 and 24% during drying processes. However, the lowest dry apparent densities and thermal conductivities were reached when precursors with an intermediate Blaine were used, 0.62 g/cm^3 and 0.079 W/m°K, respectively. The considerable expansion and the elongated morphology of the pores formed in 27SOAL seem to have a beneficial effect and enhance the insulation properties of the produced IPs. Despite the minor modifications made by adjusting the precursors Blaine, all IPs presented similar properties and remained compliant with the first criteria of acceptability in terms of dry apparent density (<0.80 g/cm^3) and thermal conductivity (<0.150 W/m°K) but failing in reaching the intended compressive strengths values. In terms of the second criteria of acceptability where no restrictions on compressive strength are made, the more stringent requirements on thermal conductivity values (<0.100 W/m°K) were also attained, but apparent densities lower than 0.50 g/cm^3 were not achieved. Hence, only minor adjustments could be made in the properties of the central point formulation. Moreover, the lowest apparent densities and thermal conductivity were observed in IPs produced using precursors with an intermediate Blaine, which had been already used during the production of the reaming points of the experimental domain. Based on such findings, no major improvements in the insulation properties of the reaming points of the experimental design could be foreseen and therefore, further testing to assess the influence of the precursors Blaine was discarded.

Table 4.5.7 The effects of the precursor's fineness on the properties of foamed IPs.

Blaine (cm^2/g)	**1800**	**2700**	**4500**
Apparent density 28 d (g/cm^3)	0.89±0.2	0.82±0.1	0.88±0.1
Dry apparent density 28 d (g/cm^3)	0.70±0.1	0.62±0.2	0.67±0.1
Thermal conductivity λ 28 d (W/m°K)	0.085	0.080	0.092
Dry thermal conductivity λ 28 d (W/m°K)	0.084	0.079	0.090
Specific heat capacity28 d (J/m^3·°K)	$2.6\cdot10^7$	$2.4\cdot10^7$	$3.6\cdot10^7$
Dry specific heat capacity28 d (J/m^3·°K)	$2.4\cdot10^7$	$2.4\cdot10^7$	$3.1\cdot10^7$
Thermal diffusivity 28 d (m^2/s)	$3.3\cdot10^{-7}$	$3.3\cdot10^{-7}$	$2.6\cdot10^{-7}$
Dry thermal diffusivity 28 d (m^2/s)	$3.2\cdot10^{-7}$	$3.1\cdot10^{-7}$	$2.6\cdot10^{-7}$

* % based on precursors mass (slag + silica fume).

4.5.1.2.2 Air-entraining agents

A full factorial design of experiments was also set to analyze the effects of air-entraining and foam stabilizer agents. In this set of experiments, only K7 formulation was considered as a reference binder produced with a precursor with 4500 cm^2/g of SSA, according to 3.3. The dosage (by mass addition) of air-entraining agent dosage (EA) and S/L ratio were selected as the variables to be investigated. The lower and upper limits of EA addition and S/L ratio were defined as 10.0-20.0 wt%, and 0.70-1.30, respectively (see Table 4.5.8). The foam stabilizer dosage was kept as one-third of EA mass. An additional amount of demineralized water was supplied to the mixtures in order to compensate for the loss of flowability provoked by EA and stabilizing agents. The intended overall solid-to-liquid ratio was considered to determine the content of water to be added. All IPs produced here followed the procedure describe in 4.5.1.2, and a minimum of two replicates were produced per formulation.

The central point formulation, coded as 10_E15, was also used to select the adequate curing conditions prior to performing the full factorial DoE. Three different curing conditions were tested comprising: i) room conditions, ii) 24 h at 60 °C and iii) 48 h at 40 °C. During this curing period, all specimens were kept in sealed plastic vials being afterward demolded and kept at room conditions until testing. After 48 h at room conditions, the material still presented signs of excessive moisture and a fragile structure indicating that slightly elevated temperatures were necessary to enhance polymeric reactions. This is a common practice in the production of porous and lightweight IPs as it has already been described in the introductory part of this section. The beneficial effects of slightly elevated temperatures were notorious independent of the curing temperature used (40 or 60 °C), and well-consolidated structures were formed at in conditions. Hence, the acceptability thresholds defined in Table 4.5.1 were used to define the most suitable curing conditions. In both cases, apparent density (< 1 g/cm^3) and thermal conductivity values (<0.180 W/m°K) were in the vicinity of the defined thresholds but extended curing periods at moderated temperatures were found to beneficiate strength development. Samples cured for longer periods at 40 °C exhibit an average 7 d compressive strength of 2.5 MPa, while of their 60 °C counterparts such value was only 1.5 MPa. At the risk of ignoring possible interactions between curing conditions and the other variables investigated, such curing conditions were adopted throughout these experiments.

Table 4.5.8 Design of experiments: parameters investigated, and accessory variables. The central point formulation is highlighted, and the details of the reference paste are given for comparison purposes.

Formulation	Code	DoE parameters		Accessory variables
		S/L ratio	EA dosage (mass %binder)	Stabilizer dosage (mass %$_{\text{binder}}$)
Reference paste	K7	1.30	0	0.0
Initial DoE	13_E10	1.30	10	3.3
	13_E20	1.30	20	6.6
	10_E15	1.00	15	5.0
	07_E10	0.70	10	3.3
	07_E20	0.70	20	6.6
Extra formulations	10_E10	1.00	10	3.3
	115_E15	1.15	15	5.5
	10_E20	1.00	20	6.6

In the initially defined DoE, S/L boundaries were defined at 0.70 and 1.30. The selection of such broad limits intended to explore a significant region in the surrounding area of the central point formulation. Porous IPs with similar S/L have been reported (Ascensão, 2017) but such could be replicated here. The formulations located at the lower S/L limit presented severe segregation and stratification and could not be properly demolded. These phenomena suggest an excessive usage of water and forced the redefinition of the initial DoE conditions. The S/L lower boundary was than limited to 1.0, and a new central point defined at 1.15 S/L (see Table 4.5.8). The 10_E15 formulation remained in DoE as an extra validation point. Despite this approach not being totally in accordance with DoE principles, the results collected were treated and interpreted as such.

Visual inspection

All the produced IPs presented a fine detachable layer (<1mm) on their top surface which can be seen as some remnant stratification. The thickness of such layer increased as the EA content rises and S/L ratio decreases and has a maximum thickness in 10_E20 samples (≈5 mm). Nonetheless, these detachable layers could be easily removed manually or with a compressed air jet without causing any deleterious effect on the IPs structure. Figure 4.5.8 shows an illustrative image of a cylindrical 10_E15 sample before and after the removal of such a detachable layer.

Apart from these superficial layers, all IPs presented a homogenous appearance with minor cracks being formed on the surfaces of some samples. Such superficial cracks were not observed in samples 115_E15 and 10_E15. Moreover, and despite the considerable shrinkage of the parent dense binder, no considerable volumetric changes occurred during curing. The formation of highly porous materials with broader pore size distributions is known to facilitate water evaporation, which in turn, reduces the internal stresses formed and drying shrinkage. The characteristics of the porous structures formed will be later discussed in detail.

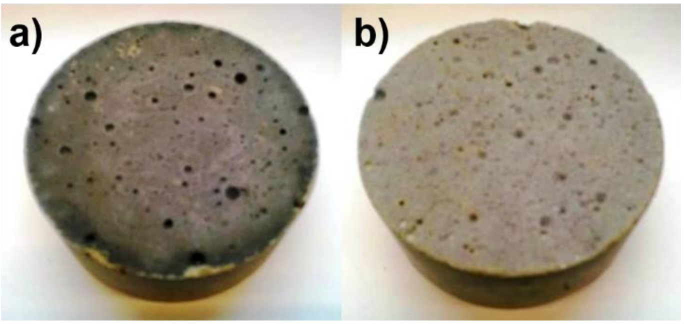

Figure 4.5.8 Illustrative image of porous IPs before (a) and after (b) the removal of the fine detachable layer form on its top surface.

Gel structure- FTIR analysis

Figure 4.5.9 shows the IR spectra of the parent dense binder and porous IPs made thereof. The IR spectra of the dense binder have shown three main peaks associated with chemical bonds in alkali-activated structures that corresponded to T-O (T=Al, Si) bonds stretching and bending vibrations at ≈ 470 cm^{-1}, Si–O bonds bending vibration at ≈700 cm^{-1} and, the asymmetric and symmetric vibration of Si–O–T bonds at 907 cm^{-1}. The presence of iron oxide phases - that should be visible given the oxide composition of the main precursor- it is denoted in IR spectra by a band around 600-700 cm^{-1} (Hertel, 2016), that appears in this case overlap with the band corresponding to Si–O bonds bending vibration. A broad peak between 2500-3700 cm^{-1} and a smaller peak around 1645 cm^{-1} were also visible and represent H_2O molecules within the IPs structure, corresponding to the H-O-H bonds deformation and O-H groups stretching vibrations, respectively. Two small peaks located between 1400-1450 cm^{-1} and between 870-880 cm^{-1} were also visible. Those peaks represent the O-C-O stretching vibrations from carbonate groups. The formation of such carbonate groups is often attributed to the reaction of free Ca cations with atmospheric CO_2. As can be seen, some changes in the molecular and bond structure were imposed by the addition of air-entraining agents and stabilizing agents into the mix design. The IR spectra of those additives are also given in Figure 4.5.9. The chemical structure of the air-entraining agent (fatty alcohol ethoxylate) presented several pronounced peaks in the low region of the spectra and two sharp peaks located between 2850-2910 cm^{-1}, while the stabilizing agent (methyl hydroxyethyl cellulose) is mainly characterized by three broad bands located between 400-600 cm^{-1}; 800-1100 cm^{-1} and 2500-3700 cm^{-1}. The majority of peaks that characterize the chemical structure of theses additive appear partially overlapped with the peaks of parent binder, and therefore could not be all clearly identifiable in IR spectra. However, the appearance of two sharp peaks located between 2850-2910 cm^{-1} and the increase of the broad bands around 840, 1200, 1400 cm^{-1} was clearly visible. These molecular changes seem to not be directly correlated to the dosage of admixtures used. Nevertheless, an increase of the peak located in the region of 3000–3700 cm^{-1} was clearly visible in 10_E10 and 10_E15 samples. As peaks in these regions are associated with the stretching and bending vibrations of O-H bonds, the increase of their intensity can be attributed to the existence of more hydroxyl groups in the molecular structures of the porous IPs produced with such mixture designs.

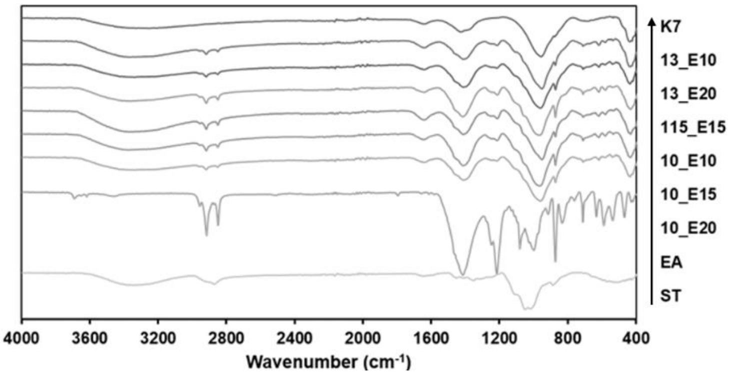

Figure 4.5.9 FTIR spectrum of the parent binder (K7), air-entraining and stabilizing agents, and the produced porous IPs.

Strength development

The flexural and compressive strengths of the different IPs are shown in Figure 4.5.9. A minimum of two replicates per formulation were tested after 28 d of curing according to the EN 196-1 (EN196-1, 2016). The strength development of porous IPs was significantly impaired relative to the parent binder. The highest flexural and compressive strength was achieved by the reference binder, 2 MPa, and 12 MPa, respectively. The IPs flexural strength was reduced from 71 to 90% relative to the reference binder while such a reduction in terms of compressive strength varied 31 to 80 %. The combined effects resulting from the modifications imposed on the reference binder are better depicted on the counterplots and surface responses in Figure 4.5.11.

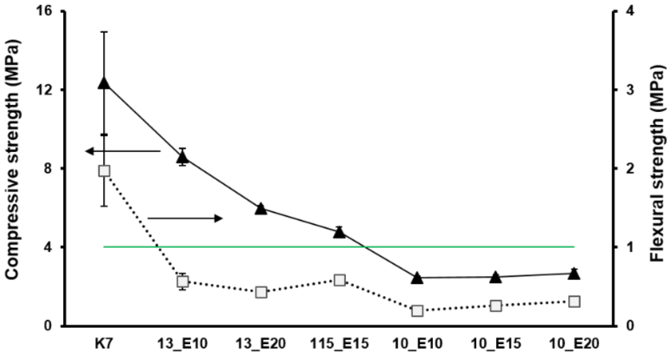

Figure 4.5.10 Compressive and flexural strength of porous IPs produced with air-entraining and foam stabilizer agents after 28 d of curing. The green line marks the threshold in which above the porous IPs meet the defined acceptability criteria in terms of compressive strength. The lines are drawn as a guide to the eye.

The strength development of porous IPs was significantly impaired relative to the parent binder. The highest flexural and compressive strength was achieved by the reference binder, 2 MPa, and 12 MPa, respectively. The flexural strength of porous IPs was reduced 71.3 to 89.9% relative to the reference binder while such reduction varied 30.5 to 80.1% in terms of compressive strength. The combined effects resulting from the modifications imposed on the reference binder are better depicted on the counterplots and surface responses in Figure 4.5.11.

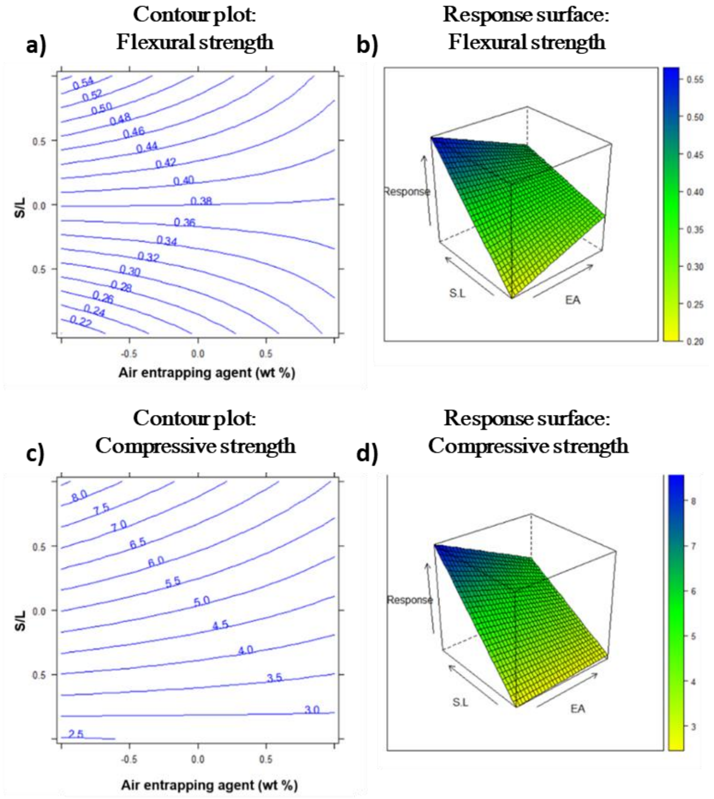

Figure 4.5.11 Flexural (a,b) and compressive strength (c,d) contour plots and the surface response of porous IPs produced with air-entraining and foam stabilizer agents after 28 d of curing.

As can be seen, the reduction of flexural strength was mainly dictated by S/L ratio, where the amount of EA was less significant. However, at higher S/L increase EA dosages seem to favor strength development while the opposite trend appears to exist at lower S/L. The maximum flexural strength reached by the central point formulation (0.6 MPa) is relatively higher than predicted in the surface response in Figure 4.5.11 (≈0.4 MPa). Such discrepancy can be attributed to experimental leverage in central points (0.1) being unlikely the existence of a slight inflection not accounted in DoE model. To verify the existence of such local maximum, additional replicates could have been produced. However, due to the low magnitude of the values involved and to absence of flexural strength requirements defined in the acceptability criteria such experiments were not performed here. Moreover, all IPs presented flexural strength values of the same order of magnitude and in no regions of the experimental domain flexural strength higher than 1 MPa were predicted. On the other hand, the surface response of compressive strength was more illustrative of the interactions between the variables studied. In the area below the central point, compressive strength values were almost exclusively governed by S/L ratio, meaning that the extra water supplied to compensate the loss of flowability had more deleterious effects than the dosage of the foaming agents' themselves. All IPs in this region are expected to present compressive values inferior to 5 MPa, and in order to be compliant with 4 MPa threshold criteria, S/L should not be significantly lower than 1.15. It also means that, if needed to be compliant with the remaining acceptability criteria, EA dosage can be increased without imposing a significant decrease of compressive strength. Such observations are further validated by the predicted compressive strength in the validation points, 10_E15 and 15_E10 samples, which are in good agreement with the results of their experimental realizations, 2.5 MPa, and 4.8 MPa, respectively.

On the other hand, in the region above the central point both variables exerted a much more significant influence on strength development. The growing influence of EA dosage was clearly despicable by the vertical rotation of counter lines. At the upper limit of S/Lratio, increase EA dosage from 10 wt% to 20 wt% decreased compressive strength from 8.6 MPa to 6.0 MPa, representing a 30 % reduction.

Nonetheless, all IPs in this region of the experimental domain surpassed the defined acceptability criteria for compressive strength, meaning that EA dosage and S/L ratio can be modified in order to optimize the remaining properties, or even to reduce production costs. The latter is expected to be reduced by increasing the solid content of the mix design or by reducing the amount of foaming agents added. In both cases, compressive strength will be enhanced, and therefore such criteria are not a limiting factor if S/L ratio above 1.15 is provided.

Apparent density

Figure 4.5.12 shows the apparent density of the porous IPs produced. As can be seen, the modifications made on the parent binder were able to significantly reduce apparent density. Despite the different levels reached, the apparent density of all porous IPs was reduced during aging, and even further after oven-drying for 48 h. The reduction of apparent density seems to be independent of S/L ratio and EA dosage as reductions of similar magnitude have been experienced over time by all IPs. However, 10_E10 and 10_E15 exhibit only minor reductions of apparent density during drying, which suggests the formation of more porous structures that facilitate drying processes during the initial 28 d of curing. Such hypothesis was later confirmed by MIP results which have shown higher levels of porosity and a boarded size distribution on those samples. These considerable reductions of apparent density upon drying can be also correlated to gel structures formed. As can be seen in Figure 4.5.9, the reduction of the broader band between 2500-3700 cm^{-1} visible in IR spectra denotes the existence of less H_2O molecules on the structures of those samples.

From Figure 4.5.12 it can also be seen that decreasing S/L ratio and rise EA dosage beneficiated the formation of less dense IPs. Samples 10_E20 didn’t follow such a general trend and presented higher apparent density relative to others produced with an equal S/L ratio. Such increase can be explained by the higher segregation observed. The less-dense segregated layer was removed and the apparent density of the remaining bodies increased.

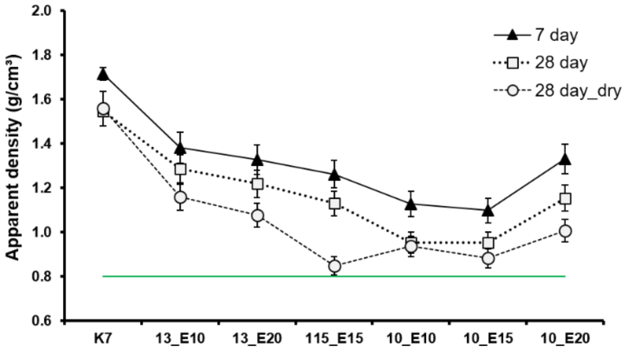

Figure 4.5.12 Apparent density of IPs produced with air-entraining and foam stabilizer agents after 7 d and 28 d of curing. The curves are drawn as a guide to the eye.

To visualize the combined effects of S/L and EA dosage on apparent density, counterplots and surface response were also produced, figure 4.5.13. The predicted apparent density values of the validation points slightly exceeded the results from their experimental realizations. The dry apparent density estimated in the central point and 10_E15 samples were approximately 1.0 g/cm^3, while the values measured did not exceed 0.9 g/cm^3. Despite predicting models had been able to properly describe strength development within the experimental domain, such is not the case in terms of apparent density. The existence of a region of minimum values defined between 115_E15 and 10_E10 could not be properly predicted. Limiting the experimental domain to regions were severe segregation did not occur or performing central composite designs could be used to improve the accuracy of the model. However, as the central point provided the porous IPs with the lowest dry apparent density, the region in the center of the experimental domain most likely constitutes the lower limit of these systems in terms of density and no further attempts of optimization were made. The central point formulation was able to produce porous IPs with densities near to 0.8 g/cm^3, and therefore compliant with the defined criteria of acceptability.

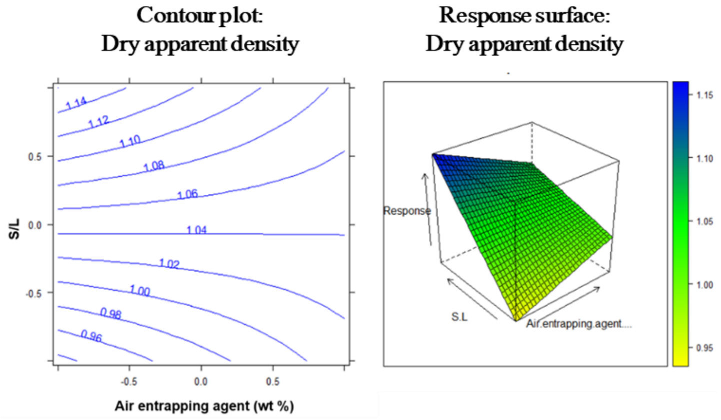
Contour plot: Dry apparent density

Response surface: Dry apparent density

Figure 4.5.13 Dry apparent density contour plots and the surface response of porous AAMs produced with air-entraining and foam stabilizer agents after 28 d of curing followed by 48 h oven dry at 65 °C.

Thermal properties

To access the insulation performance of the produced IPs, cylindrical samples with 10 cm diameter and 4 cm height were produced. After 28 d of curing, thermal conductivity (λ), specific heat capacity (cp) and thermal diffusivity (a) measurements were conducted on both sides of the samples (three measurements per each side). The samples top surface tended to present lower thermal conductivity values, but such differences were generally lower than 6%, which indicates a homogeneous matrix. Such minor differences can be attributed to the slightly irregular topography on the samples' top surfaces, which may have prevented a proper contact with the probe. The 10_E20 upper surfaces presented considerably lower values of thermal conductivity, which possibly resulted from the combination of two distinct factors, a non-homogeneous distribution of the foaming agents and the considerable irregularity of their top surfaces. However, the average values were considered representative of the insulation potential of these porous IPs and the average thermal conductivity, specific heat capacity and thermal diffusivity are shown in Table 4.5.9. After performing 28 d measurements, IPs were kept for an additional period of 48 h at 65 °C to further remove water from their structure and accessed possible differences relative to non-oven dried samples. The modifications imposed on the parent binder had a clear repercussion on all the thermal properties assessed.

Table 4.5.9 Thermal characteristics of porous AAMs produced with air-entraining and foam stabilizer a) thermal conductivity, b) specific heat capacity, and c) thermal diffusivity.

Code	λ 7 d	λ 28 d (W/m°K)	Dry λ	cp 7 d	cp 28 d (J/m^3·°K)	Dry cp	a 7 d	a 28 d (m^2/s)	Dry a
K7	0.587	0.457	0.275	$1.6\cdot10^6$	$1.6\cdot10^6$	$1.2\cdot10^6$	$3.6\cdot10^{-7}$	$2.9\cdot10^{-7}$	$2.3\cdot10^{-7}$
13_E10	0.415	0.283	0.176	$1.3\cdot10^6$	$1.1\cdot10^6$	$9.3\cdot10^5$	$3.3\cdot10^{-7}$	$2.6\cdot10^{-7}$	$1.9\cdot10^{-7}$
13_E20	0.380	0.257	0.158	$1.2\cdot10^6$	$1.1\cdot10^6$	$8.1\cdot10^5$	$3.3\cdot10^{-7}$	$2.5\cdot10^{-7}$	$2.1\cdot10^{-7}$
10_E15	0.372	0.178	0.118	$1.2\cdot10^6$	$8.7\cdot10^5$	$7.0\cdot10^5$	$3.2\cdot10^{-7}$	$2.3\cdot10^{-7}$	$1.7\cdot10^{-7}$
10_E10	0.338	0.218	0.146	$9.4\cdot10^5$	$8.7\cdot10^5$	$8.1\cdot10^5$	$5.3\cdot10^{-7}$	$2.3\cdot10^{-7}$	$1.9\cdot10^{-7}$
115_E15	0.294	0.162	0.112	$1.2\cdot10^6$	$8.3\cdot10^5$	$6.5\cdot10^5$	$2.6\cdot10^{-7}$	$2.0\cdot10^{-7}$	$1.8\cdot10^{-7}$
10_E20	0.420	0.233	0.144	$1.3\cdot10^6$	$8.4\cdot10^5$	$7.6\cdot10^5$	$3.4\cdot10^{-7}$	$3.7\cdot10^{-7}$	$2.7\cdot10^{-7}$

After 7 d, the reference binder presented thermal conductivity, specific heat capacity, and thermal diffusivity values of 0.587 W/m°K, $1.6 \cdot 10^6$ J/m^3·K, and $3.6 \cdot 10^{-7}$ m^2/s, respectively. Within the experimental domain of the DoE, dry thermal conductivity ranged from 0.420 to 0.338 W/m°K, reaching a maximum reduction of 42 % in 10_E10. Similar modifications were also observed in terms of specific heat capacity and thermal diffusivity, which varied between $9.4 \cdot 10^5$- $1.3 \cdot 10^6$ J/m^3·°K, and $3.3 \cdot 10^{-7}$-$5.3 \cdot 10^{-7}$ m^2/s, respectively. The maximum reduction of specific heat capacity was observed in 10_E10 (42%), while the minimum thermal diffusivity value was observed in 115_E15, representing a reduction of 28 % relative to the parent binder. From Table 4.5.9, can also be observed the influence of curing in the thermal properties of IPs materials. Independently of S/L ratio and EA dosage, thermal conductivity, specific heat capacity, and thermal diffusivity were all reduced during maturation and even further decreased after oven-drying. This aging effect seems related to drying processes and independent of S/L ratio and EA dosage as all IPs experienced comparable reductions over time.

As shown in Figure 4.5.14, counterplots and surface responses of thermal conductivity, one of the acceptability criteria, were built to evaluate possible regions of interest. Independently of the drying stage, all plots exhibited similar distributions. As in the case of apparent density, the region of minimum thermal conductivity values between 10_E15 and 115_E15 samples was not identified and therefore such models could not be validated. Such limitations could be overcome by performing central composite designs but the concave nature of the surface formed when including the thermal conductivity results the validation points will most likely demonstrate the existence of a local minimum around the central area, in this central region are expected to be almost compliant with the most demanding acceptability criteria in terms of thermal conductivity (<0.10 W/m°K). These reduced thermal conductivities are in good agreement with the lower apparent density of IPs located within this region, that were the nearest to reach the threshold of 0.80 g/cm^3. In order to be simultaneously compliant with compressive strength requirements increase S/L ratio up to values near 1.15 was found to be necessary. The oven-dried 115_E15 samples were able to be nearly compliant with the first criteria of acceptability, having presented an apparent density of 0.85 g/cm^3, thermal conductivity of 0.11 W/m°K and compressive strength of 4.8 MPa. Further decrease of S/L ratio to 1.0 was found to be detrimental as 10_E15 presented slightly higher apparent density (0.88 g/cm^3) and thermal conductivity values (0.12 W/m°K), and compressive strength of 2.5 MPa. EA addition should be limited to 15 wt% of the binder mass as no significant improvements were observed when higher EA dosages were used.

The results presented here also demonstrate the limits of this foaming process. As the region in the center of the experimental domain presented the lowest thermal conductivity values, no further reduction was expected to be achieved. Hence, the second and more demanding acceptability criteria could not be attained simply using EA and foam stabilizing agents. The combined use of EA, foam stabilizer and Al powder were therefore attempted, and the results gathered are discussed in the following section.

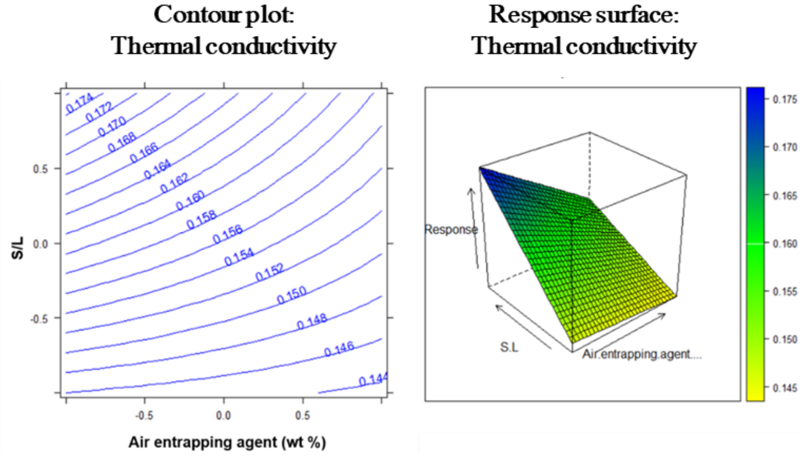

Figure 4.5.14 Thermal conductivity contour plots of porous IPs produced with air-entraining and foam stabilizer after 28 d of curing followed by 48 h oven dry at 65 °C.

Porous structure

Figure 4.5.15 shows the pore size distribution of the parent binder and porous IPs. In general, MIP data show that porous IPs have higher porosity values and a broader pore size distribution. As S/L decreases, more porous structures were formed. A systematic effect of EA dosage was also observed since higher cumulative pore volumes were promoted as EA dosage rose, Figure 4.5.15b. The modifications imposed on the parent binder also impacted the pore size distribution of the porous structures formed. Conversely to the parent binder that exhibits a structure mainly composed by mesopores, increase EA dosage and decrease S/L ratio promoted the formation of porous structures mainly composed of macropores. S/L ratio was found to be the dominant factor contributing to the formation of broader pore size distributions, while the influence of EA dosage was found to be less significant.

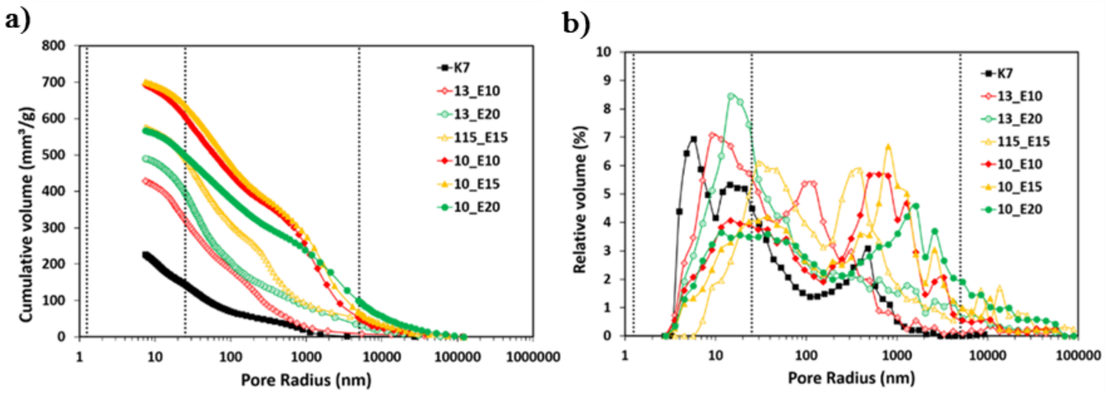

Figure 4.5.15 Cumulative pore volume (a) and relative pore size distribution (b) of the reference binder and the produced porous alkali activated materials.

In order to further investigate the differences in the void structure of porous IPs, computed tomography (Micro CT) analyses were performed in two selected IPs. Cylindrical samples with an approximated volume of 0.5 cm^3 were collected from larger specimens. The total porosity and the fractions of open and closed pores were evaluated. The porosity results of 10_E10 and 10_E15 samples are presented in Table 4.5.10.

Table 4.5.10 Porosity of 10_E10 and 10_E15 samples.

Porosity	Micro CT	
	10_E10	10_E15
Total porosity (%)	24.53	63.87
Closed porosity (%)	11.45	0.05
Open porosity (%)	14.77	63.85

The 10_E10 IPs presented low total porosity values with an approximately equal portion of open and closed pores. Conversely, the existence of an almost exclusively open pore structure and a three-fold increase of total porosity was observed in 10_E15. These results are considerably distinct from the open porosity values obtained using MIP techniques, where total pore volume and pore size distribution were similar in 10_E10 and 10_E15. Other physical properties as apparent density, thermal conductivity, and mechanical strength do not suggest such significant differences in the architecture of the porous structures formed. The reduced volume of the samples analyzed and the existence of bottleneck effects can potentially explain such discrepancy on the porosity levels observed.

4.5.1.2.3 Combined used of air-entraining agents and aluminum powder

Design of experiment

As it was previously shown, Al powder can be used in alkaline mediums to produce hydrogen and reduce the apparent density and thermal conductivity of dense IPs if one is willing to sacrifice a considerable portion of their mechanical performance. Such was not a limiting factor in the second acceptability criteria as only self-bearing capacity was required. In addition, the efficient use of Al powder requires a sufficiently viscous binder as it was demonstrated in the initial part of this section. In fact, EA and foam stabilizing agents acted as thickening agents and considerably increased the viscosity of the mixtures, which could potentiate the foaming effect of Al powder.

Based on the results of the DoE where air-entraining and foam stabilizers were used, three formulations were selected to be doped with a fixed dosage of Al powder (0.20 wt% mass addition). The formulations selected were 13_E10, 10_E10, and 115_E15. In addition to properties, the relatively reduced dosage of foaming agents also contributed to their selection. Aluminum doped formulations will be referred by adding an A2 mark to the references of their Al free counterparts, e.g., as 115_E15_A2 will refer to the aluminum-doped central point formulation.

The addition of Al powder was expected to further reduce the samples, apparent density, compressive strength, and thermal conductivity. Therefore, 13_E10_A2 was expected to present reasonable strength, apparent density, and thermal conductivity, while in the case of 10_E10_A2 and 115_E15_A2, very low apparent density and thermal conductivity were could be anticipated. The results of the control sample produced with the same Al dosage but without any air-entraining or foam stabilizer.

Strength development and thermal properties

The apparent density and compressive strength of Al-doped IPs and their Al free counterparts after 28 d of curing are shown in Table 4.5.11, while their thermal properties are shown in Table 4.5.12. As previously discussed, Al single addition to K7 binder was not able to significantly modify the mechanical and thermal properties of the materials formed. However, in the case of IPs containing air-entraining and stabilizing agents the effects of Al powder were considerable. A considerable decrease of apparent density, thermal conductivity, and specific heat values was visible in all IPs. The apparent density was reduced to values ranging from 0.28 to 0.39 g/cm^3, representing a reduction of around 70% in all IPs relative to their Al-free counterparts. Dry apparent density was even further reduced being the minimum value reached 0.27 g/cm^3 in 10_E10_A2 samples. The minor reduction of apparent density upon drying can be attributed to the highly porous structures formed that allowed water evaporation to occur during the initial 28 d of curing. A similar trend was observed in terms of thermal conductivity. Dry thermal conductivity of Al-containing IPs varied from 0.058 and 0.064 W/m°K, while such values in their Al-free counterparts varied from 0.112 and 0.176 W/m°K. The specific heat capacity of Al-containing IPs was also reduced while thermal diffusivity slightly rose (Table 4.5.12).

The 13_E10_A2 and 115_E15_A2 IPs presented similar apparent densities and thermal properties, but higher reductions were achieved when Al- powder was added to IPs with a higher S/L ratio and lower EA dosages. These results imply that such mixture designs maximize the amount of entrapped hydrogen and potentiate Al foaming effect. In all IPs the decrease in such properties was accompanied by a considerable reduction of mechanical strength. All Al-containing IPs could be demolded and presented self-bearing structures, but only the compressive strength of 13_E10_A2 could be determined. The compressive strength of those IPs was not able surpass 1 MPa, equivalent to a > 90% reduction provoked by Al addition. The detrimental effects of Al powder were more severe than anticipated and the decline of 13_E10_A2 mechanical strength higher than expected. Hajimohammadi *et al.* (2017b) have shown that increasing the availability of Al species can benefit the formation of more resistant binders, however, deleterious physical effects such as the increase of porosity and the reduction of pore wall thickness clearly overwhelmed such positive effects. In addition, it was also interesting to notice that no detachable layer was formed, and no signs of stratification were visible.

Table 4.5.11 Apparent density, oven-dry apparent density and compressive strength of porous IPs produced by combining different foaming strategies.

Code	Apparent density 28 d (g/cm^3)	Dry apparent density 28 d (g/cm^3)	Compressive strength 28 d (g/cm^3)
K7	1.56±0.1	1.55±0.1	12.3±2.6
K7_A2	1.54±0.1	1.47±0.1	11.4±2.1
13_E10	1.29±0.1	1.16±0.1	8.6±0.4
13_E10_A2	0.37±0.1	0.36±0.1	0.6±0.1
115_E15	1.13±0.1	0.85±0.1	4.8±0.2
115_E15_A2	0.39±0.1	0.37±0.1	-
10_E10	0.95±0.1	0.94±0.1	2.5±0.1
10_E10_A2	0.28±0.2	0.27±0.2	-

Table 4.5.12 Average thermal properties of porous IPs produced by combining different foaming strategies 28 d of curing.

Code	λ 28 d (w/m°K)	Dry λ 28 d (w/m°K)	cp 28 d (J/m^3·°K))	Dry cp 28 d (J/m^3·°K))	a 28 d (m^2/s)	Dry a 28 d (m^2/s)
K7	0.457	0.275	$1.6\cdot10^{6}$	$1.2\cdot10^{6}$	$2.9\cdot10^{-7}$	$2.3\cdot10^{-7}$
K7_A2	0.454	0.262	$1.6\cdot10^{6}$	$1.1\cdot10^{6}$	$2.9\cdot10^{-7}$	$2.3\cdot10^{-7}$
13_E10	0.283	0.176	$1.1\cdot10^{6}$	$9.3\cdot10^{5}$	$2.6\cdot10^{-7}$	$1.9\cdot10^{-7}$
13_E10_A2	0.082	0.065	$3.6\cdot10^{5}$	$2.6\cdot10^{5}$	$2.4\cdot10^{-7}$	$2.6\cdot10^{-7}$
115_E15	0.162	0.112	$8.3\cdot10^{5}$	$6.5\cdot10^{5}$	$2.0\cdot10^{-7}$	$1.8\cdot10^{-7}$
115_E15_A2	0.082	0.064	$3.5\cdot10^{5}$	$2.6\cdot10^{5}$	$2.5\cdot10^{-7}$	$2.6\cdot10^{-7}$
10_E10	0.218	0.146	$9.8\cdot10^{5}$	$8.1\cdot10^{5}$	$2.3\cdot10^{-7}$	$1.9\cdot10^{-7}$
10_E10_A2	0.073	0.058	$2.3\cdot10^{5}$	$1.5\cdot10^{5}$	$3.2\cdot10^{-7}$	$3.9\cdot10^{-7}$

Al powder fulfilled the purpose of its addition by increasing the insulation performance of the previously developed porous IPs. Its combined effects with air-entraining and foam stabilizer agents were able to deliver porous IPs compliant with the second and most demanding criteria of acceptability being produced samples with apparent density and thermal conductivity values considerably below the thresholds of 0.5 g/cm^3 and 0.10 w/m°K, respectively.

Increasing EA dosage does not seem vital to achieving low apparent density and thermal conductivity values, while the increase of S/L does not significantly beneficiated mechanical performance. Having in consideration that none of the formulations discussed here can be employed in applications where loads will be experienced, the formulation 10_E10_A2 provides the most efficient usage of air-entraining agents and thus should be recommended for thermal insulation purposes.

Acoustical absorption

Despite not being the primary scope of this work to produce acoustical insulating materials -and therefore no being defined in the acceptability criteria- owing to the very low apparent densities of the IPs produced by combining EA and Al powder, their acoustical properties were also ascertained. The absorptive properties of porous IPs were determined using a Kundt tube as prescribed by ISO 105342 and ASTM E1050. This direct incidence methodology allows to collect a simple numerical index (noise reduction coefficient, NRC) that quantifies the general sound-absorbing efficiency of a certain material. In addition, the Kundt method also provides information on the absorptive properties as a function of frequency which can be drastically altered even if similar NRC are maintained.

All the IPs tested present reasonable sound absorptive capacity as the sound absorption coefficient (α) was almost always greater than 0.2 across the spectrum of frequencies tested (Figure 4.5.16). Moreover, all the IPs presented NRC values greater than 0.33, being the maximum value reached by 10_E10_A2 (0.46). These NRC values are considerably higher than those reported for OPC-concrete with 100% replacement of course aggregates by rubber crumb (0.07) or fibers covered with crumb rubber (0.24) (Medina, 2016) and in line with cork-containing mortars (up to 0.53) (Tavasci, 2017). Along with the reduced apparent density and highly porous structures of the developed materials, the nanoscale porosity intrinsic to all IPs is known to provide an effective sound barrier through which sound waves cannot pass (Gandoman, 2015). Nonetheless, the compositional differences between the samples were also explicit in their acoustical profile. All mixtures presented a peak of absorption located in the low-frequency region between 280 and 320 Hz. The absorption coefficients of this peak varied from 0.90-0.95 in IPs produced with a lower EA dosage, while in IPs with higher EA dosage did not surpass 0.6. A second absorption peak was observed at higher frequencies between 1000 and 1040 Hz in 13_E10_A2 and 115_E10_A2 IPs. The absorption coefficient of this peak was higher in 13_E10_A2 almost reaching the value of 1. Further differences between these two IPs could be observed in the 360-760 Hz region where 115_E15_A2 presented better absorption capacity. The differences in the acoustical profile cannot be simply attributed to the different compactness of their structures as those IPs present similar dry apparent density values, 0.36 and 0.37 g/cm^3, respectively. Therefore, the location and magnitude of sound absorption peaks should arise from microstructural differences imposed by the mixture design. Increasing the mixture solid content seems to favor higher absorption coefficients in narrow regions of the spectrum, while increased EA dosages had a more generalized positive effect in a broader frequencies' region.

However, the acoustic profile was completely modified when combining low S/L ratio and EA dosages. The absorption peak located in the low-frequency region was maintained at values higher than 0.9 but slightly translated towards lower frequencies. At higher frequencies, the absorption coefficient progressively rose from 0.20 to near 1.0 at 880 Hz and maintained on similarly elevated levels until 1160 Hz. Afterward, the sound absorption coefficient decreased to 0.7 at 1500 Hz. Reducing the apparent density is known to have a positive effect on sound absorptive properties (Gandoman, 2015; Gao, 2017) and therefore a generally better acoustic performance could be expected in 10_E10_A2 (ρ_{dry} = 0.27 g/m^3). Such could be also observed by the highest NRC of those IPs (0.46). Further investigations remain necessary to thoroughly understand the combined effects of low S/L and EA dosage on IPs sound absorptive capacity but the acoustic performance of 10_E10_A2 in the medium frequencies' region- which is generally defined between 500 to 1500 Hz- is promising in terms of acoustic insulation for dwellings. The elevated sound absorption of 10_E10_A2 in this region makes possible to foresee that the produced IPs can constitute a dual-propose building solution that is simultaneously able to provide excellent thermal and acoustic insulation.

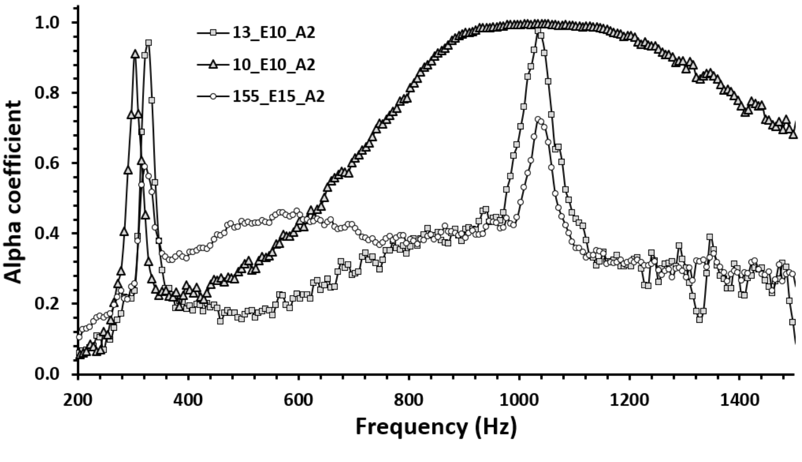

Figure 4.5.16 Representative acoustic absorption of oven-dried IPs produced with Al powder, air-entraining and foam stabilizer agents.

4.5.2 Development of lightweight inorganic polymers

Design of experiment

A different method to produced IPs with good thermal insulating properties is to incorporate lightweight aggregates into their mixture design. As shown in 4.4, such approach has been attempted by several authors who used perlite (Vaou, 2010), vermiculite (Medri, 2015), expanded glass aggregates (Palmero, 2015; Huiskes, 2016), extruded or expanded polystyrene (Colangelo, 2018; Kakali, 2018), cork granules (Roper, 2017; Novais, 2019) and rubber scraps (Wang, 2019) as coarse aggregates to produced lightweight composites. The used of small-scale aggregates as cenospheres and hollow glass microspheres has also been attempted (Nematollhi, 2017; Lu, 2019; Hajimohammadi, 2019). The latter approach was followed in this work and the effectiveness of the use of hollow glass microspheres (MLWA) as small size aggregates were evaluated.

The same parent binder used throughout foaming experiments (K7) was used as a reference to produce these lightweight IPs. The particle size distribution of the hollow glass microspheres used is shown in Figure 45.17. Due to the reduced particle size of MLWA, an additional amount of water was supplied in order to compensate for the loss of flowability. The effects MLWA dosage and added water on the physical and mechanical properties, and thermal conductivity of the produced lightweight materials were evaluated. All binders were produced following the procedure described in 4.5.1 being employed 2 extra minutes to mix the MLWA. The IPs were cured during 72 h in a moist curing chamber at 20±1 °C and 95±1 %HR, being afterward demolded and kept at room conditions. The IPs were coded after their K7/MLWA mass ratio and the final S/L ratio (accounting with extra water added). For instance, M5_95 stands for formulations where the added mass of MLWA was five times less than the mass of K7, and the recalculated S/L ratio of the binder was 0.95. The IPs mixture portions are given in Table 4.5.13.

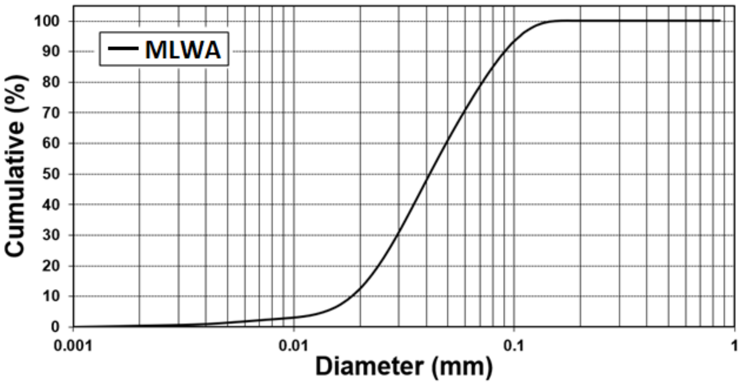

Figure 4.5.17 Particle size distribution of hollow glass microspheres (MLWA).

Table 4.5.13 Mixture design of lightweight inorganic polymers (by mass %).

	Mixture portion (wt%)					
Code	**Slag**	**Silica fume**	**KOH (14M)**	**H_2O**	**Added H_2O**	**MLWA**
K7	52.40	4.10	18.15	25.35	0.00	0.00
M5_75					31.81	20.00
M5_85					22.97	20.00
M5_95					16.02	20.00
M6_95					16.02	16.67
M7_95					16.02	14.29

Strength development

The 28 d flexural and compressive strength of the lightweight IPs is shown in Figure 4.5.18. The deleterious effect of MLWA was clearly visible on the mechanical performance of the produced IPs. Independently of the conditions used, MLWA addition provoked a roughly three-fold reduction of compressive strength, while a less severe negative impact was seen on flexural strength. Nonetheless, all IPs were nearly compliant with the 4 MPa threshold defined in the first acceptability criteria. The comparable mechanical properties of all MLWA-containing IPs indicated that, within the experimental conditions tested here, the presence of MLWA determined the mechanical properties of lightweight IPs. Such considerations are in line with the findings of the historical PCA discussed in 4.4, which indicated a significant loss of strength when lightweight aggregates were added to the IPs mix design.

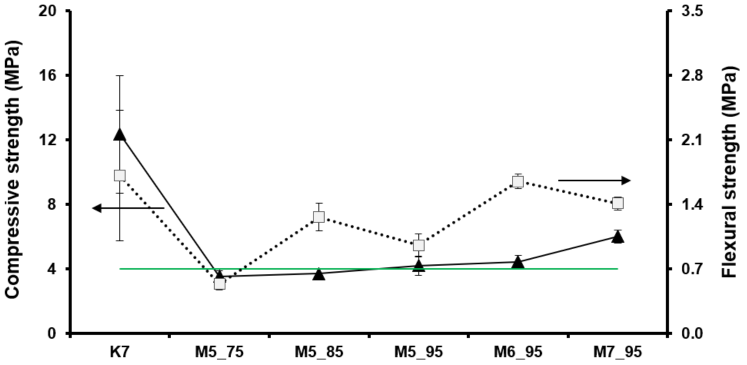

Figure 4.5.18 Compressive and flexural strength of lightweight inorganic polymers. The green line marks the threshold in which above lightweight IPs meet the defined acceptability criteria in terms of compressive strength. The lines between samples are drawn as a guide to the eye.

Unlikely foamed IPs where the nature and dosage of the foaming agents influence the structural assemblage of the gels formed (Hajimohammadi, 2017b), in the case of MLWA such is not expected on a significant scale. Hence, the impacts MLWA on strength development are most likely related to the inferior capacity of lightweight aggregates to endure mechanical loads and to the formation of fragile interfacial transition zones. As so, and considering the compositional differences between the samples produced, it could be anticipated that increase the solid content in the binders and reducing the dosage of lightweight aggregates would raise strength values. Such an assumption was experimental verified as can be seen in Figure 4.5.18.

Apparent density

The apparent density of MLWA-containing IPs followed a similar trend to strength development. In IPs with equal MLWA dosage, apparent density rose from 0.62 to 0.68 g/cm^3 as the amount of added water decreased (Table 4.5.14). A further increase of apparent density was observed by reducing MLWA in mix design, being maximum of value reached by M7_95 IPs (0.79 g/cm^3). The apparent density of all MLWA-containing IPs was reduced upon oven drying between 10 and 15%. Such considerable mass loss after 28 d of curing suggests that MLWA promoted the retention of water within the structures, which in turn, can have resulted in more progressive and less aggressive drying processes. In fact, crack or other visible defects were not formed on the surfaces of MLWA-containing IPs during curing as shown in Figure 4.5.19.

Table 4.5.14 Apparent and oven-dry apparent density of lightweight inorganic polymers after 28 d of curing.

Code	Apparent density 28 d (g/cm^3)	Dry apparent density 28 d (g/cm^3)
K7	1.56±0.01	1.55±0.01
M5_75	0.62±0.03	0.56±0.03
M5_85	0.66±0.03	0.57±0.03
M5_95	0.68±0.02	0.58±0.02
M6_95	0.73±0.01	0.64±0.03
M7_95	0.79±0.03	0.69±0.03

Figure 4.5.19 Lightweight alkali-activated materials produced with hollow glass spheres.

Assuming that the effects of MLWA are almost exclusively physical, then direct correlations between IPs' physical properties can be also expected. The correlation between apparent density and compressive strength are shown in Figure 4.5.20. Such correlation can be well-described by a linear equation. The relative low slope of the trend line implies that in order to achieve a further decrease of density a significant portion of compressive strength needs to be sacrificed. However, three of the five formulations tested were able to produce IPs within the limits of the criteria of acceptability in terms of density and compressive strength. Those samples corresponded to the formulations with the highest solid loads, namely M5_95, M6_95, and M7_95.

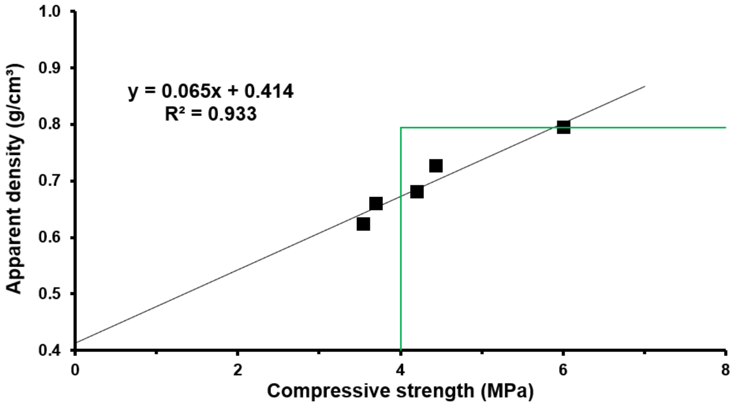

Figure 4.5.20 Compressive strength of lightweight IPs as a function of apparent density. The green lines mark the thresholds limits of the first acceptability criteria in terms of apparent density and compressive strength.

Thermal properties

The thermal properties of MLWA-containing IPs were assessed following the same procedure as in the case of foamed IPs. No significant differences were found between the top and bottom surfaces of the samples in terms of thermal conductivity, specific heat capacity and thermal diffusivity measurements, which indicates a homogeneous dispersion of MLWA within the alkali-activated binder. Hence, the average thermal conductivity, specific heat capacity, and thermal diffusivity values were considered representative and are shown in Table 4.5.15.

Table 4.5.15 Average thermal properties of lightweight AAMs produced hollow glass spheres after 28 d of curing.

Code	λ 28 d (w/m°K)	Dry λ 28 d (w/m°K)	cp 28 d ($J/m^3\cdot°K$)	Dry cp 28 d ($J/m^3\cdot°K$)	a 28 d (m^2/s)	Dry a 28 d (m^2/s)
K7	0.457	0.275	$1.6\cdot10^6$	$1.2\cdot10^6$	$2.9\cdot10^{-7}$	$2.3\cdot10^{-7}$
M5_75	0.098	0.077	$4.9\cdot10^5$	$3.7\cdot10^5$	$2.0\cdot10^{-7}$	$2.1\cdot10^{-7}$
M5_85	0.120	0.083	$3.2\cdot10^6$	$4.1\cdot10^5$	$2.1\cdot10^{-7}$	$2.1\cdot10^{-7}$
M5_95	0.124	0.088	$3.4\cdot10^6$	$4.4\cdot10^5$	$2.0\cdot10^{-7}$	$2.0\cdot10^{-7}$
M6_95	0.140	0.097	$3.3\cdot10^6$	$4.8\cdot10^5$	$2.2\cdot10^{-7}$	$2.0\cdot10^{-7}$
M7_95	0.164	0.107	$3.5\cdot10^6$	$4.8\cdot10^5$	$2.6\cdot10^{-7}$	$2.3\cdot10^{-7}$

After 28 d of curing, the thermal conductivity MLWA- containing IPs ranged from 0.098 to 0.164 W/m°K, representing a 64-79% reduction relative to the parent binder. Among MLWA-containing IPs, increasing the binder solid load rose thermal conductivity values from 0.098 to 0.124 W/m°K, while a further increment was promoted by increasing binder portion in the mix design, from 0.124 to 0.164 W/m°K. Conversely, the lowest thermal conductivity values were reached by combining high MLWA dosages and altering the parent binder formulation with significant water dosages.

Like the reduction observed in apparent density values, thermal conductivity was also significantly reduced upon drying, between 21 and 35 %. The highest reduction was observed in M7_95, which suggests that increasing binder dosages had difficult water evaporation during the initial 28 d of curing. A similar decrease was also observed in terms of specific heat capacity and thermal diffusivity, who in dried IPs varied between $3.7\cdot10^5$- $4.8\cdot10^5$ $J/m^3\cdot°K$, and $2.0\cdot10^{-7}$-$2.3\cdot10^{-7}$ m^2/s, respectively. The maximum reduction of specific heat capacity (70 %) and thermal diffusivity (8 %) relative to the dried parent binder was observed in M5_75 samples.

Figure 4.5.21 shows the thermal conductivity of lightweight IPs as a function of apparent density. The data corresponding to the reference binder is not included here.

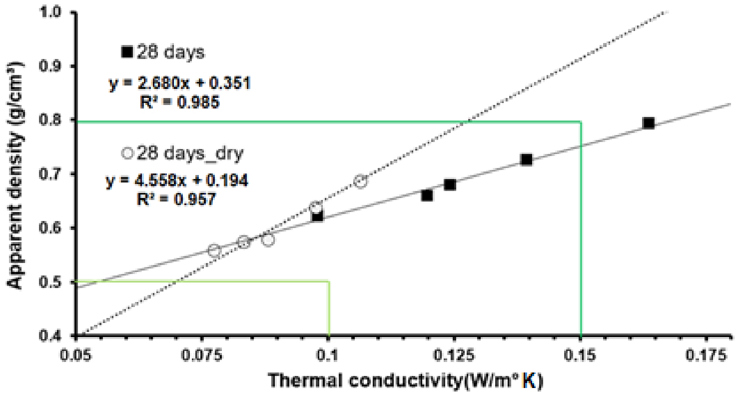

Figure 4.5.21 Thermal conductivity of lightweight IPs as a function of apparent density. The green lines mark the thresholds limits defined in the acceptability criteria in terms of apparent density and thermal conductivity. The lightest green color defines the most stringent insulating criteria.

In general, thermal conductivity values were reduced with the decrease of apparent density. Such correlations are in line with mainstream literature and can be well described by linear equations. Yet, all mixtures comprising both room-cured and oven-dried samples presented apparent densities ranging from 0.56 to 0.79 g/cm^3. The IPs' thermal insulation performance was enhanced after removing the excess of free-water from their structures, making thermal conductivity values varying from 0.077 to 0.107 W/m°K. The relocation of thermal conductivity to lower values can be attributed to the highly conductive nature of water previously present in IPs structure (Panias, 2015). These reduced thermal conductivity values are largely below the 0.150 W/m°K threshold defined in the first acceptability criteria and when considering also strength requirements (>4 MPa), it can be seen that M5_95 and M6_95 were compliant with all the first acceptability criteria. Therefore, a good compromise solution between reasonable compressive strength and low density and thermal conductivity values was reached when MLWA dosage did not surpass 20 wt% of the original binder and the amount of added water to compensate the loss of flowability did not reduce the binder's final S/L ratio to values under 0.95.

Oven-dried M5 mixtures with densities ranging from 0.56-0.58 g/cm^3 presented the lowest thermal conductivity values, being the minimum value reached by M5_75 samples (0.077 W/m°K). These reduced thermal conductivity values largely surpassed even the most demanding acceptability criteria (<0.100 W/m°K) but all IPs have failed to reach apparent density values below 0.5 g/cm^3.

From the findings above it can be foreseen that further reducing apparent density would require to increase MLWA dosage or reduce the mixtures' solid content. Equally expected would be the extremely fragile nature of the IPs produced, as can be predicted from the linear relations observed in Figure 4.5.20. Despite strength development only being a limiting factor within the apparent density range defined in the first criteria of acceptability (0.50 to 0.80 g/cm^3), the formulations presented here seem to be near the boundary's conditions in which a viable binding material is formed. In fact, mixtures with higher MLWA dosage (M4_95) and lower solid content (M5_65) were attempted but could not be demolded after 24 h of curing. Despite those two mixture designs had equally failed to produce stable IPs structures, different causes can be pointed out. On one hand, the deleterious effects of increasing MLWA dosage can be attributed to the reduced availability and excessive dispersion of binding phases in the systems, while on the other hand, reducing the binders solid load by supplying an additional amount of water had decreased the concentration of the dispersion and reduced the pH of the alkaline solution, winch in turn, had prevented the precursors dissolution and reorganization into stable binding phases. Without modifying S/L ratio, the mixture design could have been easily tailored to promote higher strength developments by introducing silicates species in the activating solution. Apart from the negative economic and environmental impact of this approach, it was previously shown in 3.3 that IPs produced with a mixture of potassium silicates and hydroxides in the activating solutions present higher densities than their hydroxide-only counterparts. Therefore, the introduction of silicates species may have favored the formation of more binding phases and produced stable IPs but will most likely fail in delivering lightweight materials with densities lower than 0.50 g/cm^3. Further modifications of the solid precursor's chemical composition and, processing and curing parameters have not been attempted but should be explored in future works.

As general conclusion of these experiments it can be said that within the experimental range defined increasing the solid content and/or reduce the dosage of MLWA promoted the formation of binding phases in the systems and therefore resulted in higher strength developments, while reducing the dosage of lightweight aggregates or increase the formulation solid content limited the thermal insulating performance of the developed materials. By investigating the effects of MLWA dosage in binders with different solid contents, insights were provided concerning how strength, density, and thermal conductivity vary within the limits studied. Based on the insights gathered IPs compliant with demanding insulating requirements were produced. Despite the developed lightweight IPs presenting slightly higher density and thermal conductivity values than the porous IPs previously described in 4.5, their enhanced mechanical features will allow their use in applications where some resistance to mechanical loads is required. Moreover, the production process and the parameters affecting the properties of lightweight IPs are relatively simpler to control than the ones involved in the production of porous IPs. Such technical advantages may well be overlooked when considering the large-scale industrial production of lightweight IPs, as the cost of the MLWA used here (around 10 €/kg) may justify the choice of rather complex mix designs. Apart from economic and technical considerations, the results have demonstrated that lightweight CaO-FeO_x-Al_2O_3-SiO_2 AAMs with excellent insulation properties can be produced using hollow glass spheres as small-size lightweight aggregates. Future investigations should be dedicated to further optimize the specific strength and thermal conductivity of the developed products, and to seek more viable and ecological alternatives to hollow glass spheres as can be the case of cenospheres.

4.6 Final considerations

In this section, the possibility of producing highly performant thermal insulation materials by alkali activating $CaO-FeO_x-Al_2O_3-SiO_2$ residues was evaluated. A historical analysis of the existing literature on alkali-activated insulating materials was performed and used to identify the most promising processing routes. Based on such assessment pre-made foams, in-situ foaming agents and lightweight aggregates were used to produce a myriad of porous and lightweight IPs from $CaO-FeO_x-Al_2O_3-SiO_2$-rich precursors with different technical properties. Before and furthermost it was found that each processing route has its own specific processing parameters that need to be carefully selected in order to produce highly performant insulating materials.

Preliminary trials have shown that pre-foams produced relatively dense IPs (<0.69 g/cm^3) but with fragile structures. The considerable amount of water introduced in the systems by water-based foams has a severely detrimental impact on strength development. As to achieve lower apparent densities higher foam dosages were required, such processing route was considered inadequate for the $CaO-FeO_x-Al_2O_3-SiO_2$-rich binders developed here and disregarded from further testing. All the remaining processing routes were able to provide IPs with reduced density and efficient thermal conductivity. Figure 4.5.22 and 4.5.23 show the apparent density of the developed porous and lightweight IPs as a function of compressive strength and thermal conductivity, respectively. Comparable results used during the historical analysis were included here for direct comparison.

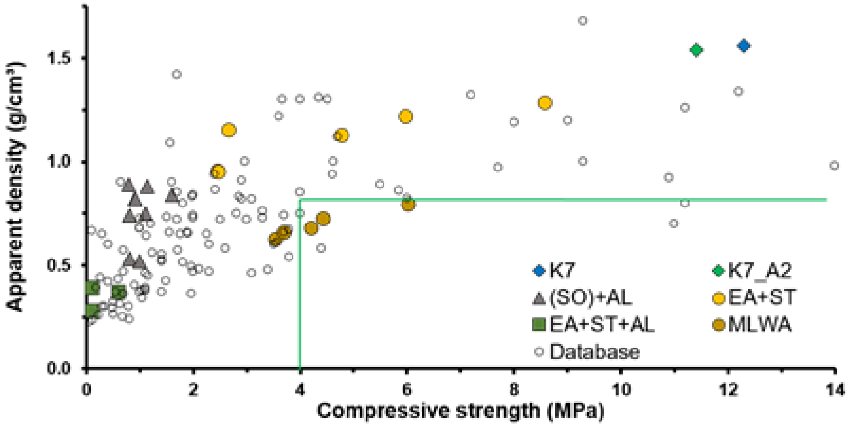

Figure 4.5.22 Compressive strength of porous and lightweight IPs as a function of apparent density. The green lines mark the thresholds limits of acceptability criteria. For comparison purposes, data points used during historical PCA are also given being represented by unfilled circular dots.

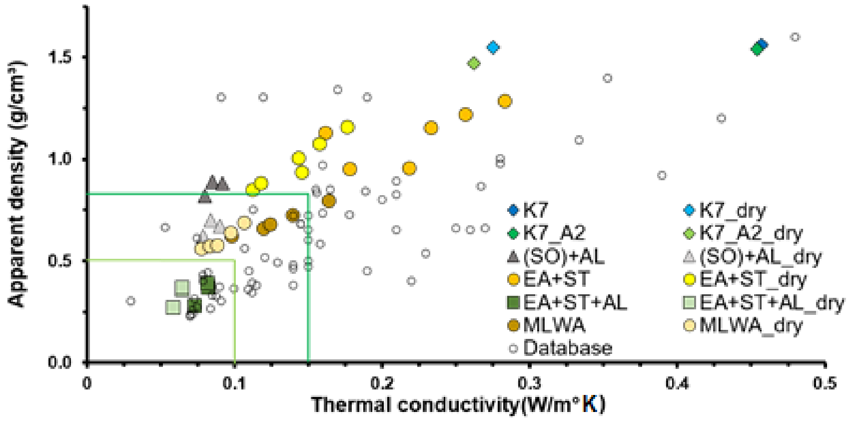

Figure 4.5.23 Thermal conductivity of porous and lightweight IPs as a function of apparent density. The green lines mark the thresholds limits of acceptability. For comparison purposes, some data points used during historical PCA are also given being represented by unfilled circular dots.

As can be seen, the use of microspheres as small-size lightweight aggregates were the only processing route able to provide IPs compliant with all requirements defined in the first acceptability criteria. After 28 d of curing, three of the formulations tested were able to deliver IPs with a compressive strength that exceeded 4 MPa and apparent density and thermal conductivity values lower than 0.80 g/cm^3 and 0.15 W/m°K, respectively. Such strength development required to limit the water dosage added to the parent binder, which however did not have a significant reflection on apparent density and thermal conductivity. Imposing a drying period at slightly elevated temperatures further reduced the apparent density of MLWA-containing samples nearly reaching the most stringent criteria defined 0.50 g/cm^3. Thermal conductivity values lower than 0.10 W/m°K were also achieved when applying such a drying period. As these solutions possess enough compressive strength to be considered for structural purposes, they can be proposed as a waste-based highly performant alternative to conventionally used materials in buildings' envelopes. Figure 4.5.24 shows the thermal transmittance as a function of the wall thickness of the developed MLWA-containing formulations.

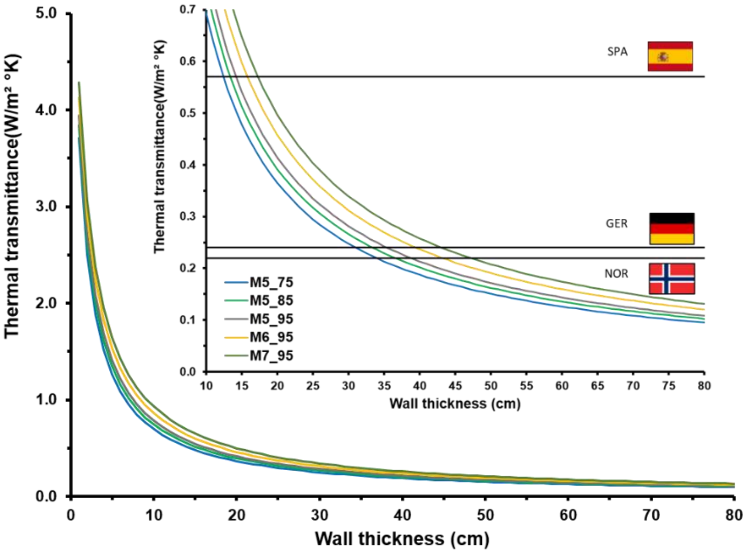

Figure 4.5.24 Dry thermal transmittance of lightweight inorganic polymers as a function of wall thickness. The insert figure shows a close-up and the thermal transmittance specifications in some EU countries.

As can be seen, the variation of thermal transmittance is defined by two distinct regimes. In the first regime, meaning walls with a thickness inferior to 10 cm, thermal transmittance rapidly declines when the wall thickness increases. Considering a 10 cm wall, the thermal transmittance varies from 0.70 to 0.93 W/m^2 °K according to the thermal conductivity of each MLWA-containing IPs as shown in Table 4.5.15. However, independently of the formulation used, all walls with a thickness inferior to 10 cm failed to surpass the minimum values of thermal transmittance defined in EU national constructions codes. Even when considering the EU less demanding specifications, as in the case of the Spanish regulation, the minimum wall thickness required to surpass the legal threshold imposed is 15 cm for M5_95 and M6_95 formulations, and 18 in the case of M7_95. When considering M5_75 and M5_85 IPs the minimum wall thickness required slightly decreases (13 and 14 cm, respectively) but such IPs were not compliant with the compressive strength criteria previously set.

In the second part of the thermal transmittance curve, it can be seen that the beneficial impact of increasing the wall thickness became much more progressive, hence reinforcing the relevance of the thermal properties intrinsic to the developed materials. In this regime, reductions on thermal conductivity values have a tremendous influence on the minimum wall thickness required to be compliant with national specifications. Considering the most demanding constructions codes in terms of thermal transmittance enforced in the EU zone, e.g. Norway, where thermal transmittance should not surpass 0.22 W/m^2 °K- the minimum thickness required to walls constructed with M7_95 is 48 cm, while in the case of M5_95 only 39 cm would be required. The approximately 22% higher thermal conductivity value of M7_95 had an equal correspondence in terms of the minimum wall thickness required (+23%). To achieve similar thermal transmittance values, the M6_95 formulation would require an intermediate thickness of 44 cm, which corresponds to a 10% increase relatively to M5_95. When considering the thermal transmittance limits enforced in the largest EU market (Germany, <0.24 W/m^2 °K), such thickness can be further reduced to 36, 40 and 44 cm, respectively.

Despite that M5_75 and M5_85 IPs did not present enough strength development to be compliant with the defined 4 MPa threshold (3.5 and 3.7 MPa, respectively), it would be advisable to consider their application into buildings' envelopes according to Figure 4.5.24. The minimal thermal conductivity presented by M5_75 (0.077 W/m°K) would allow being compliant with the Norwegian and German construction codes using only 34 and 32 cm walls, respectively. Strategies to enhance the strength development in those formulations and surpass the 4 MPa threshold may include an initial period of curing at a slightly elevated temperature similar to those imposed on pre- and in-situ foaming samples.

The different insulation potential between the IPs developed according to different processing routes can be seen in Figure 4.5.25. For a clear comparison, only IPs that presented the lowest thermal conductivity values per processing route were included here. Considering exclusively insulation performance it can be seen that porous IPs produced with air-entraining and stabilizing agents are clearly not competitive. A 50 cm wall would be necessary to compliant with Norwegian construction codes in terms of thermal transmittance, while equal performance can be achieved with less than 35 cm using other processing routes. The combined use of Al-powder, air-entraining and stabilizing agents were able to deliver IPs with the lowest thermal transmittance being only required 26 cm to be compliant with the most stringent EU construction codes. However, the low mechanical resistance of this type of solution prevents their use for structural purposes and therefore cannot be directly compared with MLWA-containing IPs. Despite the lower wall thickness required, the higher dosages of additives and activating solutions required should be also considered as it will increase the production cost and environmental impacts of such mixture designs.

MLWA-containing IPs were the only products that could satisfy structural requirements. However, due to the high costs involved in their production, it was considered appropriate to alter the concept of the solutions proposed. The production of multilayer sandwich panels that intercalate a large insulating layer in between two thin dense layers intended to produce biphasic construction elements that simultaneously present high mechanical resistance and low density and thermal transmittance. Based on the observations previously made regarding IPs insulation and mechanical performance, environmental impacts, and production costs, 27SOAL formulation was selected to be used as the insulation section of multilayer panels. The detail description of such formulation can be found in 4.5.1, while the production of multilayer panels is later presented in a dedicated section.

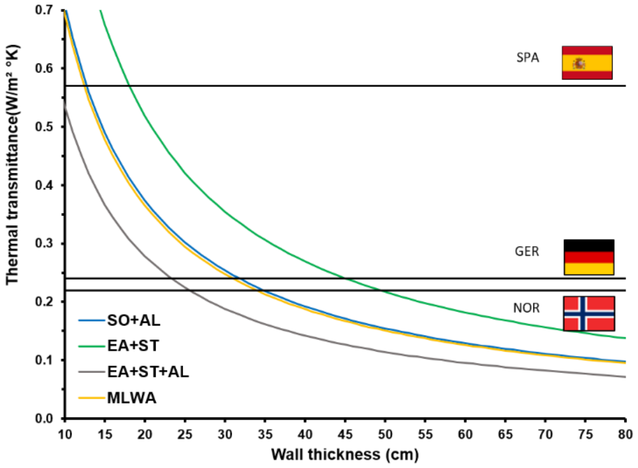

Figure 4.5.25 Dry thermal transmittance of porous and lightweight IPs as a function of wall thickness according to different processing routes.

References

Ascensão, G., Seabra, M. P., Aguiar, J. B., & Labrincha, J. A. (2017). Red mud-based geopolymers with tailored alkali diffusion properties and pH buffering ability. Journal of cleaner production, *148*, 23-30. https://doi.org/10.1016/j.jclepro.2017.01.150

ASTM E1050 Impedance and Absorbtion of Acoustical Materials Using A Tube, Two Microphones and a Digital Frequency Analysis System.

Colangelo, F., Roviello, G., Ricciotti, L., Ferrándiz-Mas, V., Messina, F., Ferone, C., & Cheeseman, C. R. (2018). Mechanical and thermal properties of lightweight geopolymer composites. Cement and Concrete Composites, 86, 266-272. https://doi.org/10.1016/j.cemconcomp.2017.11.016

Bai, C., & Colombo, P. (2018). Processing, properties and applications of highly porous geopolymers: a review. *Ceramics International*, *44*(14), 16103-16118. https://doi.org/10.1016/j.ceramint.2018.05.219

Denissen, J., Kriskova, L., & Pontikes, Y. (2019). Kinetics of pore formation and resulting properties of lightweight inorganic polymers. Journal of the American Ceramic Society. https://doi.org/10.1111/jace.16301

EN 196-1:2016- Methods of testing cement - Determination of strength.

EN ISO 105342, 2001: Determination of sound absorption coefficient and impedance in impedance tubes- part 2 Transfer-function method. CEN, Brussels.

Gandoman, M., & Kokabi, M. (2015). Sound barrier properties of sustainable waste rubber/geopolymer concretes. *Iranian Polymer Journal*, *24*(2), 105-112. https://doi.org/10.1007/s13726-014-0304-1

Gao, X. (2017). Alkali activated slag-fly ash binders: design, modeling and application. https://research.tue.nl/en/publications/alkali-activated-slag-fly-ash-binders-design-modeling-and-applica

Hajimohammadi, A., Ngo, T., & Mendis, P. (2017b). How does aluminium foaming agent impact the geopolymer formation mechanism?. Cement and Concrete Composites, 80, 277-286. https://doi.org/10.1016/j.cemconcomp.2017.03.022

Hajimohammadi, A., Ngo, T., Provis, J. L., Kim, T., & Vongsvivut, J. (2019). High strength/density ratio in a syntactic foam made from one-part mix geopolymer and cenospheres. *Composites Part B: Engineering*, *173*, 106908. https://doi.org/10.1016/j.compositesb.2019.106908

Hertel, T., Blanpain, B., & Pontikes, Y. (2016). A proposal for a 100% use of bauxite residue towards inorganic polymer mortar. Journal of Sustainable Metallurgy, 2(4), 394-404, https://doi.org/10.1007/s40831-016-0080-6

Hertel, T., Novais, R. M., Alarcón, R. M., Labrincha, J. A., & Pontikes, Y. (2019). Use of modified bauxite residue-based porous inorganic polymer monoliths as adsorbents of methylene blue. *Journal of Cleaner Production*, *227*, 877-889. https://doi.org/10.1016/j.jclepro.2019.04.084

Huiskes, D. M. A., Keulen, A., Yu, Q. L., & Brouwers, H. J. H. (2016). Design and performance evaluation of ultra-lightweight geopolymer concrete. Materials & Design, 89, 516-526. https://doi.org/10.1016/j.matdes.2015.09.167

Kakali, G., Kioupis, D., Skaropoulou, A., & Tsivilis, S. (2018). Lightweight geopolymer composites as structural elements with improved insulation capacity. In *MATEC Web of Conferences* (Vol. 149, p. 01042). EDP https://doi.org/10.1051/matecconf/201814901042

Liu, Y., Yan, C., Zhang, Z., Gong, Y., Wang, H., & Qiu, X. (2016). A facile method for preparation of floatable and permeable fly ash-based geopolymer block. *Materials Letters*, 185, 370-373 https://doi.org/10.1016/j.matlet.2016.09.044

Lu, B., Qian, Y., Li, M., Weng, Y., Leong, K. F., Tan, M. J., & Qian, S. (2019). Designing spray-based 3D printable cementitious materials with fly ash cenosphere and air entraining agent. Construction and Building Materials, 211, 1073-1084. https://doi.org/10.1016/j.conbuildmat.2019.03.186

Medina, N. F., Flores-Medina, D., & Hernández-Olivares, F. (2016). Influence of fibers partially coated with rubber from tire recycling as aggregate on the acoustical properties of rubberized concrete. Construction and building Materials, 129, 25-36. https://doi.org/10.1016/j.conbuildmat.2016.11.007

Medri, V., Papa, E., Mazzocchi, M., Laghi, L., Morganti, M., Francisconi, J., & Landi, E. (2015). Production and characterization of lightweight vermiculite/geopolymer-based panels. Materials & Design, 85, 266-274. https://doi.org/10.1016/j.matdes.2015.06.145

Nematollahi, B., Ranade, R., Sanjayan, J., & Ramakrishnan, S. (2017). Thermal and mechanical properties of sustainable lightweight strain hardening geopolymer composites. Archives of Civil and Mechanical Engineering, 17(1), 55-64. https://doi.org/10.1016/j.acme.2016.08.002

Novais, R. M., Ascensão, G., Ferreira, N., Seabra, M. P., & Labrincha, J. A. (2018b). Influence of water and aluminium powder content on the properties of waste-containing geopolymer foams. *Ceramics International*, *44*(6), 6242-6249. https://doi.org/10.1016/j.ceramint.2018.01.009

Novais, R. M., Carvalheiras, J., Seabra, M. P., Pullar, R. C., & Labrincha, J. A. (2019). Red mud-based inorganic polymer spheres bulk-type adsorbents and pH regulators. *Materials Today*. https://doi.org/10.1016/j.mattod.2019.01.014

Palmero, P., Formia, A., Antonaci, P., Brini, S., & Tulliani, J. M. (2015). Geopolymer technology for application-oriented dense and lightened materials. Elaboration and characterization. Ceram. International, 41(10), 12967-12979. https://doi.org/10.1016/j.ceramint.2015.06.140

Panias, D., Balomenos, E., & Sakkas, K. (2015). The fire resistance of alkali-activated cement-based concrete binders. In F. Pacheco-Torgal, J.A. Labrincha, C. Leonelli, A. Palomo, P. Chindaprasirt, Handbook of Alkali-activated Cements, Mortars and Concretes (pp. 423-461). Woodhead Publishing. https://doi.org/10.1533/9781782422884.3.423

Roper, D. S., Kutyla, G. P., & Kriven, W. M. (2017, January). Properties of cork particle reinforced sodium geopolymer composites. In Developments in Strategic Ceramic Materials II: A Collection of Papers Presented at the 40th International Conference on Advanced Ceramics and Composites, January 24-29, 2016, Daytona Beach, Florida (Vol. 36, No. 7, p. 79). John Wiley & Sons. https://doi.org/10.1002/9781119321811.ch8

Tavasci, P. (2017) Technical Report 17RE00048- Vibration and noise absorbent concretes, OB1: Know how development on sound absorbing concrete for outdoor and indoor applications.

Vaou, V., & Panias, D. (2010). Thermal insulating foamy geopolymers from perlite. *Minerals Engineering*, *23*(14), 1146-1151. https://doi.org/10.1016/j.mineng.2010.07.015

Wang, R., Gao, P., Tian, M., & Dai, Y. (2019). Experimental study on mechanical and waterproof performance of lightweight foamed concrete mixed with crumb rubber. Construction and Building Materials, 209, 655-664. https://doi.org/10.1016/j.conbuildmat.2019.03.157

Chapter 5

Functionalization of building materials

The adoption of a multi-layer geometry made possible to consider the functionalization of the thin outer layers of panels, otherwise economically unreasonable if considering the entire wall section. The following section will describe the incorporation of phase change material into the mixture design of dense IP mortars as an attempt to provide a thermal regulating function to the external layers of biphasic panels. A comprehensive bibliographic review was firstly performed on thermal storage systems with particular emphasis being given to latent heat storage systems and the use of phase change materials in building materials. Chapter 5 is entirely based on unpublished data that is firstly discussed here.

5.1 Thermal storage systems

The concept of thermal comfort encompasses a strong personal component and construction codes only aim to define an acceptable thermal gradient representative of general comfort conditions. To be compliant with such comfort conditions, heating or cooling (or both) are employed often coupled with ventilation systems (HVAC). The operative time and cost of these types of solutions vary according to the necessities of each specific building, but the energy consumption of HVAC systems accounts for around half of the energy used in buildings and 10–20% of total national energy consumption in developed countries (Pérez-Lombard, 2008). As HVAC systems utilize these considerable amounts of energy, they also pose significant challenges for the energy supply grid, especially in peak energy load time (Boyle, 2004) In addition, these systems also have significant deleterious environmental impacts and can represent potential risks for public health; namely by allowing the entrance and proliferation of external pollutants and contaminants, bacteria, fungi or due to their own degradation when deficient maintenance is provided. In the next few decades, the expected population growth and the consequent expansion of the built area, the increase of indoor occupation time and the provision of ever-higher comfort standards, are expected to exacerbate these problematics. Thus, the development of alternative energy solutions is considered a pressing matter. Thermal energy storage (TES) systems can be used to replace or at least minimize the operative time of HVAC systems (Cabeza, 2007) while simultaneously transferring operative periods to segments of the day where energy costs are significantly lower (Khudhair, 2004). TES systems use energy surpluses and shortages to absorb and release energy and, in this way, guarantee proper comfort levels, offering energy-saving and offset energy peak loads (Zeinelabdein, 2018). Combining thermal energy storage (TES) systems with proper insulation of the building envelope can contribute to minimize energy consumption and help to achieve near-zero energy buildings. The concept of combining insulant and thermal responsive materials in biphasic panels was the underlying motivation to the IP products developed in this chapter.

Thermal energy storage systems can be designed based on physical or chemical processes. In the case of TES based on chemical processes, termed as thermochemical energy systems (TCES), the energy absorbed and released is originated during the dissociation and synthesis of chemical compounds in reversible reactions (Zeinelabdein, 2018). These types of systems are characterized by high energy densities, a wide range of operative temperatures, stable storage, and easy transportation (Ding, 2012; Kalaiselvam, 2014). These positive features are, however, accompanied by low heat transfer in high-density conditions, generally elevated costs, and lack of long-term performance examinations (Kalaiselvam, 2014). Table 5.1.1 shows a comparison of capacity, power, efficiency, and costs between thermochemical, latent and sensible heat-based systems. Thermochemical energy systems provide higher energy storage density but present higher investment costs compared to latent and sensible heat storage systems. In fact, economic factors are frequently the limiting factor and primary constraint for TCES wider use (Abedin, 2011).

Table 5.1.1 Performance comparison between thermal storage systems (Hauer *et al.*, 2011).

Thermal system	Capacity (kW h/t)	Power (MW)	Efficiency (%)	Cost (€/k W h)
Sensible heat	10-50	0.001-10	50-90	0.1-10
Latent heat	50-150	0.001-1	75-90	10-50
Thermochemical heat	120-250	0.01-1	75-100	8-100

In systems based on sensible and latent heat, energy transfers occur due to the accumulation and release of sensible (sensible heat storage, SHS) or latent heat (latent heat storage, LHS). Figure 5.1.1 shows the variation of sensible and latent heat storage as a function of temperature.

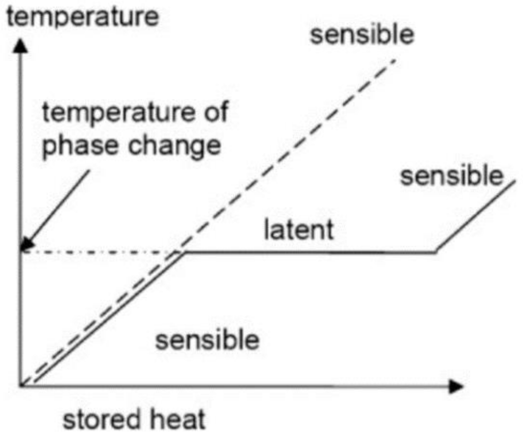

Figure 5.1.1 Schematic representation of sensible and latent heat storage as a function of temperature (Zeinelabdein *et al.*, 2018).

In traditional constructions, thermal energy storage is frequently achieved by increasing the thermal mass of building components. This construction technique can be seen as an SHS system where total storage capacity is increased by raising the volume of material. In SHS systems no phase changes occur, and heat capacity is given by the ratio between heat stored and the temperature gradient (Zhang, 2016). Liquids (e.g. water), oils, and solid (e.g. metal, rocks) materials can be used in SHS, being water one of the common substances with high volumetric heat capacity (4182 kJ/m^3 K). In Table 5.1.2 the thermal properties of some common building materials are given for comparison. As one can see, ordinary construction materials present limited volumetric heat capacity meaning that large volumes are required to achieve significant storage; this is extremely unappealing to the construction sector where real estate value is based on the available area.

Table 5.1.2 Thermal properties of some common building materials at 20 °C (Dincer *et al.,* 2002).

Material	Density (kg/m^3)	Specific heat (J/kg K)	Vol. thermal capacity (10^6 J/m^3 K)
Clay	1458	879	1.28
Brick	1800	837	1.51
Sandstone	2200	712	1.57
Wood	700	2390	1.67
Concrete	2000	880	1.76
Glass	2710	837	2.27
Aluminum	2710	896	2.43
Iron	7900	452	3.57
Steel	7840	465	3.68
Water	988	4182	4.17

On the contrary, to accumulate a similar amount of energy, LHS systems require smaller mass and volumes as they present higher energy densities and volumetric heat capacity. The increased energy densities allow augmenting the buildings' thermal mass without reducing living areas or increasing structural loads. Therefore, LHS systems can be incorporated in pre-existing buildings or even in lightweight constructions.

Zeinelabdein *et al.* (2018) provided a comparison between the required mass and volume of two SHS (water and rock) and two LHS (one organic and one inorganic material) substances to store the same amount of energy (10^6 kJ) during a temperature increase of 15 °K, Table 5.1.3.

The results show that LHS systems can provide up to an 11-fold volume reduction and a 15-fold reduction in terms of mass relative SHS systems. These significant reductions allow maintaining the available area while simultaneously reducing the operative time of HVAC systems. Other of the main advantages of LHS systems include their technical simplicity and cost efficiency over TCES, and their well-defined and adjustable transition temperature (where absorption and discharge of energy take place).

In the following sections, a more comprehensive bibliographic review is provided on latent storage systems, the different types of phase change materials, their characteristics, and potential uses in the construction sector.

Table 5.1.3 Required mass and weight of two SHS and LHS substances to store 10^6 kJ during a temperature rise of 15 °K (Zeinelabdein *et al.,* 2018).

	Sensitive heat storage (SHS)		**Latent heat storage (LHS)**	
	Rock	**Water**	**Organic**	**Inorganic**
Required weight of storage (kg)	67000	16000	5300	4350
Required volume of storage (m^3)	30	16	6.6	2.7

5.2 Latent heat storage systems characteristics and performance overview

In LHS systems, energy is stored and released during the phase transition of a certain material(s) over a defined temperature range. As so, these substances are frequently referred to as phase change materials (PCMs), and their usage in energy storage systems has been growing over the last years. When the temperature rises to a point where phase transition is possible, thermal energy is accumulated, hence, reducing the increase of temperature of the surrounding environment. By contrast, whenever the temperature decreases, the accumulated energy is released, representing an internal thermal load that minimizes the temperature drop, Figure 5.2.1.

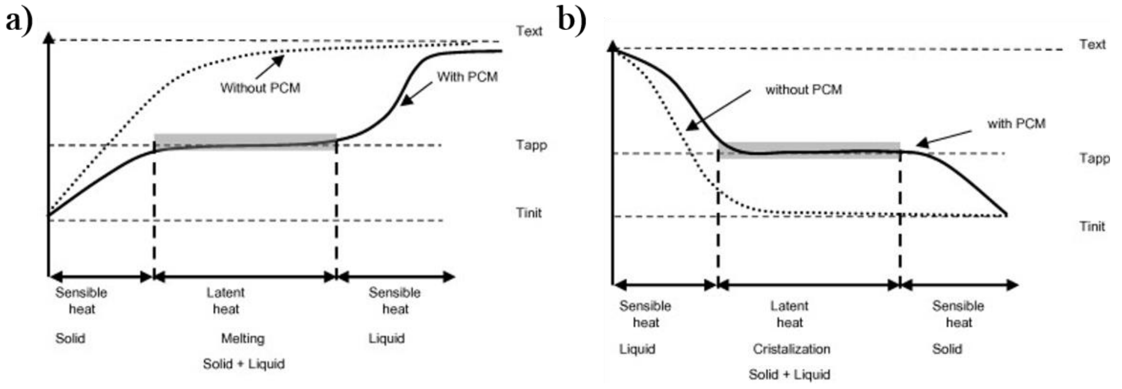

Figure 5.2.1 Schematic representation of the phase change materials effect on temperature variation: a) absorption and b) restitution period. T_{ext}, $T_{app,}$ and T_{init} represent the external, application and initial temperature, respectively (adapted from Ventolà *et al.,* 2013).

Therefore, PCMs use indoor temperature fluctuations to control indoor temperature. This notion is based on the regenerative use of energy, which allows PCMs to act as thermal buffers or regulators who autonomously attenuate temperature fluctuations in inside environments. Figure 5.2.3 provides a schematic representation of the thermodynamic principles involved in phase transitions. A solid-liquid PCM is given as an example but similar thermodynamic principles stand for all phase transitions.

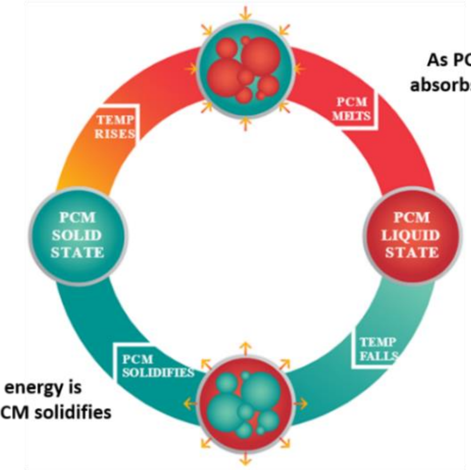

As temperature rises, PCM melts

As PCM melts, it absorbs heat energy

As heat energy is released, PCM solidifies

As temperature falls, heat energy is released.

Figure 5.2.3 Phase change materials principles (adapted from Microtek Laboratories)

Phase transitions can be classified according to the phases involved and so PCMs (not exclusively). Phase transitions can be either: solid-solid (between two different solid states); solid-liquid (fusion/solidification); solid-gaseous (sublimation/ de-sublimation) and liquid-gaseous (vaporization/condensation). In transitions occurring between solid-solid and solid-liquid states (and vice versa), an inferior amount of latent heat is stored and released compared with transitions involving gaseous phases. However, at atmospheric pressure, gaseous phases require large volume containers, and therefore, their application in TES is challenging.

5.2.1 Solid-solid phase change materials

Solid-solid phase change materials can be classified into four main compounds categories based on their chemical composition; organic, organometallic, inorganic, and polymeric (Fallahi, 2017). In these materials, the absorption and release of heat occur during reversible phase transitions between crystalline or semi-crystalline phases and another crystalline, semi-crystalline, or amorphous phases. Despite the lower quantities of latent heat involved in these phase transitions (Cárdenas, 2013; Nomura, 2010), this type of PCM presents some technical advantages that make them competitive with solid-liquid PCMs. As solid-solid PCMs retain their bulk properties, no leaching occurs, and the need for encapsulation is avoided. PCM capsules can decrease thermal transfer effectiveness and significantly increase production costs. This feature allows solid-solid PCMs to be directly blended with other materials such as concrete or gypsum (Fallahi, 2017). In addition, solid-solid PCMs do not require nucleation to prevent supercooling and experience less phase-segregation and volumetric changes upon phase transition. In the case of confinement (see Figure 5.4.1), the superior volumetric stability of these materials also rends the design of the containers more flexible and, therefore more easily incorporate in TES systems. Promising solid-solid PCMs for TES applications include pentaerythritol [$C_5H_{12}O_4$], pentaglycerine [$CH_3 - C - (CH_2 - OH_3)$], neopentyl glycol [$(CH_3)_2 - C - (CH_2 - OH_2)$], and mixtures of thereof (Zeinelabdein, 2018).

5.2.2 Solid-liquid phase change materials

Contrarily to solid-solid, solid-liquid PCMs do not retain their bulk properties upon phase transition. In these PCMs, when transition temperature(s) is surpassed the ordered crystalline structures are changed to disordered amorphous ones due to the breakage of supramolecular bonds. The crystalline ordered arrangement becomes then a randomly oriented liquid state, Figure 5.2.4.

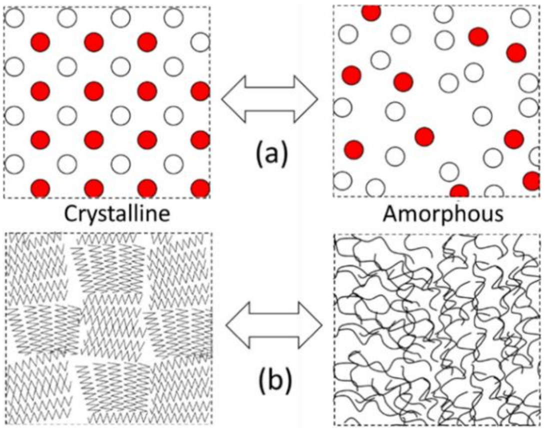

Figure 5.2.4 Schematic representation of the phase transition process of solid-liquid PCM: (a) salt-hydrate type system changing from ordered crystalline to a disordered non-crystalline phase, and (b) paraffin type system changing from a lamellar crystal to a random disordered phase (Fallahi *et al.,* 2017).

In the reverse process, when temperature decrease below the phase transition temperature, nucleation starts, and the molecules are re-arranged again into crystalline structures. The crystallization process is affected by many factors such as the cooling-rate, type of molecules and the presence of impurities (that act as nucleating agents) or added nucleating agents to avoid supercooling. Supercooling and other technical problems of each class of solid-liquid PCMs will be discussed in the ensuing sections. Despite some volumetric instability upon phase transition (the volume can increase up to 10% during melting (Zeinelabdein, 2018), the superior heat storage capacity and cost efficiency relative SHS and solid-solid PCMs make solid-liquid PCMs the most viable candidates for the construction sector. In fact, solid-liquid PCMs are the most commercialized type of PCMs (predominantly hydrated salts, paraffins, water-salts eutectic) covering a temperature range from -40º to 120ºC, Figure 5.2.5.

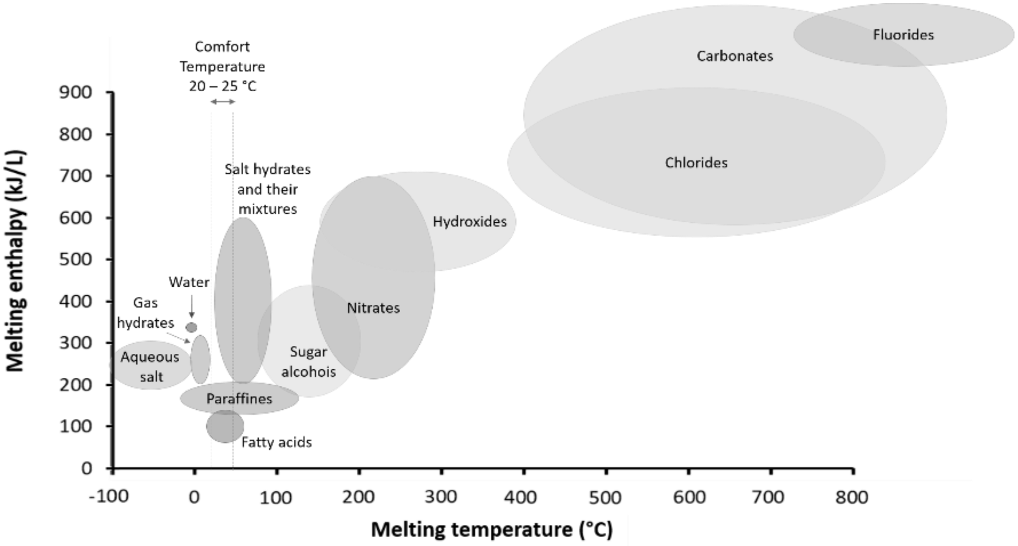

Figure 5.2.5 Classification of solid-liquid phase change materials based on their enthalpy and melting point (adapted from Zhou *et al.*, 2012).

In systems used to control buildings' indoor temperature, only PCMs with phase transition near to human comfort zone should be employed. Table 5.2.1 shows some commercially available solid-liquid PCM having a phase transition between 20-25 °C.

Table 5.2.1 Commercially available solid-liquid phase change materials with phase change temperature between 20-25 °C.

PCM (by supplier)	Class	Melting temp. (°C)	Heat fusion (kJ/kg)	Specific heat (kJ/kg °K)	Thermal cond. (W /m °K)
Climator					
Climesel 21	Salt hydrated	21-26	134	N.A.	0.75-0.93
Climesel 23	Salt hydrated	23	148	N.A.	0.75-0.93
Climesel 24	Salt hydrated	24-27	140	N.A.	0.75-0.93
EPS Ltd.					
A22	Organic	22	145	2.22	0.18
A22H	Organic	22	216	2.85	0.18
A23	Organic	23	145	2.22	0.18
A24	Organic	24	145	2.22	0.18
A25	Organic	25	150	2.26	0.18
A25H	Organic	25	226	2.15	0.18
Honeywell					
Astorstat HA17	Organic	21.7-22.8	N.A.	N.A.	N.A.
Environ. Proc. Sys.					
E21	Salt hydrated	21	150	N.A.	N.A.
PCP Ltd					
PC-25	Salt hydrated	25	150	N.A.	0.54-1.10
Microtek lab.					
Micronal 24D	Paraffin	24	97	N.A.	N.A.
Nextek 24D	Paraffin	24	170	N.A.	N.A.
Emerest					
Emerest 2325	Organic	20	134	N.A.	N.A.
Emerest 2326	Organic	20	139	N.A.	N.A.
PLUSS					
OM21	Organic	21	250	N.A.	0.14/0.21
FS21R	Organic	20.5-20.7	183	N.A.	0.10/0.30
FS21	Organic	20-21	130	N.A.	0.10/0.30
HS21	Inorganic	18-22	185	1.40 (L)	0.59/0.82
HS22	Inorganic	22-23	185	3.04-2.20	0.56/1.13
HS24	Inorganic	24-25	185	2.3 (L)	0.55/1.05
Rubitherm					
RT21	Paraffin	21	155	2.0	0.2
RT21 HC	Paraffin	21	190	2.0	0.6
RT22 HC	Paraffin	22	190	2.0	0.2
RT 24	Paraffin	24	160	2.0	0.2
RT 25	Paraffin	25	170	2.0	0.2
RT 25HC	Paraffin	25	230	2.0	0.2
SP 21E	Inorganic	21-23	170	2.0	0.6
SP 22 A17	Inorganic	22	150	2.0	0.6
SP 24E	Inorganic	24-25	180	2.0	0.6
SP25 A8	Inorganic	25	180	2.5	0.6
SP25 E2	Inorganic	24-26	180	2.0	0.6

Solid-liquid phase change materials classification

Solid-liquid phase change materials can be divided into three main groups according to their chemical composition: i) inorganic, ii) organic, and iii) eutectic mixtures (Figure 5.2.6). The addition of each class of PCMs into building materials present several advantages and disadvantages inherent to their chemical composition.

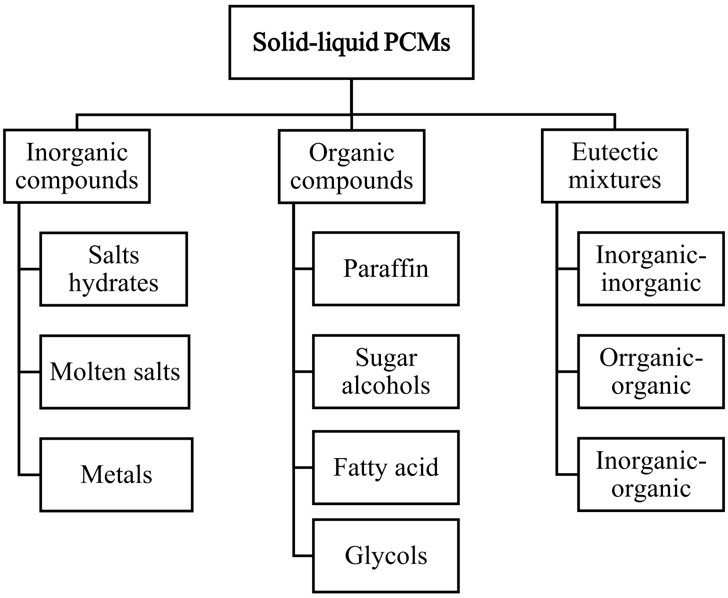

Figure 5.2.6 Classes of solid-liquid PCMs based on their chemical composition.

Inorganic PCMs

Inorganic PCMs can be hydrated or molten salts, and metallic alloys. In general, these types of PCMs present several desirable features such as high latent heat of fusion, thermal conductivity (around 0.5 W/m°K) and volumetric storage capacity, and reasonable volumetric stability upon phase transition. Inorganic PCMs are widely available, and their cost is frequently lower relative to organic PCMs. Table 5.2.2 gives examples of some inorganic PCMs with transition temperate near to the human comfort zone.

Table 5.2.2 Thermal properties of some inorganic solid-liquid phase change materials with phase transition between 20 and 25 °C.

PCM compound	Melting temp. (°C)	Heat fusion (kJ/kg)
Iron (III) bromide hexahydrate	21-27	105
Manganese (II) nitrate hexahydrate	25.5	148
Calcium chloride Hexahydrate	24-28	125-174

Among inorganic PCMs, hydrated salts are the most frequently employed in latent heat storage systems. The phase transition of these salts occurs due to reversible hydration and dehydration processes. During these processes, each salt gives origin to a particular crystalline structure, and therefore, it is possible to accomplish desirable phase transition temperatures by varying the salt chemical composition. In addition, hydrated salts present high latent heat accumulation capacity, conductivity, and enthalpy; are inflammable, compatible with plastic containers and economic (Zeinelabdein, 2018). Such properties could make their use favorable for indoor temperature control, but their incongruent melting, phase segregation and supercooling restrict their application in building materials (Sharma, 2002; Khudhair, 2004). Incongruent melting can be attributed to the different densities of dehydration reaction products (phase segregation). Hydrate and anhydrous salts tend to settle, hindering their complete recombination with water molecules during ensuing thermal cycles. This phenomenon results in a continuous decrease in thermal performance and compromises PCMs' cyclic stability (Cabeza, 2007). Incongruent melting and phase segregation can be prevented by modifying the salts' chemical compositions, by mechanical stirring or by addicting thickening agents to the solution. By increasing the solution viscosity, the formed crystals remain dispersed, thus facilitating their later dissolution.

Supercooling phenomena characterize hydrated salts in which crystallization does not occur immediately below the melting point. In these cases, the crystallization and release of latent heat are only possible if the temperature significantly decreases below the melting point (Carvalho, 2013). Hence, supercooling widens PCMs' transition zone, decreasing their attractiveness for applications operating in short temperatures ranges, i.e. building materials. Furthermore, supercooling can impose fast volumetric changes that can compromise the containers' tightness and cause PCMs leakage over time. This is of particular interest for stainless steel reinforced building materials since hydrated salts are known to promote severe corrosion of metallic elements. Additionally, in concrete and concrete-like materials, even if PCM leakage does not occur, high volumetric variations can result in severe microcrack formation, ultimately reducing the materials' mechanical properties and long-term performances. Supercooling can be minimized by using nucleating agents, by segregating some salt crystals to later act as nuclei, or by using specific containers that enhance nucleation (Zeinelabdein, 2018).

Molten salts and metallic alloys have several interesting features such as volumetric stability upon phase transition, and high thermal conductivity and heat fusion per unit of volume. However, they show high-temperature phase transition making their application only desirable in high-temperature processes, e.g., solar power plants and waste heat recovery (Cárdenas, 2013).

Organic phase change materials

Despite initially discarded in the development of thermal energy storage systems, organic PCMs have later reemerged in several fields of application. Organic PCMs are chemically stable and present reasonable thermal capacity, high latent heat fusion, and a wide range of phase transition temperatures (Khudhair, 2004). They also show congruent melting and insignificant degradation and supercooling (Sari, 2003), and are compatible with most of common construction materials.

Organic PCMs can be classified into two major groups, paraffin, and non-paraffin (Silva, 2016). Among non-paraffin PCMs, fatty acids have emerged in some TES applications due to their desirable properties and renewable origin. Saturated fatty acids can be described with the general formula [$CH_3(CH_2)_n$•COOH]. The most commonly used saturated fatty acids include caprylic, capric, myristic, palmitic and stearic acids where the number of carbon atoms per molecule can range from 8 to 18. These saturated fatty acids present transition temperatures from 16 to 65 °C, and relatively high heat of fusion, between 100 and 200 kJ/kg (Yang, 2018). Nevertheless, their application into construction materials is highly precluded by their flammability and varying toxicity, mild corrosivity and distinct odor (Sari, 2003). Their three-fold higher cost relative to paraffin and the shortage of substances with transition temperatures around human thermal comfort pose additional challenges to their implementation in the construction sector.

Paraffin belong to the group of acyclic saturated hydrocarbons (i.e., alkanes) that can be described with the general formula [C_nH_{2n+2}], where n is the number of carbon atoms. Except for paraffin waxes, the application of n-alkanes in the construction sector is expected to have a restrict as the high purity of their raw materials significantly increases their production costs (Cabeza, 2007; Zeinelabdein, 2018). Paraffin waxes consist of a mixture of straight-chain hydrocarbon molecules containing between 20 and 40 carbons. In contrast with pure alkanes where phase transition occurs in a well-defined temperature, paraffin waxes generally melt within a temperature range that increases as the number of carbons rises. Paraffin waxes main advantages are their vast range of phase transition temperatures up to 70 °C, the reasonable storage density (Yang, 2018), the low vapor pressure, the absence of phase segregation, and their cyclic stability. For instance, Shukla *et al.* (2008) compared the thermal cycling stability of three inorganic and four organic PCMs over 1000 cycles. Their findings suggest that among the tested PCMs, paraffin waxes were more suitable for LHS purposes based on the stability of their melting temperature and latent heat of fusion.

Moreover, paraffin waxes are safe, non-corrosive, inexpensive and abundantly available. Conversely, paraffin waxes are incompatible with plastic containers, have poor conductivity and carry flammability risks (Zalba, 2003; Cai, 2009; Yang, 2018). Significant efforts have been made to overcome the latter (e.g., inclusion of high conductive nanoparticles and flame-retardants and flame-extinguishing products (Song, 2010; Yang, 2018) to enhance paraffin waxes performance and safeness. Table 5.2.3 shows the main physical properties of some organic solid-liquid PCMs with phase transition between 20 and 25 °C, (Sharma, 2002; Zeinelabdein, 2018).

Table 5.2.3 Thermal properties of some organic solid-liquid phase change materials with phase transition between 20 and 25 °C.

PCM compound	Melting temp. (°C)	Heat fusion (kJ/kg)
Paraffin C_{16}-C_{18}	20-22	152
Polyethylene glycol E 600	20-25	146
Polyglycol E 600	22	127.2
Dimethyl sabacate	21	120-135
Octadecyl 3-mencaptoproypylate	21	143
Paraffin C_{17}	21.7	213
n-Heptadecane	20.8-21.7	171
Paraffin C_{13}-C_{24}	22-24	189
Black paraffin	25-30	150
Lithium Chloride Ethanolate	21	188

Eutectic and non-eutectic mixtures

Eutectic and non-eutectic mixtures of organic and/or inorganic PCMs can be produced in order to tailor phase transition(s) and thermal energy capacity (Zhou, 2012). By controlling the mixture portions is possible to target specific melting point(s) and achieve superior thermal energy storage capacity relative to the individual constituents of the mixture (Tyagi, 2011). Table 5.2.4 shows the thermal characteristics of some eutectic mixtures appropriate for application in TES systems.

Table 5.2.4 Thermal properties of some eutectic mixtures with phase transition between 20 and 25 °C (Zhou *et al.*, 2012; Zeinelabdein *et al.*, 2018).

PCM compound	Melting temp. (°C)	Heat fusion (kJ/kg)
45% Capric + 55% Lauric acid	21	143
61.5% Capric + 38.5% Lauric acid	19	132
82% Capric + 18% Lauric acid	19.1-20.4	147
75.2% Capric + 24.8% Palmitic acid	22.1	153
26.5% Myristic + 73.5% Capric acid	22.4	152
34% Myristic + 66% Capric acid	24	147.7
50% Calcium chloride + 50% Magnesium chloride hexahydrate	25	95
66.6% Calcium chloride dihydrate + 33.3% Magnesium chloride hexahydrate	25	127
45% Calcium nitrate tetrahydrate+ 55% Zinc nitrate hexahydrate	25	130
66% Calcium chloride hexahydrate + 33% Magnesium chloride hexahydrate	25	127
Octadecane + Docosane	25.5-27	203.8
Octadecane + Heneicosane	25.8-26	173.93

By definition, eutectic mixtures of two or more constituents melt and solidify congruently and without segregation. In non-eutectic mixtures, multiples phase transitions coexist, potentiating phase segregation, and degradation. This fact compromises non-eutectic mixtures cyclic stability, rendering unfeasible their use in TES systems. The limitations of eutectic mixtures mainly concern the scarcity of thermodynamic data and long-term performance studies. Also, some fatty eutectic mixtures, as fatty acids itself, present a strong and unpleasant odor that limits their application in building components (Thambidurai, 2015).

Technical requirements and criteria of selection

The selection of the PCM best suited for a specific application should consider several technical requirements as highlighted in the previous sections. PCMs must demonstrate several relevant properties, especially thermal energy storage capacity under relevant application conditions. Another of the most relevant points is stability upon thermal cycling, meaning upon repeated phase transitions. PCMs must survive a considerably large number of cycles without suffering degradation. Along with these general technical requirements, determining the feasibility of a specific PCM for latent storage systems require careful thermodynamic, kinetic and chemical examinations (Tyagi, 2011; Zhou, 2012). Table 5.2.5 shows the technical criteria for PCM selection as summarized by Zhou *et al.* (2012).

Table 5.2.5 Technical selection criteria of phase change materials.

Thermodynamic properties	1) Melting temperature in the desired temp. range 2) High latent heat of fusion per unit volume 3) High thermal conductivity 4) High specific heat and high density 5) Small volume changes on phase transformation 6) Small vapor pressure at operating temperatures 7) Congruent melting
Kinetic properties	1) High nucleation rate to avoid supercooling 2) High rate of crystal growth
Chemical properties	1) Complete reversible freezing/melting cycle 2) Chemical stability 3) No cyclic degradation 4) No corrosiveness 5) No toxicity or flammability

In addition to technical considerations, PCM selection should also consider economic factors such as cost and large-scale availability. These factors will play a vital role in determining the economic viability of PCM-containing building materials. Although the economic assessment of PCM-containing inorganic polymers has not been defined as the scope of this work, some considerations regarding the PCM market and prospects will be present in the following section.

5.3 Market analysis and prospects

As the market of thermal insulating materials, the demand for advanced PCMs is estimated to continue to grow on account of more energy-efficient stringent construction codes, the efficient harnessing of alternative energy sources, and the need for reducing greenhouse emissions and buildings' operating costs. Despite the high production and encapsulation costs, the lack of awareness and the high investments continuing to be restraining factors, PCMs global market is projected to register a compound annual growth rate (CAGR) of 17.7% between 2017 and 2024, nearly reaching 4.500 million US dollars of revenue by 2024 (Markets and markets, 2019; Global markets insights, 2019). By segment, building and construction are projected to be the most important markets during the considered period. In 2017, building and construction represented 23% of PCMs end-use, and the projected CAGR for this segment was 22.0% in 2019. Region-wise, Europe is the largest and more fast-growing market. The increase in demand for PCMs in Europe is led by the enforcement of more energy-efficient regulations and the ever-growing operative costs of buildings. The increase of awareness about newly-developed PCM-containing materials is expected to stimulate the European market further. The Americas are the second-largest market for PCMs, while Asia-Pacific presents the most favorable growth prospects. The growth in the region is expected to benefit from low-cost structures and the increase of demand in segments such as HVAC systems, textiles, shipping, packing & transportation, and thermal energy storage systems.

By 2016, organic PCMs had the largest market size by value, while inorganic PCMs dominated in terms of volume. Paraffin held the maximum share of the global market due to its easier microencapsulation process and higher economic value. However, encapsulation technology encompasses a significant portion of the research made in the field and production costs can further benefit from advances in this area. Salt hydrates are projected to be the fastest-growing product in the coming years owing to their cost-effectiveness, and niche temperature range covered (Global markets insights, 2019).

The PCM market is highly diversified with an increasing number of small, medium, and large-scale manufacturers around the world (Zeinelabdein, 2018). Some of the relevant players operating in the market are Henkel, Sasol, Phase Change Products Pty Limited, Honeywell, Croda International PLC and The Dow Chemical Company. Other significant players include Rubitherm, Climator, Microtek Inc. and PLUSS (Zeinelabdein, 2018; Global markets insights, 2019).

In a recent study, Fullenkamp *et al.* (2019) referred the average cost of commercially available PCMs to be around 8 USD/kg, varying from 5 to 50 USD/kg for wholesale orders. Considering the expected competition between involved players to secure shares of a growing market, a reduction in PCMs acquisition cost can be expected. The latter market prospects should be considered by third parties, namely in the construction sector, when assessing the long-term economic viability of PCM-containing building materials.

References

Abedin, A. H., & Rosen, M. A. (2011). A critical review of thermochemical energy storage systems. The open renewable energy journal, 4(1). https://doi.org/10.2174/1876387101004010042

Boyle, G. (2004). Renewable energy. Renewable Energy, by Edited by Godfrey Boyle, pp. 456. Oxford University Press, May 2004. ISBN-10: 0199261784. ISBN-13: 9780199261789, 456.

Cabeza, L. F., Castellon, C., Nogues, M., Medrano, M., Leppers, R., & Zubillaga, O. (2007). Use of microencapsulated PCM in concrete walls for energy savings. Energy and Buildings, 39(2), 113-119. https://doi.org/10.1016/j.enbuild.2006.03.030

Cai, Y., Wei, Q., Huang, F., Lin, S., Chen, F., & Gao, W. (2009). Thermal stability, latent heat and flame retardant properties of the thermal energy storage phase change materials based on paraffin/high-density polyethylene composites. Renewable Energy, 34(10), 2117-2123. https://doi.org/10.1016/j.renene.2009.01.017

Cárdenas, B., & León, N. (2013). High-temperature latent heat thermal energy storage: Phase change materials, design considerations and performance enhancement techniques. Renewable and sustainable energy reviews, 27, 724-737. https://doi.org/10.1016/j.rser.2013.07.028

Carvalho, I. M. S. (2013). Dimensionamento de um sistema de teto arrefecido integrando materiais de mudança de fase.

Climator. [cited 2019, 13/05]; Available from: ⟨http://climator.com/⟩].

Dincer, I. (2002). On thermal energy storage systems and applications in buildings. Energy and buildings, 34(4), 377-388. https://doi.org/10.1016/S0378-7788(01)00126-8

Ding, Y., & Riffat, S. B. (2012). Thermochemical energy storage technologies for building applications: a state-of-the-art review. International Journal of Low-Carbon Technologies, 8(2), 106-116. https://doi.org/10.1093/ijlct/cts004

Hauer, A. (2011, February). Storage technology issues and opportunities. In Committee on Energy Research and Technology (International Energy Agency), International Low-Carbon Energy Technology Platform, Strategic and Cross-Cutting "Energy Storage–Issues and Opportunities (Vol. 15).

EPS. [cited 2019, 13/05]; Available from ⟨http://www.pcmproducts.net/⟩.

Fallahi, A., Guldentops, G., Tao, M., Granados-Focil, S., & Van Dessel, S. (2017). Review on solid-solid phase change materials for thermal energy storage: Molecular structure and thermal properties. Applied Thermal Engineering, 127, 1427-1441. https://doi.org/10.1016/j.applthermaleng.2017.08.161

Kalaiselvam, S., & Parameshwaran, R. (2014). Thermal energy storage technologies for sustainability: systems design, assessment and applications. Elsevier.

Khudhair, A. M., & Farid, M. M. (2004). A review on energy conservation in building applications with thermal storage by latent heat using phase change materials. Energy conversion and management, 45(2), 263-275. https://doi.org/10.1016/S0196-8904(03)00131-6

Microtek Laboratories. [cited 2019, 13/05]; Available from ⟨https://www.microteklabs.com/⟩.

Nomura, T., Okinaka, N., & Akiyama, T. (2010). Technology of latent heat storage for high-temperature application: a review. ISIJ International, 50(9), 1229-1239. https://doi.org/10.2355/isijinternational.50.1229

Pérez-Lombard, L., Ortiz, J., & Pout, C. (2008). A review on buildings energy consumption information. Energy and buildings, 40(3), 394-398. https://doi.org/10.1016/j.enbuild.2007.03.007

Rubitherm. [cited 2019, 13/05]; Available from: ⟨https://www.rubitherm.eu/⟩.

Sari, A., & Kaygusuz, K. (2003). Some fatty acids used for latent heat storage: thermal stability and corrosion of metals with respect to thermal cycling. Renewable Energy, 28(6), 939-948. https://doi.org/10.1016/S0960-1481(02)00110-6

Sharma, A., Sharma, S. D., & Buddhi, D. (2002). Accelerated thermal cycle test of acetamide, stearic acid and paraffin wax for solar thermal latent heat storage applications. Energy Conversion and Management, 43(14), 1923-1930. https://doi.org/10.1016/S0196-8904(01)00131-5

Shukla, A., Buddhi, D., & Sawhney, R. L. (2008). Thermal cycling test of few selected inorganic and organic phase change materials. Renewable Energy, 33(12), 2606-2614. https://doi.org/10.1016/j.renene.2008.02.026

Silva, T., Vicente, R., & Rodrigues, F. (2016). Literature review on the use of phase change materials in glazing and shading solutions. Renewable and Sustainable Energy Reviews, 53, 515-535. https://doi.org/10.1016/j.rser.2015.07.201

Song, G., Ma, S., Tang, G., Yin, Z., & Wang, X. (2010). Preparation and characterization of flame retardant form-stable phase change materials composed by EPDM, paraffin and nano magnesium hydroxide. Energy, 35(5), 2179-2183. https://doi.org/10.1016/j.energy.2010.02.002

Thambidurai, M., Panchabikesan, K., & Ramalingam, V. (2015). Review on phase change material based free cooling of buildings—the way toward sustainability. Journal of Energy Storage, 4, 74-88. https://doi.org/10.1016/j.est.2015.09.003

Tyagi, V. V., Kaushik, S. C., Tyagi, S. K., & Akiyama, T. (2011). Development of phase change materials based microencapsulated technology for buildings: a review. Renewable and sustainable energy reviews, 15(2), 1373-1391. https://doi.org/10.1016/j.rser.2010.10.006

Ventolà, L., Vendrell, M., & Giraldez, P. (2013). Newly-designed traditional lime mortar with a phase change material as an additive. Construction and Building Materials, 47, 1210-1216. https://doi.org/10.1016/j.conbuildmat.2013.05.111

Yang, X. H., & Liu, J. (2018). Advances in Liquid Metal Science and Technology in Chip Cooling and Thermal Management.

Zalba, B., Marın, J. M., Cabeza, L. F., & Mehling, H. (2003). Review on thermal energy storage with phase change: materials, heat transfer analysis and applications. Applied thermal engineering, 23(3), 251-283. https://doi.org/10.1016/S1359-4311(02)00192-8

Zeinelabdein, R., Omer, S., & Gan, G. (2018). Critical review of latent heat storage systems for free cooling in buildings. Renewable and Sustainable Energy Reviews, 82, 2843-2868. https://doi.org/10.1016/j.rser.2017.10.046

Zhang, H., Baeyens, J., Caceres, G., Degreve, J., & Lv, Y. (2016). Thermal energy storage: Recent developments and practical aspects. Progress in Energy and Combustion Science, 53, 1-40. https://doi.org/10.1016/j.pecs.2015.10.003

Zhou, D., Zhao, C. Y., & Tian, Y. (2012). Review on thermal energy storage with phase change materials (PCMs) in building applications. Applied energy, 92, 593-605. https://doi.org/10.1016/j.apenergy.2011.08.025

5.4 Phase change materials in building materials: incorporation methods and available products

Phase change products are currently commercially available in multiple forms such as suspensions, dry powders, wet cakes, and granules, or in broad range encapsulated products such as spheres, pouches, tubes, panels (Figure 5.4.1). The integration of these products into building materials or elements can be done via several methods such as direct incorporation, immersion, encapsulation, shape-stabilization and form stable composites (Memon, 2014). These methods are briefly described in the following sections of this chapter.

Direct incorporation

Direct incorporation is by far the simplest and more economical method to integrate PCMs into building elements. PCMs are directly added during the production process of conventional construction materials (e.g., gypsum, cement paste, mortar, or concrete) either in the form of liquid (aqueous solution) or solid (powdered form). No additional pieces of equipment are required, and only minor changes need to be implemented in existing production processes. Notwithstanding, this application technique frequently raise leaching and compatibility issues. Special care should be taken when designing cement and cement-like based materials to guarantee that PCMs do not interfere with reaction process and formed products, reduce bonding between paste and aggregates (if any), and diminish the mechanical and durability properties of the material (Memon, 2014).

Immersion

Another technique to incorporate PCMs into building materials consists of immerging concrete, brick blocks, wallboards, tiles or other porous materials in molten PCMs. Capillary forces or vacuum impregnation assure that liquid PCMs are retained in the materials porous structures (Novais,2015; Zeinelabdein, 2018). The limitations of this process are mainly related to the porosity levels needed to ensure appreciable levels of PCMs incorporation, the duration of the saturation period and the insufficient long-term thermal performance due to leakage. Novais *et al.* (2015) suggested to overcoming the latter by applying an external film of a polymeric resin.

Encapsulation

Encapsulation techniques can be characterized according to the shell scale and divided between macro, and microencapsulation (Khudhair, 2004). In both cases, PCM shells should present adequate mechanical resistance and sufficient deformability to accommodate external and internal solicitations without losing their integrity. Internal solicitations are transversal to all fields of application and PCMs as they result from volume changes occurring during phase transition. External solicitations assume particular importance in the construction sector during concrete and mortars manufacturing process. Moreover, PCMs' shells should be resistant to corrosion, thermally stable and allow an effective heat transfer. Encapsulation main advantages include a significant decrease in the risk of leakage and flammability (if any).

Macroencapsulation

Macroencapsulation is a technical solution where PCMs are confined in plastic pockets, plastic or metallic tubes, spheres, or panels of variable volumes (from milliliters to liters), Figure 5.4.1. These products can be directly incorporated into building components but typically present low thermal transfer coefficients as the confinement elements itself act as a thermal barrier.

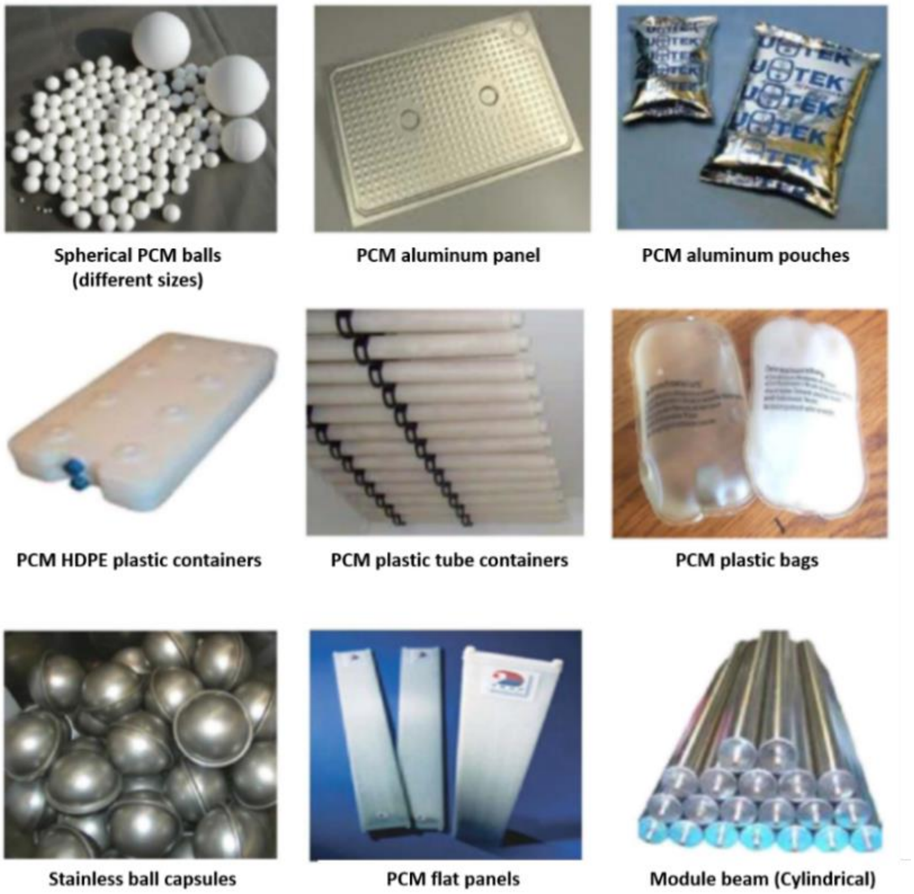

Figure 5.4.1 Macroencapsulated phase change materials available in the market (adapted from Zeinelabdein *et al.,* 2018).

Microencapsulation

In microencapsulation, a solid (powdered) or liquid (suspensions) PCM is confined within microcapsules of diameters ranging from 1 e 100 µm, Figure 5.4.2 (Schmidt, 2007). Several different microencapsulation methods had been attempted, but in situ polymerization seems to obtain a significant consensus over the remaining techniques since it is possible to achieve smaller capsules and excellent shell structure. Notice that diminishing the capsule size reduces the complexity of their integration into building materials and enhances heat transfer due to the increased heat exchange surface. Other microencapsulation methods include pan coating, air-suspension coating, centrifugal extrusion, vibrational nozzle, spray-drying, interfacial polymerization, and emulsion polymerization (Memon, 2014; Fullenkamp, 2019).

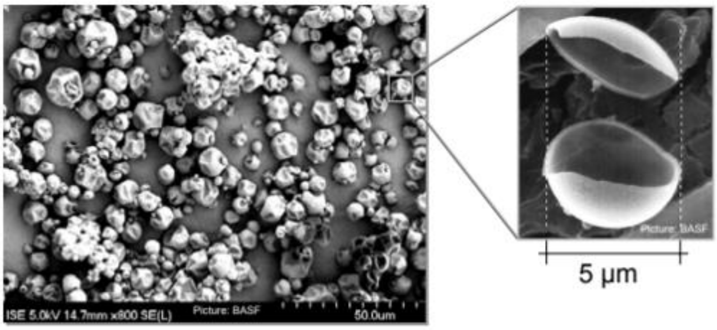

Figure 5.4.2 Microencapsulated paraffin wax (Schmidt *et al.,* 2007)

PCMs' shells are frequently made of high-density polymers being the most notable polymethyl methacrylate, PMMA (Konuklu,2015; Lucas, 2019). PMMA is known to melt around 160 °C (William, 2006) and ignite at 460 °C, forming carbon dioxide, water, carbon monoxide, and low molecular weight compounds, including formaldehyde (Zeng, 2002). This makes most of the microencapsulated PCMs inappropriate for high-temperature applications, and special precautions should be taken when considering PCM-containing building materials for fire and high-temperature purposes. Environmental stress cracking was reported to contribute to leaching and associated loss of efficiency (Castellón, 2011). Castellón *et al.* (2011) suggested using semi-crystalline polymeric shells in virtue of their higher resistance to cracking induced by environmental stress. Nevertheless, Uddin *et al.* (2002) and Sharma *et al.* (2002) had shown the cyclic stability of microencapsulated products upon 1000 cycles (Figure 5.4.3), while Konuklu *et al.* (2015) reported their successful incorporation in cement, lime and gypsum matrices.

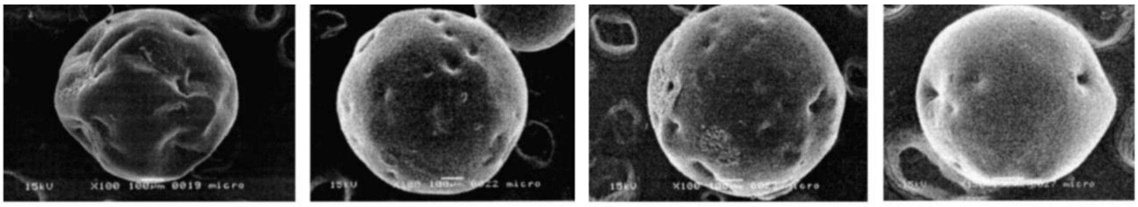
0 cycle 200 cycle 500 cycle 1000 cycle

Figure 5.4.3 Microencapsulated paraffin wax geometrical profile evaluated by SEM analysis after a different number of thermal cycles (Uddin *et al.,* 2002).

The inner-shell spatial arrangement can also assume different configurations. Mono and polynuclear or matrix encapsulation can be used to tailored PCMs' performance without influencing the interaction with the surrounding material, Figure 5.4.4 (Khudhair, 2004; Tyagi, 2011).

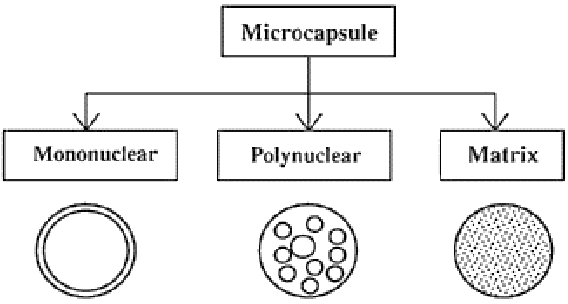

Figure 5.4.4 Different microcapsules configurations (Tyagi *et al.,* 2011).

In general, microencapsulated products present good compatibility with construction materials without imposing severe detrimental effects on their physical properties, while the high superficial area guaranteed by microencapsulation increases heat transfer capacity.

Shape stabilization

In shape stabilization, a PCM is dispersed (usually paraffin) in high-density polyethylene (HDPE) or styrene, and butadiene mixture. The blended material is molten at high temperatures followed by rapid cooling. The support material solidifies endowing tightness and rigidity to the shape-stabilized material when operating near to the PCM transition temperature. Since the mass percentage of PCM can be as high as 80%, large specific heat and thermal storage are achieved (Memon, 2014). The performance of shape-stabilized PCMs can be further improved by adding graphite or carbon fibers as a thermally conductive component (Zhang, 2006).

Form-stable composites

Form-stable PCMs composites are produced using highly porous materials as skeletons to absorb liquid PCMs. Supporting materials as diatomite, expanded perlite and graphite, silica fume, vermiculite, kaolin, and granulated blast furnace slag can be found in the literature. As in shape stabilization, these supporting materials improve thermal conductivity and increase PCMs' thermal stability. Form-stable composites can be obtained by natural immersion, but vacuum impregnation increases retention capacity, hence thermal energy storage capacity. Form-stable PCMs composites can later be incorporated in common building materials to improve their thermal features. As an example, Xu and Li (2013) used paraffin/diatomite PCM composite as a cement replacement in dosages up to 30 % by weight. Thermal tests made on 200x100x15 mm^3 panels show that both internal and external faces of PCM-containing panels presented lower temperatures during heating stages and higher temperatures during cooling stages. It worth to mention that the incorporation of paraffin/diatomite composite resulted in a considerable reduction of compressive and flexural strength.

5.5 Microencapsulated PCMs in binders

Among the described methods, the addition of microencapsulated products in hydraulic binders had shown promising results. The simple addition method and the possibility of use paraffin waxes have both technical and economic benefits (Lucas, 2019). Lucas *et al.* (2019) studied the effects of microencapsulated paraffin waxes in cement, cement-lime, lime, and lime-gypsum rendering mortars. Mortars with varying PCM dosages were used to coat the inner faces of $20\times20\times20cm^3$ test cells with a 3mm thickness layer. The test cells were then submitted to repeated thermal cycles with temperatures ranging from 10 to 40 °C, being a steady-state period of 10 min sustained at maximum and minimum temperatures. The results have shown a significant decrease in the thermal gradient as the PCM dosage rose. Lime mortars containing 30% PCM achieved the best thermal performance. The thermal gradient was reduced by 8.7 °C, representing a reduction of approximately 33%. A thermal delay was also clearly visible near to PCM transition temperature (23 °C) during both heating and cooling stages, Figure 5.5.1. PCM-containing lime mortars exhibited enhanced mechanical performances despite the substantial increase of open porosity and water absorption values. The authors attributed these results to reduced internal porosities and better particle packaging. The importance of considering PCM economic impact on the mortars' final cost was also highlighted by the authors, which considering both strength development and potential energy savings recommended a 20 wt% PCM dosage.

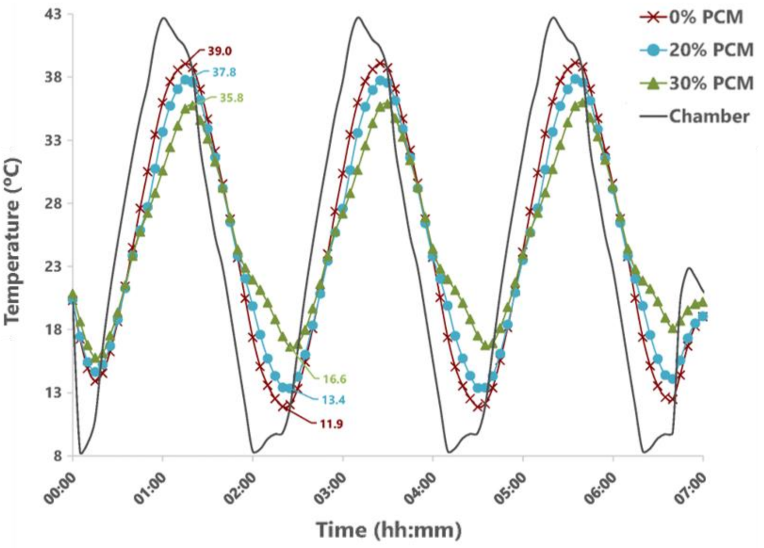

Figure 5.5.1 Thermal profile of lime mortars (Lucas *et al.*, 2019).

It is important to note that beneficial effects on strength development were only observable in lime mortars. On the contrary, in cement, cement-lime, and lime-gypsum mortars, the addition of equal dosages of PCMs had impaired strength development. This distinct behavior was attributed to the different ways of how PCM capsules could be incorporated on binders' microstructures. Hunger *et al.* (2009) studied the effects of microencapsulated materials on self-compacting concrete. Through modeling and in-situ experiments, they observed that increasing PCM content up to 5 wt% reduced the hydration temperature peak by 28 %. The heat released during hydration processes can be temporarily stored in PCMs, partially offsetting the maximum temperature reached. In addition, several broken PCM capsules were observed, and the released wax can further influence the binders' hydration process and produce fragile wax-interfaces within the cementitious matrix. These effects denote the influence of microencapsulated PCMs on the reaction kinetics and can contribute to explaining the different strength developments between cement and lime-based mortars.

The research in this field has been predominantly focused on studying the effects of microencapsulated PCMs in hydraulic binders with particular emphasis on cement-based systems. To the best of our knowledge, only a few studies explored the integration of PCM microcapsules in alkali-activated binders, Figure 5.5.2.

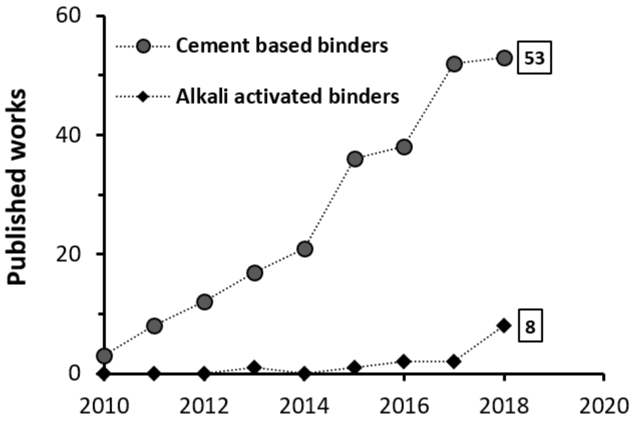

Figure 5.5.2 Cumulative works published for "cement" or "concrete" or "mortars" and "microencapsulated phase change materials", and "geopolymer" or "inorganic polymer" or "alkali activated materials" and "microencapsulated phase change materials". Data collected from the Scopus database in May 2019.

Shadnia *et al.* (2015) used class F fly ash, sand, and a sodium hydroxide solution to produce IP mortars where the sand was progressively substituted by microencapsulated PCM (up to 20 vol%). SEM observations showed good bonding between the polymeric matrix and the PCM capsules, but a considerable reduction of compressive strength was also observed. However, all the IPs presented compressive above 15 MPa after 28 d of curing. Differential scanning calorimetry was used to characterize the specific heat curves of the produced IPs. PCM-containing mortars have shown endothermic peaks around the PCMs' transition temperature while no peaks were observable in PCM-free mortars. To further evaluated the effectiveness of PCM-containing mortars, 30×30×30 cm^3 plywood cubicles were built and covered with IPs containing different PCM dosages. The cubicles were exposed to natural conditions during a 24 h period, and the temperature at the slabs' top and bottom and inside the cubicles was monitored.

The results of these thermal tests had shown similar trends to those reported by Lucas *et al.* (2019). The maximum temperature reached on the bottom slab, and inside the cubicles decreased as PCM content rose. In the 20 % PCM cubicles, the maximum temperature of the bottom slab was reduced 6.2 °C while the inner air maximum temperature was reduced 5.5 °C. The time necessary to reach maximum temperature was also modified being reported a 70 min delay in 20% PCM test cells. Conversely, when the external temperature decreased, a more abrupt temperature decay was seen in test cells that contain PCM-free mortars. All these findings demonstrated, to different extents, the superior thermal properties of PCM-containing building materials. Notice that in these works different types of binders were used, which seems to suggest that PCMs ability to attenuate temperature variations is not significantly affected by the binders' nature.

Notwithstanding, the opposite may not be true as the binder's nature and type of PCM used were shown to dictate the beneficial or detrimental nature of the effects produced by PCM addition. Cao *et al.* (2018a) studied the thermal performance of fly-ash-GGBFS slag concrete containing different dosages and types of microencapsulated PCMs. They have found an almost linear correlation between the increase of PCM dosage and the reduction of density, while an opposite trend was found relatively to open porosity. This was probably related to the adjustments made on binder-aggregates mass ratio necessary to compensate for the loss of flowability. More interesting, however, was the reduction of thermal conductivity and the increase of energy storage capacity as the content of PCM rose. Concrete walls with different thicknesses were used to evaluate the effects of different types of PCM on power consumption required to stabilize the inner temperature of a testing cell at 23 °C.

Given a 75 mm wall, the introduction of 5.4 wt% PCM reduced power consumption by 24 % and 36 % depending on the type PCM used. Smaller capsules containing polar functional groups exhibited a more uniform dispersion and better interfacial bonds with the cementitious matrix, resulting in lower thermal conductivity and higher thermal energy storage capacity (Cao, 2018a, b). In another work, Cao *et al.* (2018c) investigated the role of the hygroscopic nature, size, and concentrations of PCM microcapsules on time-dependent viscosity and reaction rate. It was found that increasing the PCM concentrations decreased polymerization reaction rate, probably as a result of higher initial viscosities. Such dependency was particularly visible in the case of PCM capsules containing polar functional groups and less severe when hydrophobic polymer shells were used. These results were attributed to the higher amount of water absorbed by the microcapsules with polar functional groups. Based on the results gathered, their research group developed empirical and numerical models to quantify time-dependent viscosities changes and to simulate the thermal performance of building materials containing microencapsulated PCM. Contrary to previously existing models, the asymmetric shape of the melting curve was taken into consideration, which had considerably increased the accuracy of the model proposed (Cao, 2018a).

In a slightly different approach, Afolabi *et al.* (2019) produced form-stable PCMs to be later incorporated in alkali-activated binders. In their work, expanded graphite was used as supporting material to encapsulate an organic PCM. The liquid paraffin wax was infused by vacuum impregnation, and a calcium chloride/sodium silicate mixture was used to seal the composite. Red mud, sand, and a sodium trisilicate solution were used to produce an alkali-activated mortar where the sand was replaced by up to 30 wt% by the developed materials. The produced composite was shown to be chemically and thermally stable, and no signs of leakage were visible. The thermal performance of the PCM-containing walls was confronted with conventional solutions and demonstrated slower heating and cooling rates, Figure 5.5.3.

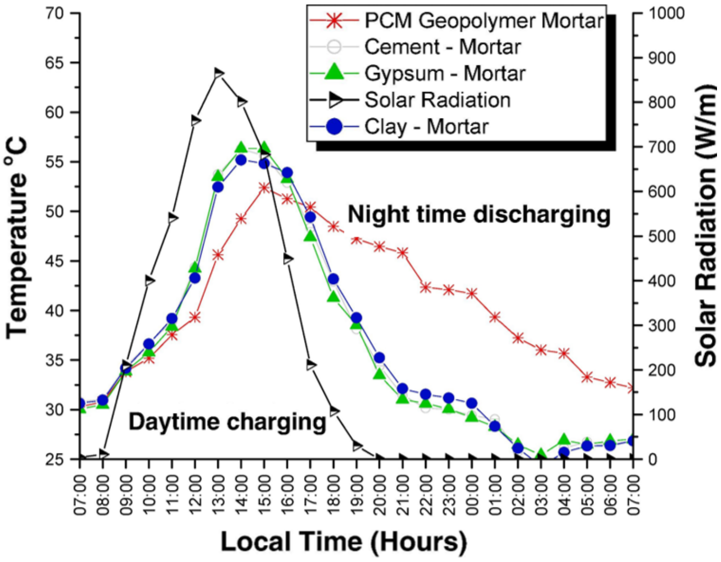

Figure 5.5.3 The temperature of different mortar surfaces during a 24 h period (Afolabi *et al.*, 2019).

A similar procedure has adopted by Wang *et al.* (2016), Sukontasukkul *et al.* (2016), Kastiukas *et al.* (2016) and Hassan *et al.* (2018) who have encapsulated paraffin waxes in different supporting materials such as lightweight expanded perlite, clay, and waste aerated blocks. The PCM-impregnated aggregates were then used to produce thermally responsive fly-ash, ground granulated blast furnace, clay, and tungsten mud-based thermally responsive IPs. All these materials beneficiated from impregnated aggregates, presenting reduced thermal conductivity and enhanced heat capacity. In general, the produced IP mortars presented reasonable density and compressive strength values compliant with common construction applications. Interestingly, no literature was found addressing the impregnation of porous IPs materials. Future investigations can transpose the impregnation methods described herein to porous IPs materials. The use of waste-based supporting IPs can potentially cope with the thermal and economic constraints of current encapsulation methods while further reducing the use of prime raw materials (e.g., expanded graphite or perlite).

In recent efforts, Jacob *et al.* (2016; 2018) proposed an alternative method to use IPs materials in TES systems. In their works, hemispherical shells with a diameter of 2.5 cm were fabricated using fly-ash based binders, Figure 5.5.4. The hollow shells were filled with a molten salt eutectic mixture of barium, potassium and sodium chloride, and exposed to thermal cycles up to 600 °C. The scope of this work was to produce PCM-capsules for high temperatures applications, but the PCM selection can be easily adjusted according to the envisioned application. Although the produced capsules had failed to prevent PCM leakage, these works constituted a first attempt to show the potential use of low-cost IPs binders as PCM macrocapsules. This type of solution can be of particular interest in applications where high-temperature-resistant materials are required.

Figure 5.5.4 Alkali activated fly ash-based hemispheres (Jacob *et al.*, 2018).

References

Afolabi, L. O., Ariff, Z. M., Megat-Yusoff, P. S. M., Al-Kayiem, H. H., Arogundade, A. I., & Afolabi-Owolabi, O. T. (2019). Red-mud geopolymer composite encapsulated phase change material for thermal comfort in built-sector. Solar Energy, 181, 464-474. https://doi.org/10.1016/j.solener.2019.02.029

Cao, V. D., Pilehvar, S., Salas-Bringas, C., Szczotok, A. M., Bui, T. Q., Carmona, M., ... & Kjøniksen, A. L. (2018a). Thermal performance and numerical simulation of geopolymer concrete containing different types of thermoregulating materials for passive building applications. Energy and Buildings, 173, 678-688. https://doi.org/10.1016/j.enbuild.2018.06.011

Cao, V. D., Pilehvar, S., Salas-Bringas, C., Szczotok, A. M., Do, N. B. D., Le, H. T., ... & Kjøniksen, A. L. (2018c). Influence of microcapsule size and shell polarity on the time-dependent viscosity of geopolymer paste. Industrial & Engineering Chemistry Research, 57(29), 9457-9464. https://doi.org/10.1021/acs.iecr.8b01961

Cao, V. D., Pilehvar, S., Salas-Bringas, C., Szczotok, A. M., Valentini, L., Carmona, M., & Kjøniksen, A. L. (2018b). Influence of microcapsule size and shell polarity on thermal and mechanical properties of thermoregulating geopolymer concrete for passive building applications. Energy Conversion and Management, 164, 198-209. https://doi.org/10.1016/j.enconman.2018.02.076

Castellón, C., Martorell, I., Cabeza, L. F., Fernández, A. I., & Manich, A. M. (2011). Compatibility of plastic with phase change materials (PCM). International Journal of Energy Research, 35(9), 765-771. https://doi.org/10.1002/er.1723

EPCM as TES materials for building applications. International Journal of Sustainable Energy, 38(6), 561-582. https://doi.org/10.1080/14786451.2018.1543307

Global markets insights, Inc. [cited 2019, 13/05]; Available from: ⟨http:// https://gminsights.com//⟩].

Hassan, A., Ismail, N., Mourad, A. H., Rashid, Y., & Laghari, M. (2018). Preparation and Characterization of Expanded Clay-Paraffin Wax-Geo-Polymer Composite Material. Materials, 11(11), 2191. https://doi.org/10.3390/ma11112191

Hunger, M., Entrop, A. G., Mandilaras, I., Brouwers, H. J. H., & Founti, M. (2009). The behavior of self-compacting concrete containing micro-encapsulated phase change materials. Cement and Concrete Composites, 31(10), 731-743. https://doi.org/10.1016/j.cemconcomp.2009.08.002

Jacob, R., Raud, R., Trout, N., Bell, S., Clarke, S., Will, G., & Bruno, F. (2018). Effect of inner coatings on the stability of chloride-based phase change materials encapsulated in geopolymers. Solar Energy Materials and Solar Cells, 174, 271-276. https://doi.org/10.1016/j.solmat.2017.09.016

Jacob, R., Trout, N., Raud, R., Clarke, S., Steinberg, T. A., Saman, W., & Bruno, F. (2016, May). Geopolymer encapsulation of a chloride salt phase change material for high temperature thermal energy storage. In AIP Conference Proceedings (Vol. 1734, No. 1, p. 050021). AIP Publishing. https://doi.org/10.1063/1.4949119

Kastiukas, G., Zhou, X., & Castro-Gomes, J. (2016). Development and optimisation of phase change material-impregnated lightweight aggregates for geopolymer composites made from aluminosilicate rich mud and milled glass powder. Construction and Building Materials, 110, 201-210. https://doi.org/10.1016/j.conbuildmat.2016.02.029

Khudhair, A. M., & Farid, M. M. (2004). A review on energy conservation in building applications with thermal storage by latent heat using phase change materials. Energy conversion and management, 45(2), 263-275. https://doi.org/10.1016/S0196-8904(03)00131-6

Konuklu, Y., Ostry, M., Paksoy, H. O., & Charvat, P. (2015). Review on using microencapsulated phase change materials (PCM) in building applications. Energy and Buildings, 106, 134-155. https://doi.org/10.1016/j.enbuild.2015.07.019

Lucas, S. S., & de Aguiar, J. B. (2019). Evaluation of latent heat storage in mortars containing microencapsulated paraffin waxes–a selection of optimal composition and binders. Heat and Mass Transfer, 1-7. https://doi.org/10.1007/s00231-019-02594-1

Markets and markets. [cited 2019, 13/05]; Available from: ⟨http://marketsandmarkets.com/⟩]

Memon, S. A. (2014). Phase change materials integrated in building walls: A state of the art review. Renewable and sustainable energy reviews, 31, 870-906. https://doi.org/10.1016/j.rser.2013.12.042

Novais, R. M., Ascensão, G., Seabra, M. P., & Labrincha, J. A. (2015). Lightweight dense/porous PCM-ceramic tiles for indoor temperature control. Energy and Buildings, 108, 205-214. https://doi.org/10.1016/j.enbuild.2015.09.019

Shadnia, R., Zhang, L., & Li, P. (2015). Experimental study of geopolymer mortar with incorporated PCM. Construction and building materials, 84, 95-102. https://doi.org/10.1016/j.conbuildmat.2015.03.066

Schmidt, M. (2007). Phase Change Materials-latent heat storage for interior climate control. BASF, Ludwigshafen, Germany.

Sharma, A., Sharma, S. D., & Buddhi, D. (2002). Accelerated thermal cycle test of acetamide, stearic acid and paraffin wax for solar thermal latent heat storage applications. Energy Conversion and Management, 43(14), 1923-1930. https://doi.org/10.1016/S0196-8904(01)00131-5

Sukontasukkul, P., Nontiyutsirikul, N., Songpiriyakij, S., Sakai, K., & Chindaprasirt, P. (2016). Use of phase change material to improve thermal properties of lightweight geopolymer panel. Materials and Structures, 49(11), 4637-4645. https://doi.org/10.1617/s11527-016-0812-x

Tyagi, V. V., Kaushik, S. C., Tyagi, S. K., & Akiyama, T. (2011). Development of phase change materials based microencapsulated technology for buildings: a review. Renewable and sustainable energy reviews, 15(2), 1373-1391. https://doi.org/10.1016/j.rser.2010.10.006

Uddin, M. S., Zhu, H. J., & Hawlader, M. N. A. (2002). Effects of cyclic operation on the characteristics of a microencapsulated PCM storage material. International Journal of Solar Energy, 22(3-4), 105-114. https://doi.org/10.1080/0142591031000092210

Wang, Z., Su, H., Zhao, S., & Zhao, N. (2016). Influence of phase change material on mechanical and thermal properties of clay geopolymer mortar. Construction and Building Materials, 120, 329-334. https://doi.org/10.1016/j.conbuildmat.2016.05.091

William F.. Smith, & Hashemi, J. (2006). Foundations of materials science and engineering. Mcgraw-Hill Publishing.

Xu, B., & Li, Z. (2013). Paraffin/diatomite composite phase change material incorporated cement-based composite for thermal energy storage. Applied energy, 105, 229-237. https://doi.org/10.1016/j.apenergy.2013.01.005

Zeinelabdein, R., Omer, S., & Gan, G. (2018). Critical review of latent heat storage systems for free cooling in buildings. Renewable and Sustainable Energy Reviews, 82, 2843-2868. https://doi.org/10.1016/j.rser.2017.10.046

Zeng, W. R., Li, S. F., & Chow, W. K. (2002). Preliminary studies on burning behavior of polymethylmethacrylate (PMMA). Journal of fire sciences, 20(4), 297-317. https://doi.org/10.1177/073490402762574749

Zhang, Y. P., Lin, K. P., Yang, R., Di, H. F., & Jiang, Y. (2006). Preparation, thermal performance and application of shape-stabilized PCM in energy efficient buildings. Energy and Buildings, 38(10), 1262-1269. https://doi.org/10.1016/j.enbuild.2006.02.009

5.6 Development of PCM-containing inorganic polymers

5.61 Mortars preparation and phase change material selection

The mortar to which PCMs were added correspond to MP30|0.88 formulation, and the detailed description of mixture portions can be seen in 3.5.5. The selection of this particular mortar had in consideration the similarly reduced shrinkage values but higher workability relative to M18 mortars. A commercially available microencapsulated paraffin (Nextek_24D, Microtek Laboratories) was selected as the PCM to be incorporated in IP mortars based on the technical considerations set in the introductory part of this section (e.g., phase transition at 20-25 °C and high heat fusion). The cost of such microencapsulated paraffin was approximately 60 €/kg. Despite the relatively high cost of such additive it was considered in line with the values presented in the literature of 5 to 45 €/kg for wholesale orders (Fullenkamp, 2019). The fundamental physical and thermal properties of the PCM selected are given in Table 5.6.1 and, a backscattered micrograph showing its structure is provided in Figure 5.6.1.

Table 5.6.1 Fundamental data of Nextek_24D PCM (Microtek Laboratories, 2019).

Commercial name	Form	Size (µm)	Melting point (°C)	Heat fusion (J/g)	Max. operating temp. (°C)	Core/shell ratio
Nextek_24D	Dry solid	15-30	24	170	250	≈ 9:1

The effects of adding similar microencapsulated PCMs in traditional rendering mortars have been described by Lucas (2011) and Ascensão (2015), showing an effective capacity to enhance the mortars' thermal performance and elevated compatibility with the matrix materials. The key differences between Nextek_24D and the PCM used on those works are the reduced free formaldehyde content of the shell (<25 ppm) and the higher heat fusion of the latter. Further detailed characterization of microencapsulated paraffin can be found in the works mentioned above. All PCM-containing mortars were produced following the procedure described in 3.3, being afterward employed one extra minute to disperse the microencapsulated PCM.

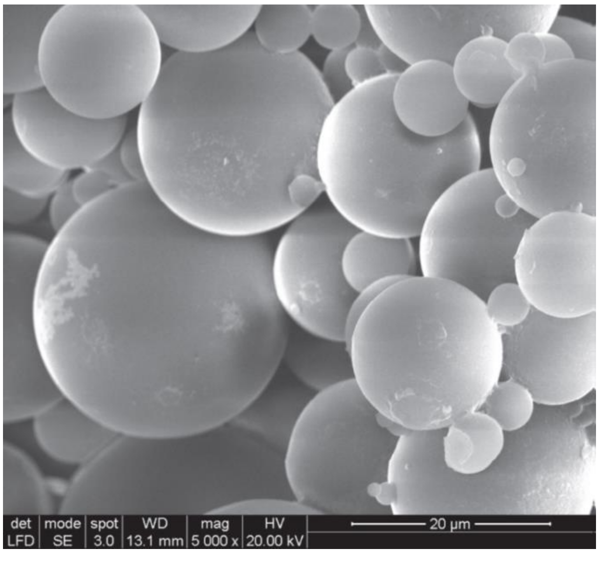

Figure 5.6.1 SEM backscattered micrograph of microencapsulated PCM (reproduced from Shadnia *et al.*, 2015).

5.6.2 Screening tests

Although the effects shrinkage reducing agents and curing temperature had already been described in Chapter 3, possible iterations with phase change materials were evaluated by performing a 2^3 full factorial DoE. The variables considered in these experiments were the dosage of PCM and SRA (2-Methyl-2.4-Pentanediol), and the temperature during the initial 24 h of curing. All IPs were named after the dosage of such additives, being their upper and lower limit shown in Table 5.6.2. A minimum of three 2x2x2 cm^3 replicates was produced per formulation, and their apparent density and compressive strength determined after 48 h of curing.

Figure 5.6.2 shows the apparent density of IP mortars after 48 h of curing. As can be seen, apparent density varied form approximately 2.39 to 2.70 g/cm^3. The single-use of SRA did not significantly affect the mortars' apparent density at an early age. Despite such results seem to contradict the results discussed in 3.6, the effects SRA on porosity and consequently mass loss related to water evaporation only had a significant expression at later ages, and therefore could not be observed here, Figure 5.6.2.

Table 5.6.2 Experimental matrix of the 2^3 full factorial DoE and the respective value of each variable per formulation.

Code	DoE parameters		
	PCM (wt%)	SRA (wt%)	Temp. (°C)
M3000|20	0.0	0.0	20.0
M3003|20	0.0	3.0	20.0
M30100|20	10.0	0.0	20.0
M30103|20	10.0	3.0	20.0
M3000|50	0.0	0.0	50.0
M3003|50	0.0	3.0	50.0
M30100|50	10.0	0.0	50.0
M30103|50	10.0	3.0	50.0

* % based on precursors mass (slag + silica fume).

However, the modifications on mortars' apparent density imposed by PCMs are not expected to evolve with time significantly, and therefore early age measurements could potentially indicate major effects. Microencapsulated PCMs typically present densities ranging from 0.6 to 1.0 g/cm^3 depending on the type of paraffin and shell used, and of shell/core ratio. Thus, if the melting point is not surpassed, PCM can be considered as lightweight small-size aggregates that increase the mortars volume per unit of mass. It can be seen that in IPs mortars cured at 20 °C the addition of 10 wt% PCM reduced apparent density to approximately 2.45 g/cm^3. However, it should be mentioned that even at low curing temperatures, PCMs can concentrate heat generated during polymerization reactions, possibly interfering with the reaction kinetics and physical properties of the produced mortars. A further but minor decrease of density was promoted by combining SRA and PCM despite the reasons for such reduction being not clear.

More interesting, however, was to observe that when mortars were cured at slightly elevated temperature and PCM assume a more active thermal role, the differences in density are less significant. This may suggest that PCM thermal effect somehow compensates for their low density. However, the possibility of PCM act as an internal curing agent seems to be contradicted by the strength development of mortars cured at 50 °C, Figure 5.6.3c,d. The negative effect of SRA on strength development was confirmed, being even the dominant factor that contributed to lowering the compressive strength of IPs cured at 20 °C. However, when IP mortars were cured at 50 °C, strength development was equally affected by the addition of SRA and PCM. The reference mortar (M3000|50) presented the highest compressive strength (81 MPa), but all IPs mortars inside the experimental domain exhibit compressive strengths higher than 40 MPa after only 48 h of curing.

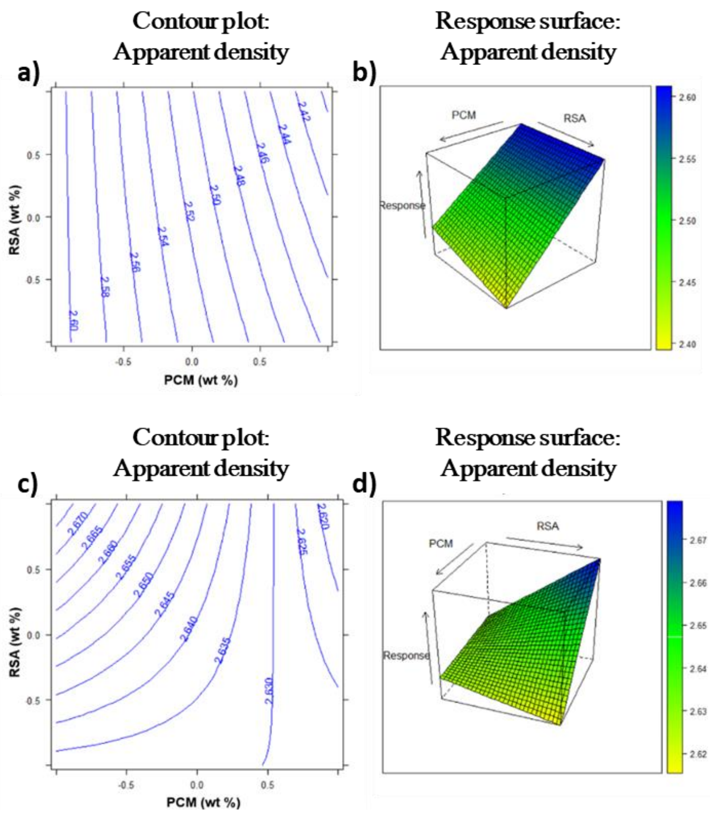
Contour plot: Apparent density

Response surface: Apparent density

Contour plot: Apparent density

Response surface: Apparent density

Figure 5.6.2 Contour plots and apparent density surface responses as a function of PCM and SRA dosage of samples cured at different temperatures (a, b) 20 °C and (c, d) 50 °C.

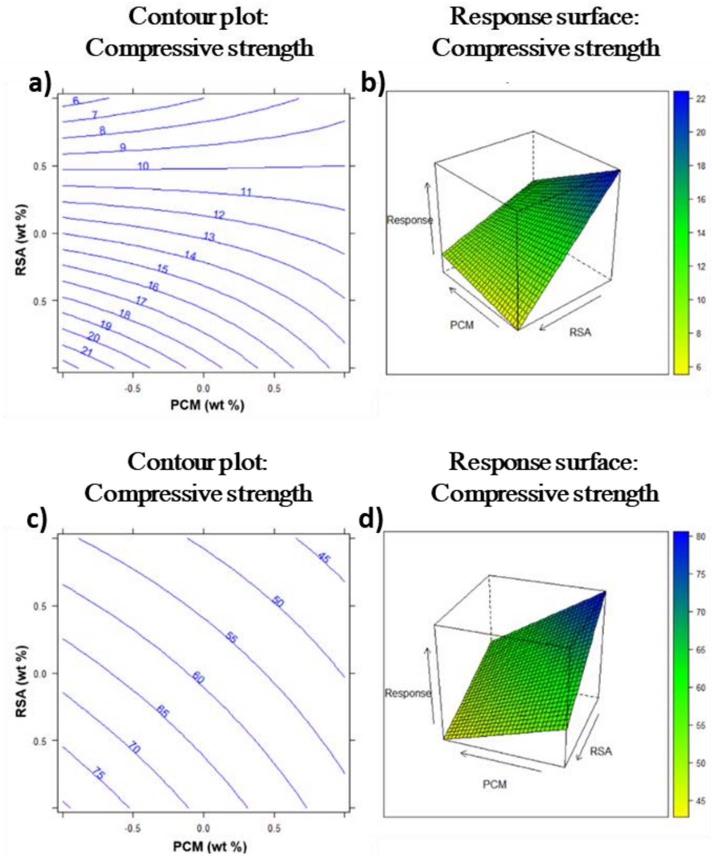
Contour plot: Compressive strength

Response surface: Compressive strength

Contour plot: Compressive strength

Response surface: Compressive strength

Figure 5.6.3 Contour plots and compressive strength surface responses as a function of PCM and SRA dosage of samples cured at different temperatures (a, b) 20 °C and (c, d) 50 °C.

Even disregarding possible late-stage strength developments these results show a significant reduction in IPs' mechanical properties provoked by PCM addition. Despite the severe level of such reduction, the use of latent heat storage materials seemed feasible. Notwithstanding, in order to achieve higher mechanical performances imposing a period of curing at slightly elevated temperatures is recommended. Yet, such need did not constitute an additional constraint when considering the production of sandwich panels as it has been already demonstrated that elevated temperatures were required to the limit shrinkage of the parent mortars and that insulation properties of foamed IPs also beneficiate from curing at slightly elevated temperatures.

5.6.3 Strength development and volumetric stability of PCM-containing mortars

To further confirm the effects of PCM on the properties of IPs mortars, 4x4x16 cm^3 monolith samples of the M3003|50 and M30103|50 formulations were produced (see Table 5.6.2) and their fundamental properties characterized after 28 d of curing. A third set of IPs was also produced with an intermediate PCM dosage (5.0 wt%), further termed as M3053|50. Eventual disruptions of the volumetric stability of the parent mortar were assessed following the procedure described in 3.5.

As can be seen in Table 5.6.3, increasing the PCM dosage led to a significant reduction of apparent density. Such reduction followed a pattern similar to the one observed in Figure 5.6.2a, which corresponded to mortars cured at 20 °C. The thermal effect of PCM during the initial stages of reaction did not have a repercussion in apparent density at later ages, and strength development was significantly impaired. Compressive strength reaffirmed the results gathered at early age and validated the surface responses proposed. The assumptions made regarding the similarity of early and later age impacts of PCM on compressive strength were confirmed.

The reduction of total porosity and average pore size has been used in literature to explain some increases in strength when PCMs are introduced in the mixture design (Lucas, 2011). Similar enhancements were not verified in the mortars developed here, therefore discarding the eventual optimization of particle packing.

The volumetric stability of PCM microcapsules and the reduction of the binding phase per unit volume favored a progressive reduction of shrinkage as the PCM dosage rose. Table 5.6.3 shows that M30103|50 mortars presented shrinkage values lower than 1 mm/m, which is generally assumed as benchmark value for cementitious and cement-like products.

Table 5.6.3 Fundamental properties of PCM-containing IP mortars after 28 d of curing.

	M3003|50	**M3053|50**	**M30103|50**
SRA (wt%)	3.0	3.0	3.0
PCM (wt%)	0.0	5.0	10.0
Apparent density 28 d (g/cm^3)	2.54±0.1	2.41±0.1	2.32±0.1
Flexural strength 28 d (MPa)	7.1±0.3	6.3±0.3	5.4±0.2
Compressive strength 28 d (MPa)	66.4±3.7	47.3±3.1	37.2±2.6
Shrinkage (mm/m)	1.10±0.10	1.03±0.04	0.80±0.05

* % based on precursors mass (slag + silica fume).

In an attempt to promote the responsible use of additives and optimize production costs, SRA dosage was reduced to 2.0 wt% of the precursors mass. Such a decision was based on the positive effect of PCM on the mortars' volumetric stability and the relatively small increase shrinkage verified in Chapter 3 when 2M dosage was reduced from 3.0 to 2.0 wt%. To verify if these competitive effects were able to deliver PCM-containing mortars with shrinkage values near to 1 mm/m, the mortars described in Table 5.6.3 were replicated with an SRA dosage of 2.0 wt% and their fundamental properties reassessed. As can be seen in Table 5.6.4, the properties of PCM-containing mortars were only marginally affected by the reduction of SRA dosage further confirming the findings described in 3.6. The presence of PCM microcapsules did not significantly modify the effects of reducing SRA dosage, and mortars with shrinkage values near

1 mm/m were obtained. Independently of SRA dosage, both flexural and compressive strength were reduced as PCM dosage rose, reaching a minimum value of approximately 6 MPa and 37 MPa, respectively.

Table 5.6.4 The effects of reducing SRA dosage on the fundamental properties of PCM-containing IP mortars after 28 d of curing.

	M3002|50	M3052|50	M30102|50
SRA (wt%)	2.0	2.0	2.0
PCM (wt%)	0.0	5.0	10.0
Apparent density 28 d (g/cm^3)	2.49±0.1	2.44±0.1	2.23±0.1
Flexural strength 28 d (MPa)	8.0±0.3	6.3±0.3	6.0±0.2
Compressive strength 28 d (MPa)	67.3±5.1	57.0±1.7	37.4±2.2
Shrinkage (mm/m)	1.20±0.11	1.12±0.07	0.99±0.05

* % based on precursors mass (slag + silica fume).

5.6.4 Carbonation tests

Despite having been shown that PCMs could be effectively added into IPs mortars and even have a beneficial impact on their volumetric stability, it was noted the lack of available studies reporting long-term effects of PCMs in the durability of cement and cement-like materials.

As the first measure to assess their impact on the durability of the developed materials, accelerated carbonation tests were performed on heat-cured reference mortars (M30|50) and on its 10 wt% PCM-containing counterparts (M30102|50), and the progression of the carbonation front and the evolution of mechanical properties were monitored.

Accelerated tests allow to roughly estimate the long-term effects of carbonation in a reasonable timeframe. However, it should be kept in mind that natural carbonation representability is arguable, and the interpretation of the results and conclusions made thereof should have the latter into consideration. The accelerated carbonation tests were performed according to the UNI EN 13295:2008. After demolding the specimens, a 10 d stabilization period was imposed before initiate carbonation tests. In this period, the specimens were kept in a controlled atmosphere at 20±1° C and 60±5 RH. After the stabilization period, half batch of each mortar was transferred to a commercial climatic chamber at equal temperature and RH but with a 3 % CO_2 concentration. This date will be referred to as time 0, and the mortars were monitored during the following 56 d. The mechanical properties of a minimum of two specimens per mortar formulation, curing condition (natural or accelerated carbonation), and age were determined. After performing mechanical tests, a phenolphthalein solution was sprayed on fractured surfaces, and the carbonated depth was measured. In Figure 5.6.4 an illustrative image shows the absence of carbonation at time 0 in PCM-containing samples. An equal absence of carbonation was also observed in the reference samples at the beginning of carbonation tests.

Figure 5.6.4 Illustrative image of the lack of carbonation in PCM-coating samples at time 0.

In Figure 5.6.5 can be seen that natural carbonation conditions only marginally affected the mortars' mechanical performance. Carbonation depth was also not affected by SRA and PCM addition, suggesting that possible differences in the pore structure formed required prolonged exposition to be manifested. These results further justify the need for accelerated tests to estimate later-age carbonation effects.

Despite the more pronounced carbonation of reference mortars at later ages, the loss of compressive strength after accelerated carbonation test was higher in PCM-containing mortars, 9 and 13%, respectively. A greater impact of PCM was observed in flexural strength. After 56 d of accelerated carbonation, the flexural strength of reference mortars significantly increased (+22%), while a two-fold reduction occurred in their PCM counterparts. Despite the introduction of PCM into the mixture design resulted in a negative impact on strength development, reasonable flexural (>3 MPa) and compressive strength (>35 MPa) could be maintained by limiting PCM dosage to 10 wt%.

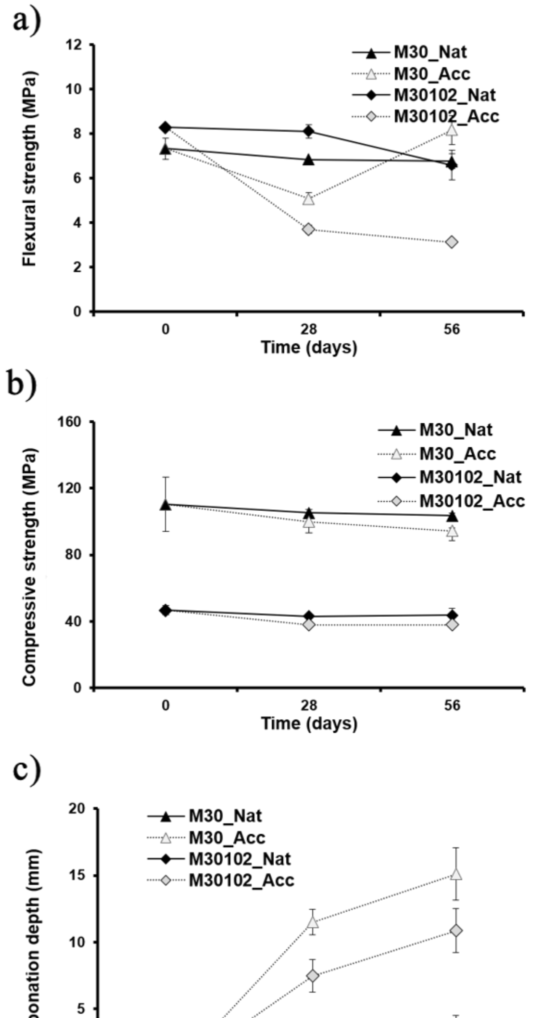

Figure 5.6.5 Comparison between the effects of natural and accelerated carbonation on (a) flexural and (b) compressive strength. In (c) the temporal progression of carbonation depth is shown.

5.6.5 Functional characterization-Thermal response of PCM-containing mortars

In order to evaluate the thermal response of PCM-containing mortars, 16x16x4 cm^3 specimens of M30|50 and M30102|50 were produced and inlaid into the top surface of a 50x50x50 cm^3 extruded polystyrene test cells, Figure 5.6.6.

The test cells were placed inside a climatic chamber and subjected to different temperature profiles, according to Figure 5.6.7. The temperature of the climatic chamber was varied between 5°C and 45°C, and the temperature on the internal and external surface of the specimens continuously monitored at its geometrical center. The thermal cycles were designed to be symmetric relative to the PCM melting temperature. In the first thermal cycle, lower heating and cooling rates and short isothermal steps (2h) were defined, representing a moderate scenario, while the second cycle intended to simulate extremely demanding conditions. Relative humidity levels were kept constant throughout these experiments at 60 %, and an initial stabilization period of two hours at 20 °C was set in both profiles.

Figure 5.6.6 Cubic test cells developed to assess the thermal responsiveness of different IP mortars.

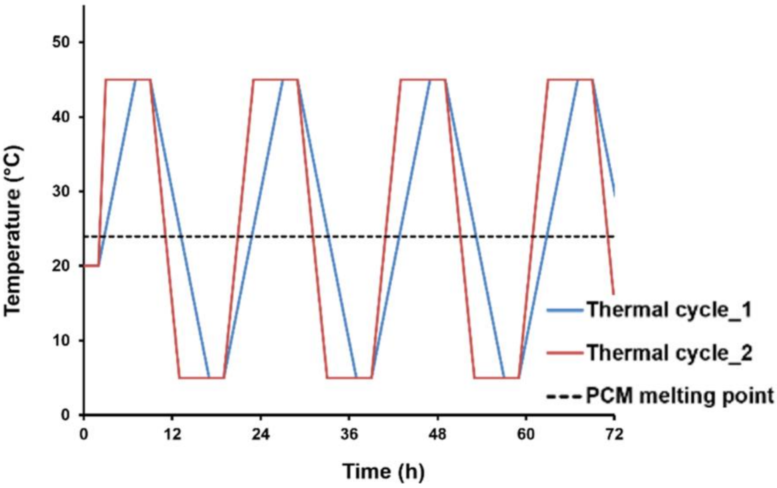

Figure 5.6.7 Thermal profiles used to assess the mortars' thermal response.

Figure 5.6.8a,b shows the temperature evolution of the specimens' internal and external surfaces. As can be seen, independently of the mortar formulation used, the maximum external temperatures are considerably higher, and the minimum temperatures considerably lower than the temperatures recorded internally. These thermal gradients also observed in PCM-free specimens denoting a thermal mass effect that should not be attributed to storage and release of latent heat.

It is fair to recognize that the addition of PCM microcapsules with reduced specific weight diminished the mortars' apparent density (approximately -11%) and, hence their thermal mass. This thermal mass effect should be accounted for in the design of PCM-containing building materials, especially when submitted to significant temperatures fluctuations.

Therefore, the differences in the thermal gradients observed between the surfaces of the test cells will not only denote the active thermal role of PCM but also comprise thermal mass contributions. A close-up image of heating and cooling stages and isothermal steps in thermal cycle 1 is provided in Figure 5.6.9.

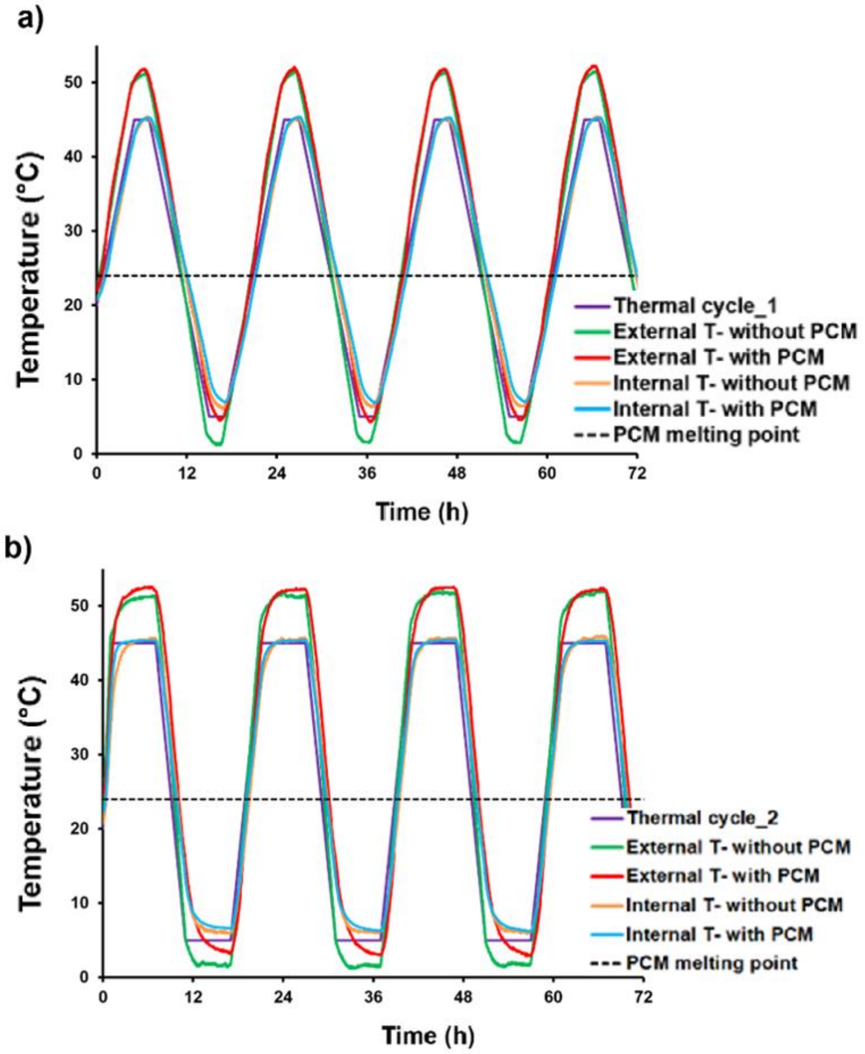

Figure 5.6.8 Temperature evolution of reference and PCM-containing mortars when subjected to different thermal profiles: a) thermal cycle 1 and b) thermal cycle 2.

As can be seen in Figure 5.6.9a, the maximum internal temperature was only marginally decreased with the introduction of PCM (-0.1 °C), while the temperature of external surfaces was increased by 0.6 °C. Similar behavior was reproduced during all heating stages of thermal cycle 1. These results could eventually suggest a poor thermal effect of the selected PCM. However, Figure 5.6.9c shows that near to PCM phase transition temperature the outer surface of PCM-containing samples presented significantly lower temperatures relative to the reference mortar. The lower temperatures and the thermal delay observed in Figure 5.6.9c demonstrates the beneficial thermal impact of PCM during heating stages in regions near to their phase transition. In this region, the internal surfaces of both mortars present similar temperatures showing that the heat load accumulated on outer surfaces is diffused through the samples, not directly reaching the inner surfaces of the test cells. When temperature surpassed 30 °C, the differences between the temperature profiles become inexistent which suggests that PCMs thermal capacity has been reached. At higher temperatures, PCM could no longer act as thermal buffers, and the temperature of both external and internal surfaces was increased relative to reference mortar. Such an increase in temperature can be attributed to the slightly inferior thermal mass of PCM-containing samples. Therefore, the thermal efficiency of the PCM-containing mortars developed here would be substantially increased during heating stages if maximum temperatures are limited to approximately 30 °C. Moreover, the thermal delay observed near to PCM melting point can be enlarged if more progressive heating regimes are provided.

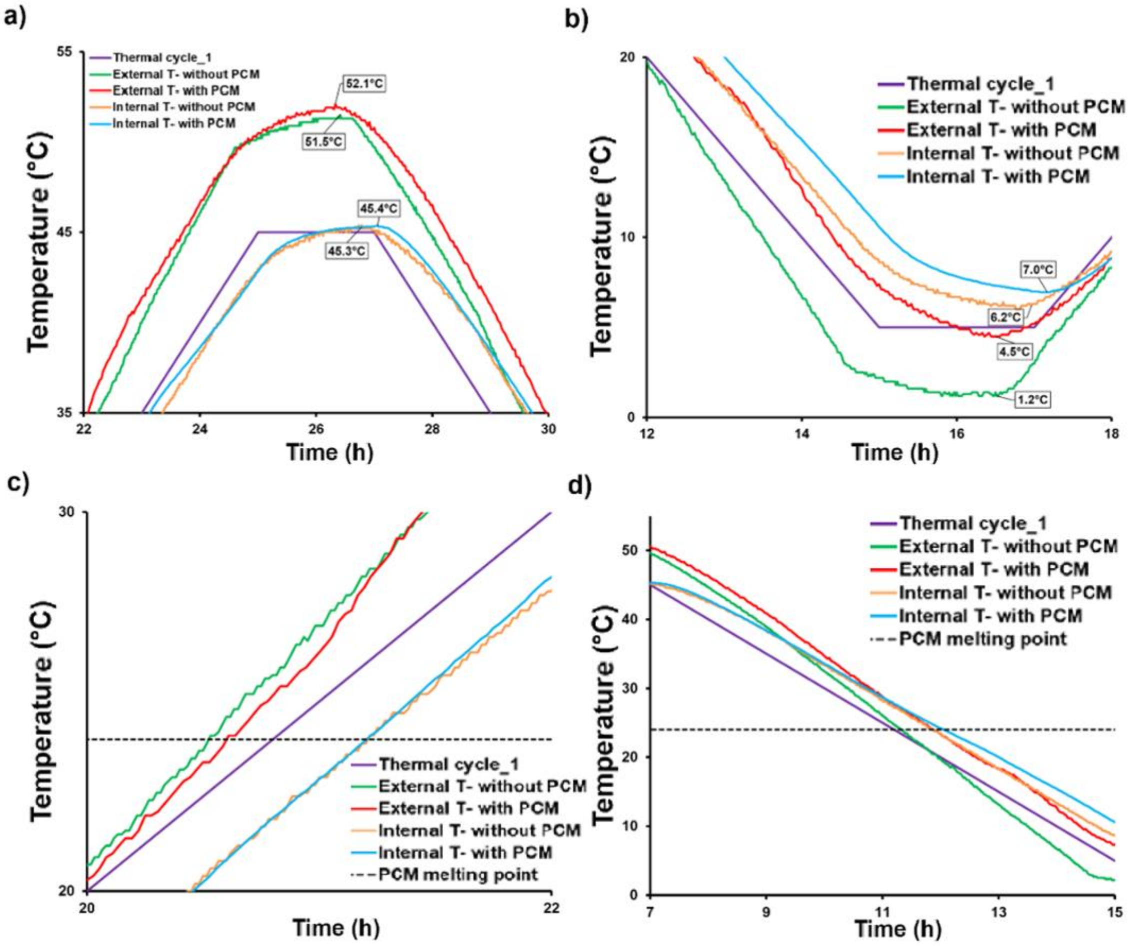

Figure 5.6.9 Temperature evolution of the reference and PCM-containing mortars during thermal cycle 1: a) isothermal step at 45 °C, b) isothermal step at 5 °C, c) heating stage and d) cooling stage.

The addition of PCM was particularly effective during cooling stages of thermal cycle 1, and in increasing of the minimum temperatures reached. As can be seen in Figure 5.6.9d, during the entire cooling stage, PCM-containing mortars exhibited higher temperatures in both internal and external surfaces. The thermal energy accumulated during heating stages was promptly discharged to the surrounding environment by the reference mortars, while a more progressive thermal evolution was observed in PCM-containing mortars. In the initial part of cooling stages, the differences in the thermal profiles cannot be linked to thermal effects involving phase transitions and should be attributed to the physical differences between the mortars compared here. As temperature decreased and got closer to 24 °C, the difference in the thermal behavior of the different mortars was further exacerbated due to the heat released during PCM solidification. The addition of 10 wt% PCM was able to increase the minimum internal temperature by 0.7 °C, while in external surfaces an increase of 3.1°C was observed, Figure 5.6.9b. In Table 5.6.5, the reductions of thermal gradients obtained by PCM addition are shown. As can be seen, considerably higher reductions were obtained on external surfaces. As the external surfaces were directly exposed to the surrounding atmosphere (i.e. heat and cooling sources), such a result could be expected.

The main thermal effects of PCM were not altered by modifying the thermal profile to present higher heating and cooling rates and longer isothermal steps, Figure 5.6.8b. The existence of a thermal delay during heating stages around the phase transition temperature of PCM was also visible in thermal cycle 2, albeit with a shorter duration. The higher rate of energy supply in this thermal cycle explains the reduction of such a period. During cooling stages, no significant differences were found between cycles 1 and 2. However, longer isothermal steps tended to attenuate the beneficial thermal impacts of PCM and approximate the maximum and minimum temperatures reached to those of the reference mortars. As consequence, the reduction in internal and external temperature gradients provoked by PCM was lower in cycle 2, and hence, its effectiveness impaired.

Table 5.6.5 Average variation of the prototypes external an internal temperature between the references mortars their PCM-containing counterparts.

	Thermal cycle	
	1	2
Maximum external temp.	+0.6 °C	+0.7 °C
Minimum external temp.	+3.1 °C	+1.7 °C
Maximum internal temp.	-0.1 °C	-0.4 °C
Minimum internal temp.	+0.7 °C	+0.3 °C
External thermal gradient	-2.5 °C	-1.0 °C
Internal thermal gradient	-0.8 °C	-0.7 °C

In summary, despite the maximum temperature and heating rates tested here not being optimal, the addition of 10 wt% PCM to the mortars formulation was able to reduce both external and internal temperature gradients proving the thermal buffering features of the developed materials. The thermal performance of the developed IP mortars would further beneficiate if more moderated temperature regimes are experienced, which in fact would better represent the climate of most EU regions.

Nonetheless, it was shown that the produced PCM-mortars can be used as passive thermal regulators even in severe climatic conditions to guarantee adequate levels of comfort, with reduced energy consumption and, by doing so, approximate current construction models of the concept of near-zero energy buildings.

Future investigations should submit the developed products to more realistic thermal profiles and confirm their thermal performance in-service conditions. Further developments in this field can comprise the utilization of multiple PCMs with different phase transition temperatures in order to autonomously respond to different thermal solicitations. Moreover, designing such a multi-purposes type of solution would be extremely important in industrial contexts to streamline future production process. The cost reduction of microencapsulated PCM, the increase of their efficiency by tailoring the thermal properties of the surrounding matrix or by modifying their chemical composition, and the digital coupling with heating and refrigeration systems are also worthy of being explored.

References

Ascensão, G. (2015). Desenvolvimento e caracterizaçao de argamassas multifuncionais. Msc thesis, Department of Civil Engineering, University of Aveiro.

Fullenkamp, K., Montané, M., Cáceres, G., & Araya-Letelier, G. (2019). Review and selection of EPCM as TES materials for building applications. International Journal of Sustainable Energy, 38(6), 561-582. https://doi.org/10.1080/14786451.2018.1543307

Lucas, S. (2011). Argamassas funcionais para uma construção sustentável. PhD thesis, Department of Civil Engineering, University of Aveiro.

Microtek Laboratories . [cited 2019, 13/05]; Available from: ⟨https://www.microteklabs.com/⟩.

Shadnia, R., Zhang, L., & Li, P. (2015). Experimental study of geopolymer mortar with incorporated PCM. Construction and building materials, 84, 95-102. https://doi.org/10.1016/j.conbuildmat.2015.03.066

Uddin, M. S., Zhu, H. J., & Hawlader, M. N. A. (2002). Effects of cyclic operation on the characteristics of a microencapsulated PCM storage material. International Journal of Solar Energy, 22(3-4), 105-114. https://doi.org/10.1080/0142591031000092210

UNI EN 13295 (2008). “Prodotti e sistemi per la protezione e la riparazione delle strutture di calcestruzzo - Metodi di prova - Determinazione della resistenza alla carbonatazione.”

Chapter 6

High-temperature resistance of alkali-activated materials

The following chapter is based on a manuscript in preparation entitled "High-temperature resistance of CaO-FeOx-Al_2O_3-SiO_2 alkali-activated materials" by Ascensão, G., Faleschini, F., Marchi, M., Segata, M, Van De Sande, J., Rahier, H., Bernardo, E. & Pontikes, Y.

The mentioned manuscript fully covers the research performed in the context of high-temperature resistance, but its results are firstly presented here. The mortar selected to assess the high-temperature performance of the developed materials corresponds to the formulation MP30|0.88 as described in 3.6. Note that no shrinkage reducing agents or phases change materials were used here as neither of those admixtures can withstand temperatures above 200 °C.

Abstract

AAMs are emerging in the construction sector by providing an opportunity to up-cycle several wastes in the production of highly performant and added-value materials for technical applications. One of the most attractive properties of AAMs is their performance under considerable thermal loads. Being generally praised for their refractory and high-temperature resistant features, the thermal behavior of AAMs is dictated by their chemical composition, phase assemblage, and crystallized phases upon exposure to high temperatures. Hence, the thermal performance of AAMs produced from CaO-FeO_x-Al_2O_3-SiO_2-rich residues may significantly differ from the most commonly described (Na_2O/K_2O)-Al_2O_3-SiO_2 ternary systems. Therefore, the purpose of this research was to ascertain the resistance to high temperatures of CaO-FeO_x-Al_2O_3-SiO_2 alkali-activated materials. Mortars specimens were exposed to different temperatures (up to 1100 °C) and heating rates (1 and 10 °C/min), and the properties of the resulting materials were evaluated in terms of visual appearance, weight loss, apparent density, and compressive strength. These analyses were further complemented by evaluating the morphological and mineralogical modifications that occurred during thermal exposure using scattering electron microscopy (SEM) and X-ray diffraction (XRD) techniques. The findings of this work demonstrated the significant effect of temperature and heating rate on the properties of the fired AAMs.

At low heating rates, there were no visible macroscopic effects on the samples apart from volumetric reduction and a gradual lightening of their color as the temperature raised. The mechanical strength of AAMs underwent an abrupt decline at 750 °C widely recovered at higher temperatures, reaching the maximum value of 184 MPa at 1100 °C that corresponds to a 115% increase compared to the parent AAM. With the increase of heating rate to 10 °C/min, a strength loss at 750 °C persisted, but the maximum compressive strength was halved (97MPa) and reached at 900 °C. At 1100 °C a significant reduction of compressive strength was observed (17 MPa), but all the samples were able to maintain their structural integrity. Except for samples exposed to 1100 °C with a heating rate of 10 °C/min, all AAMs presented residual compressive strength values higher than 40 MPa. These results have shown that CaO-FeO_x-Al_2O_3-SiO_2 AAMs present interesting refractory and high-temperature resistant features and can be potentially used as high-temperature resistant mortars and concrete or as a thermal coating to protect pre-existing cement-based concrete elements.

6.1 Introduction

The development of added-value products using secondary outputs can have a remarkably positive effect on the sustainability and economics of thermochemical technologies. Apart from the excellent mechanical and insulating features described in the previous chapters, another attractive property of AAMs is their high performance at elevated temperatures. Conversely to concrete that suffers considerable degradation and spalling at relatively low temperatures (even below 400 °C (Hertz, 2003; Rossino, 2014)), the physicochemical characteristics of AAMs allow them to act as fire spreading and thermal energy barriers that prevent the failure of construction elements. Yet, the thermal behavior of AAMs is largely dependent on several synthesis conditions such as the chemical composition of the parent precursors, the type (silicate or hydroxide solutions), concentration, and charge balancing cation (Na^+ or K^+) in the activating solution, and Si/Al molar ratio (Kong, 2008; Van De Sande, 2019a). These synthesis conditions dictate the liquidus temperature of AAMs, as well as the amount and type of crystalline phases formed.

The typical chemical composition of the slag produced during the thermochemical conversion of municipal and mined wastes can be described as a CaO-FeO_x-Al_2O_3-SiO_2 quaternary system. This chemical composition could be potentially adjusted to promote the formation of more refractory phases upon thermal exposure (i.e. by adding alumina-rich materials (Sakkas, 2014; Van De Sande, 2019a), but changing the composition of such low-value product may entail hardly bearable environmental and economic costs. Moreover, the present work did not intend to maximize the thermal properties of CaO-FeO_x-Al_2O_3-SiO_2-rich AAMs by altering their chemical composition with beneficial admixtures but ascertain the thermal performance of potassium-based AAMs previously optimize for more general construction purposes. Thus, the thermal performance of conventional construction materials as OPC-concrete, and not fire-resistant or refractory ones, should be taken as a benchmark throughout this work.

Pure (Na_2O/ K_2O)-Al_2O_3-SiO_2 ternary systems are known to present excellent thermal resistance due to the crystallization of phases as albite (liquidus temperature, 1118 °C), nepheline (stable up to 1256 °C) and carnegieite (liquidus temperature, 1526 °C) in the case of sodium; and aluminosilicates compounds with high melting points as orthoclase (liquidus temperature, 1250 °C), leucite (with a congruent melting point of 1693 °C) and kalsilite (liquidus temperature, 1750 °C) in the case of potassium (Panias, 2015). The refractory performance of potassium-based ternary systems is further beneficiated by the higher viscosity of potassium feldspar melts that turns flowability a less significant phenomenon and reinforces the advantageous character of potassium-based AAMs for high-temperature applications. Nevertheless, it is fair to mention that Na_2O-SiO_2-Al_2O_3 systems can also present excellent resistance to high temperature if a specific set of synthesis conditions that promote carnegieite formation (melting point, 1526 °C) are provided. On the other hand, K_2O-SiO_2-Al_2O_3 systems present a broader set of synthesis conditions where refractory phases are formed upon sintering (Panias, 2015), and this is particularly relevant in industrial contexts where versatile and resilient mixture designs are of utmost importance. From this point of view, the use of a potassium-based activating solution is advantageous both in terms of thermal performance and industrial processing.

However, the chemical composition of the slag produced in thermochemical conversion processes is characterized by the presence of significant contents of calcium and iron which have a direct influence on the phase composition and the morphology of the material after heating. Low-calcium systems (i.e. geopolymers) are generally preferable for producing high-temperature resistance AAMs as calcium reduces the liquidus temperature of K_2O-Al_2O_3-SiO_2 systems. Furthermore, the near absence of hydrated and chemically bonded water in those low-calcium structures (White, 2010; Park, 2018) reduces the deleterious microstructural effects of dehydration, resulting in more thermally stable AAMs. The presence of Fe can also be deleterious to K_2O-Al_2O_3-SiO_2 systems. The effects of iron are mainly determined by the amount of alumina present in the systems (Panias, 2015). If insufficient alumina is available, the iron-compounds formed are characterized by much lower melting temperatures relative to their Fe-free analogs.

Hence, the thermal performance of AAMs made from FeO_x-Al_2O_3-SiO_2 precursors with low Al_2O_3 contents is expected to be significantly impaired relative to their iron-free equivalents. On the other hand, in alumina-rich K_2O-Al_2O_3-SiO_2 systems, the introduction of Fe is not expected to preclude the crystallization of highly stable and refractory phases of mullite, leucite, and kalsilite; and can even promote the crystallization of refractory hercynite (Panias, 2015). The presence of these phases potentiates the thermal resistance of AAMs made from alumina-rich FeO_x-Al_2O_3-SiO_2 precursors and are expected to deliver excellent fire-resistant properties (Sakkas, 2014).

While several authors investigated the phase transitions and thermal characteristics of AAMs produced from precursors as metakaolin and fly-ash, that can be mainly described as Al_2O_3-SiO_2 binary systems (Bell, 2009; Degirmenci, 2018); and calcium or iron-rich ones, as ground granulated blast furnace slag (Degirmenci, 2018), ferronickel slag (Sakkas, 2014), and copper slags (Van De Sande, 2019a), the thermal characteristics of more complex CaO-FeO_x-Al_2O_3-SiO_2 quaternary systems have not been thoroughly investigated yet. From the premises described above becomes clear that calcium- and iron-containing phases will play vital roles in determining the thermal performance of those AAMs. Understanding what their combined effects are and how they are translated into the residual properties of CaO-FeO_x-Al_2O_3-SiO_2-rich AAMs after thermal exposure will be crucial for these AAMs to gain market acceptance as temperature resistant materials, and ultimately, to provide another long-term, large-scale, up-cycling solution for CaO-FeO_x-Al_2O_3-SiO_2-rich residues generated during thermochemical conversion processes.

6.2 Experimental procedure

Raw material characterization and mortars preparation

The precursor used to produce IP mortars corresponds to the slag mainly used throughout this work, and the detailed description of its characteristics can be found in Chapter 3. The bulk chemical composition of the slag can be generally described as a CaO-FeO_x-Al_2O_3-SiO_2 quaternary system, and its complete chemical composition can be found in Table 3.5.8. The Fe oxidation state was quantified as described by Close *et al.* (1958) and, the iron phases were found to be predominantly in the bivalent oxidation state (92%).

Following the principles of sustainability, the use of cement and natural aggregates was completely avoided in the mortars mix design; the vitreous slag was used both as the main precursor and aggregate as previously described in 3.5.5. Based on the previous results, the mortar mixture was designed for a binder-to-aggregate mass ratio of 0.88. Fuller distribution was applied to optimize aggregates particle size distribution corresponding to MP30|0.88 mortars described in 3.6. To assist the reader, the characteristics of the reference mortar mix design are provided in Table 6.2.1.

Table 6.2.1 Reference mortar composition (wt%).

Powdered Slag	Silica Fume (SF)	Solution	Aggregates	
			Fraction 1+0	Fraction 10+0
32.7	1.9	12.2	31.2	22.0

The finely powdered slag was used as binders' main precursor (94.5 wt% of binders' solid load) while the silica fume (SF, Elkem, >95% SiO_2) used as an admixture further increased the availability of Si species and favor strength development. Increasing Si/Al ratio is also expected to promote the formation of highly thermally stable phases (Bell, 2009) and produce compact microstructures with low porosity levels after thermal exposure (Morsy, 2019), thus improving the high-temperature resistance and residual strength of the produced materials. A potassium-based activating solution was used following a mix design previously optimized. Theoretical predictions (Panias, 2015) and empirical experimentations (Kong, 2008) in the available literature confirm the superior thermal performance of potassium-based AAMs relative to their sodium-based counterparts. The preparation of the activating solutions is described in 3.3, and the solutions used in these experiments were composed of 83.4 wt% H_2O, having a SiO_2/K_2O molar ratio of 0.68.

The mortars were produced following the procedure described in Chapter 3. The mortars were cast into $5x5x5cm^3$ metallic molds and cured for 24 h in controlled conditions (20±0.5 °C and 95±1.0% relative humidity). After demolding, the mortar specimens were individually sealed with a plastic film and thermally treated for 72 h at 50 °C, being afterward kept at room conditions (20±1.0 °C and 65±5.0% relative humidity) until testing.

Methods

High-temperature processing

After 28 d of curing, mortar specimens were heated from room temperature up to 1100 °C in a chamber furnace (Carbolite RHF). Five different target temperatures were defined: 105, 600, 750, 900, and 1100 °C. These target temperatures were chosen on the grounds of previous studies (Rossino, 2014; Van De Sande, 2019a) who have demonstrated the existence of relevant chemical transformations occurring in these temperature ranges. For each target temperature, a thermal profile with a heating rate of 1 °C/min and an isothermal step of 1 h was set. The heated specimens were let to cool down naturally inside the closed furnace. This procedure was replicated with a heating rate of 10 °C/min to assess the impact of heating rate on AAMs mineralogy, morphology, and post-heating properties. A minimum of two specimens per temperature and heating rate were tested.

Physico-mechanical characterization

The weight (0.1 g accuracy) and dimensions (0.01 mm accuracy) of each specimen were measured before and after thermal exposure to evaluate the mass loss and the volumetric changes occurring during thermal treatment (and eventual anisotropic features). The mortars' bulk density was determined by the relation between the weight and volume of each sample. Compressive strength was determined using a Universal Testing Machine (Controls) according to the EN196-1:2016.

Crystallinity and morphological characterization

The crystallinity of the starting slag and mortars produced from thereof was assessed by X-ray diffraction (XRD), carried out on a conventional Bragg-Brentano Bruker D8 Advance diffractometer equipped with Lynxeye detector (Cu Kα radiation λ=1.54059 Å, divergence slit 0.5°, Soller slit set 2.5°+2.5°, 5-70°2θ, step/size 0.02° and t/step 0.04s.) and phase identification by EVA software (database ICDD-PDF-2). Samples from green and thermally treated mortars were collected from mechanical tests, grinded, sieved (≤45µm), and kept sealed prior testing. Scanning electron microscopy (SEM - EVO® MA 15) equipped with energy dispersive X-ray spectrometry (EDS, AZtecEnergy) was used to further evaluate the differences in the sample's morphology before and after thermal exposure. All backscattered electron images (BSE) were acquired using a 20 kV acceleration voltage and a working distance of 10.0 mm.

6.3 Results and discussion

Physico-mechanical characterization

The AAMs residual properties were ascertained as a function of temperature (up to 1100 °C) and heating rate (1 and 10 °C/min). Figure 6.3.1 illustrates the color change, the cracking, and the deformation in mortars after high-temperature exposure. Below 750 °C there were no visible effects on the surface of the specimens independently of the heating rate used. Only a slight lightening of the color, which can be attributed to gradual dehydration, could be observed from 20 °C (Figure 6.3.1a) to 600 °C (Figure 6.3.1b). In fact, Figure 6.3.2 shows that mass loss mainly occurred in this temperature range. The mass loss at 105 °C can be attributed to the evaporation of free water located in large pores. Previous works (Van De Sande, 2019a) had reported a higher mass loss in this temperature range, which can be explained – along with the differences in binder chemistry- by the curing conditions (50 °C for 3 d) and curing duration (28 d) employed in this work prior to thermal testing. The further mass loss observed at temperatures up to 600 °C can be attributed to the egress of water present in small size pores, interstitial water, and chemically bonded water in hydroxyl groups (Bell, 2009; White, 2010). No anisotropic features were detected, and a uniform volumetric contraction that did not exceed 20 vol% was observed.

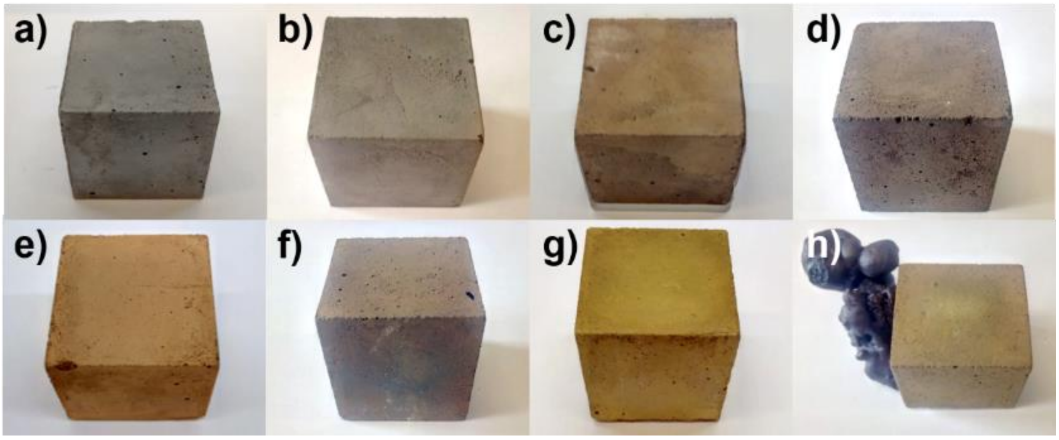

Figure 6.3.1 Alkali activated mortars specimens after 28 d of curing and thermal exposure to (a) 20 °C, (b) 600 °C, (c, d) 750 °C with heating rates of 1 and 10 °C/min, respectively, (e, f) 900 °C with heating rates of 1 and 10 °C/min, respectively, and (g, h) 1100 °C with heating rates of 1 and 10 °C/min, respectively. Mortars exposed to 105 °C are not shown here but no significant modifications on specimens' appearance could be seen relative to the ones kept at 20 and 600 °C (a). At 600 °C there were no visible differences between specimens heated with distinct heating rates, being (b) a representative example of both. Molten material present at the surface of mortars heated up to 1100 °C at 10 °C/min is illustrated in h).

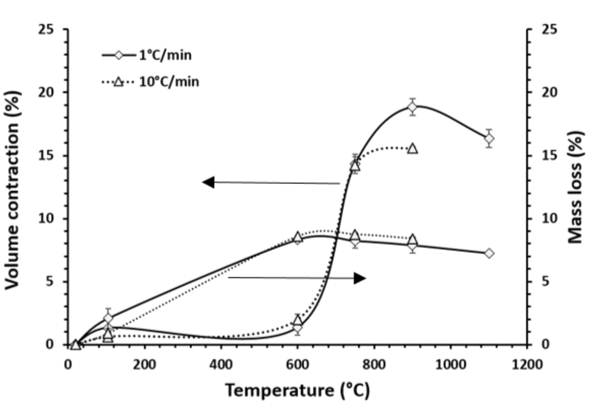

Figure 6.3.2 Mortars' volume contraction and mass loss as a function of temperature and heating rate. The curves are drawn as a guide to the eye.

The influence of the heat rate started to become evident from 750 °C, as shown in Fig. 2 c-h. The specimens heated at lower rates (1 °C/min) changed color from a light grey to a gradually more brownish and yellow color (see Figure 6.3.1 c,e,g). No cracks were visible on the surfaces of these samples, and the absence of color gradients indicates uniform mineralogical transformations. The mineralogical transformations that occurred at these temperatures explain these changes in color and are discussed later in this work.

When a higher heating rate was employed (10 °C/min), less distinguishable color changes were observed. The specimens heated up to 750 and 900 °C presented a less vivid brownish color relative to the ones heated at lower heating rates. Some color gradients were observed across the specimen's surfaces, especially when heated to 900 °C. The differences in colors indicate that temperatures gradients may have led to uneven phase transitions. In addition, some cracks and superficial degradation were visible at the surface of samples. The rapid increase of temperature fastens dehydration processes, but water release occurs at higher temperatures due to low heat and mass transfer rates (Figure 6.3.2), which in turn, results in excessive vapor pressure and gives origin to the observed crack propagation (Nurhayat, 2018). However, all samples heated up to 900 °C maintained their structural integrity. The samples heated to up 1100 °C with a heating rate of 10 °C/min present considerable molten material in their bottom surfaces (rotated in Figure 6.3.1h). Apart from the excessive vapor pressure generate, the large temperature gradients across the samples' cross-sections result in differential shrinkage, further increasing the stresses formed and more extensive crack propagation (Figure 6.3.3), allowing the runoff of molten material. Similar findings were reported by Fernández-Jiménez *et al.* (2010), who observed that steep heating and cooling rates form new or intensified pre-existing cracks due to the high thermal strain generated, ultimately leading to local failure. The viscosity of the melts also decreases as the temperature rises, further facilitating their flow. Hence, the amount of molten material is expected to be significant at temperatures higher than 900 °C, that with the increased flowability of the melts and the high amount of voids and cracks in the mortars structures resulted in the appearance of molten material in the samples surfaces, as can be seen in Figure 6.3.1h.

Figure 6.3.3 The surface of alkali activated mortar after thermal exposure to 1100 °C with heating rates of 10 °C/min. Molten material was removed from the sample surface for clarity.

In samples heated to 1100 °C with a lower heating rate, no molten material was visible after thermal exposure. The more gradual heating process diminished crack formation, which allowed to retain the molten material inside the monolith, positively affecting the mortars' structural stability and high-temperature performance. Although mortars heated up to 1100 °C with heating rates of 10 °C/min retain their cubic shape and were tested for their compressive strength, they were excluded from further physical analysis (e.g. mass loss).

The physical and mineralogical modifications that occurred upon heating had clear repercussions on AAMs residual properties. From room temperature to 600 °C a slight increase of compressive strength after thermal exposure was observed, as shown by Figure 6.3.4. The improvement of compressive strength after thermal exposure to temperatures that do not exceed 600 °C is not related to melting and crystallization processes (see section "Morphological analysis") but most likely due to the increment of on-going polymerization reactions. In section 3.4 have been shown that in very similar alkali-activated systems, exothermic reactions have not completely ceased after more than 20 d of curing. Elevated temperatures stimulate these late-stage reactions and prompt the formation of more mechanically resistant binding phases. This beneficial effect overcomes the deleterious impact of dehydration and improves AAMs mechanical features.

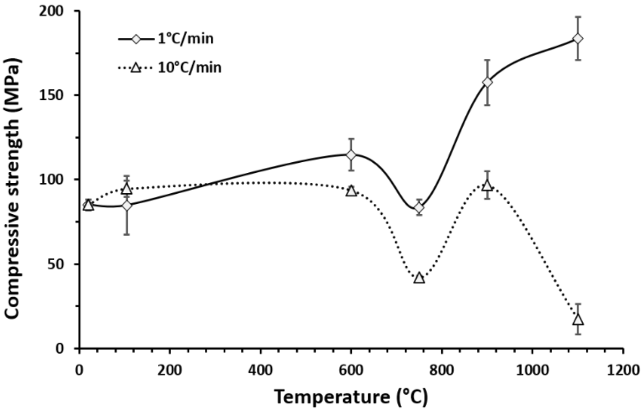

Figure 6.3.4 Mortars' compressive strength as a function of temperature and heating rate. The curves are drawn as a guide to the eye.

The increase of compressive strength in this temperature range is often associated with densification (Van De Sande, 2019a). However, it can be seen in Figure 6.3.5 that the apparent density slightly decreases at 600 °C. Although more resistant and probably denser polymeric skeletons been formed, this decrease is, however, the combined effect of water loss and shrinkage. As mass loss (≈ 8.5 wt%) was significantly higher than the volumetric contraction up to 600 °C (<2 vol%), apparent densities decrease.

The increment of on-going reactions is further supported by comparing the mechanical strength of samples thermally treated up to 600 °C with different heating rates. As can be seen, lower heating rates – meaning more prolonged residence time at elevated temperatures- favor the formation of more resistant AAMs without significantly modifying the samples' mass and volume (Figure 6.3.2) or promoting the significant formation of new crystalline phases (Figure 6.3.6). At 750 °C, considerable deterioration of AAMs mechanical properties occurred with both heating rates used. This process can be attributed to the deterioration of iron- and aluminosilicate networks (Bakharev, 2006), which are the primary reaction products of alkali activation reactions. The shrinkage of the aluminosilicate network induces internal cracks and increases the mean pore size, thus, leading to poorer mechanical performances (Bakharev, 2006). Nonetheless, totally dehydrated charge balance cations (Na+ or K+) act as flux at high temperatures and reduce the temperature at which crystallization starts. This can imply the formation of partially sintered phases around 750 °C (Fernández-Jiménez, 2010), which, however, are not fully able to compensate the decline in compressive strength provoked by shrinkage upon structure total dehydration.

An additional factor that has been reported to contribute to the loss of strength at temperatures around 800 °C is the expansion of coarse aggregates (Kong and Sanjayan, 2010). However, due to the type and granulometric distribution of the amorphous aggregates used in this work a similar phenomenon seems unlikely. The effects of the network shrinkage could be seen at the macroscopic level by the steepest increase of the volumetric contraction observed around 750 °C, Figure 6.3.2. At this temperature, increasing the heating rate was found to be detrimental to AAMs residual strength. Along with the higher crack formation due to the higher vapor pressure generated, the considerable difference of mechanical performance between mortars heated with distinct heating rates may indicate more deteriorated network structures. At 750°C, AAMs start to lose their predominantly amorphous character leading to the appearance of some broadened peaks of magnetite (Fe_3O_4) and esseneite ($CaAlFeSiO_6$), Figure 6.3.6. The amount of crystallized phases was not sufficiently high to compensate for the decrease of AAMs mechanical strength but may have contributed to the sudden densification of the samples.

As mass loss was mainly associated with dehydration processes occurring mostly before 300°C, the mass remained practically unchanged at temperatures higher than 600 °C. As a consequence, the apparent density followed a similar trend to the volumetric contraction. A minor increase of mass was visible from 750 °C to higher temperatures (Figure 6.3.2) that can be attributed to further oxidation and crystallization of iron species into magnetite and posteriorly to hematite phases. The reference mortar presented a density of 2.46 kg/m^3 and a compressive strength of 85 MPa after 28 d of curing. Using a heating rate of 1 °C/min the maximum apparent density was observed at 900 °C (2.78 g/cm^3). At the highest temperature tested (1100 °C), apparent density was reduced to 2.71 g/cm^3 which suggests the partial reduction of hematite to magnetite. The results are in agreement with XRD patterns shown in Figure 6.3.6 and with the findings of Van De Sande *et al.* (2019a) who reported a 13 wt% reduction in hematite content and a magnetite increase in the same order of magnitude (12 wt%) in Fe-rich samples from 1000 °C to 1300 °C. However, the decrease of apparent density was not detrimental to mechanical performance, and the samples heated up to 1100 °C with a heating rate of 1 °C/min presented the maximum compressive strength recorded, 183 MPa.

In those samples, when the temperature exceeded 750 °C and the crystallization of new phases becomes more extensive, the decay of compressive strength was fully reversed. Post-heating compressive strength progressively increased as the temperature rose, with an increase relative to parent mortar of 85% and 115% at 900 °C and 1100 °C, respectively. However, increasing the heating rate to 10 °C/min did not only provoke a higher decay of compressive strength at 750 °C, but it also significantly impaired the performance recovery at higher temperatures. On those samples the maximum compressive strength was halved and attained at 900 °C (97 MPa). Despite the recovery from the decay observed at 750 °C and the 13% increase relative to the parent mortar, much higher compressive strengths were observed in samples heated up to 900 °C with lower heating rate (158 MPa). At 1100 °C, the mechanical strength of samples heated with different heating rates became even more discrepant. Conversely to the samples heated at 1 °C/min that yield the maximum strength at this temperature, when high heating rates were imposed a considerable degradation of the AAMs performance occurred. However, as shown in Figure 6.3.2, these samples were not dimensionally stable with some molten material coming out the samples' structure. This explains the much lower compressive strength. The reason why in fast heated samples some material runoff might be that crystallization is not fast enough, while the viscosity decreases due to the increasing temperature. At 1 °C/min there is apparently better match between the heating and crystallization rate. Except samples exposed to 1100 °C with a heating rate of 10 °C/min (17 MPa), all samples after the thermal exposure presented compressive strength values higher than 40 MPa.

.

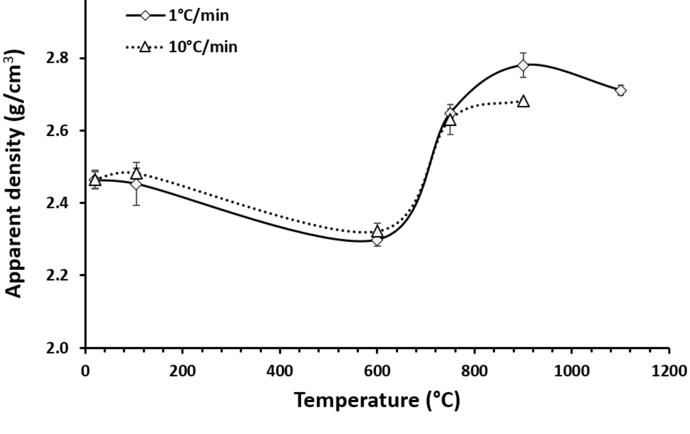

Figure 6.3.5 Mortars' apparent density as a function of temperature and heating rate. The curves are drawn as a guide to the eye.

Crystallinity

The mineralogical composition and the high-temperature mineralogical transitions are of the utmost importance to fully describe the thermal behavior of AAMs and to safely classify them in terms of high-temperature resistance. At room temperature, AAMs are predominantly amorphous materials. The amount and type of crystalline phases present in AAMs are mainly dependent on the chemical composition of their parent precursors. The powdered slag (PS) and silica fume (SF) used in this work as starting materials were almost completely XRD amorphous materials; only one crystalline peak of small intensity was detected in the XRD patterns for SF, identified as moissanite (SiC, as an impurity).

Not surprisingly, AAMs made thereof exhibit an utterly amorphous structure at room temperature, with a pronounced hump between 20-40° 2θ in their XRD patterns. Heating the samples to 105 °C did not impose any significant crystalline transformation regardless of the heating rate used (not shown here for the sake of relevance). The first signs of the formation of crystalline phases were visible in the samples heated at 600 °C. In XRD patterns of mortars heated at the rate of 1 °C/min, no crystalline peaks were detected at this temperature, Figure 6.3.6a. However, increasing the heating rate to 10 °C/min seems to have promoted the formation of a crystalline phase identified as mullite ($Al_6Si_2O_{13}$), Figure 6.3.6b. Mullite is frequently reported to crystallize at higher temperatures (>1000 °C), but some works highlighted that the characteristics of the silica source and the processing conditions (including heating rate) can reduce mullite crystallization temperature (Fernandes, 2018; Bartsch,1999; Kara, 1996). In the presence of amorphous silica, mullite formation was reported at temperatures as low as 800 °C (Fernandes, 2018). However, the crystallization of mullite at 600 °C is improbable, and its presence in the XRD pattern is most likely an artifact.

The formation of crystalline phases was further accentuated as the temperature increased, especially at temperatures higher than 900 °C. The crystallization of magnetite (Fe_3O_4) and esseneite ($CaAlFeSiO_6$) was visible at 750 °C. The crystallization of these phases could be anticipated from the high iron and calcium contents of the parent slag. At 900 °C, significant differences could be seen between the XRD patterns of samples heated with distinct heating rates. At the highest heating rate, leucite ($KAlSi_2O_6$), anorthite ($CaAl_2Si_2O_8$), and hematite (Fe_2O_3) also started to crystallize. Slightly more elevated local temperatures can have made part of the abundant esseneite and magnetite phases transit to anorthite and hematite phases, respectively. The formation of leucite, anorthite, and hematite phases was also visible in samples heated with a lower heating rate, but only to a minor extent and at 1100 °C. In samples heated at the rate of 10 °C/min up to 1100 °C, the hematite peak was smaller while the magnetite peak was more significant compared to samples heated up to 900 °C. This indicates that a partial reduction of hematite into magnetite occurs with rapid heating up to 1100 °C (Van de Sande, 2019a). The formation of esseneite and magnetite as the predominant phases in all samples can be seen as a natural consequence of the abundant availability of Si, Ca, and Fe species provided by the mix design. The addition of silica fume and potassium silicate solution could anticipate the formation of these thermally stable and refractory phases, favoring the formation of AAMs with high thermal performance. The residual properties of the developed materials were enhanced with the adoption of slower heating rates. The physico-mechanical phenomena occurring during steeper heating processes, such as the higher vapor pressure and increased shrinkage and degradation of binding phases seem to overwhelm possible positive effects from crystal formation. To further investigate such phenomena, morphological analyses were performed in samples heated up to 1100 °C, where the most significant crystallographic differences were observed.

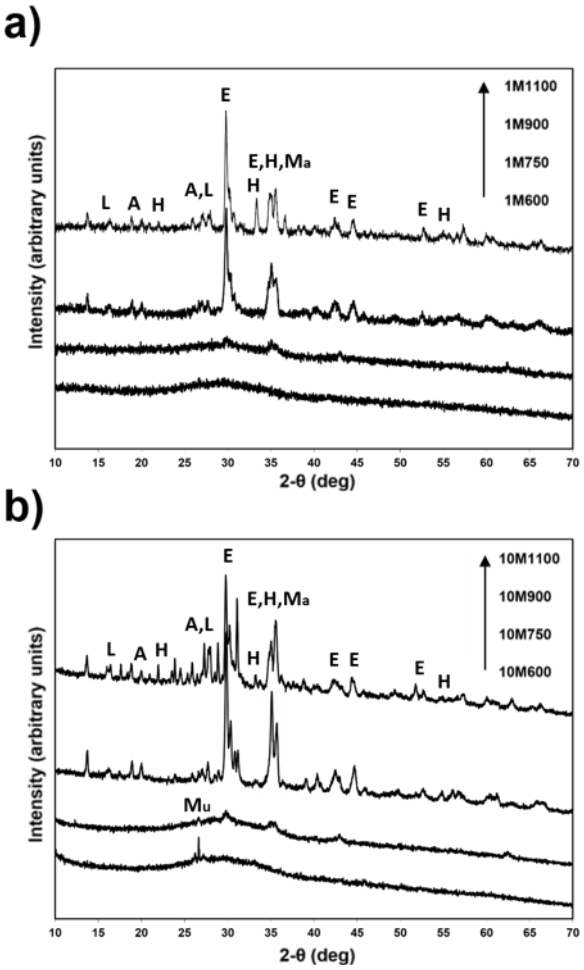

Figure 6.3.6 XRD patterns of alkali activated mortars after heated to different temperatures: a) with a heating rate of 1 °C/min and b) with a heating rate of 10 °C/min. The main peaks of each phase are indicated as follows: Mu = mullite, Ma= magnetite, E = Esseneite, L = Leucite, A = anorthite, H = hematite.

Morphological analysis

Figure 6.3.7 shows representative backscattered electron imaging micrographs of the reference mortar before being exposed to thermal treatment. A binder phase was formed (Figure 6.3.7a), but the existence of embedded unreacted particles confirms that complete dissolution was not achieved. The high solid-to-liquid ratio used (2.85) limited precursors' dissolution, but the samples show a homogeneous matrix in which undissolved particles acted as small-sized aggregates, Figure 6.3.7b. The formation of microcracks due to drying shrinkage processes has been previously reported in Chapter 3, but undissolved particles acted as physical barriers limited crack development and propagation, Figure 6.3.7b. EDS analyses revealed a binder phase predominantly composed of Si, Al, Fe, Ca, and K, while the spectra of undissolved particles was in line with chemical composition of the slag used as the main precursor and as aggregates. Some spherical pores were also observed which can be attributed to entrapped air during mixing or to undissolved SF particles removed during SEM sample preparation.

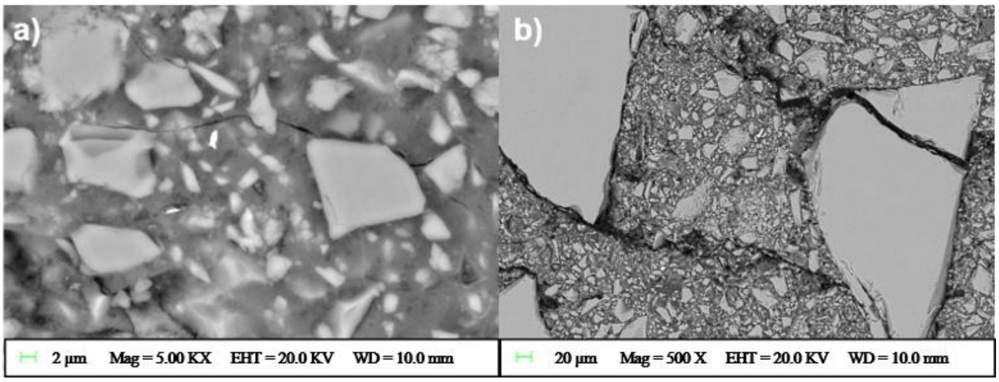

Figure 6.3.7 Backscattered electron imaging micrographs of alkali activated mortar before being exposed to elevated temperatures.

The effects of high-temperature exposure and heating rate on mortar morphology are illustrated in Figure 6.3.8. Independently of the heating rate used, a more compact microstructure with few large cracks was formed relative to the parent mortar. The morphological analysis of these samples indicates that undissolved particles previously visible at room temperature were almost completely molten, Figure 6.3.8a, b. Their previous homogeneous structure was transformed into a texture of finely exsolved phases. However, the contours of undissolved particles remain identifiable as white lines. A clearer picture of interfacial transition zones between molten aggregates and previous existing binders is better seen at higher magnification, Figure 6.3.8c, d. EDS analyses revealed the predominance of iron elements in the white areas outlining the aggregates contours, which suggest the concertation of crystalized Fe-rich phases at these locations. At higher magnifications, the morphological differences between samples heated with distinct heating rates also become more evident.

Mortars heated at 1 °C/min exhibit a continuous interfacial transition zone with no visible cracks or microscopic pores. The progressive increase of temperature that reduces vapor pressure and cracks formed upon heating; the prolonged residence time at high temperatures that may have increased the amount of molten material; and the use of potassium-based activating solutions that assist the formation of very viscous vitreous phases (Fernández-Jiménez, 2010), may have all contributed to sealing pre-existing pores and cracks. More homogeneous microstructures were formed, which agrees with the enhanced compressive strength of these mortars after being exposed to high-temperatures, Figure 6.3.2.

At the steepest heating rate (Figure 6.3.8d), the existing microstructure at room temperature had more difficulty to absorb the thermal strains generated upon heating. Apart from the already mentioned local failure and runoff of molten material, the formation of micropores along interfacial transition zones was also visible. A less compact and more heterogeneous structure was formed at the microscopic level, and the less effective bonding between the newly crystallized phases can explain the lower mechanical strength of mortars heated at 10 °C/min at all temperatures above 600 °C. These differences in mortars' morphology show that heating rate plays a vital role in the sintering process. Increasing the heating rate affects the phases crystallized but also their morphology and distribution, which in turn affects the dimensional stability of the mortars at high-temperature and their properties after cooling. The crystallization of new phases was particularly relevant at temperatures over 900 °C, but strength only increased if a low heating rate was employed. Nevertheless, all mortars were able to largely surpass the threshold temperature of 400 °C without any visible signs of degradation or spalling. This behavior clearly shows the superior thermal performance of the developed products relatively to mainstream construction materials.

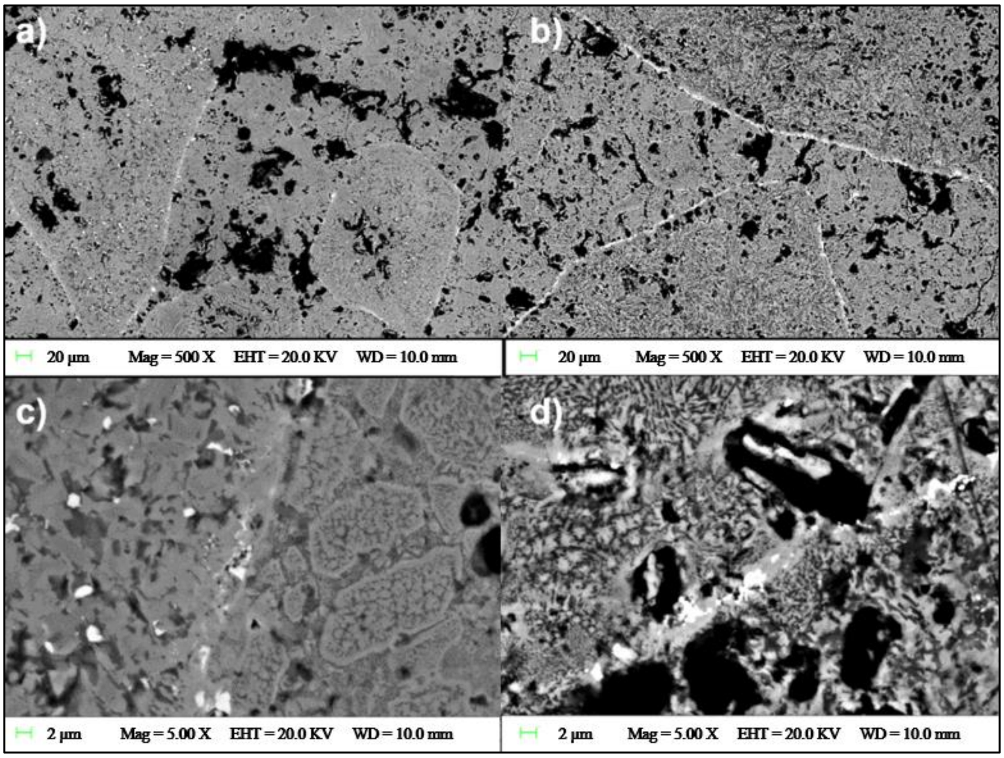

Figure 6.3.8 Backscattered electron imaging micrographs of mortars exposed to 1100 °C. a,c) with a heating rate of 1 °C/min and b,d) with a heating rate of 10 °C/min.

6.4 Conclusions

In this work, the high-temperature resistance of $CaO-FeO_x-Al_2O_3-SiO_2$ AAMs was investigated. The mix design of the AAMs was developed to use a high content of a low-value residue (85.9 wt%). This conscious option envisioned to reduce the production cost and environmental impact of the produced materials while providing an up-cycling solution to large volumes of $CaO-FeO_x-Al_2O_3-SiO_2$-rich slags generated in thermochemical conversion processes. The results of this work have shown the superior thermal performance of AAM produced from these residues relatively to mainstream construction materials. The effect of temperature and heating rate were investigated being both recognized as vital to the post-heated properties of AAMs. Lower heating rates had a beneficial effect on AAM mechanical performance. The maximum strength was observed when specimens were exposed to 1100 °C (183 MPa), almost doubling the compressive of green mortars (85 MPa). Increasing the heating rate to 10 °C/min was found to promote more severe deterioration processes that resulted in extensive crack development and even samples' deformation at 1100 °C. Along with the formation of less homogeneous microstructures, these deleterious effects were found to result in more fragile structures after thermal exposure that limits the use of the developed materials to 900 °C if high heating rates will be experienced/applied.

Nonetheless, the thermal features of benchmark materials (e.g., OPC-based products) were clearly surpassed by the developed AAMs mortars. No signs of spalling were visible and developed materials could withstand temperatures up to 900 °C with heating rates up to 10 °C/min and maintaining their structural integrity and considerable mechanical strength (> 40 MPa). Moreover, crystallographic analyses revealed the crystallization of thermally stables phases, indicating that the refractory and high-temperature resistant features of the developed $CaO-FeO_x-Al_2O_3-SiO_2$-rich alkali-activated materials could be potentially further enhanced by fine-tuning the mix design.

References

Bakharev, T. (2006). Thermal behaviour of geopolymers prepared using class F fly ash and elevated temperature curing. *Cement and Concrete Research*, *36*(6), 1134-1147. https://doi.org/10.1016/j.cemconres.2006.03.022

Bartsch, M., Saruhan, B., Schmücker, M., & Schneider, H. (1999). Novel low-temperature processing route of dense mullite ceramics by reaction sintering of amorphous SiO2-coated γ-Al2O3 particle nanocomposites. Journal of the American Ceramic Society, 82(6), 1388-1392. https://doi.org/10.1111/j.1151-2916.1999.tb01928.x

Bell, J. L., Driemeyer, P. E., & Kriven, W. M. (2009). Formation of ceramics from metakaolin-based geopolymers. Part II: K-based geopolymer. *Journal of the American Ceramic Society*, *92*(3), 607-615. https://doi.org/10.1111/j.1551-2916.2008.02922.x

Close, P., Shepherd, H. M., & Drummond, C. H. (1958). Determination of several valences of iron, arsenic and antimony, and selenium in glass. *Journal of the American Ceramic Society*, *41*(11), 455-460. https://doi.org/10.1111/j.1151-2916.1958.tb12894.x

Degirmenci, F. N. (2018). Freeze-thaw and fire resistance of geopolymer mortar based on natural and waste pozzolans. Ceramics–Silikáty, 62(1), 41-49. https://doi.org/10.13168/cs.2017.0043

EN, BS (2016). 196-1. Methods of testing cement. Part 1: Determination of strength, BSI Standards Limited 2016, ISBN 9780580845802.

Fernandes, L., & Salomão, R. (2018). Preparation and Characterization of Mullite-Alumina Structures Formed" In Situ" from Calcined Alumina and Different Grades of Synthetic Amorphous Silica. *Materials Research*, *21*(3). http://dx.doi.org/10.1590/1980-5373-mr-2017-0783

Fernández-Jiménez, A., Pastor, J. Y., Martín, A., & Palomo, A. (2010). High-Temperature Resistance in Alkali-Activated Cement. *Journal of the American ceramic society*, *93*(10), 3411-3417. https://doi.org/10.1111/j.1551-2916.2010.03887.x

Hertz, K. D. (2003). Limits of spalling of fire-exposed concrete. *Fire safety journal*, *38*(2), 103-116. https://doi.org/10.1016/S0379-7112(02)00051-6

Kara, F., & Little, J. A. (1996). Sintering behaviour of precursor mullite powders and resultant microstructures. *Journal of the European Ceramic Society*, *16*(6), 627-635. https://doi.org/10.1016/0955-2219(95)00179-4

Kong, D. L., Sanjayan, J. G., & Sagoe-Crentsil, K. (2008). Factors affecting the performance of metakaolin geopolymers exposed to elevated temperatures. *Journal of Materials Science*, *43*(3), 824-831. https://doi.org/10.1007/s10853-007-2205-6

Kong, D. L., & Sanjayan, J. G. (2010). Effect of elevated temperatures on geopolymer paste, mortar, and concrete. *Cement and concrete research*, *40*(2), 334-339. https://doi.org/10.1016/j.cemconres.2009.10.017

Morsy, M. S., Shebl, S. S., & Rashad, A. M. (2009). Effect of fire on microstructure and mechanical properties of blended cement pastes containing metakaolin and silica fume. *Silicates Industriels*, *74*(3), 59. http://www.irbnet.de/daten/iconda/CIB_DC25545.pdf

Panias, D., Balomenos, E., & Sakkas, K. (2015). The fire resistance of alkali-activated cement-based concrete binders. In *Handbook of Alkali-activated Cements, Mortars and Concretes* (pp. 423-461). Woodhead Publishing. https://doi.org/10.1533/9781782422884.3.423

Park, S., & Pour-Ghaz, M. (2018). What is the role of water in the geopolymerization of metakaolin?. Construction and Building Materials, 182, 360-370. https://doi.org/10.1016/j.conbuildmat.2018.06.073

Rossino, C. (2014). Intrinsic damage and spalling sensitivity of concrete subjected to high temperature. https://www.politesi.polimi.it/handle/10589/89809

Sakkas, K., Panias, D., Nomikos, P. P., & Sofianos, A. I. (2014). Potassium based geopolymer for passive fire protection of concrete tunnels linings. *Tunneling and underground space technology*, *43*, 148-156. https://doi.org/10.1016/j.tust.2014.05.003

Van De Sande, J., Pontikes, Y. & Rahier, H. (2019a). Thermal behavior of Inorganic polymers synthesised from Fe-rich slags. (Manuscript in preparation)

White, C. E., Provis, J. L., Proffen, T., & Van Deventer, J. S. (2010). The effects of temperature on the local structure of metakaolin-based geopolymer binder: A neutron pair distribution function investigation. *Journal of the American Ceramic Society*, *93*(10), 3486-3492. https://doi.org/10.1111/j.1551-2916.2010.03906.x

Chapter 7

Semi-industrial upscaling

One of the key challenges faced by alkaline activation technology is to transpose their unanimously recognized potential among academics to the industrial realm. A plethora of causes contributes to the so-far restricted market implementation of alkali-activated materials, being however most of them not related to technical limitations. While addressing those factors is commendable, dedicate greater efforts to grasp possible scaling effects is justifiable in a work of this nature.

Therefore, the following chapter describes the first steps taken towards the semi-industrial upscaling of the developed products and outlines the challenges encountered.

Introduction

While the development of alkali-activated materials has long been understood as a potential solution to address the sustainability concerns associated with cement-based products, much fewer attempts have been made to streamline the academic efforts made into the upscaling and commercialization of the developed products. With the exception of some start-up companies, many of the known large-scale projects have been undertaken by large industrial corporations whose primary aim is to discover processes in which utilize the residues of their industries.

By prioritizing the reduction of the economic burdens associated with the landfill of their residues, those entities forcibly focused their efforts in market segments with lower barriers of entry (e.g., road infrastructures, blocks, and pavers).

Apart from challenges related to the supply chain and cost of alkali activators, the lack of regulating frameworks for alkali-activated materials had also restricted the widespread of these emerging materials into more added-value segments. However, the growing implementation of performance-based specifications facilitates their acceptance and extends the market segments for which AAMs can be considered. In this work, waste-based AAMs were developed with a broad range of properties but added-valued structural and non-structural elements for NZEB buildings were the main envisioned application.

When considering the upscale of AAMs, one of the most significant challenges faced is their sensitivity to feedstock materials and synthesis conditions. Prediction models like ones discussed in Chapter 3 can serve as guideposts during the initial stages of development, but thorough examination of possible scaling effects will still be required, and ad hoc adjustments needed in full-scale production to ensure compliance with legislation in force and to guarantee consistency levels that meet market expectations.

Upscaling tests and results

To examine the feasibility of producing real scale sandwich panels, gradual manufacturing upscaling from standard 4x4x16cm^3 specimens to semi-industrial prototypes was performed. The conceptual model of the sandwich panels produced is given in Figure 7.1a, while the schematic representation of the casting sequence is shown in Figure 7.1b. Foamed IPs were jet into the molds immediately after cast the first layer of dense IP mortar. After 24 h of curing at 50 °C, the top surface of the foamed layer was aligned and the second layer of the dense IP mortar cast. This casting sequence intended not to limit expansive reactions and endow the foamed layer of a reasonable level of consolidation before casting the second layer of dense IP mortars.

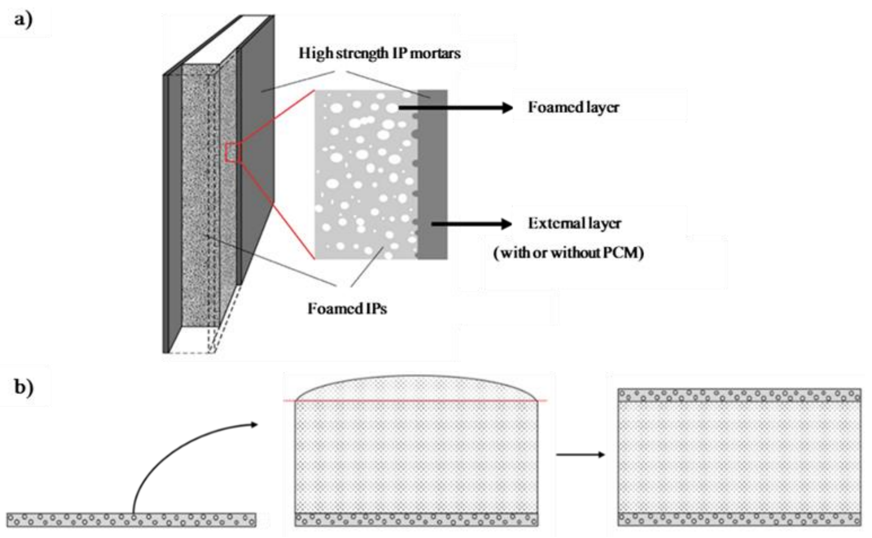

Figure 7.1 Conceptual drawing of IP-based multilayer sandwich panels and schematic representation of the casting sequence.

Based on the insights gathered in the previous chapters of this work and considering the performance of the different AAMs developed, MP30|22M0.88 mortars and 27SOAL foamed IPs were selected to produce the dense outer-layers and the thick thermal insulating section of the prototypes, respectively. In ensuing stages, MP30|22M0.88 mortar was substituted by its 10 wt% PCM-containing counterparts in one of the panels' outer layers to endow the produced prototypes of a thermally responsive character.

The mix portions and the production processes of these AAMs, the detailed description of their properties, and the motifs that grounded their selection have been already addressed and can be found in Chapters 3 to 6. To assist the reader, a summarized description of the AAMs main properties is reassumed in Table 7.1.

Notice that MP18|22M0.88 mortars can be also used to produce the panels' external layers if PCM inclusion is not considered. However, since PCM-containing mortars were used in these upscaling stages, it would be preferable in an industrial context to maintain constant the parent mortar and adding or not PCM according to product range desired. Such industrial constraints were considered and mimicked in these upscaling stages.

Table 7.1 Main physico-mechanical properties of AMMs used to produce multilayer sandwich panels.

Code	Description	App. density (g/cm^3)	Thermal cond. (W/m°K)	Comp. strength (MPa)
27SOAL	Foamed IP	0.62±0.2	0.08±0.05	0.9±0.1
MP30|22M0.88	Mortar	2.49±0.1	0.79±0.05	67.3±5.1
MP3010|22M0.88	10 wt% PCM mortar	2.23±0.1	0.80±0.09	37.4±2.2

In order to firstly assess possible scaling effects and the adhesion between dense mortars and porous foamed IPs, 30x25x10 cm^3 bi-layer panels were produced. The foamed insulation layer was maintained constant while dense layers with and without PCM were tested. The thickness of the dense layers was approximately 1.5 cm, while the foamed IP had an 8.5 cm thick. Figure 7.2 shows one of those bi-layer panels as an example.

Despite the higher quantities of materials required to prepare these medium-size prototypes, the same type of mixing device (Hobart HL200-1STD, Mixer) was used, and no significant modifications were encountered on the pastes and mortars' workability. After demolding, the surface of the dense layer has not presented any visible defects or cracks and its visual appearance was similar to the smaller specimens shown in section 3.6. The porous structure of foamed IPs also resembled the structures formed in smaller samples, and thermal conductivity measurements made in several locations of different specimens had shown thermal conductivity values ranging from 0.078 to 0.087 W/m°K. Although a two-step casting process and no connectors have been employed, the layers of the panels presented reasonable adhesion and could be demolded and handled without any problem.

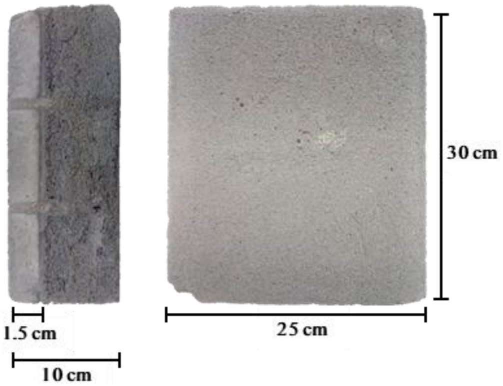

Figure 7.2 Image of bi-layered panels produced as the first upscaling stage.

Given the success of the first upscaling stage, customized molds have been produced to upscale the panel dimensions to 50x50x40 cm^3. In this case, tri-layer panels with external layers alternately with and without PCM were produced. As the quantities required to produce such large-sized prototypes could no longer be mixed using standard laboratory equipment, a 125 l concrete mixer drum was used. The cast sequence was main as described in Figure 7.2, however.

An increase of viscosity was noticed when producing larger batches of MP30|22M0.88 mortars. Slight readjustments on the mortars' composition could have been made to increase their flowability but using a vibrating table for 75 s was sufficient to avoid the formation of defects on the surfaces of the specimens, Figure 7.3a. A similar scaling effect was observed in PCM-containing mortars, but also in this case, employing vibrating equipment was enough to guarantee smooth surfaces, Figure 7.3b. Therefore, the production of denser mortars seems to be resilient to scaling effects, and considerable modifications on the mix design were unnecessary when considering the production of real-scale sandwich panels.

Conversely, the characteristics of the foamed IPs were drastically modified when producing such large insulating sections. Along with an irregular distribution of porosity, some crack formation was observed in regions where large pores were formed.

Thermal conductivity measurements were performed in different areas of the specimens being found a large dispersion among the results. In some areas, thermal conductivity values resemble those of dense binders while in others presented were similar to foamed IPs produced at a laboratory scale.

The reasons for such different structures being formed are most likely related to an uneven dispersion of the surfactant and foaming agents used (sodium oleate and aluminum powder). The rotation speed of the mixing equipment used during the development stage could not be replicated by the concrete mixer drum used (≈ 20 rpm), possibly modifying the dispersion and contributing to the partial agglomeration of those additives, which in turn, reduced their effectiveness and affected the foaming process and properties of the final materials.

Another factor that could have contributed to such phenomena is the geometry and large volume of the produced prototypes. The higher concentration of aluminum powder in some regions - and consequently gas bubbles formed- and the increased volume and mass of the specimens may have favored the burst of gas bubbles and contributed to the formation of denser structures. However, as these effects were most likely intermingled, definitive claims will not be made here as they would be premature and hardly supported without further evidence.

Nonetheless, in an attempt to overcome such deleterious scaling phenomena, the layering concept was extended to the insulating element of the prototypes. Figure 7.3c shows the cross-section of a sandwich panel prototype where the inner insulating layer was cast progressively in different moments within a 48 h period. The foamed IPs were produced using the laboratory mixer used to produce the medium–size prototypes running at nearly half of its maximum capacity, approximately 10l per formulation.

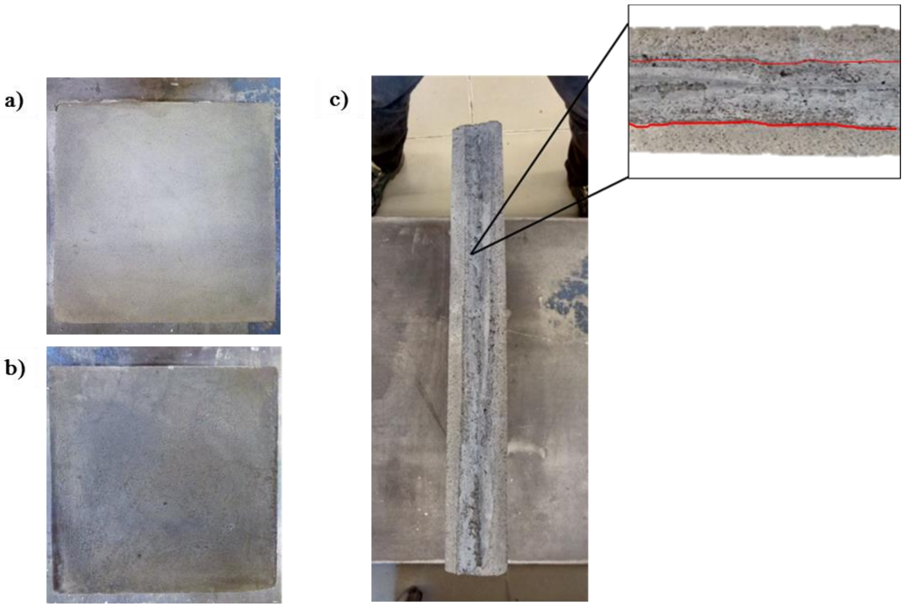

Figure 7.3 External surfaces without (a) and containing PCM (b) and the cross-section of the multilayer sandwich panels (c).

Homogenous porous structures were formed in each of the cast layers and formation of clusters of large-sized pores and cracks was avoided. Despite thermal conductivity values of freshly produced materials not being directly comparable with those of specimens matured for 28 d, before casting each insulating layer the thermal conductivity of its predecessor layer was monitored. Despite some variation, thermal conductivity values barely exceeded 0.10 W/m°K, which, if accounting for the effects of maturation, indicates the formation of porous structures similar to those observed in small and medium-size prototypes. The adhesion between dense and porous layers and, among different porous layers does not seem to be problematic.

The sandwich panels shown in Figure 7.3 served the purpose of demonstrating that sequential casting can be an effective technical solution to overcome scaling effects if investments in modifying existent equipment and production lines are not possible. The foaming process of porous IP can be further tailored (e.g., by using slightly higher curing conditions) to accelerate the IPs consolidation rate, and in turn, allow the cast of ensuing layers. Future research should also be dedicated to exploring different dispersion techniques to enhance the distribution of additives to guarantee their efficient use.

Nevertheless, the produced prototypes were considered satisfactory for final industrial upscaling after the optimization of mixing protocols. The properties of the prototypes were not examined here as they may be yet modified during ensuing upscaling stages but based on properties measured at a laboratory scale some predictions and considerations can be made.

Figure 7.4 shows the variation of thermal transmittance function of the wall thickness assuming dense outer layers with a total thickness of 2 cm. As can be seen, the initially considered 40 cm were almost enough to be compliant with the most stringent EU construction codes. An additional centimeter would be required if designing products for the Norwegian market, however. Considering Germany as the most significant EU market, a 40 cm thick panel would be compliant with the construction codes in force that require thermal transmittances values below 0.24 W/m^2

°K. A 40 cm thick panel produced for insulation purposes only has an estimated density of approximately 725 kg/m^3 or 290 kg per square meter. Given the reduced thickness of the outer layers, PCM introduction is not expected to significantly modify such physical properties of the developed panels being the estimated density and weight per square meter only slightly reduced to 710 kg/m^3 and 285 kg/m^2, respectively. Since the contribution to the panels' compressive strength of the inner insulating section is negligible, the effect of PCM addition will most likely replicate the effects observed in the starting mortars, halving the panels' compressive resistance from 70 to 35 MPa. Such compressive strength values are still compliant with structural requirements and therefore do not limit the application of thermally responsive panels. However, it should be mentioned that the selection of an adequate type of panel should also consider factors such as the risk to fire exposure (see Chapter 6), and local weather conditions and energy costs. This is list is not exhaustive, and such evaluation must be case-specific.

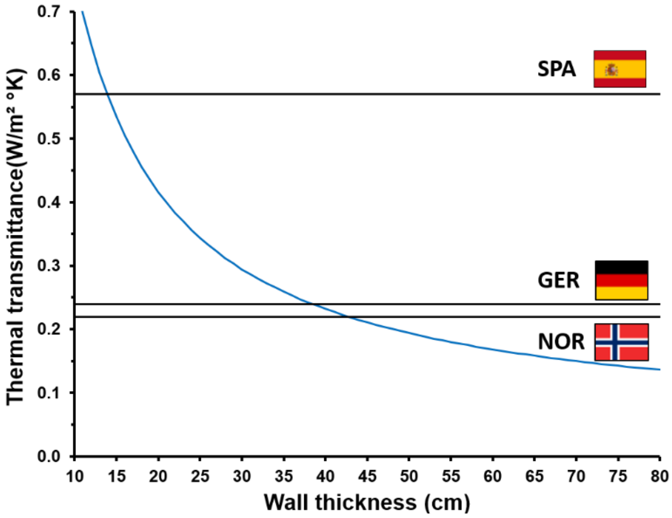

Figure 7.4 Estimated thermal transmittance of multilayer sandwich panels as a function of wall thickness according to different processing routes.

Conclusions

This chapter has described the firstly made tests to upscaling the alkali-activated materials developed from Ca-Fe-rich slags similar to those produced during the thermal conversion of landfill mined wastes. Gradual up-scaling stages have taken place from the production of small specimens up to prototypes of the commercial scale. The semi-industrial trials performed served the purpose of demonstrating the feasibility of producing real-scale thermally-responsive insulating sandwich panels and identify the most critical technical threats that require further optimization. The production of dense mortars, with or without containing phase change materials, did not demonstrate sensitivity to scaling. Therefore, the production of IP mortars has shown signs of being a robust process easily adapted to pre-existing infrastructures and widely available equipment. Conversely, up-scaling foamed IPs have shown to be more problematic and, most likely the critical task in the future industrial exploitation of this work.

Expanding the concept of layering to the insulating section of the panel has proven to be a valid strategy to overcome such limitations, but the developed products still need to be placed into use and their durability in-service conditions examined.

Chapter 8

Conclusions and Recommendations

Conclusions

Encourage the commercial deployment of alkali-activated materials requires the development of engineering-focused solutions for target applications and market segments. The present thesis embodies such vision by being focused on the development of highly performant inorganic polymers for near-zero energy dwellings.

However, the capacity to innovate and the ability to respond to market demands cannot disregard sustainable development objectives. Sustainable development is crucial to future competitiveness and ensures that society's present needs do not compromise the needs of future generations. In a context of depletion of primary resources, a strategy for sustainable competitiveness implies, among other things, managing resources efficiently and in a responsible way. For this reason, another equally important aspect of this doctoral research is the promotion of circular economic models. Incentivize industrial symbiosis between proxy sectors and produce building materials with low associated environmental impacts was also a key driver in this work.

For this purpose, vitrified residues produced during the thermochemical conversion of refused derived fuel were taken as a representative case study of a broad group of currently underutilized industrial by-products (i.e., CaO-FeO-rich) slags that could be potentially valorized via alkali activation.

Alkali-activated materials with engineered properties were developed and upscaled from a laboratory up to a semi-industrial scale. The knowledge gained throughout the process and the scientific contributions given on the fundamental understanding of CaO-FeO-rich IPs are valuable contributions that increase the maturity of such valorization technology and establish a solid groundwork for further advancements in the field.

Another key outcome of this thesis is a comprehensive analysis of the potential and limitations of using CaO-FeO-rich IPs to produce energy-efficient building materials that can be used as a guideline for future industrial developments.

Despite its greater relevance if understood as a whole, the chapters of this doctoral thesis can be presented as a stand-alone scientific oeuvre that provides valuable insights on a specific topic. In this chapter, the main conclusions reached are briefly summarized, and recommendations for future research are provided.

In Chapters 1 and 2, the fundamental principles of alkali activation are presented. Current scientific gaps and technological challenges are emphasized to provide a comprehensive description of the state-of-art. The research performed is contextualized, and its relevance highlighted.

These chapters also serve the purpose of introducing less experienced readers, hoping to arouse their interest in this fascinating field of research.

In Chapter 3, the influence of several compositional factors on the reaction kinetics and structural development of $CaO-FeO_x-Al_2O_3-SiO_2$–rich IPs was examined. Solid-to-liquid ratio and K_2O/SiO_2 molar ratio were identified as the most influential synthesis factors affecting the properties of Ca-Fe-rich IP binders. The introduction of soluble silicates in the activating solutions was found to positively impact the reaction kinetics and favor the formation of denser microstructures, which in turn, have a positive repercussion on the binders' mechanical performance. Those governing factors were used to build predictive models, and based on their outcomes, IPs binders with a high dosage of residues in their composition (> 90 wt% of solids) and enhanced properties were developed. Highly dense IP binders with low open porosity and water absorption (<5%) and high flexural (up to 7 MPa) and compressive strength (up to 175 MPa) were produced.

Apart from performance base criteria, economic factors are also fundamental when making a case for alkali-activated materials. Hence, to further assist developers and manufacturers in decision-making processes, such predictive models were expanded to incorporate a preliminary economic assessment of the developed binders. Base on technical and financial considerations, the starting binders used in ensuing development stages were defined.

Alkali-activated binders are prone to volumetric instability, and considerable shrinkage values were also observed on the developed binders. Hence, significant efforts were devoted to examining and describe the shrinkage mechanisms affecting Ca-Fe-rich IP binders and to the development of adequate shrinkage mitigation strategies.

To identify the predominant shrinkage mechanisms and evaluate its sensitivity to modifications on the precursors' characteristics, a comparative study was performed using two different slags as case studies. Drying shrinkage was identified as the governing mechanism affecting IPs volumetric stability, whereas autogenous shrinkage was largely affected by the type of residue used. The presence of metallic iron in the slag composition could be related to expansive reactions, but further dedicated research is needed to exclude other factors that may have contributed to such expansion. The expansive behavior observed significantly contributed to increasing the IPs’ volumetric stability, resulting in a three-fold reduction of shrinkage after 7 d of curing.

With a similar purpose of promoting expansive reactions, Ca-rich admixtures were added to the binders' formulations. The use of CaO-rich admixture was found as a simple and relatively inexpensive method to minimize the shrinkage of alkali-activated materials. Increasing dosages of CaO-rich admixtures up to 3.0 wt% were able to reduce shrinkage by more than 60 %. The reduction of shrinkage was proportional to the admixture content, but high dosages considerably impaired setting times and have a detrimental impact on IPs microstructure. Considering the holistic examination performed on its effects, an optimal admixture dosage of 2.0 wt% is recommended to alkali-activated systems similar to those investigated in this work.

The slag’ partial replacement by reactive Ca-rich admixtures was also investigated. At room temperature, introduce of GGBFS into the mixture design was detrimental. Shrinkage values increased, and strength development was considerably compromised. However, it was found that the effects of GGBFS addition are reverted if heat-curing is provided. In these conditions, strength development is greatly enhanced due to an increase in hydration reactions. IP structures with fine pores are formed, but the higher resistance of the polymeric networks can accommodate the higher tensile stresses generated during water evaporation, which results in lower shrinkage.

In sum, providing additional calcium sources was found to be a viable option to beneficiate the volumetric stability of IPs products. However, the potential of such shrinkage mitigation strategy might be limited by the reactivity of the precursors used as such admixtures significantly decrease the workability and setting times of IP pastes and mortars.

Conversely, the use of organic compounds as shrinkage reducing agents is not constrained by the precursors' nature as their impact in the reaction kinetics is limited. Along with their amphiphilic character that reduces the surface tension at the pore solution/air interface, organic compounds increase the total porosity of the structures formed and enlarge the average pore size. These combined effects significantly reduce the tensile stress from capillaries, resulting in more stable inorganic polymers. The increase in porosity resulted in a significant decay in mechanical properties, which, however, can be minimized with curing regimes that involve slightly elevated temperatures. Among the examined compounds, 2-Methyl-2.4-Pentanediol was found to be a more effective shrinkage reducing agent and slight less detrimental to strength development.

The principle of the maximal content of slag was extended to the aggregates used to increase further the sustainably of the solutions proposed. Slag granules were processed and used to replace sand in mortars' formulations. Reactive aggregates do not behave as sand analogs as they take an active role in polymerization. Their partial dissolution enhances the reaction kinetics with the net effects of reducing setting times, increases strength development, and slightly impair the mortars' volumetric stability.

Nevertheless, mortars produced with such aggregates revealed interesting properties, which constitutes the use of slag aggregates as a viable option to increase the sustainability and competitiveness of alkali-activated materials. By combining multiple shrinkage mitigation strategies, highly dense mortars with a total slag content that excessed 85 wt% were developed presenting low shrinkage values (≈ 1 mm/m) and, high flexural (up to 8 MPa) and compressive strength (> 55 MPa).

Apart from allowing to maximize the slag dosage in mix design and optimize the final properties of the mortars developed here, the key output of these investigations is a set of insights provided on the shrinkage mechanisms affecting AAMs and on the efficiency and effects of several shrinkage mitigation strategies that can be now outreached to related alkali-activated systems.

Chapter 4 was dedicated to a different line of research focused on the development of insulation materials from alkali-activated binders. Given the multitude of processing routes proposed in the literature, historical analysis was firstly conducted to identify the most promising processing routes to produce such materials. Based on such assessment, pre-made foams, in-situ foaming, and lightweight aggregates were used to produce thermal insulating lightweight materials with broad range properties. The parameters affecting each processing route were examined, and the materials optimized to be compliant with acceptability criteria in terms of apparent density, compressive, and thermal conductivity.

Among the different processing methods, the use of small-size lightweight aggregates was found the most adequate to develop insulating alkali-activated materials able to compliant with structural requirements. The optimized composite materials presented compressive strength exceeding 4 MPa, an apparent density of near 0.50 g/cm^3 and, thermal conductivity values lower than 0.10 W/m°K.

These solutions can be proposed as a waste-based, highly performant alternative to conventional materials used in buildings' envelopes. The predictions made indicate that walls with a thickness of approximately 35 cm will be compliant even with the more stringent EU national construction codes.

For the production of insulating material for non-structural purposes, the combined use of gas releasing, air-entraining, and stabilizing agents was found promising. By adequately tailoring mix design, IP materials could be engineered to present extremely low apparent density and thermal conductivity, 280 kg/m^{3,} and 0.06 W/m°K, respectively. The developed materials showed self-bearing capacity, but their use in applications where significant loads are foreseen can be challenging.

Chapter 5 outlines the application of the phases changes materials to produce multifunctional thermally reactive IP mortars. The addition of PCM to the mortar's formulation could effectively reduce temperature gradients, serving the purpose of proving the thermal buffering features of the developed materials. Such results indicate that IP mortars can be functionalized to act as passive thermal regulators to guarantee adequate levels of comfort with reduced energy consumption in near-zero energy buildings.

Chapter 6 was dedicated to ascertaining the high-temperature resistance of the alkali-activated mortars. The results have shown the IP mortars have superior thermal performance relative to those of mainstream construction materials. Nonetheless, the post-heating IP properties are determined by the maximum temperature of exposure and heating rate. Lower heating rates have a beneficial effect on AAM's mechanical performance, while steepest heating processes promote severe deterioration processes and result in extensive crack development. If temperature and heating rates are sufficiently high, AAMs are severely deformed. These harmful effects limited the use of the developed materials to 900 °C if high heating rates would be experienced.

Nonetheless, independently of the heating rate tested, the thermal features of benchmark materials (e.g., OPC-based products) were clearly surpassed. No signs of spalling were visible, and the developed materials could withstand temperatures up to 900 °C and maintaining their structural integrity and considerable mechanical strength values (> 40 MPa).

Finally, in Chapter 7, a precast multifunctional composite panel was presented. The motivation for this research was to develop highly performant sustainable sandwich panels with the potential to replace conventional precast insulating solutions. The challenge was to demonstrate the feasibility of producing thermally-responsive and insulating sandwich panels at a semi-industrial scale and to identified possible criticalities for future upscaling stages.

The production of optimized IP mortars, with or without containing phase change materials, was shown to be a robust process that does not suffer significant scaling effects. Conversely, the production of foamed IPs was found more sensitive to scaling, which can be challenging in industrial contexts. The modifications made in the casting sequence were effective and can constitute a possible solution to be implemented at the industrial level.

This doctoral research highlighted the so far largely neglected potential Ca-Fe-rich slags by demonstrating that they can be successfully reintegrated into the materials cycle via alkali-activation in the form of sustainable and add-valued building materials.

Nevertheless, the development of highly performant and multifunctional inorganic polymers is not trivial and requires a profound understanding of the factors influencing the properties of end products. The analysis and description of Ca-Fe-rich IPs are challenging, and little work has been previously undertaken to streamline early investigations into industrial contexts. By exploring the development of alkali-activated products with a wide range of proprieties on a multiscale level, a solid scientific basis was provided for future scaling-up developments.

By foster the widespread and large-scale utilization of waste-based building materials in key applications such as the building envelopes, this work ultimate aim is to contribute to increasing the sustainability of the construction sector and approximate current construction practices to the concept of near-zero energy buildings.

Recommendations for future research

The present Ph.D. thesis was focused on the development of sustainable and energy-efficient inorganic polymers for near-zero energy dwellings. Slags produced during the thermal conversion of landfill residues were used as precursors and taken as a case study of a broader group of CaO-FeO_x-rich by-products that can be potentially reintegrated into the materials cycle through alkaline activation technology.

The contributions made to the knowledge on the investigated materials and alkaline activation technology in general, ranged from the identification of the governing synthesis parameters to the description of how those influence the reaction kinetics, the structures formed and several fresh and hardened properties of IP binders, mortars, and lightweight materials.

The results presented and achievements made in preliminary upscaling stages clearly show that added-value materials can be produced from so far underexplored CaO-FeO_x-rich slags, but further research is still recommended at both academic and industrial levels to realize fully the potential of the findings made.

Research in the following realms should be therefore encouraged for further industrial development and implementation:

- The research performed in this work has been mainly focused on the valorization of RDF-slags, but it would be interesting to conduct investigations and develop similar products from other unexplored waste streams.
- The developed predictive models will also be greatly beneficiated if other types of precursors were considered to provide a measurement of their sensitivity to modifications on the precursors' supply chain.
- Moreover, as the most commonly used precursors in alkali activation (GGBFS, fly ash and metakaolin) already have established markets as supplementary cementitious materials, the future decrease in their availability will forcibly lead to competition with cement producers driving an increase in costs. The economics of alkali-activated will be further challenging, being recommended to explore the use of other abundant and cheap precursors.
- The development of solutions based on locally available precursors produced in proxy industries (e.g., by-dust, bagasse ash, or bauxite residues) may constitute an interesting approach to overcome such limitations.
- The same premises can be applied to activating solutions where the costs and competing markets for hydroxide and silicates activators recommend research on alternative alkali sources.
- In the field of alkali activation, a different processing route for RDF-slags and similar residues worth to be explored is the production of blended cements and one-part geopolymers/inorganic polymers. The reactions and hardening mechanisms in these systems are considerably different and deserve dedicated research. These types of products can suppress some of the technical constraints of “traditional” alkali-activated materials such as handle highly alkaline solutions or bag packaging.
- Dedicated investigation is also required to assess the long-term properties and durability of the developed products. Efforts should be made to evaluate and enhance if necessary, their resistance to chemical attacks (e.g., sulfates and chlorides) and freeze-thaw cycles.
- Implement pilot production lines and demonstrate the performance of the developed products in real service conditions is of the utmost importance to consider their commercialization.

- Despite the broad range of applications covered in this work, it would be interesting to consider also the use of RDF-slags as precursors and aggregates in concrete production.
- Given the distinct nature of hydraulic and IP binders, a vaster range of aggregates may be admitted in the production IP mortars and concrete. Explore the potential and limitations of aggregates interdicted in the production of traditional mortars and concrete may also have some significant environmental and economic benefits.
- The use or development of ad hoc superplasticizers should be considered. Apart from the expected environmental and economic gains associated with a reduction in the dosage of activating solutions, suitable water reducers would allow to produce highly performant products. Several IP properties would benefit from their use, including one of the most problematic hurdles encountered during this work, i.e., drying shrinkage.
- The market potential of IP products will be not only dictated by their technical properties but also conditioned by the competitors in the field. Interesting scientific and industrial research questions will forcibly arise when considering the development of IP products for market segments where traditional binders are under performant, e.g., fire-resistant insulating materials, confinement of radioactive materials, or space construction.
- Additional efforts should be devoted to the development and cost optimization of multifunctional alkali-activated materials. Apart from the thermally-responsive and insulation materials developed here, other types of functionalities should be examined (e.g., electrically conductive, self-cleaning, or self-healing IP materials). Deep experimental and theoretical research, as well as engineering the production and application of multifunctional AAMs will be indispensable to their wider use.
- In the context of sustainability, a deeper understanding of the production, service life, and post-use solutions for alkali-activated products is necessary. Comprehensive life and cost cycle analysis are commendable to validate alkali-activated materials in specific regional contexts.
- In the scope post-service life, the possibility of reactivating alkali-activated materials after thermal-treatment is emerging among the scientific community and would be interesting to apply such technology to the products developed in this work.

The list presented does not aim to be exhaustive and only enumerates some general areas that the author would like to address his future endeavors.

Many other application-related questions could have been listed, which will be particularly relevant when considering employing alkali-activated materials outside the scope of the construction sector. It is the authors believe that collaborations between different subfields of engineering will promote the integration of alkaline activation technology in many production schemes, which, in turn, will drive significant advances in the field and will dictate which the most important scientific questions to be addressed.